UNIVERSITÀ DEGLI STUDI DI MILANO

DOTTORATO DI RICERCA IN SCIENZE DELLA TERRA

Ciclo XXXVI

DIPARTIMENTO DI SCIENZE DELLA TERRA

PhD Thesis

THERMO-HYDRO-MECHANICAL NUMERICAL MODELLING TO ASSESS THE ROLE OF CLIMATIC FACTORS IN THE STABILITY OF ALPINE ROCK SLOPES

GEO/05

Andrea MORCIONI
Mat. R12840

TUTOR:
Prof.ssa Tiziana APUANI

CO-TUTOR:
Prof. Francesco CECINATO

COORDINATOR:
Prof.ssa Maria Iole SPALLA

Abstract

This work aims at increasing the knowledge of climate impacts on the stress-strain evolution of rock slopes, through the adoption of a multi-disciplinary approach and the development of multiphysics numerical analyses. Several case studies of past and active rockslide events in the Alpine region were analyzed, for which the effects of different couplings were explored. By means of a methodological process that includes geological and geomechanical characterization of rock slopes, the definition of a geological conceptual model, and the development of numerical stress-strain analysis, this work is intended to be a valid reference for the analysis of rock slope evolution in response to climate inputs.

Concerning the hydro-mechanical (HM) couplings, two case histories in which exceptionally heavy rainfall events led to slope failure are discussed. In particular, the Piuro landslide (Bregaglia Valley, Sondrio, Italy), which occurred in 1618, and the 2012 Cimaganda rockslide (San Giacomo Valley, Sondrio, Italy) were back-analyzed with a focus on their triggering mechanisms related to the distribution of pore pressure, resulting from extreme rainfall events. The results confirmed the dominant role of HM couplings in defining slope instability processes.

Next, the effects of surface temperature variations on slope stability were analyzed along the Cimaganda rock slope, with particular focus on a large historical rockslide. The combined effect of long- and short-term thermal evolution were numerically explored, overlapping the late-Pleistocene/Holocene warming trend to the seasonal temperature oscillations. It was shown that although slope failure events do not appear to be directly triggered by thermal cycles, the latter over a long period can lead to considerable mechanical slope degradation and strain accumulation. Moreover, a thermal monitoring system placed along the Cimaganda slope provided some preliminary evidences on the impact of current environmental loadings (from daily to seasonal) on the distribution of temperature inside the monitored rock-mass and the resulting rock-joint deformations.

Then, to assess the relationship between climate variables and the evolution of an active rockslide, the Ruinon case study (Frodolfo Valley, Sondrio) was analyzed. In particular, after a careful assessment of the factors controlling rockslide evolution via numerical stress-strain analysis and hydrogeological modelling, coupled thermo-poro-mechanical modelling was carried out. Once calibrated, the model allowed to simulate the recently measured velocity history of the rockslide and was then adopted to explore the impact of forthcoming climate changes on rockslide activity. This allowed to gain further insight into the link between climate inputs and rockslide activity, providing the basis for the development of a physics-based warning system.

The presented research allowed to:

- Correctly simulate the evolution of the analyzed Alpine rock slopes, by considering the main predisposing and triggering factors.
- Gain deeper understanding on the quantitative relationships between temperature, pore pressures and strain rates in Alpine rockslides via numerical modeling.
- Provide advice on the development and calibration of physics-based numerical models that include climate scenarios in the prediction of future landslide activity.

The presented multi-disciplinary approach (geological characterization, conceptual modeling, numerical analysis) has proven to be a valid method for the investigation of rock slopes exhibiting gravitational instability phenomena. It can be deduced that multiphysical approaches should no longer be overlooked in slope stability analyses, as their role in forecasting and predictive applications is of paramount importance.

Index

Symbols and notations

Symbols and notations

The following list collects in alphabetical order symbols and notations introduced in the text.

A.D.: Annus Domini

AGI: Associazione Geotecnica Italiana (Italian Geotechnical Association)

ARPA: Agenzia Regionale Protezione Ambiente (Regional Agency for Environmental Protection)

ASTM: American Society for Testing and Materials

B.P.: Before Present

BEM: Boundary Element Method

c: Cohesion

CM: Snow melt day degree factor

CMG: Centro Monitoraggio Geologico (Geological Monitoring Center)

Cond: Electrolytic Conductivity

C_p: Specific heat capacity

CTR: Cartografia Tecnica Regionale (Regional Technical Mapping)

D: Thermal diffusivity

DEM: Distinct Element Method

DFN: Distinct fracture Network

ds: Landslide shear-band thickness

DSGSD: Deep Seated Gravitational Slope Deformation

E: Young Modulus

FoS: Factor of Safety

f: Frequency

FDM: Finite Difference Method

FEM: Finite Element Method

g: Acceleration of gravity

G_0: Initial Gruntfest number

GBinSAR: Ground Based Interferometric Synthetic Aperture Radar

Gr: Gruntfest number

Gr_c: Critical Gruntfest number

GSI: Geological Strength Index

HM: Hydro-mechanical

IR: Infra-Red

ISRM: International Society of Rock Mechanics

JCS: Joint Compressive Strength

JRC: Joint Roughness Coefficient

Jv: Volumetric joint count

K: Bulk Modulus

k: Hydraulic conductivity

k_{eq}: Equivalent hydraulic conductivity

K_n: Normal stiffness

K_s: Shear stiffness

LE: Limit-Equilibrium

LGM: Last Glacial Maximum

LIA: Little Ice Age

M: Thermal sensitivity coefficient

MC: Mohr-Coulomb criterion

MR: Daily melting rate

N: Load-rate sensitivity coefficient

NRMSE: Normalized Root Mean Square Error

PDE: Partial Derivative Equation

P_f: Pore-pressure

P_{f0}: Reference pore-pressure

RC: Runoff coefficient

RMR: Rock Mass Rating

RMSE: Root Mean Square Error

RQD: Rock Quality Designation

SAR: Synthetic Aperture Radar

SWE: Snow Water Equivalent

T: Temperature

t: Time

T_0: Reference temperature at the landslide sliding surface

TC: Time of concentration

TDS: Total Dissolved Solids

THM: Thermo-hydro-mechanical

TM: Thermo-mechanical

T_{paleo}: Paleo-temperature

Ts: Hydraulic transmissivity

UCS: Uniaxial Compressive Strength

v: Velocity

V: Volume

λ: Thermal conductivity

γ: Strain

$\dot{\gamma}$: Strain rate

$\dot{\gamma}_d$: Reference shear stress rate

ρ: Density

ϕ: Friction angle

δ: Kronecker delta

υ: Poisson Coefficient

θ: Porosity

σ: Stress

σ': Effective stress

σ_C: Compressive strength

σ_{KK}: Volumetric stress

σ_N: Normal stress

τ_P: Peak shear strength

τ_r: Residual shear strength

τ_d: Reference shear stresses

σ_T: Tensile strength

α: Linear thermal expansion

α_V: Biot coefficient

^{12}C: Carbon-12

^{13}C: Carbon-13

^{16}O: Oxygen-16

^{18}O: Oxygen-18

^{2}H: Deuterium

Chapter 1
Introduction

The occurrence of landslide events represents the most superficial evidence of time-dependent slope evolution, related to the complex interactions between morphological, geological, environmental, and anthropical factors. Among all, a significant role of meteo-climatic factors in driving slope instability processes has been detected, acting on both the stress state and the mechanical properties of materials, in the short- (i.e., daily to seasonal) and the long-term (i.e., years to millennia) time scales. This relationship is well-known and evident for shallow soil landslides, but it is currently less clear for rockfalls and even more for large landslides and rockslides.

Over the years, numerical tools have been widely employed to analyze slope stability, as well as to study the impact of climatic factors on the mechanical evolution of slopes. In the literature, however, numerical simplifications are generally adopted (Jing 2003), leaving processes relevant to hydro-mechanical (HM), thermo-mechanical (TM), or thermo-hydro-mechanical (THM) couplings, only few explored (e.g. Gischig et al. 2011b; Wu et al. 2019). As a result, processes that may significantly contribute to slope mechanical degradation are generally neglected in numerical analyses (e.g., atmospheric temperature variations, wet-dry cycles). Moreover, ongoing climate change is revealing new complex evolutionary dynamics (e.g., permafrost degradation, extremization of freeze-thaw cycles, changes in hydrological and thermal equilibria), for which a multiphysical approach in slope stability can no longer be neglected. Research output shows the need for further efforts in the field of landslide prediction, especially to numerically quantify the impact of climatic factors (Stoffel and Huggel 2012; Gariano and Guzzetti 2016).

This work aims to increase the knowledge of climate role on the stress-strain evolution of rock slopes, through the adoption of a multi-disciplinary approach and the development of multiphysics numerical analyses. Rockslide case histories will be addressed, from historical to active events. By means of a methodological process that includes geological and geomechanical characterization of rock slopes, the definition of a conceptual models, and the development of numerical analyses, this work is intended to be a valuable example of multi-disciplinary approach for the analysis of rock slope evolution in response to climate inputs whether past, present, or future. Considering the revealed complexity of the phenomena, the use of complex, multiphysics numerical analyses will be explored to assess their potential and applicability in landslide risk mitigation actions.

1.1 Introduction to slope instability processes

Gravity-driven processes are one of the most dangerous geological hazards worldwide (Guzzetti et al. 1999; Reichenbach et al. 2018); their occurrence is the cause of economic losses, casualties, and damage to the natural environment and to human infrastructures located in the failure area or along the path of the material flow (Guzzetti et al. 2012). The recent massive expansion of tourism and commercial activities, combined with growing infrastructure and access to remote areas, leads to a considerable increase in the anthropic exposure to slope instability processes (Fischer et al. 2010; Guzzetti et al. 2012). In this context, local governments and scientific communities are increasingly motivated to raise their interest in the analysis and management of these natural processes, considering also the current scenario of exacerbating climatic conditions (Ravanel and Deline 2010; Duvillard et al. 2015; Scavia et al. 2020). In order to understand and analyze the impact of landslide processes, the scientific community has classified them into different categories based on their kinematics, volume, and type of material involved, velocity and activity state, as well as on their driving and triggering mechanisms. Understanding their nature is in fact helpful in studying their behavior, assess mechanisms of future evolution and plan effective risk prevention and mitigation actions. Over the years several approaches and classifications have been presented (Varnes 1978; Selby 1982; Cruden and Varnes 1996). The most widely recognized and used is the Cruden and Varnes classification (Cruden and Varnes 1996, recently revised by Hungr et al. 2014), which is mainly based on the kinematics and the type of material involved in the instability process.

Following the Cruden and Varnes landslide classification, it is possible to distinguish:

1. *Falls*: Falls involve free-falling rock blocks from a steep cliff, slope, or overhang, or the sudden activations of single block/boulder on the slope. The materials involved can range from single rocks to large boulders. Falls are usually rapid and can represent a significant hazard, especially in areas with vertical rock faces.

2. *Slides*: Slides are characterized by the movement of a sliding mass along one or more surfaces of rupture or shear. Based on the geometry of the sliding surface, rotational slides (when the surface is curved and concave), translational slides (the surface is planar), or complex slides (more than one type) can be identified. This classification encompasses three subcategories:

    - *Rockslide*: Rockslides involve the rapid movement of large volumes of rock. These events can be triggered by factors like climate, seismic activity, or human activities. They are often extremely harmful and can travel significant distances.

- *Debris slide*: Debris slides consist of soil, loose rock, or other soft materials that move as a single body. These processes often occur on steep slopes and can be drive by heavy rainfall or rapid snowmelt.
- *Earth slide*: Earth slides involve the slow, downslope movement of fine-grained, clay-rich soil. They typically occur in areas with prolonged rainfall or high groundwater levels, and their slow movement can be particularly hazardous to infrastructure over time.

3. *Spreads*: Spreads involve the lateral extension of material, typically along the horizontal axis, with slow movement over time. This category includes:

    - *Lateral Spread*: Lateral spreads are typically associated with particularly complex geologic conditions, where a rigid body lies over a material with plastic behavior. The instability mainly involves the upper rigid body moving laterally and deforming with tensile fractures. Rapid accelerations may occur as a result of seismic activity.
    - *Topples:* Toppling landslides are characterized by the forward rotation of a block or mass of material about an axis located at or near the base of the block. They often occur on cliffs or steep slopes where the material becomes unstable.

4. *Flows*: Flow-type landslides involve the downslope movement of material that behaves like a viscous fluid. These landslides can be particularly destructive due to their speed and the ability to cover large distances. Mainly based on the type of involved material, flow-type landslides include:

    - *Debris Flow*: Debris flows are fast-moving mixtures of water, granular soil of different grain size and other debris. They can occur in various environmental conditions; they can be channelized or not, with heavy rainfall being a common trigger.
    - *Mudflow*: Mudflows are similar to debris flows but consist mainly of fine-grained material such as clay and silt mixed with water. They often occur in areas with loose, unconsolidated soils and can be triggered by heavy rainfall or rapid snowmelt.
    - *Lahar*: Lahars are volcanic mudflows composed of volcanic ash, water, and debris. They often result from volcanic eruptions and can travel great distances, posing significant hazards to communities downstream.

Depending on the type and volume of the material involved, different landslide behavior and evolution can be expected, with own velocity and energy, leading to greater or lesser impact on both the slope environment and human activities.

The landslide hazard is defined as the probability that a landslide of a given magnitude will occur in a given period and in a given area (Nadim et al. 2005; Wang et al. 2020). The greater this probability, the greater the hazard. The hazard level is always related to the presence or absence of anthropogenic elements in the landslide area, that can be potentially damaged by its occurrence. This is described by the concept of landslide risk, which is given by the product of hazard, vulnerability, and exposure, where vulnerability and exposure are defined respectively as the ability of an element (e.g., a building) to resist the occurrence of an event and as the economic, social and cultural value of the element itself (Cutter et al. 2003; Uzielli et al. 2008). If the hazard level is high but no potentially damaging elements are present in the area, then the risk level will be low. On the other hand, if the landslide area is characterized by widespread human activity, the risk can be very high even for low hazard levels.

The first step toward the prevention and mitigation of landslide risk is to identify the area most prone to gravitational instabilities, that is, where the hazard is higher, and human activities are exposed to greater risk (Brabb 1984). In the past few decades, several authors have proposed a number of studies, both at regional and local scales, regarding the occurrence of landslides. The overall goal is to define how susceptible is a system to instability processes in the direction of predicting "where" landslides are likely to occur (Guzzetti et al., 2005, 2006; Reichenbach et al., 2018), and then how dangerous they will be and which will be their impact.

To minimize the level of risk and understand landslide evolutionary dynamics, instability processes are controlled by monitoring systems chosen according to the type of landslide (e.g., earth slides, debris flow, rockfall). These include the following traditional instruments (Casagli et al. 2010, 2023; Bazin et al. 2012; Intrieri et al. 2012; Michoud et al. 2013):

- *Geotechnical*, both deep (e.g., inclinometers), superficial (e.g., extensimeters, dystometers, ground-based radar, GPS, laser scanner) and aerial (e.g., satellite radar, laser scanner);
- *Hydrogeological* (e.g., piezometers, multi-parametric probes);
- *Hydrological* (e.g., hydrometers);
- *Climatic* (e.g., rain gauges, snow gauges thermometers, anemometer).

These instruments can be either of manual reading, giving discontinuous data in time, or of automatic reading, which provides continuous data with fixed time intervals.

Together with monitoring systems, in recent decades, there has been a massive development of numerical tools that allow to analyze the relationships between slope dynamics and external variables

(e.g., environmental, seismic) and study the physical mechanisms driving slope degradation and failures (only to cite some, Borga et al. 1998; Carrara et al. 1999; Guzzetti et al. 1999; Godt et al. 2008; Wang and Ni 2014; Reichenbach et al. 2018).

The complexity of natural systems, however, brings to a difficult definition of common procedural schemes for the spatiotemporal analysis and forecasting of instability processes (initiation, reactivation, and runout). A multi-disciplinary approach is often necessary, which, however, requires a deep understanding of all the methodological aspects. The issue concerns not only shallow landslides with rapid and prominent dynamics, but also large landslides and rock avalanches, where the huge volumes involved imply a high damage potential.

1.2 Controlling factors: the concept of progressive slope failure

The development of slope instability processes can be explained through the concept of progressive failure process (Terzaghi 1962; Eberhardt et al. 2004; Preisig et al. 2016), which will be extensively discussed in this Section as propaedeutic to the comprehension of the issues and statements addressed in this work.

The set of parameters and factors that define the stress state and the mechanical behavior of a slope are generally referred to as internal parameters. Among them, parameters crucial for landslide occurrence, and usually associated with a predisposing effect, are (Volkwein et al. 2011; Corominas et al. 2014):

- *Slope morphology*: elevation, slope gradient, exposure and roughness concur to define the slope potential energy and local stress state distribution.
- *Geology and geomechanical properties*: the rock type, the presence of geological structures (e.g., faults, folds), the intensity of fracturing, the features of discontinuities, and the degree of weathering of rock-masses can result in the development of weak mechanical zones (Jaboyedoff et al. 2011, 2013; Lahai et al. 2021).
- *In situ stress state*: a wide spectrum of topographic, tectonic, glacial loading-unloading and exhumation-generated stresses interacted at several spatial and temporal scales and preferential directions, concurring in the localization of the actual rock-mass system stress state (Ballantyne 2002; Leith et al. 2014). In addition, the slope hydrogeological setting contributes to the definition of effective stresses that control the deformation and strength of geological bodies.

Since the concomitance of particularly unfavorable conditions of internal factors (e.g., low-quality rock-masses, steep slopes, geological settings) can promote the development of gravitational instability

phenomena, they are generally referred to as *"predisposing factors"*. These parameters dictate the deformability and strength properties of slopes, defining their mechanical behavior. They are in continuous interaction with external variables, which can change their magnitude in space and time, controlling the stress state of a slope. Starting from conditions of overall stability, in which predisposing factors to landslide events may be present, processes acting on resisting and/or mobilizing forces progressively lead to conditions of mechanical degradation. These factors, generally referred to as "*preparatory factors"*, act repeatedly over time, leading the system to near-collapse conditions. The slope remains stable, even if in a precarious condition of stability, until a particular event occurs sufficient to cause its ultimate failure. This event is called the *"trigger"* or *"initiator"*. These factors are generally referred to as "external factors" and can be basically divided according to their nature into:

- *Meteo-climatic processes*: rainfall events, snow melting processes, freeze-thaw cycles and temperature fluctuations (Stoffel and Huggel 2012; Paranunzio et al. 2019; Scavia et al. 2020; Camera et al. 2021; Bajni 2022) are generally responsible of mechanical weakening processes linked to modifications of the slope water circulation patterns, weathering and erosional processes, fractures nucleation and coalescence.
- *Seismicity*: rock-mass structure could be dramatically damaged and weakened by earthquake shaking, both at the slope scale and at the micro-scale. Large earthquakes frequently act as triggering factors for rock-mass instabilities (Keefer 1984; Wasowski et al. 2011; Martino et al. 2014; Valagussa et al. 2014) even at consistent distances from the epicenter (up to 300 km, Stoffel et al. 2019). Nonetheless, the long-term effects generated by earthquakes (i.e., post-seismic effect) may lead to large deformation and fracture propagation, thus representing a temporal persisting preparatory process for rock-mass instabilities (D'Angiò et al. 2021; He et al. 2021).
- *Human activity*: anthropic activities such as quarrying and mining, excavation for infrastructures, and vibration due to blasting are responsible for the modification in the rock slope geometry and stress distribution (Selby 1982; Xu et al. 2003; Volkwein et al. 2011) as well as water pumping or recharges , in general, hydrogeological works.

Overall, the history of an unstable slope can be subdivided into four stages: (i) pre-failure, (ii) first-time failure, (iii) post-failure, and (iv) reactivation. During the pre-failure stage, the concomitant action of climatic and anthropogenic factors over long periods of time results in "progressive slope degradation", including the deterioration of mechanical properties of the rock material and discontinuity elements, as well as the increase of the rock-mass fracturing degree. At the same magnitude, the action and effectiveness of these factors depend on the morphological and geological characteristics of the slope (i.e., the predisposing factors). Where conditions predispose slopes to instability (e.g., highly fractured

rock-masses, presence of tectonic structures, etc.), the action of external factors will be more incisive. Their action continues progressively over time and can lead to precarious stable conditions, with a rate varying according to their magnitude and the predisposition of the system. When the slope reaches precarious stable condition, the action of a single factor can cause failure (i.e., triggering factor). Once the rupture has occurred, the slope is affected by new stress conditions that can result in stable or continuous unstable conditions, until a new equilibrium is reached. The action of external factors goes ahead and, again, can bring the slope to new conditions of instability. Following a failure event, the slope can potentially be more susceptible to the action of climatic factors as the new morphological, geological, and mechanical conditions can be more predisposing.

The concept illustrated above, known as "*progressive failure process*" (Terzaghi 1962; Eberhardt et al. 2004; Preisig et al. 2016), demonstrates why landslide phenomena can occur even without the presence of extreme or particularly severe triggering events, but simply through the concatenation of processes that gradually lead the slope to overall failure conditions. Often, in fact, collapse occurs without an apparent triggering factor, but simply due to the achievement of unstable conditions by continuous and prolonged action of preparatory factors.

1.3 Slope instabilities and climate factors: evidences and scientific open challenges

Among all, slope evolution is significantly affected by climate dynamics, which act on both the stress state and the mechanical properties (Eberhardt et al. 2004). Studies on the relation between landslide occurrence and meteorological events have shown a strong correlation. This is particularly evident and well known for shallow instability phenomena, especially for flow and slide processes involving debris and soil materials (Guzzetti et al. 2006; Montrasio et al. 2009; Gariano and Guzzetti 2016; Donnini et al. 2023). Studies on the relationship with rock-landslides (i.e., rock-fall and rockslide) are less frequent, but still have identified a clear dependence. The recognized relationships between climate variables and landsides occurrence (involving both soils and rocks) are currently the basis for warning procedures that consider meteorological forecasts as a tool for defining emergency plans and hazard thresholds (Gonzalez et al. 2024).

Starting from landslide inventories and historical climate series, in recent years several authors (Macciotta et al. 2015; D'Amato et al. 2016; Paranunzio et al. 2016, 2019; Matsuoka 2019; Bajni et al. 2021, 2023; Bajni 2022) have progressively introduced climate variables to implement statistical relationships on rockfall and shallow rockslide occurrence. Robust cause-effect relationships were identified. Paranunzio et al. 2016 and Matsuoka 2019 analyzed effects related to rainfall events (e.g.,

precipitation intensity and amount at sub-daily, daily, or weekly scales) as well as climate trends (e.g., thermal evolution at monthly, quarterly, or longer period scales), testifying a duality of effects involving both short-term and long-term scenarios. Davies et al. 2014, Preisig et al. 2016, Grämiger et al. 2020 and Liu et al. 2021 reported that the occurrence of rockslide events often happens in conjunction with intense or unusually prolonged rainfall events. These, in fact, result in considerable variations in the magnitude of forces acting within a slope, leading to the exceeding of critical levels. Together with rainfall, the action of snow accumulation and melting, influences rockslide occurrence, being both an immediate and cumulative source of water, especially in the mountain environment (Lucas et al. 2020; Stumvoll et al. 2020; Siva Subramanian et al. 2020).

Water pressure variation, however, usually only represents the ultimate actor in the process of rock-slope instability initiation. The continuous and persistent action of atmospheric factors over time, can significantly promote the progressive rock-slope mechanical degradation, leading to critical unstable condition. In this perspective, recent research focused on the role of atmospheric temperature variations in the development of rock-masses' degradation through heating-cooling, freeze-thaw and wet-dry cycle, ice cracking or permafrost degradation processes (Matsuoka 2008; Bakun-Mazor et al. 2013; Collins and Stock 2016; Nigrelli et al. 2018; Draebing and Krautblatter 2019; Marmoni et al. 2020; Grechi and Martino 2021; Morcioni et al. 2022; Grechi et al. 2023). Variations in the atmospheric temperature during both short- and long-term periods induce thermal stresses and strains due to the volumetric contraction and expansion of materials (Hall 1999; Gunzburger et al. 2005; Bakun-Mazor et al. 2020), promoting the process of fracture propagation and mechanical weathering. If partially saturated conditions apply, freeze–thaw cycles can affect the strength of rock-masses through both ice segregation-melting processes (i.e., repeated expansion and contraction within a joint inducing fracture propagation and failure of intact rock bridges) and thermal chemo-mechanical weathering. The triggering of many rockslides in the periglacial environment is attributed to the melting of permafrost and interstitial ice (i.e., reducing rock-mass cohesion) due to an increase in the average atmospheric temperature (Sosio et al. 2008; Fischer et al. 2010; Walter et al. 2020). Bajni 2022 in the Aosta Valley region (Italian Alps), identified three different climate indices as most representative of the rockfall and shallow rockslides triggering processes: namely the cumulated amount of effective water inputs, the cumulated number of wet-dry cycles and the cumulated number of freeze-thaw cycles. The 95% of the rockfalls occurred in not ordinary conditions for at least one among the three indices.

Much rarer are studies involving large landslides (e.g., rock avalanches and DSGDS), where identification of the driving factors appears complex because of the plurality of processes involved. A climate control has been widely recognized, although it is strongly site-specific and difficult to quantify (Bertolini and Pizziolo 2008; Preisig et al. 2016; Crosta et al. 2017; Notti et al. 2021).

Over the years, numerical modelling has been demonstrated to be a useful tool for simulating the impact of climate factors on the initiation of gravitational rock-slope instabilities; numerous Authors (e.g., Griffiths and Lane 1999; Cheng et al. 2007; Brideau et al. 2011; Gischig et al. 2011b; Wang and Ni 2014) have proposed different studies, where, however, the complexity of the natural systems leads to the development of simplified models. As a result, the effect of multiphysics couplings on slope stability is poorly explored and many natural processes as heating-cooling, freeze-thaw, wet-dry cycle, or permafrost degradation are still not fully explored in this field (Rounce et al. 2016; Falatkova et al. 2019; Wang et al. 2023). Research and direct observations to date, however, have increased awareness of their role in slope stability and highlighted the need for further study.

Moreover, inspection of the relevant bibliography reveals the lack of common criteria and comprehensive procedural schemes for the analysis of landslide evolutions under climate forcing. The issue concerns not only shallow soil landslides, whose climate control is better understood, but also large landslides, rockslides and rock avalanches, where the large volumes involved imply a high damage potential of these processes. The increasing catastrophic impact of slope instabilities on societies and infrastructures leads to the necessity of new tools for analyzing their evolution and defining warning thresholds for risk assessment and managements. Only through a wide and complete knowledge of all the factors involved, will be possible to obtain accurate and applicable tools for landslide prediction and mitigation.

1.3.1 Past climate conditions: the case of the Alpine environment

The Alpine environment is cyclically affected by strong variations in climate conditions on both short (i.e., seasonally) and long-term (i.e., climatic eras) periods, resulting in a significant effect on the slopes evolution.

The last significant climate change occurred between the late Pleistocene and Holocene age, when Alpine regions were affected by a massive long-term air warming trend. Studying isotope records and pollen data, different authors provide climate evolution in the Alpine region (Ivy-Ochs et al. 2006; Vinther et al. 2009). According to Ivy-Ochs et al. 2009 its paleo-temperature trend can be outlined as follows: during late Pleistocene age, mean temperatures were about 12°C colder than today; at the end of Pleistocene, mean air temperatures had risen to values of 3.5°C colder than today and stabilized around the current values during Holocene age, varying only by ±1 °C as shown by Davis et al. 2003 based on pollen data.

This, in addition to causing significant changes in the magnitude of climate factors involved in the process of slope stability, contributed to the development of glacier advancement and retreat processes.

Alpine valleys are in fact occupied by ice masses, the extent of which varies cyclically in response to climatic forcings on millennial scales. In conjunction with cold periods, advancement of glacial bodies is recorded, which may extend to occupy entirely Alpine valleys, with significant ice thicknesses. As reconstructed by Mey et al. 2016, analyzing the available ice extent indicators, the mean and maximum ice thickness over the Alpine region at the last massive glacial advance (i.e., Last Glacial Maximum, below as LGM) were 415 and 2445 m, respectively. During warmer periods the glacial bodies progressively recede back to the upper valleys, occupying only the higher elevations. In this way, slopes are exposed to completely new climatic conditions, and the rock-masses are progressively released from their glacial load.

The LGM, occurred during the late Pleistocene age about 28-18 kyr BP (Scapozza et al. 2014; Ivy-Ochs 2015; Wirsig et al. 2016), when the entire Alpine arc was covered by a huge ice-cap and only the highest peaks remained uncovered (Bini 1996; Bini et al. 2009; Darnault et al. 2012; Tantardini et al. 2013; Seguinot et al. 2018). The previously discussed thermal rise had subsequently led to a glacial retreat, up to the present conditions. These dynamics result in a primary mechanical effect on slope evolution related to processes of loading-unloading acting on the rock-masses.

Within the context of the Alpine environment, first-time damages are often related to periods of glacial retreat where substantial slope over-steepening, stress unloading, and kinematic de-buttressing occur. Glacial unloading leads to the development of tensile failures and large-scale stress release (Holm et al. 2004; Cossart et al. 2008). Numerical analyses showed that failure processes could initiate through the development of tensile rock-mass damage following glacial de-buttressing (Eberhardt et al. 2004). However, a large lag time typically separates the end of deglaciation and the occurrence of large-scale slope instabilities, implying the unlikelihood for glacial unloading to act as a direct failure triggering factor (Prager et al. 2008; Ivy-Ochs et al. 2009; Zerathe et al. 2014).

In addition to the stress effects, glacial and interglacial phases induce significant changes in climatic conditions, which, directly or indirectly, cause substantial effects on slope instability processes. Among all, cycles of glacier advance and retreat induce complex changes in the thermal and hydrologic regime of adjacent valley flanks, with corresponding coupled mechanical interactions that can drive fracture growth and propagation in rock-masses (Grämiger et al. 2018, 2020).

Although the impact of individual factors in the stress-strain evolution of Alpine slopes is widely recognized, their long-term and short-term interaction is difficult to understand because of its complex multiphysical structure. Analyses proposing the study of the mechanical evolution of Alpine slopes over long time scales, are generally focused on post-glacial stress-release factors, while the coupling with related climatic processes is generally neglected.

Increasing the comprehension of these natural processes is of fundamental importance for hazard assessments in Alpine valleys, many of which are undergoing rapid glacier changes. Moreover, understanding the mechanisms that have driven the stress-strain evolution of Alpine slope in the past, is critical for developing models and analyses that can predict their evolution under future climate projection.

1.3.2 Future climatic conditions

Currently, the Alpine environment as well as the entire planet, is significantly affected by changes in the mean climatic conditions, generally referred as to "Climate change". At the global scale, is being observed to a general long-term shift in temperatures and weather patterns. As reported by United Nation (https://www.un.org/en/), the average temperature of the Earth's surface is now about 1.1°C warmer than it was in the late 1800s (before the industrial revolution) and warmer than at any time in the last 100.000 years. The last decade (2011-2020) was the warmest on record, and each of the last four decades has been warmer than any previous decade since 1850. Global temperature is projected to warm by about 1.5 °C by 2050 and 2-4 °C by 2100, over the pre-industrial values (IPCC 2014).

Climate models, based on physical processes simulating the transfer of energy and materials, allow for predicting climate evolution at the global scale (Stocker 2014). By analyzing their outputs and performing a process of bias correction (Cannon 2018) and downscaling (Wilby et al. 2004; Fowler et al. 2007), it is possible to assess the localized impact of warming scenarios by evaluating climate variables such as precipitation, atmospheric temperature and air humidity.

At the local scale, model predictions and current observations, show that the Alpine region could be severely affected by significant climate variations. Warming is in fact amplified in the mountain environments, because the increase in temperatures leads to a decrease in the size of zones covered with ice and snow which reflect the sun's rays. These zones are replaced by areas of dark rock and later vegetation, which instead absorb the suns heat, increase ground temperature and contribute to more melting. Complex topography poses considerable challenges to climate models, which typically translate to uncertainties in climate projections of future temperatures, and even more so for precipitation regime. In the Alpine environment, mean and maximum air temperatures have increased considerably in the past few decades and related average temperatures have been warmer than in any measurable period (Consortium PAGES 2k 2013). Over the course of the 20th century, temperatures have risen by 2°C. The rate of this warming, observed since the beginning of the Industrial Revolution, has increased since the 1980s to 0.5°C per decade. Considering ongoing climate change, mean and extreme temperatures are expected to continue rising considerably over the next decades (IPCC 2012). Significant changes may also be expected in precipitation, especially in the seasonality of water contributions which are likely to

be associated with the projected warming trend (European Commission 2020). Although global precipitation patterns have not changed significantly over the course of the 20th century, considerable regional and seasonal changes have been observed. The increase in average temperature indirectly alters the distribution of the water resource, with a change in the hydrological cycle. Considering the case of the French Alpine region (Durand et al. 2009), since 1960, winter precipitation has significantly diminished in the south of France, while an increase has been recorded in the north.

The extremization of weather-climate variables, may results in an increased incidence of such factors in the mechanical evolution of slopes, generating new scenarios and dynamics. Their prediction represents a new research direction and a new challenge in the geomechanical and geotechnical scientific field.

Evidence of the impact of climate change on mountain slope stability is already tangible and comes from the analysis of documented slope failure events in the Alps since 1900 (Stoffel and Huggel 2012; Jemec Auflič et al. 2023). The record of rock slope failures spanning a period since the beginning of the 20th century primarily indicates a sharp increase of the number of events since 1990 (Stoffel et al. 2014). This is especially true for small rockfall events, but clear trends are also evident for large failures.

For the Central Swiss Alps, for instance, Meusburger and Alewell 2009 reported an increase of landslide events due to an increase of intense torrential rainfalls since the 1960s. For the Italian Alps, archival records show an increase of landslide activity since the mid-19th century, even if a relation with both a greater availability of historical data and changing vulnerability in increasingly urbanized areas could be present (Tropeano and Turconi 2004).

Gariano and Guzzetti 2016 conducted a literature review analysis, founding causal relationships between landslides and climate change. The type, extent, magnitude, and direction of the changes in the stability conditions of the slopes, and on the location, abundance and frequency of the landslides, are not completely clear. The effects of the warming climate trend on the landslide occurrence, as well as the definition of new risk scenario, remain difficult to quantify.

1.4 Thesis scope, objectives and structure

The scope of this work is to increase the knowledge of climate impacts on the stress-strain evolution of rock slopes, through the adoption of a multi-disciplinary approach and the development of multiphysics numerical analyses. By means of a methodological process that includes geological and geomechanical characterization of rock slopes, the definition of a geological and a geomechanical conceptual model, and the development of numerical stress-strain analysis, this work is intended to be a valid reference for the analysis of rock slope evolution in response to climate inputs. Several case studies of past and active

rockslide events in the Alpine region are analyzed, along which the effects of different physical couplings are explored.

The thesis general objectives are:

- Propose a multi-disciplinary approach useful for the development of numerical analyses applied to rock slope stability, starting with the definition of a conceptual model based on a solid geological and geomechanical characterization phase.
- Develop numerical analyses aimed at evaluating the impact of pore pressure distributions and related HM stresses resulting from extreme rainfall events.
- Develop numerical analyses useful for the assessment of the combined effect of long- and short-term atmospheric temperature evolutions in the stress-strain conditions of a rock slope.
- Explore the use of multiphysics numerical approaches in rock slope stability analyses, which can account for complex mechanical behaviors leading to increased awareness of the climatic role in the development of deformation phases of large landslides.
- Explore the use of numerical tools for the assessment of the impact of ongoing climate change on the landslide activity.

The thesis is distinguished into 6 major Chapters. After introducing the research topics and defining the aims of the work (Chapter 1), Chapter 2 explores the main methods of defining the mechanical properties of intact rock and discontinuities, as well as the geomechanical characterization of rock-masses. Finally, numerical tools commonly used for simulating rock slope behavior are presented. A special focus will be dedicated on stability analyses and numerical tools that enable multiphysics simulation, in which natural processes driven by climate dynamics can be examined. Chapters 3, 4 and 5 will report and discuss the research activities carried out. In particular, the analyses will be presented in such a methodological order as to preserve the logical approach adopted in the development of the work. It initially involved the analysis of the impact of individual climate factors, and then moved to a greater degree of complexity with the introduction of multiphysical processes.

In Chapter 3, two case studies in which exceptionally heavy rainfall led to slope failure will be discussed. First, the Piuro landslide case history, occurred in 1618, and then the 2012 Cimaganda rockslide, will be analyzed. The Piuro 1618 event (Bregaglia Valley, Sondrio) represents a famous case history of a large Alpine landslide with complex kinematics (5-7 Mm^3 of rock material involved), induced by extreme climatic conditions. Its analysis required the use of a 3-D approach with a finite difference calculation method (FDM). The 2012 Cimaganda rockslide (Spluga Valley, Sondrio), on the other hand, represents a typical case of a rock shallow landslide involving a significantly degraded and fractured rock-mass. A

2D approach with a finite element numerical method (FEM), was sufficient to correctly simulate the mechanical behavior of the slope. In both cases, the analysis aim at understanding their triggering mechanisms by simulating the distribution of pore pressures and related HM stresses resulting from an extreme rainfall event.

In Chapter 4, the effects of surface temperature variations on slope stability are explored and applied to the Cimaganda rock slope, with a particular focus to the historical rockslide (7.5 Mm^3). Using a distinct element approach (DEM), analyses are aimed at reconstructing the stress history of the slope and evaluate whether temperature may serve as a driving factor for slope instabilities, evaluating the effect of both long-term (years to centuries) and short-term thermal variations (daily to seasonal). Moreover, a thermal monitoring system will be presented, providing some preliminary evidences on the impact of environmental loadings (from daily to seasonal) on the distribution of temperature inside the monitored rock-mass and the resulting rock-joint deformations.

In Chapter 5 the Ruinon rockslide case history (Frodolfo Valley, Sondrio), will be presented. In this case, the geomechanical complexity of the problem and the activity of the rockslide, required the adoption of a multiphysics approach, which was supported by a good availability of both mechanical and climatic data due to the presence of an efficient monitoring system. In a first step, the identification of predisposing factors was carried out through a 3D FEM analysis. Then, the hydrogeological regime was reconstructed using a 3D FEM approach and the output of the analysis were imported into a 3D DEM model, where the role of HM factors in triggering the deformative acceleration stages of the rockslide were verified. At last, the application of a 1D thermo-poro-mechanical mathematical model was explored and the impact related to climate changes on Alpine landslides was discussed.

The research developed by each case study will be presented following the methodological approach adopted in this work, which includes geological and geomechanical characterization of rock slopes, definition of a geological conceptual model, and development of numerical analysis; finally, after presenting the numerical modelling results, their critical discussion will answer the research questions step by step.

Chapter 6 summarizes the research outcomes and provides some directions for further future development of the study.

Chapter 2
Rock slope instabilities: issues and approaches

Considering that this work will mainly focus on the analysis of gravitative instabilities of rock slopes, this Chapter addresses the common methods for defining the mechanical properties of rock-masses and introduces the main numerical tools used in literature to simulate their evolution. These concepts are preparatory to the analyses presented in the subsequent Chapters, with a particular reference to the geomechanical characterization and the numerical simulation applied in the presented case studies, and they do not claim to be exhaustive of all the wide literature on the theme.

2.1 Mechanical behavior of rock slopes

The mechanical behavior of rock slopes refers to their ability to react in the presence of different external forces and environmental conditions. Understanding their behavior is a key step in assessing their stability on different time scales. Rock slopes are composed of rock-masses, which consist of intact rock material (rock matrix) cut into discrete blocks by discontinuity elements, mainly represented by bedding or foliation planes, fractures and joints. Fracture intensity and orientation depend on the former action of different geological processes (Pollard and Aydin 1988), often resulting in sets of discontinuities (families), with spacing and length varying according to a probability density functions (e.g. negative exponential; Priest and Brown 1983). As a result, rock-masses behave as a discrete, anisotropic, and heterogeneous medium (Hudson and Harrison 1997; Jing 2003) where their overall strength and deformability are controlled by the frequency and orientation of discontinuous elements.

The rock matrix is generally assumed as a continuous and isotropic element, where, however, the presence of microfractures or preferential orientations in its mineral constituents can drive fracture propagation and the direction of damage (Liu et al. 2015). This results in a strong dependence on the scale of observation, which must be carefully evaluated. If the extent of discontinuities is small relative to the scale of analysis, then the medium can be considered continuous and the behavior of the rock matrix will determine the solution of the problem. On the other hand, if the effect of discontinuities cannot be neglected, then, a discrete approach becomes essential and the mechanical and geometrical properties of its constituents will drive the evolution of the whole system (Liu et al. 2020).

Focusing on rock slope instability processes, a "*discontinuum medium*" scheme (i.e. small volumes of rock-masses with frequent and persistent discontinuities) can be associated with rockfall events, with shape and volume of unstable blocks controlled by the pattern of discontinuities and their kinematic

driven by the orientation of joints, ranging from planar ruptures, wedge slides and toppings. With large-scale problems (i.e. large volumes with no dominant structural patterns), the global behavior of the rock-mass can be regarded as that of an "*equivalent-continuum*" medium with strength and deformability representative of the global rock-mass behavior. As an example, large slope failures are usually related to rock-masses with randomly oriented discontinuities, which give soil-like behavior to the slope.

Over time rock slopes show a general complex time-dependent evolution, related to the progressive mechanical degradation of the material (and consequently of the strength properties) and the propagation of the fracturing network (Eberhardt 2008; McColl 2012). The concept of progressive failure, presented in Section 1.2, has wide application in the case of fractured rock-masses. One of the first authors to introduce the concept of progressive rupture was Terzaghi, according to whom, in rock systems, it is unlikely that there exists a priori an infinitely persistent network of natural discontinuities such as to form a surface along which a landslide phenomenon can be triggered (except for very small mobilized volumes); rather, it is believed that the persistence of families of discontinuities is actually limited and that a complex interaction between existing discontinuities and fracture propagation through intact rock bridges is required to bring the slope to failure (Terzaghi 1962). For the process of fracture propagation to occur, it is necessary that the stress state acting at the propagating front falls beyond the strength limit. Therefore, the heterogeneity and planes of anisotropy that characterize intact rock represent points of weakness as well as preferential directions in their propagation. The critical development of microcracks called the process of "static fatigue", seems to be the mechanism responsible for the time-dependent behavior of rock masses and the delayed attainment of failure, even when they are subjected to a constant stress state over time (Li X. et al., 2016).

Rock slopes evolve under the influence of several processes, acting with changing magnitude and timing over different timescales, from years to thousands of years (Ballantyne 2002). The evaluation of both present and past conditions is further complicated by the poor knowledge of long-term processes and the uncertainties in the reconstruction of mechanical and hydraulic properties in formerly past environments. To analyze the evolution of rock systems in relation to different external inputs, multiple numerical tools have been proposed over the years, which, thanks to significant technological improvements, have found widely application in recent decades. Their use, however, cannot be separated from a careful and accurate characterization of rock systems in all its principal constituents. The more extensive the site-specific geomechanical knowledge, the more accurate and reliable the numerical results will be.

Laboratory geomechanical detection methods

At the rock-sample scale, mechanical properties of intact rocks can be detected by laboratory tests (e.g., uniaxial and triaxial compression, direct and indirect tension), where the influences of petrographic and microstructural characters are analyzed by providing strength and deformability values of the material. Standardized procedures are provided for the execution of the main geomechanical tests; among them:

- *Uniaxial compression test*- ASTM standards D7012-14 (ASTM 2014);
- *Point load test* - ASTM standards D5731-08 (ASTM 2008a);
- *Triaxial compression test* - ASTM standards D2664-04 (ASTM 2004);
- *Indirect tension test* – ASTM standards D3967-23 (ASTM 2023).

Observed behavior permitted the development of several failure criteria where linear or curvilinear relations are generally used (e.g., Coulomb 1776; Tresca 1864; Mises 1913; Griffiths 1921; Drucker and Prager 1952; Wiebols and Cook 1968; Mogi 1971; Lade 1977; Hoek 1988; Wang and Lin 2018).

On the same way, the mechanical features of discontinuity surfaces can be carefully analyzed, with shear tests on decimeter-scale samples, to investigate peak and residual strength and stiffness (ASTM standards D50607-08 ASTM 2008b). Results are useful for establishing failure criteria accounting for joint roughness and strength (e.g., Patton 1966; Jaeger and Cook 1969; Kulhawy 1975; Barton 1976; Barton and Choubey 1977).

According to the ISRM Suggested Methods (ISRM 2015; Kulatilake et al. 2016), normal and shear joint stiffness can be detected by processing the results of direct shear tests. Normal stiffness (Kn) is defined during the normal loading phase by analyzing the σ_N/displacement curve. Kn by definition is given by the ratio of the normal tension to the average normal displacements and represents the ability of the joint to resist deformations caused by the applied force. The shear stiffness (*Ks*) is defined in the second step of the mechanical test (i.e., shear load phase), considering the pre-peak linear section of the horizontal stress-displacement curve. Plotting the stiffness values obtained at the first shear cycle as a function of the normal stress applied to the specimen, yields a linear distribution that, as with normal stiffness, allows *Ks* to be expressed as a function of stress.

Field-surveys geomechanical detection methods

The complex mechanical behavior of rock-masses can be characterized only partially by mechanical tests. Although large-scale tests and investigations in boreholes, excavations, or tunnels, allow direct observations of rock-masses their behavior is often very localized and not easily to replicate. Therefore, from intact rock parameters and discontinuity conditions, empirical approaches and indexes have been

developed to quantify the equivalent strength of rock-masses. One of the simplest and most widely used is the Rock Quality Designation Index (RQD, Figure 2.1) proposed by Deere et al. 1966 to quantify fracture intensity from core logs, given by the percentage of recovered core pieces longer than 0.1 m.

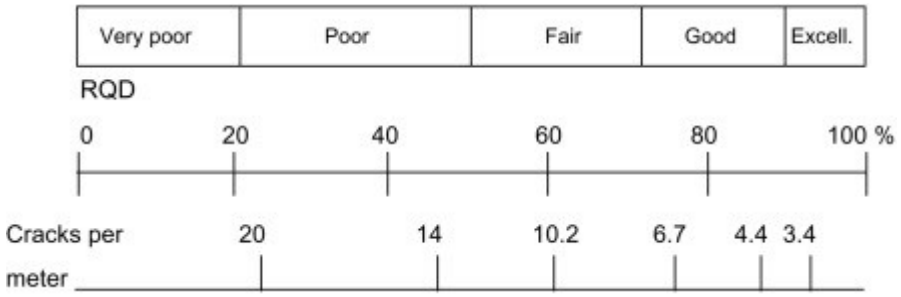

Figure 2.1 – Definition of the Rock Quality Designation index and related quality classes, from (Schön 2015).

Due to its simplicity of application, RQD is frequently used in core logging and represents an input value for more complex geomechanical classifications. The RQD is also related to the volumetric joint count (J_v, i.e., the number of joints intersecting a rock-mass volume of one m^3), through the relation proposed by (Palmstrom 1974).

Geomechanical classifications are empirical tools that, by direct observation of the rock-mass features, give quality indexes that can be used for the definition of mechanical properties. The elements that are generally investigated are the rock matrix strength, the RQD index, the geometry of discontinuities (e.g., orientation, spacing), the condition of discontinuity surfaces (e.g., roughness, weathering), the presence of water and the stress state. These factors are collected by performing detailed geomechanical surveys defined by methodical and standardized procedures (ISRM 2015).

Developed by Bieniawski 1974, the Rock-mass Rating (RMR, Figure 2.2) represents a geomechanical classification system that allows quality indices to be correlated with strength and deformability parameters of the rock-mass. It was mainly conceived for shallow tunnels and mining operations to establish the global quality of rock-masses, but it was also extended to slope instability issues (Romana et al. 2015). The rock-masses are subdivided into five categories, from “very good” to “very poor”. A rock-mass classified as “very good” is a strong medium, poorly fractured, without significant seepage processes and low alteration degree. On the other hand, if the cluster is “weak”, has low strength properties and will potentially have the possibility of developing frequent slope stability problems.

Another widely employed classification system is the rock Quality system (Q-classification system), presented by Barton et al. (1974) and almost exclusively used for the excavation of tunnels. The Q-system is based on three fundamental ratios, representing block size, frictional strength, and stress

regime, described by six different parameters collected through geomechanical surveys. due to its simplicity and accuracy has found great use in the field of rock mechanics, as testified by the numerous work published using this classification method (see for example, Barton 1988; Grimstad and Barton 1993; Løset 1997; Grimstad et al. 2002; Norwegian Geotechnical Institute 2015).

A. Classification Parameters and Their Rating

Parameter			Range of values						
1.	Strength of intact material, MPa	Point-load strength index	> 10	4 – 10	2 – 4	1 – 2	< 1 (prefered for this low-range uniaxial compressive test)		
		Uniaxial compr. strength	> 250	100 – 250	50 – 100	25 – 50	5 – 25	1 – 5	< 1
	Rating		15	12	7	4	2	1	0
2.	Drill core quality, *RQD*, %		90 – 100	75 – 90	50 – 75	25 – 50	< 25		
	Rating		20	17	13	8	3		
3.	Discontinuity spacing, mm		> 200	60 – 200	200 – 600	60 – 200	< 60		
	Rating		20	15	10	8	5		
4.	Condition of discontinuities		Very rough surface; not continuous; no separation; unweathered wall rock	Slightly rough surfaces; separation < 1 mm; slightly weathered walls	Slightly rough surfaces; separation < 1 mm; highly weathered walls	Slickensided surfaces; gouge < 5 mm thick; or separation 1-5 mm continuous	Soft gouge > 5 mm thick; separation > 5 mm; continuous		
	Rating		30	25	20	10	0		
5.	Ground water	Inflow per 10 m tunnel length, l/m	None	< 10	10 – 25	25 – 125	> 125		
		Summary water pressure	0	< 0.1	0.1 – 0.2	0.2 – 0.5	0.5		
		General conditions	Completely dry	Damp	Wet	Dripping	Flowing		
	Rating		15	10	7	4	0		

B. Rating Adjustment for Discontinuity Orientation

Strike and dip orientations		Very favorable	Favorable	Fair	Unfavorable	Very unfavorable
Rating	Tunnels and mines	0	– 2	– 5	– 10	– 12
	Foundations	0	– 2	– 7	– 15	– 25
	Slopes	0	– 5	– 25	– 50	

C. Rock Mass Classes by Summary Ratings

Rating	100 – 81	80 – 61	60 – 41	40 – 21	< 21
Class number	I	II	III	IV	V
Rock description	Very good	Good	Fair	Poor	Very poor

D. Rock Classes by Stand-up Span Time

Class number	I	II	III	IV	V
Average stand-up time	20 yrs for 15 m span	1 year for 10 m span	1 week for 5 m span	10 h for 2.5 m span	30 min for 1 m span
Cohesion of rock mass, kPa	> 400	300 – 400	200 – 300	100 – 200	< 100
Friction angle of rock mass, deg	> 45	35 – 45	25 – 35	15 – 25	< 15

Figure 2.2 - Rock-mass Rating classification (Bieniawski 1979).

A fundamental step toward a quantitative parameterization of the strength and deformability of rock-masses was taken by (Hoek and Brown 1980). They proposed a nonlinear empirical failure criterion for rock-masses which is nowadays applied for stability assessment problems and engineering projects. The criterion is based on the idea that starting from intact rock properties, the global strength of rock-masses

can be evaluated by increasing the scale of the problem to include discontinuities using an empirical relation analyzing the spatial pattern of joints and their conditions (Hoek 1988; Hoek and Brown 1997; Marinos and Hoek 2000). To support the practical adoption of this approach, Hoek and Brown 1997 introduced the Geological Strength Index (GSI, Figure 2.3), with which the rock-mass can be described with an index ranging from 5 to 95, relying only on the qualitative and simple handling description of the structure and weathered joints and avoiding multi-parameter classification schemes.

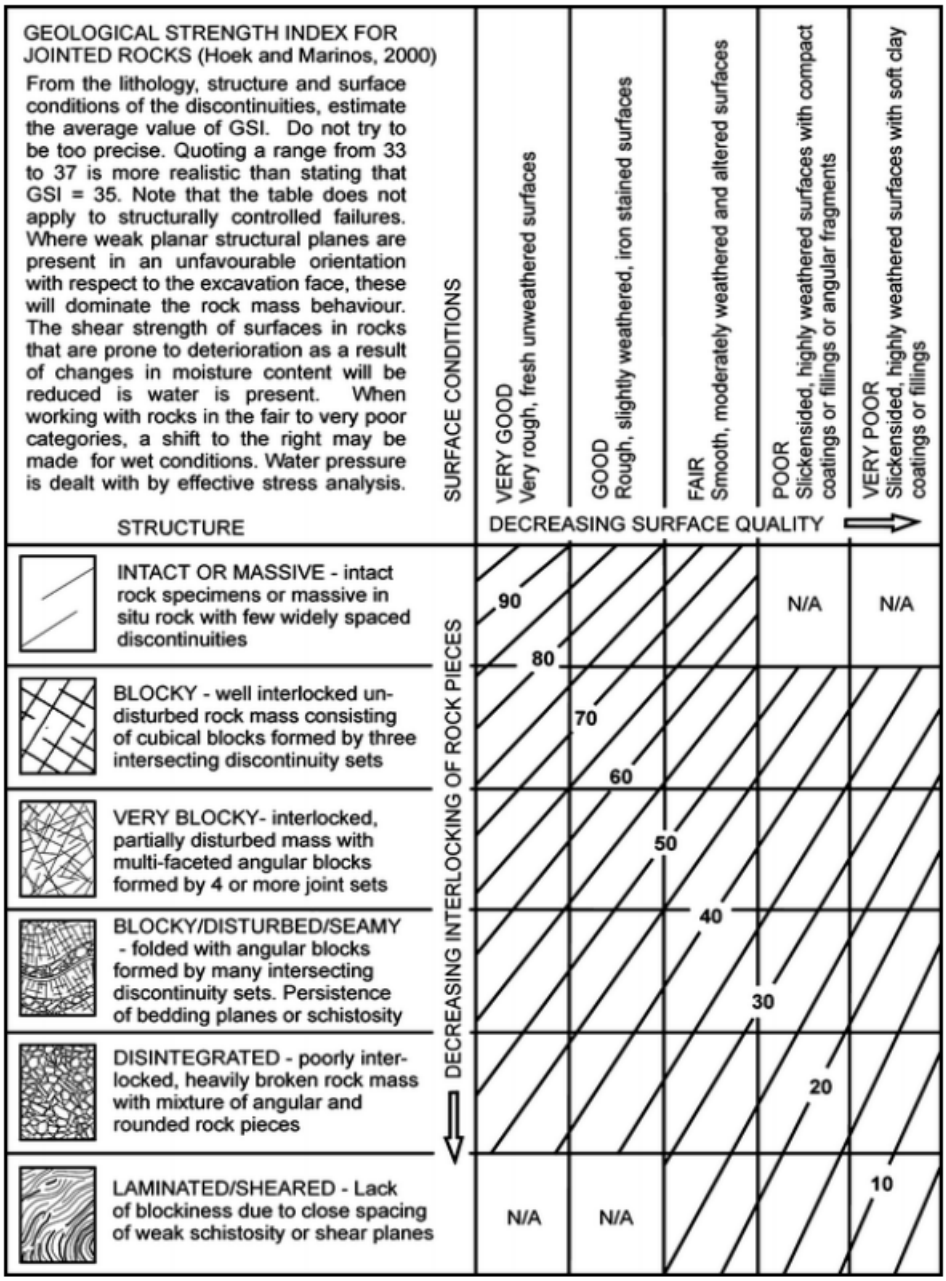

Figure 2.3 – Scheme for the definition of the Geological Strength Index (GSI; Marinos P and Hoek 2000)

The ease of application has allowed for widespread use of the GSI, which has subsequently been adapted for the description of weak, heterogeneous, and complex rock clusters and correlated with quantitative descriptors (Marinos and Hoek, 2000; Hoek et al., 2002; Hoek et al., 2005; Marinos et al. 2005; Cai et al., 2004; Hoek et al., 2013).

2.2 Numerical analysis applied to slope stability

Numerical methods are widely used for the simulation of rock systems and analyze the physical processes affecting them, including the development of gravitational instability phenomena. These methods are part of a very broad framework that includes different methodological approaches that, focusing on the topic of slope stability, can be classified into: deterministic limit equilibrium (Borga et al. 1998; Burton and Bathurst 1998; Aleotti and Chowdhury 1999; Godt et al. 2008) and numerical stress-strain (Griffiths and Lane 1999; Cheng et al. 2007; Brideau et al. 2011; Gischig et al. 2011a; Wang and Ni 2014). Deterministic methods provide quantitative information on landslide potential by calculating the factor of safety and assess its spatial distribution (Thiebes et al. 2013, 2014; Camera et al. 2015; Gu et al. 2015). The factor of safety is defined as the ratio of resisting forces to driving forces acting along a potential failure surface, and is usually calculated through the limit equilibrium (LE) formulation (e.g. Bishop 1955; Morgenstern and Price 1965; Janbu 1973). Stability analyses by limit equilibrium methods have been performed generally by considering the plane strain assumption, adopting a 2D cross-section of the slope taken as representative of the real case. However, slope failures occur in three dimensions, and the significance of this geometrical difference, cannot always be neglected. LE methods require a simplified topographic surface geometry that does not allow evaluation of the role of morphology in the stress distribution, which is of primary importance in natural slopes.

Deterministic LE methods are widely employed to solve geotechnical engineering problems at the slope scale, finding good acceptance in the practitioner community over the years, through the development of different numerical software (Cheng et al. 2007; Ureel and Momayez 2014; Liu et al. 2015; Rawat and Gupta 2016). Despite its inherent limitations and a large number of simplifying assumptions, due to its simplicity, computational speed and ease of programming, the LE method is one of the most widely used deterministic approaches for geoengineering remediation.

Numerical stress-strain models represent a good alternative to LE methods to quantify slope stability and simulate slope mechanical evolution under different external loads. Several authors adopted numerical approaches to solve complex problems of slope stability, notably using the Strength Reduction Technique (e.g., Donald and Giam 1988; Griffiths and Lane 1999; Wei et al. 2009; Tschuchnigg et al. 2015), that allow to quantify the stability of a slope through the definition of a factor of safety (*FoS*).

The strength reduction method is based on the progressive reduction of the mechanical parameters governing the global shear strength (e.g., cohesion and friction angle), until slope collapse is achieved (Varona P. & Loring D.L., 2005). A starting value of the factor of safety (FoS_{trial}) is chosen, which will then be progressively increased for each attempt, reducing the parameters according to the relationships:

$$c_{trial} = \frac{1}{FoS}\ (c) \qquad \text{(Equation 2.1)}$$

$$\phi_{trial} = arctan(\frac{1}{FoS})\ tan\,\phi \qquad \text{(Equation 2.2)}$$

The value of the factor of safety (FoS_{trial}) used to derive the parameters that lead the slope to collapse corresponds to the critical factor of safety commonly derived from deterministic methods.

Stress-strain numerical methods, represent a powerful and versatile alternative approach to LE slope stability analysis. While in the latter, only global equilibrium equations and (interface) constitutive laws are enforced, the former allows to achieve an exact solution of the mechanical problem, by also accounting for compatibility equations, thereby allowing to calculate internal strains and displacements. In addition, with the advancement in computing capabilities, the development of 3D simulations requires reasonable computational costs even on large models, allowing the topographic factor to be included in the analysis of natural slope stabilities (Wei et al. 2009; Wolter et al. 2013; Morcioni et al. 2023a). The potential of these tools and their applicability in the study of the impact of climatic factors on slope stability, lies in their ability to physically couple processes of different natures.

In addition to basic numerical methods (i.e., stress-strain), extended methods are also employed (Jing 2003), generally known as mathematical models. A mathematical model is usually adopted to describe a geomechanical system through a set of variables and a set of equations that establish relationships between them. The real model is the set of functions that describe the relationships between the different variables and is generally used to describe very complex processes of advanced multiphysics interaction. Because of their complexity they are generally adopted with a one-dimensional approach. Their applicability in the slope stability field is for example related to understanding the phenomena that occur at the shear band of landslides (Veveakis et al. 2007; Seguí et al. 2020) or to fully describe complex natural processes such as soil water infiltration and its couplings (Shao et al. 2016).

2.2.1 Fundamentals of stress-strain modeling

Numerical stress-strain analyses introduce constitutive laws to intact rock and discontinuities, allowing the definition of the nature and magnitude of stresses and deformations, through the resolution of equations of elasticity, plasticity or more complex behavior. Numerical computation codes have been

greatly implemented in recent years, thanks to the increased capacity of modern calculators, finding wide use in geomechanical and geotechnical fields. In general, numerical modeling consists of idealizing a real and complex natural system (such as a rock-mass), with a conceptual model that reproduce it, allowing its physical-mathematical analysis. The compatibility between the numerical model and the natural system is greater the more robust the assumptions made and the parameter values introduced into the calculation are. The modeling approach can be distinguished into "*continuous*" or "*discontinuous*". For the continuous method, it is assumed that all elements constituting a rock-mass are in connection with each other, defining a continuous body. Discontinuity systems that define rock blocks, as well as anisotropies and/or preferred directions of material weakness, are implicitly represented in the behavior of the rock-mass. Some discontinuous elements of primary importance, such as faults or tectonic lines, can be introduced individually as isolated elements crossing the continuous body (Figure 2.4a).

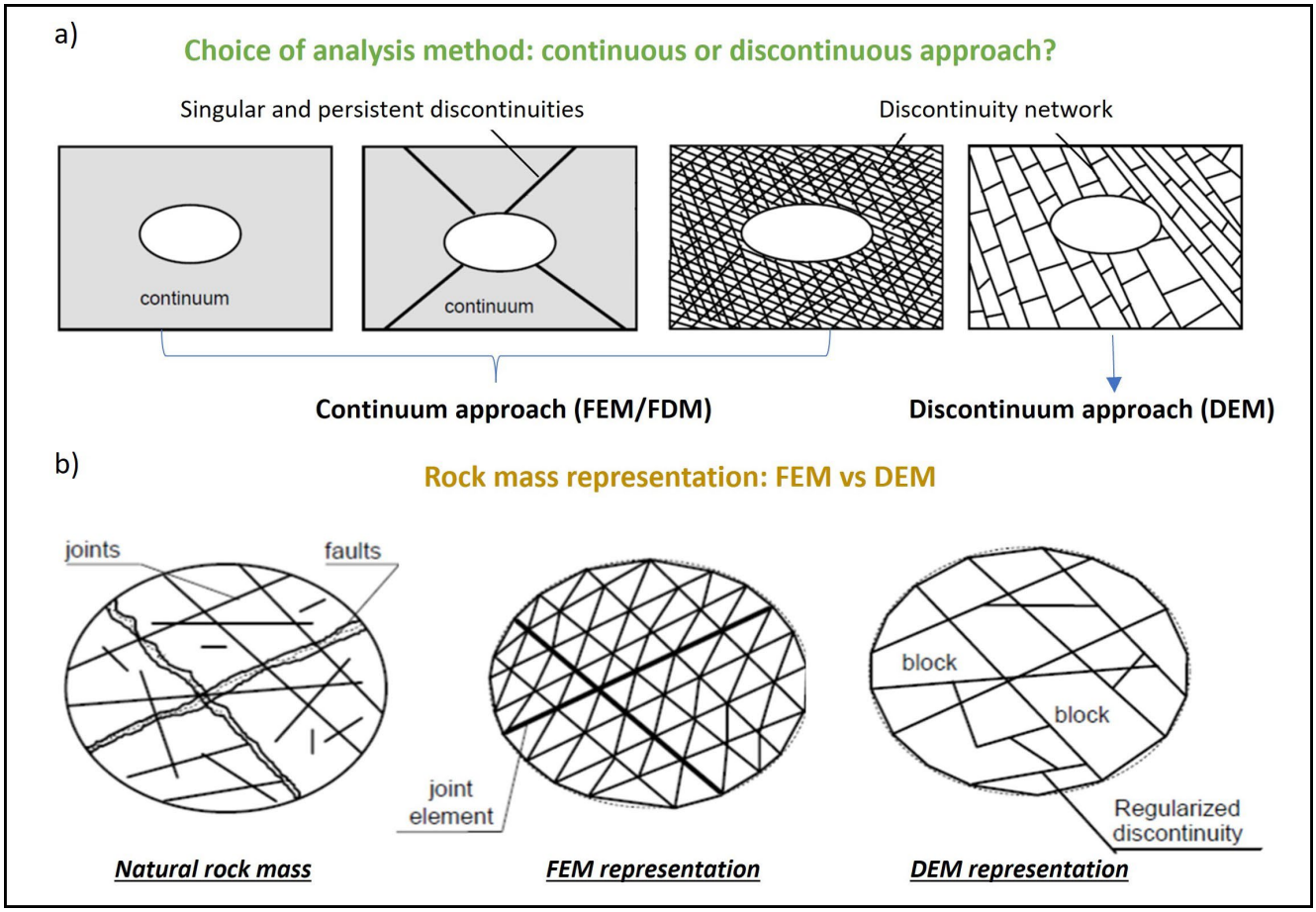

Figure 2.4 – a) Choice of analysis method based on the geometry and persistence of the discontinuities affecting the rock-mass. In the case of isotropic rock-masses, rock-masses affected by few persistent discontinuities, or intensely fractured rock-masses, a continuous method is generally associated. In the case of moderately fractured rock-masses, on the other hand, a discontinuous method will be associated. b) Differences between continuous-type and discontinuous-type computational codes in the representation of the natural system. In the first case (FEM) only the most persistent fractures are represented; discontinuity systems are considered implicitly in the material behavior. In the second case (DEM) all discontinuity systems are made explicit; they control the behavior of the mass and represent the interfaces between deformable or nondeformable rigid blocks (Jing 2003).

Continuous methods

From a mathematical point of view, analyses performed by continuum approach methods are based on solving partial differential equations that control the behavior of the rock-mass by approximating them with simpler functions of known trend. Going into more detail among continuum analysis methods, we can distinguish the finite element methods (FEM) from the finite difference methods (FDM) and the boundary element method (BEM) (Bathe KJ. 1982).

In FEMs, the continuum is discretized into a given number of subdomains (or cells) through the creation of a grid composed of primitives of coded shape (triangles and quadrilaterals) and defined by a precise number of nodes (Figure 2.4b). The basic assumption made in finite element computation codes is that the solution of complex functions is returned for each cell through a linear combination of functions called "shape functions". These are in general polynomial functions with the purpose of returning nodal values to each subdomain with the desired approximation; in particular, the greater the number of nodes used for discretization, the greater the polynomial degree and thus the degree of approximation will be low.

Finite difference methods (FDM), on the other hand, are based on approximating partial derivatives of complex functions with finite difference equations. A mathematical model described by differential equations is then transformed into an algebraic problem. A lattice of points called "grid points" is superimposed on the domain under analysis at which the approximation is carried out (usually equi-spaced square lattices are used to simplify the problem).

By solving the analysis so that it simultaneously satisfies the continuity conditions, boundary conditions and the system of differential equations governing material behavior, a strain entity is assigned to each cell (for FEM) or each point on the continuum (for FDM). Considering the entire analysis domain, a strain and stress distribution consistent with the equilibrium state of the slope will be obtained.

Unlike FEM and FDM methods, the BEM approach initially searches for a weak global solution through the numerical solution of an integral equation. The introduction of elements using different orders of shape functions, similar to FEM, has greatly improved the applicability of BEM to stress analysis problems (Jing 2003). The most important original developments in the application of BEM in rock mechanics can be attributed to the early work reported in (Cheng 1966; Bettes 1977; Zienkiewizc et al. 1983), quickly followed by many others, such as those reported in Naylor, DJ et al. 1981; Pande et al. 1990; W 1990.

The main advantage of BEM is the reduction of one model dimension, with mesh generation and thus much easier preparation of input data than FEM and FDM. In addition, the solutions within the domain are continuous, unlike the discontinuous point solutions obtained with FEM and FDM. However, in

general, the BEM is not as efficient as the FEM in dealing with material heterogeneity because it cannot have as many subdomains as there are elements in the FEM. Also, BEM is not as efficient as FEM in simulating nonlinear behavior of materials, such as in plasticity processes and damage evolution, because domain integrals often occur in these problems. BEM is more suitable for solving fracture problems of inhomogeneous and linearly elastic bodies (Jing 2003).

Discontinuous methods

When rock-masses cannot be considered as an equivalent continuum, but as a discontinuous and anisotropic medium (i.e., its mechanical and hydraulic behavior is strongly influenced by the fracture network), it will be necessary to switch to a discontinuous approach (DEM) (Burman 1971). These, unlike the continuum ones, consider the discontinuity systems explicitly, assigning them a model of behavior that will then affect the overall evolution of the slope (Figure 2.4b). Shear strength along a discontinuity is generally defined through elasto-plastic parameters (cohesion and friction angle), specifying and distinguishing peak and residual values. Barton's nonlinear strength criterion, which is defined by the JRC and JCS parameters, also finds great application.

Blocks that are isolated from discontinuity systems can be considered either rigid or deformable, assigning to the latter a constitutive model as in the case of discontinuities. Of fundamental importance in this type of modeling, therefore, is the representation of discontinuities in terms of geometry and mechanical behavior. They are considered as interaction zones between blocks that have the potential to overlap and move in space and time. To account for the large natural variability of the parameters that control and characterize discontinuity systems, probabilistic analyses that take into account their statistical distribution are often applied. In the case of rigid blocks, the solution returned by the model is limited to solving the dynamic equations of motion of the bodies. Considering the interaction forces between the blocks and the laws of behavior valid at the interfaces, the displacements and motion of each block constituting the slope are obtained. In the case of deformable blocks, the method of resolution is more complex because the solution prescinds from a matrix stress-strain analysis such as that performed in finite elements.

The representation of discontinuity elements in a discontinuous model (especially 3D) passes through the definition of a Distinct Fracture Network (DFN). A DFN model is derived from a set of statistical distribution properties defining the joint geometrical features: fracture sizes, orientations, and positions. Combined with a density factor and a random seed, it is used to generate discontinuity networks. A DFN realization is thus a fracture set whose characteristics obey the statistical description of the DFN model. Fractures are modeled as 3D disk following a classical description of fracturing, i.e. several fracture

families whose respective densities are defined from apparent fracture intensity along boreholes or scanlines, from bulk density or from bulk number of fractures. The DFN density is thus calibrated to these 1D-observed fracture intensities or 3D-expected fracture densities. Different probability distributions are used to describe the location, size, density and direction of joints. DFN methods are widely used in literature to simulate rock-masses in complex geomechanical framework, allowing to consider the uncertainty and spatial variability of natural systems (Einstein and Baecher 1983; Wong et al. 2020; Liu et al. 2021).

Moreover, in a distinct numerical approach, the process of crack propagation within a jointed rock-mass can be simulated via the so-called Voronoi tessellation, which creates randomly sized polygonal blocks (Bishop 2009). Their sides represent randomly oriented elements which allow failure along new pathways (i.e. new discontinuities). Assigning them mechanical properties of intact rock, the process of fracture propagation and the failure of rock bridges can be simulated: fracturing occurs when the joint strength between Voronoi blocks is exceeded.

For all that has been discussed so far, the choice between computational codes that solve in the continuous or discrete depends on numerous site-specific factors that are essentially related to the geometry and intensity of fracturing, as well as the scale of the problem (Section 1).

A continuous-type approach is most suitable for analyses of poorly fractured rock-masses, where discontinuities marginally affect the general evolution of the slope; alternatively, they may be particularly suitable for intensely fractured masses, to such an extent that their behavior can be likened to that of an equivalent continuum. The discrete-type approach, on the other hand, is more suitable for moderately fractured materials where the behavior of the cluster is strongly controlled by the presence of discontinuity systems that isolate potentially unstable blocks (Jing 2003).

Hybrid models are frequently used in rock engineering, basically for flow and stress-strain problems of fractured rocks. The main types of hybrid models in literature are the BEM/FEM, DEM/FEM and DEM/BEM models. The combination of two different numerical approaches makes it possible to harmonize the required problem geometry with the available numerical techniques, thus providing an effective representation of the rock-mass. The hybrid FEM/BEM was first proposed in Barbosa and Ghaboussi 1990, then followed in Munjiza et al. 1995, 1999 as a general stress analysis technique. In rock mechanics, it has been used mainly for simulating the mechanical behavior of underground excavations (Wittke 1990). The hybrid DEM/BEM model was implemented for coupled HM analysis of fractured rocks, using combinations of DEM, and BEM approaches, involving the definition of a DFN. In Southwell 1956, a hybrid DEM/FEM model was described, in which the DEM region consists of rigid blocks and the FEM region can have non-linear material behavior.

The hybrid models have many advantages, but special attention needs to be paid to the continuity or compatibility conditions at the interfaces between regions of different models, particularly when different material assumptions are involved, such as rigid and deformable block region interfaces (Jing 2003).

2.2.2 Multiphysics approaches

The potential of numerical approaches, especially in the slope-stability applications, lies in their ability to couple mechanical stress-strain analysis with the simulation of other natural processes such as heat transport or water flow (coupled models). This coupled formulation implies that the modeled processes occur simultaneously, with effects on both the mechanical system and the evolution of the coupled natural process. This allows for more realistic simulation of natural systems, bringing closer the real behavior of the rock slopes to the modelled one.

The couplings between the processes of heat transfer (i.e., thermo-T), fluid flow (i.e., hydro-H) and stress-strain (i.e., mechanical-M) in fractured rocks, have become an increasingly important subject since the early 1980s (Lorig 1985; Liao and Hencher 1997), mainly due to the modelling requirements for the design and performance assessment of underground radioactive waste repositories, gas/oil recovery, hot-dry-rock thermal energy extraction, contaminant transport analysis and environment impact evaluation in general (Jing 2003). In recent years, THM models are becoming very powerful in simulating complex geomechanical processes related to the exploitation of geothermal energy, injection of CO2, and to analyze issues related to permafrost degradation and frost cracking that are becoming increasingly common in the environmental field due to climate change. Some recent papers have provided fully coupled THM models for simulating the behavior of geotechnical materials (e.g., Gawin et al. 1996; Neaupane and Yamabe 2001; Zhou and Ng 2015).

The term “coupled processes” implies that the rock-mass response to an external perturbation, such as the construction and operation of a nuclear waste repository, cannot be predicted with confidence by considering each process independently. The coupling models are based on heat and multiphase fluid flow in deformable and fractured porous media, and have been mainly developed according to the thermo-elasticity theory of solids, as well as the poro-elasticity theory. The coupling effects are formulated as three interrelated PDEs, expressing the conservation of mass, energy and momentum, for describing fluid flow, heat transfer and deformation (Shi and Goodman 1985).

Coupled processes and models represent a major advance in rock mechanics, which has only been accomplished in the past few decades. Their extensions to include chemical, biochemical, electrical,

acoustic and magnetic processes have also started to appear in the literature and are an indication of future research directions (Dejong et al. 2013).

Since slope instability processes can be notably influenced by the THM coupled processes (Section 1.3), some studies have been carried out to assess slope stability under multi-field coupling effects. In terms of evaluating slope stability under the TM effects, several researchers have studied processes affecting periglacial and glacial environment (e.g. see (Gunzburger et al. 2005; Gischig et al. 2011), as well as the thermally induced rock failures (Bakun-Mazor et al. 2020). Others have been focused on assessing slope stability in consideration of the HM coupled effects (Preisig et al. 2016; Donati et al. 2020; Liu et al. 2021). To date, few studies have been conducted to evaluate slope stability in consideration of the coupled THM effects (Wu et al. 2019; Wang et al. 2023). This is mainly related to the assumptions and simplifications that need to be adopted in the development of numerical analyses, especially when applied to slope stability where the goals of the analysis lead more to focus on the triggering mechanisms. Direct observations, however, reveal that it is of crucial importance to consider the multiphysics effect when the stress-strain evolution of slopes is analyzed.

2.3 Numerical tools adopted in this work

In this work, different numerical software, identified as the best tool for the simulation of the investigated processes, were adopted. They included both continuous and discontinuous methods for solving mechanical (stress-strain) problems and for simulating natural processes such as groundwater circulation and thermal diffusion. The computational software adopted for each case history (Section 1.4) are presented below, in order to simplify the discussion in the respective Sections. In some cases, the coupling between different computational codes was explored. Added to them is a mathematical numerical model, developed in the MATLAB environment in Sections 5.8 and 5.9, which for clarity and completeness in the discussion will be fully presented in Section 5.8. The reasoning behind the choice of the different calculation methods and software for each case study is discussed in the corresponding chapters, so that the choices can be better argued and justified.

FLAC3D - Itasca

FLAC3D (version 7.0 – Itasca 2019; Zabuski 2019; de Ojeda et al. 2021) is a finite difference (FDM) code, with a 3D implementation, particularly suited to analyze geotechnical problems. In FLAC3D, natural rock slopes are modeled as a continuum medium, discretizing the domain by a continuous grid, where each zone behaves according to an assigned linear or nonlinear constitutive law. Due to its explicit

finite volume formulation, the code is able to deal with large strains (e.g., large displacements), and capture instabilities including cases of yield and failure over large areas, or total collapse. Moreover, using mechanical interfaces, the software can also simulate discontinuities such as faults and singular geological elements. Complex geometries can be easily modeled allowing the simulation of sliding along weak surfaces and the evolution of deformations over time. Different authors (Itasca 2019; Zabuski 2019; de Ojeda et al. 2021) clearly showed the potential for using continuum FDM codes to simulate stress distributions in rock slopes, to investigate mechanisms of large slope deformation and landslide development. FLAC3D allows modeling of groundwater circulation through a permeable medium, taking into account the fluid-solid interaction (HM coupling) in which variations in pore pressure induces variations in effective stresses and vice versa (two-way coupling). FLAC3D also enables calculation of thermal couplings (TM) and simulation of temperature distribution by diffusion.

In this work FLAC3D was adopted for the analysis of the Piuro landslide with an HM approach (Section 3.2).

RS2 – Rocscience

RS2 is a 2D numerical code (RocScience 2017), based on the finite elements formulation (FEM). The software allows the introduction of discontinuities, through the definition of elements called 'joint boundary elements' (Hammah et al. 2008), thus defining a hybrid numerical configuration. Strength and stiffness properties can be assigned to these elements, allowing the simulation of rock-mass behavior.
The use of this software in the field of slope stability is generally linked to the development of analyses following the strength reduction (SR) approach, for the calculation of the strength reduction factor (SRF - Clayton et al. 2020; Tandon et al. 2022; Valentino 2023) . However, RS2 presents great potential given by the possibility of analyzing the presence of a discontinuity system in a continuous environment and by the flexibility in simulating HM processes (Wang and Li 2021).

In this work RS2 was adopted for the analysis of the 2012 Cimaganda rockslide with an HM approach (Section 3.3)

UDEC - Itasca

UDEC (version 7.0 - Itasca Consulting Group 2018) is a 2D numerical code based on the distinct element method (DEM) formulation, particularly suited to analyze the behavior of discontinuous media. In UDEC, the jointed rock-mass is modeled as an assemblage of distinct deformable or undeformable blocks, that are in mechanical interaction through contacts representing discontinuities (Cundall and

Hart 1992). Deformable blocks are defined by a continuum mesh of triangular finite-difference zones, where each zone behave according to an assigned linear or nonlinear stress-strain law; blocks can thus deform, translate, rotate and interact with each other.
Rock joints are treated as interfaces between intact blocks, along which contact forces and stresses are examined. Deformability and strength properties of interfaces are represented by spring-slider elements located at contact points between a block corner and an adjacent block edge (Lorig and Cundall 1989). If the prescribed tension or shear strength limit is exceeded, failure of the interface is assumed. Stresses can accumulate at slip fronts and additional failure or slip propagation can occur until the stress state drops below the strength limit. UDEC is thus suited to evaluate the stress-strain evolution of a discontinuous medium like the rock-mass at hand (Zhang et al. 1996; Strouth and Eberhardt 2009; Grämiger et al. 2017, 2018, 2020; Rwechungula and Cheng 2021).
UDEC allows modelling fluid flow through the fractures. Blocks can be simulated either as impermeable or porous media. Moreover, steady-state pore pressures can be assigned to zones within deformable blocks and boundary conditions may be applied in terms of fluid pressures. UDEC also enables calculation of thermal couplings and simulation of temperature distribution by diffusion. The thermal model simulates the transient flux of heat in materials and the subsequent development of thermally induced stresses. The heat flux can be modeled by either isotropic or anisotropic conduction.

In this work UDEC was adopted for the TM analysis applied to the Cimaganda rock slope (Section 4.2).

3DEC – Itasca

The 3DEC code (version 7.0 - Itasca Consulting Group 2019), is the 3D implementation of UDEC. The approach of analysis remains the same as presented for the 2D version, as well as the hydraulic and thermal coupling possibilities. The transition from a 2D to a 3D approach allows better definition of the relationships between morphological and geological features, although some geometric simplifications are sometimes necessary to reduce the computational load. 3DEC is very useful for the study of rock-masses through the introduction of 3D discontinuity networks using distinct fracture model (DFN - Yin and Chen 2020; Liu et al. 2021; Wu and Hsieh 2021).
In this work 3DEC was adopted for the HM analysis applied to the Ruinon rockslide (Section 5.7).

MOOSE

MOOSE (Multiphysics Object-Oriented Simulation Environment) is a FEM open-source C++ framework , developed by the Idaho National Laboratory (Icenhour et al. 2018). It is a powerful tool for simulating multiphysics processes because of its nonlinear solver, that supports efficient coupling

between systems of physical equations. Multiple physical processes can be solved in an implicit, fully coupled way. MOOSE's project has generated a growing developer community of scientists and researchers actively involved in its continued development. Currently, MOOSE provides physics modules for solving problems in mechanics, porous flow, phase field modeling, and geochemical processes. All these modules are available to users, and any physics library can be included in the analyses. The input file represents the core of the simulation, where separate components are used to define all the required elements. They include: the mesh geometry, the variables to solve for, the terms of the system of equations to be solved (called kernels), the boundary conditions, the initial conditions, and the calculation settings (solver options and timesteps). An external input mesh file, containing the geometric and topological information for MOOSE, can also be provided and called in the input file. The MOOSE simulator can output results in a variety of formats, from comma-separated plain text to common binary formats, that can be easily read with a popular post-processing software.

In this work MOOSE was adopted for a stress-strain and HM analysis applied to the Ruinon slope (Section 5.5).

COMSOL Multiphysics

COMSOL Multiphysics (Version 5.4 - www.comsol.com), is a FEM code able to simulate devices and processes in all fields of engineering, manufacturing, and scientific research in both 1D, 2D or 3D. It provides fully coupled multiphysics and single-physics modeling capabilities. COMSOL facilitates conventional physics-based user interfaces and coupled systems of partial differential equations (PDEs). Beside the classical problems that can be addressed with application modules, the core Multiphysics package can be used to solve PDEs in weak form in both drag-and-drop tools (Form Editor) or programming (Method Editor). Compared with traditional commercial computational software, it allows greater freedom in defining the equations governing the investigated physical problems and in setting the domain boundary conditions. In the field of rock slope stability this software is not generally adopted for mechanical calculation, due to its numerical continuous nature. However, it is widely adopted for the simulation of slope physical processes such as the hydraulic and thermal ones linked to slope stability issues (Grämiger et al. 2018, 2020; Wang et al. 2023).

In this work COMSOL was adopted to simulate thermal diffusion processes in Section 4.2 and 5.9.

SEEP3D – Geostudio

SEEP3D is a finite element software (Seequent 2022) of the GeoStudio suite (https://www.geoslope.com/). The software allows simulating hydrogeological flow in complex geological structures under steady-state or transient conditions. Thanks to flexibility in defining boundary conditions, it has great potential for coupling multiphysical processes, from solute and gas transport to heat transfer and freezing processes. SEEP was firstly developed by the United States Army Engineer Waterways Experiment Station to simulate a variety of problems involving seepage. It can model simple saturated steady-state problems or sophisticated saturated-unsaturated transient analyses with atmospheric coupling to the ground surface. The 3D approach also allows to preserve the geological setting in the numerical analysis and analyze the complex relationship between the hydraulic bodies that define a slope. The governing equation used in its models is the Laplace equation solved in both 2 and 3 dimensions. SEEP allows for different hydraulic conductivities along the major and minor axes (anisotropic conditions) to be defined.

SEEP3D uses blocks (called “regions”) to represent hydrogeological units or engineering elements as impermeable walls, wells or underground tunnels. The finite element mesh pattern is inherent to each region in the domain. Therefore, as the regions are connected together, the mesh is constructed automatically, ensuring complete mesh compatibility between the regions. Once the domain is set up and boundary conditions and material properties are applied, the problem is ready to be analyzed using one of SEEP3D's built-in iterative solvers that can handle linear, nonlinear, steady-state, transient, and adaptive analyses. Post-processing includes contouring the total head (equipotential lines) or pore pressure, drawing the flux vectors, and calculating the flux potential values at the nodes. These values can be used to draw the flow lines together with the equipotential lines (i.e., flow networks). The piezometric surface (i.e., pore pressure equal to 0), can also be displayed.

The great potentiality of this software is that the distribution of the modeled variables (e.g., pore pressure) can be imported into other software of the GeoStudio suite for numerical calculation of coupled physical processes such as heat transport (i.e., using TEMP3D software). Alternatively, the value of modelled variables at each grid node can be exported to be introduced into different computational software with their x, y, z coordinates.

In this work SEEP3D was adopted to develop the hydrogeological model of the Ruinon slope (Section 5.6).

Chapter 3
Rainfall as major rockslide driving factor

3.1 Introduction: research question and objectives

Rainfalls and rapid snowmelts are considered the most significant factors causing slope failure for both rockslides and rockfalls (Maraun et al. 2022). In the Alpine environment there are several examples of slope collapse induced by water pressure changes, e.g. Val Pola 1987 (Crosta et al. 2004), Brenva 1997 (Barla and Barla 2001), Preonzo 2012 (Loew et al. 2017). In other cases, pore pressure has been deemed responsible of accelerating downslope movement of landslide bodies, as for example in the Ruinon rockslide (Carlà et al. 2021) or the Vallemaggia rockslide (Preisig et al. 2016). The degree of hydro-mechanical (HM) coupling depends on the specific slope conditions, being influenced by the surface topography, the hydrogeological properties of the materials involved (i.e., the spatial distribution and density of fractures) and the slope mechanical state (Preisig et al. 2016).

Rainfall processes related to rock slope instability can include: (i) increase of water pressure (i.e., reduction of effective stresses); (ii) failure of rock bridges (i.e., rock-mass strength reduction); (iii) joint infilling swelling, dissolution and leaching (i.e., mechanical degradation). These processes could act at different time scales, depending on the intensity and duration of the rainfall events.

Groundwater in Alpine valley flanks is subjected to strong seasonal fluctuations, mainly driven by snowmelt processes and heavy rainfall that contribute to surface recharge, temporarily raising the water table (Hansmann et al. 2012; Lucas et al. 2020; Stumvoll et al. 2020). Even if observations in stable Alpine valley flanks have highlighted reversible rock slope deformations (Hansmann et al. 2012; Loew et al. 2017; Rouyet et al. 2017), such coupled HM processes may play an important role in driving cyclic fracture propagation over longer time scales (Preisig et al. 2016; Grämiger et al. 2020). This phenomenon is called HM fatigue (Bonzanigo 1999; Parriaux et al. 2010), causing continuous evolution of hydrodynamic parameters due to the dependency of rock-masses permeability on effective stress, shear slip, aperture and dilation of fractures (Preisig et al. 2012; Riva et al. 2017).

Preisig et al. 2016 observe that in Alpine valleys, pore pressures are usually increased two times per year: (i) in Spring due to snow melt, often accompanied by heavy rainfall; and (ii) in Fall because of intense rainfall periods. These pore pressure fluctuations are typically in the range of 0.01–0.05 MPa for soil slopes, and 0.1–0.5 MPa for rock slopes (Bonzanigo 1999; Parriaux et al. 2010).

Several techniques were exploited to numerically analyze HM coupling in geological media, involving both continuum and discontinuum approaches. In general, the goal is to analyze the mechanical response

of the slope to different hydrogeological scenarios, also identifying site specific thresholds for triggering of slope acceleration phases (Bonzanigo 1999; Crosta and Agliardi 2014). Despite the simple formulation, continuum models are affected by great uncertainties mainly related to the definition of hydraulic parameters, given the discontinuous nature of fluid flow in rock-masses. The use of statistically-based DFN is progressively increasing in the last few years, leading to a conjugate discontinua description of geological media with statistical description of rock-mass anisotropy and heterogeneity (Fischer et al. 2010; Elmo et al. 2014, 2015; Sturzenegger et al. 2015).

Despite the above presented studies and approaches, many authors agree that additional research is needed to improve the understanding and quantification of the relationships between rainfall-driven processes and rock-slope failures.

Focusing on stress-strain modeling analyses, studies presented in the literature involve the simulation of HM processes by introducing a static piezometric level, which is forced to vary by imposing a rising scenario. Only few works analyze meteorological events through a transient analysis, coupling mechanical calculation with hydrogeological water circulation. Especially in the case of localized failures in rock slopes, this is of critical importance in order to reconstruct the evolution of hydraulic pressures within the discontinuity network, and faithfully assess the HM mechanisms leading to the development of instability. In literature this is generally neglected because of computational challenges and is simplified by introducing a piezometric surface (more frequently a line in a bi-dimensional analysis), interacting with a prior-established landslide slip surface.

Moreover, large landslides with a complex geological structure are often difficult to analyze using classical modeling methods, due to their complex kinematics and hydrological features (Lignon et al. 2009; Mergili et al. 2014). Most of the published works analyze the stability of large landslides with a 2D approach, even if they represent a typical 3D problem. A 2D approach leads to neglecting structural and morphological differences across the failure surface, as well as the development of localized pore pressure changes induced by topographical constraints and hydrogeological structures (Wolter et al. 2013).

This Chapter will present two case studies in which exceptionally heavy rainfall led to slope failure. In particular, the Piuro landslide case history, occurred in 1618, and the 2012 Cimaganda rockslide, will be analyzed.

The Piuro 1618 event represents a famous case history of a large Alpine landslide with complex kinematics (5-7 Mm^3 involved), induced by extreme climatic conditions (Scaramellini et al. 1988). It occurred during the so-called Little Ice Age (LIA), characterized worldwide by colder temperatures (Mann et al. 2009), snowy winters and dry summers with frequent floodings. The consequences of such

peculiar climatic conditions are documented in the geomorphological activity, especially in soil erosion processes, debris-flow activities, and flooding (Grove 2001). During this period, between the 16th and 19th centuries, several large landslides also occurred in the Alpine region (e.g. Monte Crenone and Arth-Goldau rock avalanches (Scapozza et al. 2015; De Pedrini et al. 2022). The climatic conditions peculiar to that period, may have favored the development of such gravity phenomena, although, due to the lack of meteorological data, quantitative cause-effect analysis may only be hypothesized (Stoffel and Beniston 2006).

The 2012 Cimaganda rockslide, on the other hand, represents a typical case of a rockslide involving a significantly degraded and fractured rock-mass. It occurred on a slope with peculiar geomechanical characteristics that also predisposed the development of a large rockslide in historical times involving 7.5 Mm^3 of rock material. Regarding the 2012 event, the exact triggers are known, represented by a heavy rainfall event that saturated the rock-mass located at the base of the slope.

Numerical modeling of these two landslide events required a different modeling approach that necessarily had to take into account the different scales of analysis. For the Piuro landslide, it was necessary to adopt a 3D approach because of the geometries of the geological elements that predisposed its development, as well as the distribution of stresses and the pore pressures. For the 2012 Cimaganda rockslide, the limited volume, the geological homogeneity of the investigated portion of the slope, and the geomechanical setting enabled a 2D approach to capture the general evolution of the slope with reasonable detail. A FEM approach was adopted in which a discontinuity network was also explicitly introduced, thus defining a hybrid numerical configuration.

In both cases, a numerical modeling analysis was developed with the aim of reproduce water infiltration processes, reconstruct the distribution of hydraulic pressures associated with a triggering event, and simulate geometries and volumes of landslide masses (i.e., back analysis). Evaluation of stress-strain fields aims to reproduce the development of the slip surface without introducing any prior knowledge of its location in the model. The simulated outputs are then compared with those observed in the field in order to validate the results. Both numerical analyses were preceded by a careful geological and geomechanical characterization phase that led to the definition of a robust conceptual model of both slopes.

In Section 3.2 the 1618 Piuro landslide will be investigated. After presenting the geological, geomorphological, and geomechanical data collected involving both in-siu and laboratory analyses (Section 3.2.2), a conceptual geological-mechanical model of the slope will be presented in Section 3.2.3. Starting from this model, the HM analysis will be finally developed in Section 3.2.4.

In Section 3.3 the Cimaganda case history will be analyzed, with a particular focus on the 2012 event. After presenting the geological, geomorphological, and geomechanical data collected involving both in-siu and laboratory investigations (Section 3.3.2), a geological-mechanical model of the slope will be presented in Section 3.3.3. Starting from this model, the HM analysis will be finally developed in Section 3.3.4. In Section 3.4, some research outcomes based on the evidence from the analyses developed will be provided.

The Piuro landslide HM numerical analysis has been published in Morcioni et al. 2023.

3.2 The Piuro case study

3.2.1 Study area

The Piuro landslide is located in the central Italian Alps, along the Bregaglia Valley, which extends with an Est-West direction from the village of Chiavenna to the Engadin region Figure 3.1 a-b). The landslide develops on the southern flank of the valley, in correspondence of the Piuro village.

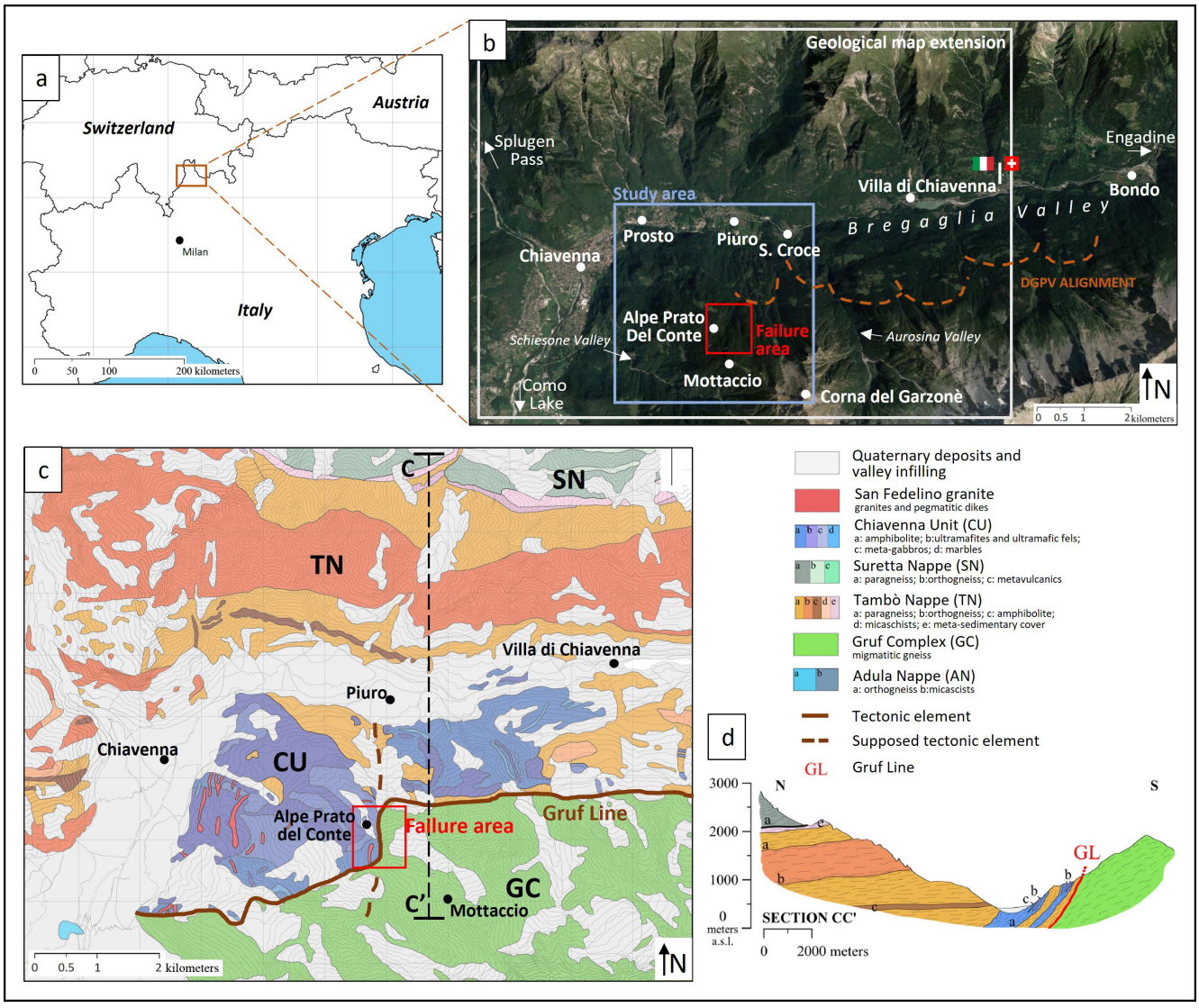

Figure 3.1 a) Location of the study area; b) Satellite photo of the lower Bregaglia valley showing the location of the failure area, the extent of the 3D model and geomorphological features; c) Geological settings of the study area (from (Montrasio and Sciesa 1988)); d) Geological cross section with a N-S direction.

The geological framework is of particularly complexity as the valley crosscuts the stack of the Upper and Middle Pennidic Nappes which include, from top to bottom, the Suretta and Tambò nappes, the Chiavenna Unit and the Gruf Complex (Figure 3.1 c-d). While the northern slope is mainly composed

by gneissic rocks and micaschists belonging to the Crystalline Basement Units of the Tambò and Suretta Nappe (Middle and Upper Pennidic), on the southern one mafic and ultramafic rocks of the Chiavenna Unit prevail. The regional tectonic line known as the Gruf Line, runs in the upper portion of the southern slope, almost parallel to the valley axis (E-W) and is characterized by a recrystallized and verticalized mylonitic rock band (Figure 3.1 c).

The Gruf Line is considered an extension of the Engadin Line, with same geological origin and kinematics (Wenk 1984; Tibaldi and Pasquarè 2009). Recent seismic activity and morphological evidences along the Engadin-Gruf system (Tibaldi and Pasquarè 2009) show that these elements could be still active (Albini et al. 1988; Ismes 1994). South of the Piuro village, the Gruf Line is cut by a sub-vertical fault with a North-South direction (Figure 3.1 c). To the north of the Gruf Line, ultramafic rocks of the Chiavenna Unit with intercalated gneissic bodies of the Tambò Unit are present; to the south, migmatitic gneissic rocks of the Gruf Complex outcrop. The fault makes the ultramafic rocks of the Chiavenna Unit in contact with the migmatitic gneissic ones of the Gruf Complex (Figure 3.1 c). This tectonic framework, with strong rheological differences, may be one of the factors that predisposed the slope to gravitational instability phenomena.

The Quaternary geomorphological evolution of the Bregaglia Valley is related to the superposition of glacial, gravitational and alluvial processes. During the Last Glacial Maximum (LGM), Engadin glacier filled the whole valley and only the highest peaks and ridges were ice-free (Tantardini et al. 2022). The trimline of the LGM glaciers in the Italian Bregaglia Valley varies from 2250 m a.s.l. to 2170 m a.s.l. moving E to W (Tantardini et al. 2022) and minor lateral glaciers were confined at higher altitudes.

The southern slope is morphologically articulated, with steep portions interrupted by plateaus and terraces, where glacial deposits are well preserved with morainic ridges stretched parallel to the main valley axis (E-W). Trenches and counter-slopes that highlight areas subject to Deep Seated Gravitational Slope Deformations (DSGSDs) are widespread along the entire slope (Figure 3.1b). They are particularly concentrated at an elevation of about 1300 m a.s.l., where morphological conditions and the presence of the sub-vertical tectonic lineament (Gruf Line) may have promoted their development with a direction parallel to the valley axis. As shown by Tibaldi and Pasquarè 2009, the alignment of DSGSDs on the southern slope suggests a correlation between slope instability and the geological structure of the valley. In addition, numerous scarps and detachment zones affect glacial terraces on both sides of the valley, reflecting the intense post-glacial activity of the DSGSDs.

As evidence of the intense geomorphological activity, the valley has been recently affected by significant landslide events. In August 2017, a large mass of rock material with volumes comparable to those of the Piuro event, failed from the slopes of the Cengalo Peak, destroying part of the village of Bondo and

permanently altering the morphology of the valley (Walter et al. 2020). In August 2019, a rockslide of several thousand of cubic meters, affected the slopes located north of the village of Villa di Chiavenna, causing the evacuation of some inhabitants. More recently, in July 2021, the Piuro area was affected by a debris flow detached from the northern slope in correspondence with the Perandone Valley. It was triggered by heavy rainfalls and caused the interruption of the national road SS37 connecting the village of Chiavenna with Swiss territory.

3.2.1.1 The Piuro landslide

On September 4, 1618, a large landslide destroyed the ancient village of Piuro causing the death of at least 1000 people. The village of Piuro, located in the middle of the Alps, was an important trading centre between the Mediterranean region and Northern Europe, well known for its silk trade and soapstone production. Therefore, the event had a significant social and economic impact among communities of all Alpine regions and was well documented by chronicles and paintings during the subsequent decades (Scaramellini et al. 1988).

The failure area of the 1618 event is placed on the southern slope of the Italian Bregaglia Valley, between 1300 and 1700 m a.s.l., east to the locality “Alpe Prato del Conte”. The dynamic of the event is reported in historical writings and chronicles collected by Scaramellini et al. 1988. The sliding mass is described as a “mixture of rocks, mud and water that slid down the slope”, reaching the bottom of the Valley and wiping out the ancient village of Piuro (Figure 3.2).

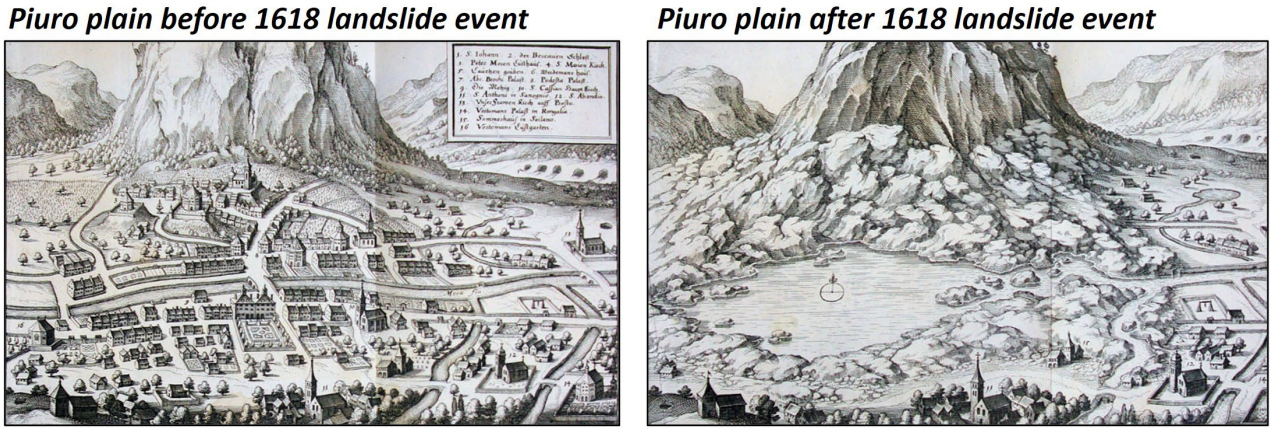

Figure 3.2 Historical drawings showing the village of Piuro before and after the 1618 event (from Scaramellini G., 1988)

Dust and debris covered the entire valley as far as the nearby town of Chiavenna, where the event was distinctly heard. The Mera River, which flows through the valley, was dammed for a few hours. According to historical writings, a large area upstream of the landslide deposit was submerged by a lake

created by the Mera River, until the water overflowed, without flooding the town of Chiavenna (Falappi 2012). The volume of the sliding mass is estimated at values of 5-9.5 Mm^3 based on the stratigraphical reconstruction of the landslide deposit on the Piuro Plain (Pigazzi et al. 2022). Historical sources (Scaramellini et al. 1995) testify that the catastrophic event was preceded by heavy rainfall that affected the area for the whole week preceding the event. The day before the failure event, new fractures opening and loud noises were seen along the slope. Mudslides and rockfalls also reached the village area only a few hours before the event, destroying some forests and crops.

Shortly after the occurrence of the landslide event, different hypotheses were made within the local community to explain why it happened. Some ascribed it to divine punishment against an exaggerated opulence earned with commercial trades; others related it to the heavy rainfall occurring just before the event, and yet others blamed it on an earthquake caused by "very strong underground winds locked up in the many cavities of the mountain", mined to extract stones. During the last decades, based on historical documents and paintings, some authors started to analyze the landslide event to define geometries, volumes, preparatory and triggering factors. Previous studies collected in (Scaramellini et al. 1995), suggested a possible detachment zone of the landslide and the extent of its deposit. The triggering cause was identified as strong rainfall, as suggested by historical sources describing how the catastrophic event was preceded by heavy rain affecting the Piuro area for the entire previous week (Scaramellini et al. 1988). However, the lack of a scientific approach left several questions open, as the precise location and geometry of the landslide scar and its deposit, the volume of the landslide body, as well as the sliding mechanism. In recent years, the Interreg AMALPI18 project (https://www.amalpi.org/) aimed at promoting the scientific knowledge of some large Alpine landslides between the Swiss and Italian territories including that of Piuro, to raise awareness on slope instability topics through a cross-border geo-cultural trail (the AMALPI Trek; Apuani and Scapozza 2023). In this framework Pigazzi et al. 2022 identified the landslide deposit by providing a reconstruction of its geometry and volumes based on geological and geomorphological surveys, and on the stratigraphic analysis of two boreholes drilled in the Piuro Valley floor. Moreover, the work by Pigazzi et al. 2022 confirmed the location of the landslide scars by the observation of trenches and scarps affecting the southern valley slope. Based on field surveys, a relation with geological elements was highlighted and two possible scars were outlined by the alignment of morpho-structures.

3.2.2 Data collection

With the aim of identifying the geomorphological and geomechanical features that highlight the presence

of the landslide, and that potentially led to its development, geological and geomechanical surveys were carried out along the slope. This chapter will discuss in detail the detected features that most characterize the study area. Particular emphasis was given to the geomechanical characterization of the failure area, with the aim of collecting enough data for the definition of a strong and valid mechanical model. For this, detailed geomechanical surveys and laboratory tests were carried out.

In addition, the observed geomorphological features were compiled into a geomorphological map, to describe processes that characterize the study area.

3.2.2.1 Geological settings

The Piuro landslide failure area is characterized by the tectonic contact between the Gruf Complex and the Chiavenna Unit (Figure 3.3). in the area the contact has a N-S trend, related to a sudden rotation of the Gruf line with a general E-W trend along the main valley. Surveys in the field, showed a gradual transition between ultramafic and gneissic rocks belonging to the Chiavenna unit and the Gruf complex, respectively.

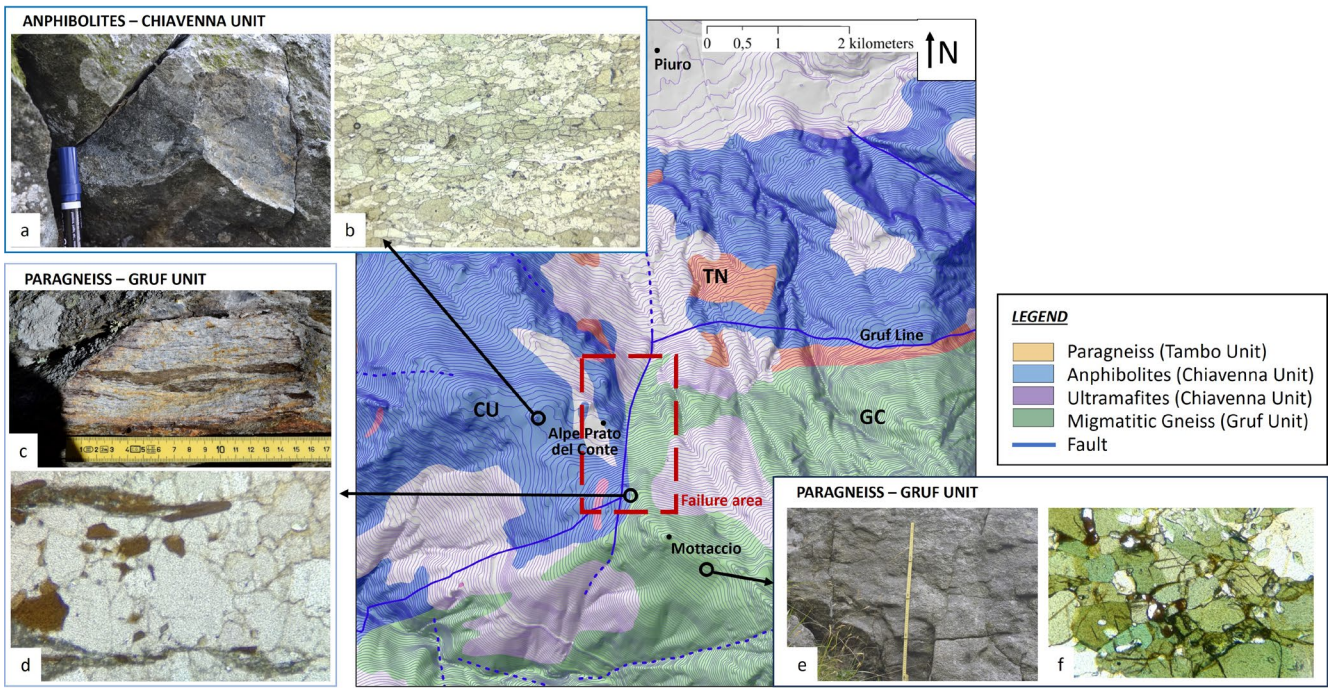

Figure 3.3 – Geological settings of the Piuro slope defined by the interplay between 3 different tectonic units. Anphibolite rock belonging to the Chiavenna Unit macroscopic (a) and optical microscope view (b). Migmatitic gneiss outcropping at the contact between Gruf and Chiavenna Unit macroscopic (c) and optical microscope view (d). Gneissic lithology distinctive of the Gruf unit macroscopic (e) and optical microscope view (f).

The Chiavenna Unit exhibits banded amphibolites, massive amphibolites, ultramafites (serpentinites with olivine and magnetite, talc-schists, chlorite-schists and amphibole-schists) and marbles. In the

landslide failure area, this Unit is mainly composed by banded amphibolites with biotite or epidote and rarely clinopyroxenes, and massive amphibolites made by millimetric to centimetric horneblende and plagioclase (Falappi 2012). The Gruf Complex includes biotite-feldspar migmatitic gneiss. Biotite orthogneiss with abundant centimetric mafic enclaves and migmatitic paragneiss with alternation of leucocratic (quartz and feldspar) and melanocratic (biotite, sillimanite and garnet) centimetric bands outcrops along the Piuro detachment zone (Montrasio and Sciesa 1988).

In correspondence of the transition between the two Units, mafic and gneissic rocks are highly foliated with pervasive planes of sub-millimiter to millimeter thickness. The prevailing lithology appears to be paragneiss with alternating bands of different mineralogical composition. The Tambò Nappe is not so widespread in the study area. It is present only as interbedded bodies in the Chiavenna Unit as paragneiss composed by millimetric to centimetric bands of quartz and quartz with feldspar layers alternated to biotite or white mica rich gneiss.

Optical microscopic observations of the three main lithologies characterizing the failure area (Figure 3.3) showed their composition and texture. The amphibolite samples (Chiavenna Unit) are mainly composed of amphiboles and plagioclase minerals (Figure 3.3 a-b). Plagioclase is found in aggregates of lenticular shape elongated parallel to the foliation, individual crystals have polysynthetic gemination with narrow and broad bands. The amphibole is elongated in a main direction (preferential shape orientation). Amphibolite presents a nematoblastic microstructure (hornblende prisms arranged in the foliation plane) with grain <1 mm. Transition paragneiss (migmatitic paragneiss belonging to the Gruf Complex) are composed of quartz, k-feldspar, plagioclase, brown-green biotite, white mica (Figure 3.3 c-d). The texture is gypsum-occhiadine characterized by the presence of centimeter-sized lentiform polycrystalline aggregates (porphyroblasts). The latter are largely composed of k-feldspar and feldspar crystals with myrmechitic textures. The foliation is weakly defined by the presence of phyllosilicate beds. Biotite beds are often anastomosed and locally joined by coarse lamellae of pale mica with the flaking traces perpendicular to the foliation. The undeformed magmatic gneisses of the Gruf complex are mostly composed of quartz, plagioclase, alkali feldspar, biotite, muscovite ± garnet, sillimanite (Figure 3.3 e-f). They are fine-grained and display an equigranular and interlobate texture characterised by rounded, subhedral to anhedral, up to 0.2 mm large quartz, plagioclase and perthitic alkali feldspar.

3.2.2.2 Geomorphological features

Geomorphological field surveys carried out along the slope, identified a failure zone, a sliding/accumulation zone and a deposition zone (Figure 3.4).

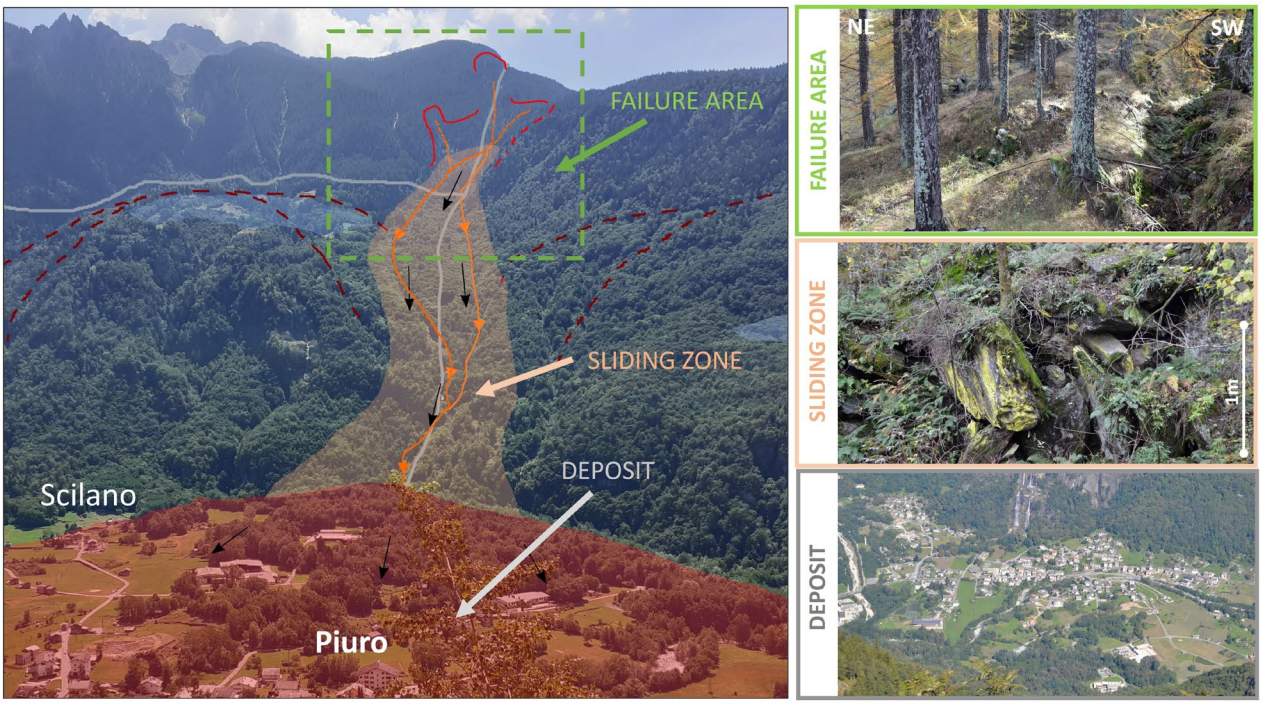

Figure 3.4 - Photo of the Piuro landslide taken from the opposite slope. Failure, sliding and deposit zones are highlighted.

Considering the topics covered in this work, this Section will mainly analyze the elements and processes that characterize the failure area. For detailed analysis about the characterization and reconstruction of the 1618 landslide deposit, please refer to the work presented in Pigazzi et al. 2022 and Pigazzi et al. 2023. All the geomorphological data and observations collected during the field surveys were collected into a map that shows the geomorphological shapes and deposits of the area. A cutout of the detachment area is presented in this work (Figure 3.5). The complete map of the entire Piuro slope is presented in Pigazzi et al. 2022.

The detachment zone is characterized by the presence of very pronounced morphologies with steep rock slopes interrupted by wide morpho-structural plateaus. Steep scarps were observed in correspondence of the Alpe Prato del Conte locality at an altitude of about 1430 m a.s.l. Here, flat morphologies covered by quaternary deposits are abruptly interrupted by traction trenches and steep rock-scarps Figure 3.5). Trenches have an ESE-WNW orientation and are characterized by a metric opening whose walls consist of strongly disjointed rock-masses (Figure 3.5).

The rock-scarps are tens of meters high and have a variable orientation moving eastward. At the Alpe Prato del Conte locality they are consistent with the direction of the trenches (ESE-WNW), varying to E-W and then NE-SW moving eastward (Figure 3.5). Other rock-scarps with NE-SW orientation are clearly evident upstream of the Alpe Prato del Conte toward the Mottaccio locality, at an elevation of about 1700 m a.s.l.

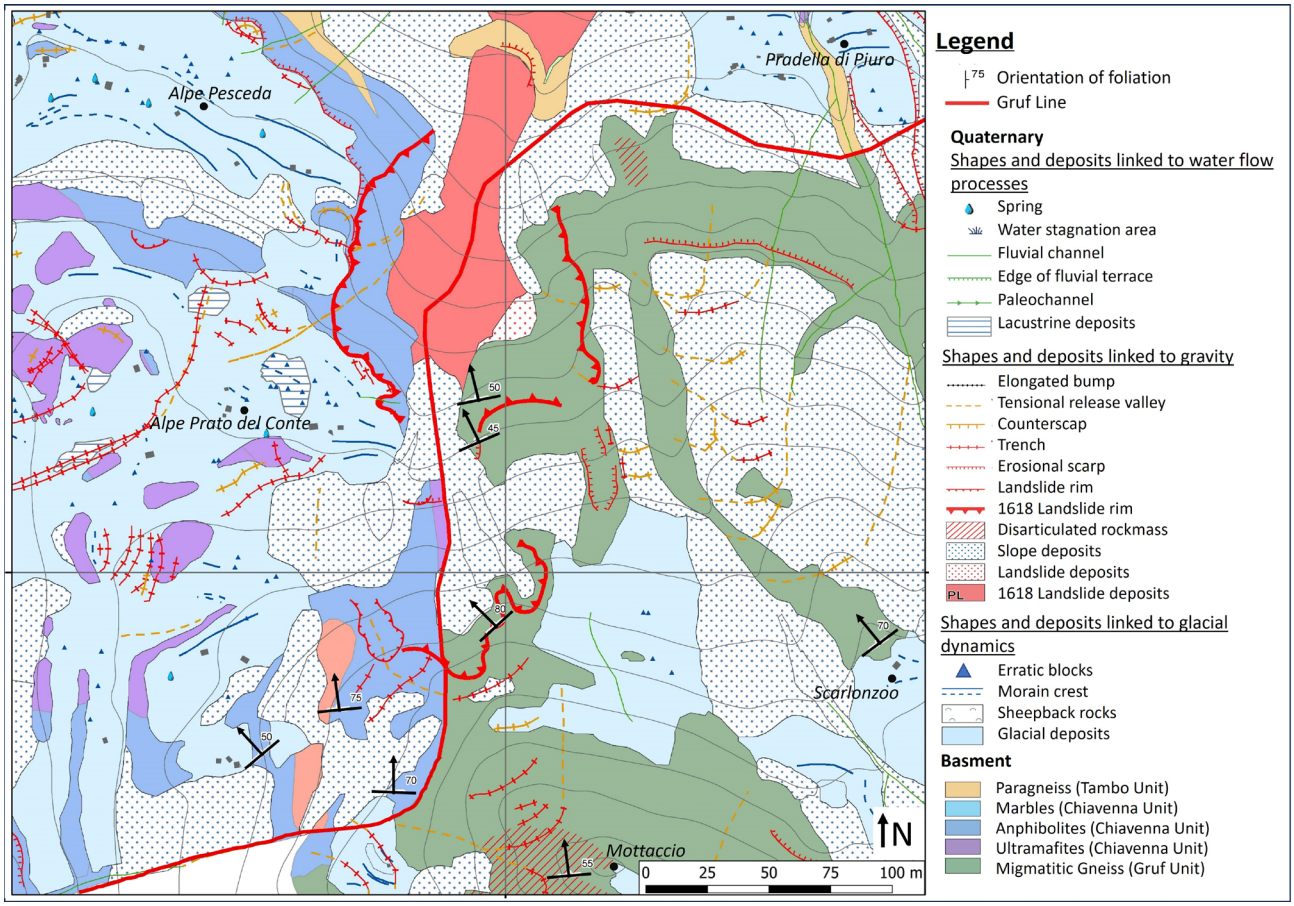

Figure 3.5 - Geomorphological map of the 1618 failure area.

According to Pigazzi et al. 2022 and other previous works (Scaramellini et al. 1995), the rock-scarps at Alpe Prato del Conte represent the area where the slope failure occurred during the 1618 event; the upper scarps, close to the Mottaccio peak, may have been originated by secondary gravitational events related to stress-release processes. A coeval genesis between lower and upper scarps is not visible in the field, but cannot be completely excluded. Rock scarps are still active, as highlighted by rockfall deposits present at their base without vegetation and featuring small boulders, that become larger moving downstream.

Along the slope, and in particular in the area of the failure event, two quaternary units were recognized: the glacial deposits of the Laghi Supersinthem (Late Pleistocene, Bini et al. 2014) and the slope and alluvial sediments of the post-glacial unit (Latest Pleistocene to recent). The glacial deposits consist mostly of massive homogenous to mildly graded and poorly stratified diamictons made up of gravels, cobbles and blocks, with a fair amount of sand and fines. Clasts are usually equidimensional from sub-angular to rounded, rarely faceted. Source is both local (paragneiss of the Tambò Nappe, orthogneiss of the Tambò Nappe and Gruf Unit, as well as amphibolites of the Chiavenna Unit) and regional (granitoids, micaschists and metapelites that are absent in the lower Bregaglia Valley). These deposits have been

interpreted as ablation tills and were found from about 500 m up to 2000 m a.s.l. on the slope. In the Prato del Conte area, glacial deposits are involved by slope failures, as they are bordered by scarps and affected by trenches that dislocate the underneath basement rocks (Figure 3.5).
The Postglacial unit, unconformably overlays both the bedrock and the Laghi Supersynthem sediments. In the failure area they are mostly represented by slope deposits, composed by decimetric to metric equidimensional to oblate angular to sub-angular clasts with open-frame texture or clast-supported with sands and minor fines, where clasts petrography is strictly related to the source areas.
These deposits are cut by deep incisions with an approximately N-S trend (Figure 3.5), which represent transporting material channels. From the failure area moving southward, toward the valley floor, chaotic deposits are present with metric rock boulders, often in a silty and sandy matrix (Figure 3.4). These deposits are ascribed to the 1618 event (Pigazzi et al. 2022). In the area investigated for the present work, only landslide transit deposits are present and located in a steep channel that descends from Alpe Prato del Conte towards Piuro (Figure 3.4, Figure 3.5).
The sliding mass, while moving down toward the valley floor, involved the glacial deposits constituting the morphological terrace of Alpe Prato del Conte, Pradella di Piuro and Alpe Moscone, which are clearly cut by the steep North-South morphological channel (Figure 3.5)

3.2.2.3 Geomechanical characterization

With the aim of defining the geomechanical features of the Piuro landslide failure area, a geomechanical characterization including detailed field surveys and laboratory tests on intact rock and discontinuities was performed. This allowed to outline the main characters governing the mechanical behavior of rock-masses and to obtain the data necessary for the elaboration of valid numerical models of the slope under investigation.

Field surveys

Geomechanical surveys, carried out along the few accessible walls of the main landslide scarp, showed a high variability of the mechanical quality of rock-masses related to lithology and fracturing degree. Following the ISRM suggested methods (ISRM 1981), four detailed geomechanical surveys were performed in the detachment area of the 1618 event (Figure 3.6).
Overall, four main discontinuity systems can be recognized: 300°/65°(*K1*), 60°/80° (*K2*), 180°/30° (*K3*), 350°/85° (*K4*).

- *K1* is set along the dominant foliation planes parallel to the Gruf Line, which is directed about 60°- 240° cutting the Valley axis at a low angle. It shows smooth surfaces with mean Joint

Roughness Coefficient (JRC) values of 8 and Joint Compressive Strength (JCS) of 110 MPa, detected following the ISRM suggested methods (ISRM 1981).

- *K2* is consistent with the regional 330°- 150° directed lineaments, widespread on both sides of the Valley and responsible for major secondary valley incisions. Joints show features of shear kinematics planes with very smooth surfaces (mean JRC values of 6 and JCS of 150 MPa).
- *K3* is a planar system with sub-horizontal surfaces cutting the vertical ones. It plays a significant role in the definition of rock-mass instability blocks along the slope. Joint surfaces show roughness features with mean JRC values of 11 and JCS of 100 MPa.
- *K4* dips vertically to the north and is mainly related to singular discontinuities with high persistency and very high spacing (> 10 m). Joint surfaces are rough (mean JRC values of 9 and JCS of 115 MPa).

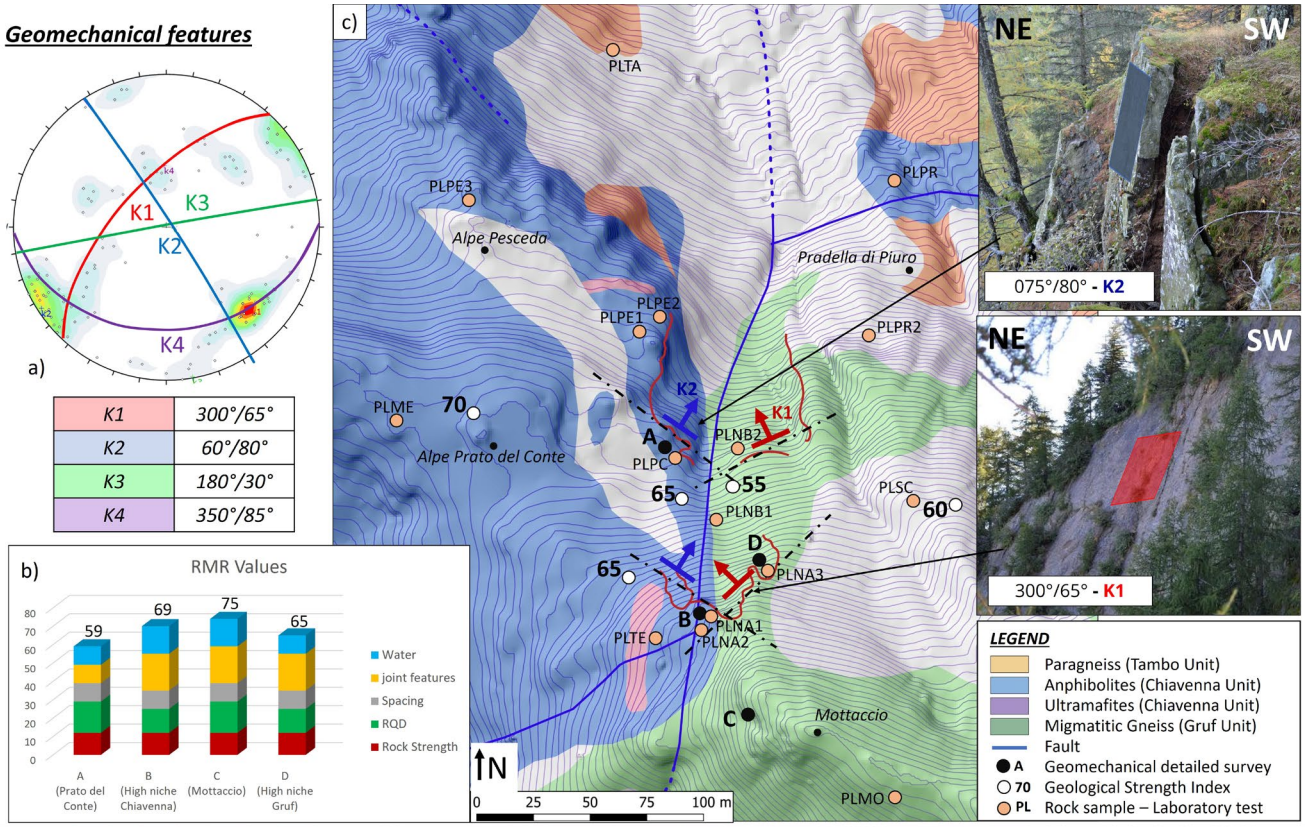

Figure 3.6 - Geomechanical features of the study area; a) Lower hemisphere stereographic projection of the main discontinuity sets detected from all the geomechanical surveys. Joint orientation is expressed by dip direction/dip; b) Rock-mass Rating values obtained from the four geomechanical detailed surveys conducted; c) Geological map showing the location of rock sample collected and geomechanical surveys conducted. Photos showed two rock-masses outcropping in correspondence of the lower and upper landslide niche. Two main discontinuity sets are highlighted with different colors.

The calculated RMR (Rock-mass Rating; Bieniawski 1974) and the evaluated GSI (Geological Strength Index; Marinos P and Hoek 2000) reveal a generally discrete to good rock-mass mechanical quality (RMR ranging from 59 to 74, GSI ranging from 55 to 65; see Figure 3.6). Due to a more intense

fracturing and a higher weathering degree of the rock-masses, lower values were detected at the Alpe Prato del Conte locality, close to the subvertical tension trenches and along the main scarps of the lower niche. Moreover, in correspondence of the Mottaccio locality, upstream of the detachment zone, highly fractured rock-masses (with metric openings of discontinuities) were detected. The fracturing condition is predominantly subvertical with E-W and N-S directions; two sets of discontinuities with lower inclination are also present, one dipping toward NW and one dipping to E horizontally. The discontinuity network isolates cubic blocks greater than one cubic meter and represent a preferential zone of water infiltration during rainfalls.

According to the orientation of the main landslide scarps, the right flank of the 1618 event is set along the *K1* discontinuity system, while the left flank is set along the *K2* one (Figure 3.6). As a result of the geometrical features of the discontinuity network, gravitational instability along the slope is favored by the orientation of the vertical joint systems relative to the slope direction. High persistent *K1* and *K2* shear surfaces may act as a sliding plane of significant volumes of rock material, that can be isolated upstream by the *K4* tensile system or even by the planar *K3* system. Moreover, in the presence of highly fractured rock-masses with highly persistent and opened joints rockfalls events are frequent, mainly as toppling or sliding evolution of blocks and rock-towers.

Laboratory tests

Intact rock

A rock sample collection campaign was carried out in the area of the 1618 landslide detachment (Figure 3.6), covering both the Chiavenna Unit and the Gruf Complex. Marginally, samples from the Tambò Fault were also collected, mainly for petrographic analysis.

To study the mechanical behavior of intact rock, uniaxial compression tests under unsaturated conditions were conducted according to ASTM standards (D7012 – 14; ASTM, 2014). The following Table 3.1 collects the results obtained on the tested specimens. For the gneissic samples of the Gruf complex, the tested lithology is characterized by migmatitic paragneiss with alternation of leucocratic (quartz and feldspar) and melanocratic (biotite and sillimanite) millimetric bands. It follows that a dependence of the mechanical behavior in relation to the direction of the load with respect to the mean orientation of the foliation planes, was observed. Strength and deformability of the material are found to be slightly higher if the load is applied perpendicular to the foliation planes. The rock exhibits a uniaxial compressive strength (UCS) varying from 73 to 108 MPa with a Young modulus (E) of 20-32 GPa and a mean Poisson ratio (υ) of 0.34.

Table 3.1 – Results from uniaxial compressive tests conducted on samples collected along the slope. See figure 3.6 for they location.

Uniaxial compressive tests					
Sample code	**Geological Unit**	**Density [g/cm^3]**	**Young Modulus [GPa]**	**Poisson ratio**	**Uniaxial compressive strength [MPa]**
PLNB1	Chiavenna	2.80	45.0	0.40	165.00
PLTA	Tambò	2.50	30.0	0.41	80.00
PLNA1	Gruf	2.65	30.0	0.38	108.20
PLNA2_a	Gruf	2.60	32.3	0.40	107.20
PLNA2_b	Gruf	2.60	22.0	0.36	73.43
PLNA2_c	Gruf	2.60	20.0	0.25	99.73

In contrast, the amphibolite of the Chiavenna Unit has a more massive texture that gives the material greater compressive strength and less deformability. Values of compressive strength (UCS) of 165 MPa, Young modulus (E) of 45 GPa and a Poisson ratio (υ) of 0.4, were obtained. They were also compared with data obtained from previous tests conducted on amphibolite collected in the Valchiavenna region (master's and bachelor's theses in Earth and geological sciences – Università degli Studi di Milano), showing behavior congruent with that obtained in this work. The mechanical behavior of the Tambò Unit reflects a higher degree of weathering of the tested material, with lower strength and deformability properties than the previous ones. As an example, the laboratory certificate for a uniaxial test conducted on a sample of gneissic rock is given below (Figure 3.7).

UNIAXIAL COMPRESSIVE TEST			ASTM D7012-14. Metodo D
CLIENT:	Andrea Morcioni	DATA:	2022-06-23
LOCALITY:	Piuro Landslide	WORKER:	M. Perfido, A.Morcioni, P.Di Pietro
SAMPLE:	PLNA2_C	MACHINE:	Pressa Controls (500N), Advantest 9, software Controls Triaxrocks
DEPTH (m):	Outcropping		
LITHOLOGY	Ortogneiss	TIPO DI PROVA:	Monoassiale a controllo di spostamento

PICTURE

NOTE: Axial load applied perpendicularly to the plane of schistosity

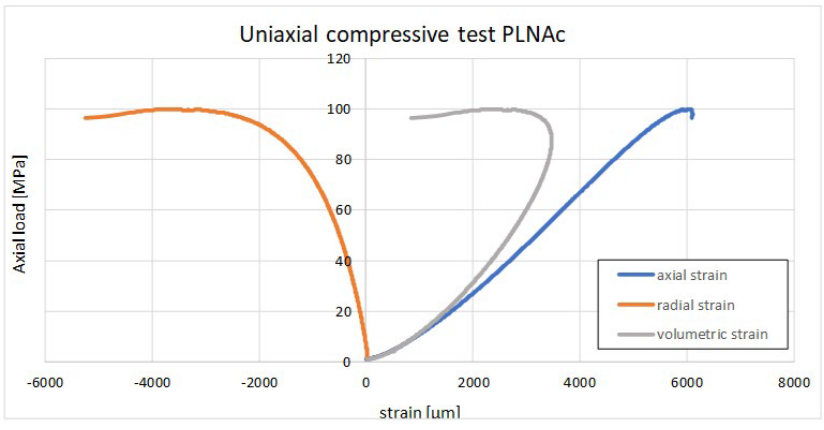

Compressive uniaxial strength	σ_c	99.73	MPa
Elastic modulus - tangent 50% of σc	$E_{t50\%}$	20.00	GPa
Elastic modulus - secant 50% of σc	$E_{s50\%}$	16.34	GPa
Mean elastic modulus	E_{av}	17.80	GPa
Poisson Coefficient	ν	0.25	-

Note: breaking after 1775 s (about 29.5 minutes). Fracture along an inclined plane between 20 and 25 °

Figure 3.7 - Laboratory certificate for a uniaxial test conducted on a gneissic rock sample.

Discontinuities

To study the mechanical behavior of discontinuities, a direct joint shear test was performed according to ASTM standards (D5607 – 08; ASTM 2008) on a representative discontinuity surface belonging to the *K1* set. The joint surface has been sampled at the high niche (*PLNA* in Figure 3.6), according to the ISRM standards for the outcropping joints (ISRM 2015). From the sampled surface, five specimens were obtained, useful for performing the laboratory mechanical test. Each specimen was subjected to three shear mechanical cycles in order to investigate both peak and residual values of the material. Results are summarized in Table 3.2.

Table 3.2 - Results from direct shear joint tests conducted on a discontinuity sample belonging to the K1 set.

Direct shear joint tests						
Test	σ_N (MPa)	Loading rate (MPa/s)	n° cycle	τ_P (MPa)	τ_r (MPa)	Shear displacements at peak (mm)
GB1_T1	1.0	0.08	1	1.06	0.71	1.357
GB1_T2	1.0	0.08	2	0.64	0.73	11.57
GB1_T3	1.0	0.08	3	0.70	0.66	13.60
GB2_T1	1.5	0.08	1	1.27	0.98	0.97
GB2_T2	1.5	0.08	2	0.62	0.73	0.90
GB2_T3	1.5	0.08	3	0.46	0.74	2.55
GB3_T1	2.0	0.08	1	1.70	1.16	1.12
GB3_T2	2.0	0.08	2	1.12	1.11	8.16
GB3_T3	2.0	0.08	3	1.07	1.13	7.16
GB4_T1	4.0	0.08	1	2.73	2.60	2.03
GB4_T2	4.0	0.08	2	2.00	2.13	4.54
GB4_T3	4.0	0.08	3	1.85	2.08	1.91
GB5_T1	6.0	0.08	1	4.61	3.60	7.84
GB5_T2	6.0	0.08	2	2.97	3.60	2.30
GB5_T3	6.0	0.08	3	3.06	3.12	2.46

At the first mechanical shear cycle (i.e., undisturbed surfaces), a softening behavior is shown, related to the presence of asperities that generate frictional resistance. Since the surface is not smooth, the upper block needs high stress (i.e., peak resistance) to overcome the asperities and slide on the lower one. According to the Mohr-Coulomb criterion, a value of peak friction angle (ϕ) of 34.8° with a cohesion (c) of 0.25 MPa was obtained (Table 3.3). Shear cycles after the first one (i.e., disturbed surfaces), showed a hardening behavior with lower shear strength. In fact, the surface is progressively abraded and modeled to a smooth plane. The residual friction angle dropped to a value of 25.0° (Table 3.3).

At each mechanical cycle, the morphological changes reported on the joint surface (roughness, alteration, distance between the two blocks) were analyzed, using manual (Barton comb) techniques. The results showed a strong dependence between surface morphology and slip resistance, with a progressive flattening of the surface as the cutting cycles progressed.

Table 3.3 – Shear strength parameters calculated from Barton-Bandis (Barton and Bandis 1982) and Mohr-Coulomb (Coulomb 1776) equations.

Shear strength						
Barton-Bandis criterion			*Mohr criterion*			
JCS	83	[MPa]	ϕpeak	34.79	[°]	**First mechanical cycle**
JRC	7		c peak	0.26	MPa	
ϕresidual	28.89	[°]	ϕresidual	31.65	[°]	
			c residual	0	MPa	
			ϕresidual	25.02	[°]	**Last mechanical**
			c residual	0	MPa	

Following the ISRM suggesting methods (ISRM 2015; Kulatilake et al. 2016), normal (*Kn*) and shear stiffness (*Ks*) were defined (Section 2.1). The detected values vary between 1.50 GPa/m to 4.08 GPa/m for *Kn*, and between 1.01 GPa/m to 1.45 GPa/m for *Ks*, depending on morphological and surface weathering conditions. As an example, the laboratory certificate for a joint direct shear test conducted on a sample belonging to the K1 discontinuity set is given below (Figure 3.8).

JOINT DIRECT SHEAR TEST

Client:	Morcioni Andrea	DATA :	18/12/2020
Loaclity:	Piuro Landslide - Mottaccio	Test n°	1
Type:	Outcropping natural joint	OPERATOR:	Morcioni Andrea, Lombardini Sofia
Name of the sample:	GB_3	NOTE:	

FEATURES OF THE SAMPLE

Geometrical features	Width [mm]	86	Mechanical features	JRC	7
	Length [mm]	73		JCS [MPa]	83
	Area [mm^2]	6278			

FEATURES OF THE TEST

Step 1: axial load		Step 2: shear load	
Velocity [MPa/s]	0.1	Velocity [N/s]	Manual hydraulic pump
Target [MPa]	2		
N° steps	4		

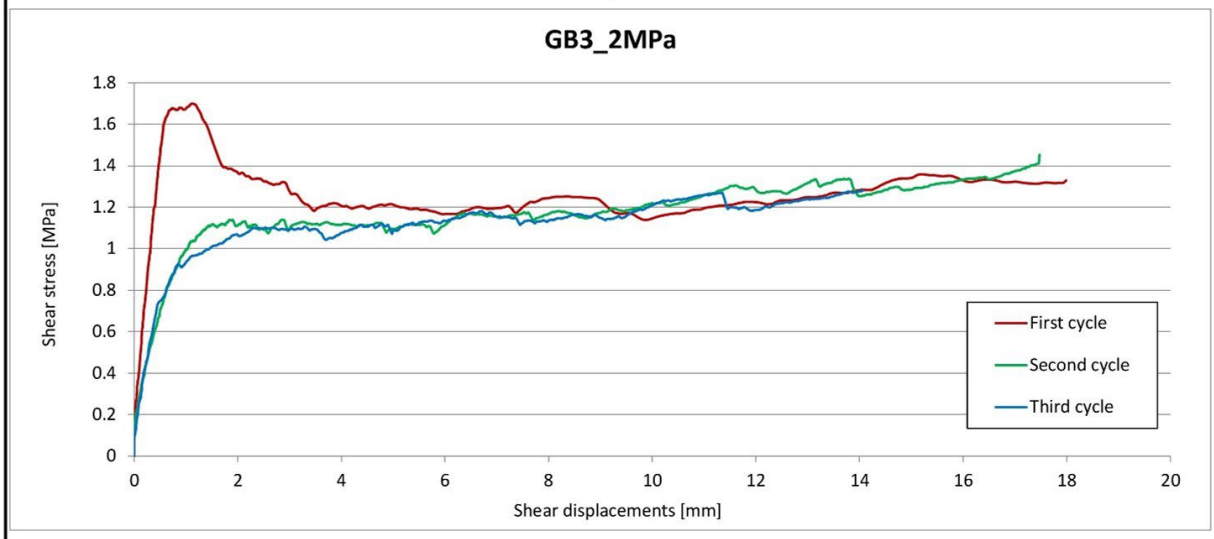

Picture of the sample surface (top)

First shear cycle	Third shear cycle
	

Figure 3.8 - Laboratory certificate for a direct shear test conducted on a discontinuity rock sample belonging to the K1 system.

3.2.3 Definition of a geomechanical conceptual model

Summarizing the observations highlighted and discussed in the previous Sections (3.2.2.1, 3.2.2.2, 3.2.2.3), the mechanical evolution of the Bregaglia southern slope above the village of Piuro, is related to the presence of significant tectonic elements (Section 3.2.2.1, Figure 3.1). The first one, with an E-W direction (Gruf line), runs parallel to the main valley axis and drives the development of large-scale tension release processes. Morpho-structures field evidences are represented by the presence of numerous deep seated gravitational slope deformations (DSGDS) aligned along the slope and culminating in apical plateaus in correspondence of the Gruf line outcropping. The second tectonic element, with a N-S trend, cuts and deform the previous one in correspondence of the Piuro landslide failure area. Its presence is highlighted by deep morphological incisions moving from the top of the slope to the bottom of the valley, following the same direction trend. As reflected by field evidences, it is clear that these two elements play a significant role in the slope mechanical evolution, and therefore must be necessarily considered in a conceptual geological and geomechanical model of the slope.

The geological setting is mainly defined by the interplay of three tectonic units that outcrop along the slope: the Chiavenna Unit, the Gruf Unit, and the Tambò Nappe (Section 3.2.2.1, Figure 3.1). If the extension of the Gruf Unit is well delineated and bounded on the N and W by the previously described tectonic elements, the limit between the Chiavenna and Tambò Units is more difficult to define. However, the mechanical behavior of the slope on this section, seems to be more influenced by the presence of the mafic and ultramafic rocks belonging to the Chiavenna Unit. As evidenced by field investigations in the study area (Section 3.2.2), this Unit has in fact a greater areal extent and rheological importance compared to the Tambò Nappe, occurring only as intercalation bodies. The presence of lithologies belonging to the Tambò Unit increases considerably moving eastward toward Villa di Chiavenna locality, where it becomes the predominant geological unit (Figure 3.1).

With the goal of defining the geological framework of the Piuro landslide failure area, the portion of the slope S and W the Gruf line can therefore reasonably be represented by a single unit homogeneously composed of mafic and ultramafic rocks of the Chiavenna Unit. Consequently, the geological conceptual model of the slope is characterized by a direct contact between gneissic (Gruf) and mafic (Chiavenna) lithologies in correspondence of the N-S tectonic element. On the other hand, along the E-W one, the contact is more gradual and characterized by the presence of highly fractured lithologies that could be in first assumption be assimilated to the Tambò Unit.

Moving to a geomechanical prospective, the rock-masses outcropping along the slope are moderately fractured with medium to good mechanical qualities (Section 3.2.2.3). Geomechanical surveys carried out, showed a general mechanical homogeneity of the rock-masses outcropping, with no significant

differences between the geological units. The discontinuity sets identified are repeated congruously throughout the investigated area, considering both geometrical and mechanical features. Except for a few cases (e.g., Mottaccio locality), the slope evolution does not seem to be governed by significant or particularly persistent discontinuity elements. Rather, its geomechanical evolution is believed to be controlled by the different rheological behaviors of geological unit outcropping and the tectonic elements affecting it. Following these observations, a model of the slope will be constructed in the next section 3.2.4 (Figure 3.9).

3.2.4 Hydro-mechanical analysis

In this Section, the stress-strain evolution of the Piuro slope is analyzed. Starting from the geological conceptual model defined in Section 3.2.3, a mechanical 3D model is now defined including all the data and observations collected in previous Section 3.2.2.

The development of mechanical failure elements and zones of high deformation induced by rainfall events is here analyzed through a coupled HM analysis and applied to the Piuro landslide. The aim is to assess whether the 1618 event was promoted by the complex geological settings of the slope and whether its triggering factor may be represented by an intense rainfall event, as reported by historical writings.

Starting from the key points discussed in Section 3.2.3, it is considered valid to follow a continuum numerical modeling approach, in order to analyze the rheological contrast and the mechanical role of the tectonic elements separating outcropping geological units along the slope. With this aim, the representation of rock-masses as continuous media in which the presence of discontinuities is represented implicitly, is considered a valid approximation.

3.2.4.1 Methods

Numerical analysis of the Piuro rock-slope was performed using the finite difference (FDM) code FLAC3D (version 7.0 – Itasca 2019; Zabuski 2019; de Ojeda et al. 2021), presented in Section 2.3.

Modelling approach – Definition of a mechanical model

The model domain develops along the southern slope of the Bregaglia Valley. It extends from Prosto to Santa Croce villages to the N and from the Corna di Garzonè peak to the Schiesone Valley to the S (Figure 3.1). It includes Bregaglia Valley with Mera River, Aurosina Valley with Aurosina River and Schiesone Valley with Schiesone River. The base of the model has a rectangular shape with a short side

(the E-W side, parallel to the Bregaglia Valley) of 3600 m in length and the long side (the S-N side, perpendicular to the Bregaglia Valley) of 4200 m. It covers an area of 15,768,800 m^2 calculated on the topographical surface. The highest elevation of the model is 2385 m a.s.l. in correspondence of the Corna di Garzonè peak and the lower one is 364 m a.s.l in correspondence of the Prosto Village along the Mera River.

Starting from the conceptual model of the slope defined in Section 3.2.3, the development of the mechanical model required a number of steps. The first one involved the reconstruction of the topography prior to the 1618 landslide event. This is based on the 2015 Digital Terrain Model of the Lombardy Region (5 m of resolution), modified by reproducing the pre-failure topography conditions, considering the volumes of the failed rock-mass and assuming a continuity with the lateral slopes. Since the aim of this study is to analyze the triggering mechanisms of the 1618 failure, only the portion of the slope representing its detachment zone was reconstructed. This is considered acceptable, since the morphology of the valley bottom is not expected to affect the stress-strain evolution in the upper part of the slope where the slope failure occurred.

A second step involved the 3D reconstruction of the geological elements outcropping along the slope, using the software Geomodeller (Version 3, Intrepid Geophysics 2014). Starting from geological maps (Figure 3.9a, Montrasio and Sciesa 1988) it was possible to define the 3D geology by considering orientation data measured along the slope and their relationships with the topography (Figure 3.9b).

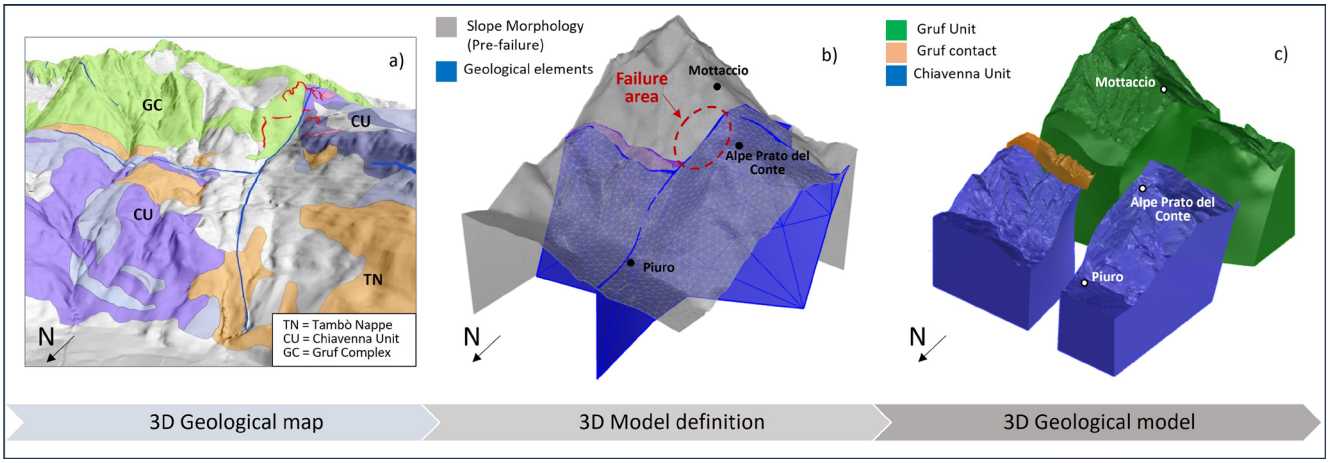

Figure 3.9 – Definition of the geological model used for numerical calculation.

Planar elements representing faults and tectonic lineaments were then exported from Geomodeller and imported as surface bodies in the meshing tool Rhinoceros (version 6.0, McNeel 2010). Here, through Boolean operations between the topographical surface and geological planar elements, the blocks representing the different tectonic units were created: Chiavenna unit, Gruf unit and Tambò unit. These

blocks were then introduced in a subsequent step in FLAC3D as separate units with a finite volume. Blocks were discretized into a finite-difference grid by the definition of hexahedral zones (Figure 3.10a), which enable simple and high-performance definition (Abbassi et al. 2013). A maximum zone size of 80 m was set, letting the software automatically creating a best-fitting grid considering the input morphology, allowing a significant reduction in computation time. Given the overall extension of the model domain, resulting in a side length of over 3 km, a zone size of 80 m is deemed sufficient to capture the general behavior of the slope. A total number of 121,228 zones were thus created resulting in 866,260 nodes.

Contact between blocks representing the geological separation between tectonic units were set as mechanical interfaces, which can deform following assigned strength and stiffness parameters (Table 3.4). On the other hand, adjacent zones that are not characterized by geological evidence of the presence of a fault (Figure 3.1) were merged using the "attaching" tool, defining a single coeval body.

Boundary conditions of fixed zero velocity are specified along the bottom boundary of the model domain and fixed normal zero velocity was set along the side boundaries (Figure 3.10b).

As the model was defined and the boundary conditions were set, mechanical properties were introduced using the Hoek & Brown failure criterion (Hoek 1988; Section 2.1).

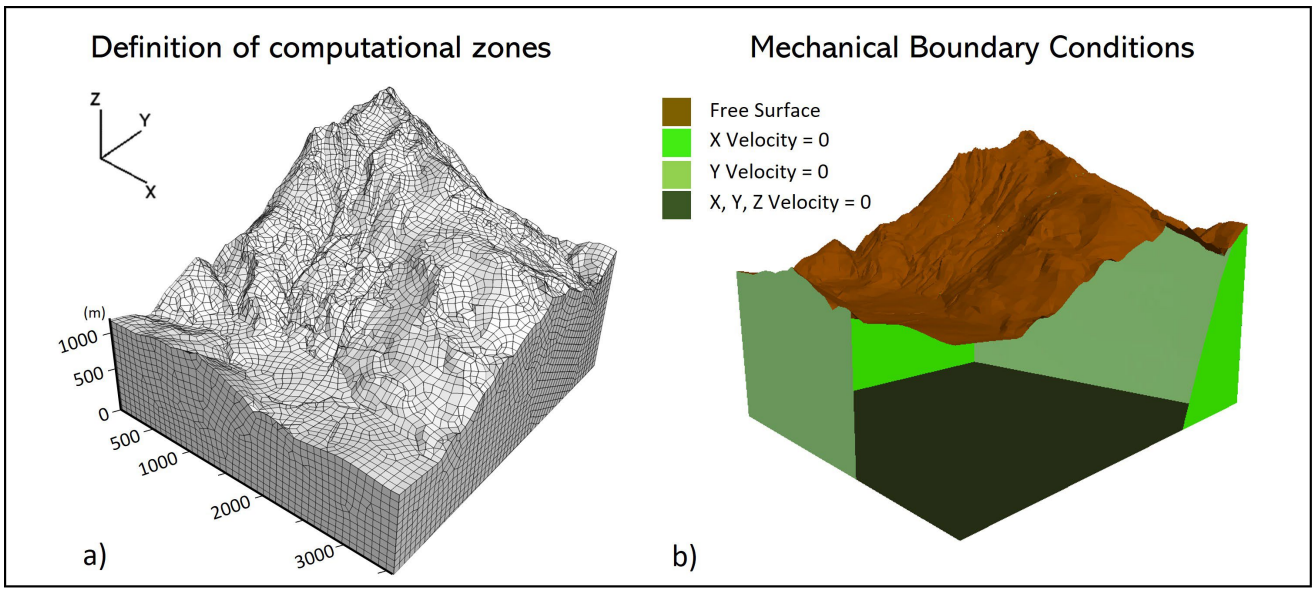

Figure 3.10 – a) Discretization of the model into hexahedral computational zones; b) Mechanical boundary conditions including fix velocity at the base of the model and roller boundaries at its sides.

Rock-mass strength parameters were calculated by applying the GSI approach considering results from geomechanical surveys and laboratory tests (Section 3.2.2.3). The resulting parameters estimated for the study area are presented in Table 3.4 and Figure 3.11. Two different mechanical property scenarios were

calculated considering the measured maximum and minimum values. For interfaces, the Mohr-Coulomb criterion was adopted, and relevant strength and deformability parameters were defined from laboratory tests.

Table 3.4 - Mechanical elasto-plastic properties of blocks and interfaces.*) Derived from laboratory tests conducted as part of the present study. **) Derived from laboratory tests conducted by Apuani T. (Master's and bachelor's theses in Earth and Geological sciences – Università degli Studi di Milano - work not published).

Mechanical properties of Blocks			
	Chiavenna Unit (scenario1/ scenario2)	Gruf Unit (scenario1/ scenario2)	Tambò Unit (scenario1/ scenario2)
Uniaxial Strength [MPa]	165*/ 150**	110* / 100*	80* / 70**
GSI	70 / 60	65 / 55	50 / 50
m_i	26 / 26	28 / 28	16 / 16
D	0.8 / 0.8	0.8 / 0.8	0.8 / 0.8
E_i [MPa]	45000 / 40000	40000 / 30000	30000 / 25000
m_b	4.36 / 2.404	3.486 / 1.923	0.612 / 0.454
s	0.0106 / 0.00233	0.00498 / 0.00109	0.000513 / 0.00024
a	0.501 / 0.503	0.502 / 0.504	0.506 / 0.508
Poisson ratio (υ)	0.4** / 0.4**	0.3* / 0.3*	0.4** / 0.4**
Density [Kg/m^3]	2800*	2600*	2500*
Interfaces* (scenario 1/ scenario 2)			
Peak friction angle [°]		35 / 28	
Peak Cohesion [MPa]		1 / 0.1	
Residual friction angle [°]		25 / 25	
Residual Cohesion [MPa]		0 / 0	
Tensile strength [MPa]		1 / 0.1	
Normal Stiffness [GPa m^{-1}]		5 / 5	
Shear Stiffness [GPa m^{-1}]		1/ 1	

Considering that the aim to evaluate the role of geological features along the slope as preparatory factors for the 1618 landslide event, the development of a landslide body was not forced in the model by artificially introducing a sliding surface.

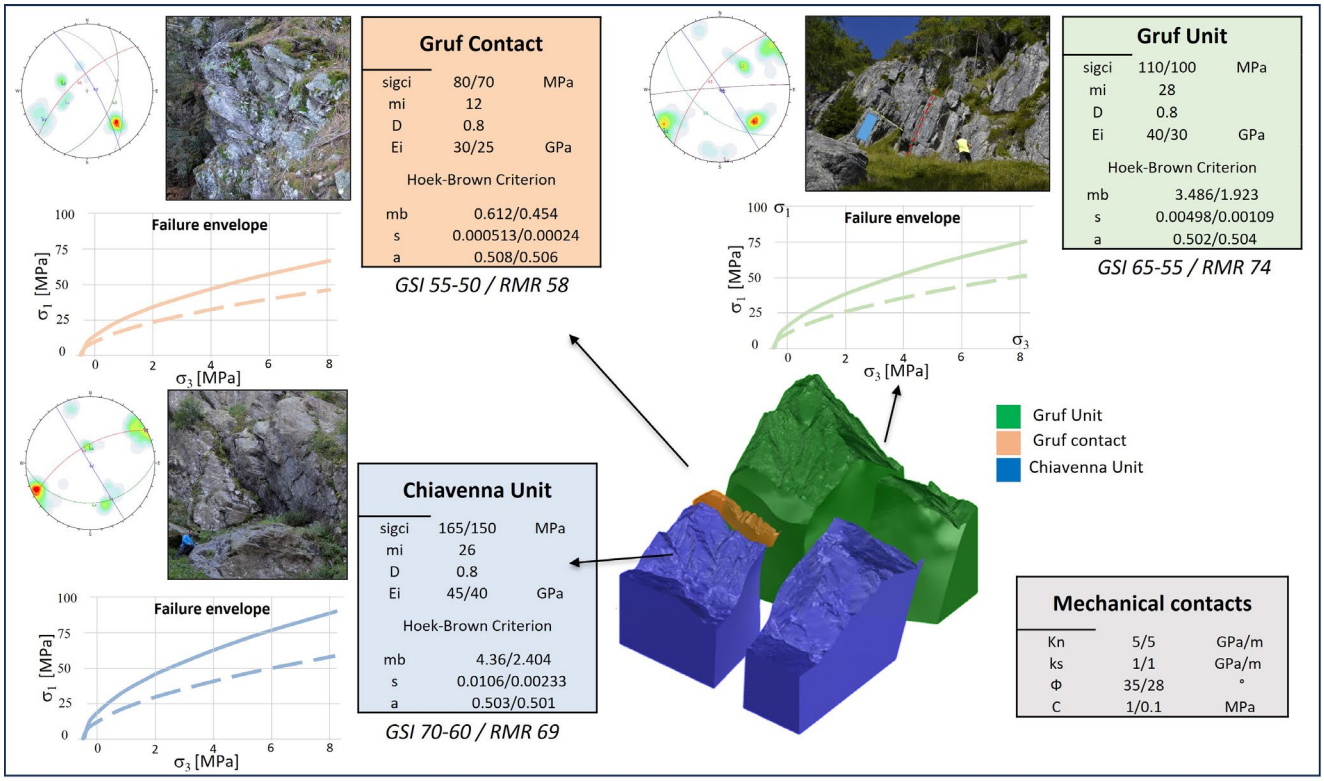

Figure 3.11 - Geomechanical definition of the slope by introducing properties resulting from site-specific survey and laboratory activities. The double value reported refers to two different geomechanical scenarios.

Modelling approach – Definition of a hydrogeological model

A 3D transient groundwater flow simulation was carried out using the FLAC3D software in order to simulate the triggering rainfall event. Due to the absence of direct piezometric measurements in the slope, some hydrogeological assumptions were made. The basal water table was introduced accounting for the presence of the Mera, Aurosina, and Schiesone rivers flowing on the bottom of the valleys surrounding the Piuro slope. The resulting basal piezometric level would cross the slope of interest only on its lower part, laying largely below the detected slip failure surface of the studied landslide (Figure 3.12a). This level represents the starting condition for the subsequent transient hydrogeological analysis. The principal assumption in the hydrogeological model is that the slope is only recharged by water infiltrating from its surface during rainfall events. Deep groundwater recharge is not considered in this stage of the modelling procedure. This assumption was necessary as lateral and deep flow contributions are difficult to estimate in the absence of measured data. As the aim of this work is to analyze the failure mechanisms developed in the subsurface of the slope, this assumption is not considered to exert a significant influence in the magnitude of pore pressures at shallow depths. Groundwater flow modelling is used, in this context, to reproduce the pore pressure evolution over space and time, without studying the groundwater flow system in detail.

Rock-mass' principal hydraulic conductivities were calculated by define the permeability tensor, considering joint orientation, JRC, aperture and fracture frequency of each discontinuity set (Lotti et al. 2012). A value of equivalent hydraulic conductivity $k_{eq}=1.51\cdot10^{-7}$ m/s was calculated considering the collected data from geomechanical surveys (Section 3.2.2.3). Even if a small difference was found between the Chiavenna ($1.75\cdot10^{-7}$ m/s) and Gruf Unit ($1.27\cdot10^{-7}$ m/s), as a first step of the analysis a homogenous hydrogeological unit was introduced, in order to reduce computational costs. The material was assumed to be isotropic in agreement with field observations that showed a fracture network composed of a system of discontinuities orthogonal to each other (Section 3.2.2.3). Moreover, in this model the interfaces were assumed to be fully permeable.

The definition of the landslide triggering factor involved the analysis of the rainfall regimes. According to historical notes, the 1618 failure was preceded by a heavy rainfall event that persisted during the entire week before the landslide occurred. However no measured data are available. To identify a possible rainfall triggering value, meteorological data relative to the most significant landslide events that affected the Valchiavenna and Valtellina region in recent decades were collected, considering the closest climate station available (Valtellina 1987: Chiavenna station; Cimaganda 2012 rockslide: San Giacomo Filippo station; Villa di Chiavenna 2019 rockslide: Villa di Chiavenna station; Chiavenna 2021 landslide: Villa di Chiavenna station). They were related to the rainfall probability curves calculated for the Piuro area based on data collected by ARPA's (Regional Agency for Environmental Protection) measurement stations (http://iris.arpalombardia.it/; Figure 3.12b). This method is based on the current meteorological data set and assumes that the pluviometric regime did not vary during the past centuries. Although this can lead to significant errors when forecasting and early-warning scenarios are analyzed, in this paper the method is only applied to find a reasonable rainfall data with which to perform the HM analysis.

Based on the meteorological data, a hypothesis coincident with a return period of 200 years, corresponding to a duration of 5 days and a total accumulated water of 345 mm, was made. This trigger rainfall value was introduced as constant rainfall intensity, and a vertical infiltration value of $8\cdot10^{-7}$ m/s was calculated assuming the absence of surface runoff. The infiltration function evaluated over time represents the input data for the transient HM analysis, in which the hydrogeological boundary conditions are represented by (Figure 3.12a):

- Function over time of vertical water infiltration along slope surfaces ($8\cdot10^{-7}$ m/s for 432,000 sec);
- Zero pore pressure along the Piuro Valley floor, Aurosina Valley, and Schiesone Valley, simulating the presence of streams;
- No flow along the sides and at the base of the model.

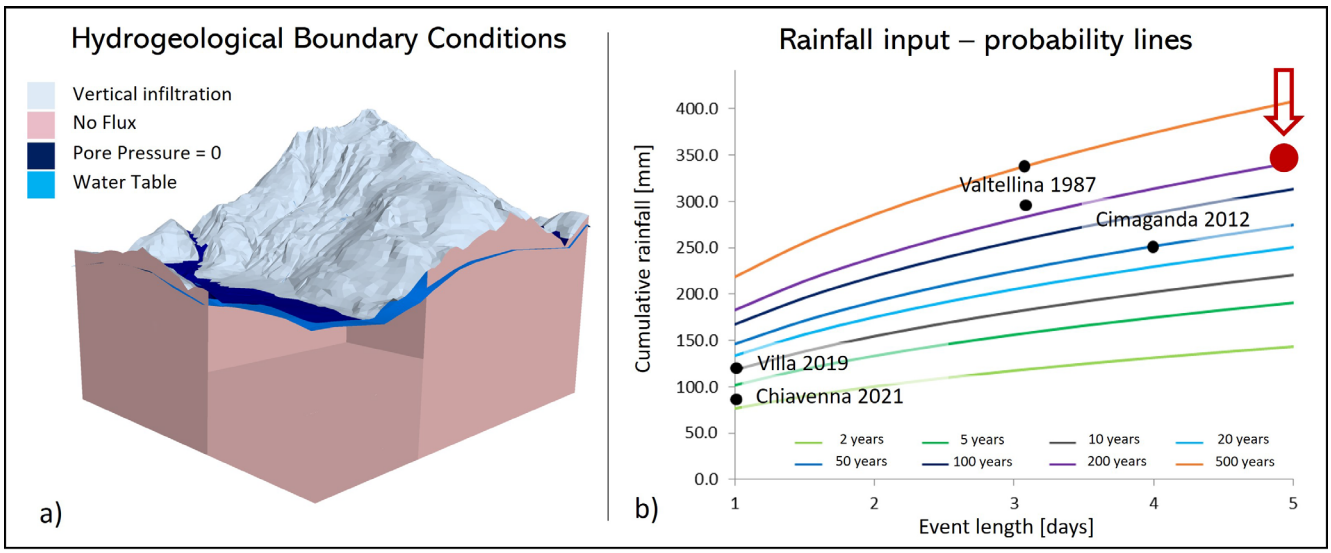

Figure 3.12 - Definition of HM analysis; a) Boundary conditions of the hydrological model; b) Rainfall probability curves for different return periods. Red circle indicates input value, defined by evaluating rainfall scenarios in the study area.

Modelling procedure

The modeling procedure involved in a first step the definition of the stress state along the slope under elastic conditions, which was followed by the calculation of plastic deformations under both dry and saturated conditions.

Given the complexity of the geometries and the large number of elements in the model, the initial elastic stress field due to the gravity load and topography constraints was calculated by a mechanical initialization until force-equilibrium was reached in dry conditions (*Step 1*). Once the initialization procedure was completed, the effect of groundwater in the effective stress state was evaluated introducing a static piezometric level, determined considering the local ordinary hydrogeological regime (Figure 3.12a*; Step 2*). The effective stress state distribution resulting from *Step 2* was used as the starting point for the subsequent elasto-plastic calculation, where, once the elastic displacements and velocities (deemed meaningless) were set to zero, the global equilibrium state was recalculated (*Step 3*).

A lowering of strength and deformability properties, representing the mechanical degradation of the rock-masses, was then established by reducing the GSI index (and consequently the Hoek & Brown strength parameters) from the geomechanical "scenario 1" to "scenario 2" (Section 3.2.4.1, Table 3.4) consistently with field observations, and elasto-plastic equilibrium was recalculated (*Step 4*). Next, the effects of a triggering rainfall event were simulated using a fully coupled HM analysis. Rainfall and hydrogeological conditions were reproduced by a transient groundwater flow analysis, specifying a vertical infiltration along the slope (Section 3.2.4.1). The HM formulation was solved by the FLAC3D code using an explicit finite difference scheme with an automatically computed timestep of 18 seconds (*Step 5*).

Following the concept of progressive failure mechanism, *Steps 1 to 4* aim at reproducing the preparatory stages leading the system to a progressive mechanical degradation. This causes a general strength reduction and an increase in the slope deformations. In the last *Step 5*, the introduction of rainfall would represent the ultimate collapse triggering factor.

3.2.4.2 Results

The output of the above outlined numerical analysis is evaluated in terms of stress-strain field redistribution in the rock-mass domain and the development of plastic strain and failures. The impact of groundwater circulation in the stress-strain field, is assessed by comparing results between different steps of the analysis. To evaluate localized stress changes and possible plastic strain localization, some monitoring points were defined at different depths along the slope where the failure zone of the 1618 event was located. Different 2D sections with N-S direction orthogonal to the valley axis were analyzed. Following the modelling procedure presented in Section 3.2.4.1, at the first initialization *Steps* (*1-2*), it was possible to reconstruct the stress states along the slope given by gravity, considering topographic constraints. The pore pressures are zero in correspondence with valley bottoms, and gradually increase with depth consistent with the water table boundary conditions (Figure 3.13a).

Figure 3.13b shows the vertical effective stress contours (σ'_{ZZ}) and the orientation of the stress tensor. It can be observed that the major principal stresses (σ'_1) are directed according to the maximum slope gradient and have an orientation parallel to the slope surface with an inclination angle of about 40°. Their inclination decreases rapidly in the valley floor.

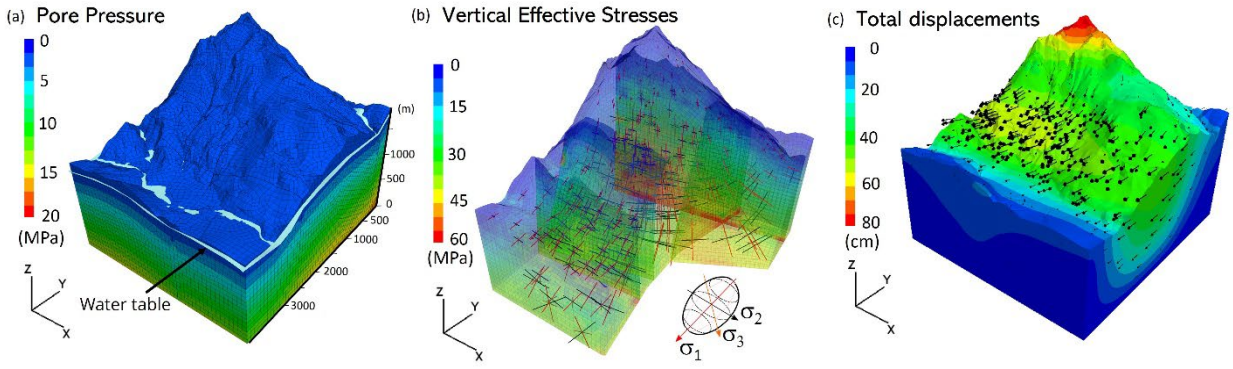

Figure 3.13 - Pore pressures (a), effective stresses (b), and total displacements (c) simulated along the modelled slope at the initialization phase.

The distribution and magnitude of the simulated total displacements are consistent with the slope morphology: their vertical component (of the order of 1 m) is maximum in the upper portion of the slope,

while the horizontal one (of the order of 0.9 m) is largest in its central part (Figure 3.13c). At *Step 3*, using high strength parameters for the rock-mass and with standard hydrogeological conditions, no failure conditions are reached, neither within rock-mass elements nor along geological interfaces (Figure 3.14 b-c).

The reduction of geomechanical properties (*Step 4*) induces a significant increase in the number of failed elements and a slight increase in the shear strain modulus. An area of large displacements (with maximum values of 1 m) develops along the N-S lineament at an altitude of about 1400 m a.s.l., close to the Alpe Prato del Conte locality. Consistently, plastic shear and tensile failures begin to develop in the same area up to a maximum depth of 200 meters from the slope surface (Figure 3.14 d-f). Even if an instability attitude is evident along this portion of the slope, a critical condition is not yet reached at this stage.

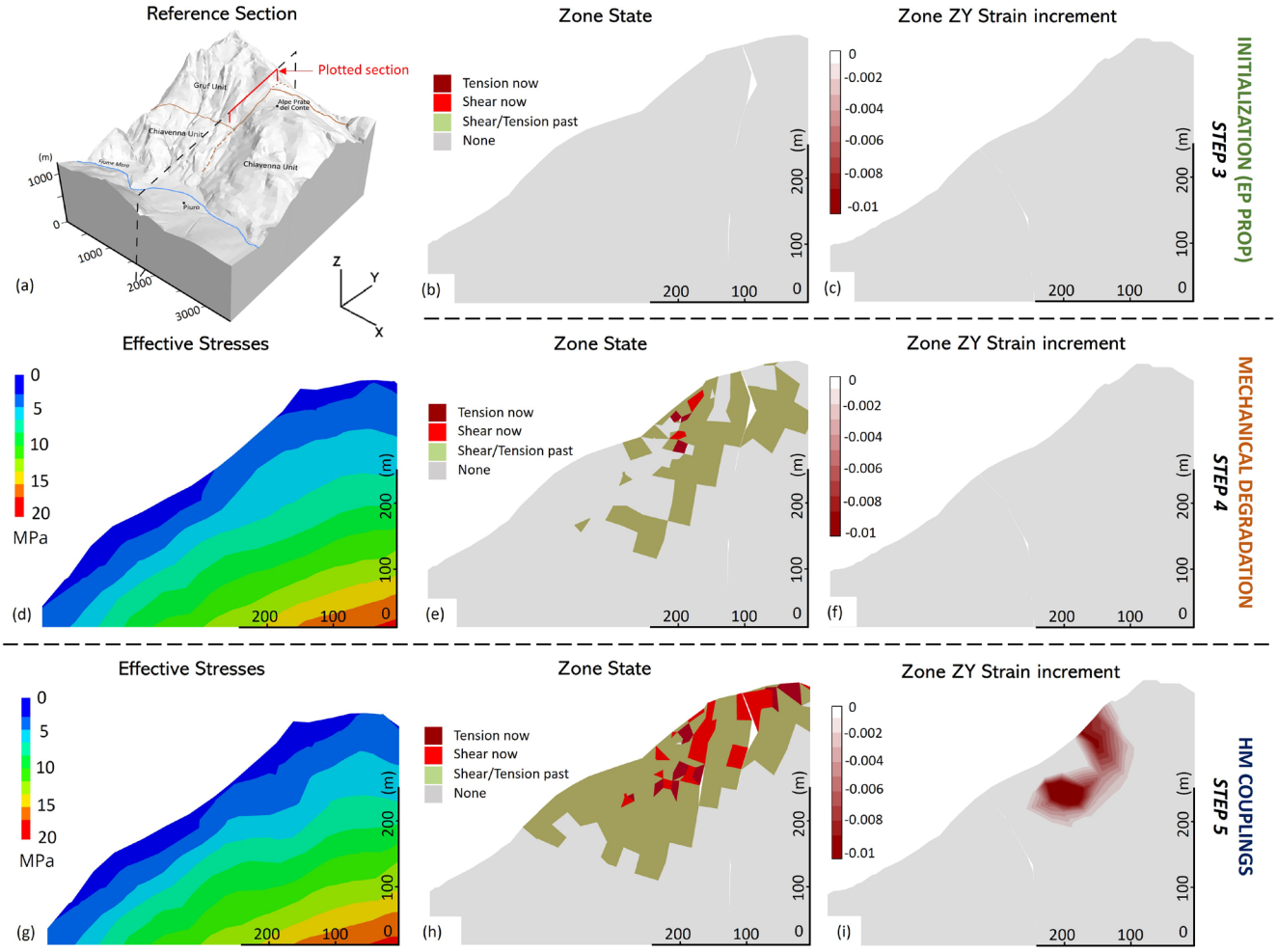

Figure 3.14 - (a) Location of the 2D section showing effective stresses (d,g), zone state (b,e,h), and ZY strain increment (c,f,i) simulated for different steps of the analysis.

Finally, the introduction of vertical water infiltration with a fully coupled transient HM analysis (*Step 5*), leads to the development of localized excess pore pressures along the slope. The simulated water flow moves toward the base of the slope both northward (in the direction of Piuro) and southward (in the direction of the Schiesone Valley) consistently with the hydraulic conductivity values introduced in the model. Pore pressure increase occurs at the toe of the slope due to an accumulation of water and a consequent rise in the groundwater level. Significant pore pressure increase occurs also in correspondence of the Alpe Prato del Conte locality, where gentler dipping slopes allow water accumulation. In this portion, a significant decrease in the effective stresses until a depth of 300 m was observed (see Figure 3.14 g-i). This was sufficient to generate a large increase in shear and tensile straining leading to failure, as is apparent by comparing Figure 3.14d and Figure 3.14g. At the end of the simulated rainfall event, tensile zones are identified upstream the Alpe Prato del Conte locality toward the top of the slope, whereas shear plastic zones are present at its base. Focusing on the top portion of the slope, a surface along which shear strains concentrate is observed to develop during the HM simulation (Figure 3.14i). It extends from elevations of 1300 m up to 1600 m a.s.l. and reaches a maximum depth of 150 m.

In terms of total displacements (the resultant of the modulus of the 3D displacement vectors), the simulation results in large values localized along the N-S lineament at an elevation of about 1400 m a.s.l., in correspondence to the 1618 failure area identified in the field (Figure 3.15).

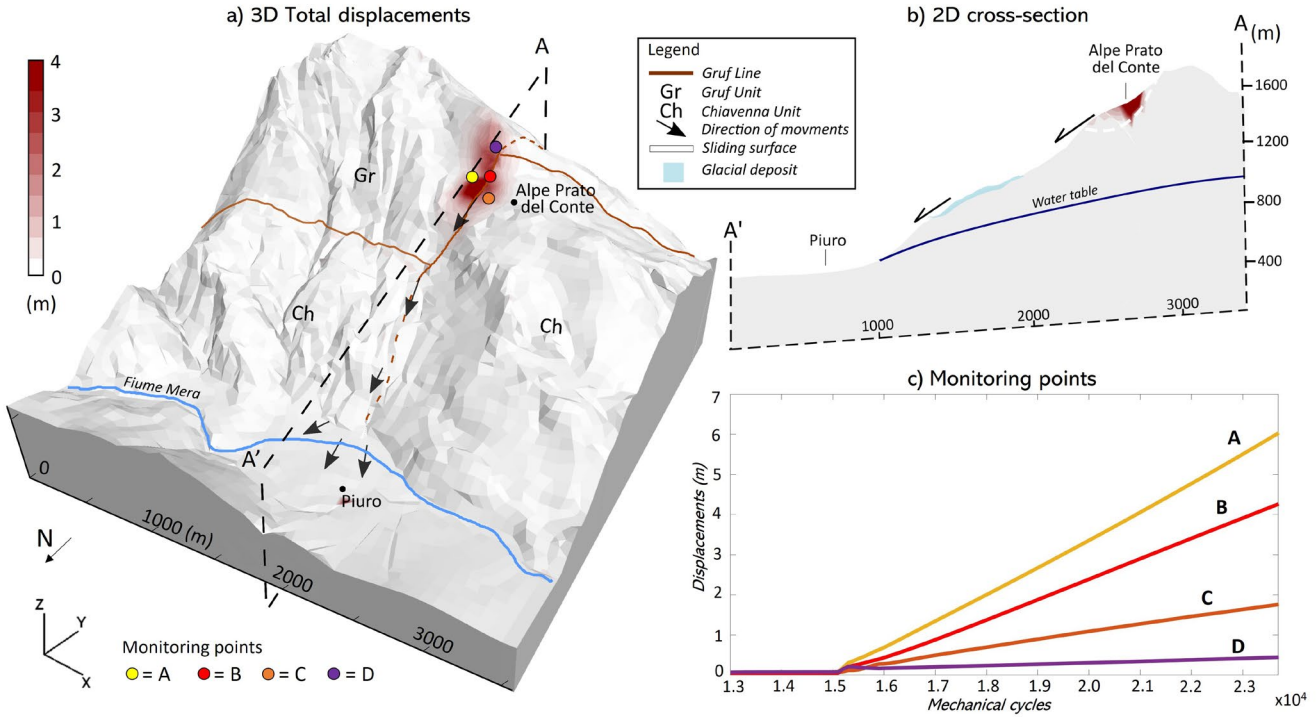

Figure 3.15 - a) 3D total displacements simulated at the end of the HM coupled analysis. b) 2D total displacements along a N-S cross-section crossing the failure area. c) Graph of measured displacements at monitoring points (fig a) with mechanical cycles (defined as the number of timesteps performed).

Maximum values up to 5 m are reached at the end of the transient HM analysis, with clear mechanical disequilibrium.

Analyzing the evolution of the displacement values recorded by the monitoring points located in the failure area of the 1618 event, it can be observed that during the simulated rainfall process, plastic conditions are reached. This is highlighted by the sudden rise in shear strain rate and simulated displacements, indicating the achievement of irreversible conditions. This is most evident for the points located in the surroundings of the main failure zone of the slope (*A, B, C* points in Figure 3.15), and is less evident in the upper part where the deformations are markedly smaller (*D* point in Figure 3.15). At the end of simulation, the maximum shear strain and total displacement distribution clearly show the presence of a critical, composite sliding surface approximately corresponding to the observed one.

3.2.5 Discussion

In the first phase of the study, in-situ geological and geomechanical surveys, supported by laboratory mechanical testing, enabled the development of a robust geological model of the Piuro slope. By geomorphological observations, it was evident that its mechanical evolution is potentially driven by the presence of tectonic elements separating geological units with different rheological behavior. To verify the role of these elements as preparatory factors for the landslide event that affected the Piuro slope in 1618, a 3D stress-strain analysis was developed. In addition, following historical reports, the effect of intense rainfall on the distribution of stresses and plastic deformations was subsequently explored, and its possible triggering role was evaluated.

By comparing results between different steps of the analysis, the role of pore pressure increment in the stress-strain evolution of rock-slopes was highlighted, demonstrating that induced damage and slope displacements are strongly enhanced in the presence of HM couplings. Regarding the modeling approach, *Steps 1 to 4* represent the preparatory process that leads the system to a gradual mechanical degradation, causing an overall reduction in strength. Considering the purposes of the present analysis, the mechanical degradation of rock-masses was enforced by introducing the weakest values among those measured in the study area. At the end of *Step 4* and before the introduction of the rainfall factor, plastic shear strains and resulting displacements are concentrated along the N-S lineament at an altitude of about 1400 m a.s.l., close to the Alpe Prato del Conte locality. Even if collapse conditions are not reached, a predisposition to instability is quite evident.

These observations clearly highlight how the N-S geological element plays a significant role as a predisposing factor to gravitational instability along the analyzed slope, in total agreement with previous studies conducted for the Piuro landslide (Scaramellini et al. 1988, 1995; Pigazzi et al. 2022). The use

of a 3D modeling approach allowed the introduction of the complex geological structure characterizing the southern slope of the Bregaglia Valley. Results are in agreement with the observations of previous authors, who underlined the importance of including 3D topography when analyzing the stress-strain evolution of rock slopes and complex large landslides (e.g., Jaboyedoff et al. 2011; Wolter et al. 2013). The development of pore pressures and the distribution of localized stresses caused by 3D topographic constraints are not negligible.

The considered rainfall scenario was sufficient to generate an increase in pore pressures and induce a significant increment of plastic deformations and displacements. Although the actual magnitude of the rainfall event is unknown, the assumed value for this work is consistent with the current measurements in the area, and it allowed to demonstrate the role of heavy rainfall as a triggering factor for the 1618 event, in agreement with the historical writings.

Simulation results are in accordance with previous studies that identified the failure scar in correspondence of the Alpe Prato del Conte locality. At the end of the transient HM analysis, highest values of total displacements are concentrated along the N-S geological element at an elevation of 1500 m a.s.l. and at a depth of 100 m, defining a cluster of maximum deformation east of the Alpe Prato del Conte plateau. Displacements of lower magnitudes are also present upstream, moving toward the Mottaccio peak. This is in agreement with geomorphological mapping, that detected the presence of a main scarp at an elevation of about 1500 m a.s.l. and secondary and minor scarps at larger altitude (Section 3.2.2.2).

Regarding the dynamics of the event, field surveys and the nature of the landslide deposit suggest an involvement of both rock and glacial materials (mixed deposits made by soil and cobblestones). Numerical simulations showed how the initiation of the instability should have occurred along the geological bedrock. However, considering the geomorphological framework of the failure area and the materials outcropping along the slope, the sliding mass must have involved glacial deposits that covered the Alpe Prato del Conte plateau and glacial terraces located downstream during the run-off of the failed mass. This is confirmed by field observations in the detachment zone, where rock scarps interrupt flat morphologies made by glacial deposits as well as the morphological terrace of Pradella di Piuro and Alpe Moscone, which are clearly cut by the landslide deposit. Since this work mainly focused on reproducing the preparation and triggering of the main deep-seated sliding mechanism, the adopted model did not include the soil material covering the bedrock. Future work could explore the subsequent dynamic evolution of the landslide involving both the bedrock and soil cover. To this end, a hybrid modelling approach following the continuum-discrete-distinct method should be explored (e.g. Ma et al. 2019; Pu et al. 2022).

Analyzing the displacements trend and the location of the slip surface, the volumes of the failed mass simulated by the model amount to approximately 7 Mm^3. Considering the material taken along the downstream path and the volumetric expansion of the material after failure (around 30%), total values of about 10 Mm^3 can be estimated. These are higher volume values than those suggested by (Pigazzi et al. 2022), based on the stratigraphical reconstruction of the deposit on the Piuro plain. However, it must be observed that the grid size used for domain discretization is 80 meters. For a more accurate assessment of the sliding volumes, it is necessary to decrease the grid size to lower values. This will lead to an increase in computational costs that must be addressed especially during the fully coupled HM analysis.

3.3 The Cimaganda case study

3.3.1 Study area

The study area is located along the San Giacomo Valley (Central Italian Alps), between the village of Chiavenna and the Splügen Pass (Figure 3.16a-b). The studied rock-slope is sited on the left flank of the valley, in correspondence of the Cimaganda village. The valley, furrowed by the Liro Torrent, follows a N-S striking direction and represents the natural divide between the Lepontine and Rhaetian Alps.

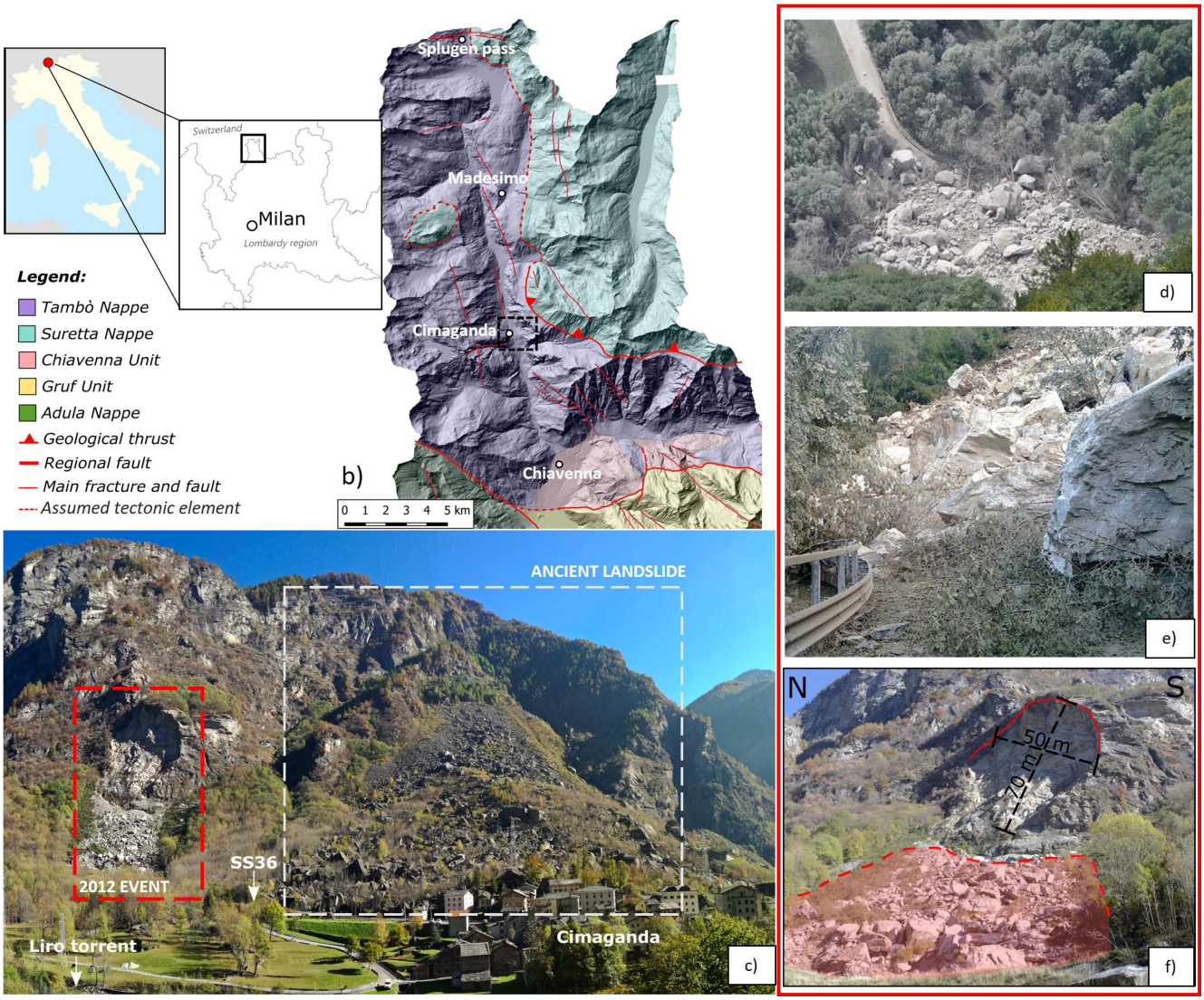

Figure 3.16 – a) Location of the study area. b) Distribution of the principal DSGSD bodies along San Giacomo and Bregaglia Valley. c) Failure area and deposit of both 2012 and historical Cimaganda event. d-e) 2012 rockslide event. f) 2012 rockslide failure scarp with its geometrical features; rockslide deposits are highlighted in red.

The geological framework of the area is related to the Alpine Pennidic nappe arrangement, characterized by the emplacement of two sub-horizontal gneissic bodies: the Suretta and Tambò Units (Figure 3.16a). They consist of polycyclic and poly-metamorphic basement mainly composed by paragneiss and

orthogneiss lithologies (Montrasio and Sciesa 1988). The tectonic contact between the two units gently dips to the E–NE and is characterized by the presence of a meta-sedimentary cover unit (Spluga-syncline) composed by quartzites, marbles and schists. The contact widely outcrops on the E slope of the valley at an elevation of about 1900-2200 m a.s.l., showing significant deformation and thickness variations.

The morphology of the valley is characterized by high sub-vertical rock cliffs, where gravitational processes dominate the current slope dynamics. Post-glacial rockfall talus cone and landslides deposits are particularly frequent along the entire valley floor, with blocks even greater than 10 m^3. The last relevant rockslide event, in May 2018, involved a rock volume of about 5,000 m^3 over the Gallivaggio sanctuary, a few kilometers south of the Cimaganda site (Carlà et al. 2021). Deep-seated gravitational slope deformations (DSGSDs), favored by the combination of high-relief landscapes and lithostructural framework, frequently affect both valley flanks with different states of activity. Morphological evidence of DSGSDs (trenches, counter-slopes and splitting of ridges) are particularly frequent along the tectonic contact between the Tambò and Suretta units (Aldighieri and Mazzoleni 2011).

An example is represented by the Cimaganda rockslide (below as *historical Cimaganda rockslide*), which collapsed in ancient times mobilizing a volume of material on the order of 7.5 Mm^3 (Figure 3.16c - Mazzoccola 1993). The event is marked by morphological evidences along the E flank of the valley, in correspondence of the Cimaganda village. It represents the failure evolution of a DSGSD, bounded upstream by the structural terrace of Bondeno and on the lateral sides by the Stua and Avero valleys. The rockslide detachment zone is wedge-shaped and is characterized by high subvertical rock cliffs. It is bounded by brittle geological elements consisting of (i) a system of vertical fractures with a N-S direction parallel to the slope orientation, (ii) a persistent discontinuity set merging towards NW defining its left flank and (iii) a WSW-ENE subvertical fault defining its right flank. The rockslide deposit is cone-shaped with angular blocks of gneissic rock reaching the valley bottom (Figure 3.16c). Two distinct portions in the accumulation area have been recognized: the first one is localized at lower altitudes and is characterized by huge blocks with volume larger than 100 m^3; the second one, made up by smaller blocks, is partially colonize by vegetation and localized at higher altitudes, partly overlapping the first one. Due to the high energy of the event, the rockslide deposit has risen to the opposite slope, damming the Liro torrent and partly modifying its path, leading to the deposition of thin and lacustrine deposits upstream of the accumulation zone. The age of the rockslide event is difficult to estimate as no information or citation data have been found in the local historical archives. Lichenometric dating was performed by Mazzoccola 1993 on the rockslide deposit giving the upper limit of its age. Results indicate an age before the 900 A.D. for the principal massive episode. Other secondary and more recent events

probably involved the main detachment zone, leading to the current slope morphology.
Along the rock slope the presence of highly persistent and opened fracture systems parallel to the valley axis, leads to periodic slope failure phenomena which, in most cases, involved limited volumes of rock material. However, they represent a serious treat for the Cimaganda village and for the SS36 national road, which is the only connection between Chiavenna and the Splügen Pass. The right flank of the Cimaganda rockslide is particularly active, due to the presence of high rock cliffs. The last most important failure event, occurred in September 2012 (below as *2012 Cimaganda rockslide*) mobilized 20,000 m^3 of rock material, blocking the SS36 national road and isolating the upper valley for a few days (Figure 3.16d-f).

3.3.1.1 The 2012 Cimaganda rockslide event

The 2012 Cimaganda rockslide occurred on September 27 after a period of intense rainfall, which totalized 267.8 mm in 4 days at the *San Giacomo Filippo - Lago del Truzzo* meteorological station and 209.4 mm at the *Madesimo - Spluga* station (https://www.arpalombardia.it/).
The rockslide scarp is located at about 1100 m a.s.l. with a size of 50-60 m in width, 60-70 m in length and 5-10 m in depth (Figure 3.16f). At the detachment, the slope consists of steep wooded scarps, rising with progressive steps until the Bondeno terrace, located at an elevation of about 1700 m a.s.l. The rockslide mass traveled down the slope destroying the forest below and blocking the national road SS36 for a segment of about 60 m. The deposit is composed by angular blocks of gneissic rock, heterogeneously distributed from the failure scarp to the bottom of the valley. The largest blocks are found in the central part of the deposit, with volumes of several tens of meter cubes. Block sizes tend to decrease towards the lateral boundaries, as well as towards the top of the rockslide deposit, where boulders smaller than 1 m^3 dominate. Huge boulders with a volume of more than 100 m^3 are even present at the lower and central part of the deposit.
The factors that predisposed the area to failure mainly consist of particularly favorable geomechanical and morphological settings, characterized by an intensely fractured and weathered rock-masses, and steep slopes. The trigger should be sought in the intense rainfall event that preceded the landslide failure, which may had resulted in a major increase of pore pressure within the collapsed rock-mass.

3.3.2 Data collection

With the aim of identifying the geomorphological and geomechanical features that potentially led to the development of the gravity-driven instability processes along the Cimaganda rock slope, geological and

geomechanical surveys were carried out covering both the historical and the 2012 rockslide events.
This Section will discuss in detail the results of the field surveys, mostly characterizing the study area. Particular emphasis was given to the geomechanical characterization of the slope, with the aim of collecting enough data for the definition of a strong and valid mechanical model of the slope. For this, detailed geomechanical surveys and laboratory tests were carried out. In addition, field surveys data were compiled into a geomorphological map, describing shapes and processes that characterize the study area.

3.3.2.1 Geological settings

The geological framework of the Cimaganda rock slope is related to the arrangement of the Tambò and Suretta Alpine Pennidic units (Montrasio and Sciesa 1988; Figure 3.16b). Field surveys showed that rock-masses are mainly composed by paragneiss belonging to the Corbet Zone (crystalline basement of the Tambò nappe), with a discrete homogeneity along the slope (Figure 3.17a-c). Some lithological variations were found with intercalation of orthogneiss bodies within the paragneiss, more frequent along the bottom of the slope (Figure 3.17).
The tectonic contact with the Suretta unit, gently dipping toward E-NE, is located above the crown of the historical rockslide at about 1800 m a.s.l. It is highlighted by a bundle of persistent and highly foliated meta-sedimentary rock of the Spluga Syncline, with lower mechanical quality than the surrounding lithologies. Due to the persistent quaternary cover, the contact between the two nappes is not visible.
Moving to the rock walls upstream of the "Bondeno" locality, a change in the petrographic and textural characters was observed, thus highlighting the transition into the Suretta nappe. The outcropping material is of a gneissic type (paragneiss), with a much sharper and pervasive schistosity than the same lithotypes belonging to the Tambò nappe.
The structural foliation of the gneissic rock-masses gently dips to the NE with good homogeneity along the entire slope, both for the Tambò unit and the Suretta.

3.3.2.2 Geomorphological features

The study area presents a great geomorphological variability, typical of the Alpine environment in which different morphogenetic processes follow each other in time and space. The analysis of geomorphological elements focused mainly around the historical Cimaganda rockslide, with the aim of identifying shapes and processes that characterize the study area, as well as elements that may indicate

instability and tensional release processes. All the geomorphological data and observations collected during the field surveys were compiled into a map (Figure 3.17f).

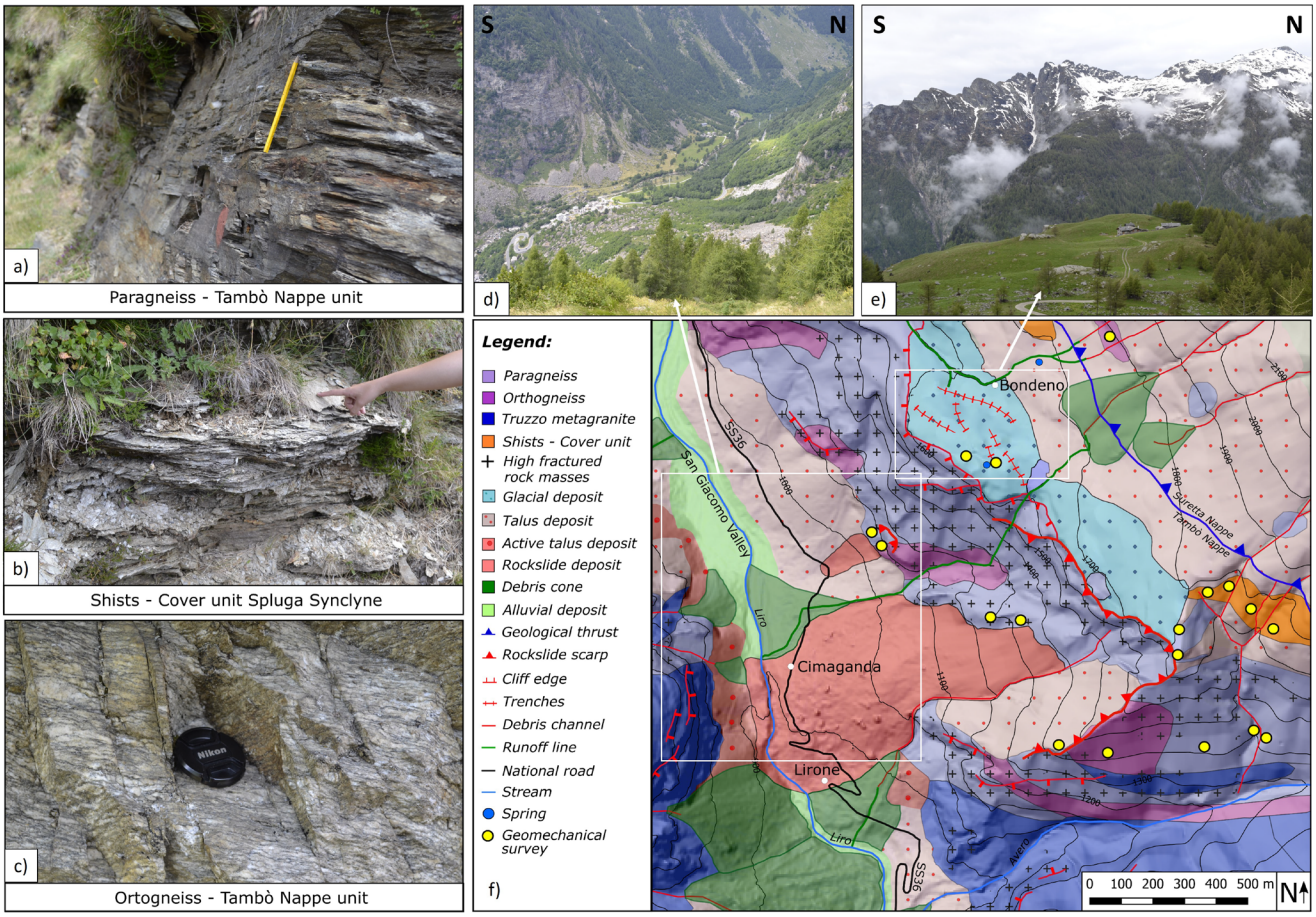

Figure 3.17 – Geological and geomorphological features of the Cimaganda rock slope. a,b,c) Main lithologies outcropping. d) View of the Cimaganda valley floor, where the relationship between slope and fluvial dynamics is clearly visible. e) Tensional release trenches and counter slopes at Bondeno locality. f) Geomorphological map.

Along the valley bottom it was possible to delineate the morphological elements of the two rockslide events that characterize the slope behind Cimaganda, distinguishing niches, scarps and deposits. The latter, in particular, are composed of huge blocks that can even reach volumes of tens of cubic meters; going up toward their detachment zone, block size gradually decreases until they become less than one cubic meter.

The San Giacomo Valley, in this section, is characterized by very steep slopes, culminating in high rock cliffs. Post-glacial cover, consisting of fully vegetated slope deposits, predominate at their base, except for a few singular cases where active debris are present (Figure 3.17d). Frequent are the streams that furrow the slopes, deepening to define valleys or gullies that represent preferential ways for surface water runoff. At their confluence with the main valley, they end in broad fans to which a "mixed" gravity and fluvial origin has been ascribed. In the Cimaganda area, the Liro stream does not seem to be

particularly active in erosive terms, due to a low morphological gradient that results in a limited water flow energy. In fact, it flows over a fluvial plain consisting of fine materials deposited by the river itself. The origin of this plain and the deposition of the material could be attributed to the development of a small lake upstream of the historical Cimaganda rockslide deposit, which reached the valley floor causing the obstruction of the river (Mazzoccola 1993).

If the valley floor is characterized by a continuous overlap of gravitational and fluvial forms, the structural terrace of Bondeno consists mainly of gentle deposits of glacial origin, to which multiple gravity-driven elements are added. Firstly, the presence of trenches and counter slopes that shape and characterize the terrace near the escarpment edge is highlighted (Figure 3.17e). Due to their position and origin, they therefore represent clear morphological evidence of the tensional release processes affecting the slope.

Along the morphological edges that drop towards the main valley, it is possible to observe the presence of natural steps mainly related to the subsidence of the material that sink under the gravity load; this is highlighted by the presence of uprooted trees and rocky towers in precarious conditions of stability (see Figure 3.17d and Figure 3.18e-f). These elements clearly indicate the presence of a deep gravitational deformation process affecting the slope. The rockslide events under analysis may therefore represent its most rapid and superficial evidence.

Along the Bondeno structural terrace, rock-masses show clear evidence of glacial cycles, with striae and scoured rocks that indicate an ice flow direction corresponding to the main valley axis. Morphologies and glacial deposits (moraines and erratics) related to the last retreat phases of the San Giacomo glacier, are quite widespread where flat morphologies allow their preservation.

From a geomorphological point of view, it is also worth highlighting the presence of peaty material and water stagnation in some points located around the villages of Gualdera and Mottolo. They could represent evidences of water circulation and summit stagnation by means of suspended water bodies in the slope under investigation.

3.3.2.3 Geomechanical characterization

With the aim of defining the geomechanical features of the Cimaganda slope, a geomechanical characterization including detailed field surveys and laboratory tests on intact rock and discontinuities was performed. This allowed to outline the main characters governing the mechanical behavior of rock-masses outcropping and to obtain the data necessary for the elaboration of a valid numerical model of the slope under investigation.

Field surveys

Following the ISRM suggested methods (ISRM 1981), geomechanical field surveys were performed in the study area, along the 2012 failure scarp and at the top of the Cimaganda slope in correspondence of the historical rockslide niche (Figure 3.18).

Focusing on the fracturing conditions of the rock-masses, at least three systems of discontinuity (*K1*, *K2* and *K3*) were identified. Joint geometrical parameters as orientation (dip direction and dip), spacing (distance normal to joint tracks) and trace (length of joint segment) were collected and analyzed with a statistical approach, as follows:

- *K1*, representing pervasive foliation of gneissic rocks, gently dips towards NNE with a low inclination angle (dip direction/dip: 34°±10°/27°±3°; spacing: 1.5±0.7 m; trace: 9±3.5 m). It can be related to the regional tectonic contact between Tambò and Suretta nappes. Mean detected values of Joint Roughness Coefficient (JRC) and Joint Compressive Strength (JCS) were respectively 7 and 66 MPa.
- *K2*, with shear kinematic features, dips towards NW with an inclination angle of 70° (dip direction/dip: 287°±25°/70°±10°; spacing: 2±0.9 m; trace: 4±1.8 m). It shows very smooth surfaces with high persistency features (mean JRC values of 4 and JCS of 114 MPa).
- *K3* dips vertically towards SW (dip direction/dip: 222°±20°/79°±5°; spacing: 2.5±1 m; trace: 4.1±2.1 m), and has strike at low angle with the main San Giacomo Valley axis. Joint surfaces show roughness features with mean JRC values of 9 and JCS of 83 MPa.

The calculated RMR (Rock-mass Rating; Bieniawski 1974) and the evaluated GSI (Geological Strength Index; Marinos P and Hoek 2000) reveal a good rock-mass mechanical quality (RMR ranging from 60 to 65, GSI ranging from 45 to 65; see Figure 3.18). At the crown of the historical Cimaganda rockslide, in the upper part of the slope, lower GSI values (50 ± 5) were detected, due to a more intense fracturing conditions and a higher weathering degree of the rock-masses.

Gravity-driven instability processes as rockfalls and shallow rockslides seem to be particularly favored by the geometrical orientation of the joint systems relative to the slope direction. High persistent *K2* shear surfaces with low mechanical properties (smooth and weathered surfaces) may act as a basal sliding plane of significant volumes of rock material, that can be isolated upstream by the *K3* tensile system. The *K3* system in particular, has an orientation parallel to the valley axis with sub-vertical inclination, very extensive persistence and considerable aperture values. These elements, in addition to promoting the separation of rock blocks, also promotes the circulation of rainfall water within the rock-mass, that can accumulate and create significant water pressures.

A complex geomechanical framework was found in the upper part of the Cimaganda slope, where the presence of highly fractured rock-masses with persistent and opened joints, leads to the development of rock-towers which can evolve in rockfalls and rockslide events (Figure 3.18e-f). Strong degraded rock material with a thick weathering layer was also found in this area.

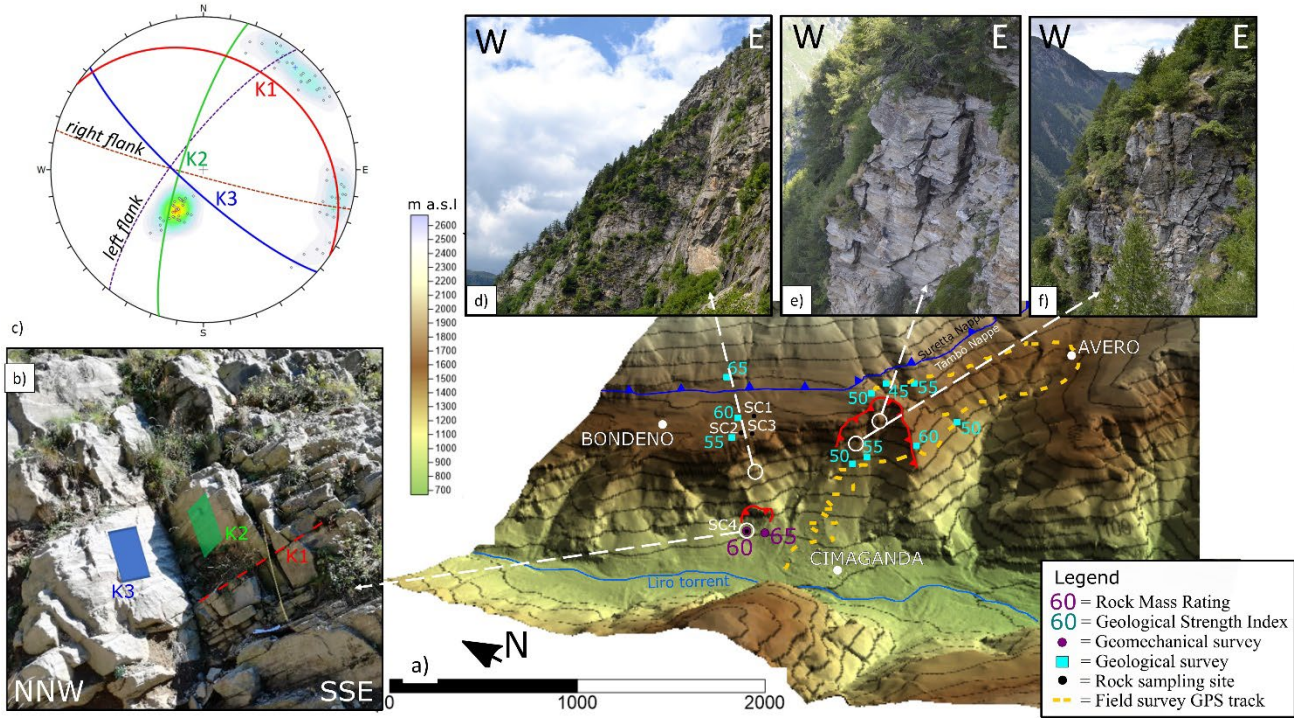

Figure 3.18 – Geomechanical features of the Cimaganda rock slope. a) 3d representation of the Cimaganda slope with location of geological and geomechanical surveys performed, as well as rock material sampling sites. b) Rock-masses outcropping along the 2012 rockslide scarp; three main discontinuity sets are highlighted with different colors. c) Stereo-net representing the orientation of the discontinuity sets and the flanks of the historical rockslide event. d-f) Rock-masses outcropping along the slope with a high degree of fracturing, persistency and aperture of the discontinuity elements.

Laboratory tests

Intact rock

To investigate the mechanical behavior of both intact rock and discontinuities, uniaxial compressive tests on rock samples and direct shear tests of joint surfaces were conducted according to the ASTM standards (D7012 – 14 and D5607 – 08). A rock material collection campaign was carried out covering the entire Cimaganda slope.

Three sampling sites (*SC1*, *SC2* and *SC3* in Figure 3.18) are located in the proximity of the Bondeno locality and are essentially represented by outcrops isolated among the quaternary deposits. Site *SC4*, on the other hand, is located on the 2012 rockslide scarp.

The prevailing lithology is of gneissic type with clear evidences of degradation throughout the slope; this is particularly evident in the sampling sites located at the crown of the ancient rockslide (*SC1*, *SC2*

and *SC3*). Low lithological and textural variability was observed in the collected samples moving from the base of the slope where orthogneiss bodies prevail, toward its summit where paragneiss are present. Samples collected at the *SC4* site, exhibit a uniaxial compressive strength (UCS) of 100 MPa with a Young modulus (E) of 22 GPa and a Poisson ratio (υ) varying from 0.25 to 0.43. The behavior of the material is typical of a poorly weathered massive rock. This could be related to the fact that the analyzed material was collected from the 2012 rockslide scarp, where fresh material was unearthed by the landslide event itself.

In contrast, the paragneiss lithology sampled at *SC1*, *SC2* and *SC3* sites, shows a more foliated texture that gives the material greater deformability and lower mechanical strength. In addition, the rock was extremely weathered, with very frequent microfractures weakening the overall strength of the material. Values of compressive strength (UCS) varying from 36 to 70 MPa with a Young modulus (E) of 10-26 GPa and a Poisson ratio (υ) of 0.22-0.3, were obtained. The following Table 3.5 collects the results obtained on the tested specimens.

Table 3.5 - Results from uniaxial compressive tests conducted on rock samples collected along the slope. See figure 3.16 for they location.

Uniaxial compressive tests					
Sample code	**Lithotype**	**Density [g/cm^3]**	**Young Modulus [GPa]**	**Poisson ratio**	**Uniaxial compressive strength [MPa]**
SC1_M1	Paragneiss	2.60	14.50	0.30	60.26
SC1_M2	Paragneiss	2.60	26.40	0.22	70.50
SC1_M3	Paragneiss	2.60	10.50	0.22	36.61
SC2_M1	Paragneiss	2.60	13.40	0.33	60.00
SC2_M2	Paragneiss	2.60	22.80	0.24	49.00
SC4_M1	Orthogneiss	2.70	22.94	0.43	102.68
SC4_M2	Orthogneiss	2.70	21.66	0.37	102.37
SC4_M3	Orthogneiss	2.70	22.30	0.24	99.83

As an example, the laboratory certificate for a uniaxial test conducted on a sample of gneissic rock is given below (Figure 3.19).

UNIAXIAL COMPRESSIVE TEST			ASTM D7012-14. Metodo D
CLIENT:	Andrea Morcioni	DATA:	2020-06-01
LOCALITY:	Bondeno	WORKER:	M. Perfido, A.Morcioni
SAMPLE:	SC1-M1	MACHINE:	Pressa Controls (500N), Advantest 9, software Controls Triaxrocks
DEPTH (m):	Outcropping		
LITHOLOGY	Gneiss - Tambò nappe	TIPO DI PROVA:	Strain controlled uniaxial tests

PICTURE

β = 30°

*β Angle between the failure plane and the direction of the maximum principal stress

NOTE: Axial load applied perpendicularly to the plane of schistosity

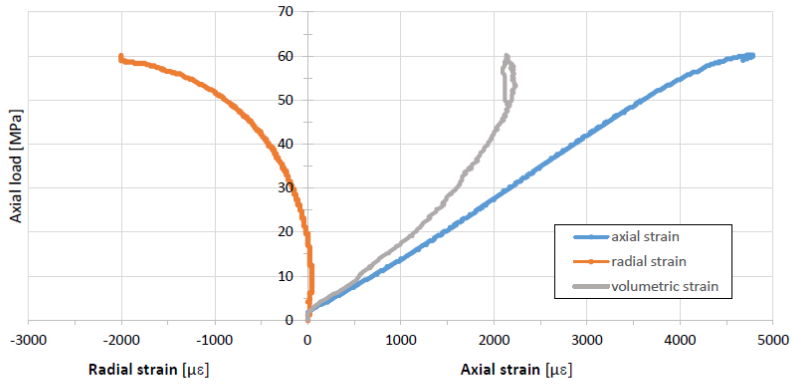

Compressive uniaxial strength	σ_c	60.26	MPa
Elastic modulus - tangent 50% of σc	$E_{t50\%}$	14.50	GPa
Elastic modulus - secant 50% of σc	$E_{s50\%}$	13.90	GPa
Poisson Coefficient	ν	0.30	-

Figure 3.19 - Laboratory certificate for a uniaxial test conducted on a gneissic rock sample.

Discontinuities

To study the mechanical behavior of discontinuities, direct joint shear tests were performed according to ASTM standards (D5607 – 08; ASTM 2008) on representative discontinuity surfaces belonging to the *K2* and *K3* set. The *K2* joint surface has been sampled along the Bondeno terrace (*SC1* site in Figure 3.18), according to the ISRM standards for the outcropping joints (ISRM 2015). From the sampled surface, three specimens were obtained, useful for performing the laboratory mechanical test. Each specimen was subjected to three shear mechanical cycles in order to investigate both peak and residual values of the material. Results are summarized in Table 3.6.

Table 3.6 - Results from direct shear joint tests conducted on a discontinuity sample belonging to the K2 set.

Direct shear joint tests – K2 set						
Test	σ_N (MPa)	Loading rate (MPa/s)	n° cycle	τ_P (MPa)	Shear displacements at peak (mm)	JRC
SC1a_T1	1.5	0.08	1	0.93	19.25	2
SC1a_T2	1.5	0.08	2	0.95	20.53	2
SC1a_T3	1.5	0.08	3	0.97	21.81	2
SC1b_T1	3.0	0.08	1	1.5	18.77	2
SC1b_T2	3.0	0.08	2	1.79	18.62	1
SC1b_T3	3.0	0.08	3	1.86	20.71	1
SC1c_T1	6.0	0.08	1	3.15	19.48	2
SC1c_T2	6.0	0.08	2	3.49	18.45	2
SC1c_T3	6.0	0.08	3	3.57	19.87	2

Results from the direct joint shear tests showed a mechanical behavior typical of a very smooth surface. Joint shear resistance in fact, did not show a peak phase distinct from a residual one, due to the complete absence of morphological asperities on the joint surface. In addition, the results showed evidences of an extremely weathered surface, with rock fragmentation upon application of the tangential loads. This results in a hardening behavior (i.e., increased difficulty to relative sliding between the blocks as relative sliding progresses) due to the formation of dust and pieces of rock that pose resistance to the movement. This observation is consistent with the results of uniaxial tests performed on material taken at the same sampling site, which had shown poor mechanical strength.

According to the Mohr-Coulomb criterion, a value of peak friction angle of 28° with a null cohesion was obtained (Table 3.7). Moving to the last shear mechanical cycle, a friction angle value of 25° was detected.

Table 3.7 – K2-set shear strength parameters calculated from Barton-Bandis (Barton and Bandis 1982) and Mohr-Coulomb (Coulomb 1776) equations.

Shear strength K2						
Barton criterion			*Mohr criterion*			
JCS	75	[MPa]	ϕpeak	28.0	[°]	**First mechanical cycle**
JRC	2		C peak	0	MPa	
ϕresidual	25.4	[°]	ϕresidual	25.0	[°]	**Last mechanical cycle**
			C residual	0	MPa	

The *K3* joint surface has been sampled along the 2012 rockslide scarp (*SC1* site in Figure 3.18), according to the ISRM standards for the outcropping joints (ISRM 2015). From the sampled surface, four specimens were obtained, useful for performing the laboratory mechanical test. Each specimen was subjected to five shear cycles in order to investigate both peak and residual values of the material.

However, during the execution of the tests, two specimens broke when the shear strength of the first mechanical cycle was reached. Results are summarized in Table 3.8.

Table 3.8 - Results from direct shear joint tests conducted on a discontinuity sample belonging to the K3 set.

Direct shear joint tests – K3 set							
Test	σ_N (MPa)	Loading rate (MPa/s)	n° cycle	τ_P (MPa)	τ_r (MPa)	Shear displacements at peak (mm)	JRC
SC4_Aa_T1	1.0	0.08	1	1.32	0.77	0.80	10
SC4_Aa_T2	1.0	0.08	2	0.97	0.74	1.54	9
SC4_Aa_T3	1.0	0.08	3	0.84	0.72	1.17	7
SC4_Aa_T4	1.0	0.08	4	0.81	0.72	0.71	5
SC4_Aa_T5	1.0	0.08	5	0.78	0.69	0.52	5
SC4_Bb_T1	1.5	0.08	1	1.40	0.85	1.24	6
SC4_Bb_T2	1.5	0.08	2	1.16	0.96	1.86	5
SC4_Bb_T3	1.5	0.08	3	1.00	0.95	2.60	4
SC4_Bb_T4	1.5	0.08	4	0.97	0.94	4.99	4
SC4_Bb_T5	1.5	0.08	5	0.96	0.94	3.98	4
SC4_Ab_T1	2.0	0.08	1	2.34	1.16	1.10	10
SC4_Ab_T2	2.0	0.08	1	1.35	1.03	1.24	10
SC4_Ab_T3	2.0	0.08	2	1.12	1.02	1.98	9
SC4_Ab_T4	2.0	0.08	3	1.05	1.04	3.79	8
SC4_Ab_T5	2.0	0.08	4	1.00	1.01	5.44	8
SC4_Ba_T1	3.0	0.08	5	2.89	2.11	1.33	10
SC4_Bd_T1	4.0	0.08	1	3.46	2.95	1.42	9
SC4_Bd_T2	4.0	0.08	2	2.93	2.80	2.41	8
SC4_Bd_T3	4.0	0.08	3	2.79	2.77	3.05	7
SC4_Bd_T4	4.0	0.08	4	2.78	2.76	4.75	7
SC4_Bd_T5	4.0	0.08	5	2.74	2.73	4.69	6
SC4_Bc_T1	6.0	0.08	1	5.12	3.95	1.60	7

The mechanical behavior of this discontinuity set is completely different from the previous one, reflecting a higher degree of roughness and a less pronounced altered state of the material. At the first mechanical shear cycle (i.e., undisturbed surfaces), a softening behavior is shown, related to the presence of asperities that generate frictional resistance. Since the surface is not smooth, the upper block needs high tangential stress (i.e., peak resistance) to overcome the asperities and slide on the lower one. According to the Mohr-Coulomb criterion, a value of peak ϕ of 48° with a c of 0.25 MPa was obtained (Table 3.9). Shear cycles after the first one (i.e., disturbed surfaces), showed a hardening behavior with lower shear strength. In fact, the surface is progressively abraded and modeled to a smooth plane. The residual friction angle dropped to a value of 33° (Table 3.9). At each mechanical cycle, the morphological changes reported on the joint surface (roughness, alteration, distance between the two blocks) were analyzed, using manual (Barton comb) techniques. The results showed a strong dependence

between surface morphology and slip resistance, with a progressive flattening of the surface as the cutting cycles progressed.

Table 3.9 – K3-set shear strength parameters calculated from Barton-Bandis (Barton and Bandis 1982) and Mohr-Coulomb (Coulomb 1776) equations.

Shear strength K3						
Barton criterion			*Mohr criterion*			
JCS	70	[MPa]	ϕpeak	48.00	[°]	**First mechanical cycle**
JRC	8		C peak	0.25	MPa	
ϕresidual	33.20	[°]	ϕresidual	34.00	[°]	
			C residual	0	MPa	
			ϕresidual	33	[°]	**Last mechanical cycle**
			C residual	0	MPa	

Following the ISRM suggesting methods (ISRM 2015; Kulatilake et al. 2016), normal (*Kn*) and shear stiffness (*Ks*) were defined (Section 2.1). The detected mean values of *Kn* vary between 1.50 GPa/m (*K2*) and 4.08 GPa/m (*K3*), depending on morphological and surface alteration conditions. The mean values of shear joint stiffness *Ks* vary from 1.01 GPa/m (*K2*) to 1.45 GPa/m (*K3*), following the above described shear strength parameters. As an example, the laboratory certificate for a joint direct shear test conducted on a sample belonging to the K3 discontinuity set is given below (Figure 3.20).

JOINT DIRECT SHEAR TEST

Client:	Andrea Morcioni	DATA :	26/11/2020
Loaclity:	Cimaganda (SO)	Test n°	1
Type:	Outcropping natural joint	OPERATOR:	Morcioni Andrea
Name of the sample:	SC4_Ab	NOTE:	

FEATURES OF THE SAMPLE

Geometrical features	Width [mm]	90	Mechanical features	JRC	10
	Length [mm]	95		JCS [MPa]	60
	Area [mm^2]	8550			

FEATURES OF THE TEST

Step 1: axial load		Step 2: shear load	
Velocity [MPa/s]	0.1	Velocity [N/s]	Manual hydraulic pump
Target [MPa]	2		
N° steps	4		

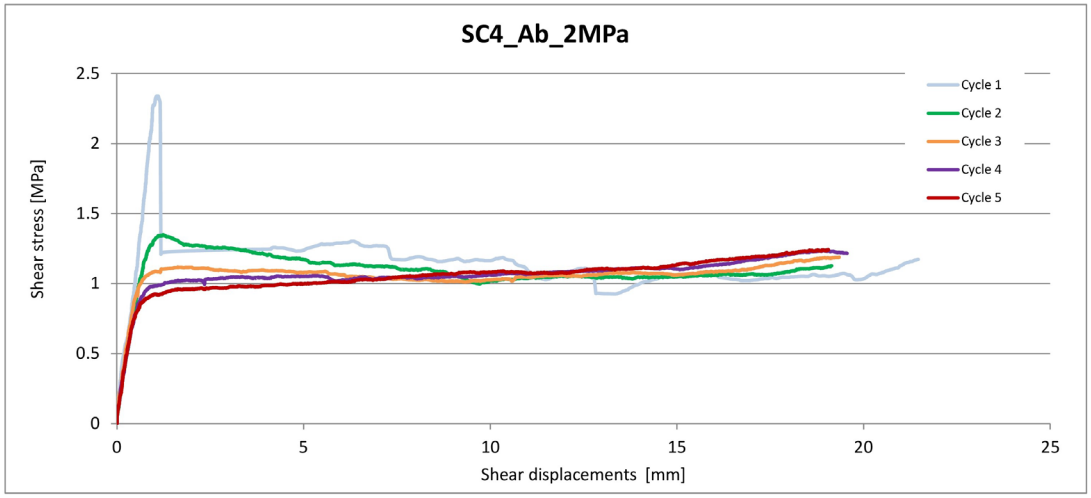

Picture of the sample surface (top)

Mechanical cycle 1	Mechanical cycle 5
	

Figure 3.20 - Laboratory certificate for a direct shear test conducted on a discontinuity rock sample belonging to the K3 system

3.3.3 Definition of a geomechanical conceptual model

Summarizing the observations highlighted and discussed in the previous Section 3.3.2, the geological setting of the slope is characterized by no significant or sudden lithological variations able to define differences in the mechanical behavior of the outcropping rock-masses. A relevant geological element

is represented by the sub-horizontal tectonic contact between the Tambò and Suretta Units, however placed far and at higher elevations from the section of slope affected by the gravity processes. It is highlighted by a metasedimentary body characterized by a transition zone with high schistosity and high degree of fracturing conditions (Figure 3.16 - Figure 3.17b), expressed by the presence of a morphological plateau.

The overall mechanical behavior of the slope would seem to be governed by the persistent discontinuity network characterizing the rock-masses with low mechanical properties. In particular, the mechanical state of the rock-masses outcropping along the slope appears to be strongly controlled by 3 main discontinuity sets (Figure 3.18 –a-b). As evidence of their high representativeness, they have been recognized systematically in all the outcrops analyzed. Of particular importance is the *K3* set, identified with an approximately NW-SE direction parallel to the valley axis and dipping toward the SW with an high angle. This set seems to control, at all the scales of observation, the mechanical behavior of rock-masses, isolating potentially unstable material (Figure 3.18 –d-f). The combination of the morphological features of the slope and the joint properties belonging to this family (aperture, persistence and orientation), generates structures that are particularly prone to gravity-driven processes, resulting in a typical discontinue behavior of the slope.

Concerning the *K2* set, with NE-SW direction, it exhibits lower persistence and intensity of fracturing than what observed for the *K3* family. From slope-scale analyses, however, it can be observed that the discontinuities belonging to the *K2* system also play a major role in the development of instability phenomena along the slope, representing the basal slip and lateral release surfaces for gravitational phenomena. By photogrammetric analyses performed on the 2012 rockslide scarp, it was possible to assess that the material released by the rockslide event was defined by the *K2-K3* interaction.

Regarding the condition of the investigated joints, modest roughness is shown for the *K1* and *K3* families, contrasted by low roughness of the *K2* set. In general, the discontinuities detected on the landslide scarp appear to be slightly weathered with JCS values even higher than 100 MPa. On the other hand, the joints detected at the crown of the historical landslide, are characterized by a high degree of weathering with thick, highly discolored superficial layer.

It is also relevant to point out that locally, very considerable aperture values were measured in the *K3* discontinuities, even close to one meter on the outcrops in the upper part of the slope. The mechanical state of the rock-masses outcropping on the slope under study, appears to be "good" with discrete GSI and RMR values.

3.3.4 Hydro-mechanical analysis

In this Section, the stress-strain evolution of the Cimaganda rock slope is analyzed. Starting from the geological conceptual model defined in Section 3.3.3, a geo-mechanical 2D model is now defined including all the data and observations collected in previous Section 3.3.2.

The development of mechanical failure elements and zones of high deformation induced by rainfall events is here analyzed through a coupled HM analysis and applied to the 2012 Cimaganda rockslide event. The aim is to define the triggering mechanisms occurred during the failure event linked to an intense meteorological event. The analysis is meant to increase knowledge of the mechanisms responsible for the recent gravity evolution of the Cimaganda rock slope, useful for the prior identification of possible events similar to the one that occurred in September 2012. In addition, the analysis aimed to validate the model presented in Section 3.3.3, by reconstructing the 2012 failure event.

3.3.4.1 Methods

The numerical HM stress-strain analysis was performed using the 2D FEM numerical code RS2 (RocScience 2017), described in Section 2.3.

Modelling approach

The cross section of modeling, coincident with the rockslide direction of movement, extends from the Liro Torrent up to the top of the slope at a height of about 1800 m a.s.l. (Figure 3.21), considering the pre-failure topographical conditions (2002 Digital Terrain Model of the Sondrio Province).

In the model, the rock-mass is assumed to behave as an elasto-plastic medium, according to the Generalized Hoek & Brown strength criterion (Figure 3.21). Pervasive planes of schistosity were represented by introducing a jointed material; planes orientation and Mohr-Coulomb strength parameters where specified to confer an anisotropic behavior at the rock-mass.

Boundary conditions at the base and on both sides of the model, were introduced far enough to avoid boundary effects in the area of interest, preventing displacements along both *X* and *Y* axes. The mesh used is uniform with 6 nodes triangular elements.

A multiple joint network, made by the two main sets *K2* and *K3* was then introduced (Figure 3.21). By using Baecher joint network model (Baecher et al. 1978), which allows a statistical distribution of joints orientation, frequency and intensity, and by assigning Mohr-Coulomb strength parameters, each set of discontinuity was fully represented (Figure 3.21). Strength parameters were derived both from laboratory analysis and from Barton-Bandis model, developed using JRC and JCS data, corrected in

relation with the scale effect (Barton and Bandis 1982). Value of shear and normal stiffness of joint surfaces derived from the interpretation of laboratory direct shear tests (Figure 3.21).

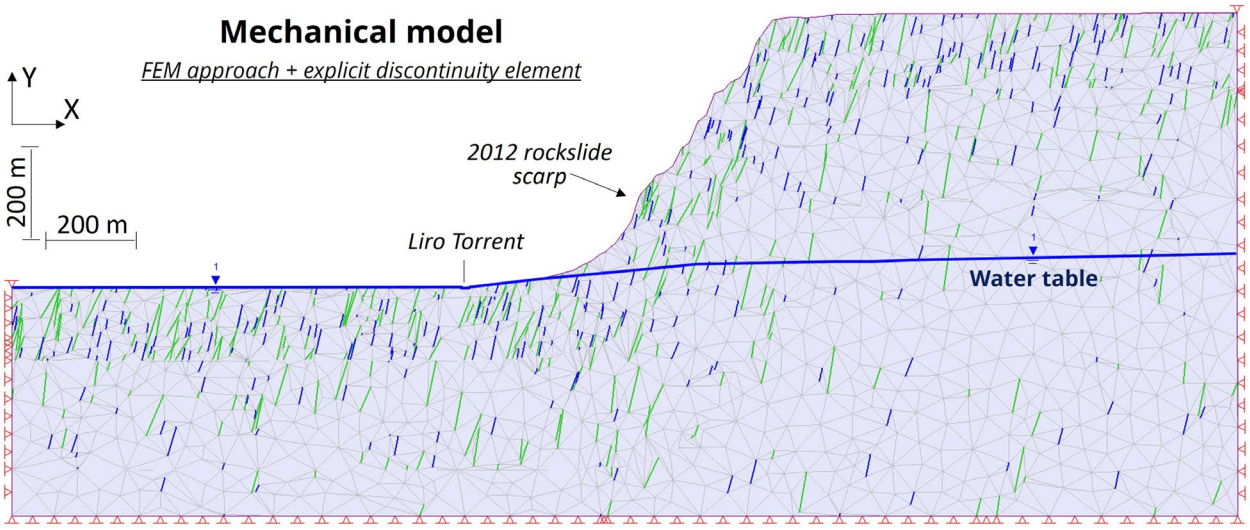

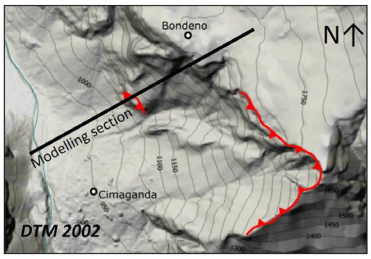

Joint network: geometrical features

SET	Type	Dip Dir. [°]	Dip [°]	Representation	Mean length [m]	Intensity of fracturing
K1	Shistosity	34	27	Implict	/	/
K2	Joint	287	78	Explict	58.2	0.00013
K3	Joint	222	79	Explicit	34.3	0.00013

Joint network: mechnical properties

SET	Type	C_P[MPa]	C_i[MPa]	ϕ_P [°]	ϕ_r [°]	k_N[GPa/m]	k_S[GPa/m]
K1*	Shistosity	0.2	0	32.5	24	4.08	1.47
K2**	Joint	0.15	0	28	25	3	1.32
K3**	Joint	0.25	0	48	33	4.08	1.47

* Derived from field surveys; ** Derived from laboratory tests

Material properties

sigci	175/60	MPa
mi	26	
D	0.8	
Ei	35/20	GPa

Hoek-Brown Criterion

GSI	60/55
mb	4.185/3.285
s	0.00483/0.002
a	0.50284/0.504

Figure 3.21 – Mechanical model of the Cimaganda rock slope.

Concerning the hydrogeological characterization, rock-masses principal hydraulic conductivities were calculated by means of the permeability tensor eigenvectors and eigenvalues considering joint orientation, JRC, aperture and fracture frequency of each discontinuity set (Lotti et al. 2012). Equivalent hydraulic conductivity value of the rock-mass of $k_{max}=1.61\cdot10^{-3}$ m/s and $k_{min}=2.83\cdot10^{-7}$ m/s were calculated from the collected data.

The definition of the rockslide triggering factors involved the analysis of the rainfall regimes and the definition of hydraulic boundary conditions for the development of a transient HM analysis (Figure 3.22a). The 2012 failure was preceded by a rainfall event with a cumulated precipitation of 267 mm in four days, resulting in a return period event of more than 50 years ("San Giacomo Filippo" ARPA station, at 2064 m a.s.l.). The triggering rainfall dataset was divided into periods of constant rainfall intensity, and for each of these, vertical infiltration values were calculated assuming no surface runoff, reasonable condition coherent with field observations (Figure 3.22b). The evaluated infiltration over time function represents the input data for the following transient HM analysis.

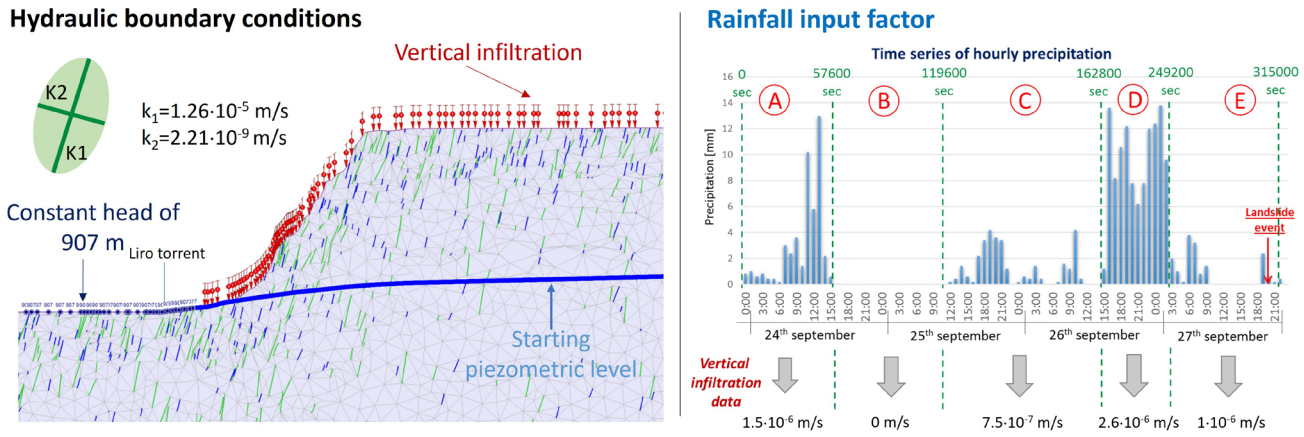

Figure 3.22 – Hydraulic boundary conditions for a transient HM analysis.

Modelling procedure

Starting with a fully dry model, the following steps were performed; for each step, an elasto-plastic equilibrium was carried out:

- The system was led to elastic equilibrium under gravity load. At the end of this step resulting displacements were reset (*Step 0*).
- Elasto-plastic mechanical strength parameters were introduced to the rock-mass, and to the joint network, considering the best conditions, i.e. the mechanical highest values detected in the studying area (*Step 1*).
- The effect of groundwater was evaluated considering a static piezometric level supposed as the local ordinary hydrogeological regime (Figure 3.21). Due to the absence of direct measurements of groundwater levels in the slope, some hydrogeological assumptions were necessary. The water table was introduced accounting the presence of the Liro torrent on the bottom of the valley and considering the general absence of groundwater outflows along the slope. The resulting piezometric level cross the slope only on its lower part, laying below the slip failure surface of the studied rockslide (*Step 2*).
- The application of a second perturbation to the system, representing the mechanical degradation of the rock-masses, was established reducing the GSI index (i.e., the Hoek & Brown strength parameters) from 60 to 55 (*Step 3*).
- The mechanical properties of the intact rock and of the joint sets were downgraded (while maintaining an overall rock-mass GSI of 55), introducing the lowest parameters detected in the study area (*Step 4*).

- The effects of the triggering rainfall event were simulated using a semi-coupled HM analysis (i.e., variations in pore pressure within the joint network and the rock matrix's porous space affect effective stresses and thus deformation distributions, but deformations do not affect pore pressure). Rainfall and hydrogeological conditions were reproduced by a transient analysis, specifying a vertical infiltration along the slope and a constant head at its toe to simulate the presence of the Liro torrent (*Step 5*).

Following the concept of progressive failure mechanism, *Steps 1 to 4* stand for the preparatory factors which led the system to a mechanical degradation (Section 1.2). At last, the introduction of rainfall infiltration represents the collapse triggering factor.

3.3.4.2 Results

At the first steps of the analysis (S*teps 1-2*), introducing the best mechanical properties and ordinary hydrogeological conditions, the general evolution of the slope was simulated (Figure 3.23).

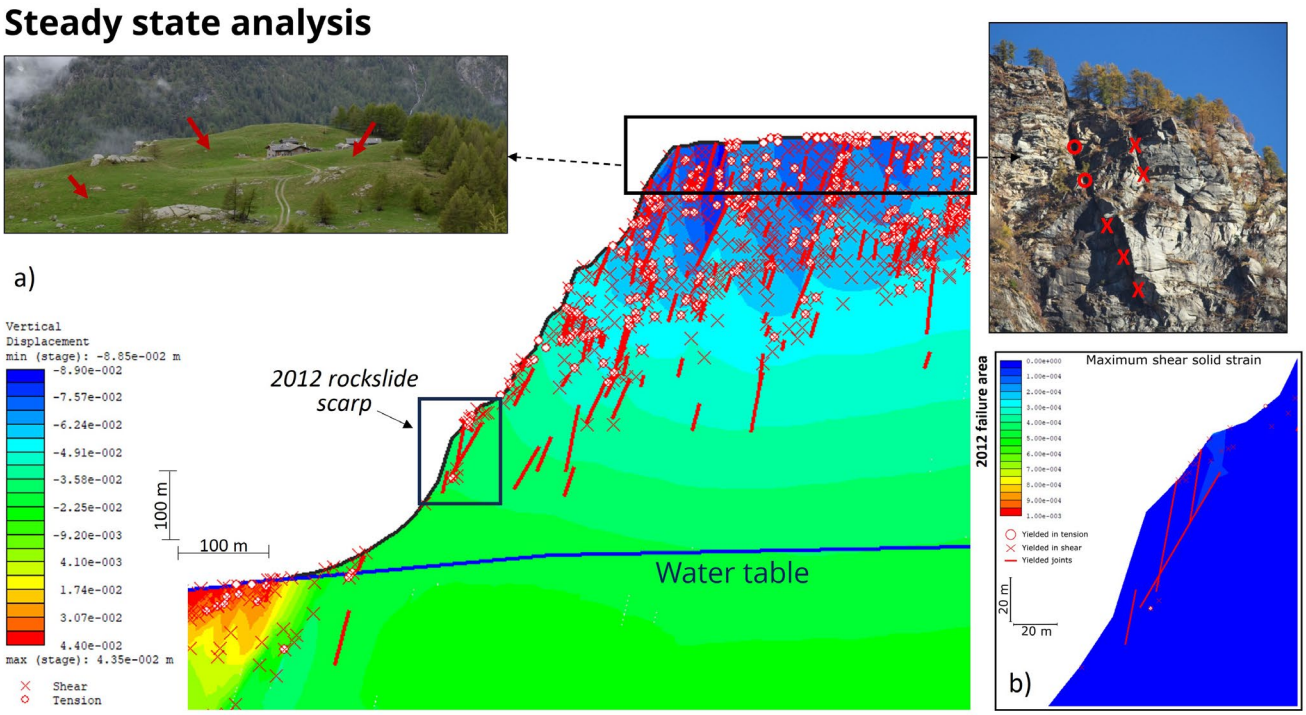

Figure 3.23 – Results from the steady state numerical analysis. a) Plot of vertical displacement and yielded elements obtained introducing a static piezometric level (i.e., ordinary conditions). b) Distribution of maximum shear solid strain and plastic joints along the 2012 failure area.

The preparation to instability is highlighted by the presence of yielded elements located at the top of the slope and in correspondence with the pre-failure scarp. The distribution and entity of the simulated

displacements are in accordance with the direct measurements carried out during geological surveys: the vertical component of displacements (in the order of 10^{-2} m) clearly identifies areas in subsidence at the top portion of the slope; meanwhile the horizontal one (in the order of 10^{-1} m) concentrates at its central portion, close to the location of instability events. At the 2012 failure area, the presence of discontinuity elements in plastic conditions shows a predisposition to instability (Figure 3.23b).

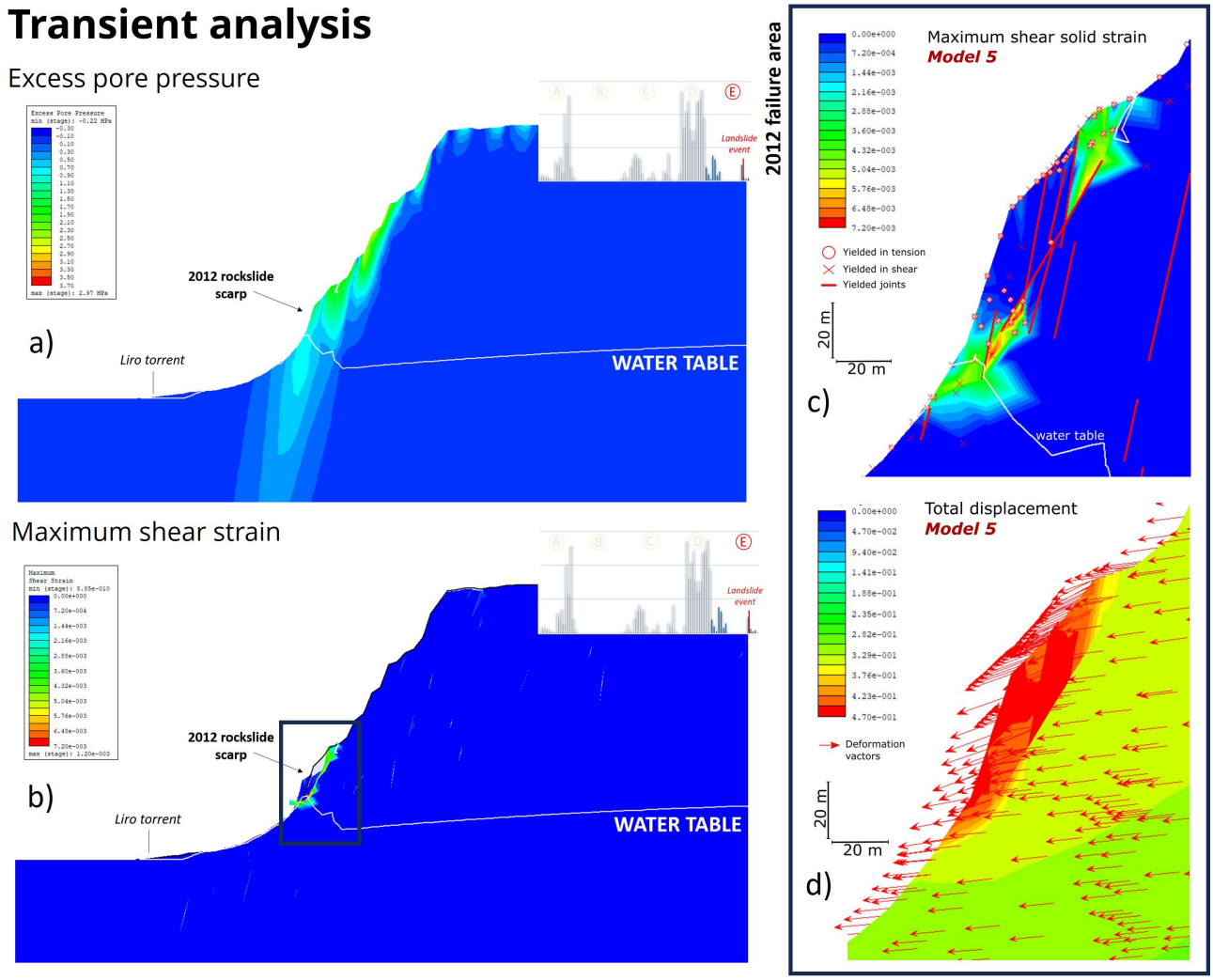

Figure 3.24 – Results from the transient numerical analysis. a) Distribution of excess pore pressure at the end of the simulated rainfall event. b) Distribution of maximum shear strain at the end of the simulated rainfall event; instability in highlighted by the development of a sliding surface. c) Distribution of maximum shear strain at the 2012 failure area. d) Distribution of total displacements at the 2012 failure area.

The introduction of worse geomechanical properties induces a significant increase in the yielded elements and a slightly increase of the displacement's modulus. Focusing on the central part of the slope where the 2012 rockslide event occurred, a shear strain surface begins to develop, with a tension crack opening at the top of the pre-failure cliff. At the end of *Step 5* the slope is in condition of gravitational instability, however without a hydrogeological triggering factor, a critical condition (i.e. collapse) is not

yet reached. Finally, the introduction of rainfall infiltration, induced a limited and temporary rising of piezometric level (Figure 3.24a), with localized excess of pore pressure, sufficient to lead the slope to a critical state (Figure 3.24b). The maximum shear solid strain and total displacement distribution (in the order of $5 \cdot 10^{-1}$ m) clearly show the presence of a critical composite shear sliding surface approximately corresponding to the observed one in terms of geometry and volumes involved (Figure 3.24c-d).

3.3.5 Discussion

In this Section, the Cimaganda case study was presented, in which the interaction between geomechanical features and climate loadings causes frequent gravitational instability processes.

Based on the results of a geomechanical characterization and subsequent laboratory investigations, a geological model of the slope was developed, with the aim of identifying evolutionary scenarios and simulate the 2012 rockslide event induced by heavy rainfall.

The adopted hybrid numerical configuration (FEM approach plus explicit discontinuous network), allowed to improve an integrated analysis in which discontinuous and continuous elements can interact with each other resulting in fracture propagation through rock-mass. Considering preparatory and triggering factors involved in the analysis, it allowed to apply the concept of progressive failure mechanism, focusing on the propagation of damaged elements both discontinuous and continuous. This represents a considerable difference with DEM approaches, in which failure and fracture propagation is admitted only along existing discontinuity elements (Hammah et al., 2008).

The modeling analysis showed that the progressive failure mechanism within the Cimaganda rock slope appears to be favored by the joints orientation and is essentially related to tensile or shear failures propagating from the discontinuity elements.

The adopted numerical method allowed also the improvement of groundwater seepage analysis, necessary to the introduction of the rainfall event. The simulation of the triggering mechanisms faithfully to what happened in September 2012 (amount of rainfall and hydrogeological infiltration times) allowed to validate the proposed geomechanical model for the Cimaganda rock slope. Mechanical properties of intact rock and discontinuities introduced in the model, well simulate the behavior of the slope. In addition, it should be noted that simulated instability is associated with the worst geomechanical properties of the surveyed rock-mass and non-ordinary hydrogeological settings, which means that even if the slope is predisposed to instability processes, these are promoted by peculiar mechanical and climatic conditions.

This analysis revealed the decisive role of the pore pressure evolution within the Alpine slopes. A rainfall event such as the one simulated in the present work, is sufficient to cause a substantial rise in the piezometric level and bring rock-masses to saturation conditions, even in the absence of a particularly developed hydrogeological body. This, together with the presence of unfavorable geomechanical conditions, is sufficient to define the development of failure events. Rupture mechanisms related to such dynamic processes, appear to be driven by the progressive development of a shear surface along which plastic elements are concentrated and progressively propagate from existing discontinuity elements. The presence of sub-vertical discontinuities, as in the case of the present study, promotes both rainfall infiltration and also the tensional release of rock material. These observations demonstrate how for the study of slope evolution in response to climatic forcing, it is therefore of critical importance to couple robust geomechanical characterization with numerical stress-strain analysis.

3.4 Conclusion

This Chapter discussed two different case studies representing common mechanical evolutionary scenarios of Alpine rock slopes: the large Piuro landslide which involved an entire slope with volumes in the order of $1 \cdot 10^6$ m^3 and the 2012 Cimaganda rockslide, resulting from the collapse of a singular rock-mass.

In both cases, the adopted approach involved careful geological and geomechanical characterization of the slope, the development of a conceptual geological model, and an HM numerical simulation.

Regarding the Piuro landslide, a particularly complex geological setting was shown to have been responsible for the development of slope instability. This required the use of a numerical 3-D approach that allowed to verify the decisive role of geological elements such as faults and tectonic contacts, and to analyze the 3-D distribution of interstitial pressures as a consequence of an intense rainfall event. Assigning low geomechanical properties to the outcropping material, a predisposition for gravitational instability in correspondence of the Piuro landslide failure area was detected. Subsequent introduction of a persistent rainfall event through an HM analysis, was sufficient to generate localized increase of pore pressures and trigger the 1618 event. The simulated volumes and geometries are compatible with observations carried out in the field, validating the model.

Even in the absence of particularly developed hydrogeological bodies (i.e., a piezometric level close to the topographical surface), morphological and hydraulic forcings are still able to generate groundwater suspended bodies with significant localized increasing of pore pressure.

The analysis of the 2012 Cimaganda rockslide revealed an evolutionary scenario different from the previous one, mainly driven by the peculiarly predisposing geomechanical setting with a typical discontinuous behavior. The presence of persistent and open discontinuity elements with sub-vertical orientation parallel to the slope, results in the release of potentially unstable material. In addition, the presence of highly degraded material highlights an advanced evolutionary state of the slope, which can therefore easily undergo instability processes.

The geological and geomechanical setting detected agreed with the use of a 2D approach, where, the introduction of discontinuity elements was necessary through the incorporation of a discontinuous network in a FEM approach. The results of the HM analysis showed that the rainfall input, was sufficient to generate a limited and temporary rise in the piezometric level at the base of the slope, bringing it to water saturation. This resulted in the development of water over pressures in correspondence of discontinuity elements, that progressively resulted into inelastic deformations leading to slope failure at the end of the rainfall event.

Both analyses confirmed the dominant role of HM couplings in the definition of slope instability processes. The concept of progressive degradation of Alpine slopes, widely shown in previous Chapters, finds here new evidences and verifications. According to field evidences, slopes were brought to failure considering an unfavorable geomechanical scenario in which the action of a single rainfall event can lead to collapse. The slope degradation process, which can be analyzed with a much longer observation time than that of a single rain event, involves a greater impact of water and pore pressure on the deformation state of slopes, which are therefore more sensitive to this type of process. In the next Chapter, the progressive degradation process of rock-masses will be analyzed in detail, evaluating the effect of thermal factors (i.e., atmospheric temperature) in the mechanical evolution of rock slopes. In this way it will be possible to explore, with a different time scale, the action of climatic factors, increasing the knowledge of such processes and take a step toward a multiphysics numerical approach.

Chapter 4
The role of atmospheric temperature variations in the stress-strain evolution of Alpine slopes

4.1 Introduction: research question and objectives

The Alpine environment is affected by significant variations of climate conditions on both short- and long-term periods, mainly revealed by changes in subsurface temperature, hydrological regimes and groundwater circulation. In general, studies (see Section 1.3) have shown that the effectiveness of surface thermal forcing is related to its cyclic and continuous action, resulting in a daily cumulative effect that can contribute to driving rock-masses toward unstable conditions on large time scales. The effects of heating-cooling cycles are negligible when considered in the short and medium term, while in the long term they can significantly influence the mechanical behavior of rock-masses and act as a thermal fatigue process (Hall 1999; Gunzburger et al. 2005). Thermal expansion-contraction cycles cause perturbations in the stress fields that can induce both the growth of pre-existing cracks and the genesis of new ones (Eppes et al. 2016), resulting in rock-mass degradation.

To address the effects of temperature on rock slope stability, in the last decades, several monitoring systems were proposed. In the engineering sector, rock slope monitoring systems are generally linked to construction sites, or to protect infrastructures and buildings (Li et al. 2018; Scaioni et al. 2018; Ma et al. 2020). Thermal observations are generally limited to air temperature; only recent scientific studies have shown data regarding rock face temperature (Brideau et al. 2011; Blikra and Christiansen 2014; Collins and Stock 2016; Eppes et al. 2016; Collins et al. 2017; Marmoni et al. 2020) and thermal changes within the rock-mass (Magnin et al. 2015; Fiorucci et al. 2018). Racek et al. 2021a, proposed an easy and modular monitoring system composed of crack meters, a climate station, solar radiation sensors, and a compound borehole temperature probe. Racek et al. 2021a monitored different sites in the Czech Republic providing both thermal and mechanical data, measuring temperature variations up to 3 m deep. These studies have shown a clear dependence of atmospheric temperature variations on the deformation state of rock-masses, with particular reference to the aperture measured along discontinuities. The relationship is very clear at the seasonal scale while of minor magnitude at the daily scale. Temperature variations are generally confined to the first 0.5 m for daily oscillations while they can exceed 3 m at the long-term seasonal scale.

Monitoring systems are usually expensive and difficult to maintain and are limited to a single-point

measurement of rock temperature, without information on its spatial distribution over the whole rock-mass. As a consequence, the temperature of the rock-mass is known only in few points even if it can differ significantly due to variations in morphological and exposure conditions (Gruber et al. 2003). This limitation can be overcome by using infra-red (IR) cameras, which enable to measure temperature changes over the entire rock face (Teza et al. 2012; Sobrino et al. 2016; Grechi et al. 2021; Racek et al. 2021b). With this approach, the intensity and the evolution in time and space of temperatures can be constrained with respect to local climatic conditions, morphological features (i.e., surface irregularities and differently exposed surfaces) and jointing conditions of the target under investigation.

Due to its great potential, IR demonstrated to be a useful non-invasive remote sensing technique in various scientific fields, among which is the detection of unstable blocks on a rock slope face (Guerin et al. 2019). When open joints are within the thermal active layer, air-filled discontinuity networks can strongly influence the in-depth heat propagation, leading to fragmentation of the heat front. Such an effect is responsible for significant differential heating–cooling cycles of isolated sub-volumes or rock blocks. In this way it is possible to detect rock blocks detached from the main wall, as they are surrounded by discontinuity elements with air insulating heat transfer. For instance, during the cold season, wide continuous cracks can be mapped as they appear warmer due to duction of warmer air from inside the mass (Baroň et al. 2014).

Regarding slope stability and stress-strain analyses of rock-masses, only a few works in the literature consider also the mechanical impact of surface thermal variations through numerical modeling.

In this framework, the importance of including short-term temperature variation was first highlighted by Gischig et al. 2011b, c using a simplified elastic rock-slope model and showing that TM stresses can induce rock-mass deformation and joint failures even at greater depths below the thermo-active layer. Then, the role of long-term temperature changes supporting deglaciation in the Alpine environment, was explored by Baroni et al. 2014, performing a numerical analysis applied to the Adamello Valley. Based on these observations Grämiger et al. 2018 performed a numerical analysis showing that TM stresses could represent a significant factor driving rock-mass damage in periglacial environments, especially for exfoliation joints failures. Moreover, several studies based on field data measurement and physical models, showed the capability of periodic temperature oscillations to induce plastic damage on discontinuous elements (Gunzburger et al. 2005; Bakun-Mazor et al. 2020).

Numerical modeling methods are also useful for analyzing heat flow within rock-masses and for simulating temperature distribution along a slope. These are essential tools when the installation of monitoring systems is infeasible or too expensive, but also when the time scale of analysis is very long, as in the case of simulating the stress history of Alpine slopes or to predict their future evolution.

As an example, Marmoni et al. 2020, studied the spatial distribution of daily near-surface temperature variations and the heat flux propagation through a jointed rock-mass in a rocky quarry wall, pointing out the importance of coupling monitoring methods with numerical ones.

In this Chapter, considering all these observations, the effects of surface temperature variations on slope stability are explored and applied to the Cimaganda rock slope (Section 3.3). Analyses are aimed to evaluate whether temperature may serve as a driving factor for slope instabilities, evaluating the effect of both long-term (years to centuries) and short-term thermal variations (daily to seasonal).
In a first step, a coupled TM numerical modelling was developed considering (i) glacial debuttressing resulting from the Last Glacial Maximum (LGM) deglaciation, (ii) paleo-temperature redistribution and (iii) seasonal temperature fluctuations (i.e., heating-cooling cycles).
In a second step, preliminary data collected by a TM monitoring system installed along the Cimaganda slope were analyzed. The aim is to provide preliminary evidences of the temperature fluctuation impacts (from daily to seasonal) on the distribution of temperature inside a rock-mass and the resulting deformations along discontinuities. This represents an initial exploratory data collection that can be enhanced in the future to identify TM and climatic relationships.

In Section 4.2.1 the geological, geomorphological, and geomechanical features of the historical Cimaganda rockslide will be discussed by recalling the observations and data presented above in Section 3.3. In Section 4.2.2 the climatic history of the slope will be presented, with a special focus on its past evolution. Starting from the geomechanical model presented in Section 3.3.3, a TM analysis will be developed in Section 4.2.3. Finally, in Section 4.3 the installation of a TM monitoring station will be presented. In Section 4.4, conclusions based on the main evidences from the developed analyses will be provided.
The TM numerical analysis applied to the Cimaganda rock slope has been published in Morcioni et al. 2022.

4.2 Thermo-mechanical numerical analysis applied to the Cimaganda rock slope

In this Section, a TM analysis was defined and applied to the Cimaganda rock slope. Analyses are aimed to evaluate whether atmospheric temperature may serve as a driving factor for slope instabilities, evaluating the effect of both long-term (years to centuries) and short-term thermal variations (daily to seasonal). In the next two paragraphs, the geological and geomechanical features of the Cimaganda slope, which have already been discussed extensively in the Section 3.3, will be initially taken up. Next, the climatic variables that have affected and characterize the study area will be discussed in order to define the input factors of the present analysis.

4.2.1 The Cimaganda rock-slope

As widely discussed in the Section 3.3.2 and 3.3.3, the Cimaganda rock slope presents peculiar geomechanical and morphological features, resulting in extensive gravitational instability processes throughout the area. In particular, it was highlighted that the mechanical behavior of the outcropping rock-masses follows a typical discontinuous behavior, resulting in the isolation of potentially unstable rock material. This set-up appears to be particularly favorable for the development of gravitational instability processes, as demonstrated by the numerical modeling analyses developed for the 2012 rockslide event (Section 3.3). Another particularly significant feature is the presence of a strong degree of degradation of the outcropping rocks, with thick patinas of alteration, smooth and discolored joint surfaces, and the development of microfractures giving low mechanical properties to the material. The climatic history of the slope could represent one of the main forcings that had led to the development of these weathering processes, thus representing preparatory factors for gravity-driven instability. Among them, of particular importance, could be the cycles of glacial advance and retreat that affected the entire Cimaganda slope as evidenced by the presence of striae and scoured rocks (Section 3.3.2). To them, thermal variations and hydraulic dynamics driven by climatic loads over the short and long term, are superimposed.

4.2.2 Data collection

The collection of geological, geomorphological, and geomechanical data for the Cimaganda rock slope has already been extensively discussed in Section 3.3.2, to which please refer for a complete discussion. The collected data allowed the definition of a robust geological and geomechanical model of the slope,

validated with a back-analysis of the 2012 event. In consideration of the aims of the analysis presented in this Section, the climatic evolution of the study area in both the short and long term, is now addressed. The goal is to define the most significant factors in the evolution of the Cimaganda rock slope, which will represent input factors in subsequent stress-strain analyses.

4.2.2.1 Past and current climate regime

During the Pleistocene age, in the last 2.6 million years, European Alpine valleys were affected by several glacial and interglacial periods (Bini 1996), related to significant variations in the mean atmospheric temperatures driven by climate dynamics at the global scale (Section 1.3.1).

Ice extension during the Last Glacial Maximum (LGM) in the Valchiavenna region has been reconstructed by Tantardini et al. 2022 in agreement with Bini et al. 2009. During the LGM the whole San Giacomo Valley was occupied by ice and only the highest peaks and ridges were ice-free. The ice thickness between the valley bottom and the trimline was 450 m in the upper valley, at the Montespluga Lake, and increased downstream up to 1550 m at San Giacomo Filippo village due to the topographical and morphological constrains (Tantardini et al. 2013). In correspondence of the Cimaganda slope the ice level reached an elevation of 2150 m a.s.l, resulting in a glacial thickness of 1230 m. The San Giacomo glacier joined the Engadin-Bregaglia glacier in the Chiavenna area, making a single body which flowed southwards until it joined the Adda glacier.

As described by Tantardini et al. 2013, after LGM expansion, the San Giacomo glacier passed from a single and wide body to a smaller tongue forced to flow into the valley floor. As melting proceeded, the glacier thickness decreased and progressively receded back to the upper valley. In agreement with studies conducted in the Alps and Engadin region (Florineth and Schlüchter 1998; Olhendorf C 1998; Maisch et al. 2003; Bini et al. 2009; Ivy-Ochs 2015), for the study area at hand it is reasonable to assume glacial maximum conditions until 19-18 kyr BP, followed by a general melting phase. Once deglaciation in the principal San Giacomo Valley was completed and ice-free conditions were reached, valley flanks have been no longer subject to glacier advances.

During late Pleistocene and Holocene age, deglaciation in Alpine regions was supported by a change in climate conditions with a general long-term air warming trend. According to Ivy-Ochs et al. 2009 and Davis et al. 2003 using pollen data, during LGM mean temperatures were about 12 °C colder than today and began to rise following the deglaciation process; at the end of Pleistocene, mean air temperatures had risen to values of 3.5 °C colder than today and stabilized around the current values during Holocene age.

Current climate conditions exhibit typical features of an Alpine environment. Elevations in the San Giacomo Valley range from 333 m a.s.l. of the Chiavenna Village up to 3279 m a.s.l. of the Pizzo Tambò. Air temperature data relative to the last decades recorded by the 3 climate stations located along the valley, were analyzed in order to evaluate their annual evolution (https://www.arpalombardia.it/). Daily and monthly average temperature series are shown in Figure 4.1 together with the weather stations location. Annual fluctuations with negative average values during winter and positive values during summer were observed. Fitting the time series with a periodic sine function, a mean annual amplitude of 10.2 °C was identified. While mean annual temperatures depend on altitude, the amplitude of seasonal oscillation is not strongly affected by elevation (Figure 4.1).

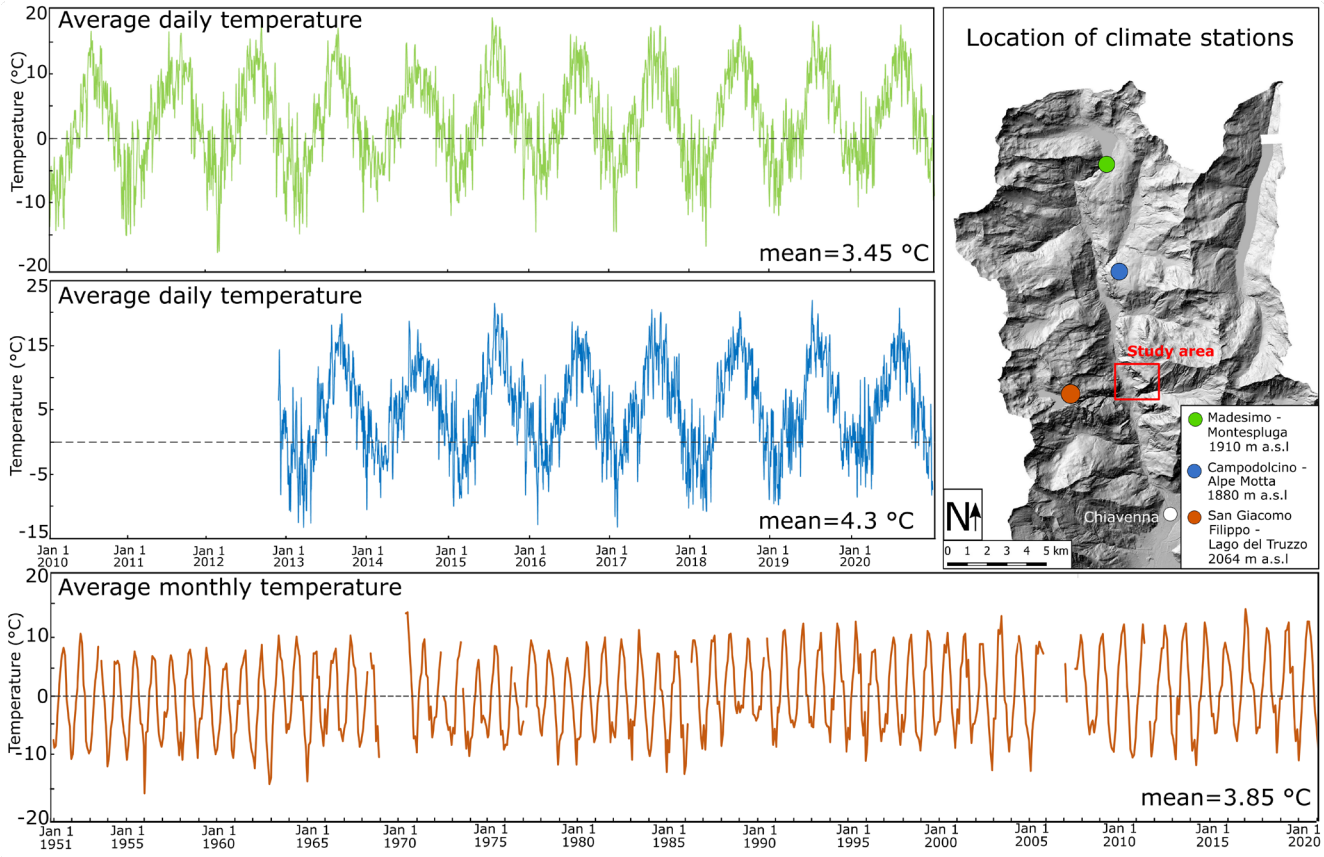

Figure 4.1 - Daily or monthly average air temperature histories recorded by the 3 climate stations located along the San Giacomo Valley during the last decades.

4.2.3 Thermo-mechanical analysis

Starting from LGM condition, the combined effects of (i) glacial debuttressing (ii) paleo-temperature redistribution and (iii) seasonal temperature fluctuations are explored in this Section, focusing on the propagation of failure elements within the rock-mass domain. The analysis is aimed to evaluate whether

temperature may serve as a driving factor for rock slope instabilities, evaluating the effect of both long-term (years to centuries) and short-term thermal variations (daily to seasonal). Simulation of highly degraded areas along the slope surface, as well as the reproduction of mechanical scenarios that allude to the development of large-scale slope instabilities (e.g., historical Cimaganda rockslide), will be analyzed and used as model validation.

4.2.3.1 Methods

Numerical analysis of the Cimaganda rock-slope was performed using the 2D DEM code UDEC (version 7.0 - Itasca Consulting Group 2018), suited to evaluate the stress-strain evolution of a discontinuous medium like the rock-mass at hand and the Cimaganda rock slope (Section 2.3). Transient long-term temperature distributions were calculated using the FEM code COMSOL Multiphysics (Version 5.4 - www.comsol.com), that allows greater flexibility compared to UDEC in defining boundary conditions and simulate thermal processes (Section 2.3).

To analyze the effects of temperature changes in the stress-strain field along the slope, a linear thermoelastic behavior of the rock-mass was assumed. Variations in the stress state are thus induced by thermal strains resulting from isotropic volumetric expansion or contraction of rock blocks, governed by a constant thermal expansion coefficient. For each block, considering the constraint exerted by the presence of the surrounding blocks at all locations but the slope surface, thermally induced volumetric strains will cause stress state changes, which can even propagate at depths greater than the so-called thermally active layer (maximum depth at which a surface temperature change is propagated). Changes in the stress state within the rock-mass domain will affect interfaces between intact blocks for which an elasto-plastic behavior is assumed. As the stress state evolves, the shear stress at interfaces may reach failure conditions, thus inducing plastic straining.

Modelling approach

The cross section represented in the numerical model (Figure 4.2a), taken along the historical Cimaganda rockslide's direction of movement, extends from the west to the east slope of the San Giacomo Valley and is based on the 2015 Digital Terrain Model of the Lombardy Region, modified by reproducing the pre-failure topography conditions, assuming a continuity with the lateral slopes.

The mechanical model includes two rock-mass basic components: discontinuities and intact rock (Figure 4.2b). Discontinuities are represented by a multiple joint network based on the three different systems identified with geomechanical surveys (Section 3.3.2.3). The UDEC built-in joint generator was used,

to reproduce with a statistical approach similar joint patterns to those observed in the field. Relevant parameters for the joint generation procedure are represented by the dip angle (angle between joint track and x-axis), trace (length of joint segment), and spacing (distance normal to joint tracks). They were determined based on geomechanical field measurements performed on rock-masses outcropping along the slope (Section 3.3.2.3). A statistical analysis of collected parameters was performed and representative values were obtained: for each of them, a mean value and a standard deviation representing random fluctuation around the mean were provided (Section 3.3.2.3). Considering scale effects, the geometrical values directly measured at outcropping rock-masses were scaled up by a factor of 100 in the model. Also, to account for a confinement effect, joint spacing was increased at depths greater than 1000 m by a factor of 2 and at depths greater than 2500 m by a factor of 4 (Figure 4.2b).

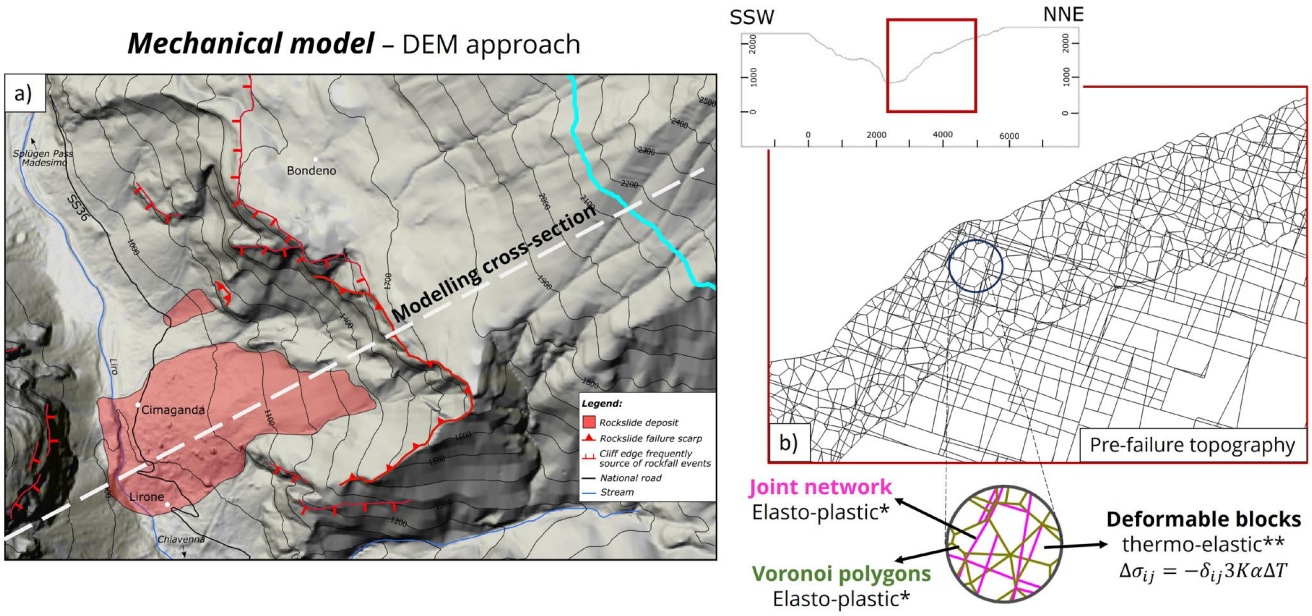

Figure 4.2 – a) Location of the modelling cross-section. The LGM trimline is also highlighted (light blue line). b) Cross-section and mechanical model of the slope.

Discontinuities were assigned an elasto-plastic Mohr-Coulomb constitutive law including slip-weakening of ϕ and c (Table 4.1). The joint model aims at simulating displacement-weakening by loss of frictional, cohesive and tensile strength: once shear or tensile failure is reached, strength properties instantaneously drop from peak to shear residual values and null tensile strength.

Joint strength parameters were derived from both direct-shear laboratory tests (*K2* and *K3* discontinuity sets; Section 3.3.2.3) and from Barton-Bandis model (*K1* set), developed using JRC and JCS data evaluated during geomechanical surveys (Section 3.3.2.3) and corrected in relation with the scale effect (Barton and Bandis 1982).

So-called Voronoi tessellation was introduced to simulate intact rock, while allowing for the possibility of newly formed discontinuities (Rwechungula and Cheng 2021; Wu et al. 2023). The Voronoi tessellation procedure in UDEC is controlled by two factors: the "Average edge length" and the "Iteration number". The Voronoi algorithm begins by distributing points randomly within the region to divide. Then, an iteration procedure moves the points depending on the iteration number: the higher the number of iterations, the more uniform the spacing between points will be. Next, triangles are created between all points and the Voronoi polygons are defined by constructing perpendicular bisectors of all triangles that share a common side (Itasca Consulting Group 2018). Polygons were built with an average edge length of 100 m and iteration number of 5 (software default value). Considering the extension of the slope and the geometrical properties of discontinuities, these values allowed a proper geometrical representation with a good computational cost.

Table 4.1 - Mechanical elasto-plastic properties of discontinuities, Voronoi polygons and blocks.

Mechanical properties of Discontinuities and Voronoi polygons				
	*K1**	*K2**	*K3**	*Voronoi**
Peak friction angle [°]	32.5	28.0	48.0	53.0
Peak Cohesion [MPa]	0.1	0.1	0.2	5.0
Residual friction angle [°]	24.5	25.0	33.0	28.0
Residual Cohesion [MPa]	0	0	0	0
Tensile strength [MPa]	0	0	0	1.0
Residual tensile strength [MPa]	0	0	0	0
Normal Stiffness [GPa m^{-1}]	1.5	1.5	4.0	20.0
Shear Stiffness [GPa m^{-1}]	1.0	1.0	1.5	10.0
Mechanical properties of blocks				
Density* [kg m^{-3}]	2700			
Bulk Modulus* [MPa]	$4.0 \cdot 10^4$			
Shear Modulus* [MPa]	$1.4 \cdot 10^4$			
Thermal expansion coefficient** [K^{-1}]	$9.5 \cdot 10^{-6}$			

* Derived from site-specific laboratory tests; ** Derived from literature.

Rock strength parameters were calculated by applying the GSI approach (Marinos and Hoek 2000) considering results from geomechanical surveys and uniaxial compression tests (Section 3.3.2.3). This resulted in estimated values of c (5.0 MPa), ϕ (53.0°) and σ_T (1.0 MPa) that were assigned to Voronoi contacts assuming a Mohr-Coulomb constitutive law (Table 4.1).

Rock blocks, resulting from the intersection of discontinuities and Voronoi polygons, were set as deformable and discretized into a triangular finite-difference mesh. Blocks were assigned thermo-elastic properties considering a homogeneous and isotropic material (Table 4.1), where mechanical properties

derived from site specific laboratory tests (Section 3.3.2.3) while thermal expansion properties were taken from the literature (Cermak and Rybach 1982; Robertson 1988; Grämiger et al. 2018). Considering that TM analyses are computationally intensive, models require an as simplified as possible geometry. Hence, the modelled area was restricted to the east slope of the San Giacomo Valley, where the historical Cimaganda rockslide developed, and Voronoi tessellation was introduced only in the uppermost 500 m of this area (Figure 4.2b). Roller boundaries were applied to the lateral sides of the model, whereas the bottom boundary was fixed. Domain borders were placed far enough from the area of interest to avoid boundary effects.

The adopted modelling strategy, involving the use of two software was developed using the modelling strategy outlined in the following scheme (Figure 4.3) and discussed in the next paragraphs.

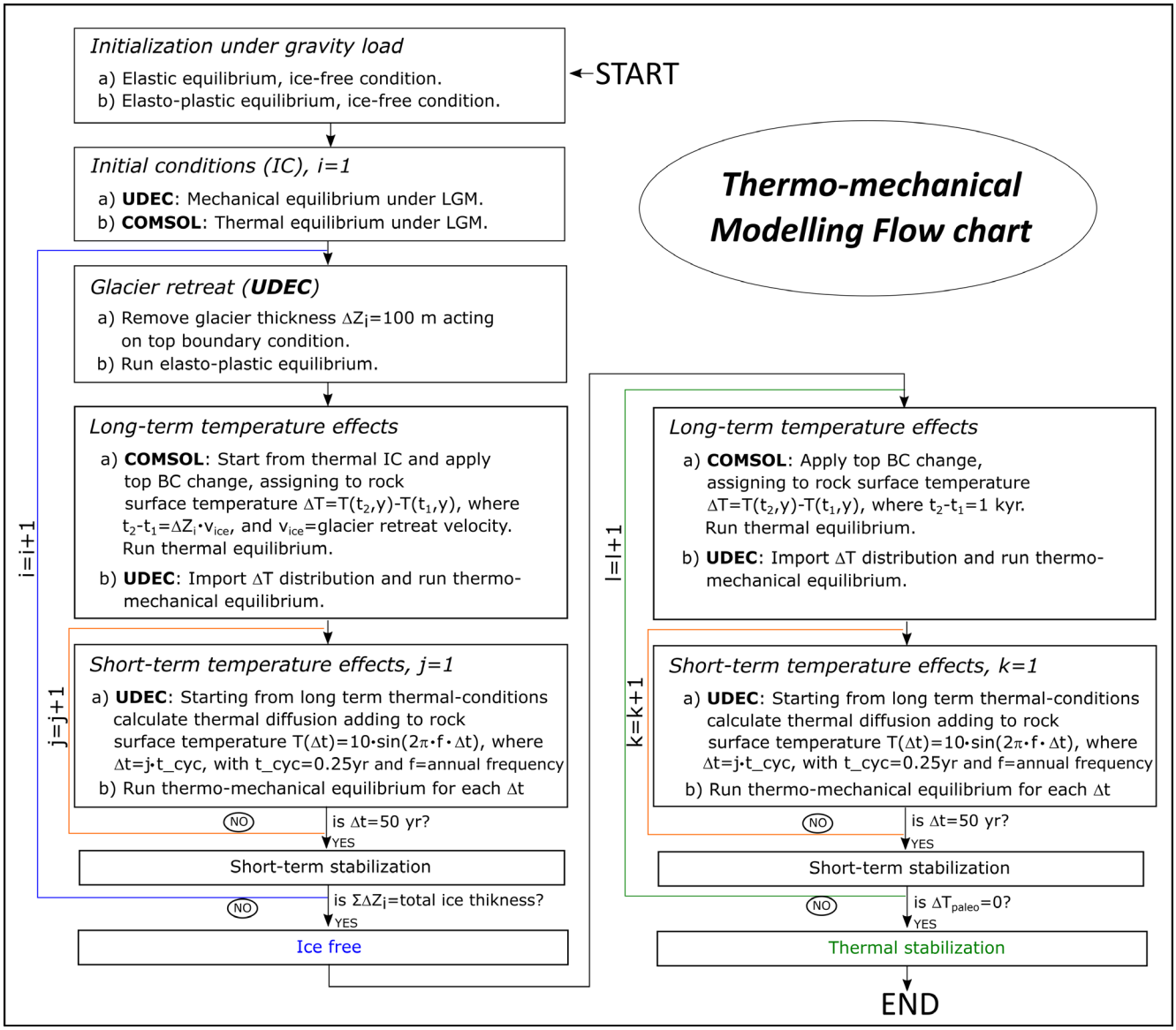

Figure 4.3 - Thermo-mechanical modelling flowchart.

Modelling procedure

Initialization

The initial elastic stress field due to the gravity load and topography constraints under ice-free conditions was calculated by a mechanical initialization simulation until force-equilibrium was reached. In this phase, the strength of discontinuities was set sufficiently high (i.e., c and Φ were increased by one order of magnitude) to prevent failure. Then, Mohr-Coulomb elasto-plastic properties were activated thus allowing joints to yield, and equilibrium stresses were recalculated. After this 2-step initialization procedure, the extent of mechanical damage and stress-strain distribution in the slope are deemed to represent the ice-free, pre-LGM mechanical conditions in the San Giacomo Valley. Next, the glacial load corresponding to the LGM ice level was introduced as an isotropic load boundary condition, at the slope surface (Figure 4.4). Assuming an ice density of 900 kg m^{-3}, ice loads were defined by the following simplified relation:

$$\sigma_{XX} = \sigma_{YY} = Z \cdot \rho_{ICE} \cdot g \qquad \text{(Equation 4.1)}$$

where Z is the ice thickness, ρ_{ICE} the ice density and g the gravity acceleration.

At LGM, the ice level in correspondence of the Cimaganda village reached an elevation of 2150 m a.s.l, resulting in a glacial thickness of 1230 m (Tantardini et al. 2013). LGM ice boundary stresses were thus applied to the slope portion covered by ice, and another elasto-plastic calculation step was performed until mechanical equilibrium. This was set to represent the starting point of the analysis, hence resulting accumulated displacements were reset to zero.

Glacier retreat

Once the initialization procedure was completed, the effect of glacial unloading was explored by reducing the ice thickness acting on the Cimaganda rock slope following Eq. 4.1. To simulate the progressive and continuous deglaciation process, the numerical analysis was performed starting from LGM conditions and representing the glacial retreat with thirteen stages of ice surface lowering, until the ice-free condition was reached. Each stage corresponded to the removal of a 100 m thick ice layer, and, for each stage, mechanical equilibrium was calculated (Figure 4.4a). Stepwise debuttressing is a valid approach to minimize unbalanced forces and reach numerical mechanical equilibrium without excessive computational cost. Moreover, for long-term mechanical studies on glacial time scales, modelling ice as a hydrostatic stress boundary condition leads to more realistic results compared to explicitly representing the ice body in the integration domain as an elastic solid material (Leith et al. 2014). In fact, the latter assumption would lead to significant overestimation of the damage associated with glacier retreat (Grämiger et al. 2017).

Long-term temperature effects

The effects of long-term thermal changes related to the paleo-temperature evolution during LGM deglaciation, were numerically simulated and superposed to the ice unloading effects.

Temperature distributions along the valley cross section were simulated in COMSOL Multiphysics considering the rock-mass as a continuous medium. The process of heat transport is governed by thermal conduction defined by thermal diffusivity (D), which depends on thermal conductivity (λ), specific heat capacity (C_P) and rock density (ρ) following the relation $D = \lambda(\rho C_P)^{-1}$. Values of λ = 2.9 W m^{-1} K^{-1} and C_P = 780 J Kg^{-1} K^{-1} were chosen for the problem at hand, corresponding to generalized values for gneissic lithologies found in the literature (Cermak and Rybach 1982; Robertson 1988; Grämiger et al. 2018).

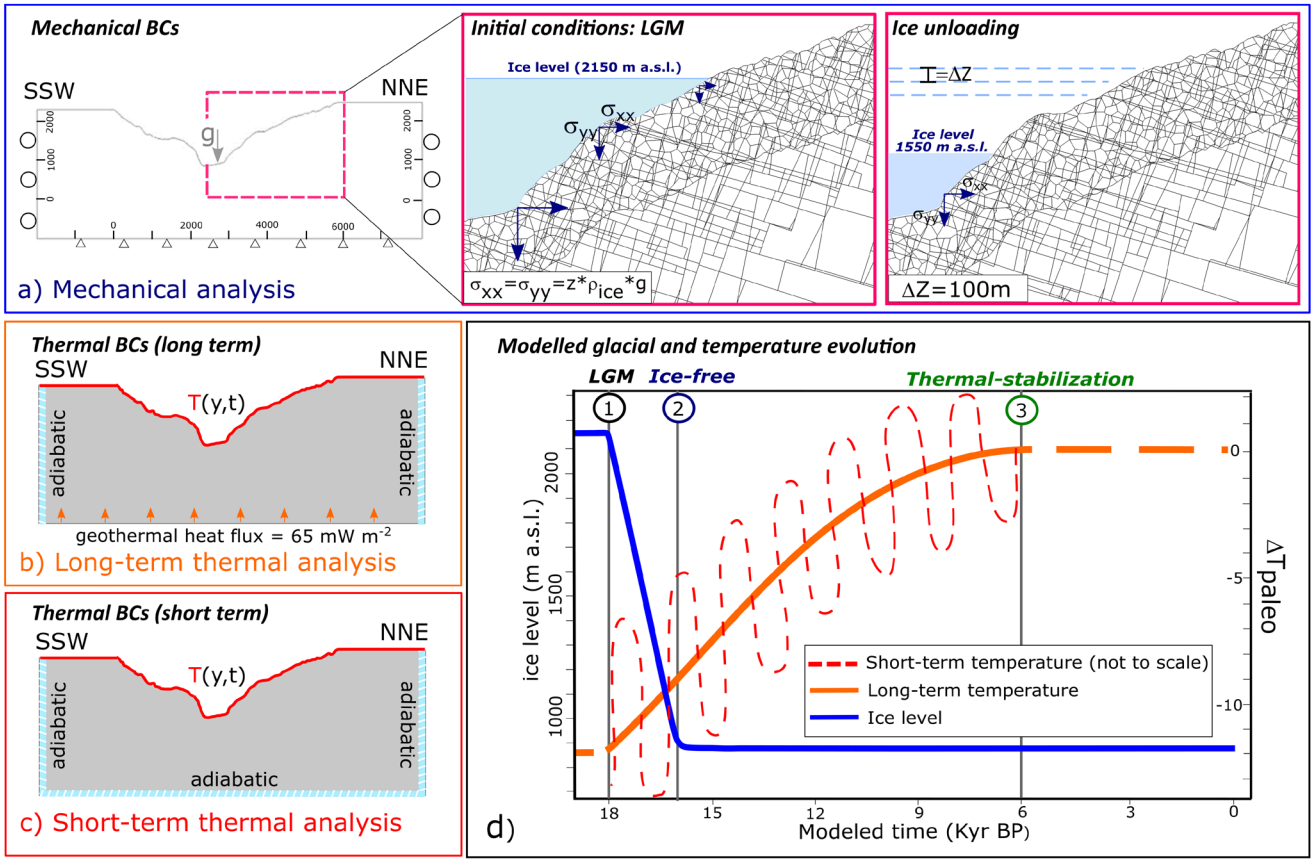

Figure 4.4 - a) Model geometry and boundary conditions of the mechanical model. b) Boundary conditions of the thermal model for the long-term thermal analysis. c) Boundary conditions for the short-term thermal analysis. d) Schematic modelled glacial and temperature evolution. The blue line shows the simulated ice level starting from the LGM conditions. The orange dashed line shows the modelled long-term temperature evolution (ΔT_{paleo}) fitting paleo-temperature reconstructions for the Alpine region (modified from Grämiger et al., 2018). The red dashed line represents the seasonal temperature fluctuation overlapped to the long-term variations; frequency and amplitude are not to scale.

Adiabatic boundary conditions define the lateral sides of the thermal model, while a constant vertical geothermal heat flux of 65 mW m^{-2} (Swisstopo 1992) is applied along the lower boundary (Figure 4.4b).

A prescribed temperature history was assigned to the slope surface, representing the main driver of temperature evolution within the rock-mass governed by the ice level (i.e., ice-air interface) position. Specifically, below the glacier cover, rock surface temperatures were held constant at 0 °C, while above the ice level, they were set to depend on environmental conditions, as a function of altitude (y) and time (t). Rock surface temperatures were thus defined by:

$$T(t,y) = 0 \qquad \textit{for } y \leq \textit{glacier elevation}$$

$$T(t,y) = 15.3 - (0.005 * y) + \Delta T_{paleo}(t) \qquad \text{for y > glacier elevation} \qquad \text{(Equation 4.2)}$$

where 15.3°C is the mean rock surface temperature at the reference elevation of y = 0 m; 0.005°C m^{-1} represents the rate of temperature variation with altitude (y); $\Delta T_{paleo}(t)$ is the factor that accounts for the paleo-temperature change relative to the present (Figure 4.4d), matching past air temperature reconstructions (Ivy-Ochs et al. 2009; Grämiger et al. 2018). The function defined by Eq. 4.2 was elaborated by Grämiger et al (2018) based on rock temperature data recorded in the Upper Rhone Valley. Considering similar lithologies and comparable climate factors, it was considered valid for the study area at hand, in the absence of site-specific rock surface temperature data.

Initial temperature conditions were obtained upon calculating steady-state thermal equilibrium under the LGM ice extension (Figure 4.3). Transient temperature evolution was evaluated for each mechanical step of deglaciation defined during the glacial retreat analysis (i.e., every 100 m of ice lowering; Figure 4.3). Considering a melting rate of 0.6 m yr^{-1}, deglaciation is completed at 16 kyr B.P. (Figure 4.4b). Once ice-free conditions were reached, temperature distributions were evaluated every 1 kyr, since paleo temperature stabilized around the current mean values ($\Delta T_{paleo}(t) = 0$) at 6 kyr B.P. (Figure 4.4d).

The transient temperature fields calculated by FEM were then imported into the DEM code, by assigning a temperature value to each grid-point as input data. UDEC was then run to a TM equilibrium, considering thermo-elastically induced strains, bringing about changes in the stress field (Figure 4.3). This represents a TM semi-coupled approach, where temperature variations may result in stress changes, but mechanical changes do not result in temperature variations. This restriction is not believed to be of great significance for quasi-static practical rock engineering problems (Itasca, 2011).

Adopting a standard thermo-elastic isotropic constitutive law, thermally induced stresses in the rock-mass domain are thus given by:

$$\Delta\sigma_{ij} = \delta_{ij} 3K\alpha\Delta T \qquad \text{(Equation 4.3)}$$

Where $\Delta\sigma_{ij}$ is the change in stress, δ_{ij} is Kronecker delta ($\delta_{ij} = 1$ for $i = j$ and $\delta_{ij} = 0$ for $i \neq j$), K is the bulk modulus, α is the linear thermal expansion coefficient, and ΔT is temperature change.

The above relation is applied by the DEM code assuming a constant temperature in each triangular zone

of the mesh, which is obtained by an interpolation from the surrounding grid-points. TM coupling is thus provided by the influence of temperature change on the volumetric strain of a zone, through the thermal expansion coefficient α. Thermally induced stresses are superposed to the previously calculated mechanical stress state.

Short-term temperature effects

The annual seasonal temperature fluctuations were finally introduced in the simulation and their effect superposed to that of the long-term temperature changes and ice unloading. Due to the significant number of involved cycles, short-term temperature distributions were computed directly within UDEC with a transient thermal analysis, in order to simplify the coupling procedures (Figure 4.3).

Blocks between discontinuities were assigned the same diffusive thermal properties as those defined for the FEM long-term analysis. Below the glacier cover, temperatures were held constant at 0 °C, while, above the ice level, rock surface temperatures were set to depend on environmental conditions defined by altitude, time (paleo temperature changes relative to present) and seasonal fluctuations. Introducing short-term temperature effects, Eq. 4.2 that defines the rock surface temperatures, now becomes (Grämiger et al. 2018):

$$T'(t,y) = 0 \qquad \textit{for } y \leq \textit{glacier elevation}$$
$$T'(t,y) = 15.3 - (0.005 * y) + \Delta T_{paleo}(t) + Asin(2\pi f t) \qquad \text{for y} > \text{glacier elevation} \qquad \text{(Equation 4.4)}$$

The term $Asin(2\pi f t)$ represents the sinusoidal temperature annual signal. The amplitude A was set to 10°C, as discussed in Section 4.2.2.1 when analyzing the time series of temperature data recorded in the study area.

Starting from the long-term temperature distributions, a sinusoidal temperature history with 20°C=*2A* peak-to-peak amplitude and one-year period was imposed at the ice-free slope surface. Boundary conditions in the rest of the domain assumed zero heat flux at both bottom and lateral sides of the model, so that the short-term thermal effect can be consistently superposed to the long-term temperature distributions (Figure 4.4d).

Modelling annual cycles throughout the entire late Pleistocene and Holocene period was deemed practically unfeasible, due to the extremely high computational cost with standard calculation facilities. Hence, a sensitivity analysis was performed to assess the impact of annual temperature oscillations on mechanical damage in the rock-mass domain, quantified through the magnitude of shear and normal displacement rates and the occurrence of plastic straining recorded along discontinuities with elasto-plastic properties. An initial significant damage signal, reflecting the effects of suddenly applying a

sinusoidal temperature fluctuation to the slope surface, was observed. The magnitude of the damage signal progressively decreases to a stable level and becomes negligible after about thirty peak-to-peak cycles, when the system reached a quasi-static equilibrium. These results are in accordance with Gischig et al. 2011b who observed a consistent decrease in the damage signal after five years using a simplified rock-slope model with elastic properties.

Evidences from a sensitivity analysis allowed to significantly reduce the number of annual cycles to be modeled. For each step of modelling (i.e., for every change in ice level and long-term temperature distribution), a number of annual cycles Nc=50 was assumed to be sufficient to accommodate the effect of the new sinusoidal thermal boundary conditions (this corresponds to parameter Nc reported in the modelling flowchart of Figure 4.3). The conductive heat equation was solved by the UDEC code via a Finite Differences implicit scheme with a timestep of 1 day. A TM equilibrium calculation step was performed every 0.25 yr following Eq. 4.3.

4.2.3.2 Results

The output of the above outlined numerical analysis is evaluated in terms of stress-strain field redistribution in the rock-mass domain and the development of plastic shear strain and tensile failures along discontinuities. The impact of temperature in the stress-strain field and in the development and propagation of fractures within the rock-mass, is assessed by comparing results from the purely mechanical glacial unloading analysis with those from the long-term and short-term TM analyses. To evaluate localized stress changes, some monitoring points were defined at different depths along the slope at which the evolution of simulated normal and shear stress and displacement rates were recorded. Considering that block interface elements (discontinuities and Voronoi polygons) behave as an elasto-plastic medium, the stress path at the selected points was plotted and compared to the corresponding strength envelope, analyzing the role of thermal loads in the occurrence and propagation of plastic failures.

Glacial retreat mechanical analysis

As a result of topographical constrains, during LGM the glacial overburden was maximum at the bottom of the valley and progressively reduced moving upwards along the slope. The ice thickness acting on the valley floor was 1230 m, resulting in a maximum normal stress of about 10.5 MPa.

Debuttressing leads to a general stress reduction within the rock-mass domain and a progressive stress redistribution along the slope. Volumetric stresses (σ_{kk}) decrease with a maximum variation of 20 MPa at the bottom of the valley, following the glacial loading pattern (Figure 4.5a). Differential stresses (σ_{max}

– σ_{min}) acting on the valley floor at a depth of 100 m increased from 5 MPa to 15 MPa (Figure 4.5b), as a result of reduction in the minimum principal stress component (σ_{min}). In contrast, the valley flanks experienced only a slight differential stress variation, consistently with the smaller ice loading action (Figure 4.5a-b).

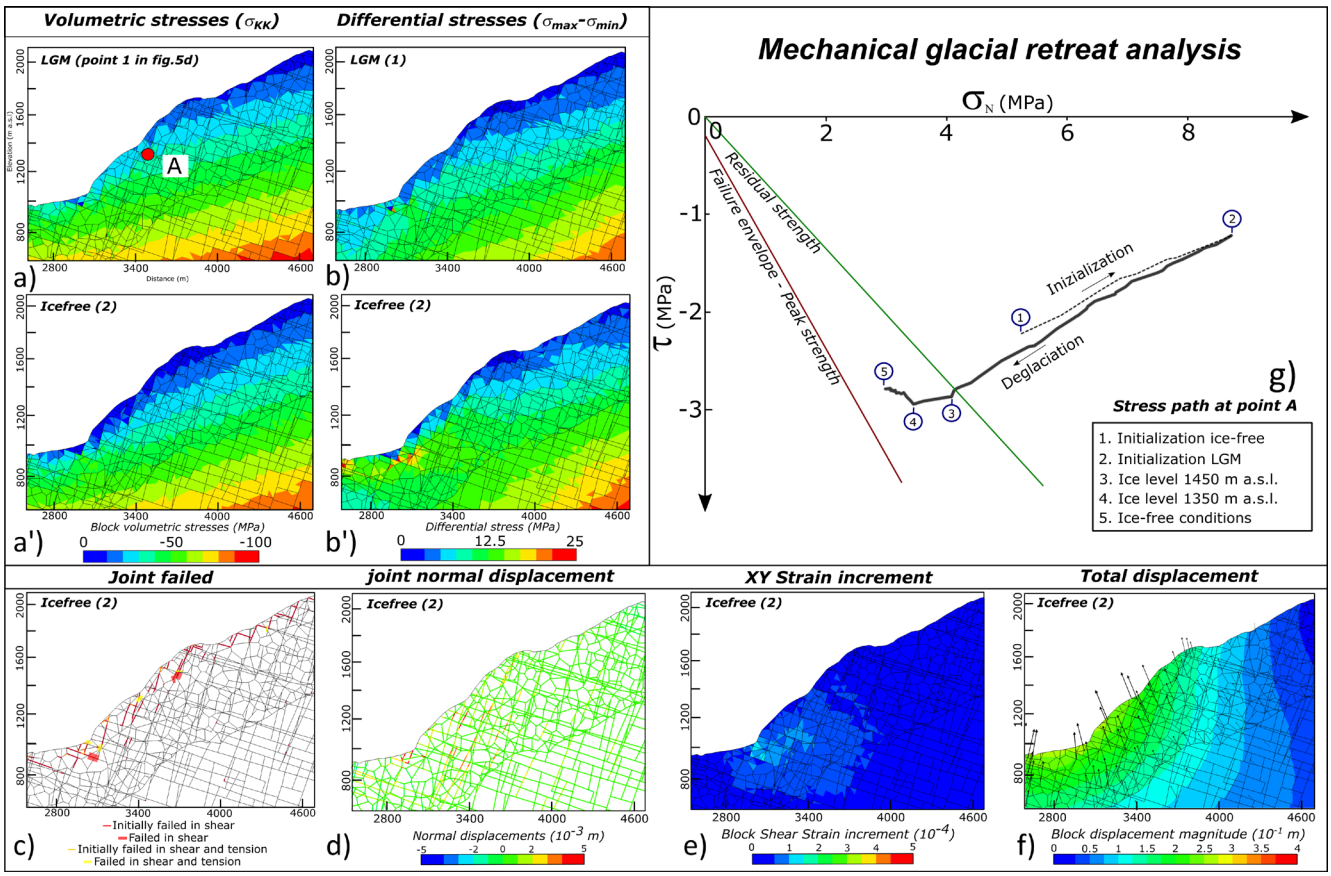

Figure 4.5 - Volumetric stresses (a-a') and differential stresses (b-b') simulated along the slope at two different steps of the analysis: LGM and Ice-free. In plots (a-a') and (b-b') extensive stresses are positive, while compressive ones are negative. The effects of ice unloading are shown by the spatiotemporal damage distribution (c) and the normal displacements (d) of discontinuities, the shear strain increment (e) and the total displacements (f) of blocks. The stress path recorded at point 'A' is presented in (g).

Stress redistribution along the slope was thus not homogeneous, leading to a variable damage pattern. Simulated new tensile and shear failures mainly occurred as a propagation of discontinuities that had already undergone plastic failure at LGM. Further damage mainly occurred at the valley bottom and at the midportion of the slope where the magnitude of stress changes was largest (Figure 4.5c). It can be observed that debuttressing also induced opening of the subvertical discontinuities, along which normal displacements reach values over $5 \cdot 10^{-3}$ m as shown in (Figure 4.5d). Expectedly, total displacements show a general uplift, as a result of elastic rebound due to unloading processes, reaching the maximum values at the valley floor (Figure 4.5f). Overall, considering a purely mechanical analysis, the effect of

ice removal does not seem to create significant rock-mass damage, as it mainly results in a post-glacial elastic volume increase.

Figure 4.5g shows the stress path simulated at monitoring point A, located along a mid-slope subvertical joint at a depth of 100 m. During initialization at ice-free equilibration, the stress state lies (in absolute value) below the peak failure strength envelope (stress-path point 1 in Figure 4.5g). Additional LGM ice loading caused an increase in the normal stresses, thus the stress state moved further away from the failure envelope (point 2 in Figure 4.5g). Then, progressive ice unloading induces a normal stress decrease and a shear stress increase, and the unloading path is roughly coincident with the loading one, implying reversible (elastic) loading conditions. However, when the ice level reached an elevation of 1350 m a.s.l and the slope surface above monitoring point A became ice-free, the stress state moved closer to the failure envelope (point 4 in Figure 4.5g). As deglaciation proceeded, normal stress in the considered joint further decreased, so that by the end of deglaciation, the joint ended up more critically stressed compared to the initial ice-free conditions, although failure was not attained.

Long-term thermo-mechanical analysis

The transient thermal analysis performed with the FEM approach allowed to evaluate the temperature redistribution along the slope during deglaciation, considering both ice level lowering and climate conditions changing. The initial temperature field for the transient thermal analysis was defined under LGM conditions with a stationary solution (Figure 4.6a).

Thermal gradients are shown to be highly influenced by the extent of the glacier cover, holding the ground surface temperature at 0° C. During deglaciation, the slope is progressively exposed to atmospheric conditions, that depend on the altitude and on the paleo temperature factor (Section 4.2.3.1). Considering that the 0°C isotherm for the mean ground temperature during LGM is located at 500 m a.s.l. (Eq. 4.2), during deglaciation ice-free rock surface portions are gradually exposed to negative temperatures, resulting in a progressive cooling of the slope. Ice-free valley conditions are reached at 16 kyr B.P. (Figure 4.6b), when the 0°C isotherm has risen to 1400 m a.s.l. (Eq. 4.2). Figure 4.6e shows the differences between LGM and ice-free temperature distributions. It can be observed that the slopes portion located between the LGM ice level and the ice-free 0°C isotherm experienced a net cooling process (blue scale colors), while, in the rest of the slope, temperature globally increased (red scale colors). Simulated temperature variations are restricted to the slope subsurface within a maximum depth of thermal diffusion of about 300 m (Figure 4.6e). The deglaciation-induced temperature difference distribution suggests that the slope surface experienced significant thermal shocks due to sharp temperature gradients, with special reference to (i) the top and (ii) the lower-mid portion of the scarp.

The latter area, shown in previous Section to be affected by most of the debuttressing-induced mechanical damage, is bound to especially suffer from thermally induced degradation.

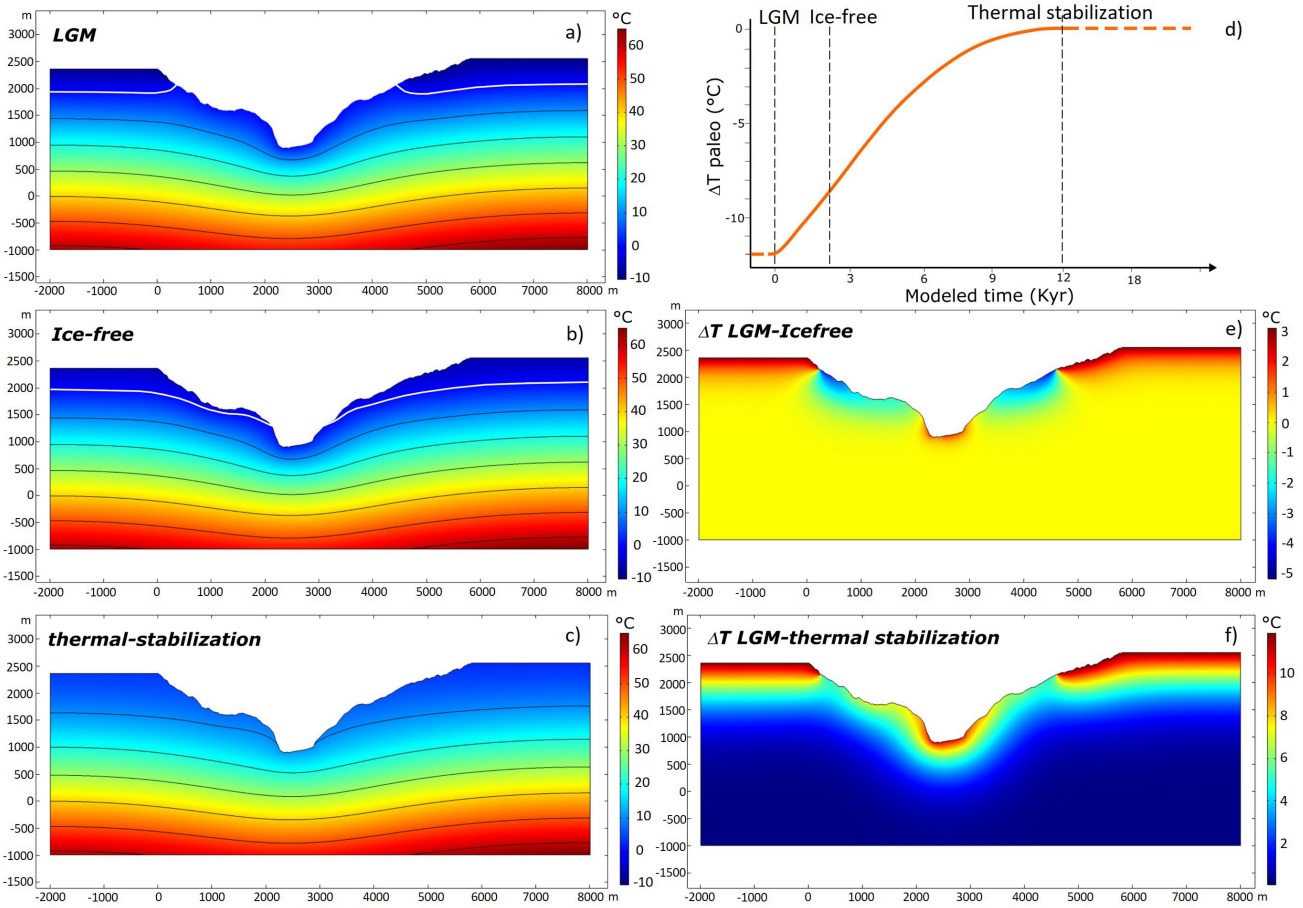

Figure 4.6 - Results of the thermal FEM transient analysis. a) Temperature distribution during LGM; d) Temperature distribution at ice free conditions; a) Temperature distribution at thermal stabilization (end of the heating process); d) Evolution of the DT_{paleo} factor from LGM to thermal stabilization; e) Temperature changes between LGM and ice-free conditions; f) Temperature change between LGM and the thermal stabilization condition. In subfigures b and c it can be observed that no temperature variations are represented by green colors, blue scale colors indicate a cooling process, while red scale colors indicate a heating process.

Once deglaciation is completed, temperature distribution is no longer affected by the ice level lowering and depends only by the ΔT_{paleo} factor (Eq. 4.2). This results in a progressive heating of the slope until 6 kYr B.P., when temperature changes relative to present become negligible (ΔT_{paleo}=0; Figure 4.6d). Considering that the ΔT_{paleo} factor is independent of altitude, the heating process in this phase can be considered homogeneous along the entire slope, causing the maximum depth of temperature diffusion to increase to values of about 1000 m (Figure 4.6f). At the end of the analysis, the 0° C ground isotherm has risen to 3000 m a.s.l. (Eq. 4.2) and the slope has experienced an overall heating process (red scale colors in Figure 4.6f).

Temperature fields were then imported in the DEM model as input data for the long-term TM analysis, where the effects of paleo-temperature changes, associated with the deglaciation process, were explored.

Compared to a purely mechanical model, the TM one accounts for additional stresses due to the temperature variations along the slope (Eq. 4.3).

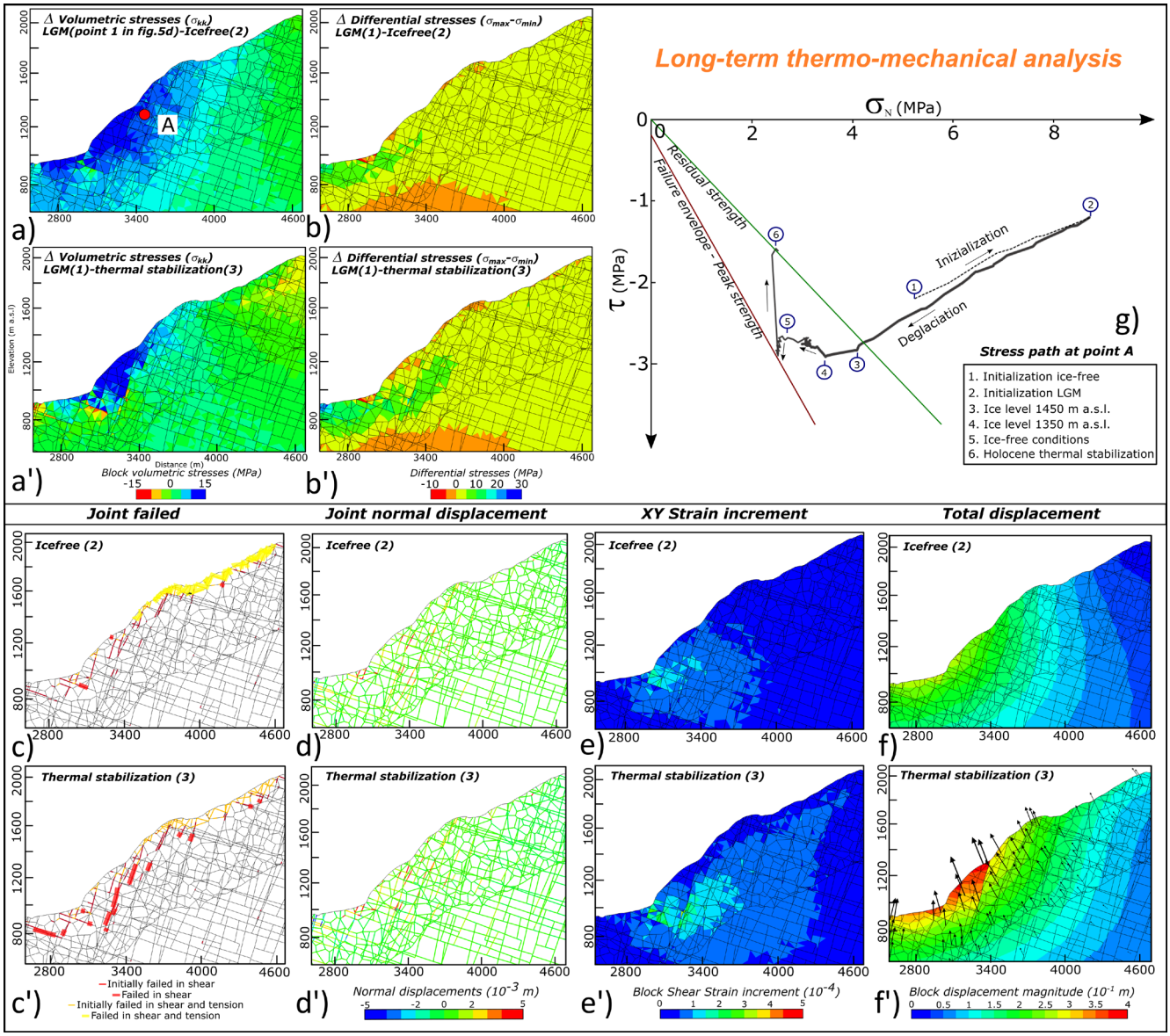

Figure 4.7 - Simulation results show the increment of volumetric stresses (a-a') and differential stresses (b-b') along the slope at two different steps of the TM analysis: 'ice-free' and 'thermal stabilization'. In plots (a-a') and (b-b') extensive stresses are positive, while compressive ones are negative. Increments are referred to the LGM stress distribution presented in Figure 6. The effects of ice unloading and long-term temperature change at 'ice-free' and 'thermal stabilization' conditions, are shown by plotting the spatiotemporal damage distribution (c-c') and the normal displacements (d-d') of discontinuities, the shear strain increment (e-e') and the total displacements (f-f') of blocks. The stress path recorded at point 'A' is presented in (g).

In Figure 4.7a,b the variation in volumetric stresses (σ_{kk}) and differential stresses (σ_{max}-σ_{min}) between the LGM, ice-free and Holocene thermal stabilization conditions are shown. During deglaciation (from 18 up to 16 kyr B.P.), the effects of glacial unloading and slope surface cooling, which causes a rock-mass volume contraction, leads to a general stress reduction within the rock-mass domain. Focusing on

the mid-slope area, volumetric stresses decrease (Figure 4.7a), while differential stresses increase (Figure 4.7b) as a result of a reduction in the minimum principal stress component (σ_{min}).

The subsequent temperature and stress redistribution between the ice-free and the Holocene thermal stabilization conditions (from 16 up to 6 Kyr B.P.), is characterized by an extensive, overall heating of the slope. The rise in temperature induced a general volumetric expansion of the rock blocks, causing increments in the volumetric stresses along the entire slope, with maximum values of $\Delta\sigma_{kk}$ = 10 MPa (Figure 4.7a'). Differential stresses progressively increased, starting from the valley floor and extending upslope, identifying a region of high differential stresses at the toe of the slope (Figure 4.7b'). Monitoring the out-of-plane stresses, a noticeable variation in their magnitude could be observed, resulting in some cases in assuming the maximum principal stress value, especially at shallow depths where the slope morphology highly affects the stress distribution.

During deglaciation, the progressive cooling and contraction of rock blocks promoted both tensile and shear failures along the subsurface, as well as the opening of sub-vertical discontinuities (Figure 4.7c). The subsequent heating phase promoted damage at greater depths where the confining stress level is higher, mainly as shear failures of subvertical discontinuities, with significant additional slip propagation as shown in Figure 4.7c'. The volumetric expansion of blocks also induced a closure of discontinuities, especially at depth, where the stress increment is larger (Figure 4.7d').

Focusing on the mid-slope area, where the historical Cimaganda rockslide occurred, a shear strain localization region is observed to begin to develop at the end of the deglaciation (Figure 4.7e) and to progressively expand as a result of the heating process (Figure 4.7e'). This region corresponds to the area of most significant differential and volumetric stress increase. Intensive shear straining within the elastic rock blocks gradually caused plastic yield along discontinuities and boundaries of the Voronoi polygons: a significant increment in the extent of joint failure and slip propagation along sub-vertical discontinuities was observed (Figure 4.7c'). As a result, simulated total displacements concentrate at this portion of the slope (Figure 4.7f).

Examining the stress-path recorded at monitoring point A (Figure 4.7g), introducing the long-term temperature effects a different stress state is attained compared with the purely mechanical analysis (Figure 4.5). Until the joint remains below the ice level and slope temperature is kept constant by the glacier cover (points 2-4 in Figure 4.7g), the stress path is coincident with the mechanical one. However, when monitoring point A becomes ice-free, temperature changes penetrate to depths of 300 m (Figure 4.6f) and the rock-mass is subjected to a cooling process, resulting in ΔT = -1°C. When deglaciation is completed (point 5 in Figure 4.7g), stress conditions move closer to the failure envelope. The subsequent phase (points 5-6 in Figure 4.7g), characterized by a global heating trend (ΔT~7°C), leads to an increase

in shear stress: the stress path thus reaches the failure envelope causing joint failure, and the instant attainment of residual strength conditions, according to the adopted joint constitutive law (point 6 in Figure 4.7g).

Short-term thermo-mechanical analysis

Introducing short-term thermal effects, as the slope surface is exposed to atmospheric conditions it is suddenly affected by temperature cycling on a seasonal basis, that are superposed to the long-term temperature changes. Considering that the diffusion depth of seasonal temperature changes is limited to the first tens of meters, the yearly temperature oscillations affect only the shallowest blocks along the slope surface, causing their cyclic isotropic expansion and contraction. However, thermally induced volumetric strains lead to stress variations which can propagate at depths well below the thermally active layer. Compared with the purely mechanical and long-term TM analyses, when additional short-term temperature fluctuations are considered, the extent of unstable rock-mass increases, extending further toward the top of the slope. New damage occurs mainly along the slope surface, represented by (i) tensile failures of discontinuous elements that represent the sides of blocks directly affected by the thermally induced volumetric changes, and (ii) plastic shear failures along sub-vertical joints, driving the process of TM stress propagation (Figure 4.8a-b).

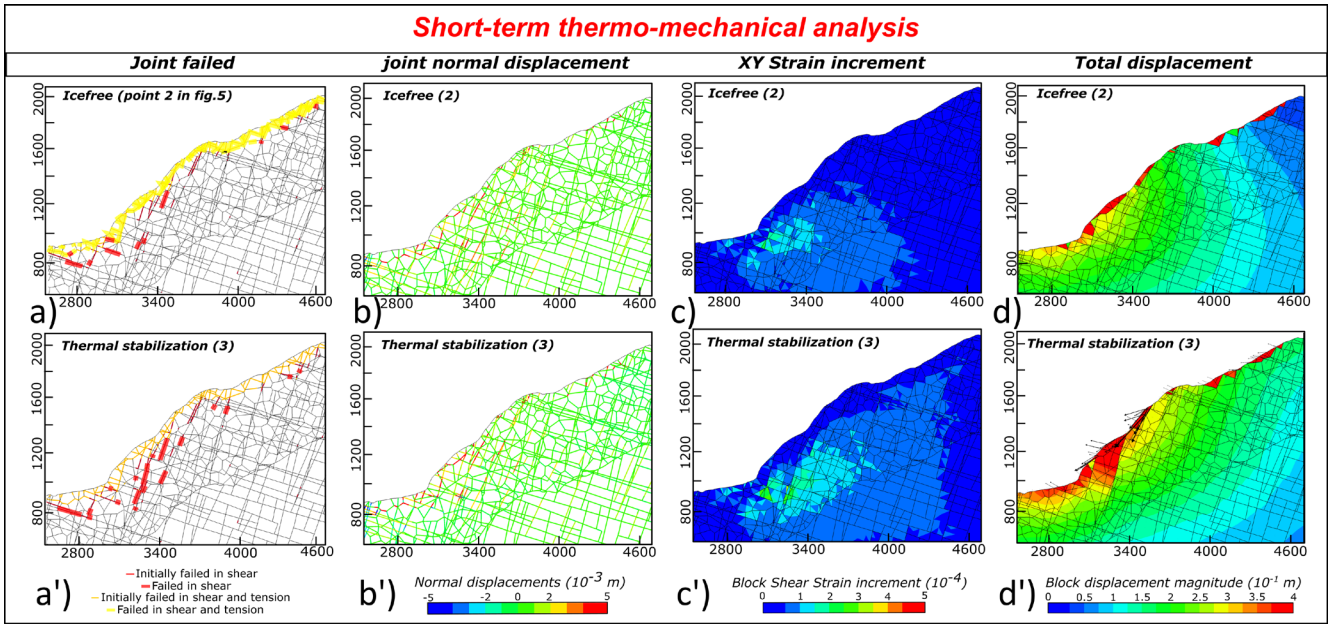

Figure 4.8 - The combined effects of ice unloading, long- and short-term thermal loading at 'ice-free' and 'thermal stabilization' conditions, are shown by plotting the spatiotemporal damage distribution (a-a') and the normal displacements of discontinuities (b-b'), the shear strain increment (c-c') and the total displacements of blocks (d-d').

Focusing on the mid-slope area where the historical Cimaganda rockslide occurred, the shear strain localization region that begins to develop at the end of the deglaciation and progressively propagates as a result of paleo-temperature heating, is now more extended (Figure 4.8c). Irreversible displacements take place, as a result of the combination of elastic glacial rebound and long- and short-term thermal effects, especially along the shallower blocks that are directly affected by short-term temperature fluctuations (Figure 4.8d).

The effect of depth propagation of thermo-induced stresses and strains is clearly visible by analyzing the stress path recorded at monitoring point A and plotted in Figure 4.9a.

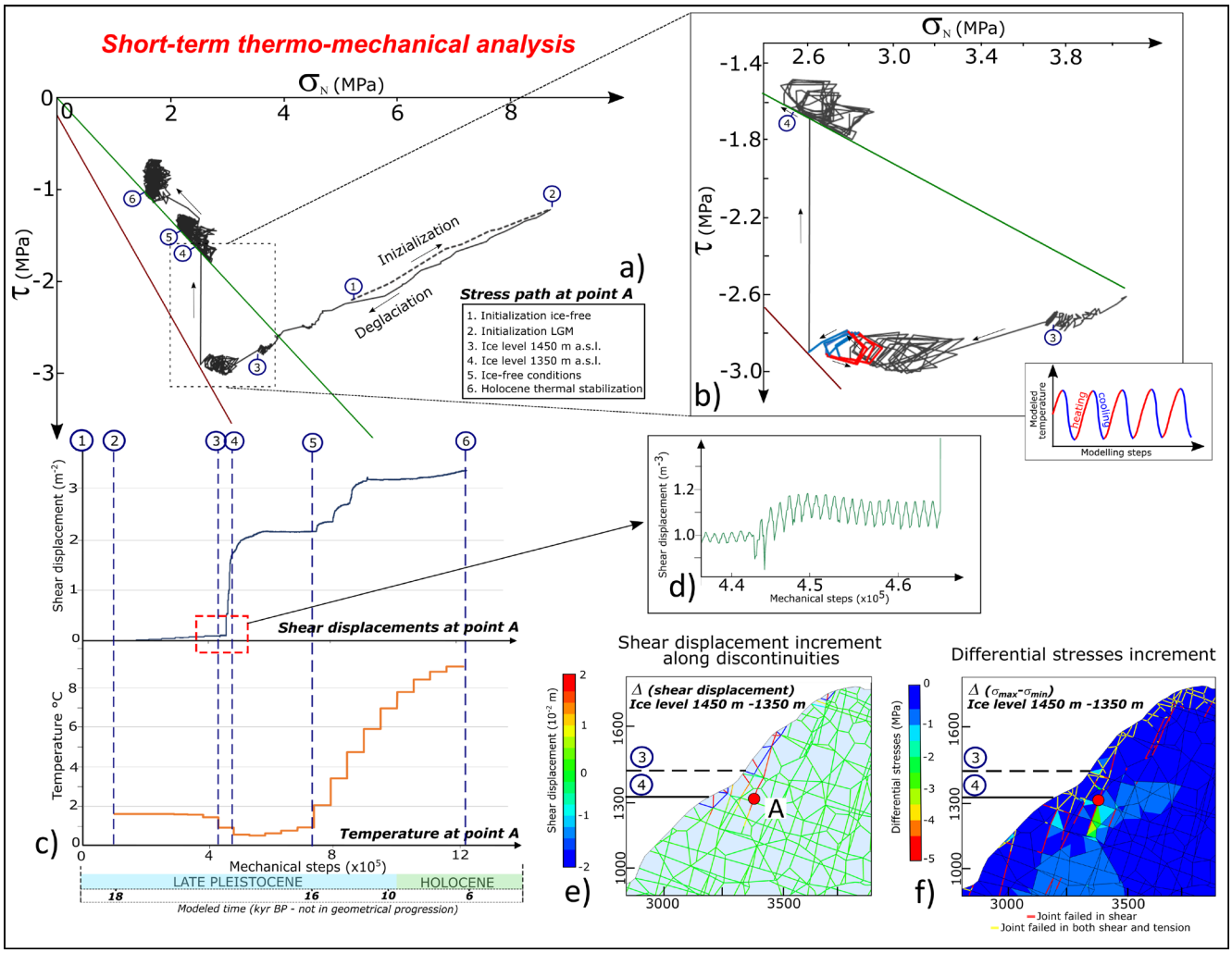

Figure 4.9 - a) Stress path recorded at point 'A'; b) Details of the stress path showing the TM cyclical stresses and the stress drop after reaching the peak strength envelope; c) Temperature and shear displacement histories at point A; d) Details of shear dislocation; e) Increment of shear displacement along discontinuities between pre-failure condition of point 'A' (ice level at 1450 m a.s.l.) and post failure condition (ice level at 1350 m a.s.l.); f) Increment of differential stresses between pre-failure condition of point 'A' (ice level at 1450 m a.s.l.) and post failure condition (ice level at 1350 m a.s.l.). Extensive stresses are positive, while compressive ones are negative.

Until the monitored joint remains covered by ice, no changes in the stress path were observed compared to the previous analyses. When ice level reached an elevation of 1450 m a.s.l., the slope surface above monitoring point A started being subjected to seasonal temperature fluctuations, and TM induced cyclic stresses are recorded in the stress path (point 3 in Figure 4.9a). However, at this stage, the discontinuity and the surrounding blocks are not already completely ice free, hence stress variations are of low magnitude (about 50 KPa, Figure 4.9b).

TM cyclic stresses become highly significant when ice level reaches an elevation of 1350 m a.s.l., and the monitored joint is completely ice-free. In fact, heating phases cause an expansion of blocks, inducing in turn an increment in normal stresses with an amplitude of ~0.1 MPa at monitoring point A; on the other hand, cooling phases cause a contraction of blocks inducing a decrease of normal stress and a shear stress increase (hence an overall decrease of shear strength, as the failure envelope is approached) with an amplitude of ~0.1 MPa. After 21 peak-to-peak annual thermal cycles, failure is attained (Figure 4.9a-b). It is important to note that temperature at monitoring point A is not affected by seasonal temperature fluctuations, as shown in Figure 4.9c. In fact, monitoring point A is located at a depth greater than the thermo-active layer, so temperature values are only affected by the long-term changes. Variations in the stress state are thus induced only by contractive/expansive thermal volumetric strains of rock blocks located above monitoring point A, closer to the slope surface.

It can be observed that the development of TM stresses within the elastic blocks brings about rupture propagation along the elasto-plastic interfaces. Slip dislocation along discontinuities follow the thermally induced cyclic pattern, involving both directions of shear: although a small amount of permanent dislocation remains after each full cycle, most of the slip occurring during the summer period is recovered in the subsequent winter one (Figure 4.9c). These features apply as long as the discontinuity remains within the elastic domain; when plastic failure conditions are reached, irreversible slip occurs, and will accumulate during the entire process (Figure 4.9d). The transition from peak to residual resistance results also in a stress redistribution in the rock-mass domain, as highlighted by the increment of differential stresses ($\Delta(\sigma_{max}-\sigma_{min})$) shown in Figure 4.9f. Thus, the stress redistribution induced by failure may promote critical loading of neighboring discontinuities, supporting the process of fracture propagation.

4.2.3.3 Discussion

For this case study, the combined effect of long- and short-term thermal loading was explored overlapping the warming trend resulting from the Last Glacial Maximum (LGM) conditions to the

Holocene age and the seasonal temperature oscillation. By comparing ice-unloading analysis with the TM ones, the role of temperature in the stress-strain evolution of rock-slopes was highlighted, demonstrating that induced damage and displacements are significantly increased in the presence of TM stresses. Results are in accordance with other TM studies that identified the importance of including long-term temperature changes supporting Alpine deglaciation (Baroni et al. 2014; Grämiger et al. 2018) and the role of periodical thermal loads in the propagation of rock-mass failures along a natural slope (Gunzburger et al. 2005; Bakun-Mazor et al. 2020).

At the end of the simulated deglaciation process, no critical conditions for slope stability were observed, and the occurrence of plastic failure is limited along pre-LGM failed elements. The subsequent introduction of both long- and short-term TM stresses leads to a substantial increase in the occurrence of plastic yield and slip propagation along discontinuities. During deglaciation, as soon as the slope is exposed to atmospheric conditions, seasonal temperature oscillations induce significant new tensile failures along the slope subsurface. Even if the effects of temperature fluctuations are progressively accommodated by the system, normal and shear displacements continue to accumulate along critically stressed and failed discontinuities. This results in accumulated inelastic deformation along joints, is able to induce surface block instability. Considering the modelling approach, these TM effects can be interpreted as a large-scale fatigue process, involving incremental slip along critically stressed discontinuities following seasonal cyclic loading. Unlike the short-term thermal loading, the long-term one (i.e., paleo-temperature changes from LGM conditions up to present) is monotonic, it occurs over a much longer time scale and includes larger values of temperature variations. Hence, the diffusion of long-term signals reaches larger depths enhancing stress-strain field variations, as emphasized by the occurrence of deep plastic yield during the heating phase that follows deglaciation. While the short-term temperature variations mainly induce instability at the slope surface, long-term thermal effects can represent an important factor in the development of large-slope deformations.

The application of the analysis on a slope along which a large instability event occurred, allowed to calibrate the modelling approach and to validate results. As corroborated by geomechanical field surveys (Section 3.3.2.3), the rock-slope evolution is mainly controlled by the presence of opened joints and highly persistent sub-vertical discontinuities, that promoted instability events along the entire slope (Figure 3.18). This field evidence supports the numerical simulation results, confirming the occurrence of new plastic shear and tensile failures, leading to superficial rock-mass instabilities, especially if seasonal temperature fluctuations are considered. In accordance with field observations, damage is particularly evident at the top portion of the slope in correspondence of the Bondeno structural terrace, where highly disarticulated rock-masses outcrop (Figure 3.18).

At the end of the numerical analysis (i.e., simulated current conditions) the predisposition to instability along these elements is quite evident. Shallow rock sliding such as the documented 2012 Cimaganda rockslide event, could be easily initiated if destabilizing driving forces are introduced in the model (Figure 3.18; Figure 4.10).

Focusing on the central part of the slope where the historical rockslide event occurred, in the numerical model it can be observed that a shear straining region begins to localize at the end of deglaciation and progressively propagates as a result of the heating process.

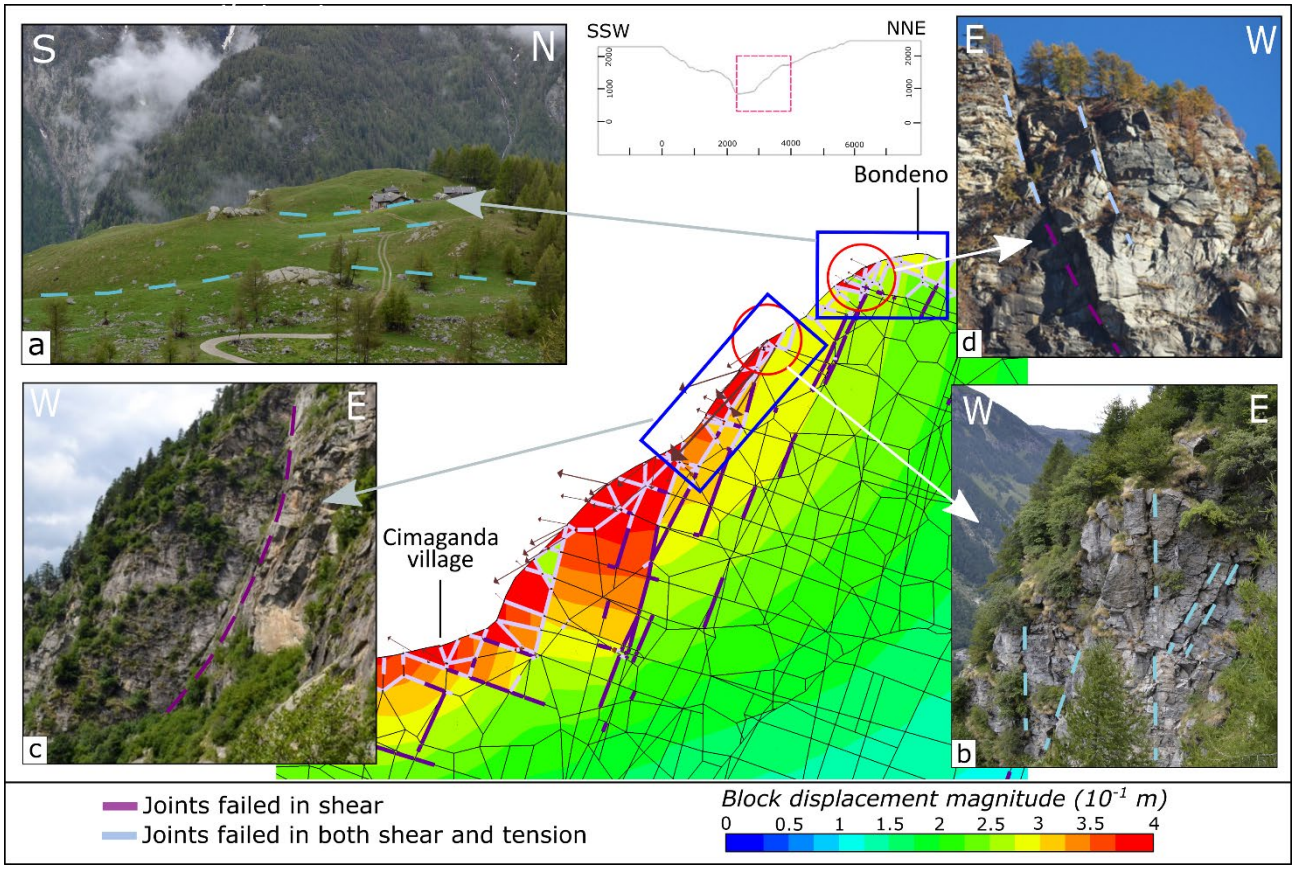

Figure 4.10 - Total displacement and damage distribution simulated at the end of the TM analysis. Results can be related to the state of the rock-masses outcropping along the slope.

The presence of such strain localization area does not bring about critical deep-seated instability conditions, but it clearly defines a preferential region for the development of a failure zone, at a depth roughly corresponding to that of the detected historical Cimaganda rockslide sliding surface (Figure 4.10). Moreover, this area corresponds to the portion of the slope where the magnitude of simulated displacements (of the order of 10^{-1} m) takes the maximum values (Figure 4.10). The resulting displacements and the development of a deep shear strain localization zone are in agreement with the evidence of the historical Cimaganda rockslide collapse. Even if a critical condition for slope stability is

not reached in the simulation, a preferential zone where damages concentrate was observed. This zone is bound to develop further, once other destabilizing factors are considered and introduced in the model.

4.3 Installation of a thermo-mechanical monitoring station

Based on results of TM numerical modeling, showing a significant influence of atmospheric temperature variations on the mechanical evolution of the Cimaganda rock-slope, the installation of a TM monitoring system was explored. The aim was to monitor over time the evolution of temperature along a representative rock-mass and measure the deformation state of relevant joints.

The monitoring system was installed in August 2022 on a rock-mass outcropping at the top of the Cimaganda slope (Figure 4.11a), in correspondence of the crown of the historical landslide at an elevation of 1635 m a.s.l. (46°22'35.25"N, 9°22'5.27"E). The installation was carried out by the Czech Academy of Sciences (Institute of Rock Structure and Mechanics, Department of Engineering Geology) and Charles University of Prague (Department of Physical Geography and Geoecology), which already have experience in TM monitoring of rock-masses (Racek et al. 2021a, b, 2023). The instrumentation installed for the Cimaganda case study has the same technical characteristics as those presented in Racek et al. 2021a.

In Section 4.3.1, installed instruments will be briefly discussed in order to define the monitored parameters. For an accurate description of their technical characteristics (e.g., instrument accuracy, sensitivity, range of functionality) refer to Racek et al. 2021a.

Installation took place in August 2022, and the monitoring system went into full operation the following month. The system has been upgraded in May and November 2023 by fixing some technical issues that had occurred during the first working months. Results of this monitoring campaign will be briefly presented in the Section 4.3.2.

4.3.1 Methods

The installed TM monitoring system includes:

- An automatic climate station aimed to monitor atmospheric temperature, rainfall, humidity, and wind speed every 10 minutes (Figure 4.11c). The control unit is equipped with a GSM modem, which sends the data automatically to the server of the provider every day at midnight. Sensors and the control unit are powered by a 12V battery.
- A 3 m long borehole equipped with a compound thermal probe composed by 11 thermocouples placed at distance of 0.05 m, 0.1 m, 0.2 m, 0.3 m, 0.5 m, 0.75 m, 1 m, 1.5 m, 2 m, 2.5 m, 3 m from the rock face surface (Figure 4.11d). The sensors are placed in a sub-horizontal borehole drilled into a stable part of the rock slope to ensure lifespan of the whole system. The direction

of drilling was chosen perpendicular to the surface of the slope and thus to the direction of maximum incidence of the solar radiation and propagation of heat flux with depth. Temperature sensors in the borehole have the same technical characteristics of the air sensors and are placed in the center of copper rings with a diameter sufficient to stick to the borehole wall (Figure 4.11e-f). In this way sensors measure the rock-mass temperature evolution at different depths. The head of the borehole is insulated to prevent air and water inflow. Moreover, to ensure that the temperature values recorded are not affected by the air circulation inside the borehole, sensors are separated by a thermal insulation material. Additionally, one thermocouple is placed directly on the rock surface measuring the slope surface temperature.

- Four induction crack meters, which measure relative block displacements along four different discontinuities (Figure 4.11g-h). These instruments (Gefran PZ-67-200) are able to record movements in the order of $1 \cdot 10^{-5}$ m (Racek et al. 2021a). Considering their technical features, they are particularly suitable for harsh conditions such as Alpine environmental conditions with large temperature changes, snow cover, ice accumulation or rain. The temporal resolution of the measurement is set to one hour.

During the first months of activities some technical issues were faced, related to some electrical compounds in the thermocouples placed at depths greater than 2.5 m and to a couple of crack meters not working properly. These issues where solved in April 2023 when pyranometers were also installed. At the end of August 2023, a connection problem led to the datalogger's batteries running out. The batteries were replaced in November 2023, when also a new data connection system was installed. Because of these technical issues, the recorded data present some gaps in time.

In April 2023 the monitoring station has been equipped with two opposite facing pyranometers to compute the solar radiation balance of the rock face (difference between incoming and reflected radiation). They have been placed on an L-shaped holder at a distance of approximately 0.1 m from the rock surface, with one hemisphere facing the rock surface and the other facing the sky, to measure incoming and reflected solar radiation. Outputs from the pyranometers are processed by a converter and sent with the monitored meteorological variables to the data server.

Unlike the climate station which is directly connected to its own server via GSM modem, the crack meters and thermocouples are connected to a datalogger (Tertium technology, 2019), which store data that are sent to a server via the Internet of Things (IoT) SigFox network or can be wirelessly transmitted at a distance of up to 100 m using Wi-Fi. The crack meters and dataloggers are powered with two AA batteries, which typically last 6-12 months according to the local climate conditions.

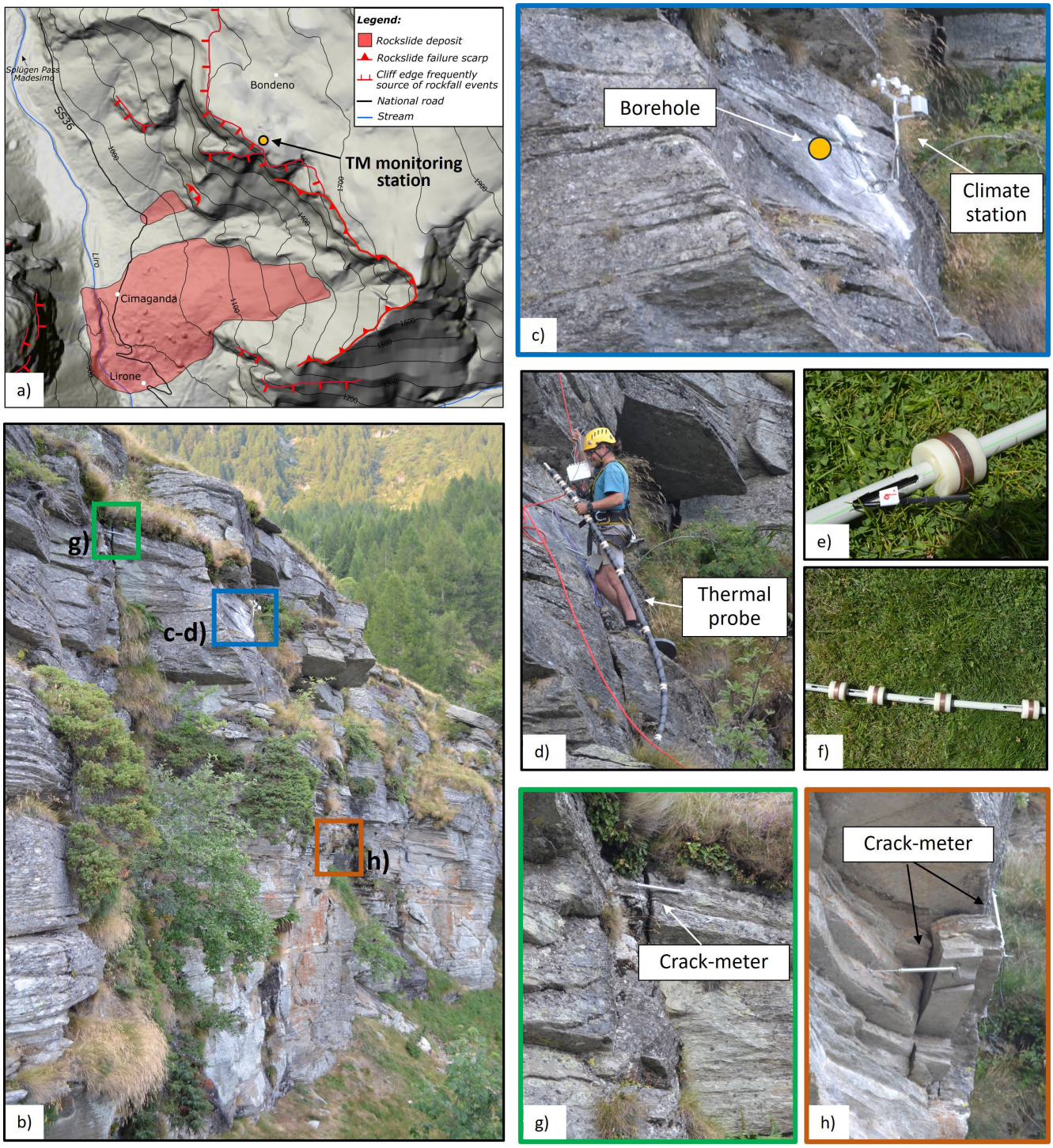

Figure 4.11 – a) Location of the thermo-mechanical monitoring system. b) Monitored rock-mass. c) Climate station including instruments for the monitoring of air temperature, rainfall, humidity and wind; the location of the borehole is also shown. d) Thermal probe installed in the borehole. e-f) Thermal sensors composing the thermal probe; inside the borehole the copper ring is in contact with the rock wall. g) Crack meter measuring the opening of the monitoring joint belonging to the K3 family; h) Crack meter monitoring an unstable rock block.

Considering the instrument installed, the TM monitoring system allow to monitor temperature trends within the rock-mass and on its surface, the aperture of discontinuities and the influence of climate variables. In this way, it is possible to study the thermal evolution with depth and climatic forcings, getting evidences on the thermal properties of the rock material (i.e., thermal conductivity). Crack meters

give quantitative information on the state of discontinuities (opening), allowing the study of the relationships between thermal loading and rock-masse deformation.

Analyzing the geomechanical features of the monitored rock-mass, a congruence with the observations discussed in the previous Section 3.3.2 was highlighted. Focusing on the rock-mass fracturing conditions, the three systems of discontinuity identified along the slope *(K1*, *K2* and *K3* in Section 3.3.2), were defined also in correspondence of the monitored rock-mass.

Field surveys coupled with numerical modelling, highlighted a key role of subvertical discontinuity elements in the mechanical evolution of the slope, driving gravitational instability processes as toppling or shallow sliding. In addition, their orientation, parallel to the rock surface, results in a potentially highest action of thermal cycles, as they are located perpendicular to the direction of blocks deformation. Indeed, the process of expansion and contraction of the blocks may have a significant impact on these elements. Considering these observations, in the TM monitoring system, it was considered valid to measure the evolution of subvertical joints belonging to the *K3* family. The four crack meters were then installed to monitor: two sub-vertical joints with centimetric aperture affecting the entire rock-mass with high persistence (k3 set; Figure 4.11g), and two discontinuities of millimeter aperture isolating an unstable block (Figure 4.11h). The first one, because of its orientation and persistence, is crossed by the thermal probe.

4.3.2 Preliminary results and discussion

To date, the monitoring system has been active for 1.5 year starting from August 2022. During the first months of activities, however, some technical issues were faced, resulting in some gaps in the temporal continuity of the data. Considering the data collected so far, it is possible to examine the evolution of temperature and joint-deformation in a single climate year only. The Figure 4.12 and Figure 4.13 show the temperature data and the joint aperture recorded from August 2022 to August 2023. At this stage of the work, given also the limited time period covered, the research was limited to ensuring the functionality of the instrumentation and analyzing the main trends in the collected data to check their congruence. More advanced elaborations are deferred to a subsequent stage of the work when also the availability of data on which to identify relationships will be greater.

The recorded air temperature (Figure *4.12*a) evolves following daily variations, which on sunny days can reach an average of 25° while on low irradiance winter days is limited to a few degrees. Superimposed on them is the seasonal evolution, which in the period under consideration had an amplitude of about 20°.

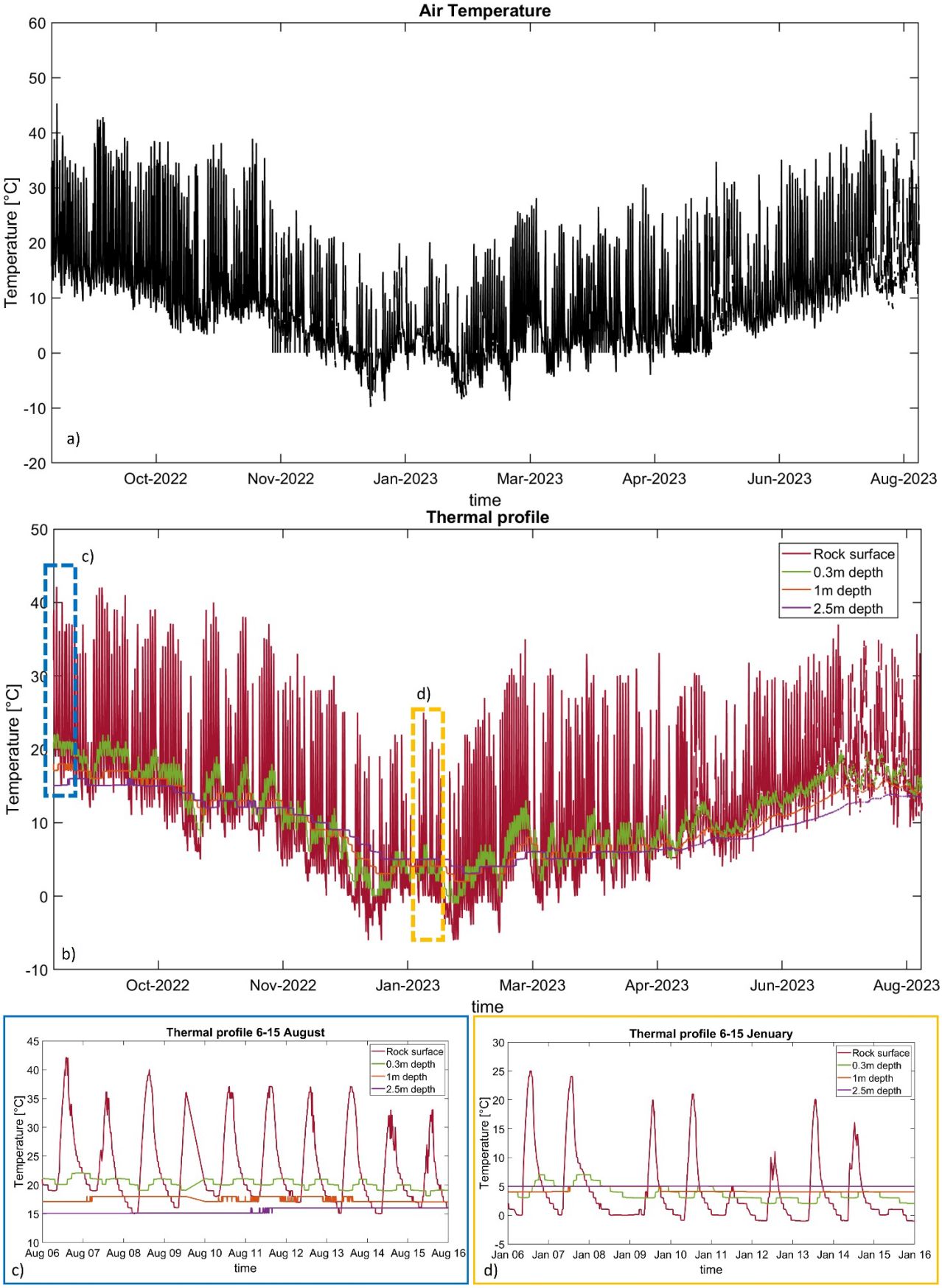

Figure 4.12 – Data from the TM monitoring station (reading interval 10 min). a) Air temperature data; b) Temperature recorded at 0, 0.3, 1.0 and 2.5 m depth; c) Temperature recorded at 0, 0.3, 1.0 and 2.5 m depth during summer; d) Temperature recorded at 0, 0.3, 1.0 and 2.5 m depth during winter.

By analyzing the temperature recorded in the rock-mass, the greatest fluctuations are recorded at its surface where variations up to 30° are observed between day and night under sunny conditions. The highest temperature recorded at the rock surface was 42°C on August 6, 2022 when the air temperature was 35°C. The minimum temperature was -6°C on December 12, 2022 when the air temperature was -9.8°C.

The temperature trend of the rock-mass directly reflects the air temperature variations with daily and seasonal temperature ranges. However, the temperature recorded on the rock-mass surface can reach values even higher than those in the air. This is probably related to the optimal orientation of the slope respect to the incidence of the solar radiation, which amplifies the thermal effects.

Data measured by thermocouples inside the borehole, allowed to define both diurnal and annual temperature fluctuations with different amplitudes at various depths (Figure 4.12b). It can be observed that diurnal thermal variations affect only the shallowest portion of the rock-mass with a maximum thermal active depth of 0.75 m in the summer period and 0.30 in the winter one. Analyzing the whole year, appreciable variations were recorded also at greater depths, with variations of 13.2° at 2 m (16.2°C recorded in September 2022 and 3°C in January 2023) and 12° at 2.5 m (15.15°C recorded in September 2022 and 3.15°C in January 2023). From April 2023 to August 2023, the temperature varied by 7° at 2.5 m depth (Figure 4.12b).

Negative temperatures were recorded inside the rock-mass only in the top 30 cm depth and relative to the coldest period monitored. At greater depths the temperature is always positive.

The joint aperture data recorded by crack-meters, show a thermally induced dilatation behavior of the rock-mass. Figure 4.13 shows the aperture data (1 hour resolution) measured by a crack-meter placed along a discontinuity belonging to the *K3* set (Figure 4.11g) from August 2022 to June 2023. From the graph, it is possible to see the influence of temperature variations in the opening of discontinuities, which increases as temperature decreases. The relation is evident both at seasonal and daily scale, with annual amplitude of 0.0020 m and average daily amplitude of 0.0003 m. It is important to note that these are elastic deformations that are fully recovered as soon as the temperature values return to the starting levels of the period under consideration. No plasticity phenomenon would appear to be measured by the system, within the limited time range.

These evidences correspond to what observed in numerical modeling (Section 4.2.3), where a cyclic evolution of aperture and stresses was observed by following the seasonal thermal input (cooling in winter and heating in summer). In particular, the graph in Figure 4.9d shows the aperture of a joint belonging to the *K3* family simulated by the TM model (same orientation as the one monitored here). The simulated deformations were also of the elastic type with amplitudes in the millimeter range.

Comparing the modeled and measured amplitudes, therefore, a good compatibility is observed. This confirms the validity of the model presented in the Section 4.2.3 and the representativeness of the parameters introduced in it, both mechanical and thermal.

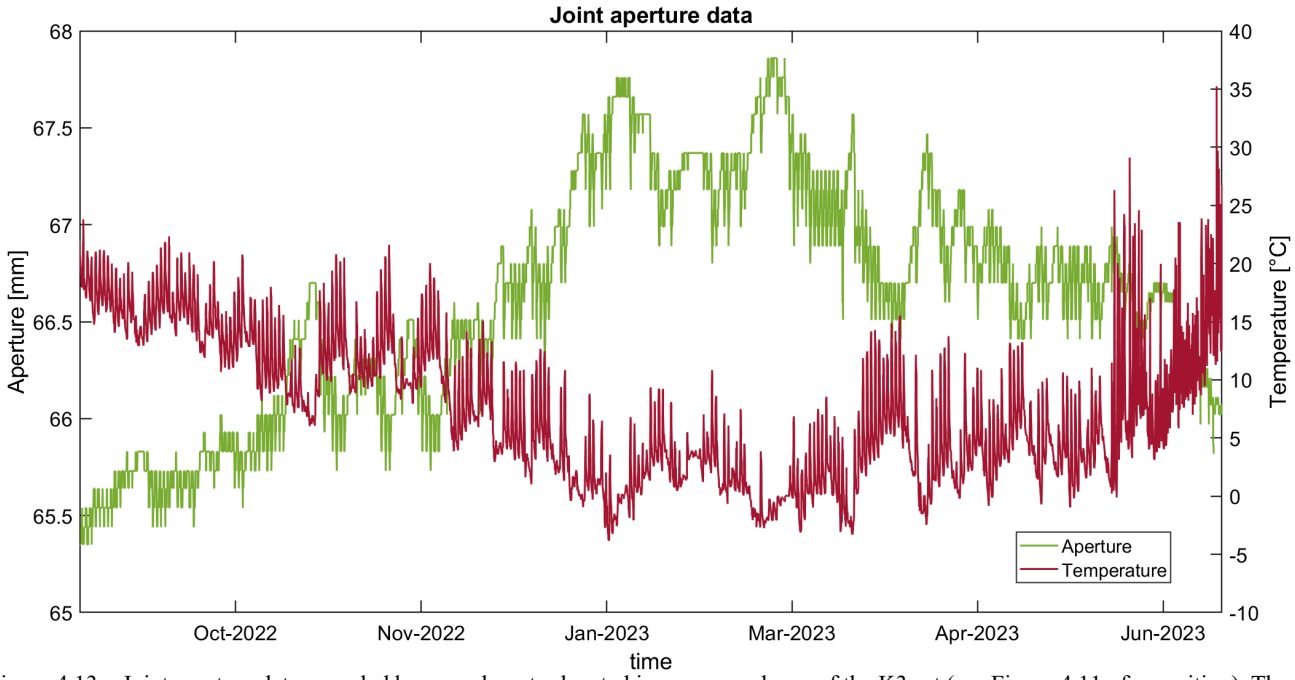

Figure 4.13 – Joint aperture data recorded by a crack meter located in correspondence of the K3 set (see Figure 4.11g for position). The aperture data are related to the air temperature.

Increasing the time range of monitoring may reveal strain accumulation phenomena that are not currently evident. The magnitude of measured deformation is sufficient to result in changes in the hydraulic opening of joints and a potential increase in the permeability of the rock-mass, in correspondence to periods of maximum aperture. This results in an increase in the infiltration capacity during spring periods, which in the Alpine environment coincide with a maximum water supply due to intense precipitation and nival melting. This results in a potential increasing hazard (i.e., higher possibility of occurrence of gravitational instability events) due to an increased presence of circulating water, that, as highlighted in the Chapter 3, is a predominant triggering factor.

The data presented in this Section are intended as partial results, as the time range considered is low. In addition, some data are missing in the time series, related to the occurrence of some technical issues during the initiation phase of monitoring. In spite of this, the analysis of the first recorded data allowed to preliminary outline a TM behavior of the rock-mass and confirm the relations already pointed out during the numerical modeling analysis. It also allowed to demonstrate the validity in using these monitoring tools for understanding thermal effects on rock-masses.

Increasing the amount of data available will be possible to identify:

- A thermal gradient with depth;
- The number of T<0 exceedances and quantify frequency of freeze-thaw cycles in time;
- The maximum depth of reaching T<0;
- Trends in the joint deformation pattern;
- Incidence of freeze-thaw cycles in the deformative evolution of joints;

As soon as data are available for a time range of at least two years, it will be possible to set up TM numerical modeling of the rock-mass, calibrated to the recorded data. The result will be a valuable tool that can analyze the response of the rock-mass in relation to different thermal inputs, including future climate projections. Thanks to the installation of pyranometers that measure incoming solar radiation, it will be possible, in a next step of the analyses, to explore the introduction of this variable as an input factor for numerical simulations.

It will also be possible to compare the recorded data and the identified relationships with other TM monitoring stations installed in different climatic and geological settings, to identify trends and impacts of the temperature in various environments.

Application of other TM monitoring techniques (e.g., IR cameras) may be explored on the Cimaganda site, as well as upgrading the monitoring station with new instrumentation.

4.4 Conclusions

In this Chapter, the thermal evolution of the Cimaganda slope was explored by the development of a TM numerical model. Moreover, a thermal monitoring system provided preliminary field evidences about the daily to seasonal rock-mass temperature evolution and corresponding joint deformation.

In the numerical analysis, the long-term (i.e., millennial scale) and the short-term (i.e., seasonal scale) thermal evolution was assessed with the aim of verifying the preparatory role of atmospheric temperature toward the development of gravitational instabilities. A significant impact of thermal inputs in regulating the mechanical evolution of the slope was observed, with the development of both reversible and unreversible deformations along discontinuities. The identified depth of active slope involvement rises as the time scale increases, consistent with a greater diffusive capacity of thermal inputs. As shown, long-term thermal evolution causes volumetric changes in rock blocks even at considerable depths, with the development of plasticity zones and strain concentration. In this term, the effectiveness of the long-term heating process that followed deglaciation in the Alpine environment was verified and applied on the case study of the historical Cimaganda rockslide. At the end of the modeling analysis, a predisposition to failure at the slope scale was observed to occur.

Considering numerical studies conducted in the Alpine environment, strains and total displacement resulting from the presented TM analysis are comparable with the effects induced by other widely acknowledge preparatory factors, pointing out the significance of considering atmospheric temperature in the evolution of rock-slopes. As an example, numerical studies conducted in the upper San Giacomo Valley on the Vamlera DSGSD with similar geological frameworks and geometries, have shown a similar trend and magnitude of displacements considering the effects of deglaciation using a time dependent constitutive law (Apuani et al. 2007).

The short-term thermal evolution was investigated with both numerical modeling and preliminary monitoring activities. In both cases, a dependency between thermal inputs and joint deformation was observed, with cyclical changes in the aperture values in response to both daily and seasonal heating and cooling thermal cycles. This causes predominantly reversible deformation that can continue over time weakening the rock-mass material (i.e., thermal fatigue). In addition, it has been observed that the magnitude of measured deformation is sufficient to result in significant changes in the hydraulic opening of joints and a potential increase in the permeability of the rock-masses, in correspondence to periods of maximum aperture.

Comparing the simulated aperture values with the monitored ones, a good match was observed, testifying the validity of the model due to the robust geomechanical characterization phase presented in the previous Chapter 3.

The study presented in this Chapter has led to an awareness of the role of atmospheric temperature in the stress-strain evolution of Alpine slopes. Although instability phenomena do not appear to be triggered directly by single thermal cycles, over a long period they can considerably weaken the system by strain accumulation. Rock-masses are thus brought into unstable conditions, where the action of a triggering factor can cause ultimate rupture. In fact, the effects of increased pore pressures in rock clusters induce deformations with an order of magnitude greater than that of temperature (Chapter 3), which, however, may find greater effectiveness in an already severely degraded system.

Hence, TM stresses induced by temperature variations along the slope surface at both long- and short-term timescales, can represent a significant preparatory factor to rock-slope instability in the Alpine environment. Temperature factors should not be neglected when the stress-strain evolution of rock slopes is analyzed, as well as during the assessment of rock fall susceptibility. This is bound to become an increasingly important aspect, in light of forthcoming climate change-related temperature exacerbation.

It is now evident that for a complete and accurate analysis of the mechanical evolution of a rock slope, it is necessary to include all the aspects that contribute to the definition of the physical process at hand, especially in the Alpine environment. With this focus, in the next Chapter a coupled multiphysics approach will be explored to fully analyze the impact of climatic factors in the development of gravitational slope instability events.

Chapter 5
Exploring the link between climate variables and landslide evolution: the Ruinon Case Study

5.1 Introduction: research question and objectives

As widely discussed in previous Chapters, the mechanical evolution of rock slopes is driven by complex interactions among intrinsic and external factors (climatic, anthropic, seismic), controlling both materials behavior and the stress state. With particular reference to climatic factors, both preparatory roles (i.e., progressive degradation of material and propagation of fracturing) and triggering effects to gravitational instability events (i.e., triggering of collapse by exceeding mechanical strength limit conditions) have been recognized.

Several studies have also shown clear relationships between recorded deformations of active rockslides and variations of climatic factors, especially considering the rainfall regime (Hansmann et al. 2012; Preisig et al. 2016; Loew et al. 2017; Rouyet et al. 2017). Studies on the thermal load relationships are rarer, except for active rock walls resulting from a primary collapse event (Gischig et al. 2011a).

Rockslide processes evolve over long times (up to thousands of years) and exhibit a combination of long-term creep-like deformation, related to progressive failure, and superimposed episodic or seasonal accelerations, related to hydro-mechanical (HM) coupled responses. This can result in continuous acceleration and self-stabilizations of the rockslide body. Studies are mainly focused on identifying a relationship between climate variables and rockslides deformations, in order to develop early-warning systems that can identify threshold values above which significant acceleration events occur.

Slip acceleration events, in fact, have some precursor signals useful for civil defense and emergency activities (Crosta et al. 2017). Examples include geomorphological precursors (scarp extension and rupture), geotechnical precursors (slope deformation, fractures opening and changes in the cover characteristics) and hydrological precursors (changes in river flows and development of water springs along the slope) (Lan et al. 2022). Quantitative analysis of these signals requires a continuous monitoring effort. In the past, traditional monitoring activities involved point and local measurement techniques as topographical and ground-based geotechnical. However recent advances in automation and remote sensing have provided new significant opportunities. Inclinometers, robotic total stations, continuous GPS and satellite or ground based synthetic aperture radar, allow a more continuous and spatially distributed monitoring and mapping of surface displacement and velocity fields, while multiple LiDAR

surveys can provide a detailed geometrical description (Strozzi et al. 2005; Cascini et al. 2010; Crosta et al. 2017; Palis et al. 2017; Simeoni et al. 2020). Several studies define threshold values and analyze the evolutionary stages of a landslide from monitoring data (among those Crosta and Agliardi 2003; Bazin et al. 2012; Intrieri et al. 2012; Crosta et al. 2013; Michoud et al. 2013; Seguinot et al. 2018). Studies have led to a progressive awareness of rockslide processes and their evolutionary mechanisms, which, combined with the development of extensive and integrated monitoring systems, allows for effective risk management (Carlà et al. 2019, 2021; Dei Cas et al. 2021, 2022; Schneider et al. 2023). Nevertheless, forecasting rockslide evolution (i.e., acceleration events or final collapse phases) remains difficult. As demonstrated by several studies, in fact, the temporal pattern of displacements is not linear, but depends on complex variables like the stress boundary conditions, magnitude and temporal distribution of external loadings (Crosta et al. 2017), as well as the material behavior changing over time following deformation processes (Eberhardt et al. 2004).

Throughout the years different numerical approaches able to forecast the evolution of a rockslide have been presented. Overcoming the concept of slope's factor of safety (Fellenius 1936; Bishop 1955; Morgenstern and Price 1965; Spencer 1967; Janbu 1973; Chen and Morgenstern 1983), several empirical models have been proposed to predict the time of failure and the expected displacements of rockslides. They are essentially based on the direct observation that the acceleration displacements preceding the collapse exhibit a finite-time singularity of the velocity (Saito 1965, 1969). The definition of the rockslide collapse time (Voight 1988) is thus calculate by considering the inverse of the measured velocity: when the inverse of velocity reaches zero (i.e., displacement tends to infinity), the rockslide accelerates catastrophically, representing slope failure (Helmstetter et al. 2004; Sornette et al. 2004). However, while these methods are effective for the development of real-time early warning systems, they are not able to forecast slip activation events, as they neither include physics nor geometrical factors (e.g., material properties and landslide geometries).

As demonstrated in previous Chapters, these limitations are overcome by stress-strain models, useful to reproduce site-specific conditions, allowing to evaluate rockslide initiation mechanisms and simulate the induced displacement field. The use of these tools for define warning thresholds is however not always affordable, due to the oversimplification required to implement the calculation analyses. Simplifications are often necessary due to lack knowledge of such complex natural processes that require a large amount of data to be accurately described (e.g., geological, hydrological, hydrogeological and geotechnical), or may be necessary due to the computational effort. This leads to assumptions that sometimes may not be negligible in setting landslide alert thresholds.

Recent advances in the prediction of landslide behavior have shown that models should be enriched with

an accurate description of the mechanical behavior of materials involved and the processes that can directly change their properties (such as strength and friction coefficient) without requiring changes in the loading stresses, allowing transition between different creep stages. In recent years, in fact, several authors focused on the time-dependent behavior of rockslide shear band materials (Vardoulakis 2002a; Goren and Aharonov 2007; Veveakis et al. 2007; Goren et al. 2010; Pinyol and Alonso 2010; Cecinato and Zervos 2012; Alonso et al. 2016), providing a time-dependent assessment tool able to simulate rockslide behavior and predict failures, combining internal and external factors (Seguí 2020). The Authors also showed a significant role of temperature at the sliding surface, as a key factor in the creep stage transition (Seguí and Veveakis 2021). Monitoring and modeling this factor, which is predominantly controlled by the friction heating of the sliding mass, is considered a novel analytical approach in defining landslide evolution prediction methods (Seguí et al. 2020).

Research works show the need for further efforts in the field of forecasting of rockslide and rock slope evolution, especially to quantify the impact of climate-driven factors. Deciphering the role of climate factors is in fact a key research challenge that must be addressed to develop adaptation strategies for preventing and mitigating the impacts of ongoing climate change (Crozier 2010; Stoffel et al. 2014; Gariano and Guzzetti 2016; Paranunzio et al. 2019; Bajni et al. 2021, 2023; Camera et al. 2021). The variability of climate forcings in time and space, need to be progressively introduced into models for predicting future rockslides evolution, and not only in the reconstruction of past events. Through the development of a physically based multiphysics approach, which integrates geo-climatic monitoring efforts, material properties, stress state and site-specific trends of the driving variables, it will be possible to obtain a valid forecasting tool, also able to account for future climate changes.

In this Chapter, the case study of the Ruinon rockslide (central Italian Alps) will be analyzed, which presents very pronounced characters of activity and dependence on climatic variables. Thanks to these features and the availability of an efficient monitoring system, a multiphysical approach will be explored to define the link between climate variable and the evolution of the rockslide.

In Section 5.2 the study area and the main features of the Ruinon rockslide will be presented. This Section will provide a list of publications, studies, and data available on this case study, which were used for the development of the analyses presented in this work, after a validation process. The collected data will be presented in Section 5.3 in the following order: geological, geomorphological, geomechanical, hydrogeological, climatic, and hydrological data. Data from the literature *("data available to date"*) and data collected for the development of this work through a survey campaign conducted in the summer of 2022 (*"integration of previous data"*), will be presented separately. In Section 5.4 all the data collected

were used for the development of a robust geological and hydrogeological model. Based on this, in Section 5.5, a 3D stress-strain analysis with a continuous approach was developed with the aim of exploring the morphological and mechanical role in the development of gravitational instabilities along the Ruinon slope. In Section 5.6 a hydrogeologic analysis focused on the reconstruction of groundwater flow is developed. The outputs of this will be used as input for a HM analysis using a 3D discontinuous approach, presented in Section 5.7, to evaluate the role of the hydrogeological component in the development of rockslide acceleration stages. The data collected and the evidence developed during the modeling process led to the development of a 1D thermo-poro-mechanical model of the sliding surface (Section 5.8), with the goal of defining a physically based numerical relationship between pore pressure and rockslide velocity. In Section 5.9, such a model will be used to explore its application in assessing the impact related to climate change in the activity of large Alpine landslides, such as is the case of the Ruinon rockslide.

The analyses presented in Sections 5.5 and 5.8 have been published in Morcioni et al. 2023a and Morcioni et al. 2023b, respectively.

5.2 Study area

The Ruinon rockslide is located in the Upper Valtellina region (Central Italian Alps), between the villages of Bormio and Santa Caterina Valfurva, along the Frodolfo valley (Figure 5.1a).

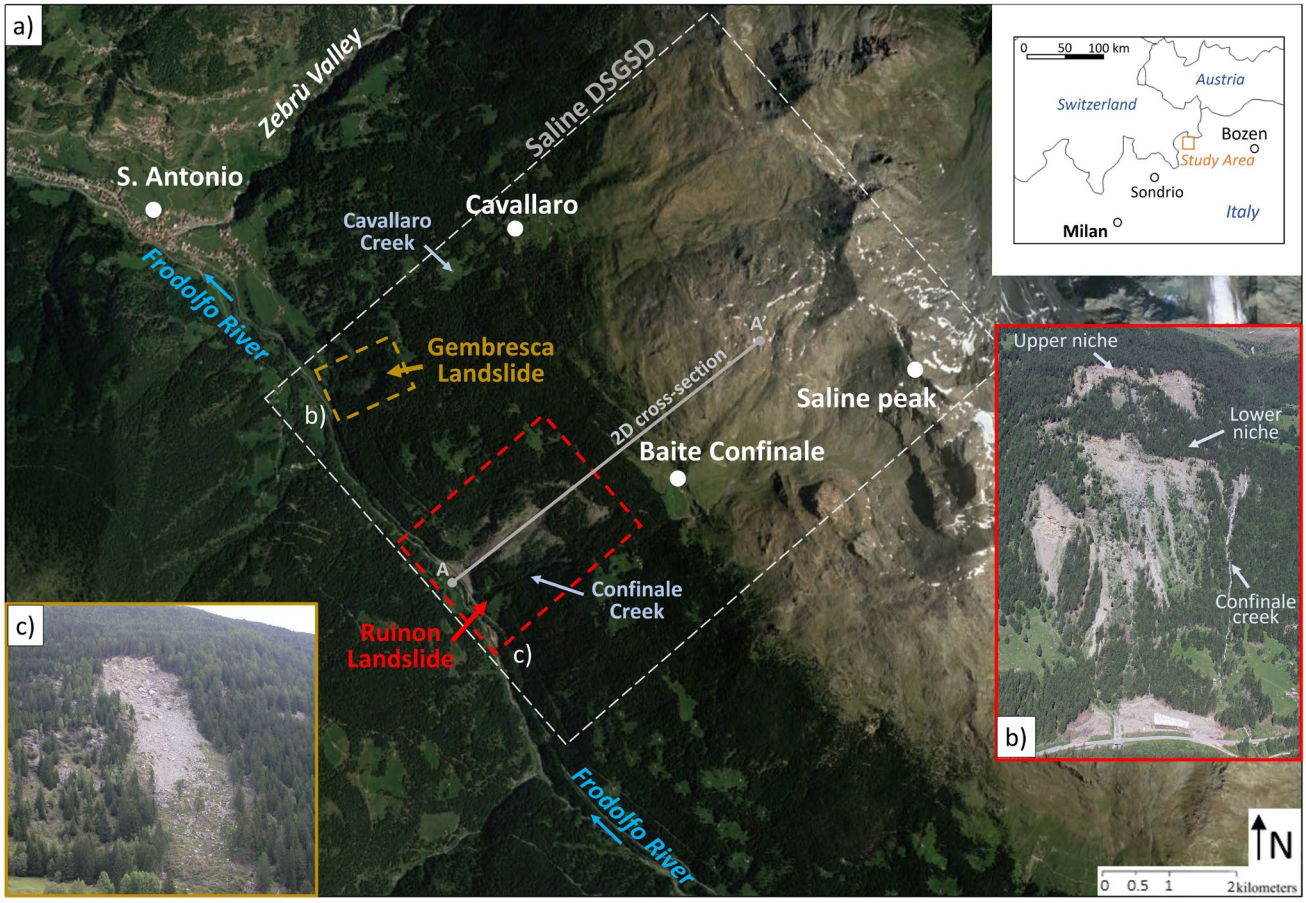

Figure 5.1 – a) Satellite image of the study area showing the main landslide bodies present. b) Image of the Ruinon rockslide where the niches and the Confinale creek are shown c) Image of the Gembresca rockslide.

Throughout its history, the valley has been affected by geomorphological dynamics, including glacial, fluvial, and gravitational processes, that have modeled its shape and caused a gradual mechanical degradation of the slopes (Agliardi et al. 2001). As a result, the valley flanks are morphologically very steep slopes affected by gravitational phenomena, mainly controlled by climate regimes. The Ruinon rockslide (Figure 5.1b), represents only one of the major gravitational processes affecting the slope. Other instability events involving smaller sliding mass volumes are present in the study area, mainly promoted by highly fractured rock-masses. Among the main ones, there is the Gembresca rockslide (Figure 5.1c), which involves a sliding mass of approximately 10,000 m^3 and is currently in a dormant condition but could be reactivated by not particularly intense external forcings (Griffini 2004). The Ruinon and Gembresca rockslides are part of a system of gravitational instability that involves the entire

slope and is known in the literature under the name of "Saline" Deep Seated Gravitational Slope Deformations (DSGDS) (Crosta and Zanchi 2000; Agliardi et al. 2001; Crosta and Agliardi 2003) (Figure 5.1a).

Upstream of the two rockslide bodies, in a range between 1650 m a.s.l. and 2830 m a.s.l., rock scarps, traction trenches, tensile fractures, and structural depressions valleys are present, approximately parallel to the main valley axis (predominantly in the WNW-ESE direction), indicating a significant gravitational activity of the slope (Crosta and Zanchi 2000; Agliardi et al. 2001; Crosta and Agliardi 2003). Ancient landslide deposits are also present along the valley bottom, suggesting an intense geomorphological activity of the slopes, even in earlier geological eras.

5.2.1 The Ruinon Rockslide

The Ruinon rockslide is considered one of the most active cases in the Alpine region. Over the years several geological and geotechnical studies have been carried out, with both scientific and engineering purposes. Among all, the following documents were used for the elaboration of this work.

Technical-engineering studies for the definition of geometries, material properties, and the design of engineering works:

- Assessment of the stability conditions of the Ruinon landslide and surrounding areas (2004). Author: Griffini L., client: Istituto di Ricerca per l'Ecologia e l'Economia Applicate alle Aree Alpine (IREALP), technical report. *Below as: Griffini 2004.*
- Intervention to protect and enhance the territories of upper Valtellina through the defense of settlements and infrastructure from the Ruinon landslide – preliminary project (2013). Author of the geological report: Griffini L., client: Lombardy Region. *Below as : Griffini 2013.*
- Geological and geotechnical reports in: executive (2020) and final (2021) projects for the design of the hydraulic by-pass of the Frodolfo River in the section underlain the Ruinon rockslide, Valfurva (SO). Author of the geological relations: Griffini L., client: Lombardy Region. *Below as: Griffini 2020 and Griffini 2021.*
- Drainage of water upstream of the Ruinon rockslide in Valfurva (Sondrio) with energy recovery from renewable sources (2015). Author: Merizzi G., client: Lombardy Region. *Below as: Merizzi 2015.*
- Feasibility project for the tunnel bypass to SS 300 Gavia - Identification of the route (2022). Client: Lombardy Region. *Below as: Regione Lombardia 2022.*

Technical-engineering studies for the definition of geometries, material properties, and the design of monitoring systems:

- Application of ground-based radar interferometry for rockslide monitoring: the Ruinon rockslide in Valfurva (SO) (2002). Author: Canuti P. (CNR-GNDCI n.2543), client: Lombardy Region. *Below as: Canuti 2002.*
- Revision of threshold values from GBInSAR data following the November 2012 event (2013). Author: Crosta G. et al., client: Regional environmental protection agency (ARPA Lombardy). *Below as: Crosta 2013*.
- Geotechnical modeling service and identification of criticality thresholds in rockslide areas monitored by the ARPA CMG (2018). Author: Crosta G., client: Regional environmental protection agency (ARPA Lombardy). *Below as: Crosta 2018.*

Scientific studies for data processing and identification of rockslide evolution mechanisms, presented in:

- Deep Seated Slope Deformations: Huge, Extraordinary, Enigmatic Phenomena *(Crosta and Zanchi 2000)*.
- Structural constraints on deep-seated slope deformation kinematics *(Agliardi et al. 2001)*.
- Failure forecast for large rockslides by surface displacement measurements *(Crosta and Agliardi 2003)*.
- Ruinon rockslide (Valfurva, Italy) activity in relation to rainfall by means of GBInSAR monitoring *(Del Ventisette et al. 2012)*.
- Long-term evolution and early warning strategies for complex rockslides by real-time monitoring (*Crosta et al. 2017)*.
- Damage-Based Long-Term Modelling of Paraglacial To Postglacial Evolution of Alpine Rock Slopes *(Riva 2017)*.
- Monitoring and analysis of the exceptional displacements affecting debris at the top of a highly disaggregated rockslide *(Carlà et al. 2021)*.

In addition to these studies, data from the geological and geotechnical monitoring system currently installed along the rockslide body (year 2022), were provided by the "Centro di Monitoraggio Geologico (CMG)" of the ARPA Lombardia agency, as part of this work.

Starting from the geometrical features of the rockslide body, the above documents show a main sliding surface located at approximately 70–90 m depth and an estimated total volume of the sliding mass of 20 Mm^3 (Crosta and Agliardi 2003; Griffini 2004; Del Ventisette et al. 2012; Crosta et al. 2017). The area of instability extends along the southwest slope of Confinale peak, characterized by NW-SE orientation, SW exposure and an average inclination of 35° (Figure 5.1).

The main active body extends at elevations between 1600 and 2100 m a.s.l., and is nested at the toe of a deep-seated gravitational slope deformation (Saline DSGSD), which affects the entire slope up to its top at 3000 m a.s.l. (Crosta and Zanchi 2000; Agliardi et al. 2001). Two different rockslide scarps identify the main active body: the so-called *"Upper niche"*, which develops between about 2050 and 2100 m a.s.l. (Figure 5.1b), and the *"Lower niche"*, located at 1900– 1950 m a.s.l. (Figure 5.1b); the two rock scarps have considerable heights, of the order of tens of meters. Along the left side of the rockslide runs the Confinale creek, which represents a potential significant water supply element.

Even if the local name "Ruinon" (meaning ruined slope) reveals a persistent instability of the slope, no gravitational events in the area were reported before 1960. The rockslide has been showing intense activity since 1981, and it experienced a major acceleration in 1987–1988 following heavy rainfall that affected the entire region causing the Valtellina floods. In 1984, following the occurrence of debris flows, the first geological investigations were carried out, and in 1997, after severe rockfalls, an in-situ monitoring network was installed by the "ARPA Lombardia" agency, under assignment of Lombardy Region. Slope hazards related to the evolution of the rockslide threaten the national road SS300, that runs through the valley bottom connecting the villages of Bormio and Santa Caterina Valfurva. A major risk is that a general collapse could obstruct the Frodolfo river, creating an unstable dam that would be potentially hazardous for villages along the valley. In June 1998, a debris flow interrupted the national road, and the 1997 monitoring system was implemented and upgraded to an automated mode. Between spring 2014 and fall 2016, accelerated displacements led to frequent road closures because of a possible progression of the sliding mass downslope of the lower scarp.

In June 2019, rockslide velocities increased to much higher values than ever before, reaching more than 1 m/day for 5 months (Carlà et al. 2021). Although a failure of the rockslide still did not occur, a large amount of debris moved downstream reaching the valley floor. A rock block of about 90 m^3 rolled down, damaging the national road, and forcing its prolonged closure. The most active areas in recent years have been the central and western parts of the lower body, and new scarps developed in the northwest portion. Due to the intense gravitational activity, especially after the 2019 events, the rockslide body consists of strongly disoriented phyllite boulders of the size of meters to decameters in diameters, embedded in a silty matrix. A large deposit of debris covers the entire slope, down to the bottom of the valley.

Geotechnical and seismic surveys allowed to define the nature of the rock-mass below the rockslide deposit, showing a lithological uniformity with extremely fractured phyllites lying on undisturbed phyllites. Boreholes drilled in 1988–1989, identified a deep shear zone of gravitational origin characterized by up to 2 m thick layers of cataclastic granular material and a highly weathered silty matrix. They were defined by a sudden decrease of the RQD index, with values tending towards zero within the undisturbed phyllites body (Griffini 2004).

The installation of inclinometers allowed to highlight the presence of secondary composite surfaces affecting the debris cover. However, many uncertainties remain with regards to the deep pattern of deformation since inclinometers have been sheared off quickly after installation, due to the high activity of the shallower debris. The presence of multiple weak layers, highlight that significant internal differential movements could exist from the sliding base up to the surface.

The slope exhibits a complex hydrogeological setting governed by the presence of the Confinale creek, flowing on the left flank of the rockslide body (Figure 5.1b). Previous authors (Griffini 2004, 2013; Crosta 2018) recognized the presence of an aquifer located within the rockslide body attributable to the high permeability material (debris and highly disarticulated rock-masses) laying over a silty low-permeability layer, corresponding to the sliding surface. However, groundwater circulation and aquifer recharge system were not well understood. By previous studies (Canuti 2002; Crosta and Agliardi 2003; Griffini 2004; Del Ventisette et al. 2012; Crosta 2013, 2018; Crosta et al. 2017; Carlà et al. 2021) it has been recognized that pore water pressures highly influence the activity of the rockslide. Analysis of displacement-time and velocity–time behavior showed impulsive rockslide acceleration events when the piezometric level rises, which are superimposed on slow and constant slope movements. A key role of rainfall and snowmelt as an accelerating factor for the rockslide has been observed (Crosta and Agliardi 2003) with accelerations primarily occurring in late spring to summer.

After the 2019 event, significant actions concerning the improvement of passive structures to protect the National Road and reduce the risk of flooding, in case of collapse, have been carried out (Griffini 2020, 2021; Regione Lombardia 2022). The monitoring system has been reinforced, and new geological surveys have been carried out for the construction of a Frodolfo river by-pass tunnel. In the last few years, the deviation of water from the Confinale creek (Merizzi 2015), combined with a climate dry period, seems to have led to a gradual stabilization of the rockslide.

5.3 Data collection

Due to the high geological significance in terms of size, hazard, and associated risk of this rockslide, numerous studies meant at geological and geomechanical characterization of the slope have been carried

out over the years. The works were mainly focused on the identification of the rockslide body geometries and on the assessment of the mechanical parameters of the outcropping materials. With reference to the technical reports presented in the previous paragraph, the following information are provided:

Table 5.1 - Data reported by the technical reports available for the development of this work.

Document	***Data***
Assessment of the stability conditions of the Ruinon rockslide and surrounding areas (Griffini 2004).	• Stratigraphy of 3 borehole cores drilled in 2004; • Geomechanical tests on intact rocks (10 Monoaxial, 8 Triaxial and 11 Brazilian tests) and discontinuities (3 Direct joint shear tests); • Geomechanical model of the slope; • Stability analysis (DEM approach); • Processing of surface monitoring data.
Intervention to protect and enhance the territories of upper Valtellina through the defense of settlements and infrastructure from the Ruinon rockslide (Griffini 2013).	• Stratigraphy of 12 borehole cores drilled in 2013; • Standard penetrometric test (SPT); • Hydraulic borehole tests (Lefranc and Lugeon type); • Geomechanical tests on intact rocks (6 Monoaxial, 3 Triaxial and 5 Sonic tests) and discontinuities (2 Direct joint shear tests); • 24 Granulometric tests on soils; • Geological and geomechanical model of the slope.
Executive project: Design of the hydraulic by-pass of the Frodolfo River in the section underlain the Ruinon rockslide, Valfurva (SO) (Griffini 2020).	• Stratigraphy of 7 borehole cores drilled in 2020; • Standard penetrometric test (SPT); • Hydraulic borehole tests (Lefranc-type); • Geomechanical tests on intact rocks (4 Monoaxial tests); • 17 Granulometric tests on soils; • Geotechnical tests on soils (6 Direct shear); • Geophysical surveys (Refraction seismic and electrical tomography).
Executive project: Design of the hydraulic by-pass of the Frodolfo River in the section underlain the Ruinon rockslide, Valfurva (SO) (Griffini 2021).	• Stratigraphy of 4 borehole cores drilled in 2021; • Standard penetrometric test (SPT); • 31 Granulometric tests on soils; • Geotechnical tests on soils (9 Direct shear); • Geophysical surveys (Refraction seismic and electrical tomography).
Revision of threshold values from GBInSAR data following the	• Geological and geomechanical model of the slope; • Processing of surface monitoring data.

November 2012 event (Crosta 2013).	
Geotechnical modeling service and identification of criticality thresholds in landslide areas monitored by the ARPA CMG (Crosta 2018).	• Geological and geomechanical model of the slope; • Processing of surface monitoring data.

Hydrogeological studies, on the other hand, are still insufficient, leaving large gaps in the identification of preferential feeding zones and recharge times of groundwater bodies which interfere with the rockslide.

This Section aims to collect bibliographic data on the Ruinon case study, and present results of a recent survey campaign conducted in the framework of this work during summer 2022, in order to validate the available data and integrate prior knowledge. Part of the characterization data presented in this work and referred to the 2022 survey campaign were developed in collaboration with two master's theses in Earth science (Stazzonelli N., 2023 and Cupelli C., 2023 - Università degli Studi di Milano).

5.3.1 Geological features

The geological framework of the Valfurva region is related to the Austroalpine Nappe arrangement (Figure 5.2), which is composed by a crystalline basement of the pre-Permian age, with a N to E vergence. In the study area, the Campo Nappe with the Bormio Phyllites (metapelite unit) outcrops (Figure 5.2a; Bonsignore et al. 1969). This formation exhibits a pervasive schistosity with millimeter to centimeter spacing, defined by a submillimeter alternation of white mica films, opaque minerals, and quartz-feldspathic microlithon, conferring a mylonitic texture to the rocks (Montrasio et al. 1990). Rock-masses are strongly deformed with isoclinal and minor transposed folds, recording a polyphase tectonic and metamorphic evolution during the Varisican and the Alpine orogeneses (Conti et al. 1994; Gregnanin and Valle 1995; Froitzneim and Manatschal 1996).

Locally, phyllites are characterized by the inclusion of magmatic bodies of late to post-Varisican and late Alpine age (Andesite in Figure 5.2b; Senaldi 2017), and other bodies of the Campo Nappe unit as marbles and prasinites (Montrasio et al. 1990).

Based on Griffini 2004 and Griffini 2013, an interpretative structural geological model of the slope is proposed. It provides 4 successive deformation phases accompanied by a magmatic event; the most pervasive are represented by the *D3* and, subordinately, the *D2* phases, clearly present in the lower

portion of the slope and only locally at higher elevations. The *D3* deformation phase generates structural elements plunging toward the NW with variable inclinations of less than 30°. Moving toward the higher sectors of the slope (NE direction) it becomes more pervasive, generating isoclinal folds in the *S2* foliation in the range between 1900 m a.s.l. and 2000 m a.s.l., and obliterating the structure formed in the *D2* phase above 2000 m a.s.l. Phases *D1* and *D4* generate rare and poorly pervasive deformation structures in the substrate that exhibit irregular spatial distribution and are only recognized above 2250 m a.s.l.

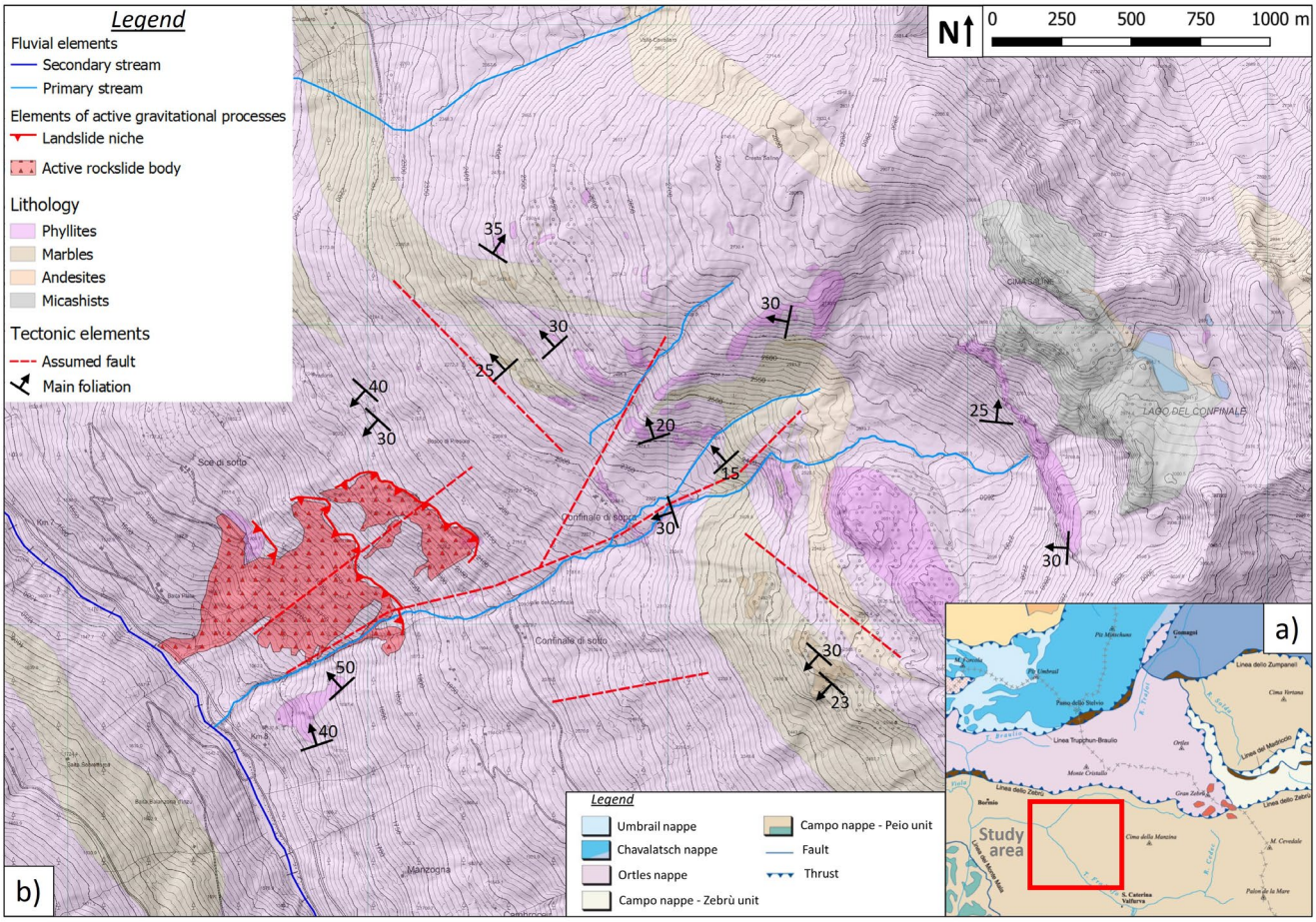

Figure 5.2 – Geological settings of the Study Area. a) Tectonic scheme showing the relationship between the different geological units present (Montrasio et al. 1990). b) Geological map of the Ruinon slope (Griffini 2013 and personal surveys); topographic basis: CTR ed. 2012 scale 1:10,000.

The portion of the slope affected by the Ruinon rockslide is characterized by the presence of a single lithotype (phyllites), with an asymmetrical metric-scale fold structure, which is poorly to moderately fractured. In addition to these, minor tectonic lineaments (fractures and faults) are present (Figure 5.2b), with direction respectively of:

- *F1*: ENE-WSW direction, approximately coincident with the T. Confinale in the section between 2200 and 2300 m a.s.l.; the orientation of *F1* was estimated to have NNW dip and inclination between 60° and 70°;
- *F2:* with NNE-SSW direction, passing through the "Baite di Confinale di Sopra" and truncated against F1 at about 2200 m a.s.l.; the orientation of *F2* was estimated to have ESE dipping and inclination of 70° to 75°;
- *F3*: with NE-SW direction arranged approximately following the Ruinon rockslide length this structure is considered subvertical.

5.3.2 Geomorphological features

Along the entire SW slope of the Confinale peak, morphological features typical of DSGSDs deformation processes, such as trenches and counter scarps can be recognized (Figure 5.3). The entire slope from an elevation of 1300 m a.s.l. to its top at 3000 m a.s.l., is affected by a deep gravitational movement, as already described as Saline DSGDS by Agliardi et al. 2001. Lateral boundaries are represented respectively by the Confinale valley at SE and the Cavallaro valley at NW (Figure 5.1a). The occurrence of long-term gravitational displacement is expressed by a wide-range of impressive morpho-structures, that are found all throughout the slope (Figure 5.3). Agliardi et al. 2001 developed a conceptual model regarding the kinematics, age, and state of activity of the Saline DSGSD. Results showed that deformations started after the Late-Wurmian age (15,000±11,000 years B.P.), as widely recognized for similar processes in the Alpine environment. Deformations continued until few centuries ago, not excluding a present-day low-rate activity. Numerical modelling indicates post-glacial relaxing as the main driving factor of the deep slope deformation.

The geomorphological survey conducted in the summer of 2022 as part of the present work, validated the dynamics recognized by previous studies (Agliardi et al. 2001; Griffini 2013; Riva 2017) and increased knowledge about the geomorphological evolution of the slope, highlighting the elements discussed below.

In the upper part of the slope, the cumulated movement resulted in ridge splitting of the Saline peak, with a huge triangular scarp with downslope vertical component of around 150 m (Riva 2017). The kinematic is controlled by the presence of a tectonic lineament crossing the entire Confinale slope with a WNW-ESE direction, steeply dipping downslope. It is represented by a swarm of fractures that drove the occurrence of various past and ongoing rock slope instability processes along the slope.

Moving downward, antithetic rectilinear scarps are encountered with lengths up to several hundred meters and vertical throw up to 3-4 m. These structures have well-preserved surfaces-oriented N-S and

NNW-SEE, representing the surface expression of steeply sloping shear zones (as already recognized by Agliardi et al. 2001). In the area of the “Baite Confinale di Sopra", around 2300 m a.s.l., a synthetic scarp of even kilometer-long lengths can be observed, often associated with counterscarps that define semi graben structures characterized by decametric width filled by blocks and debris (Figure 5.3a, d).

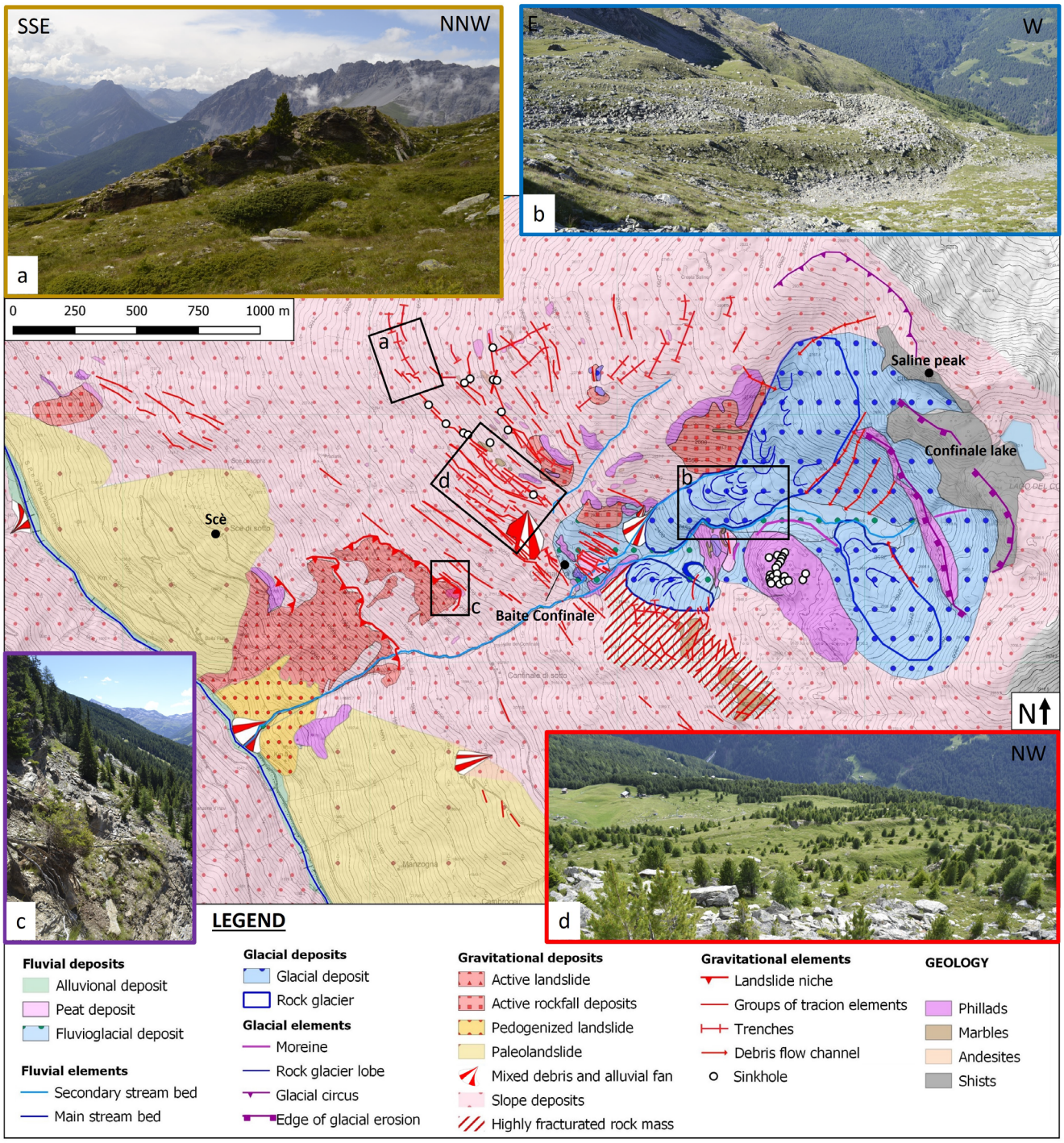

Figure 5.3 – Geomorphological map; topographic basis: CTR ed. 2012 scale 1:10.000. a) Traction trenches b) Rock glacier with advance lobes c) upper part of the Ruinon rockslide active body d) synthetic scarps, trenches and semi-graben of even kilometer-long lengths.

Moving further downward, close to the active Ruinon rockslide body, linear and convex scarps are present, with also trenches and tension cracks, which are up to 5 m wide and characterized by current activity (collapses and the exposure of fresh rock surfaces). The area affected by the active rockslide is gradually expanding backward and laterally. Upstream of the detachment niches, the abundance of trenches interrupting the grass cover testifies to the evolution of the scarps by retreat; the development of new rockslide scarps to the right of the main rockslide body, on the other hand, testifies to progressive lateral expansion. Thus, the Ruinon activity distribution could be expected as a retrogressive and enlarging rockslide, typical of a roto-translational mechanism. The active rockslide body consists of strongly disoriented boulders with equivalent diametral size of meters to decameters, embedded in a silty matrix (Figure 5.3c).

Other types of gravitational deposits are the “slope deposits”, present throughout the slope as heterometric material with gravel, sand and fine matrix, as well as bodies of “talus deposits” placed at the base of rocky outcrops consisting of heterometric clasts, generally without matrix (Figure 5.3).

At higher altitudes, between 2600 and 2900 m a.s.l., along the vertical walls below the Saline peak, evidences of rapid flows can be recognized, which propagate downstream moving large amounts of debris until they stop in correspondence of flat morphologies (Figure 5.3). Evidence of slow movements involving surface deposits is observed along the slope, as for example on the left side of the Confinale creek at an elevation of 2450 m a.s.l.

Glacial morphologies such as shaped rocks and glacial scarps are widespread and well noticeable along the slope (Figure 5.3). Above 2250 m a.s.l., within the Confinale valley, glacial morphologies and deposits are present; between elevations of 2750 and 2950 m a.s.l, several scarp margins and glacial erosion scars are visible, while between 2900 and 3000 m a.s.l. west of the Saline peak, a glacial cirque with associated fill deposits is visible. Accumulation deposits such as moraine cordons and periglacial rock glacier are present between elevations 2300 m a.s.l. and 2550 m a.s.l., characterized by the presence of advance lobes (Figure 5.3b).

On the lateral sides of the Confinale river, especially in its uppermost portion, where the slopes are flat, deposits due to surface water runoff are present. They consist mainly of remobilized glacial deposits and alluvial deposits with stratified gravels with a medium to coarse sandy matrix.

As previously documented, marble bodies outcrop along the slope; these may promote the development to distinctive karst processes. Upstream of “Confinale di Sopra” and in the “Presure Forest”, the presence of calcareous substrate lithology, predominantly marble, and a series of trenches with WNW-ESE and NNE-SSW direction intersecting each other, generate intensely fractured zones where water can easily infiltrate into areas recognized as "sinkholes" (Figure 5.3). These karst structures have also been

observed on the hydrographic left of the Confinale river, between elevations of 2600 and 2650 m a.s.l, where there is the presence of open fracture systems with NW-SE and NE-SW orientation.
The morphology of the slope at the lower elevations is characterized by the presence of accumulation deposits and systems, specifically dejection conoids of mixed debris material, eroded from rockslide bodies by the action of water courses (Figure 5.3). Ancient landslide deposits are also present at the toe of the slope (e.g., Scè rockslide), with estimated deposits thickness up to 100 m (Figure 5.3). These testify diffuse instability since paraglacial stages.

5.3.3 Geomechanical features

5.3.3.1 Data available to date

Over the years, several geotechnical campaigns have carried out in the Ruinon rockslide area, in order to assess the fracture intensity and the mechanical quality of the rock-masses. In particular, detailed field surveys, borehole drilling with stratigraphical analysis, geophysical surveys and laboratory geomechanical tests have been conducted.
As discussed in Section 5.3.1, the geological setting of the Ruinon slope is characterized by a lithological homogeneity consisting mainly of phyllite rocks, with intercalations of marble bodies. In addition, magmatic intrusions of prasinites and andesites are present, outcropping in the upper portion of the slope. Multiple deformation phases have affected the rock substrate. The most pervasive one is represented by the *D3* phase (Section 5.3.1, Griffini 2004, 2013; Senaldi 2017), generating structural planes plunging toward the NW with variable inclinations of about 30° and isoclinal folds. In addition, minor tectonic elements (fractures and faults) with ENE-WSW (*F1*), NNE-SSW (*F2*) and NE-SW (*F3*) directions, are present. They are mostly concentrated in the area upstream of the main rockslide body, even though their presence is not evidenced by particular fracture increments or lithological changes.
Previous works remarked a good congruence and homogeneity of discontinuity systems affecting the rock-masses along the slope; the main ones are:

- Discontinuity system connected to the schistosity planes dipping toward NW (more rarely SE) with 10° to 30° of inclination (maximum 50°)
- Discontinuity system with direction perpendicular to the line of maximum morphological gradient: SW dip, inclination 50° to 70°;
- Discontinuity system with direction parallel to the line of maximum morphological gradient: NW dip, inclination of 70° to 80°;

- Subvertical discontinuity system with E-W direction.

Rock-mass quality values obtained by previous Authors (Griffini 2004, 2013) around the rockslide body are in the range of "fair" classes, with Geological Strength Index (GSI) values ranging from 50 to 75. Local decrease of rock-mass mechanical properties and GSI values is observed in correspondence of highly fractured or folded outcrops at the rockslide upper niche. Riva 2017 showed a variation in mean GSI value of around 10-15 points inside and outside the Saline DSGSD body.

Direct In-situ geomechanical tests

From 1988 to the present, 34 boreholes have been drilled in the study area. Some of them were instrumented with inclinometers to measure rockslide displacements and detect sliding surfaces (Figure 5.4).

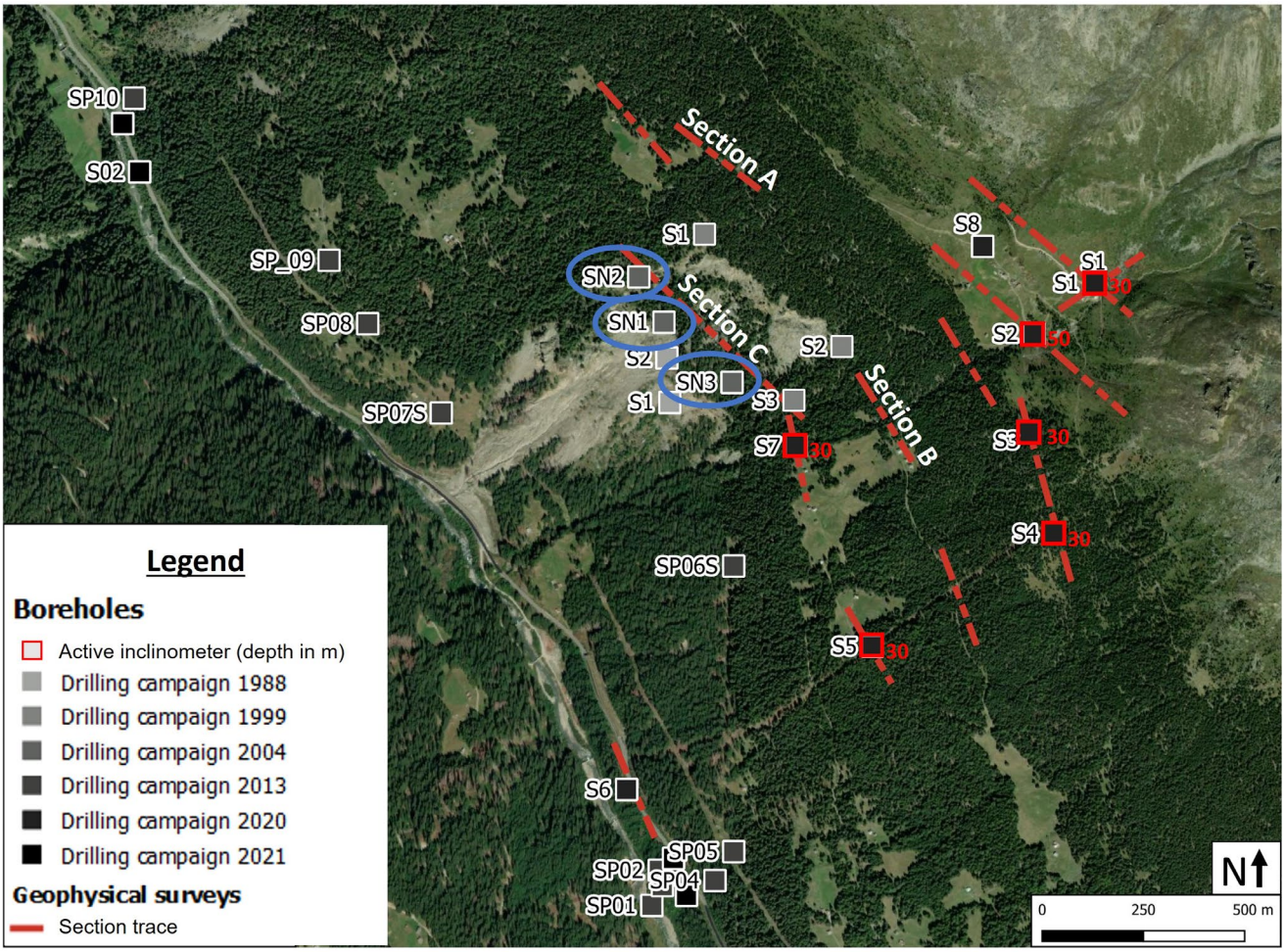

Figure 5.4 – Location of the boreholes and geophysical section traces made from 1988 to 2021.

The list of boreholes drilled in different years is summarized in Table 5.2.

Table 5.2 - List of the boreholes drilled along the Ruinon rock slope (Griffini 2004, 2013, 2020, 2021).

		Coordinates			Clockwise orientation from N		
Year	Code	N	E	Elevation (m a.s.l.)	Trend	Inclination	Depth (m)
1988	S1 (1988)	5144115.00	611932.00	1795.0		Vertical	91.0
	S2 (1988)	5144225.00	611925.00	1860.0		Vertical	95.0
1999	S1 (1999)	5144530.14	612017.77	2070.0		Vertical	120.0
	S2 (1999)	5144253.11	612357.02	2102.5		Vertical	120.0
	S3 (1999)	5144120.68	612238.49	1980.0		Vertical	93.0
2004	SN1 (2004)	5144312.90	611917.66	1917.5		Vertical	100.0
	SN2 (2004)	5144424.82	611855.44	1940.0		Vertical	96.4
	SN3 (2004)	5144164.65	612085.81	1925.0		Vertical	101.6
2013	SP_01 (2013)	5142874.37	611887.79	1522.1		Vertical	30.0
	SP_02 (2013)	5142961.29	611906.08	1514.0		Vertical	30.0
	SP_03 (2013)	5142923.10	611913.56	1517.1	18°	10°	40.0
	SP_04 (2013)	5142935.68	612043.45	1581.8	18°	5°	47.0
	SP_05 (2013)	5143007.17	612089.81	1640.6		Vertical	106.0
	SP_06S (2013)	5143711.72	612089.81	1582.7	53°	60°	121.1
	SP_06H (2013)	5143711.72	612089.81	1582.7		Vertical	140.1
	SP_07S (2013)	5144089.12	611367.99	1545.9	36°	20°	191.0
	SP_07H (2013)	5144089.12	611367.99	1545.9	36°	60°	129.8
	SP_08 (2013)	5144309.46	611186.30	1563.2		Vertical	162.5
	SP_09 (2013)	5144465.72	611090.75	1600.0		Vertical	167.0
	SP_10 (2013)	5144865.92	610609.58	1397.1	140°	5°	50,0
2020	S1 (2020)	5144410.05	612981.03	2332.5		Vertical	30.0
	S2 (2020)	5144284.22	612830.87	2250.0		Vertical	50.0
	S3 (2020)	5144040.21	612818.01	2260.0		Vertical	29.6
	S4 (2020)	5143792.03	612879.88	2225.0		Vertical	30.0
	S5 (2020)	5143513.61	612432.88	1957.5		Vertical	30.0
	S6 (2020)	5143160.46	611825.29	1532.5		Vertical	50.0
	S7 (2020)	5144007.54	612244.14	1955.0		Vertical	30.0
	S8(2020)	5144500.08	612704.69	2290.0		Vertical	80.0
	PZ1 (2020)	5144412.48	613010.92	2335.0		Vertical	30.0
	PZ2 (2020)	5144303.34	612799.24	2255.0		Vertical	50.0
2021	S01 (2021)	5144803.00	610581.20	1394.2		Vertical	18.5
	S02 (2021)	5144684.00	610623.00	1400.0		Vertical	20.0
	S03 (2021)	5142990.41	611941.00	1565.0		Vertical	15.0
	S04 (2021)	5142899.27	611973.24	1567.5		Vertical	25.0

The processing of geomechanical and stratigraphic data (Griffini 2004, 2013, 2020), allowed to define the nature of the rock-mass below the deposits, showing a general lithological uniformity with extremely fractured phyllites laying on undisturbed phyllites. Boreholes drilled in 1988–1989 (Figure 5.4), identified a deep shear zone characterized by up to 2 m thick layers of cataclastic granular material and a highly weathered silty matrix. They were defined by a sudden decrease of the RQD index, with values tending towards zero within the undisturbed phyllites body. Boreholes drilled in 2004 (Figure 5.4), also showed the presence of highly fractured layers at a depth of 70-80 m (Figure 5.5). Due to the intense activity of the rockslide, the area in the proximity of the main body is no longer accessible by working means, and therefore drillings carried out in the 2013-2020 campaigns are not directly investigating the Ruinon sliding surface. From the RQD values evaluated on the borehole rock cores, it is possible to assign overall fair to good mechanical quality to the rock-masses inspected, sometimes even very good, but with significant reductions at specific depths. Layers of increased fracture condition have been identified at depths of 43 to 45 m, 58 to 62 m, 69 to 72 m, 82 to 85 m and 92 to 97 m.

Figure 5.5 - RQD values measured at different depths in the boreholes SN1, SN2, SN3. The presence of heavily fractured layers is evident.

To monitor deep displacements and to identify potential slip surfaces, an aluminum inclinometer pipe was placed along the entire depth investigated by boreholes S1_2020, S2_2020, S3_2020, S4_2020, S5_2020, S6_2020, and S7_2020. However, due to the unfavorable location of the boreholes, placed outside the active rockslide body, (Figure 5.4), and the limited depth reached (maximum 50 m), they are not useful to monitor the deformations occurring along the deep sliding surface identified in the 1989-2004 boreholes. Measured data showed modest shallow deformation, probably related to the

evolutionary dynamics of the entire valley slope. Overall, inclinometer analyses identified maximum displacements of about 0.1 m in 5 months at depths between 20 and 30 m. As an example, representative graphs of the N-S and E-O axis of the inclinometer "S7_2020" (i.e., the inclinometer closest to the active rockslide body; Figure 5.4) are shown in Figure 5.6. First reading was taken on May 25th, 2020, and the second one on October 15th, 2020. Azimuthal deviations indicate a preferential orientation of deformations with a NE-SW direction, following the orientation of the slope. The data indicate marked displacements along the N-S axis (parallel to the slope direction) and less noticeable deformations along the E-W one.

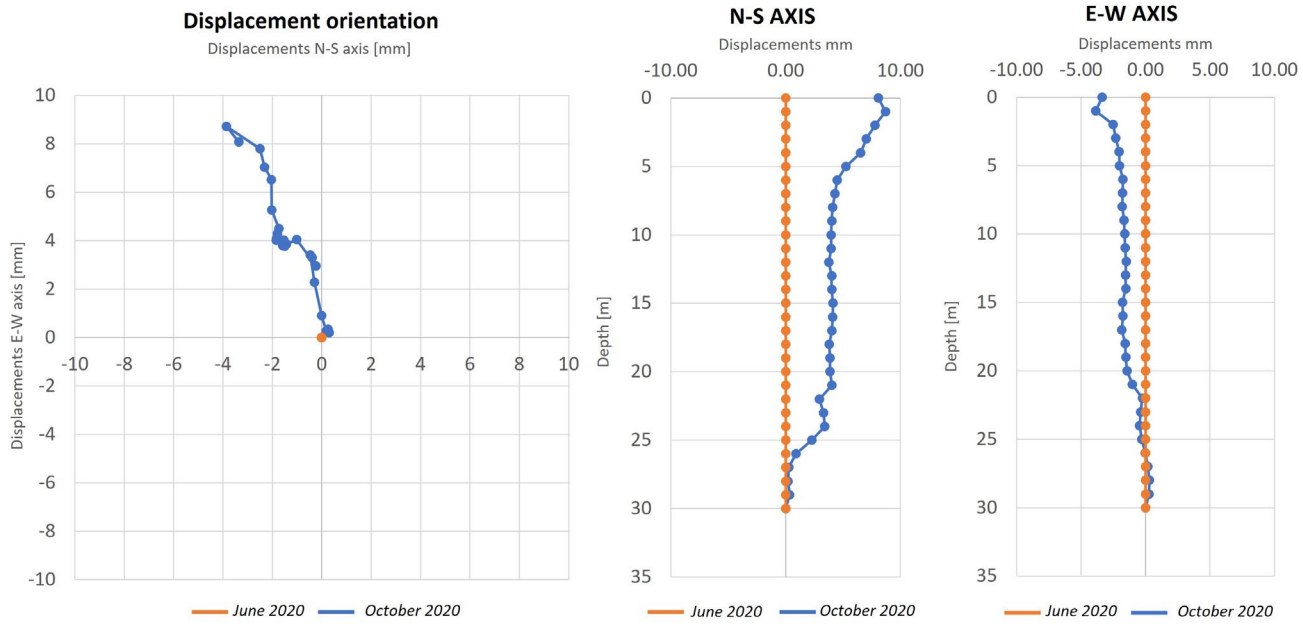

Figure 5.6 - Data recorded by the S7 inclinometer along the N-S and EW axis. The azimuthal direction of the displacements is also shown below.

Indirect In-situ geomechanical tests

Direct geomechanical investigations are complemented by geophysical surveys (Griffini 2020), carried out in the area affected by the Ruinon rockslide and at the "Baite di Confinale" locality, including refraction seismic tests and electrical resistivity tomography (Figure 5.4), allowing the characterization of the rock-mass and deposits below the topographical surface (Figure 5.7).

Energy generated in refraction seismic acquisition allowed the reconstruction of the first 100 -120 m from topographical level. From the acquired seismic data and their interpretation, three different geo-seismic units were identified:

- *First geo-seismic unit* (thickness ranging from 4 to 20 m): this unit (beyond the red line in the Figure 5.7a-b), with velocities from 900 to 1200 m/sec, can be attributed to covering materials characterized by low seismic velocities that progressively increase due to better thickening.

- *Second geo-seismic unit* (thickness ranging from 9 to 70 m): it lies between the red and blue lines of Figure 5.7a-b and is characterized by seismic velocities reaching 2500 m/s. This unit is ascribed to the presence of consolidated loose materials or highly weathered rock-masses.
- *Third geo-seismic unit*: located below the blue line of Figure 5.7a-b, is characterized by seismic velocities above 2500 m/s - 3000 m/s with further increases with depths due to a general improvement in geomechanical characteristics. This unit is probable defined by the presence of less weathered rock-masses.

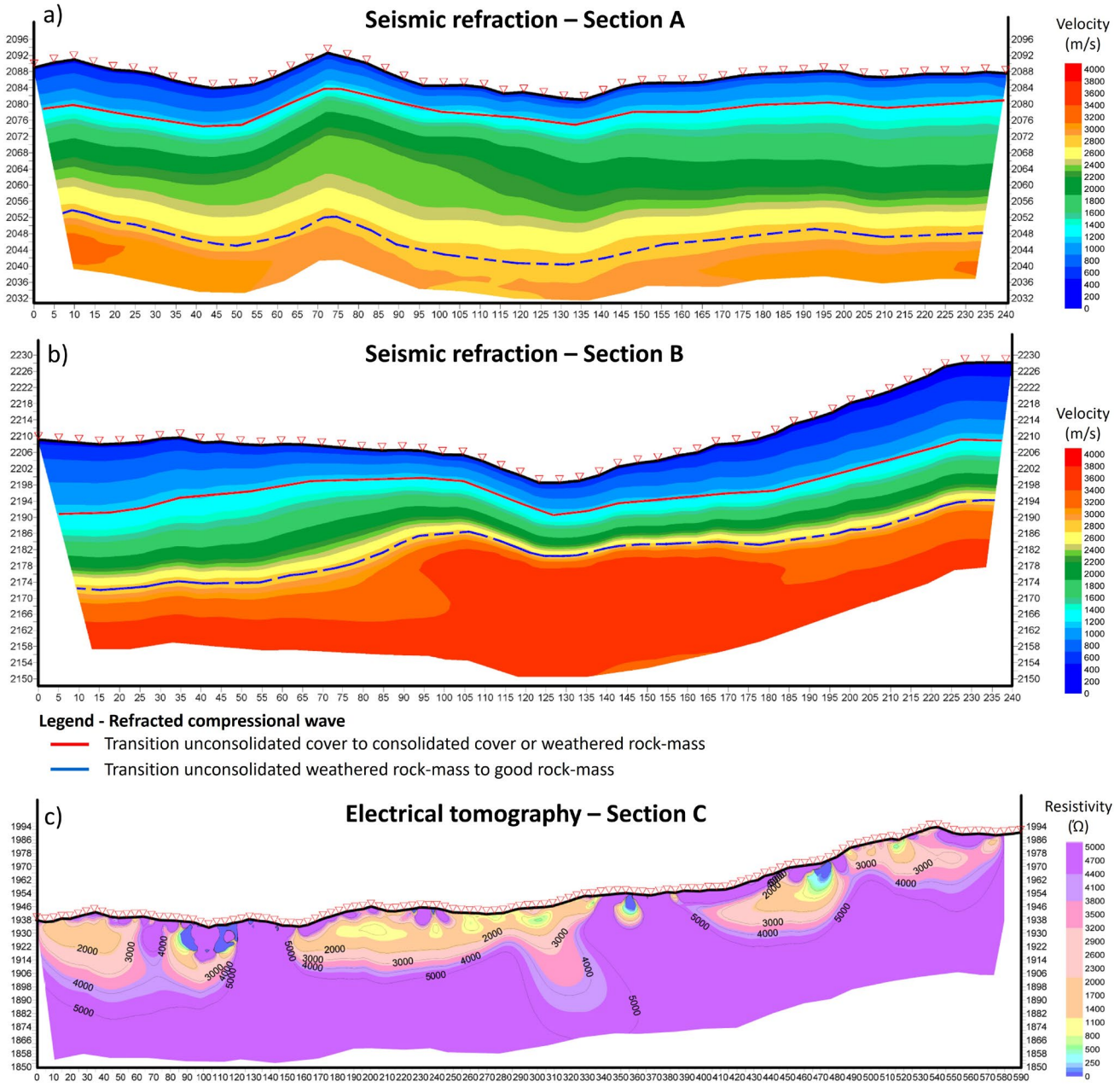

Figure 5.7 – Geophysical sections (see location on Figure 5.4). a-b) Seismic refraction section c) Electrical tomography section. From Griffini 2020.

Concerning electrical tomography, on the other hand, it allowed to investigate the nature of surface soft deposits by identifying four different units (Figure 5.7c):

- *Geoelectric unit A*: resistive, associated with the presence of surface deposits with abundant matrix;
- *Geoelectric unit B*: medium resistive, associated with the presence of debris and coarse gravels with less matrix;
- *Geoelectric unit C*: resistive, associated with the presence of coarse deposits;
- *Geoelectric unit D*: resistive, associated with the presence of gravels or beginning of the altered and fractured rock-masses.

Mechanical properties of intact rock and discontinuities

The rock material collected from the borehole cores has been analyzed by geomechanical laboratory tests in order to define the deformability and strength properties of both intact rock and discontinuities. By consulting the available documentation for the development of the present work, the following mechanical tests were performed over years (Griffini 2004, 2013, 2020, 2021):

- 20 *uniaxial compression tests* conducted in dry conditions on phyllite rock sample, collected from borehole cores material in a depth range from 40 to 190 m depth.
- 11 *triaxial tests* conducted in saturated conditions on phyllite rock sample, collected from borehole cores material in a depth range from 40 to 190 m depth. Lateral confinement σ_3 applied are equal to 3, 5, 7.5 and 14 MPa.
- 11 *Brazilian tests* conducted in dry conditions on phyllite rock sample, collected from borehole cores material in a depth range from 40 to 100 m depth.
- *5 sonic tests* conducted in dry conditions on phyllite rock sample, collected from borehole cores material in a depth range from 40 to 100 m depth.
- 3 *direct shear tests* (9 samples) conducted on random discontinuities taken at depths of 30, 60, and 90 m from 2004 borehole cores to which normal loads of 2, 4, 6 MPa were applied.
- 2 *direct shear tests* (8 samples) conducted on random discontinuities taken at depths of 160 and 186 m from 2013 borehole cores to which normal loads of 2, 4, 7, 10 MPa were applied.

Phyllites rock strength derived from mechanical testing are summarized in Figure 5.8 and Table 5.3. Phyllites shows very low uniaxial compressive strength with mean values of 40.9 ± 16.0 MPa, and minimum values even less than 20 MPa. Only for confinement of 14 MPa in a triaxial cell, mean strength values of 127 ± 41 MPa were detected.

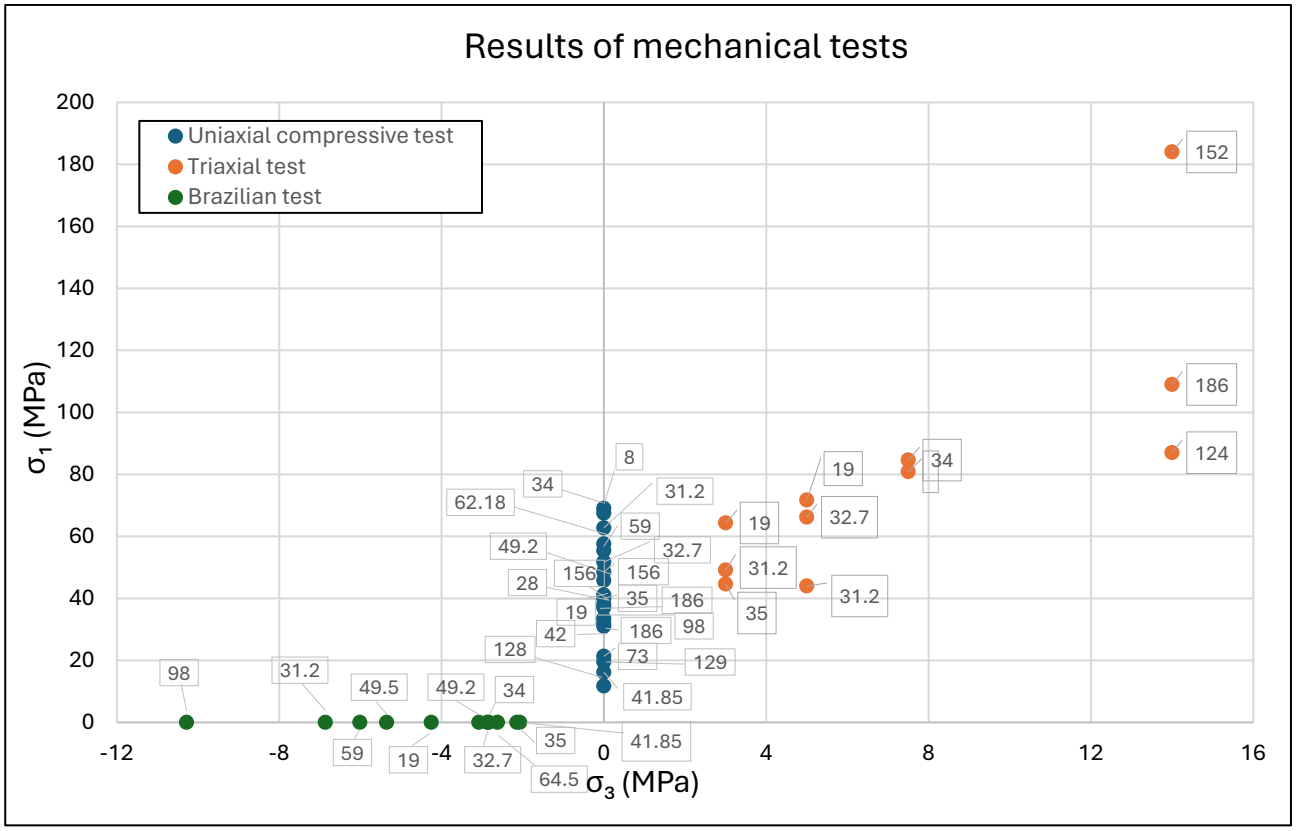

Figure 5.8 - Geomechanical test results: principal stresses at failure. In light blue uniaxial compressive strength; in orange triaxial strength; in gray tensile strength. Label numbers indicate the depth of sampling in meters.

In Table 5.3, the average values obtained from uniaxial compressive tests, triaxial tests, traction tests and sonic tests on intact phyllite rock samples, are collected.

Table 5.3 – Result of uniaxial compressive tests, triaxial tests, traction tests and sonic tests on intact phylladic rock samples.

Mechanical tests on intact rock samples							
	N° of tests	*Young Modulus [GPa]*	*Shear Modulus [GPa]*	*Poisson modulus [-]*	*Traction strength σ_T [MPa]*	*Compressive strength s_C [MPa]*	*Confinament stress [MPa]*
Uniaxial test	20	34.9 ± 20	-	0.29	-	40.9 ± 16	0
Triaxial test	3	24.3 ± 7.9	-	0.22 ± 0.05	-	52.7 ± 8.4	3
	3	37.8 ± 5.9	-	0.25 ± 0.10	-	60.6 ± 12.0	5
	2	35.4 ± 1.5	-	0.27 ± 0.01	-	82.7 ± 1.8	7.5
	3	43.0 ± 4.5	-	0.30 ± 0.13	-	127.0 ± 41.0	14
Brazialian test	11	-	-	-	5.1 ± 2.5	-	0
Laboratory sonic test	4	30.9 ± 12.4	11.8 ± 5.0	-	-	-	0

In addition, five direct shear tests on natural joints sampled at depths of 30, 60, 90 m from 2004 boreholes (nine discontinuities) and at depths of 160 and 186 m from 2013 boreholes (eight discontinuities) were performed. To obtain the failure envelopes according to a Mohr-Coulomb criterion, the discontinuities coming from the 2004 boreholes were subjected to normal loads of 2, 4, and 6 MPa; 2013 discontinuities were subjected to normal loads of 2, 4, 7 and 10 MPa. Since the joints were collected from borehole material, it was not possible to recognize their family (i.e. orientation in the field). Therefore, in order to obtain representative values, the mechanical results were grouped into a single discontinuity class. The average parameters obtained are summarized in Table 5.4.

Table 5.4 - Result of direct shear joint tests.

C_{peak} [MPa]	$C_{residual}$ [MPa]	ϕ_{peak} [°]	$\phi_{residual}$ [°]
0.59 ± 0.25	0	26.84 ± 4.00	16.67 ± 1.80

In general, results showed low strength values, probably due to a high degree of weathering and very low surface roughness, sometimes related to the presence of slippery minerals (e.g., talc, sericite). Moreover, mechanical properties are slightly affected by the depth of sampling and the stress state to which the material is subjected in the field. In fact, especially for the direct joint tests, deeper specimens showed greater stiffness and sharper response to stresses.

5.3.3.2 Integration of previous data

Geomechanical detailed field surveys

To supplement and validate the data presented in the previous Section 5.3.3.1, detailed in-situ geomechanical surveys were carried out in the summer 2022, following the ISRM suggesting methods (ISRM 2015). Geomechanical characterization involved measuring properties of discontinuity sets such as orientation, spacing, weathering degree, joint wall strength, roughness, and aperture. Moreover, to quantify the fracturing intensity of the surveyed outcrops and the mechanical quality of rock-masses, GSI values were estimated and RMR calculated (Figure 5.9).

Four detailed geomechanical investigations have been conducted in the area affected by the Ruinon rockslide and in particular at the "Baite di Confinale" locality, both in rock-masses composed of phyllites and marbles. Additionally, 31 rock-masses were described by the GSI index. The aim was to evaluate the presence of elements ascribable to the gravitational processes affecting the rock slope and to define the fracture network geometry, also finalized to the reconstruction of the water circulation system along the slope.

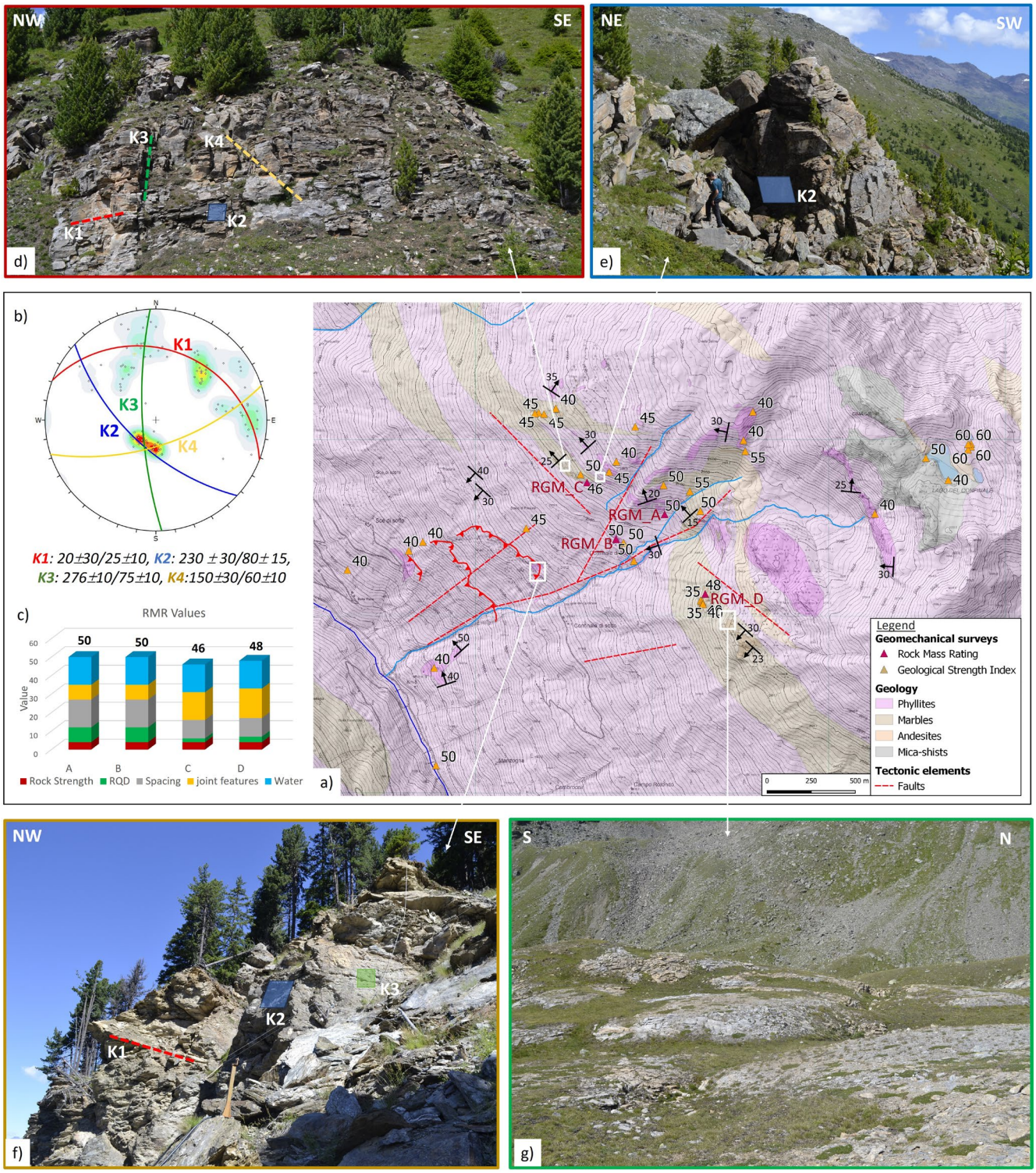

Figure 5.9 – Geomechanical features. a) Map showing the location of the geomechanical surveys performed and the GSI values detected; topographic basis: CTR ed. 2012 scale 1:10,000. b) Stereographic projection of discontinuities (lower hemisphere) measured along the slope. c) Histogram of the RMR components. d) Outcropping rock-mass at the locality of "Bosco delle Presture". The outcrop represents the side of a trench of gravitative origin with structural control. The orientation of the main discontinuity sets is highlighted using different colors. e) Outcropping rock-mass in the locality of "Bosco delle Presture" showing strong evidence of detensioning processes along the discontinuity system k2. f) Outcropping rock-mass at the high niche of the Ruinon rockslide. The high degree of fracturing and mechanical degradation is clearly evident. g) Outcropping marble rock-mass at the "Planon" locality showing geomorphological features of karst processes.

The orientations of the main discontinuity sets were shown to be congruent with the analysis presented in Section 5.3.3. In particular, four discontinuity families were identified (Figure 5.9):

- *K1*: Discontinuities parallel to the foliation planes dipping toward NE with an inclination of 20°, mean JRC equal to 10 and JCS of 60 MPa;
- *K2*: Subvertical tensile-fracture system dipping toward SW, with mean JRC equal to 8 and JCS of 70 MPa;
- *K3*: Subvertical discontinuity system dipping toward NW, with mean JRC equal to 7 and JCS of 85 MPa; it presents clear mechanical shear features;
- *K4*: Subvertical S-ward dipping discontinuity system with mean JRC equal to 8 and JCS of 72 MPa.

Based on the joint mechanical features and the RMR values, the rock-masses appear to belong to a "fair" class of quality (values ranging from 45 to 50; Figure 5.9d). The GSI values assigned, are on average resulting in a "discrete" quality. Analyzing the distribution of the detected GSI values, areas of different mechanical behavior are present. They range from the top of the slope with GSI of 50-60, to the area upstream of the detachment niche with values of 40-50 to the marble outcrops and landslide area with values of 35-40. The intensity of fracturing increases considerably in area affected by slope detensioning and active gravitational processes. As an example, in the “Bosco delle Presture” locality, kilometer-long traction trenches are present, which walls consist of highly fractured rock-masses (GSI of 40-50; Figure 5.9a-b) with metric opening discontinuities parallel to their axis (Figure 5.9 b).
In correspondence of the upper niche of the Ruinon rockslide, the rock-masses are highly fractured with dislocated rock blocks mainly identified by the *K1* and *K2* families. The unitary rock volume decreases significantly to values less than 1 m^3 (Figure 5.9 f).
Marble rock-masses outcropping on the right side of the Confinale creek, look more massive (i.e., less fractured), but with very pronounced features of persistence and opening of discontinuities, due to the development of karst phenomena. Sinkholes, caves and cavities are present, representing key points for rainfall water infiltration (Figure 5.9 g). A predisposition to dislocate block with cubic and tabular geometries, which can evolve into rockfall processes by collapse or toppling, was observed along the entire slope.

Point load laboratory tests

During the execution of the detailed geomechanical surveys rock material including both phyllites and marble lithology was sampled. This material was then subjected to point-load laboratory tests, to verify

and supplement the geomechanical database of material strength values.

Tests were performed on irregular pieces of rock, conforming to ASTM standards (ASTM D5731-08), with the load applied in both parallel and perpendicular directions to the foliation planes. Results are summarized in Table 5.5. It can be observed that the compressive strength evaluated in the loading direction orthogonal to the schistosity, in all samples of both lithologies, is much higher than in the parallel direction (Table 5.5). This behavior may be associated with the lower strength of the schistosity planes, representing planes of material weakness along which failure occurs more easily. This aspect is also clearly visible in the field, where rock blocks are predominantly dislodged along surfaces parallel to the schistosity planes. In general, the material showed typical behavior of weathered rocks, especially at the Ruinon rockslide niche where the material flakes off along the schistosity planes with minimal loading applied.

Table 5.5 - Results of point load tests performed on rock material collected along the slope.

	Point load tests		
Lithology	Load direction respect to foliation planes	N° Samples	σ_c mean (MPa)
Phyllites	⊥	6	55.16 ± 22.90
	//	6	5.02 ± 2.00
Marbles	⊥	6	55.33 ± 23.22
	//	6	18.33 ± 9.00

5.3.4 Hydrogeological features

5.3.4.1 Data available to date

The hydrogeological setting of the slope appears to be complex, characterized by the presence of trenches, sinkholes and karst morphologies upstream of the rockslide body, resulting in very high potential infiltration rates. In addition, the presence of highly fractured rock-masses, gravitational and glacial deposits, with high hydraulic conductivity contrast, could result in complex hydraulic relationships driving groundwater circulation.

Despite the evidence of a potential key role of the hydrogeological component in the mechanical evolution of the Ruinon rockslide (Griffini 2004; Crosta 2013, 2018), there are still no extensive studies on this aspect. In the following paragraphs, data collected by the hydrogeological monitoring system and by in-situ campaign for hydrological characterization of materials will be summarized. In addition, field data collected for the development of this work will be presented in order to provide a deeper

understanding of the hydrogeological setting of the slope. The collected data will be then introduced in the Section 5.6 for the development of a hydrogeological flow simulation model.

Hydrogeological monitoring system

As part of the monitoring network of the Ruinon rockslide, there are 2 piezometers for groundwater level measurement, managed by ARPA Lombardia, and 8 piezometers derived from the equipment of the 2020-2021 investigation boreholes which provide only manual water level readings (Griffini 2020, 2021). A summary table of all piezometers in the Ruinon area is shown in Figure 5.10a with their location on the map (Figure 5.10). All piezometers are permeable along the entire drilling depth. Exception is piezometer S8 (drilling depth 80 m - Figure 5.10), whose filter packs are located between 30 and 80 meters depth.

The ARPA piezometers have the following features:

- *PZ4*: automatic piezometer measuring groundwater level with a frequency of 30 minutes. Due to the amount and continuity of data available, even if located out of the body rockslide, it is the most significant for deciphering ground water fluctuation.
- *PZ2-2005*: manual piezometer; it has been out of service from 2020 due to an obstruction of the borehole, probably due to movement involving the subsurface.
- *PZ3-2015*: Manual piezometer out of service; no data are available for this piezometer.

The recorded piezometric level by PZ4 shows a strong seasonal fluctuation, with maximum values (i.e., water table close to the topographic surface) between May and June and minimum values in the winter period (Figure 5.10b). In winter 2019, this evolutionary trend was interrupted by the construction of hydraulic engineering regulation works for the Confinale creek, upstream of the piezometers' location (Merizzi 2015). The reduction of this water supply element, in conjunction with a dry period, resulted in the decrease of the groundwater level, with a complete drying of the piezometer.

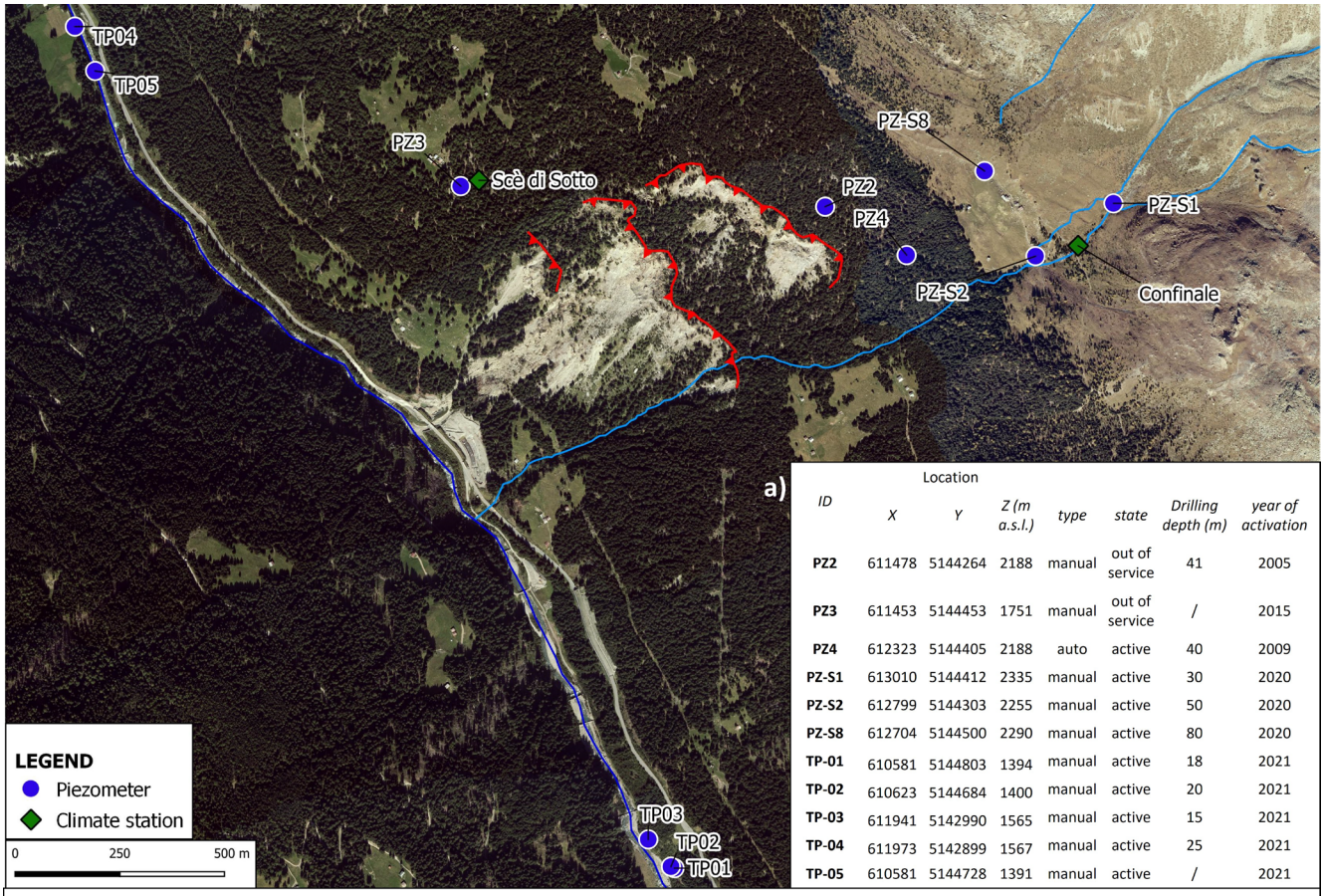

a)

ID	Location X	Location Y	Z (m a.s.l.)	type	state	Drilling depth (m)	year of activation
PZ2	611478	5144264	2188	manual	out of service	41	2005
PZ3	611453	5144453	1751	manual	out of service	/	2015
PZ4	612323	5144405	2188	auto	active	40	2009
PZ-S1	613010	5144412	2335	manual	active	30	2020
PZ-S2	612799	5144303	2255	manual	active	50	2020
PZ-S8	612704	5144500	2290	manual	active	80	2020
TP-01	610581	5144803	1394	manual	active	18	2021
TP-02	610623	5144684	1400	manual	active	20	2021
TP-03	611941	5142990	1565	manual	active	15	2021
TP-04	611973	5142899	1567	manual	active	25	2021
TP-05	610581	5144728	1391	manual	active	/	2021

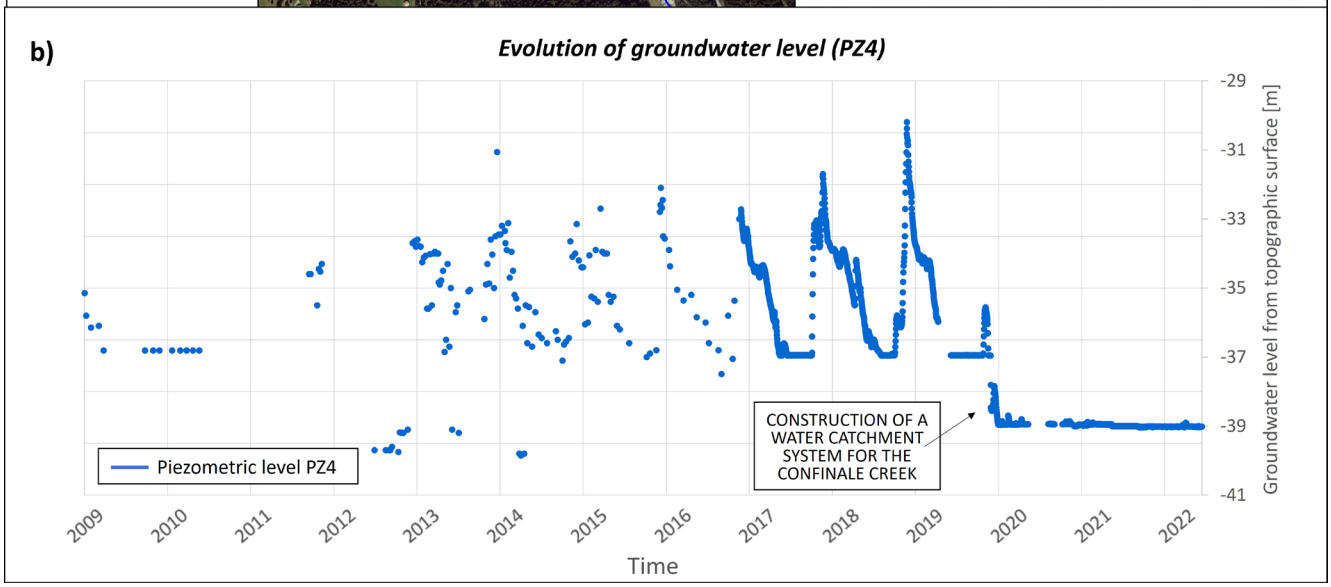

Figure 5.10 - Location of piezometers along the slope. a) summary table of all piezometers. b) graph showing the trend of piezometric level recorded by PZ4 and rainfall input measured at the Confinale climate station.

Borehole hydrogeological tests

Hydrogeological characterization tests, aimed at defining the hydraulic conductivity and transmissivity parameters (Griffini 2013, 2020, 2021) of the material constituting the slope, were carried out during the 2013 and 2020 drilling campaign. A total of 17 tests were performed, including four Lugeon tests

(Lancaster-Jones 1975) in bedrock and 13 Lefranc tests (Lefranc 1936, 1937) performed in both fractured rock-masses and loose deposits (Table 5.6). Both tests were performed following the AGI Recommendations for Geotechnical Investigations (AGI 1977). The values obtained, shown in the Table 5.6, range from 10^{-4} to 10^{-9} m/s for hydraulic conductivity (k) and from 10^{-3} to 10^{-8} m^2/s for hydraulic transmissivity (Ts). The results show that locally the rock bedrock is in a highly fractured condition and presents hydraulic conductivity values similar to those obtained for the loose deposit. This can create complex groundwater circulation dynamics, that are driven by the presence of these extremely fractured rock bodies with very high hydraulic conductivity values.

Table 5.6 - List of Lugeon and Lefranc tests performed in boreholes drilled along the slope. For the location of the boreholes, please refer to the Table 5.2 and Figure 5.4.

Hydrogeological in-situ tests							
ID Test	**Borehole**	**Type**	**Depth (m)**	**Material**	**U.L.**	**k (m/s)**	**Ts (m^2/s)**
SP08_LU01	SP_08 (2013)	Lugeon	151.3	Bedrock	2.25	$6.07 \cdot 10^{-7}$	$9.28 \cdot 10^{-6}$
SP09_LU01	SP_09 (2013)	Lugeon	153.6	Bedrock	-	$1.27 \cdot 10^{-8}$	$2.90 \cdot 10^{-7}$
SP09_LU02	SP_09 (2013)	Lugeon	157.3	Bedrock	-	$2.55 \cdot 10^{-9}$	$5.82 \cdot 10^{-8}$
SP09_LU03	SP_09 (2013)	Lugeon	164.5	Bedrock	0.75	$4.85 \cdot 10^{-8}$	$1.11 \cdot 10^{-6}$
S1_K1	S1 (2020)	Lefranc	1.4	Deposit		$9.80 \cdot 10^{-4}$	$9.80 \cdot 10^{-4}$
S2_K1	S2 (2020)	Lefranc	5.5	Bedrock		$3.20 \cdot 10^{-5}$	$3.14 \cdot 10^{-4}$
S3_K1	S3 (2020)	Lefranc	15.8	Deposit		$1.10 \cdot 10^{-5}$	$1.95 \cdot 10^{-4}$
S4_K1	S4 (2020)	Lefranc	15.8	Bedrock		$9.40 \cdot 10^{-6}$	$1.69 \cdot 10^{-4}$
S4_K2	S4 (2020)	Lefranc	25.8	Bedrock		$4.90 \cdot 10^{-6}$	$8.82 \cdot 10^{-5}$
S5_K1	S5 (2020)	Lefranc	9.8	Deposit		$1.50 \cdot 10^{-6}$	$1.13 \cdot 10^{-5}$
S5_K2	S5 (2020)	Lefranc	17.3	Deposit		$1.00 \cdot 10^{-6}$	$4.50 \cdot 10^{-6}$
S6_K1	S6 (2019)	Lefranc	8.4	Deposit		$1.68 \cdot 10^{-4}$	$3.36 \cdot 10^{-4}$
S6_K2	S6 (2020)	Lefranc	11.4	Deposit		$1.85 \cdot 10^{-4}$	$9.08 \cdot 10^{-4}$
S6_K3	S6 (2020)	Lefranc	14.9	Deposit		$1.71 \cdot 10^{-4}$	$6.00 \cdot 10^{-4}$
S7_K1	S7 (2020)	Lefranc	5.3	Deposit		$2.80 \cdot 10^{-4}$	$1.54 \cdot 10^{-3}$
S8_K1	S8 (2020)	Lefranc	10.5	Deposit		$4.30 \cdot 10^{-7}$	$1.08 \cdot 10^{-6}$
S8_K2	S8 (2020)	Lefranc	14.3	Deposit		$5.70 \cdot 10^{-7}$	$3.42 \cdot 10^{-6}$

5.3.4.2 Integration of existing data

Hydrogeological field tests: defining the hydraulic properties of materials

During the 2022 personal fieldwork, several hydraulic in-situ tests were conducted to characterize the deposits outcropping. Moreover, loose deposit samples were collected at different points, involving both

gravitational and glacial material. This Section will summarize seven infiltrometer tests conducted with a double-ring infiltrometer (ASTM D 3385) and four sand cone tests conducted with a sand volumeter (ASTM D 1556); in addition to them, five laboratory soil grain-size analyses were performed (ASTM D 6913-04) on soil samples derived from the sand cone test and along the rockslide body (Figure 5.11). Infiltrometer tests were carried out in correspondence of hydrological significant points with the aim of define the hydraulic conductivity of the deposits and explore their effective capacity to absorb water into the substrate: specifically, tests *INF1*, *INF2*, *INF3*, *INF4* and *INF6* were carried out in areas characterized by the presence of trenches and sinkholes, test *INF5* was carried out in correspondence of a peatland area, while test *INF7* is located on the hydrographic left of the Confinale creek, SE of the Ruinon rockslide (Figure 5.11).

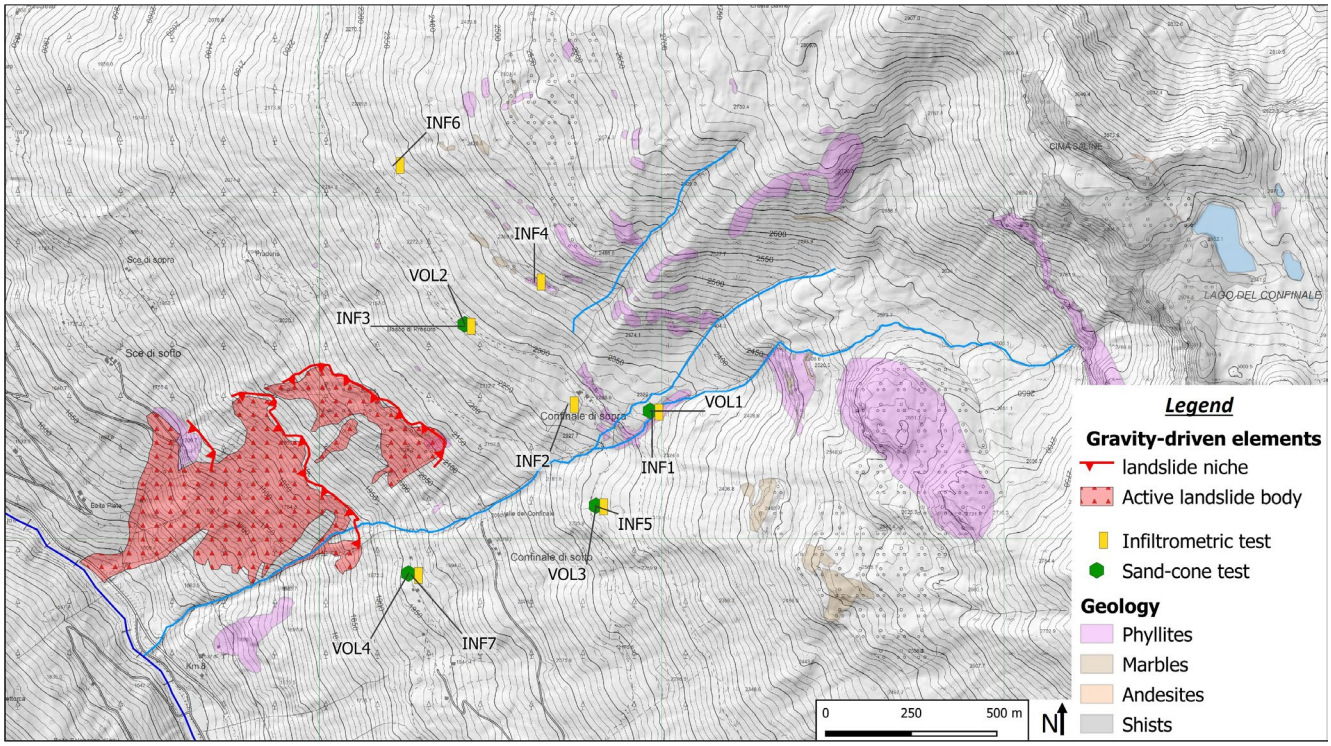

Figure 5.11 – Location of infiltrometer and sand cone tests; topographic basis: CTR ed. 2012 scale 1:10,000.

The following table summarizes the results of the analyses performed (Table 5.7). It is particularly evident that the highest hydraulic conductivity values ($2.3 \cdot 10^{-4}$ m/s, i.e., high infiltration capacity) are detected in correspondence of morphological structures related to gravitational release processes (Figure 5.11). This would seem to be related to the nature of the infilling deposits of these morpho-structures, predominantly represented by gravel with sand. The lowest hydraulic conductivity values ($3.5 \cdot 10^{7}$ m/s, i.e., low infiltration capacity) are detected along the morphological plateaus upstream of the "Baite di

Confinale" locality (Figure 5.11), where glacial deposits (silt with sand) are present. This aspect implies a significant control in the hydrogeological setting by the nature of the deposits present.

Table 5.7 - Infiltrometer tests conducted along the slope. Please refer to Figure 5.11 for their location.

Double ring infiltrometer test				
ID	X (UTM)	Y (UTM)	Water inflow rate (m^3/s)	k (m/s)
INF1	612969	5144377	$4.78 \cdot 10^{-8}$	$3.5 \cdot 10^{-7}$
INF2	612716	5144396	$1.40 \cdot 10^{-7}$	$1.2 \cdot 10^{-6}$
INF3	612424	5144631	$6.90 \cdot 10^{-7}$	$5.1 \cdot 10^{-6}$
INF4	612629	5144745	$4.24 \cdot 10^{-7}$	$3.1 \cdot 10^{-6}$
INF5	612803	5144099	$1.46 \cdot 10^{-7}$	$1.1 \cdot 10^{-6}$
INF6	612215	5145092	$3.19 \cdot 10^{-5}$	$2.3 \cdot 10^{-4}$
INF7	612262	5143899	$6.00 \cdot 10^{-5}$	$3.5 \cdot 10^{-5}$

Sand cone tests were performed in order to define the natural volume weight of the soil near gravitational traction structures (*VOL1* and *VOL2*), peatland zone (*VOL3*), and at Confinale di Sotto locality (*VOL4*) (Figure 5.11). In addition to the determination of dry weight (ϒ) values (Table 5.8), the sampled material was subjected to sieving and aerometric sedimentation for the determination of the particle size curve according to recommendations (ASTM D6913-04). Results of the granulometric analysis, implemented by means of appropriate logarithmic diagrams to obtain the grain size curves, allowed to classify the material according to A.G.I. (Italian Geotechnical Association; AGI 1977) description (Table 5.8).

Table 5.8 - Density analysis of soils with sand cone method. Please refer to Figure 5.11 for their location.

Site	**Coordinates (UTM)**		**Soil weight (kN/m³)**		**Soil size analysis**	
ID	X	Y	Υ_{dry}	Υ_0	AGI Classification	USCS
VOL1	612961	5144385	11.57	13.82	Gravelly silt, sand and clay in trace	GM
VOL2	612436	5144614	13.75	15.34	Pebbly and silty weakly sandy gravel	GP
VOL3	612808	5144097	17.03	17.38	Sandy and silty gravel	GM
VOL4	612260	5143899	16.41	18.35	Pebbly and silty gravel and sand	GM
GR_FRANA	611529	5143958	-	-	Sandy gravel and silt in trace	GM

Hydrogeological surveys: water spring distribution and monitoring

Among the activities carried out during the 2022 survey campaign, water spring mapping work was also performed, thus complementing and updating previous studies aimed to obtain a complete hydrogeological database, useful for modeling purposes. A total number of 68 springs were mapped around the Ruinon rockslide active body (Figure 5.12).

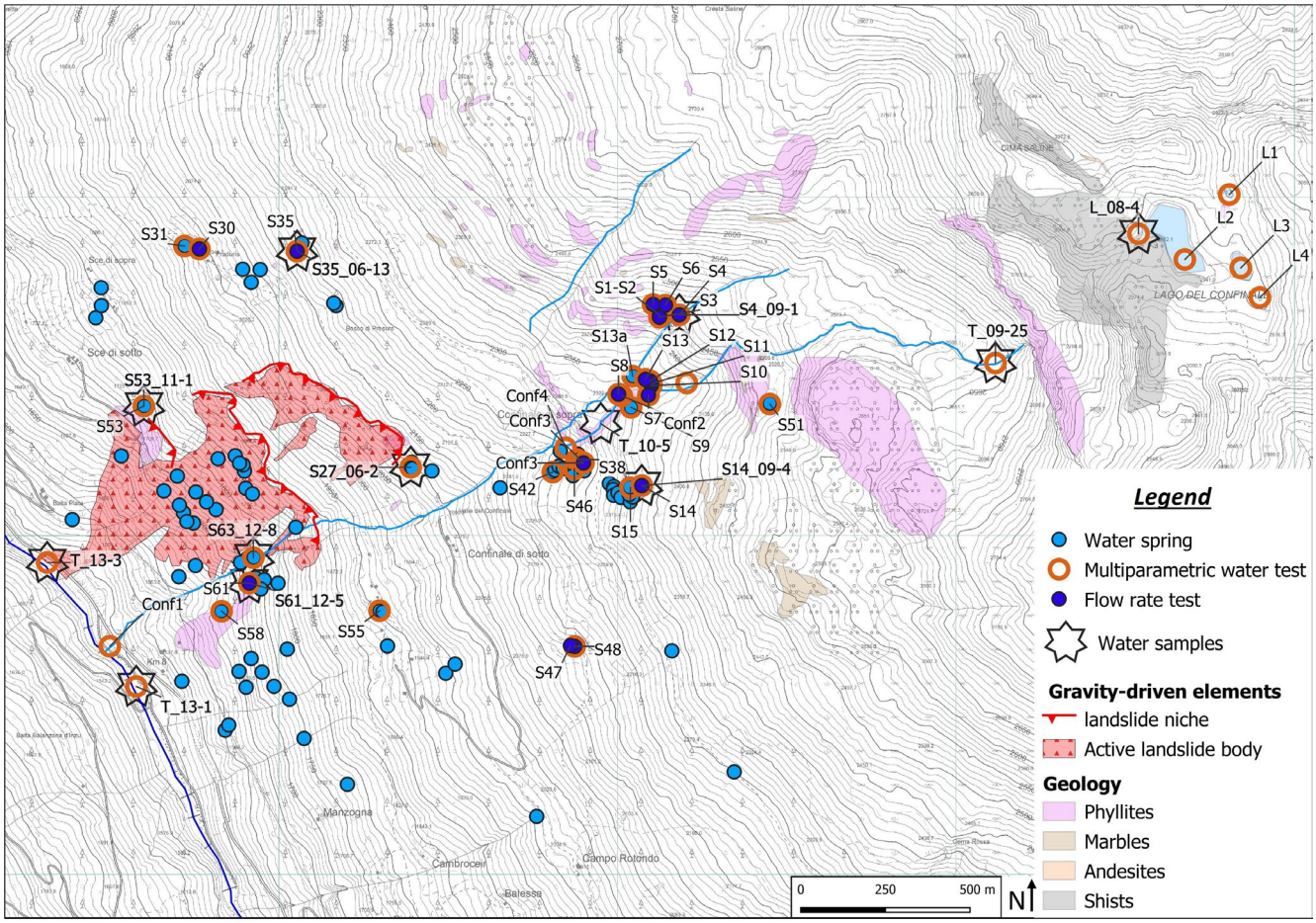

Figure 5.12 - Distribution of water springs and sampling points; topographic basis: CTR ed. 2012 scale 1:10,000.

Where possible, water flow rate was measured using simple field equipment Table 5.9. Water flow measurement was impossible in cases of low rates, presence of hydraulic engineering works or in correspondence of springs with unconcentrated flow (i.e., dispersed). As shown in the Figure 5.12, the water springs are concentrated in the lower part of the slope, along the axis of the Confinale creek and in the glacial plateaus at the "Baite di Confinale" locality. The portion of the slope upstream of the rockslide body appears dry with no water springs, probably due to the high infiltration capacity of these areas and to the presence of trenches and sinkholes. The occurrence of the majority of springs detected, have been identified as "permeability contrasts" especially in correspondence of rock glacier bodies, fluvioglacial deposit, and marbles-phyllites lithological contacts. Moreover, the alignment of water springs located at the bottom of the slope, could be ascribed to the contact between slope gravitational deposit and the historical landslides bodies, which, as such, appears to be more pedogenic. Where water flow was sufficient to perform in situ measurements, several hydro-chemical tests were performed measuring pH, Total Dissolved Solids (TDS), electrolytic conductivity (Cond.) and Temperature (T) with a multiparametric probe on both water springs, Confinale creek and lake (Table 5.9).

Table 5.9 - Water flow, chemical and physical properties measured at some springs and ampling points of the Confinale creek and lake. Blue color highlights waters with a TDS<100 mg/l, orange color waters with 100 mg/l < TDS < 170 mg/l and green color waters with TDS >170 mg/l.

ID	Coordinates (UTM)		Water flow	Chemical and physical properties				
	X	Y	(l/s)	TDS (mg/l)	Cond. (µS/cm)	A (TDS/Cond.)	pH	T (°C)
S1	613124	5144653	0.30	130	280	0.5	6.5	4.9
S2	613124	5144653	0.01	120	260	0.5	6.8	5.5
S3	613124	5144645	0.87	130	280	0.5	6.6	5.0
S4	613182	5144653	4.80	130	270	0.5	6.9	4.5
S5	613105	5144683	0.65	130	280	0.5	6.8	4.5
S6	613143	5144681	0.16	130	280	0.5	6.7	4.6
S7	613091	5144416	1.50	140	300	0.5	6.2	3.7
S8	613003	5144419	0.01	110	240	0.5	5.8	7.3
S10	613099	5144445	0.02	100	210	0.5	6.0	6.3
S11	613100	5144450	0.02	120	260	0.5	6.5	5.8
S12	613098	5144457	0.04	120	250	0.5	6.6	4.6
S13	613083	5144463	0.32	120	260	0.5	6.5	5.1
S14	613072	5144147	0.83	180	390	0.5	6.8	3.5
S18	613044	5144114	0.01	180	370	0.5	5.6	3.6
S22	612989	5144120	0.01	/	/	/	/	/
S27	612389	5144202	0.01	120	260	0.5	7.1	8.4
S28	612392	5144217	0.03	/	/	/	/	/
S30	611763	5144849	0.05	130	280	0.5	6.6	4.2
S31	611722	5144856	0.04	120	260	0.5	6.2	5.3
S35	612048	5144841	0.14	180	370	0.5	6.8	6.1
S38	612878	5144225	0.08	200	410	0.5	6.7	6.8
S40	612901	5144192	0.08	/	/	/	/	/
S41	612869	5144178	0.50	/	/	/	/	/
S42	612807	5144188	0.07	180	380	0.5	6.7	7.3
S46	612872	5144198	0.01	190	410	0.5	6.2	6.4
S47	612862	5143676	0.03	/	/	/	/	/
S48	612873	5143675	0.02	90	190	0.5	6.6	7.5
S53	611602	5144383	0.01	280	570	0.5	5.8	9.9
S54	611484	5144451	0.01	130	270	0.5	6.6	16.0
S58	611830	5143777	0.09	140	290	0.5	6.0	11.1
S59	611907	5143869	0.20	/	/	/	/	/
S61	611913	5143860	0.23	130	250	0.5	5.6	6.0
S62	611908	5143934	0.24	130	270	0.5	5.9	9.5
S65	611930	5143876	0.30	/	/	/	/	/
S66	611956	5143870	0.25	/	/	/	/	/
Conf1	611498	5143656	/	130	280	0.5	5.8	9.5
Conf2	613017	5144409	/	180	380	0.5	5.8	7.3
Conf3	612848	5144259	/	120	250	0.5	6.0	5.5
Conf4	612900	5144215	/	190	400	0.5	6.0	7.0
T_09-25	614129	5144511	/	150	310	0.5	7.0	11.0
T_13-1	611567	5143540	/	150	330	0.5	6.2	8.7
T_13-3	611323	5143920	/	160	340	0.5	6.0	8.4
L1	614810	5145006	/	< 5	< 10		5.7	3.9
L_08-4	614538	5144894	/	50	120	0.4	6.3	7.7
L2	614678	5144811	/	50	130	0.4	7.3	8.0
L3	614842	5144785	/	60	150	0.4	6.0	9.5
L4	614899	5144704	/	80	180	0.4	5.5	5.6

Three different water-chemical classes were detected based on the collected data. Category 1 (TDS < 100 mg/l – blue color in Table 5.9) collects water samples analyzed at the highest elevations. Low concentration of dissolved solids is due to the presence of nivo-glacial melt waters, and spring waters located at high altitudes, whose flow in the substrate was not long enough to enrich their content in dissolved substances, considering the siliceous nature of the rocks. Category 2 (100 mg/l < TDS < 170 mg/l – orange color in Table 5.9) is the most prevalent category, with average values attributable to the flow in a bedrock consisting mainly of phyllodes and phylladic micaschists. Category 3 (TDS >170 mg/l – green color in Table 5.9) collects water flowing in carbonate formations such as marbles. During the in-situ surveys, 12 water samples (Table 5.9) were also collected and used for isotopic and hydro-chemical laboratory analyses, which will be presented in the next Section.

In previous studies (Griffini 2021) a larger number of water springs had been detected in the same area. The reduction of water emergencies could be due to the seasonal flow regime and to a below-average rainfall in the year 2022 (Section 5.3.5). In addition, the placement of hydraulic engineering works along the Confinale creek could have affected the groundwater flow, resulting in a gradual drying of springs located along the river axis, downstream of the hydraulic engineering system, as it was also reported by the ARPA technicians employed in monitoring. Of particular significance is the drying of numerous springs arranged on the rockslide body according to two main lineaments between 1750 and 1850 m a.s.l.

Laboratory tests for chemical characterization of water

Water samples collected (Figure 5.12) were analyzed for cation and anion content and isotopic determination. Ionic analyses were performed at the “Waters and Fluids Geochemistry Laboratory” of the Department of Earth Sciences “Ardito Desio” of the University of Milan, using a Dionex ICS900 ion chromatograph (Thermo Fisher Scientific Inc.), connected to an AS-DV autosampler for cation (IonPac CS12A+CCRS500) and anion (IonPac AS9-HC+MMS300) analysis. This instrumentation is a precise and sensitive method for determining the presence of heavy metal ions, alkali metal ions, and other chemicals in a water sample. Specifically, the concentrations of lithium, sodium, potassium, magnesium and calcium (cations), fluorides, chlorides, nitrites, nitrates and sulfates (anions) were determined. Below are tables containing the results of cation (Table 5.10) and anion (Table 5.11) analyses.

Table 5.10 – Cation contents of different water samples. Please refer to Figure 5.12 for their location.

Cations (mg/l)					
ID	**Lithium (Li)**	**Sodium (Na)**	**Potassium (K)**	**Magnesium (Mg)**	**Calcium (Ca)**
T_13-1	0.008	2.56	1.00	16.62	41.51
T_13-3	0.008	2.73	1.09	16.56	43.09
S27_06-2	0.005	1.15	0.25	7.44	45.36
S63_12-8	0.005	3.14	0.46	10.06	52.01
T_09-25	0.006	2.24	0.53	13.32	45.55
L_08-4	0.005	0.51	0.33	8.05	13.03
T_10-5	0.005	2.02	0.36	8.26	44.43
S4_09-1	0.005	1.28	0.38	9.37	42.34
S14_09-4	0.006	1.17	0.40	9.69	66.08
S35_06-13	0.007	1.79	0.78	16.42	54.46
S53_11-1	0.015	4.48	2.70	32.01	69.41
S61_12-5	0.006	1.28	0.43	9.06	47.05

Table 5.11 - Anion contents of different water samples. Please refer to Figure 5.12 for their location.

Anions (mg/l)							
ID	**Florides (F)**	**Chlorides (Cl)**	**Nitrites (NO_2)**	**Nitrates (NO_3)**	**Sulfates (SO_4)**	**Bicarbonate (HCO_3)**	**Carbonate (CO_3)**
T_13-1	0.19	0.74	0.26	0.79	123.94	58.36	0.0003
T_13-3	0.20	0.90	0.20	0.97	127.99	58.05	0.0003
S27_06-2	0.15	0.46	0.23	0.53	67.02	92.10	0.0003
S63_12-8	0.15	0.42	0.25	0.87	114.94	70.14	0.0003
T_09-25	0.16	0.45	0.21	0.74	129.58	45.94	0.0003
L_08-4	0.15	0.39	0.18	0.55	30.25	42.00	0.0003
T_10-5	0.14	0.43	0.27	0.80	112.55	37.94	0.0003
S4_09-1	0.15	0.41	0.21	1.04	117.16	29.39	0.0003
S14_09-4	0.17	0.43	0.29	0.76	132.91	82.87	0.0003
S35_06-13	0.18	0.42	0.46	0.29	52.06	186.19	0.0003
S53_11-1	0.19	0.71	0.62		113.81	241.07	0.0003
S61_12-5	0.15	0.41	0.24	0.83	108.44	53.36	0.0003

The results of ion chromatography analysis were entered into Piper's classification (Piper 1944) and Schoeller's diagrams (Schoeller 1962) in order to identify the geochemical category to which the analyzed waters belong. The Piper Diagram (Figure 5.13a) allowed to determine a good homogeneity in the cation content of the samples, which mostly fall into the "Calcium - Magnesium - Chlorine – Sulfate" typology. Samples "*S27_06-2*", "*L_08-4*", "*S35_06-13*" and "*S53_11-1*" belong to the "Calcium - Magnesium – Bicarbonate" typology, due to a sulfate depletion and bicarbonate enrichment.

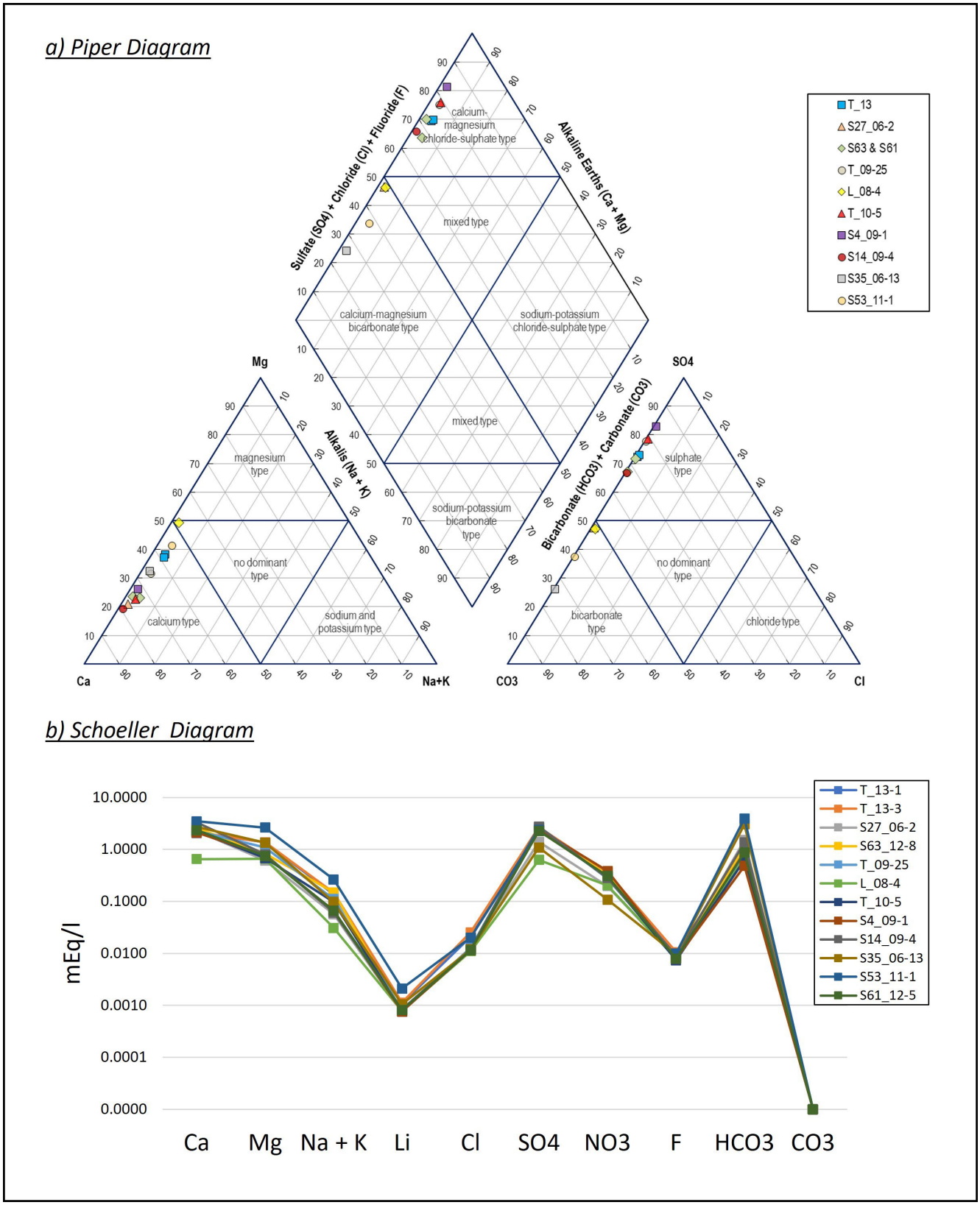

Figure 5.13 – a) Piper diagram and b) Sholler diagram for the geochemical classification of water samples.

Almost all of the samples belong to the cationic group "Calcium" thus showing enrichment in Ca and Mg compared to Na to K, with preference for Ca over Mg. The only exception is the sample from the Confinale lake (*L_08-4*) in which no specific dominance was found. The extent of relative Ca enrichment of the samples appears to be a good discriminator in the series, with sample S14_09-4 finding the highest value.

The Schoeller diagram (Figure 5.13b) allows the hydro-chemical characterization of waters through a correlation between the concentrations of the fundamental constituents (Ca, Mg, Na + K, Cl, SO_4, NO_3, and F), also allowing to distinguish between waters with weak or intense mineralization. The concentration of the major ions, plotted on Schoeller diagram (Figure 5.13b), shows that all the sampled waters belong to a single family characterized by relative depletion in lithium, chlorides and fluorides. The sample of the Confinale lake (*L_08-4*) manifests the generally most depleted values, while sample *S53_11-1* the most enriched. Overall, the waters can be described as weakly mineralized.

In addition to ion analysis, isotopic analyses were performed using a mass spectrometer and are aimed at determining the relative abundances of stable isotopes:

- 18/16 of oxygen (^{18}O, ^{16}O);
- Deuterium (^{2}H);
- 13/12 of carbon (13C, 12C).

Specifically, a photon ionization mass spectrometer (PI-MS) model Varian MAT 250 was used with the application of WS-CRDS (Wavelength-Scanned Cavity Ring-Down Spectroscopy) technology for the analysis of ^{18}O and ^{2}H. Analyses were performed by the Spin-off "ISO4" of the University of Turin. The table in Figure 5.14 summarize the results of the analyses.

Typically, $\delta^{18}O$ and $\delta^{2}H$ values vary depending on the water source and on the geological processes that affected it (Siegenthaler and Oeschger 1980; Perini et al. 2009; Masiol et al. 2021). The isotopic composition of rainfall is subject to some significant spatial and temporal effects, both at the global or local scales. The most common are: the latitude effect, the seasonal effect, the continental effect, the quantity effect, the rainout effect and the altitude effect (Masiol et al. 2021). These geographical and climatic effects do not act separately but concur simultaneously, and with different weights, in determining the isotopic composition of rainfall in the area.

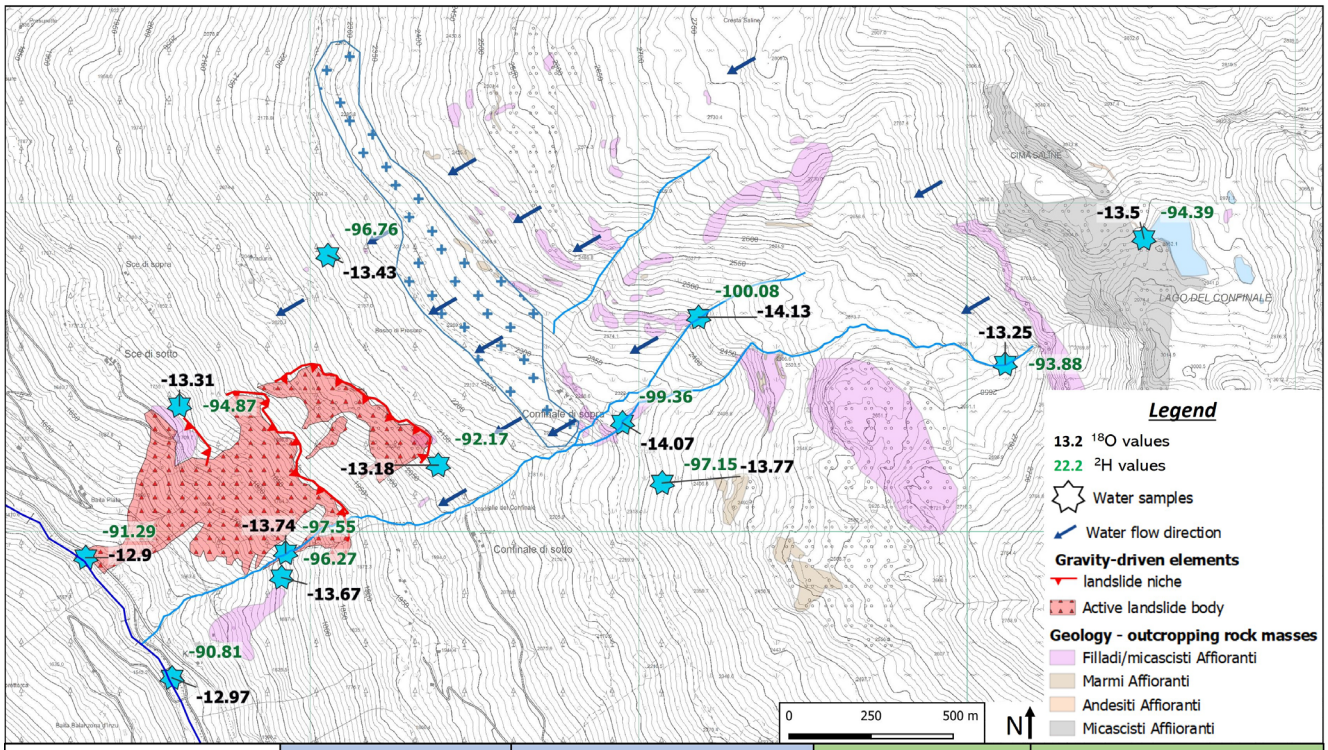

ID	1000 x δ ^{18}O vs V-SMOW2	measurement unc. (δ‰)	1000 x δ ^{2}H vs V-SMOW2	measurement unc. (δ‰)
S27_06-2	-13.18	± 0.2	-92.17	± 1
S35_06-13	-13.43	± 0.2	-96.76	± 1
L_08-4	-13.5	± 0.2	-94.39	± 1
S4_09-1	-14.13	± 0.2	-100.08	± 1
S14_09-4	-13.77	± 0.2	-97.15	± 1
T_09-25	-13.25	± 0.2	-93.88	± 1
T_10-5	-14.07	± 0.2	-99.36	± 1
S53_11-1	-13.31	± 0.2	-94.87	± 1
S61_12-5	-13.67	± 0.2	-96.27	± 1
S63_12-8	-13.74	± 0.2	-97.55	± 1
T_13-1	-12.97	± 0.2	-90.81	± 1
T_13-3	-12.9	± 0.2	-91.29	± 1

Figure 5.14 - Results of isotopic analyses. Concentration values of ^{18}O and ^{2}H are shown. Topographic basis: CTR ed. 2012 scale 1:10,000.

Overall, the isotopic values recorded in the study area are found to be consistent with the geographical and climatic characteristics of the central Italian Alps, showing on average values of -13.5 ‰ ^{18}O and -95.4 ‰ ^{2}H. The correlation of the isotopic ratios of O and H of the analyzed samples manifests a linear behavior that can be accumulated to that of the Global Meteoric Water Line (GMWL) but with a slight enrichment in δ‰ ^{2}H (Figure 5.15a).

To define the groundwater flow of the Ruinon slope, the altitude and seasonal effects were analyzed in detail. In order to assess the magnitude of the altitude effect, the variation of δ^{18}O‰ values were correlated with the change in elevation (m a.s.l.) of the collected samples (Figure 5.15b), thus obtaining a vertical isotopic gradient of -0.04‰/100 m.

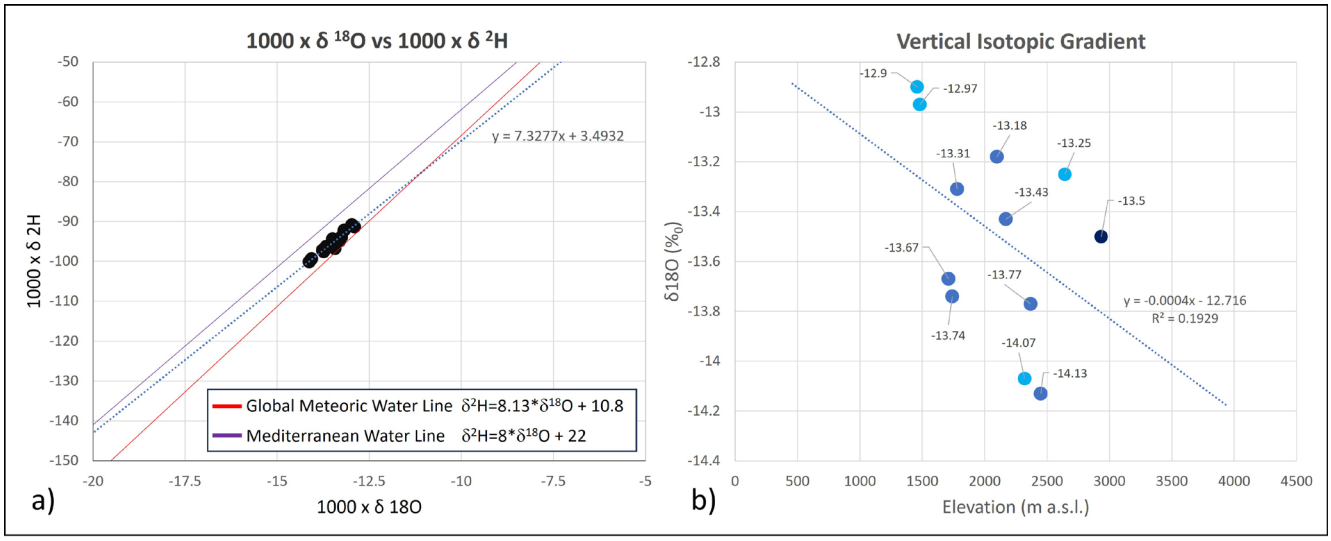

Figure 5.15 – a) Correlation of the isotopic ratios of O and H of the analyzed samples compared to the reference lines. b) Vertical isotopic gradient of $\delta^{18}O‰$.

Comparing the gradient obtained with the values determined for the neighboring Chiavenna Valley (Pinarelli et al. 2014), which are found to range between -0.15/-0.23 ‰/100 m, it can be noticed that the latter are an order of magnitude higher. This discrepancy is probably due to the small size of the population investigated in this work, the limited elevation gain and the difference in the residence times of the sampled waters in the substrate (influence of the seasonal effect). Overall, it is deemed reasonable to consider the effect of altitude, but, since the gradient is not very pronounced, it is only accounted for major elevation changes; its influence is therefore to be considered subordinate to the seasonal effect.

In addition to defining the concentration of stable isotopes of oxygen and hydrogen, the amount of carbon isotopes was also detected. The sample were defined according to the protocols presented in McCrea 1950. Below is a figure presenting the results of the analysis (Figure 5.16).

The isotopic record of carbon is related to the environmental carbon cycle; the various reservoirs of carbon on Earth (biota, CO_2 in the atmosphere, CO_2 in the oceans, etc.) are characterized by different $\delta^{13}C$, capacities, and flux rates. Carbon is continuously exchanged between these reservoirs, which constantly rebalance each other, effectively promoting fractionation that selectively concentrates different amounts of ^{13}C and ^{12}C. In order to investigate the study area results will be analyzed in order to distinguish organic carbon (derived from living organisms) and inorganic carbon (derived from the dissolution of rocks and minerals).

Calcium carbonate is composed of ^{12}C and ^{13}C in different proportions depending on its geologic history. The mineral composition of rock-masses is therefore very important because it will determine the ratio of these isotopes in the released calcium bicarbonate. Considering that rock-masses in the study area

belong to the Austroalpine Domain, it is consistent to assume that outcropping marbles are of continental origin and that their interaction with water leads to positive values of δ 13C.

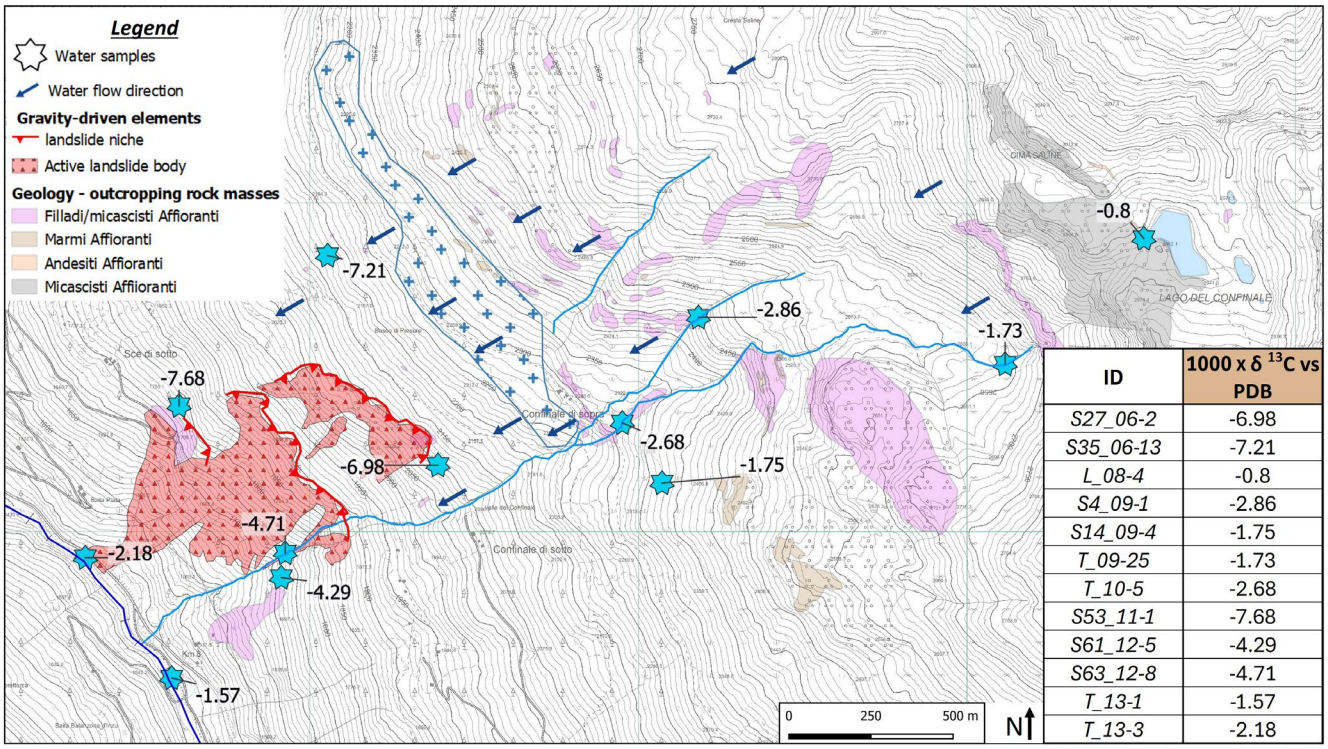

ID	1000 x δ ^{13}C vs PDB
S27_06-2	-6.98
S35_06-13	-7.21
L_08-4	-0.8
S4_09-1	-2.86
S14_09-4	-1.75
T_09-25	-1.73
T_10-5	-2.68
S53_11-1	-7.68
S61_12-5	-4.29
S63_12-8	-4.71
T_13-1	-1.57
T_13-3	-2.18

Figure 5.16 – Results of isotopic analyses. Concentration values of ^{13}C are shown. Topographic basis: CTR ed. 2012 scale 1:10,000.

By relating the values of 1000xδ^{13}C with those of bicarbonate (mg/l) calculated earlier (Table 5.11), a linear correlation is obtained. Samples "*S27_06-2*", "*35_06-13*" and "*S53_11-1*" show higher absolute amounts but without deviating from the $HCO_3/\delta^{13}C$ ratio characteristic of the investigated population. The sample that deviates most from the linear trend is sample "*S27_06-2*", which shows a relatively more pronounced δ^{13}C negativization.

Based on the hydro-chemical and isotopic data obtained, it was possible to observe that the waters of the Confinale lake are mainly derived from snow melting, due to the high negative values (-15‰ ^{18}O / -100‰ ^{2}H). The δ^{13}C content is close to 0‰ and reflects a paucity of bacterial activity consistent with the altitude and genesis of this Alpine lake. The ionic content is also very low, ascribing to the category 1 of TDS-C (Table 5.9).

Moving to lower elevations, the water of the Confinale creek (*T_09-25*) tend to take slightly more positive values (-13.25‰ ^{18}O / -93.88 ‰ ^{2}H) as dilution with rainwater increases. Also, the values of δ ‰ ^{13}C turn out to be slightly more positive. This could be due to the presence of accessory minerals such as graphite, chlorites and garnets, which could also account for the high electrolytic conductivity of the

sample (310 μs/cm) as well as the high values of magnesium (13.32 ppm) and calcium (45.55 ppm - Table 5.10).

On the other hand, the waters of the Confinale creek in proximity of the "Baite di Confinale" locality (*T_10-5*) record more negative $\delta^{18}O$ values than water upstream. This fact can be attributed to the water supply from the springs located at an elevation of 2450 m a.s.l., represented by sample "*S4_09-2*" whose values are the most negatively affected (-14.13 ‰ ^{18}O / 100.08 ‰ ^{2}H) of the entire analysis set. The strong negativization of the values could be attributable to a deep flow.

Sample *S14_09-4* also exhibits values more enriched in light isotopes than the Confinale lake (-13.77 ‰ ^{18}O / -97.15 ‰ ^{2}H) and these are also presumably attributable to deep circulation but with greater contamination from summer meteoric water. The δ‰ of ^{13}C is slightly positive and can be related to inorganic carbon input from the marbles also evidenced by high Ca content (66.08 ppm) and correlated by high TDS (180 mg/l) and electrolytic conductivity (390 μs/cm) (Table 5.9).

Samples *S61_12-5* and *S63_12-89* related to springs located between 1700 and 1750 m a.s.l. (-13.7 ‰ ^{18}O / -96.8 ‰ ^{2}H) show values consistent with a deep flow. These are presumably infiltrations of water from the Confinale creek and rock glacier spring waters that are carried deep into the trench zone located at an elevation of 2300 m a.s.l.

The values recorded at the Ruinon high niche (*S27_06-2*) are the less negative (-13.18 ‰ δ ^{18}O / -92.17 ‰ δ ^{2}H) of the whole area. These evidences lead to the hypothesis that this spring derives from a relatively shallower runoff with origin from the waters channelized at the intersection of the preferential runoff line and trenches at an elevation of 2288.5 m a.s.l. In support of this interpretation, the δ ^{13}C values of -6.98 ‰ are highly enriched in ^{12}C, resulting from a high interaction with organic material attributable to a shallower flow.

With regard to the springs located to the right flank of the rockslide body (S53_11-1), from the morphological layout of the slope and the hydro-chemical properties of the water, it is logical to assume that their supply comes from the trenches present upstream between elevation 2300 and 2350 m a.s.l. (Figure 5.12), consistent with a relatively shallow flow.

Summarizing all the hydrogeological evidences reported in this work, the map in the following page (Figure 5.17) has been developed.

Figure 5.17 – Hydrogeological map of the Ruinon slope showing the distribution of water springs and the elements that could play a significant role in the slope's groundwater circulation; topographic basis: CTR ed. 2012 scale 1:10,000. The map also shows the location of all the tests performed to characterize the hydraulic properties of the materials.

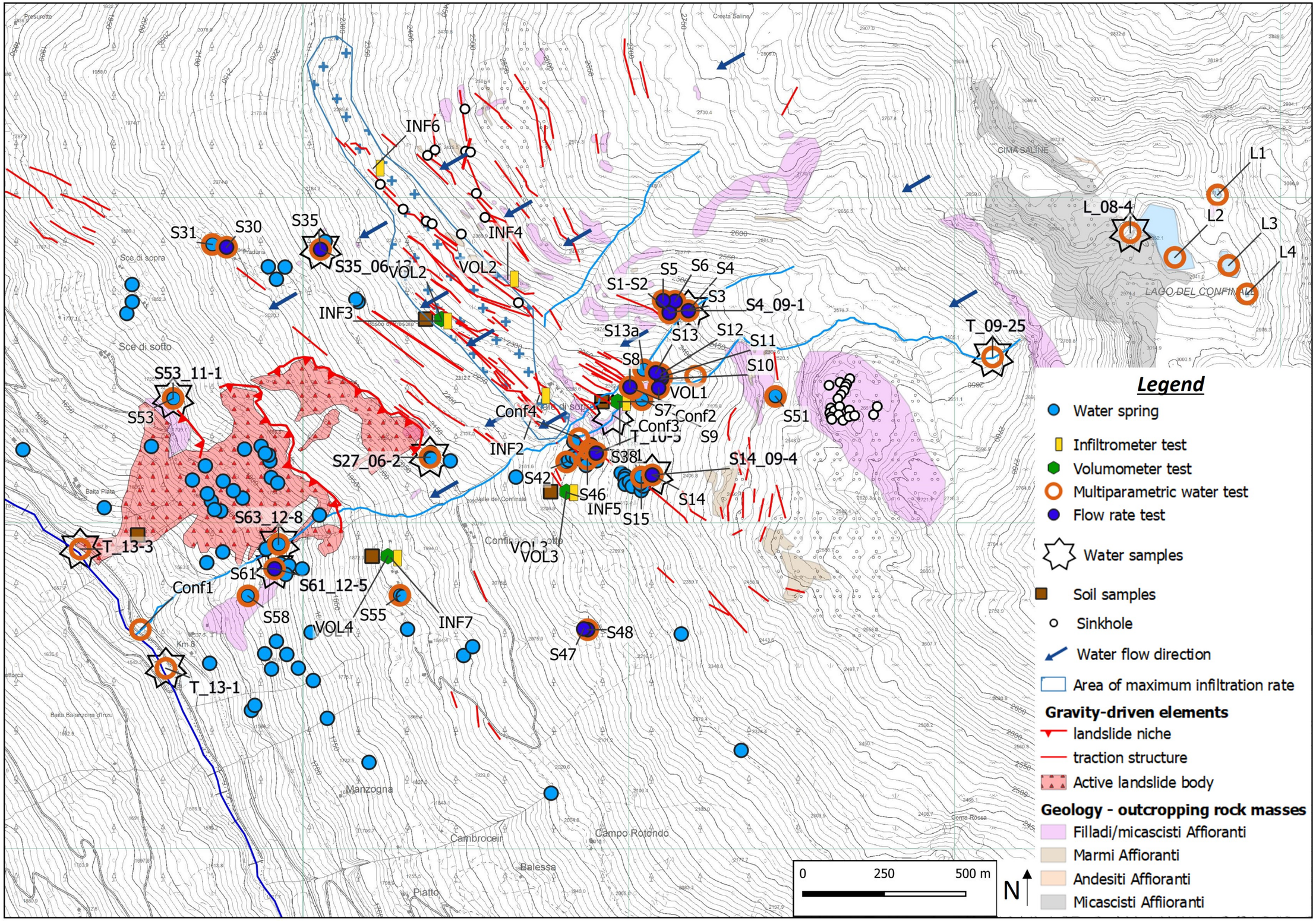
INF6
INF4
INF3
INF2
INF5
INF7
VOL1
VOL2
VOL3
VOL4
S31
S30
S35
S35_06_13
S53_11-1
S53
S27_06-2
S63_12-8
S61
S61_12-5
S58
S55
S1-S2
S5
S6
S4
S3
S4_09-1
S13a
S13
S12
S11
S10
S8
S7
S9
S38
S42
S46
S47
S48
S14_09-4
S14
S15
S51
T_10-5
T_09-25
L_08-4
L1
L2
L3
L4
LAGO DEL CONFINALE
CIMA SALINE
Cresta Saline
Conf1
Conf2
Conf3
Conf4
T_13-3
T_13-1
Sce di sopra
Sce di sotto
Pradaris
Baita Plate
Baita Balanzona d'Inzu
Km 8
Manzogna
Cambrocein
Balessa
Piatto
Campo Rotondo
Cerna Rossa
0
250
500 m
N
Legend
Water spring
Infiltrometer test
Volumometer test
Multiparametric water test
Flow rate test
Water samples
Soil samples
Sinkhole
Water flow direction
Area of maximum infiltration rate
Gravity-driven elements
landslide niche
traction structure
Active landslide body
Geology - outcropping rock masses
Filladi/micascisti Affioranti
Marmi Affioranti
Andesiti Affioranti
Micascisti Affiioranti

5.3.5 Climate and Hydrography

5.3.5.1 Climate conditions

Current climate conditions of the Ruinon slope exhibit typical features of the Alpine environment. Elevations range from 1350 m a.s.l. in correspondence of the Sant Antonio village, up to 3370 m a.s.l. of the Confinale peak. Along the slope two meteorological stations managed by ARPA Lombardia (https://www.arpalombardia.it/) are present, with a real-time transmission of the data. The Scè di Sotto station is located on the right flank of the Ruinon rockslide at an elevation of 1761 m a.s.l., whereas the Confinale station is placed upstream of the upper niche, at an elevation of 2299 m a.s.l. at the Baite di Confinale locality. Both of them are equipped with thermometers, nivometers, rain gauges, anemometers and air humidity gauges. Moreover, at the Confinale station, an automatic hydrometer that records the change in hydrometric elevations of the Confinale creek is present, allowing the estimation of its water flow.

In addition to them, there is a third climate station managed by ARPA Lombardia and located at Santa Caterina Valfurva, which, although not in close proximity to the study area, has a well-developed data set that can be useful for correlation analyses.

For this work, data recorded by the three stations between the years 2011 and 2022 were analyzed. The average monthly precipitation that characterizes the area varies from a minimum in the winter months of December and January (about 15 mm) to a maximum in August (150 mm), in agreement with values typical of an “endo-Alpine” climate (Ward and Hann 1911; Kottek et al. 2006).

Comparison of rainfall data recorded by weather stations shows a common general trend, with minor variations probably ascribed to severe and localized precipitation events. The highest average rainfall is recorded by the Confinale station, 907 mm/year, followed by the Santa Caterina Valfurva station, with 849 mm/year, and, finally ,the Scè di Sotto station with 837 mm/year. The Figure 5.18a show the rainfall data recorded from the Confinale climate station, which is considered the most representative of the study area and also the most important in defining the hydrological regime of the Ruinon rockslide.

Air temperature data for the last decade, were also analyzed to assess their evolution. Annual fluctuations with negative mean values (-5°C) in winter and positive mean values (14°C) in summer were recorded at the Confinale monitoring station. By fitting the time series with a periodic sinusoidal function, an annual mean amplitude of 9.5°C was identified.

Snowfalls occur from late October until the beginning of April, with an increasing intensity toward the second half of the winter period. Cumulative snowfalls values during a winter season vary greatly from

year to year, depending on climate conditions, but they can easily reach values of more than 3 m in 4 months (Figure 5.18).

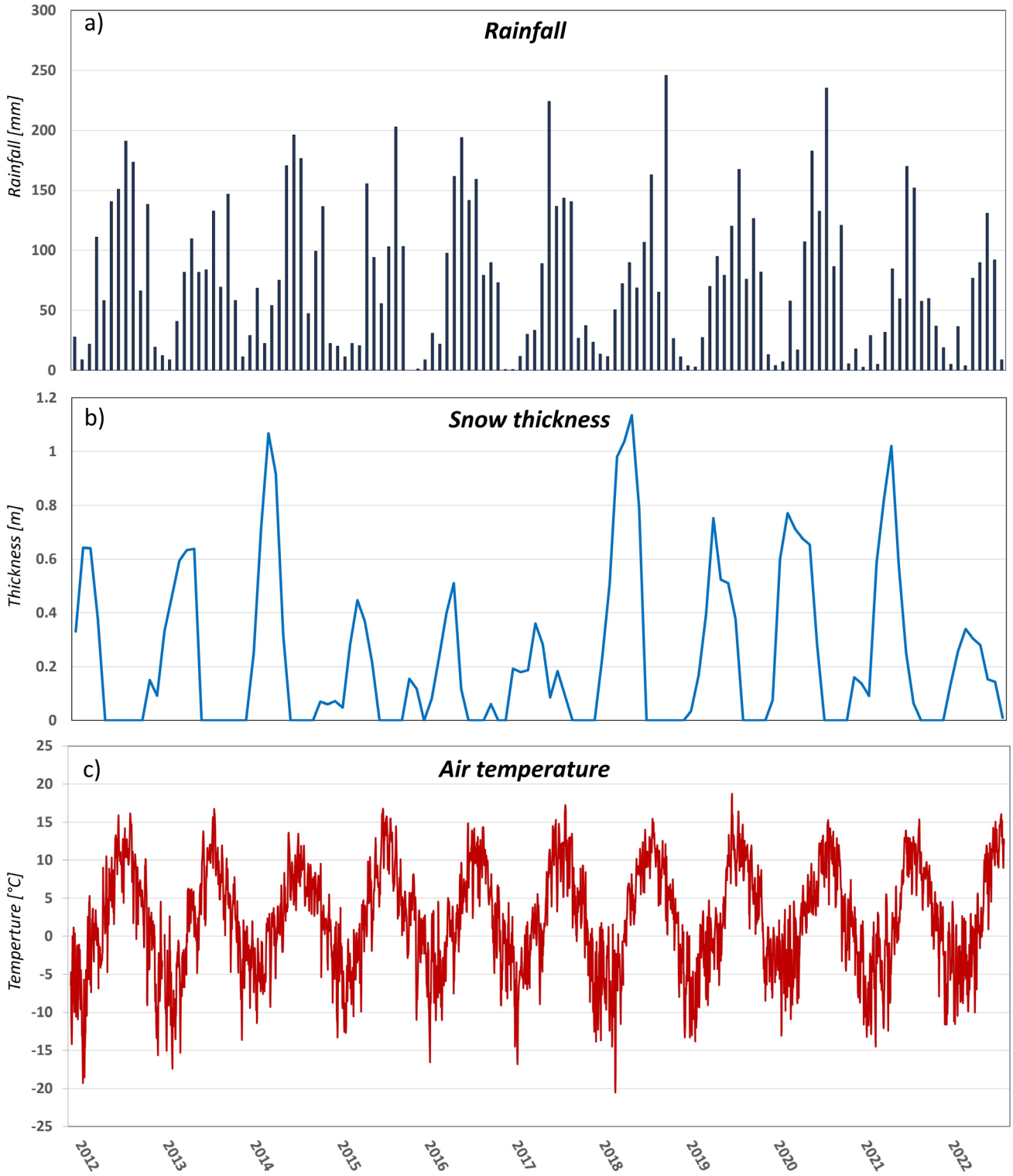

Figure 5.18 - Climate data recorded by the Confinale station a) Monthly rainfall data. b) Snow depth c) Daily temperature evolution.

The snow component is therefore of primary importance in defining the hydrological balance of the area, which is defined by the sum of snowmelt water and rainfall. With this goal, a combined analysis of rainfall, thermometric and nivometric data was performed (Figure 5.19).

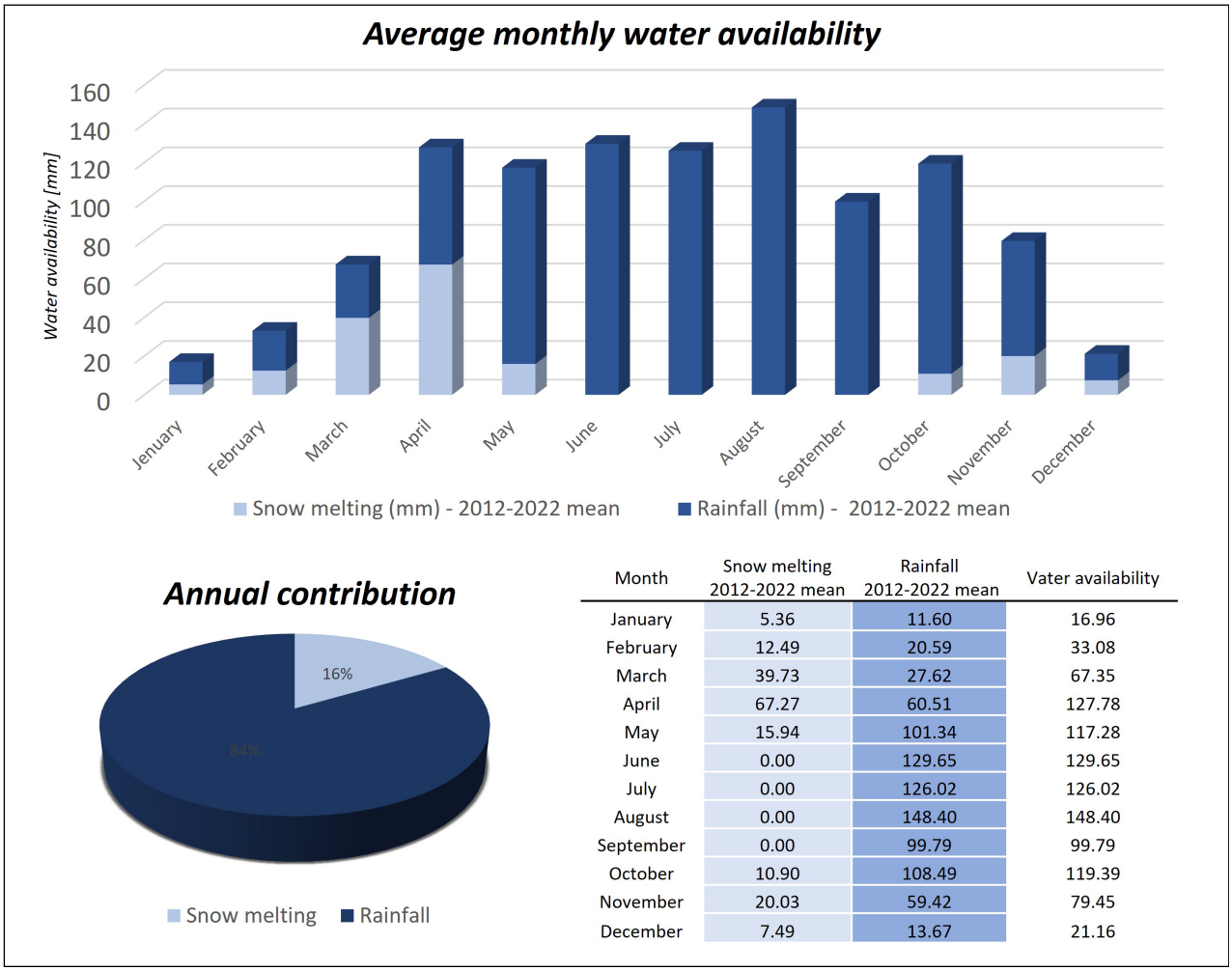

Month	Snow melting 2012-2022 mean	Rainfall 2012-2022 mean	Vater availability
January	5.36	11.60	16.96
February	12.49	20.59	33.08
March	39.73	27.62	67.35
April	67.27	60.51	127.78
May	15.94	101.34	117.28
June	0.00	129.65	129.65
July	0.00	126.02	126.02
August	0.00	148.40	148.40
September	0.00	99.79	99.79
October	10.90	108.49	119.39
November	20.03	59.42	79.45
December	7.49	13.67	21.16

Figure 5.19 - Calculation of the influence of snowmelt on water availability along the slope. It is evident that water availability increases considerably in the spring period.

Starting from the snow thickness data, snow water equivalent (SWE) values, are calculated by multiplying the absolute values of snow melt (thickness differences less than zero) by the ratio between the density of snow and water, following the equation proposed by Seibert et al. 2015:

$$SWE = Hs \frac{\rho_{SNOW}}{\rho_{WATER}} \qquad \textit{(Equation 5.1)}$$

where ρ_{snow} is the snow density and ρ_{water} is the water density. The density of snow can vary considerably (Maidment 1969; Singh 2001; DeWalle and Rango 2008).

New snow usually has the lowest densities with about 100 kg/m^3 and densities increase with aging snow due to metamorphism to about 350–400 kg/m^3 for dry old snow and up to 500 kg/m^3 for wet old snow.

In this work, a snow density value of 300 kg/m^3 is used based on work in the literature related to snow properties in the Italian Alps (Pistocchi 2016; Guyennon et al. 2019). Water density was considered at the common value of 1000 kg/m^3.

Next step is to calculate the snow melt degree day factor CM (mm/°C·day), indicating the amount of melted snow for positive daily temperature values. Following the approach of DeWalle and Rango 2008 and Bajni et al. 2021, it is possible to obtain the value of CM by equaling the value of Daily Melt Rate MR (mm/day) to the value of SWE obtained previously. In the case under analysis, a degree day factor value of 3.5 (mm/°C·day) was obtained.

The minimum daily value is selected, so that the actual amount of melted snow on a given day (mm) is obtained. Having defined the minimum value and further verified by relating it to the daily mean temperatures, the final melting value is obtained. Summing the latter with the total daily values recorded by the rain gauge, finally yields the total water availability (mm).

With an average annual snow melt of 179.21 mm, the Confinale climate station records the highest nival melt contribution (16.5%) among the three stations analyzed. Average water availability is highest in August and is controlled exclusively by rainfall (148.40 mm). The month with the highest average input from snow melt is April (67.27 mm). The average annual water availability is reported to be 1086.31 mm.

Considering return times of 2, 5, 10, 25, 50 and 100 years, and the climatic data recorded by the Confinale station, rainfall possibility signal lines were calculated (Figure 5.20).

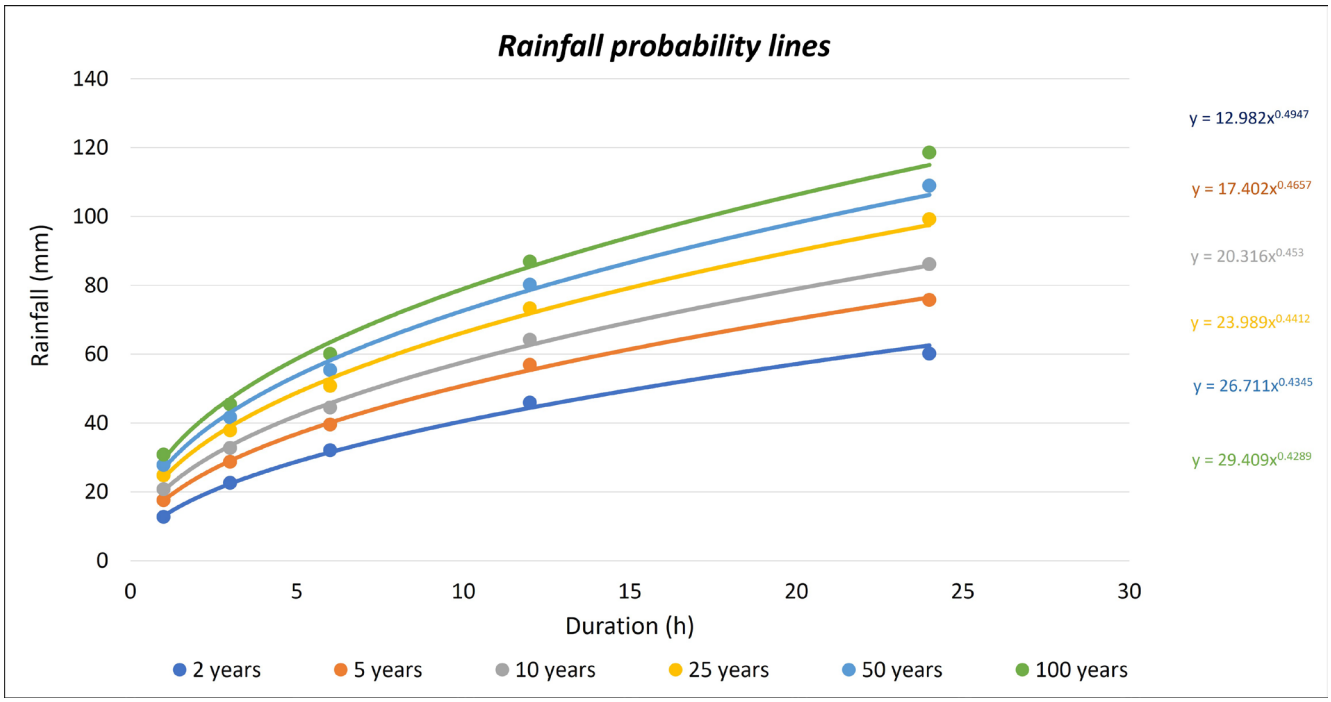

Figure 5.20 - Definition of rainfall probability lines based on climate data recorded by the Confinale station.

5.3.5.2 Hydrological study

Previous Authors (e.g., Merizzi 2015) have highlighted the potential decisive role of surface hydrological elements in the water supply to the rockslide body. Particular attention is paid to the Confinale creek, which originates from the Confinale lake and descends following the maximum inclination of the slope, flowing on the left flank of the active rockslide body. Since its proximity to active gravitational elements, it can therefore represent a significant supply element for groundwater bodies around the rockslide. This Section will focus on the analysis of the Confinale creek flow rates and on the definition of the amount of water reaching the rockslide as a result of surface water runoff.
With regard to the flow rates of the Confinale creek, by analyzing the hydraulic level data recorded by the Confinale climate station, it is possible to define a correlation between the water supply and the hydrometric level of the river. Considering a one-year time range, a clear dependence of water level with snow melting processes is noticeable. The peak value of the Confinale water level occurs in late spring (May-June), corresponding with the end of the snowmelt period. During the next months, the hydrometric level decreases according to a linear trend, interrupted by restricted peaks ascribable to intense rainfall events, until it reaches a minimum in the winter months where the creek is completely dry. Expanding the time interval (2012-2022), the same trend described above is confirmed. In particular, Figure 5.21 shows the flow rates of the Confinale creek calculated from hydrometric data and correlated with the water availability (e.g., sum of precipitation and snowmelt).

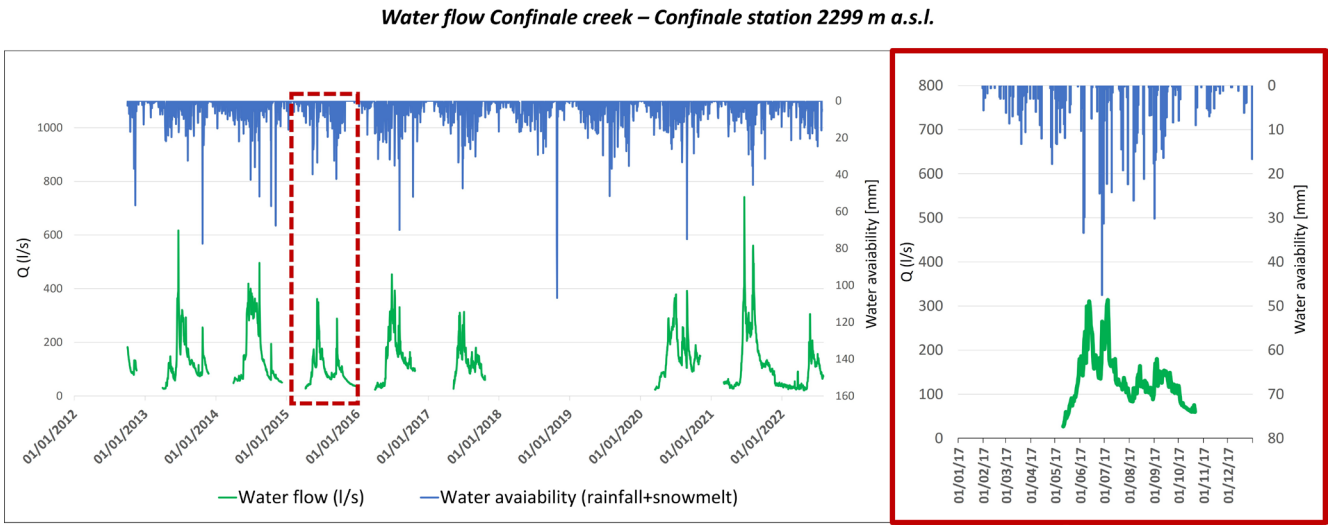

Figure 5.21 – Water flow of the Confinale creek measured in correspondence of the Confinale climate station. Flow rates are compared to water availability calculated as the sum of rainfall and snow melt.

Due to the lack of continuity in the hydrometric data for the years 2018 and 2019, it was chosen to omit these years in the representation of Figure 5.21. Annual average flow results in a value of 67.48 l/s.

Furthermore, by determining the maximum daily values, it was possible to define a maximum flow rate of 740.00 l/s, calculated over a time range of 9 years (from 2012 to 2017 and from 2020-2022).

To assess the potential surface water supply to the Ruinon rockslide body, drainage basins upstream of the upper niche were identified. In particular, all the surface runoff lines that intercept the trenches located upstream of the rockslide body were analyzed. With a morphological analysis in a GIS environment, it was therefore possible to obtain the output in Figure 5.22. In order to calculate the characteristic runoff time and the peak flow rate at the closure of each drainage basin, it was necessary to define their basic parameters such as area, maximum elevation, minimum elevation, average elevation, and average steepness (Figure 5.22).

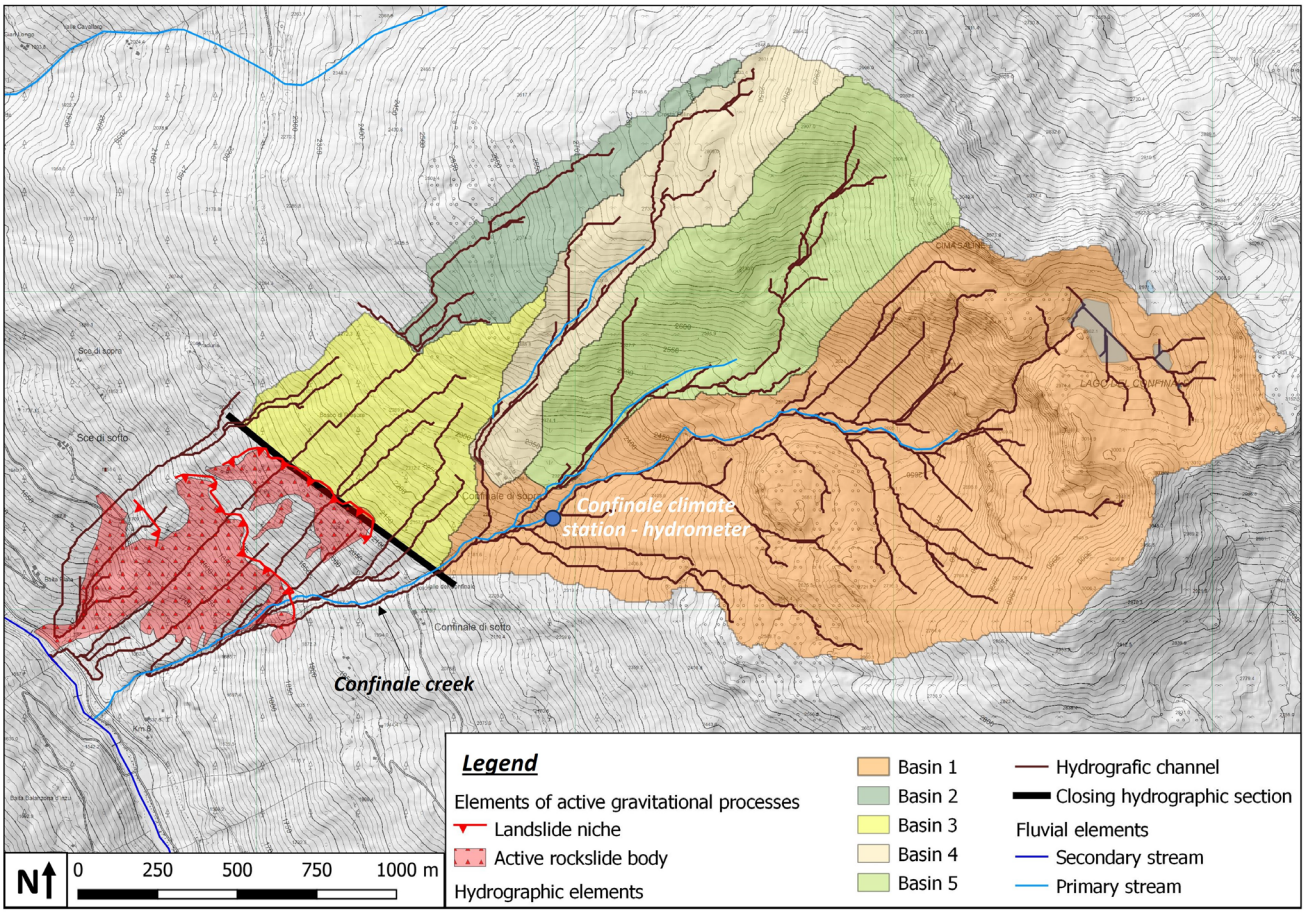

Characteristic values of drainage basins

Basin	Area [km²]	Maximum elevation [m]	Minimum elevation [m]	Mean elevation [m]	Mean slope [%]	Length of main shaft [km]	Slope of main shaft [%]
1	3.05	3161.7	2125.3	2705.7	50.2	2.93	24.9
2	0.22	2835.8	2342.8	2599.9	45.7	1.38	34.4
3	0.39	2544.8	2031.4	2223.7	52.5	0.85	42.3
4	0.39	2995.86	2274.68	2680.53	45.7	1.59	34.9
5	0.69	3057.21	2319.6	2708.85	56.9	1.6	34.9

Figure 5.22 – Definition of drainage basins based on morphological features of the Ruinon slope. The closing section of the drainage basins correspond to the upper niche of the active rockslide body.

Added to the parameters defined in Figure 5.22 is the runoff coefficient (*RC*), which is equal to the ratio of the runoff (volume of water runoff at the basin closure section) to the inflow (total amount of rainfall falling on the drainage basin). This parameter depends on the geological, geomorphological and hydrological features of the basin. For this work, the methods presented in Deppo 2002; Merizzi 2002; Bhunya et al. 2004 were applied to the definition of the runoff coefficient (Table 5.12). In particular, soil hydraulic conductivity (*FI* parameter in Table 5.12), ground vegetation cover (*V* parameter), average basin slope (*Pm* parameter), surface water network development (*D* parameter) and drainage basin shape (*P* parameter), were accounted.

Table 5.12 - Definition of parameters for the calculation of the runoff coefficient.

Parameters for the definition of the runoff coefficient (RC)									
FI parameter		*V* parameter		Pm parameter		D parameter		P parameter	
Impermeable formations present in the basin		Vegetation present in the basin		Average basin slope		Surface water network development		Shape of the basin	
Def	Val	Def	Val	Def	Val	Def	Val	Def	Val
FI>80 %	0.95	V<20 %	0.95	Pm>100 %	1	Very developed D>6 km/km^2	1	Not elongated 1<P<1.5	1
50%<FI<80%	0.75	20%<V<50%	0.75	66%<Pm<100%	0.9	Developed 4<D<6 km/km^2	0.9	Mildly elongated 1.5<P<2	0.95
20%<FI<50%	0.55	50%<V<80%	0.55	33%<Pm<66 %	0.8	Mildly developed 2<D<4 km/km^2	0.8	Elongated 2<P<3	0.9
FI<20 %	0.35	V>80 %	0.35	Pm<33 %	0.7	Not developed D<2 km/km^2	0.7	Very elongated P>3	0.85
Runoff coefficient C = FI * V * Pm * D * F									

Based on the parameters defined in Table 5.12, runoff coefficients were defined as follows (Table 5.13). By using the data obtained from the basin characterization, it was possible to calculate the associated time of concentration (*TC*), i.e., the time needed for water to flow from the most remote point in a drainage basin to its outlet. Three different relations were applied, among the most widely used of those in the literature, known as Ventura (Ventura 1905), Giandotti (Giandotti 1934) and Puglisi (Puglisi and Zanframundo 1978) relations. The relation defined by Ventura is defined as:

$$T_C = 0.127 \frac{\sqrt{S}}{\sqrt{i}} \quad \textit{(Equation 5.2)}$$

Where *S* is the basin area and *i* is the mean slope morphological gradient.

The relation proposed by Giandotti is defined as:

$$T_C = \frac{4\sqrt{A}+1.5L}{0.8\sqrt{h_{mean}- h_{min}}} \quad \textit{(Equation 5.3)}$$

Where *A* is the basin area, *L* is the length of the main shaft, h_{mean} is the mean elevation of the basin and h_{min} is the minimum elevation of the basin.

The relation proposed by Puglisi is defined as:

$$T_C = 6L^{\frac{2}{3}}(h_{max} - h_{min})^{-1/3} \quad \textit{(Equation 5.4)}$$

Where *L* is the length of the main shaft, h_{max} is the maximum elevation of the basin and h_{min} is the minimum elevation of the basin.

Table 5.13 – Definition of the runoff coefficient starting from parameters of Table 5.12. The time of concentration (TC) is also provided for each drainage basin following the relations provided by Ventura, Giandotti and Puglisi.

Definition of the runoff coefficient (RC)									
Basin	*FI*	*V*	*PM*	*D*	*P*	*Runoff coefficient*	*TC Giandotti*	*TC Ventura*	*TC Puglisi*
1	0.75	0.95	0.8	0.7	1	0.399	35.4	26.68	72.79
2	0.75	0.95	0.8	0.7	0.9	0.359	18.54	0.83	56.49
3	0.75	0.65	0.8	0.7	1	0.273	18.16	0.3	48.14
4	0.75	0.95	0.8	0.7	0.9	0.359	18.18	1.08	54.69
5	0.75	0.95	0.8	0.7	0.95	0.379	21.73	1.44	54.51

The last step for calculating maximum flow rates at the closure of the drainage basins required the evaluation of the meteorological water supply values considering the evaluated returning times defined in Figure 5.20. From the resulting data of climate analysis and considering the time of concentration, the runoff coefficients and the basin area, it was possible to obtain the flow rates for each drainage basin, for the relevant return times (Table 5.14). The time of concentration used in the definition of flow rates in Table 5.14 was calculated through Puglisi's formula (Eq. 5.4), chosen as the most representative one for the study area following a calibration process.

Table 5.14 - Calculation of flow rates with different return times at the closure of each drainage basin.

	Water flows [m^3/s]					
Basin	*2 years*	*5 years*	*10 years*	*25 years*	*50 years*	*100 years*
1	0.907	1.216	1.419	1.676	1.866	2.054
2	0.088	0.119	0.138	0.164	0.182	0.200
3	0.151	0.203	0.237	0.280	0.312	0.343
4	0.161	0.216	0.253	0.298	0.332	0.366
5	0.296	0.397	0.464	0.547	0.609	0.671

5.3.6 Ruinon geotechnical monitoring system and previous studies

With the aim of monitor slope displacements and mitigate landslide hazard, geotechnical instruments were progressively installed along the rockslide body. Currently, the area affected by the Ruinon rockslide is monitored by both shallow and deep instrumentation, mainly located in the area of the two niches and upstream of the higher one. The monitoring network includes four active piezometers (Section 5.3.4), extensometers, inclinometers (Section 5.3.3; Figure 5.4), and a ground-based interferometric synthetic aperture radar (GBInSAR – Figure 5.23).

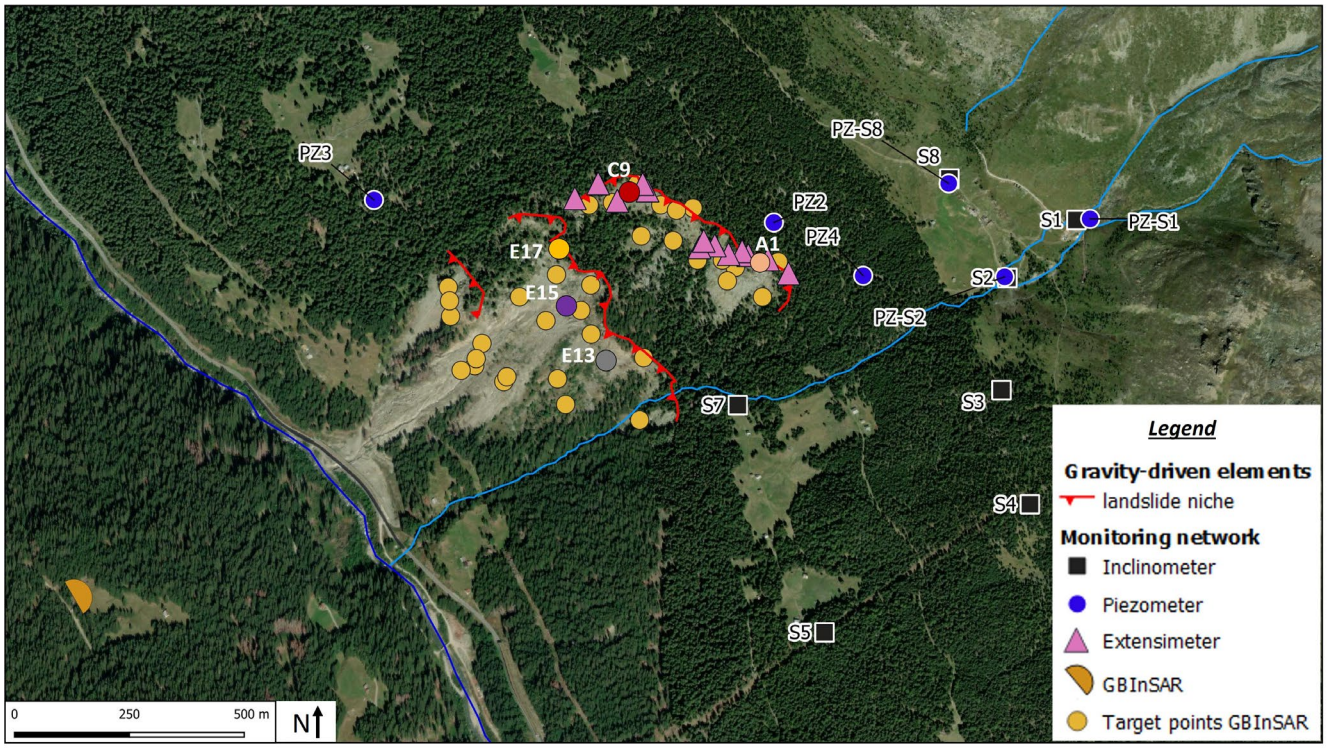

Figure 5.23 – In-situ geotechnical monitoring system of the Ruinon rockslide. The target points of the GBInSAR system presented in the Figure 5.26 are highlighted.

At date, the GBInSAR consists of 45 target points located along the rockslide body, whose position is continuously measured with a time-interval depending on the rockslide activity.

The presence of a well-developed monitoring network provides a large amount of data, and allowed to carry out several studies on the evolution of the rockslide (Del Ventisette et al. 2012; Crosta et al. 2013; Carlà et al. 2021). By analyzing the influence of driving factors and their relationship with monitored displacements, an early warning system was developed (Crosta and Agliardi 2003).

Currently, the monitoring system is managed by the Geological Monitoring Center (CMG in Italian), belonging to the Sondrio Department of ARPA Lombardia, which has installed the instrumentation and performs periodic campaigns of manual surveys (dystometric, piezometric, GPS, and inclinometric measurement campaigns). Monitoring activities began in 1988. Initial studies were mainly focused on the definition of volumes and materials involved in the gravitational instability process (Section 5.2.1). The Ruinon rockslide was picked as one of the first experimental sites monitored by a GBInSAR system (Canuti et al. 2000; Tarchi et al. 2003) that was permanently installed in 2006 (Casagli et al. 2010) as a monitoring and early warning tool (Figure 5.23).

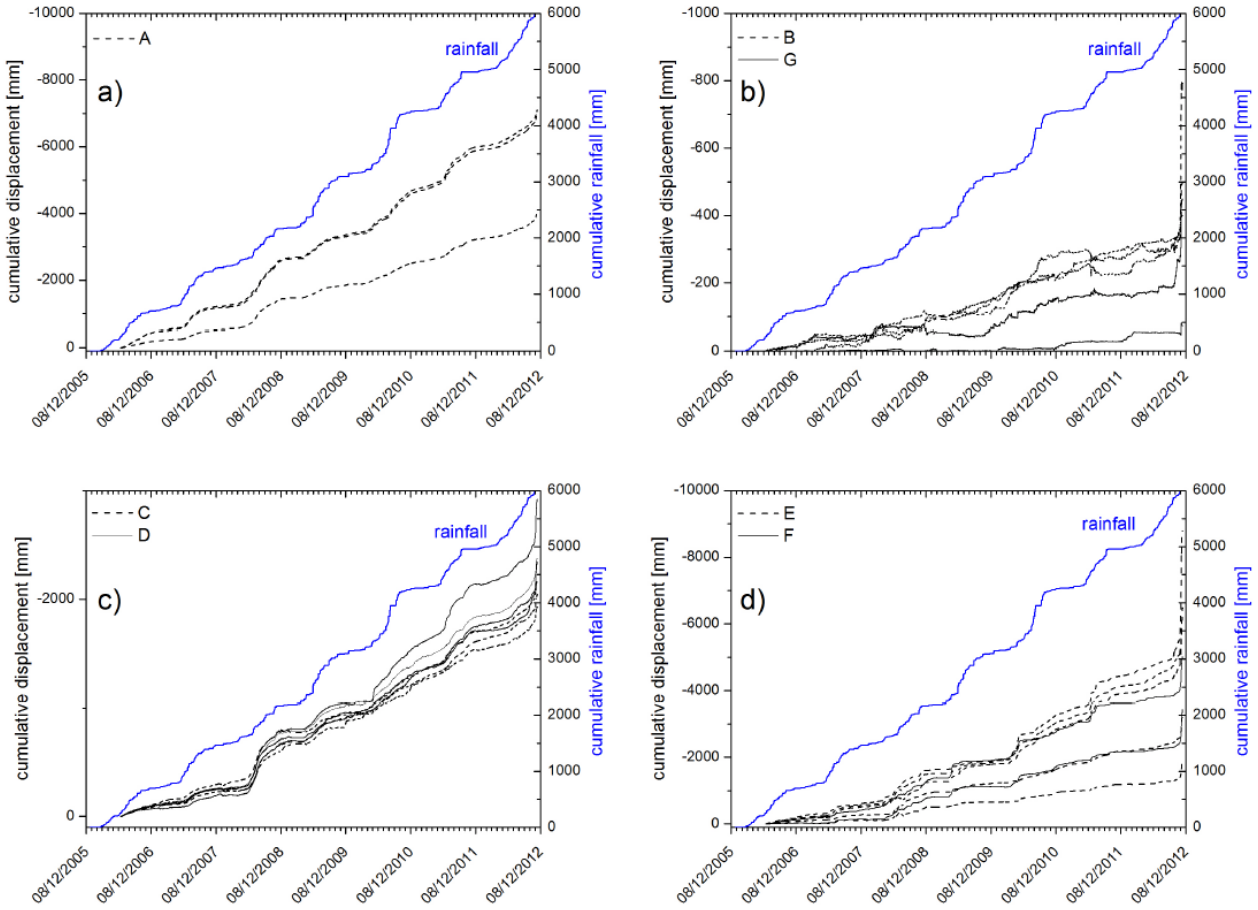

Figure 5.24 - Cumulative displacement data recorded at 6 target points of the rockslide body (Crosta 2013). A periodicity in the acceleration events that can be correlated with rainfall inputs is well evident. From Crosta 2013.

Ground-based satellite data from years 2006–2007 were analyzed by Del Ventisette et al. 2012 and Crosta 2013, defining a relation between displacements of the rockslide and the rainfall regime. Data analysis over the time period from 2006 to 2012 (Figure 5.24), showed a cyclic pattern of acceleration events with major deformations concentrated in the NE portion of the high niche and at the central body of the low niche, with escalations in the summer periods between April and August (Figure 5.24, Crosta 2013). Crosta et al. 2017 analyzed 9 years of continuous monitoring activity (2006–2014), identifying "early warning domains" within the rockslide body, defined as homogeneous domain in terms of materials, sliding mechanisms and response to rainfall inputs. For each rockslide domain, displacement rates and rainfall thresholds were defined. Carlà et al. 2021 reviewed more than a decade of GBInSAR data, analyzing the evolution of the slope in both space and time. Starting from displacement data, the thickness of the rapidly moving layer of debris was assessed. GBInSAR monitoring showed new reactivations of the rockslide phenomenon in the years of 2014 and 2016, which mainly involved the central sector of the lower niche. In June 2019, a very intense deformation event was recorded, affecting the entire rockslide body, reaching a deformation rate of more than 1 m/day and total monthly displacements of more than 10 m; similar values were also recorded in the following 3 months (Figure 5.25).

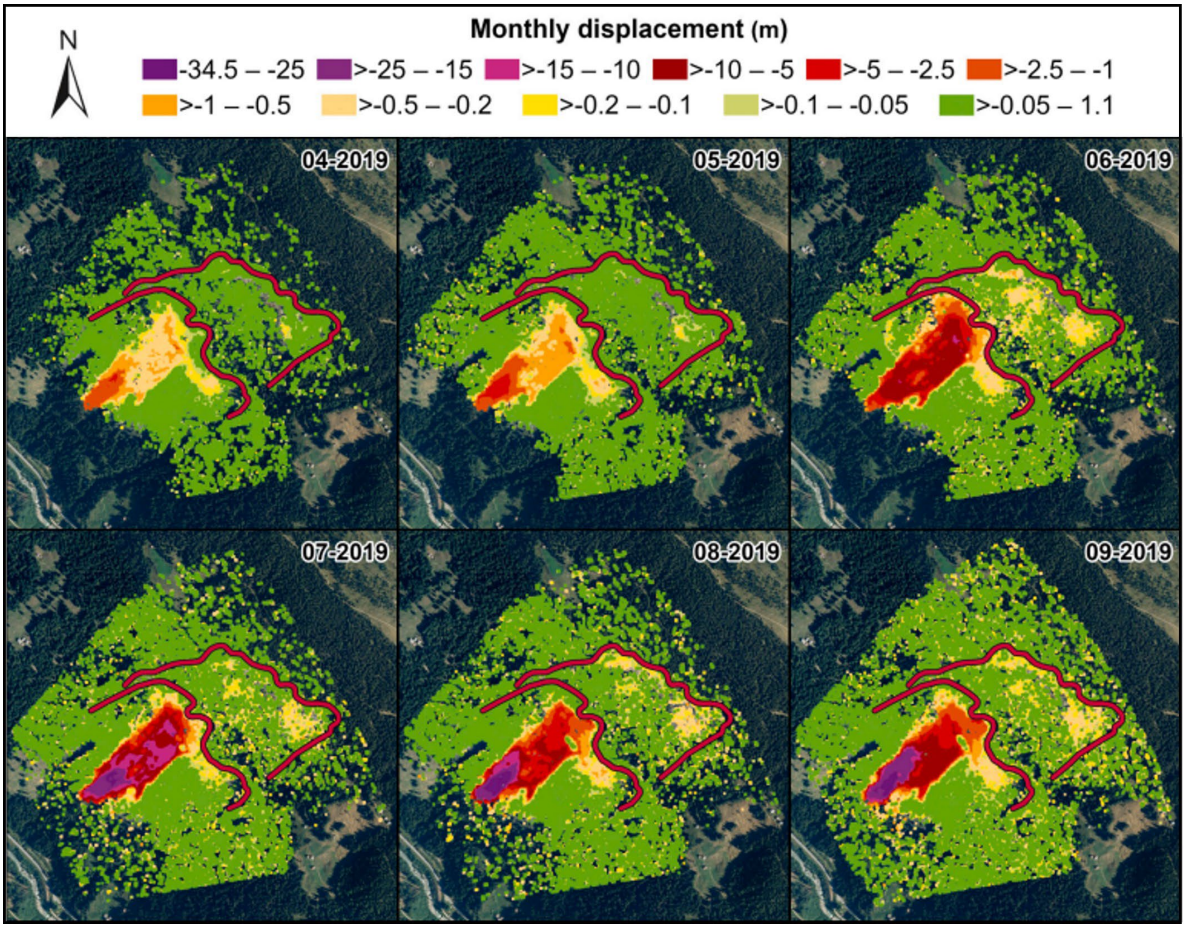

Figure 5.25 - Distribution of displacements during the 2019 acceleration event. From Carlà et al. 2021.

Velocities and displacements begin to reduce in December 2019, in conjunction with the first solid precipitation, and, reasonably, in connection with a lowering of the monitored piezometric level. The results of a numerical modeling analysis conducted by Carlà et al. 2021, suggested that the debris cover downstream of the lower niche is very close to a limit equilibrium condition and can therefore show significant deformation processes even in the absence of external forcing.

The data collected as part of this work confirmed and integrated the evidences described by previous Authors, and allowed the development of new correlations between hydrological variables and recorded displacements. Figure 5.26 shows the cumulative displacement values of the 2014-2022 period, recorded from four different monitoring points of the GBInSAR system. The results, confirmed a seasonal evolution of the rockslide behavior, marked by an increase in displacement velocities following rainfall events and snow melting processes during the spring and summer seasons. Deformation peaks were reached during periods of higher piezometric level elevation. Secondary accelerations may occur in the fall due to new rainfall, but maintaining a downward trend related to the lowering of the water table. Three episodes of rockslide acceleration are well noticeable during the years of 2014, 2016 and 2019, causing rapid shallow gravitational events, as discussed in Section 5.2.1.

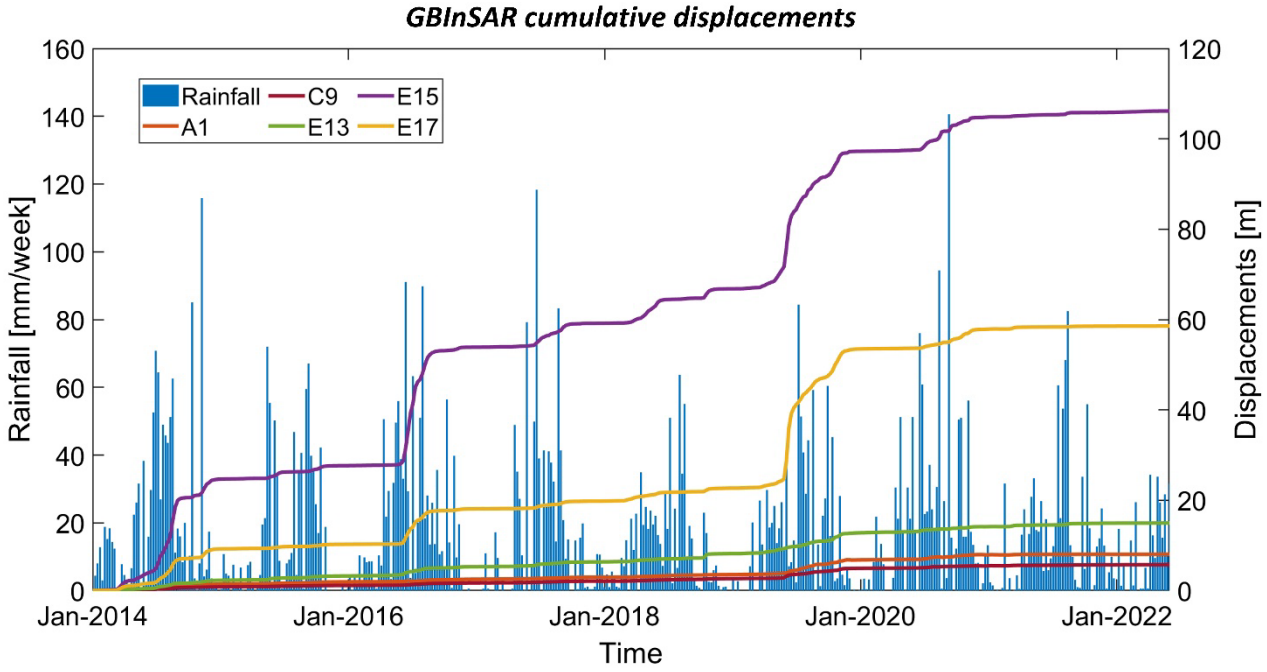

Figure 5.26 - Cumulative displacements recorded by the GBInSAR system (Figure 5.23) and rainfall data recorded at the Confinale climate station (location in Figure 5.10).

Since the early 2020s, a significant drop in the piezometric level is observed, due to both an exceptionally dry period without snowfall and the construction of hydraulic engineering works for the Confinale creek.

The river water flow, as well as some natural water springs are caught in correspondence of the "Baite di Confinale" locality, at higher elevations of the upper niche and returned further downstream via a pipeline. This reduces the waters of the creek from infiltrating inside the rockslide body and feeding the groundwater table. Parallel to the reduction of the piezometric level, a slowing down of the rockslide body is also observed, demonstrating the relationship already observed previously between rockslide activity and groundwater level.

The data recorded by the extensometers placed at the upper niche (Figure 5.23) also show a continuous evolution of the rockslide body, with, however a less pronounced activity than the points monitored by the GBInSAR radar system. The extensometers are in fact placed to measure deformations of the rock-mass, unlike the target points of the radar system, which mainly record shifts in the surface debris state. Extensometers data show a trend of creep-type behavior with sudden and very rapid accelerations (Figure 5.27). Figure 5.27 shows the cumulative evolution of displacements recorded by five extensometers. The 2019 event that resulted in a general retreat of the rockslide body is well evident. Again, there is a general slowdown in the rockslide movements from the early 2020s, with the exception of two extensometers (E3 and E7 in the Figure 5.27) that could indicate a NWward expansion during 2020 of the high rockslide niche.

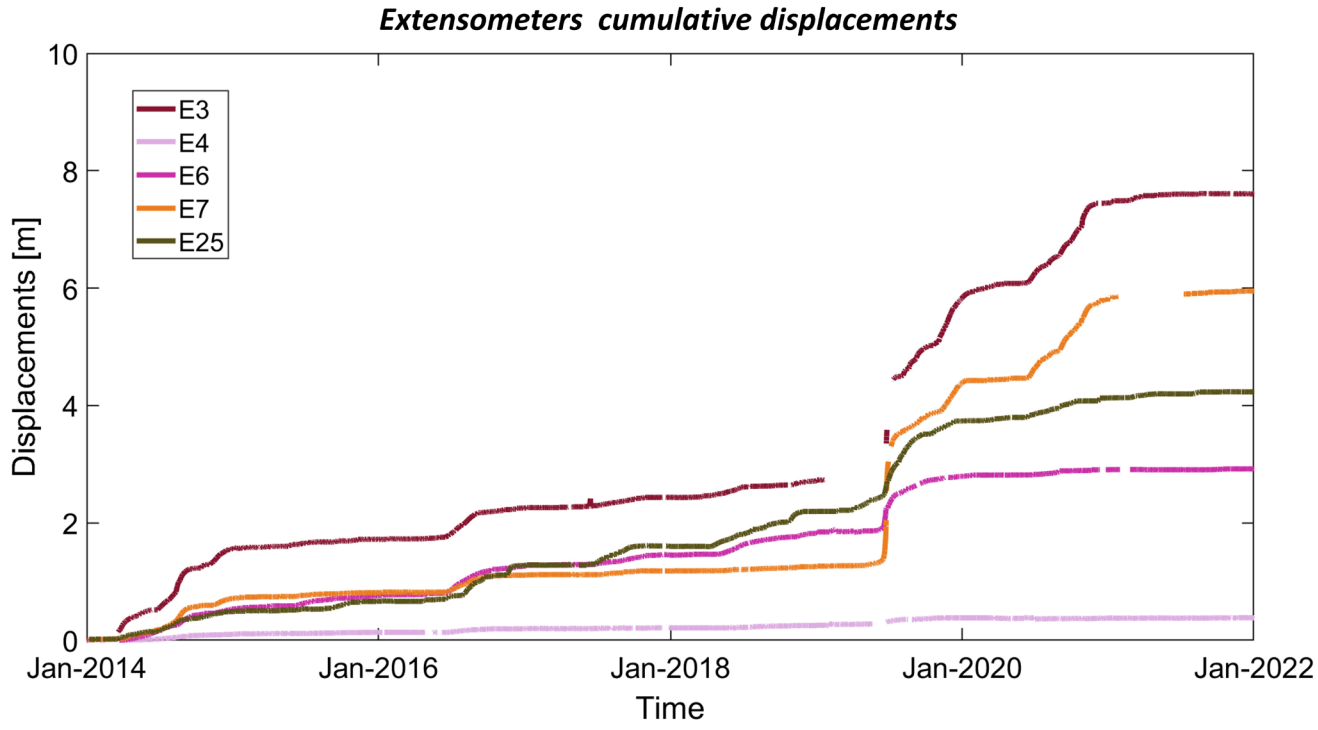

Figure 5.27 - Cumulative displacements recorded by extensimeters (Figure 5.23).

5.4 Geological and hydrogeological conceptual model

Morphological evidences

Starting from the main geomorphological evidences detected, the morphology of the slope is rough, with very steep gradients, even close to 35° at its bottom. Plateaus are present only upstream of the "Baite di Confinale" locality and at altitudes of 2600 m a.s.l. in the "Planon" locality. The slope shows clear evidences of intense gravitational activity, with the development of morphological features such as trenches, counter-slopes and semi-graben structures (Section 5.3.2; Figure 5.3) . These elements are frequent in the area of "Bosco delle Presture" and "Baite di Confinale" locality, with direction parallel to the valley axis, lengths of hundreds of meters and metric apertures. Moving toward the Ruinon rockslide body, these structures become more and more prominent with evidences of recent activity. In these areas the rock material is covered by quaternary post-glacial deposits, with rock material outcropping only at deepened trenches. The thickness of deposits ranges from 5 to 20 m, as observed from the stratigraphic logs of drilled boreholes.

Geological and geomechanical setting

Summarizing the observations discussed in the previous Sections, the geological setting of the slope is defined by an almost homogeneous bedrock of phyllite bodies (Section 5.3.1; Figure 5.2).

Locally, phyllites are characterized by the inclusion of magmatic bodies (Andesite in Figure 5.2b), and other lithological bodies of the Campo Nappe unit as marbles and prasinites. They are located at elevations above 2300 m a.s.l. and in the portion of the slope E of the main rockslide body.

The Phyllite bodies are characterized by very pervasive foliation with millimetric to centimetric layering, resulting in low material strength and high deformability properties. Intercalations of more massive bodies of marble and intrusive rocks are also present, but without significantly affecting the mechanical evolution of the slope. Their reduced geometric and geological continuity detected, combined with their location outside the main rockslide body and the area of development of the gravity elements, suggests their marginal involvement in the mechanical evolution of the slope. Geological outcrops show evidences of four deformation phases, complemented by a magmatic event. The most pervasive one is represented by the *D3* phase, clearly evident in the lower portion of the slope and only locally at higher elevations. It generates structural elements plunging toward the NW with variable inclinations of 30°, as well as isoclinal folds.

In addition to these, minor tectonic elements (fractures and faults) are present, with ENE-WSW (*F1*), NNE-SSW (*F2*) and NE-SW (*F3*) directions. They are mostly concentrated in the area upstream of the main rockslide body, even though their presence is not evidenced by particular fracture increments, as

shown by a low variation in rock-mass quality indexes or lithological changes within the investigated area.

In-situ and borehole geomechanical surveys showed a very marked fracturing state along the entire slope. In particular, very pervasive fracturing systems were observed in the outcropping rock-masses, with apertures on the order of meters in correspondence of the gravitational-release structures. A total of 4 discontinuity systems were detected (Section 5.3.3; Figure 5.9). Among them, a decisive role of *K1* and *K2* elements was recognized, which are systematically present in all the outcrops analyzed and, with their orientation and low mechanical features, promote the development of gravitational instabilities and slope deformation.

Based on the joint mechanical features and the RMR values detected with detailed geomechanical field surveys, the rock-masses appear to belong to a "fair" class of quality (RMR values ranging from 45 to 50; Figure 5.9d-e). The intensity of fracturing and the mechanical degradation degree, increases in areas affected by slope detensioning and active gravitational processes (GSI values ranging from 40 to 50; Figure 5.9 a-b, e). In correspondence of the Ruinon rockslide, the rock-masses are highly fractured with dislocated rock blocks (GSI = 40; Figure 5.9e-f). On the hydrographic left of the Confinale creek, at elevations of about 2500 m a.s.l., marble outcrops have been detected with rock-masses showing a very pronounced degree of mechanical degradation (GSI = 35; Figure 5.9e, g). The presence of cavities, sinkholes and isolated rock towers is the evidence of karst processes which may have driven the development of such condition. However, the marble unit do not seem to be mechanically involved in the Ruinon rockslide process. Instead, this area represents a significant region of rainwater infiltration.

Processing of borehole data, stratigraphic logs and seismic surveys revealed the presence of intensely fractured layers (RQD<50%) laying on an undisturbed phyllite body (RQD>50%). This zone of greater fracturing conditions has thicknesses varying from a few meters up to a hundred meters and is consistently present in all boreholes analyzed, even at higher elevations than the main rockslide body. It could be coincident with the deep landslide body represented by the Saline DSGDS, although, direct observations in lateral continuity are not present. In correspondence with the Ruinon rockslide, metric-thick bands with RQD values close to zero have been detected at depths of about 70-100 m (Figure 5.5). They represent well-developed slip planes isolating a sliding mass of about 20 Mm^3. The rockslide body is composed by extremely fractured and degraded material with rock blocks embedded in a fine sandy matrix. The thickness of this body varies from 10 m to 30/40 m and covers the entire portion of the slope starting from the upper niche and descending to the valley floor, even at lower elevations than the lower rockslide body.

Two main niches are highlighted along the slope: an upper niche at elevation of 1900 m a.s.l. and a lower niche at elevation of 2100 m a.s.l. The trend of these surfaces in the depth is not clear, but the presence of a complex system defined by the coalescence of multiple slip planes is very likely. From analysis of monitoring data (Section 5.3.6), the most active shear surface would appear to be the lower one, with translational and rotational movement resulting in displacements even in the order of tens of meters during the most intense acceleration events (Figure 5.25; Figure 5.26). The higher portion of the rockslide body, on the other hand, shows minor deformative features, although continuously expanding upstream and enlarging the right flank. These expansions are mainly related to progressive tensile failure of rock-masses which are pulled downward by the movement of the lower rockslide body.
The above discussed observations led to the geological-interpretative cross section of the slope of Figure 5.28 see next page), made in the longitudinal direction to the rockslide axis.

Rock and rock-mass geomechanical properties

The rock materials outcropping showed low mechanical properties, both through laboratory tests and in-situ investigations. In particular, very low compressive strength is highlighted with mean values of 40.9 ± 16.0 MPa and minimum values even lower than 20 MPa (Table 5.3) for samples belonging to the phyllite units at 40 to 190 m depth. In addition, discontinuity surfaces showed mechanical characters typical of very smooth and weathered surfaces (Table 5.4). The presence of clayey-talky minerals makes such surfaces particularly slippery. Considering the results of geomechanical tests and the rock-mass quality indexes estimated, the following mechanical properties (Table 5.15) were obtained applying the Hoek & Brown strength envelope equation (Hoek and Brown, 1997).

Table 5.15 - Rock-mass mechanical parameters elaborated for the Ruinon slope considering different GSI values.

Rock-mass mechanical properties			
	Low fractured rock-mass	Moderately fractured rock-mass	Highly fractured rock-mass
GSI	60	50	45
σ_c (*rock*) [MPa]	45	45	45
m_i	10	10	10
D	0.8	0.8	0.8
m_b	0.9246	0.5099	0.3786
s	0.0023	0.0005	0.0002
a	0.5028	0.5057	0.5081

Figure 5.28 - Interpretive geomechanical section of the Ruinon slope and main geognostic data. The relationship between the rock bodies and loose deposits is highlighted, as well as the trend of the rockslide sliding surface.

Ruinon slope - interpretative geomechanical cross section

Legend

Lithological units

- = Andesites
- = Phyllites
- = Marbles
- = Highly fractured phyllites
- = Shists

Structural and gravitational elements

- = Active rockslide body
- = Paleo landslide deposit
- = Slope deposit
- = Main schistosity
- = Sliding surface
- = Folding axial plane
- = Foliation
- = Fault
- = Landslide niche
- = Boreholes

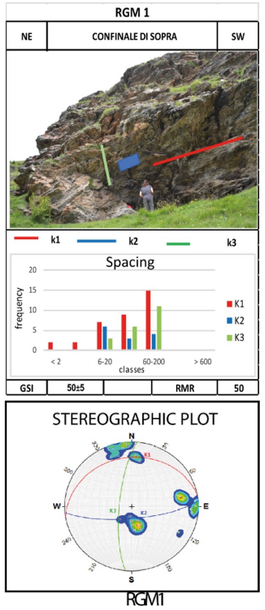

RGM1
scistosity 350°/25°

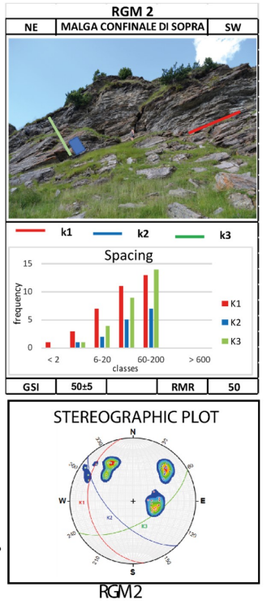

RGM2
scistosity 260°/30°

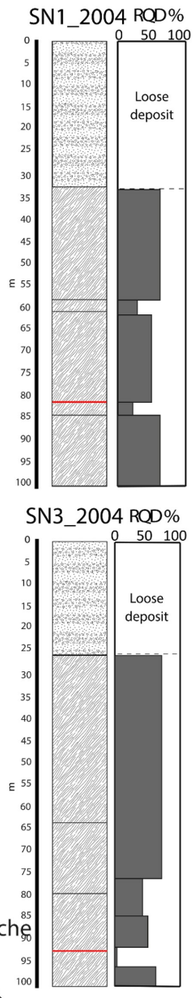

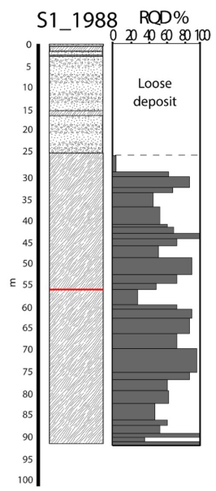

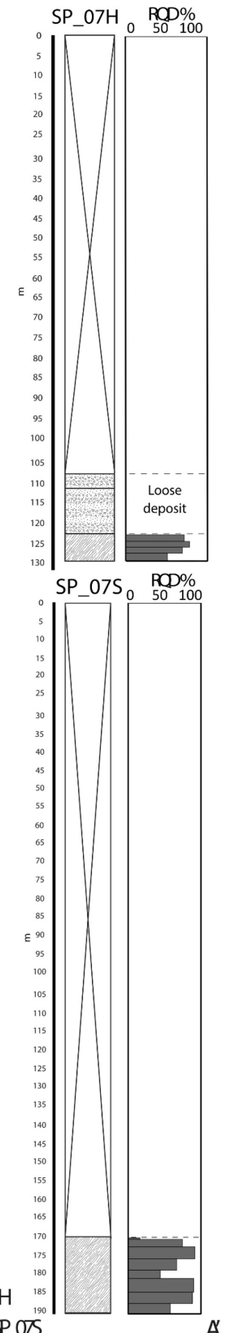

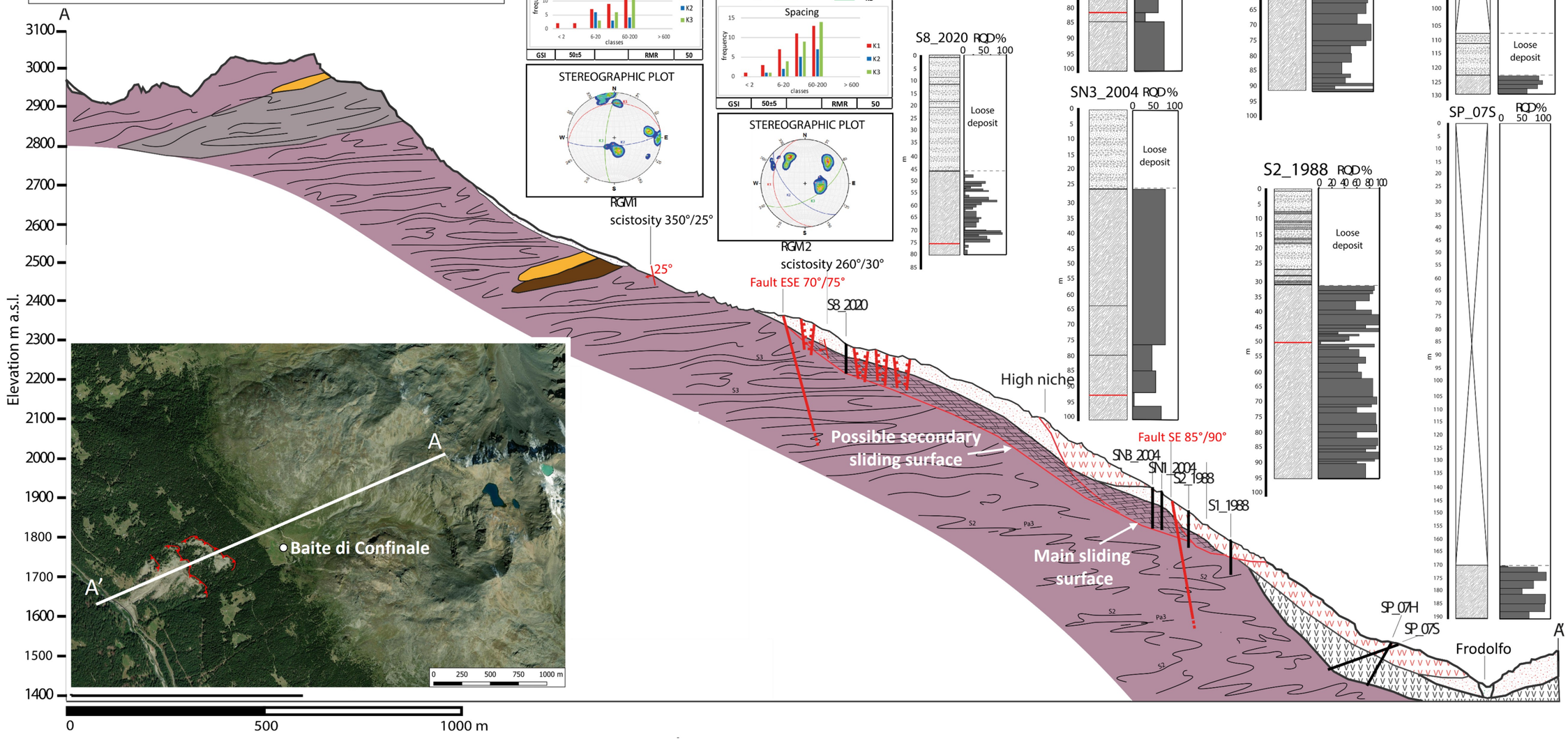

Mohr-Coulomb equivalent values, derived from the above parameters and useful for modeling purposes, are summarized in the following Table 5.16.

Table 5.16 – Equivalent Mohr-Coulomb mechanical properties of rock-masses derived from the parameters in the Table 5.4.

Rock-mass mechanical properties (equivalent Mohr-Coulomb)			
	Low fractured rock-mass	*Moderately fractured rock-mass*	*Highly fractured rock-mass*
GSI	60	50	45
c_{eq} (MPa)	0.50	0.32	0.28
ϕ_{eq} (°)	45	40	37
E_i (GPa)	35	35	35

Hydrogeological setting

As showed by monitoring data (Section 5.3.6), rockslide mobilization events occur in conjunction with intense precipitation and periods of rapid snowmelt, highlighting the potential role of water as a triggering factor (Figure 5.24, Figure 5.26). Following field observations, the hydrogeological setting of the slope is mostly controlled by the presence of trenches, sinkholes and karst morphologies upstream of the rockslide body (Figure 5.17). Field tests for hydraulic characterization of the deposits, revealed highly permeable materials in correspondence of trenches (Table 5.7), resulting in very high potential infiltration rates. In addition, the presence of the Confinale creek flowing over permeable deposits, has a great influence on groundwater feed and represents an important water supply element.

Groundwater circulation seems to be controlled by both the morphological features of the slope and the presence of bodies with different materials, that create significant hydraulic contrasts. The occurrence of water springs is concentrated where highly permeable materials such as rock glaciers, highly fractured rock-masses, or slope deposits collide with low-permeability bodies such as glacial or paleo-landslide deposits. This results in water-rich areas at the “Baite di Confinale” locality (morphological variation combined with contact between rock glacier bodies and fine deposits) and at the toe of the slope (contact between slope deposits and paleo landslide bodies). Another significant point of water outflow is represented by the alignment of springs along the main rockslide body, at an elevation corresponding to the emergence of the rockslide slip surface (Figure 5.17). This could be related to the existence of a shallow groundwater body within the rockslide and leads to the assumption of the presence of clayey - type material along the rockslide shear band, which again creates a permeability limit.

Chemical and isotopic analyses of water samples taken at different points along the slope, showed a clear connection between all the principal water bodies (Section5.3.4). Starting at high elevations, the water of the Confinale lake is primarily derived by snowmelt (low ionic content) and reflect a paucity of bacterial activity consistent with the altitude and its genesis (Table 5.9, Table 5.10, Table 5.11, Figure

5.14, Figure 5.16). Moving to lower elevations, the water of the Confinale creek has slightly different chemical features, reflecting more intense dilution with rainwater and flow over rock-masses with the presence of accessory minerals such as graphite, chlorites and garnets (Table 5.9). At the "Baite di Confinale" locality, springs present at the base of the rock glaciers bodies and along glacial deposits, show chemical features that suggest groundwater circulation at modest depths. Moving to lower altitudes, the water sampled at the toe of the slope, at elevations of about 1700 and 1750 m a.s.l., shows values consistent with deep circulation. This water probably infiltrates at the trenches located at an altitude of 2300 m a.s.l. and is carried downstream by deep groundwater flow. The values recorded at the Ruinon high niche and on the right flank of the rockslide body indicate a relatively shallow runoff, feeding from the gravitational trenches located between elevations 2300 and 2350 m a.s.l. From these evidences, two recharge areas of groundwater bodies subject to the instability process have been identified (Figure 5.29).

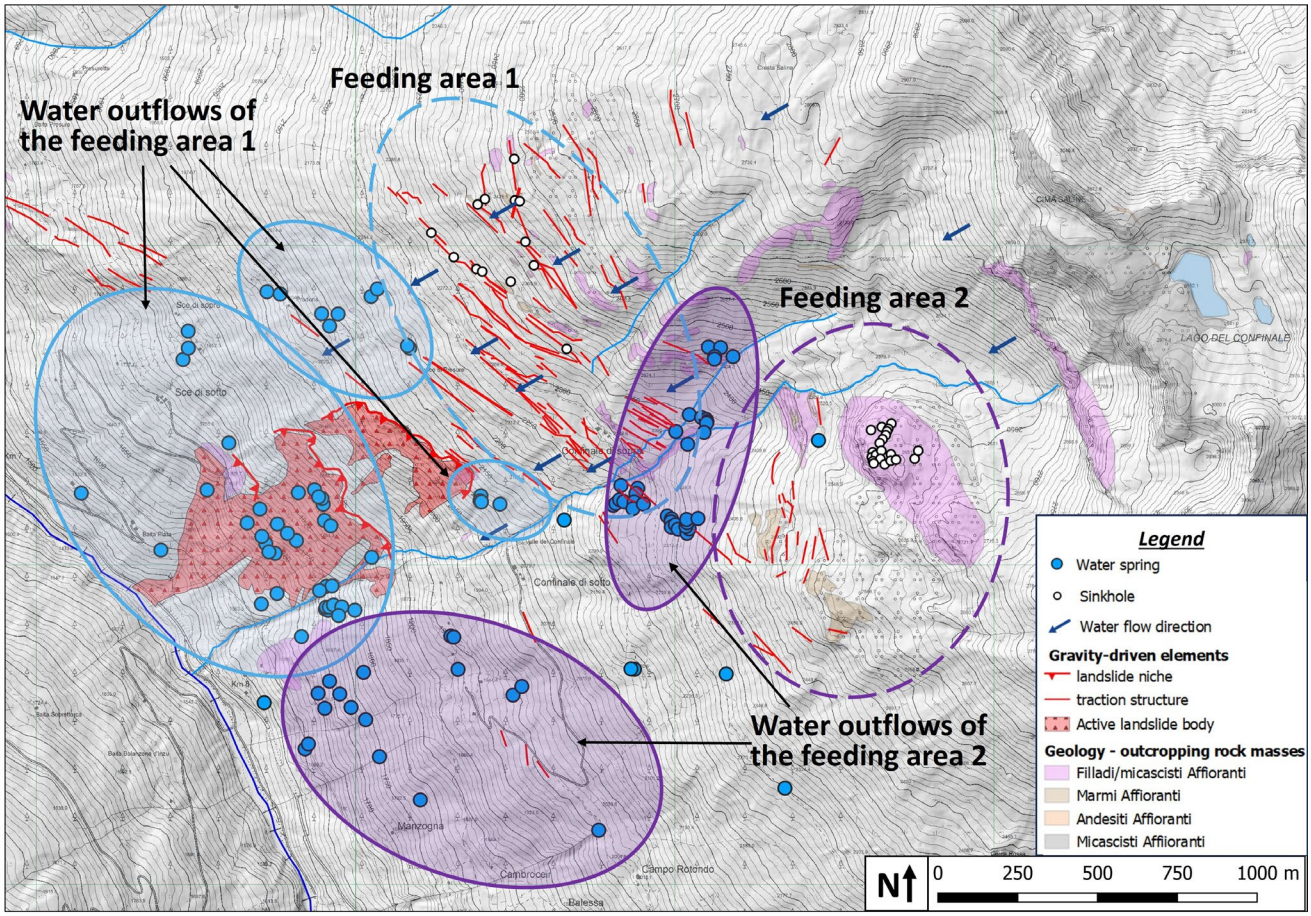

Figure 5.29 - Identification of major feeding areas and outflow zones related to the respective recharge areas.

They are essentially represented by: (i) the gravitational trenches and sinkhole systems upstream the main rockslide body and (ii) the top of the slope and the area with heavily fractured marble rock bodies. The supply elements are essentially rainwater, snowmelts and infiltrations from the Confinale creek.
With the aim of outline a hydrogeological model, it will therefore be of primary importance to consider the variability of the materials that drive the hydraulic behavior of the slope, through the definition of homogeneous hydrogeological bodies. Geological and geomorphological field observations have led to the identification of 8 stratigraphic units (i.e., bodies separated by genetic and/or depositional boundaries), represented by: rock-masses, active rockslide body, slope deposits, paleo-landslide deposits, glacial deposits, fluvio-glacial deposits and fluvial deposits. In order to parametrize these bodies and define the hydrogeological units (i.e., bodies with homogeneous hydraulic behavior), hydraulic conductivity classes are identified on the basis of:

- Nature of materials: type of deposits and rock-masses. Among them is possible to recognize: coarse loose deposit, loose deposit with fine matrix, loose deposit with abundant fine matrix, marbles and phyllites.
- Structural domain: the morpho-structural influence that faults, trenches and tensile structures can have on the hydraulic conductivity of quaternary deposits.
- Fracturing degree of rock-masses following the classes in section 5.3.3 (very fractured, moderately fractured and poorly fractured).

Taking into account these subdivisions, combining the criteria above, supported by the hydrogeological test results - as detailed below, 11 hydraulic classes have been distinguished (Table 5.17).

Table 5.17 - Definition of hydraulic conductivity classes from data obtained by in-situ hydraulic characterization tests (Section 5.3.4).

Hydraulic conductivity classes (m/s)						
	Coarse	*Coarse with fine matrix*	*Coarse with abundant fine matrix*	*Marble*	*Phyllites/ Shists*	
	D1	***D2***	***D3***	***Ma***	***Py***	
Undisturbed (Ud)	$5\cdot10^{-7}<k<5\cdot10^{-6}$	$1\cdot10^{-7}<k<1\cdot10^{-6}$	$1\cdot10^{-7}<k<1\cdot10^{-6}$	$1\cdot10^{-8}<k<1\cdot10^{-6}$	$1\cdot10^{-9}<k<1\cdot10^{-7}$	*Low fractured rock-mass (R1)*
Gravitational morpho-structures (Gd)	$1\cdot10^{-6}<k<1\cdot10^{-5}$	$5\cdot10^{-7}<k<5\cdot10^{-6}$	$5\cdot10^{-7}<k<5\cdot10^{-6}$	$k>1\cdot10^{-7}$	$1\cdot10^{-8}<k<1\cdot10^{-6}$	*Moderately fractured rock-mass (R2)*
			.		$k>1\cdot10^{-7}$	*Highly fractured rock-mass (R3)*

An initial characterization and definition of deposits hydraulic conductivity values is achieved through the interpretation of data in relation to RQD values, in the case of rock-masses, and to lithological/granulometric features, in the case of loose deposits. To support the latter classification, both data from past analyses (Lefranc, Lugeon tests) and data collected in the present work (sand cone tests and granulometric analyses) are used.

The definition of the rock-masses hydraulic units, mainly related to their degree of fracturing (*R1/R2/R3*), is performed based on hydraulic conductivity data from Lefranc and Lugeon tests. On the other hand, hydraulic conductivities for loose deposits (*D1/D2/D3*), are defined from infiltrometer and Lefranc tests.

The association of the conductivity classes on the stratigraphic units in the study area, 11 hydrogeological units with uniform hydraulic behavior are obtained as follows: low fractured phyllites (*PyR1*), moderately fractured phyllites (*PyR2*), highly fractured phyllites (*PyR3*), moderately fractured marbles (*MaR2*), slope deposit (*D1Ud*), slope deposit affected by gravitational morpho-structures (*D1Gd*), active landslide deposit (*D2Gd*), paleo-landslide deposit (*D3Ud*), glacial deposit (*D3Ud*), fluvioglacial deposit (*D2Ud*) and fluvial deposit (*D1Ud*). Added to them is the Ruinon rockslide shear band (ShB), which is characterized by very fine materials and low permeabilities (Table 5.18).

Table 5.18 - Definition of hydrogeological units considering hydraulic condictivity classes derived in Table 5.17.

Definition of hydrogeological units		
Unit	**Hydraulic conductivity class**	**Hydraulic conductivity range**
Low fractured phyllites	*PyR1*	$1 \cdot 10^{-9} < k < 1 \cdot 10^{-7}$
Moderately fractured phyllites	*PyR2*	$1 \cdot 10^{-8} < k < 1 \cdot 10^{-6}$
Highly fractured phyllites	*PyR3*	$k > 1 \cdot 10^{-7}$
Moderately fractured marbles	*MaR2*	$k > 1 \cdot 10^{-7}$
Slope deposits	*D1Ud*	$5 \cdot 10^{-7} < k < 5 \cdot 10^{-6}$
Slope deposit affected by gravitational morpho-structures	*D1Gd*	$1 \cdot 10^{-6} < k < 1 \cdot 10^{-5}$
Active rockslide deposits	*D2Gd*	$5 \cdot 10^{-7} < k < 5 \cdot 10^{-6}$
Paleo-landslide deposits	*D3Ud*	$1 \cdot 10^{-7} < k < 1 \cdot 10^{-6}$
Glacial deposits	*D3Ud*	$1 \cdot 10^{-7} < k < 1 \cdot 10^{-6}$
Fluvio-glacial deposits	*D2Ud*	$1 \cdot 10^{-7} < k < 1 \cdot 10^{-6}$
Fluvial deposits	*D1Ud*	$5 \cdot 10^{-7} < k < 5 \cdot 10^{-6}$
Rockslide shear band	*ShB*	$k < 1 \cdot 10^{-9}$

A 3D reconstruction of these units was performed in order to analyze their pattern in space and evaluate their relationship (Figure 5.30). The Geomodeller modeling software (Version 3.2.0; Intrepid Geophysics 2014), was used to build up the 3D hydrogeological units.

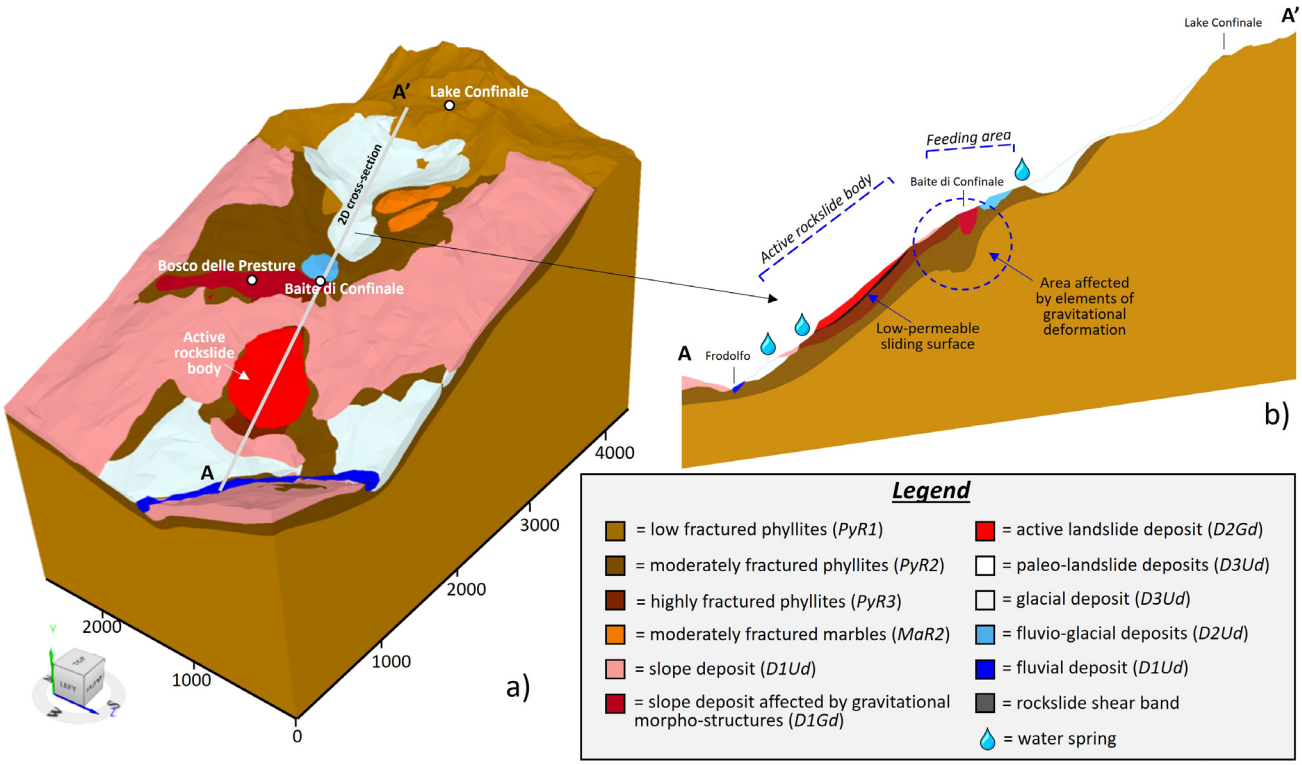

Figure 5.30 – Hydrogeological units setting, and associated properties, of the Ruinon slope. a) 3D hydrogeological units. b) 2D cross-section cutting the rockslide body along its longitudinal axis.

The starting point for the definition of the model is the distribution of the units on the morphological surface, which allowed to reconstruct their limits based on their genetic-depositional surface trend. The definition of the hydrogeological configuration at depth is supported by interpretative hydrogeological sections and the analysis of geological borehole logs. The areas of intense fracturing/medium fracturing that distinguish the rockslide body are reproduced by maintaining the bands of intense fracturing (*PyR3*) at depths of about 80 m lying over a shear band characterized by low hydraulic conductivity values (Figure 5.30b). Between the surface units and the low fractured phyllites (*PyR1*), which represent the bedrock at depth, an intermediate transitional band of moderately fractured phyllites (*PyR2*) are included (Figure 5.30b).

The geomechanical and hydrogeological model presented will be used in the next Sections to simulate groundwater flow, evaluate the relationship between the different hydrogeological units that make up the slope and validate the observations made.

5.5 Evaluation of landslide susceptibility of the Ruinon slope using a 3D FEM approach

The first step toward the numerical comprehension of a complex and active gravitational instability phenomenon, such as the Ruinon rockslide, is to explore its mechanical evolution by analyzing stress and strain distributions in response to internal (i.e., mechanical properties) and external (i.e., driving factors) variations. Among all the numerical tools (Section 2.1), stress-strain techniques represent in fact the best solution to quantify slope stability and simulate slope mechanical evolution under different scenarios, as already demonstrated in this work for the Cimaganda and the Piuro case studies (Sections 3 and 4).

In this Section, a 3D FEM numerical model, aimed to analyze the stress-strain distribution along the Ruinon slope, is presented. The goal is to define the relationship between morphological factors, mechanical parameters, hydrogeological features and the occurrence of irreversible strains along the slope, representing a key step toward understanding the processes that led to the development of the active rockslide. The analysis presented in this Section also aims to explore the use of finite element numerical tools to evaluate the most prone areas to gravitational instability, by only considering the slope morphology, the mechanical properties of the geological medium, and the gravity factor. Because of its simplicity and the limited number of parameters required by the analysis, this tool may represent a valuable approach for preliminary landslide risk assessment and the installation and implementation of monitoring systems in areas of known instability.

The model was validated by comparing numerical outputs with morphological field observations, by focusing on the geometric elements of the rockslide bodies detected in the region (depth of the sliding surface and location of irreversible deformations). A parametric analysis was carried out, and different representative piezometric level scenarios were also introduced to assess the influence of both mechanical parameters and pore pressure on the distribution of high sliding susceptibility areas in the model.

The analysis is a first step toward understanding the Ruinon mechanical evolution and is a preliminary step toward the development of more complex models, that links the external forcing of the rockslide with its internal response, to forecast its stability and velocity by identifying critical values, which can be measured in the field.

5.5.1 Methods

FEM analysis of the Ruinon rock slope was performed using the open-source C++ MOOSE (Multiphysics Object-Oriented Simulation Environment) framework, developed by the Idaho National Laboratory (Icenhour et al. 2018) and presented in Section 2.3. The geometrical model of the study area was built with *Gmsh* (Geuzaine and Remacle 2023), an external 3D finite-element mesh generator. In *Gmsh*, a model is defined using its boundary representation: a volume is bounded by a set of surfaces, a surface is bounded by a set of curves, and a curve is bounded by two endpoints. Each topological element can be uniquely named to apply a physical boundary condition. The finite element mesh of the model is a tessellation of its geometry, with simple elements of various shapes (lines, triangles, quadrangles, tetrahedrons, prisms, hexahedrons, and pyramids), arranged in such a way that if two of them intersect, they do so only along one face, edge or node, and never otherwise.
The output files of mechanical simulations were read in a binary format with *Paraview*, an open-source multiple-platform for interactive visualization (Ayachit et al. 2018).

5.5.1.1 Modelling approach

The mechanical model developed in MOOSE is based on the Tensor Mechanics module, a library of simulation tools that solve continuum problems. The rock slope is therefore simulated as a continuum and homogeneous domain, where an elasto-plastic constitutive law is assumed.
The mechanical deformation is solved by the momentum balance under static assumption, leading to the evolution of effective stresses σ', defined as:

$$\frac{\vartheta \sigma'_{ij}}{\vartheta x_{ij}} + \rho_S g_i = 0 \qquad \text{(Equation 5.5)}$$

Where ρ_S is the density of the solid and g_i the gravity vector. The total strain rate, γ_{ij}, is decomposed into a reversible (elastic), γ_{ij}^r, and an irreversible (plastic), γ_{ij}^i, part:

$$\gamma_{ij} = \gamma_{ij}^r + \gamma_{ij}^i \qquad \text{(Equation 5.6)}$$

The reversible part is assumed to follow a linear elastic relationship of the form:

$$\gamma_{ij}^r = C_{ijkl}^e \sigma'_{ij} \qquad \text{(Equation 5.7)}$$

Where, σ_{ij}' represents the effective stress tensor and C_{ijkl}^e is the elasticity tensor. The irreversible part of the strain rate follows a plastic law of the form:

$$\gamma_{ij}^{i} = \chi \frac{\partial g}{\partial \sigma_{ij}} \quad \text{(Equation 5.8)}$$

Where, g represents the plastic potential and χ is a scalar plastic multiplier. The specification of the yield criterion involved the Coulomb plastic formulation with a softening scheme, which postulated a linear relationship between shear strength on a plane and the normal stress acting on it:

$$\tau = c - \sigma_N tan\phi \quad \text{(Equation 5.9)}$$

where τ is the shear strength, σ_n is the normal stress (positive in tension), ϕ is in the angle of internal friction, and c is the cohesion. Combining the Coulomb criterion with the Mohr circle representation of stress state, and considering the admissible states, the Mohr-Coulomb (MC) failure criterion (FoS) in terms of principal stresses can be expressed as:

$$F_S = \frac{1}{2}(\sigma_1 - \sigma_3) + \frac{1}{2}(\sigma_1 + \sigma_3)sin\phi - c * cos\phi = 0 \quad \text{(Equation 5.10)}$$

As many materials described by MC plasticity, such as rocks, cannot sustain large tensile stresses, a tensile cutoff in the failure criterion was also considered (Icenhour et al. 2018). The yield surface representing the tension cutoff is defined as:

$$F_t = \sigma_3 - \sigma_t = 0 \quad \text{(Equation 5.11)}$$

Where, σ_t is the tensile strength of the material. In 3 dimensions, MC plasticity is defined by six yielding functions that are planar in the coordinates of principal stresses. They produce a region of admissible stresses in the shape of a hexagonal pyramid. Adding the tensile cutoff, the pyramid's tip is removed, turning it into a triangular-based pyramid.

The mechanical framework can be also extended to account for pore fluid pressure and the evolution of porosity by the use of MOOSE's PorousFlow module. The momentum balance equations for the fluid phase can be expressed as:

$$\beta \frac{\partial P_f}{\partial t} = \alpha_V \nabla^2 P_f - \gamma_V^{pl} \quad \text{(Equation 5.12)}$$

Where β is the compressibility factor, P_f is the pore pressure, α_V is the Biot coefficient (which is kept equal to 1 in the present work), and γ_V^{pl} the volumetric plastic strain. The pore pressure evolution is defined as:

$$P_f = P_h + \Delta P_f \quad \text{(Equation 5.13)}$$

Where, P_h is the hydrostatic pressure, and ΔP_f the excess pore pressure. Following Terzaghi's principle, the dependence of the pore fluid pressure, P_f, on the stress, σ_{ij}, is stated explicitly as:

$$\sigma_{ij} = \sigma'_{ij} - \alpha_V \delta_{ij} P_f \quad \text{Equation 5.14}$$

Where, σ_{ij}' is the effective stress (stresses are taken negative in compression). Volumetric strains control the evolution of porosity and the volume that can be occupied by a fluid. This process is fundamental to the coupling between fluid flow and solid mechanics. The total porosity, θ, is expressed as the sum of its initial value (θ_0) and the changed interconnected pore volume. In this model, the pore volume can be modified only by mechanical processes ($\Delta\theta_{mech}$). The evolution of the mechanical porosity contains two components, an elastic part:

$$\Delta\theta^e_{mech} = (1-\theta)\beta_S \Delta P_f \quad \text{(Equation 5.15)}$$

Where β_s is the compressibility coefficients of the solid, and a plastic part:

$$\Delta\theta^{pl}_{mech} = (1-\theta)\Delta\gamma^{pl}_V \quad \text{(Equation 5.16)}$$

being $\Delta\varepsilon^{pl}_V$ the increment of the volumetric plastic strain. Therefore, the total porosity is defined by the relation:

$$\theta = \theta_0 + \Delta\theta_{mech} = \theta_0 + \Delta\theta^e_{mech} + \Delta\theta^{pl}_{mech} = V_f/V \quad \text{(Equation 5.17)}$$

Where V_f is the volume occupied by the fluid. Considering the scale of the analysis (slope to regional), Darcy's law is used to relate the mass flux to the pore pressure gradient, under saturated conditions:

$$q = (v_f - v_s)\theta = -\frac{k}{\mu_f}(\nabla P_f - \rho_f g_i) \quad \text{(Equation 5.18)}$$

Where, v_f is the velocity of the fluid, v_s is the velocity of the solid, θ is the total porosity, μ_f is the viscosity of the fluid, k the permeability, and g_i the gravity vector. In the model, the permeability is considered isotropic and constant (i.e., not dependent on porosity).

5.5.1.2 Definition of the model geometry

The modeled region is coincident with the areal extent of the model presented in Section 5.4, laying between the Cavallaro valley to the N and the Confinale valley to the S (Figure 5.31a). To the W, the model limit is represented by the main valley floor with the Frodolfo river, flowing towards NW, while to the E, the boundary is represented by the mountain ridge separating the Valfurva from the Zebrù valley. The model includes the areas where the main instability phenomena of the region have been observed, namely the Ruinon and the Gembresca rockslides (Section 5.2).

The model has a squared shape base, and it covers an area of 15.8 km^2, calculated from the topographical surface. The highest elevation of the model is 3072 m a.s.l., in correspondence with the Saline peak, and the lower one is 1370 m a.s.l. along the main Valley floor.

The geometrical model was developed based on the 2015 Digital Terrain Model of the Lombardy Region (Regione Lombardia 2015) and assuming a homogeneous and isotropic medium (Figure 5.31a).

The morphology introduced in the model is therefore referable to the year 2015, corresponding with the beginning of the time interval of the monitoring data presented in the Section 5.3.6. The model was discretized into a finite-element mesh, by the definition of hexahedral zones (Figure 5.31b).

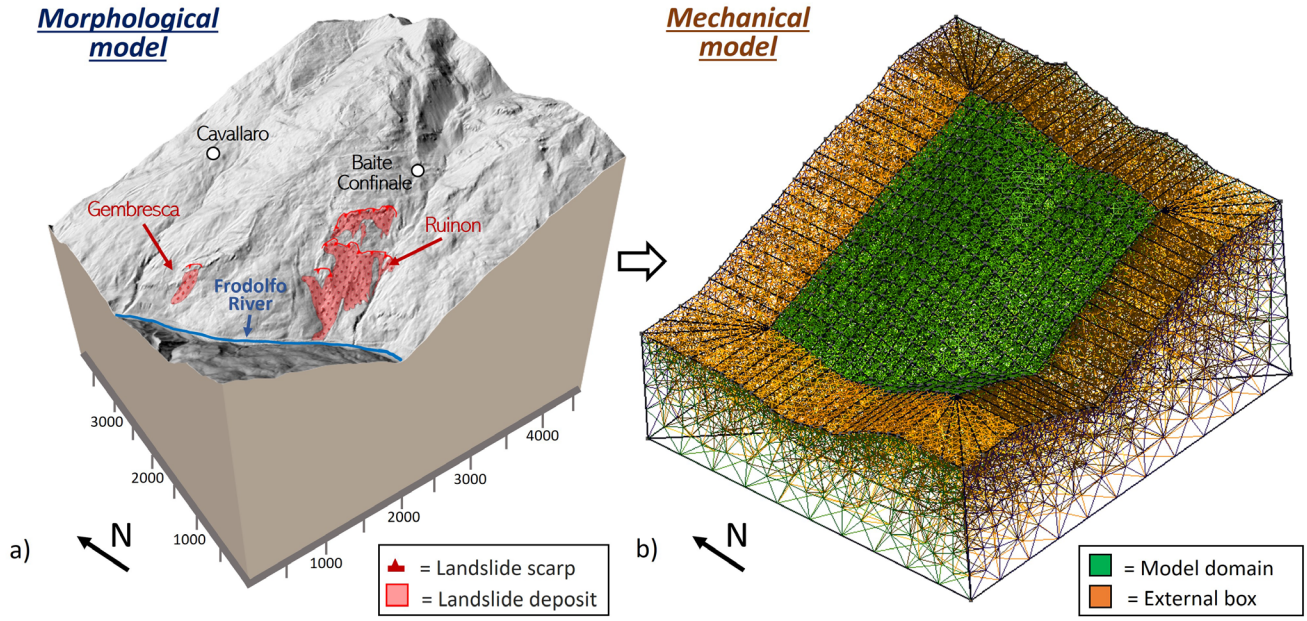

Figure 5.31 – a) Areal and morphological extension of the modeled domain. b) Definition of the computational model and external domain.

A maximum zone size of 200 m was set, allowing the meshing software to create a grid that best fits the morphology, hence obtaining a significant reduction in computational time. To speed up computational times, the mesh size increases with depth until it reaches maximum value of 500 m. Boundary conditions fixed at zero velocity were specified along the bottom boundary of the entire model, as well as at the external side boundaries. To minimize the mechanical effects due to the presence of lateral geometric constraints in the modeled area, an 'outer box' was defined by extending the lateral boundaries by 1000 m. Without this artifice, the application of Dirichlet-type mechanical boundary conditions at zero velocity, would result in the development of unrealistic stresses and strains near the boundaries and bring about significant computational errors in the area of interest.

The model was parameterized according to the mechanical parameters presented in Section 5.3.3 and summarized here in Table 5.19. As a first assumption, considering the lithological homogeneity of the study area (Section 5.3.1), the mechanical parameters presented in Table 5.19 were applied to the entire modeled domain. An elasto-plastic MC constitutive model was adopted for the model domain, whereas a linear elastic behavior was assumed for the 'outer box'.

Table 5.19 - Summary of representative mechanical parameters of the rock-masses outcropping along the Ruinon slope.

Parameter	Representative rock-mass value	Detection method
Density	2700 kg/m^3	Laboratory test (Section 5.3.3)
Young modulus	35 GPa	Laboratory test (Section 5.3.3)
Poisson ratio	0.3	Laboratory test (Section 5.3.3)
Cohesion	1 MPa	Laboratory test (Section 5.3.3)
Friction angle	35°	Laboratory test (Section 5.3.3)
Tensile strength	5.11 MPa	Laboratory test (Section 5.3.3)
Porosity	0.1	Assumption

Concerning the HM analysis, a basal water table was introduced, and free outer boundaries were defined by keeping pore pressures at constant values. The piezometric surface is represented by an external surface, introduced into the model by setting zero pore pressure along it. Then, hydrostatic pore pressures are calculated by the model, based on the location of the piezometric surface and gravity forces. In this study, the water table was defined in a simplified way considering the presence of the Frodolfo River flowing in the valley bottom and taking into account the water table level measured in the piezometer located along the slope at the Ruinon rockslide body. These represent fixed points through which the piezometric surface was drawn. The elaborated piezometric surface represents the shallowest aquifer, whose temporal evolution influences the mechanical evolution of the slope. The HM analysis presented is intended to be exploratory and representative of average hydrogeological conditions, with the aim of verifying the influence of hydrological variables in the mechanical evolution of the slope.

5.5.1.3 Modelling procedure

In a first step (*Step 1*), a static analysis was performed under dry conditions and representative mechanical properties of the slope (Table 5.19). The model was then validated, by comparing simulation results with geomorphological observations, i.e., by overlaying satellite images with model results. Four

different meshes were used as inputs to evaluate the influence of the grid size on numerical results (stress and strain distribution), and to identify the best configuration, in terms of computational cost and accuracy of the results. Once the model was validated and the best performing mesh was identified, the next two steps (*Step 2* and *3*) included a mechanical and a HM parametric analysis, respectively.

In *Step 2*, the *c* value was varied from 1 MPa to 0.25 MPa, to evaluate and quantify the effect of strength parameters in the development of irreversible deformation. As discussed in Section 5.3.3, the range of equivalent Mohr-Coulomb values identified by field investigations and laboratory tests, varies between 0.75 and 0.4 MPa; therefore, the range chosen in the parametric analysis is sufficient to evaluate the simulated deformation pattern in the presence of both good and extremely degraded rock-masses.

In *Step 3*, three different piezometric level scenarios were defined, based on the field data installed along the Ruinon slope (Section 5.3.4). The water level scenarios were defined as follows: (i) ordinary regime (water level in the piezometer at 40 m depth), (ii) maximum regime (30 m depth), and (iii) an extreme regime (20 m depth). The aim of this parametric study was to analyze the role of morphology, mechanical parameters and pore pressure in the development of irreversible strains. The evolution of effective stresses at varying groundwater level in correspondence of the Ruinon sliding surface depth, was also explored, for future development of the analysis.

5.5.2 Results

Model results were analyzed in terms of the development of irreversible deformations along the slope, as well as the redistribution of the stress–strain field within the model domain. With reference to the theoretical background presented in Section 5.5.1.1, plastic deformation defines the irreversible part of the strain tensor, highlighting area where gravitational instabilities preferentially develop. In *Step 1*, the stress-strain state along the model domain, only brought about by gravity and 3D topographical constraints, was simulated (Figure 5.32a-b-c). It can be noticed that zones of high deformation mainly develop in the eastern portion of the model and on its southern border. Focusing on the magnitude and distribution of shear plastic strain, two main clusters of large deformation were identified. The first one, corresponding to the Confinale valley, extends from the bottom of the Frodolfo valley up to an elevation of 2000 m a.s.l. The second one is located along the valley floor, with a main concentration of strains on the southern limit of the model (Figure 5.32d). The maximum shear plastic strain values detected lie in the range between 0.03 and 0.04%.

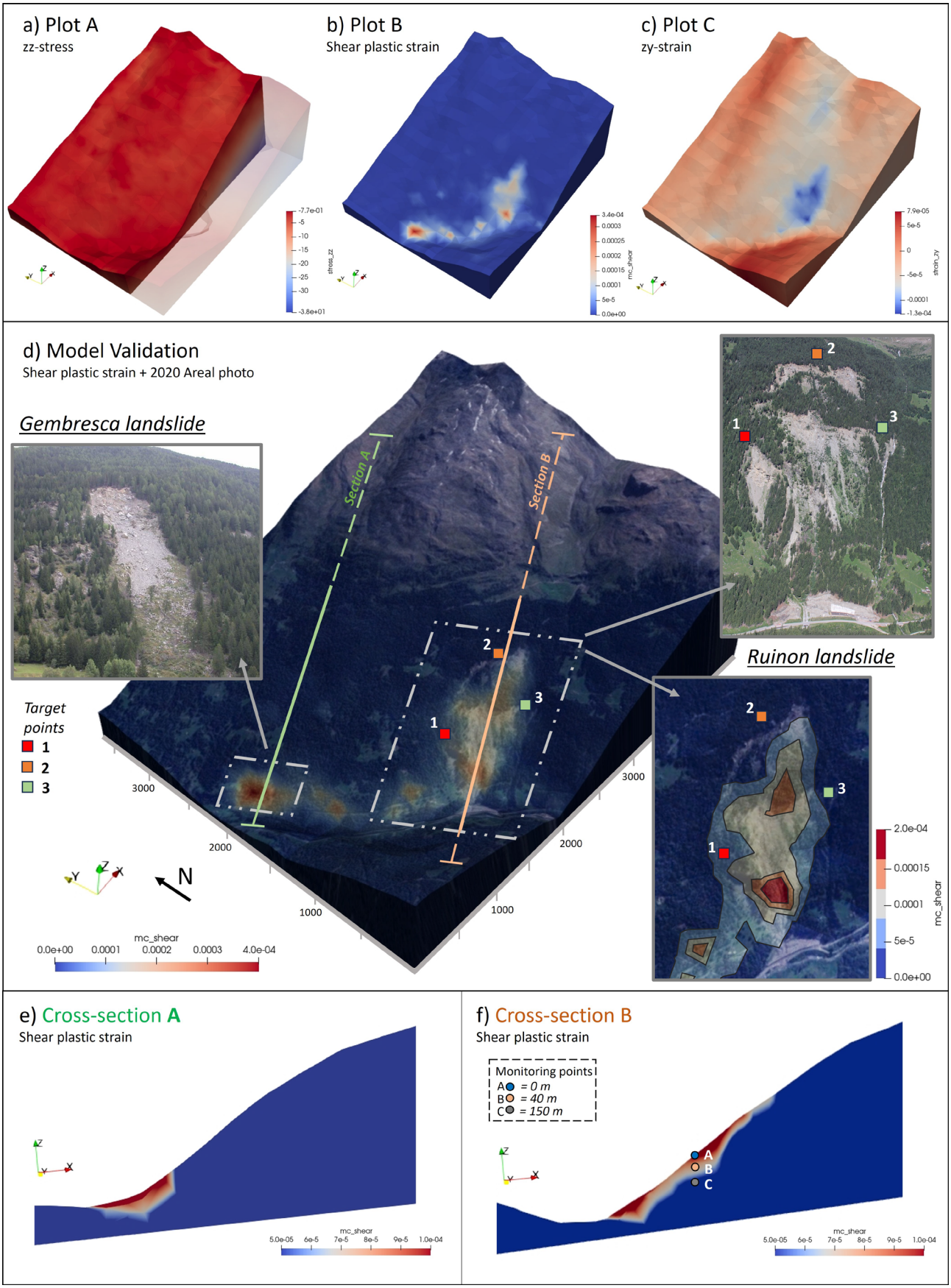

Figure 5.32 - a,b,c) Results of the stress-strain analysis in dry conditions. d) Model validation by overlapping shear plastic strains with satellite imagine of the study area. e,f) Slope cross sections along the gembresca rockslide and ruinon rockslide showing plastic deformation trends.

To validate the model and relate simulation outputs to the gravitational processes that affect the study area, a comparison between model outputs and geomorphological observations was performed. Hence, the satellite image of the study area (Google 2022) was overlaid to the model domain, by matching each pixel of the image to the model coordinates. As shown in Figure 5.32d, a good correlation was observed between the location of the simulated irreversible deformation zones and the gravitational instability events, affecting the modelled area (Ruinon and Gembresca rockslide). Moreover, analysing the 2D cross sections taken along the model domain (Figure 5.32e-f), the geometries of the rockslide bodies were reproduced with a good qualitative accuracy. Cross-Section A in Figure 5.32e explores the evolution of the Gembresca rockslide, which has been documented to involve only a shallow and limited portion of the slope (Griffini 2013), as correctly simulated by the model.

Concerning the Ruinon rockslide, the cross-section B of Figure 5.32f, cuts the slope along its active body, following its sliding direction. In this cross-section, it can be observed that the maximum irreversible deformations are simulated in the shallowest portion of the slope and become zero at a depth greater than 150 m. Geomorphological and geomechanical observations discussed in Section 5.3.3 and 5.4 highlighted a composite slip surface at about 80 m depth, and an upper scarp of the rockslide body at about 2100 m a.s.l. Considering these observations, in both 2D and 3D space, the model adequately simulates the gravitational evolution of the slope, and the observed volumes of the sliding masses are comparable with the simulation results. After model validation, different mesh sizes were tested to identify the best configuration, in terms of computational cost and accuracy of results. Sizes of 100, 150, 200, and 250 m were tested (Figure 5.33).

It may be observed that the distribution of plastic strains is consistent in all mesh configurations (Figure 5.33), where the two main clusters of irreversible deformation discussed earlier during the validation process are maintained. However, with a finer mesh, the geometries of the rockslide bodies are better defined. In addition, adopting mesh sizes of 100 or 150m the presence of deformation along the valley bottom is well reproduced.

With a mesh size of 100 m, the model simulation ends after 1000 seconds using a standard desktop multicore workstation. By increasing the mesh size, the computation time is significantly reduced, while the limits of high deformation bodies become less defined. The mesh size of 250 m is not sufficient to simulate the gravitational instabilities affecting the model domain, exhibiting a very poor definition due to the large grid size. Computation times are reduced to 20 seconds for the 200 m mesh, and to 15 seconds for the 250 m mesh. Considering the good consistency of the outputs held by the models with different mesh sizes, it was deemed appropriate to continue the analysis with the 200 m grid, on which the validation process was performed. In this way, computational times could be kept low, even

considering the subsequent introduction of the HM coupling, likely to lead to a substantial increase in simulation time.

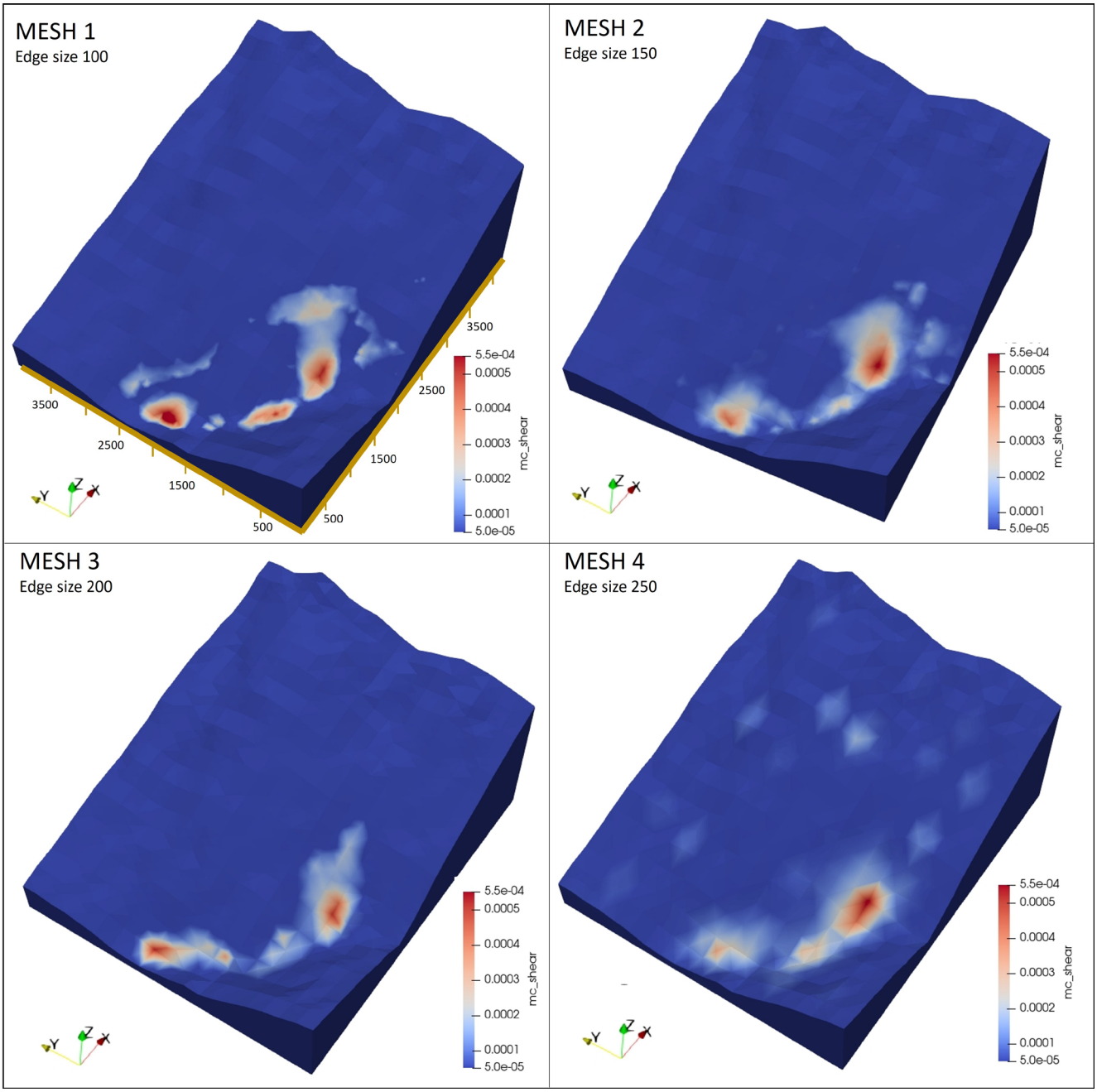

Figure 5.33 - Distribution of plastic shear strains resulted by considering different computational mesh sizes.

In *Step 2*, a parametric analysis was performed to explore the relation between *c* values and the development of plastic strains (Figure 5.34a,b,c,d,e). Moving *c* from 1 MPa to 0.25 MPa, led to a considerable increase in the development of plastic deformation. However, even if shear plastic strains increase in their magnitude, the extent of area affected by irreversible deformation and the location of

the two high strain clusters (Figure 5.34a,b,c,d), do not change significantly.

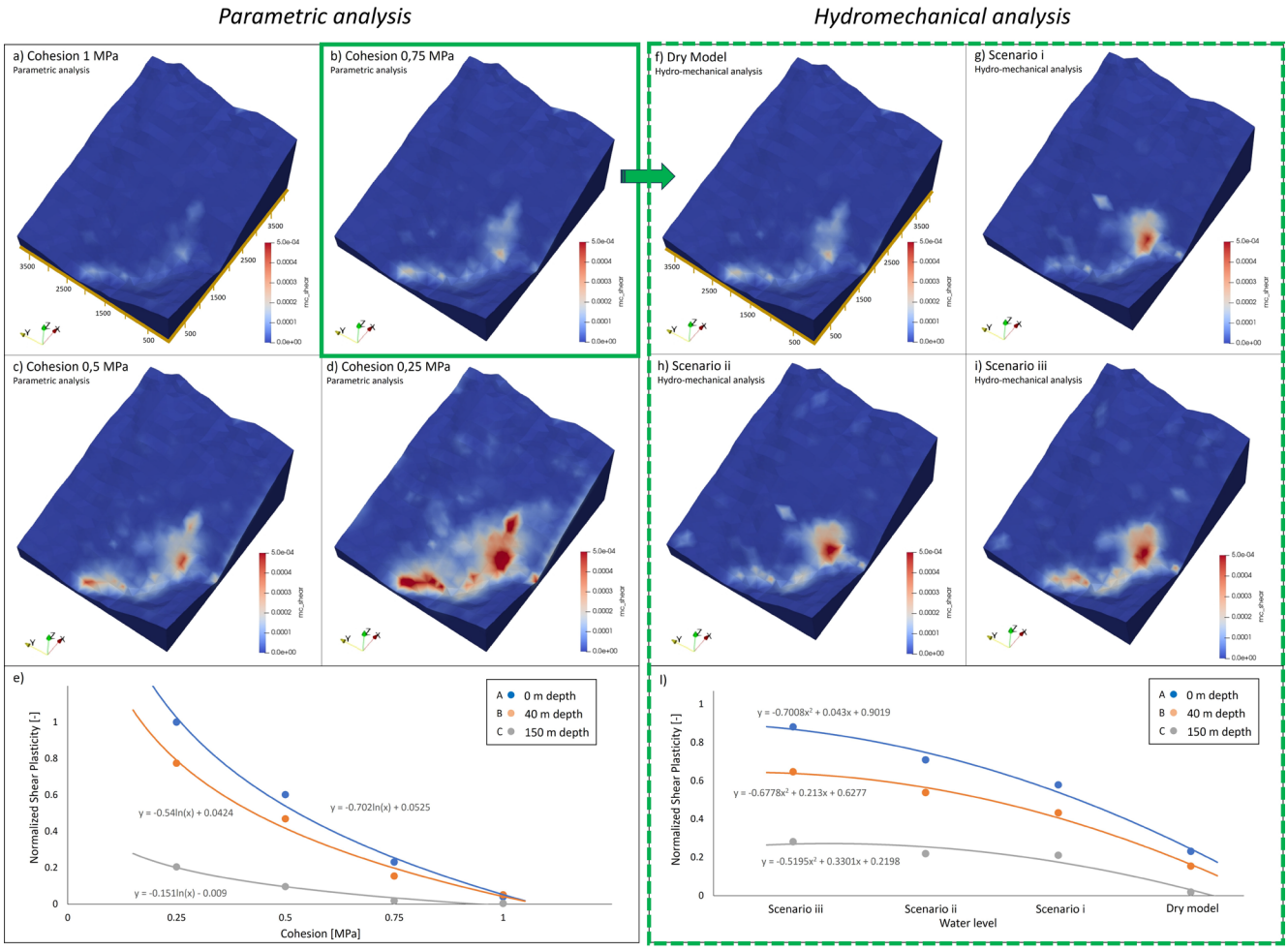

Figure 5.34 – Model outputs of parametric and HM analysis. a,b,c,d) Plots showing the evolution of plastic strains for a range of c values. e) Graph showing the evolution of normalized plastic deformations for different c values at different depths (see Figure 5.32 for the location of monitoring points). f,g,h,i) Plots showing the evolution of plastic strains for 3 scenarios of groundwater levels. e) Graph showing the evolution of normalized plastic deformations for different groundwater levels at increasing depths (see Figure 5.32 for the location of monitoring points).

To analyze the trend in strain magnitude with the evolution of mechanical parameters, a vertical profile was defined, in correspondence of the Ruinon rockslide body and three reference points A, B, C (see Figure 5.32f) were monitored: Point "A" is located on the slope surface, Point "B" inside the rockslide body (40 m depth), and Point "C" at a depth of 150 m (i.e. below the slip surface detected by geotechnical site investigations). As shown in Figure 5.34e, a logarithmic relationship could be identified between *c* values and normalized shear strain magnitude values (defined as the ratio of the measured value to the maximum simulated one) at all the three monitoring points (A, B, and C): starting from low strain values (0.001 to 0.003%) at 1 MPa of *c* (quite stable conditions of the slope), large strain values (0.05 to 0.06%) were obtained at a *c* of 0.25 MPa.

The two most shallow points A and B (orange and blue lines in Figure 5.34e) exhibited a similar behavior with curves that follow the same evolutionary trend. On the other hand, the deeper point at 150 m depth (grey line in Figure 5.34e) showed a more stable behaviour, even at very low *c* values (0.25 to 0.5 MPa). This trend is consistent with the geomechanical evolution of the slope reconstructed from site investigations, suggesting the slope to be stable at depths greater than 100 m (below the sliding surface, located at 70-90 m depth).

In *Step 3* of numerical modelling, hydrogeological factors were introduced, considering the 3 different water level scenarios defined. A clear correlation was shown between the piezometric surface level and the evolution of plastic deformation, with effects comparable to those induced by the mechanical degradation process (Figure 5.34f,g,h,i,l). Furthermore, a linear dependence between effective shear stresses and pore pressure was observed (i.e., at constant depth, as pore pressures increase, the effective shear stresses decay, according to a linear relationship). Comparing the "dry-model" with the "scenario-I drained-model" results, an increase in the magnitude of strain values was observed. As the piezometric level rises, the magnitude of plastic deformation increases, while the areal distribution of zones under irreversible deformation remains the same. However, the rising water level also induces the development of plastic strains along the main valley floor, because of the increase in pore pressures at the bottom of both valley flanks. Analyzing the monitoring points A, B, C along the Ruinon rockslide body (Figure 5.34l), a polynomial (i.e., parabolic) relation was detected between the magnitude of plastic shear strains and the simulated trend of the piezometric level. The introduction of pore pressures (transition between "dry model" and "scenario-I drained-model") generates a sudden increase in strain values (as an example, the normalized strain values recorded at point A in Figure 5.34l increased from 0.3 to 0.7), while the subsequent progressive rising of the water table causes only a limited strain growth (at the same point, normalized strain values increased from 0.7 to 0.9).

The analysis showed that decreasing the *c* values has a greater influence on strain rates respect to the increasing of pore pressure. Overall, a good correspondence with the observed geotechnical evolution of the slope is maintained, with higher plastic strain in correspondence of the shallower points and greater stability at the deepest one.

5.5.3 Discussion

A numerical 3D FEM model was defined to analyze the role of morphological, mechanical and hydrogeological factors in the development of instability processes along the Ruinon rock-slope. It assumes a homogeneous and isotropic material, with no slip surfaces established a priori. From

morphological data, geomechanical field surveys and laboratory test results, a simple mechanical model was defined using a standard elasto-plastic constitutive law. In a first step of the analysis, a static simulation was performed under dry conditions considering representative mechanical properties of rock-masses. Numerical results are shown to accurately reproduce the extent of the area affected by gravitational instabilities: overlapping satellite images with the model outputs, a good correspondence between area of simulated irreversible deformation, and the location of gravitational instability phenomena was verified. Then, mechanical and HM parametric analyses were performed, exploring different stress-strain evolutive scenarios. In both cases, a clear correlation between input factors and the magnitude of simulated strain has been shown, while the spatial distribution of irreversible deformations does not change significantly.

A homogeneous and isotropic model was adopted, not including lithological variations or the presence of significant geological elements such as faults or thrusts. This assumption is coherent with observations carried out in Sections 5.3.1 and 5.4.

Focusing on the development of the Ruinon rockslide body, the use of a simple and homogeneous model allowed to highlight the role of morphology as a main driving factor. In the dry analysis in fact, the development of irreversible deformation in correspondence with the rockslide body is not defined by any significant geological feature or lithological contact, but only by the combination of morphological and mechanical features. Even though mechanical degradation leads to an increase in strain values in terms of magnitude, the development of gravitational instability occurs in all mechanical scenarios and is therefore mainly related to the morphological features of the slope.

Concerning mechanical data, it has been demonstrated that different values of c (from 1 to 0.25 MPa) result in an increase in the magnitude of strains (0.001 to 0.06%), without a significant change in the distribution of unstable zones. The c values introduced in the different mechanical scenarios allowed to explore all the main slope geomechanical settings detected in the Section 5.4. Higher instability is linked with the worst mechanical scenario (detected at the Ruinon rockslide), while less evidence to gravitational instability is related with better mechanical properties.

The HM analysis presented showed a significant dependence between the depth of groundwater level and the development of plastic deformation, highlighting the role of the distribution of pore pressures along the slope as the main driver of rockslide activity. From these observations, combined with field monitoring investigations, came the need for more in-depth knowledge of groundwater flow patterns and the distribution of water bodies, that will be explored in next Sections.

Verified the role of morphology with a continuous and homogeneous approach, the use of a discrete element approach may be explored in future developments of the analysis so as to analyze the influence

of fracture state in promoting gravitational instability phenomena along the slope. The presented analysis also allowed to calculate the stress state along its sliding surface: the basal mean shear stresses detected at a depth of about 80 m varies between 0.2 and 0.5 MPa, depending on the groundwater level. A linear dependence between the pore pressure and the effective shear stresses has been detected allowing, as a first approximation, to use a simple linear equation to calculate the stress state along the slip surface of the rockslide, depending only on the depth of the water table. These values will be useful in the development of more complex numerical analyses presented in the next Sections.

5.6 3D Hydrogeological modelling of the Ruinon slope

From the processing of monitoring data and the results of an exploratory HM numerical analysis, a significant role of groundwater in the mechanical evolution of the rockslide is evident. However, the hydrogeological processes and the deep aquifer recharge system of the Ruinon slope are not yet well understood. These elements and features give rise to the need for a deeper understanding of the hydrogeological regime characterizing the slope, through the development of numerical modeling analysis able to simulate groundwater flow and the evolution of water bodies in relation to external hydrological inputs.

In this section, a 3D hydrogeological analysis is developed from the model presented in Section 5.4. Through the introduction of water availability data along the slope calculated as the sum of rainfall and snowmelt (Section 5.3.5), the aim is to reconstruct the hydrogeological regime of the slope and assess the presence of water bodies within the rockslide as well as its hydraulic recharge mechanisms. The model was calibrated and validated on the basis of measured and simulated piezometric level data in correspondence of the piezometer PZ4 (Section 5.3.4)

5.6.1 Methods

Three-dimensional numerical modeling of groundwater circulation along the Ruinon slope, was conducted using the SEEP3D finite element software (Seequent 2022), presented in Section 2.3.

In this software, the governing differential equation used in the formulation of the seepage analysis at constant void ratio in 3D space is:

$$\frac{\partial}{\partial X}\left(k_X \frac{\partial h}{\partial X}\right) + \frac{\partial}{\partial Y}\left(k_Y \frac{\partial h}{\partial Y}\right) + \frac{\partial}{\partial Z}\left(k_Z \frac{\partial h}{\partial Z}\right) + Q = \frac{e_0}{1+e_0}\left(\frac{\partial S}{\partial t}\right) \quad \text{(Equation 5.19)}$$

Where k_x, k_y, and k_z are the coefficients of permeability in the x, y and z directions, respectively; h is the total head; Q is the flux at the model boundaries; S is the degree of saturation; e_0 is the void ratio (assumed constant in subsequent calculation); and t is the time.

The starting point of the analysis was the set-up of the hydrogeological model presented in the Section 5.4. Then, with the aim of simulate the hydrogeological regime and study the responses of water bodies to rainfall inputs, the analysis developed in 3 main steps: (i) definition of representative hydrogeological conditions of the slope in a steady-state regime (referred to the 2014 year), (ii) transient analysis - training model (years 2015-2016), (iii) transient analysis - forecasting model (years 2017-2021).

5.6.1.1 Hydrogeological model set-up

The model areal extension includes all the significant hydrogeological elements characterizing the slope, as well as the area where the main instability phenomena of the region have been observed. The modelled region lies between the Cavallaro valley to the N, and the Confinale valley to the S (Figure 5.35a). To the W, the model limit is represented by the main valley floor with the Frodolfo river, flowing towards NW, while to the E, the boundary is represented by the mountain ridge separating the Valfurva from the Zebrù valley.

With the aim of outlining a hydrogeological model of the slope, which takes into account the variability of materials that drive its hydraulic behavior, 11 homogeneous hydrogeological bodies were defined in Section 5.4, and summarized in Table 5.18. Hydraulic parametrization, extensively discussed in Section 5.4, is now taken up in this analysis where it will be validated. A simple hydraulic model was considered, meaning a two phase media consisting of soil skeleton and water. The two parameters required by the model were thus only hydraulic conductivity and volumetric water content, which are constant in time avoiding suction process (i.e., in the unsaturated zone pore pressure is equal to zero).

Considering that the aims of the present analysis are to simulate the groundwater flow under ordinary conditions and to analyze the evolutions of the main water bodies in response to rainfall inputs, the boundary conditions imposed try to replicate the hydraulic conditions prevailing in situ. In particular, along the sides and at base of the model, no-flow conditions were imposed, while, at the surface, water in-flow conditions are applied (Figure 5.35b). Along the valley bottom, in correspondence of the Frodolfo river, constant head conditions equal to the hydrometric height of the stream were defined. In addition, to account for the presence of the Confinale creek and the volume of water infiltrating along its path, an inflow region coincident with the area in which the stream flows was introduced (red area in Figure 5.35b).

Regarding the assessment of in-flow water along the slope, regions with homogeneous infiltration capacity were specified. The same methodological procedure presented in Section 5.3.5.2 for the runoff coefficient calculation, was here applied. Considering soil hydraulic properties, ground vegetation cover, average slope, surface water network development and drainage shape, it was possible to define five regions with homogeneous runoff coefficient (Figure 5.35b). These regions were defined by following the different slope elevation ranges: regions extend perpendicular to the slope morphological gradient and cover an elevation range depending on the thickness of geomorphological bodies (Figure 5.35b). In this way, it is possible to calculate the water runoff from each region, which is added to the rainfall input of the region altimetrically below. The elevation ranges and the values of runoff coefficients, calculated considering the water availability of the year 2014, considered are summarized in Figure 5.35c.

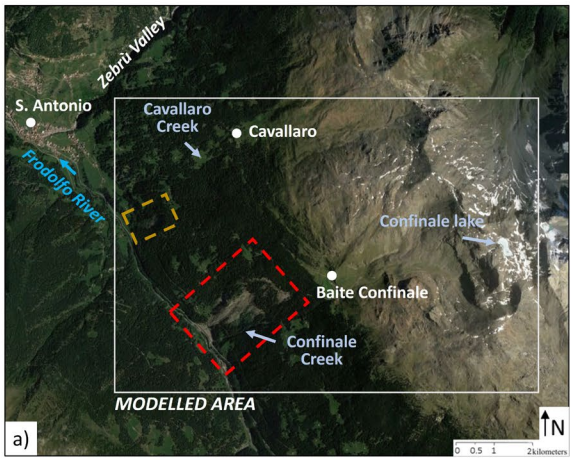

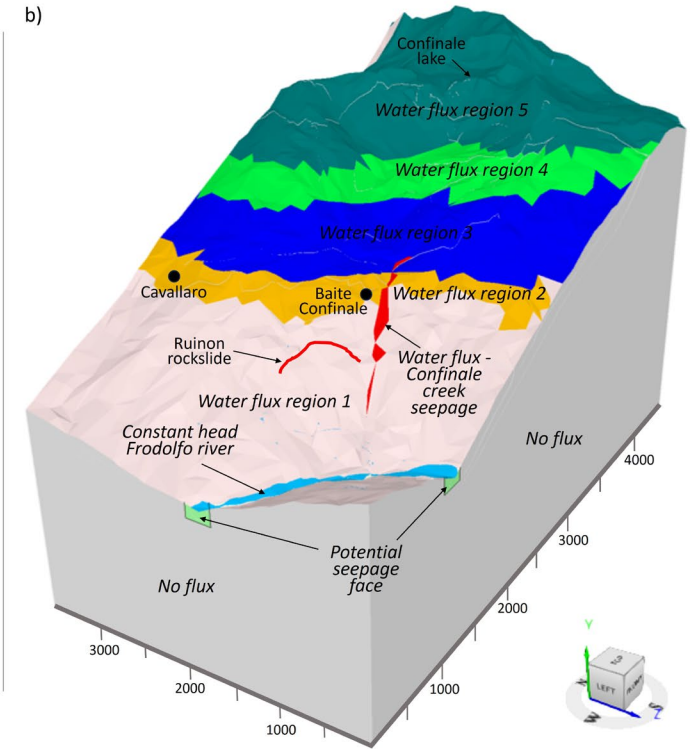

c)

Unit Water flux	Runoff coefficient	Rainfall + snowmelt 2014 [m^3/s]	Rainfall + snowmelt + runoff [m^3/s]	Runoff [m^3/s]	Total infiltration [m^3/s]
5	0,38	3,81e-8	3,81e-8	1,45e-8	2,36e-8
4	0,31	3,81e-8	5,25e-8	1,63e-8	3,62e-8
3	0,38	3,81e-8	5,43e-8	2,06e-8	3,37e-8
2	0	3,81e-8	5,87e-8	0	5,87e-8
1	0,08	3,81e-8	3,81e-8	3,04e-9	3,50e-8

Figure 5.35 – a) Areal extension of the hydrogeological model. b) Definition of hydraulic boundary conditions. c) Calculation of water inputs along the slope considering the water availability of the year 2014 as an example

5.6.1.2 Modelling procedure and input data

(i) steady-state regime 2014 – starting model

The analysis starts reproducing the representative hydrogeological conditions of the slope in a steady-state regime (*starting model*). For this purpose, the year 2014 was chosen, which had been recognized as a representative year of the climatic conditions of the slope (Section 5.3.5).

The input data for the analyses are represented by the yearly values recorded along the slope and presented in the previous Sections 5.3.4, 5.3.5. In particular, for the calculation of the amount of water infiltrating along the slope (Figure 5.35c), rainfall and snowmelt values presented in Section 5.3.5 were used (Figure 5.36). The calculation of the amount of water infiltrating along the Confinale creek was determined from the flow rates measured by the hydrometer located at the Confinale climate station, to which a reduction coefficient of 0.05 was applied. This coefficient is coherent with of literature values (Archer et al. 2020; Batista et al. 2020), the average rock-type that the creek flows through, as well as the result of infiltration tests (Section 5.3.5).

The steady-state analysis was repeated following a “trial and error” iteration procedure, adjusting the input data (mainly hydraulic conductivity values of some significant hydrogeological units) until a good representation of the mean hydrogeological conditions of the slope has been achieved. This analysis is

therefore to be intended as the first stage of the calibration process that will be carried out in the following stage ii.

ii) transient analysis - training model (years 2015-2016)

The outcome of the steady-state analysis was used as input for a transient analysis aimed at stimulating the hydrogeological regime for the years 2015-2021. The time range selected for the transient analyses is one month (2,592,000 seconds). Therefore, the input functions were calculated with a monthly average for each input parameter required by the simulation (Figure 5.36).

Model calibration was performed by comparing measured and modeled piezometric level data at the piezometer "*PZ4*" located in proximity of the Ruinon rockslide upper niche (Section 5.3.4), over the years 2015-2016. It represents the only monitoring element with temporal continuity and hydrogeological significance sufficient to verify the validity of the proposed numerical model. In addition, its location near the main rockslide body allows to verify the robustness of the model and the quality of the proposed hydrogeological conditions in correspondence of the most significant gravitational element of the slope.

In accordance with the partial output results, iterative numerical simulations were conducted between the *starting model* and the *training model* analyses, varying the hydraulic properties of some significant hydrogeological bodies (following the range of values discussed in Section 5.4), until the simulated and observed results converged to a good fitting.

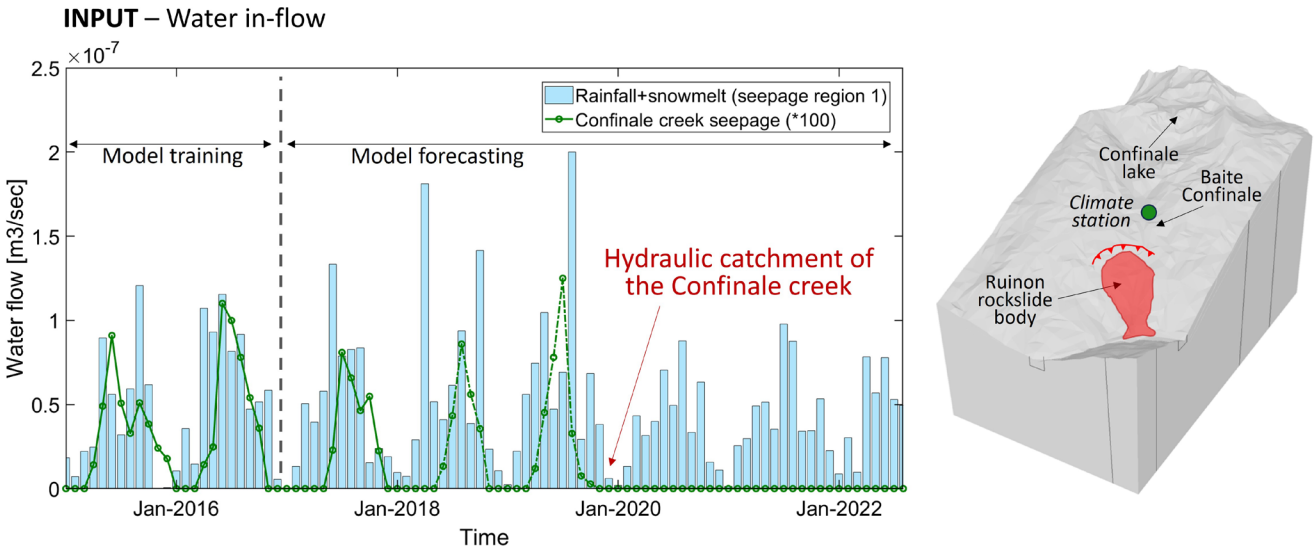

Figure 5.36 - Hydrological input data from 2015 to 2022 for numerical modeling. Regarding the water infiltration from the Confinale creek, the years 2018 and 2019 are represented by a dotted line because the data are uncertain as they are derived from the previous years' trends. The introduction of the hydraulic engineering works is highlighted by setting the creek seepage equal to zero.

iii) transient analysis - forecasting model (years 2017-2021)

Once the iteration results of the *starting* and the *training models* have reached a good accordance with monitoring observations, the hydrogeological analysis was then applied to the years 2017-2021 (*forecasting model),* by keeping the hydraulic properties defined in the calibration process unchanged.

To account for the hydraulic engineering works carried out at the Confinale creek, since November 2019, the boundary condition in correspondence of the hydraulic engineering works was set by an inflow rate equal to 0.

Model validation was performed by comparing measured and modeled piezometric level data at the piezometer "*PZ4*", at the same way of the previous calibration process.

5.6.2 Results

Numerical modeling results were evaluated in terms of the pore pressure distribution along the slope, piezometric level trends, location of water springs, and modeled water flow rate.

(i) steady-state regime 2014 – starting model

Considering the steady-state analysis (*starting model*), by introducing the annual water availability of 2014, the representative hydrogeological setting of the slope was simulated. The results of the steady-state analysis here presented are those that, following a "trial and error" iteration procedure, outcome from the calibration process performed with the *training model*.

In general, it is evident that the distribution of simulated water emergences (Figure 5.37a) reflects the in-situ observations (Section 5.3.4), with a band of springs at the base of the slope and at the rockslide body and a preferential zone of water outflow at the contact between the glacial bodies and the slope deposits at the "Baite di Confinale" location. The portion of the slope in correspondence with the Confinale creek, exhibits greater water abundance than what is simulated on the right flank of the rockslide, where drier conditions are present consistently with field observations. This is the result of a different piezometric surface trend between the right and left flanks of the rockslide, which is affected by the morphological gradient of the slope and the presence of the Confinale creek inflow.

This evolution is clearly evident by analyzing 3 cross-sections made in the SW-NE longitudinal direction, along the main rockslide axis and at the flanks of the active body. These sections, presented in Figure 5.37b,c,d, show the distribution of the modelled pore pressures and highlight the location of the piezometric level. By analyzing the A-A' cross-section carried out along the rockslide axis (Figure 5.37b), it is possible to observe that the piezometric level in the area upstream of the rockslide body, is

affected by the presence of the high hydraulic conductivity unit (trenches, gravitational fractures, etc.), with a significant deepening of the water table, which subsequently rises at the rockslide body, causing the development of springs at the base of the rockslide itself. The same phenomenon is observed upstream of the main rockslide body, where the water springs of the "Baite di Confinale" are simulated by a rise in piezometric level due to a permeability contrast between glacial and slope deposits.

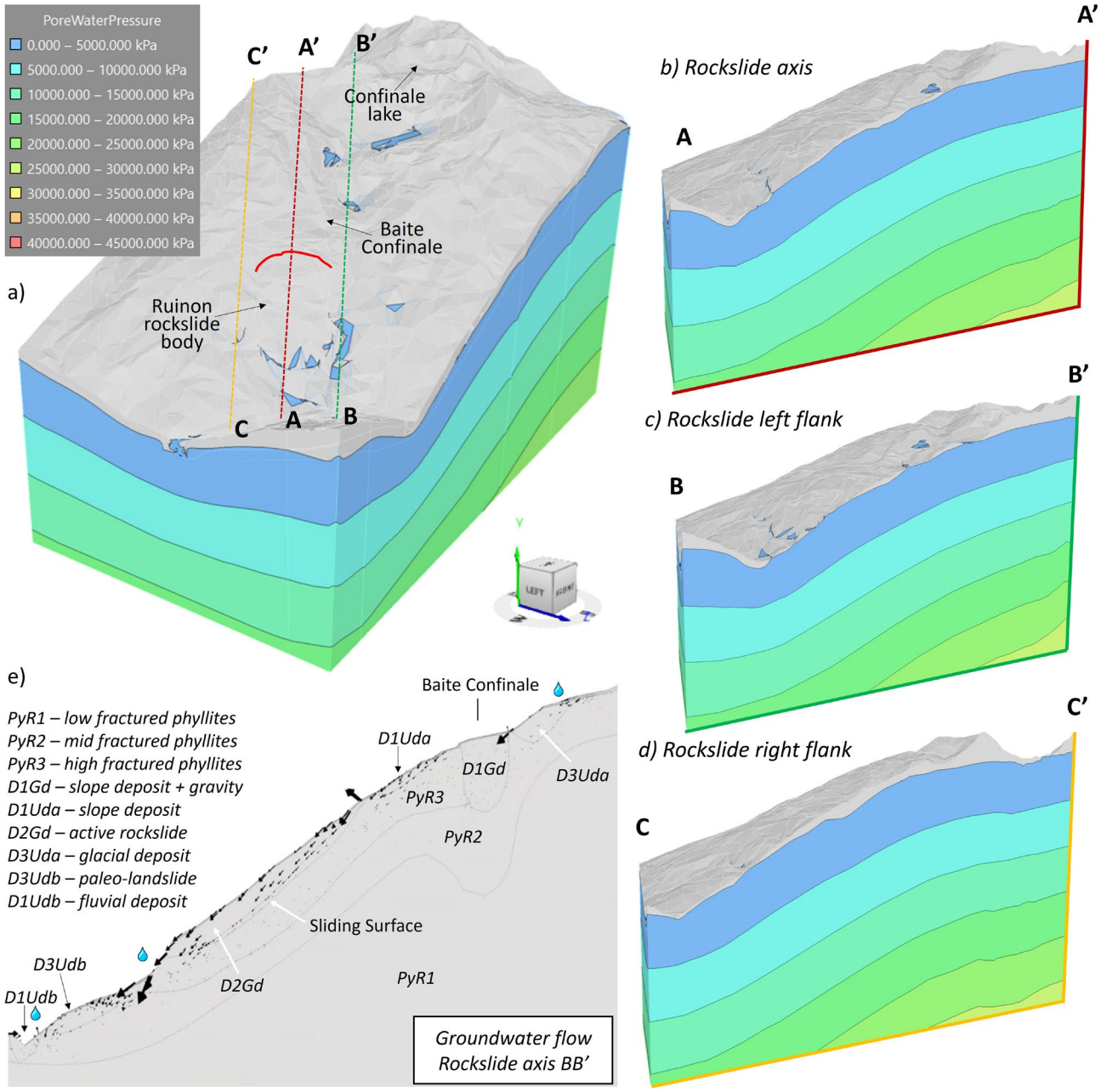

Figure 5.37 - Steady state modeling results. a) Distribution of pore pressures along the slope. the intersection of the piezometric surface and the topographic surface are highlighted by the blue spots. b) Cross section made along the rockslide axis showing the distribution of pore pressures. c) Cross section made along the left flank of the rockslide showing the distribution of pore pressures. d) Cross section made along the right flank of the rockslide showing the distribution of pore pressures. e) Groundwater flow along the rockslide axis section: arrows indicate flow directions, drops are springs; the different hydrogeological units are highlighted

The B'-B section developed on the left side of the rockslide (Figure 5.37c), along the course of the Confinale creek, shows conditions of higher water availability with a simulated piezometric level significantly closer to the topographic surface. Intersections between piezometric level and topographic surface are very frequent, resulting in an abundance of water springs. At the Confinale lake, the piezometric level is close to the topographic surface but without intersecting it. Due to its nearness to the model boundary, and to the large-scale of observation (i.e., size of geometric bodies), its recharge system could not be accurately simulated. The feeding of the lake could be related to surface runoff processes in the debris units, which are not investigated in the presented numerical analysis. However, a hydrogeological flow connection is observed between the Confinale lake and the springs located further downstream. These observations agree with the results of the hydrogeological study presented in Section 5.3.4 and confirm the reliability of the modeling analysis with respect to the quantity and quality of the available data.

The right flank of the rockslide (C'-C section Figure 5.37d), on the other hand, appears much drier with deep water table (on the order of hundreds of meters). The piezometric level never intersects the topographic surface in this area, consistent with field observations. These conditions are probably related to the robust development of the high-permeability trench hydrogeological unit along this section, which causes a substantial lowering of the water table in the area upstream.

ii-iii) transient analysis

Model calibration was achieved by performing the transient analysis, considering 2015-2016 monthly water availability (*training model*) and comparing the simulated and measured piezometric level at the piezometer PZ4. In particular, the hydraulic conductivity values assigned to the different hydrogeological units were initially fixed according to the range of values presented in the Section 5.4, with particular reference to the active rockslide body, highly fractured rock-masses and trench units, which most influence the piezometric level at the Ruinon rockslide. Values of the hydraulic properties of the hydrogeological units were varied until a good fit between measured and simulated values of piezometric level was obtained.

With hydraulic conductivities values of $2 \cdot 10^{-6}$, $5 \cdot 10^{-7}$ and $5 \cdot 10^{-6}$ m/s, the model faithfully simulates the piezometric level trend as shown in Figure 5.38a. The piezometric levels achieved in terms of maximum and minimum values are correctly simulated by the model, while there is evidence of a slightly divergent response to external rainfall inputs from in situ measurements. This could be related to the time intervals (30 days) considered, and the introduction of average values of monthly rainfall, which prevents an accurate estimation of the time of recharge and discharge of water within the slope.

The capability or goodness of the model is also evaluated by plotting the modelled vs measured piezometric level values, sampled with a time interval of two months (Figure 5.38b). In the present problem the points are well distributed along a linear alignment with a coefficient of determination R^2 equal to 0.75 (where 1 is perfectly fitting model). The goodness of the model can also be expressed as Root Mean Square Error (RMSE), or as Normalized Root Mean Square Error (NRMSE), respectively defined as:

$$RMSE = \sqrt{\frac{\sum_{i=1}^{n}(h_m - h_s)^2}{n}} \quad \text{(Equation 5.20)}$$

$$NRMSE = \frac{RMSE}{h_{max} - h_{min}} 100 \quad \text{(Equation 5.21)}$$

Where h_m is the measured piezometric level and h_s the simulated one.

For this test, it is assumed that a calibrated model results in a NRMSE parameter value of less than 15 percent, in accordance with the main literature available (ASTM 2008c; Wels et al. 2012). Results indicate a NRMSE parameter equal to 10.8 (Figure 5.38b), consistent with a good calibration of the model which is considered valid that for the purposes of the present study (i.e., simulate the general hydrogeological evolution of the slope). Further adjustments of the input data and simulation attempts could improve the performance, but they would require considerably more computational time considering the 3D approach adopted. Moreover, it must also be stressed that such effort does not justify the attempt to fit the measured and simulated response at a single monitoring point that is not totally representative of the general slope behavior.

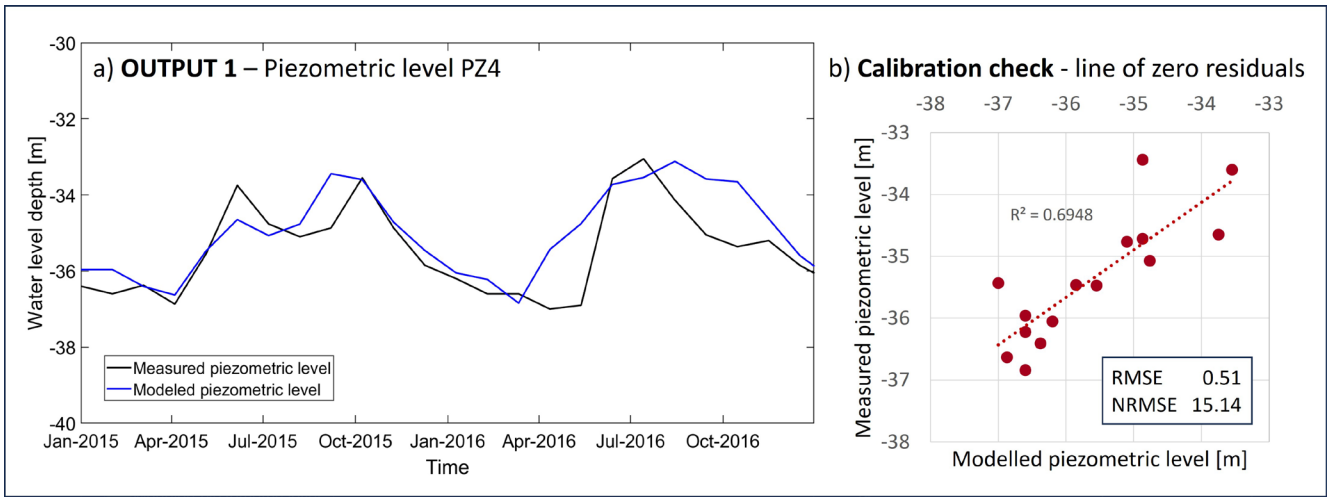

Figure 5.38 - Output of the training hydrogeological transient analysis. a) Simulated piezometric level at monitoring point PZ4 during the training period from 2015 to 2026. b) Verification of the accuracy of the calibration process.

To verify the robustness of the model, it is now validated by solving the analysis unchanged the calibrated hydraulic property values of the hydrogeological units and considering the time range 2017-

2021. The results of the validation process are shown in the Figure 5.39a, which correctly reproduce the fluctuation of the measured piezometric level, with congruent annual variation ranges. However, for the year 2018, it can be noticed a discrepancy between simulated and measured level. This is mainly related to the fact that for the years 2018 and 2019 the hydrometric levels of the Confinale creek were not available, and they have been necessarily estimated based on data of previous years and the rainfall regime, (Section 5.3.5). For the year 2019, this assumption was sufficient to correctly simulate the piezometric level trend, while for the year 2018 some corrections seem to be required. However, since the general piezometric level trend was correctly simulated, the aim of this study has been achieved and further refinement of the analysis is deferred to future developments. Moreover, it is worth mentioning that the evolution of the simulated piezometric level after the 2020 Confinale Creek water deviations is consistent with monitoring data. This demonstrates the validity of the developed model and the accuracy in defining the hydraulic boundary conditions.

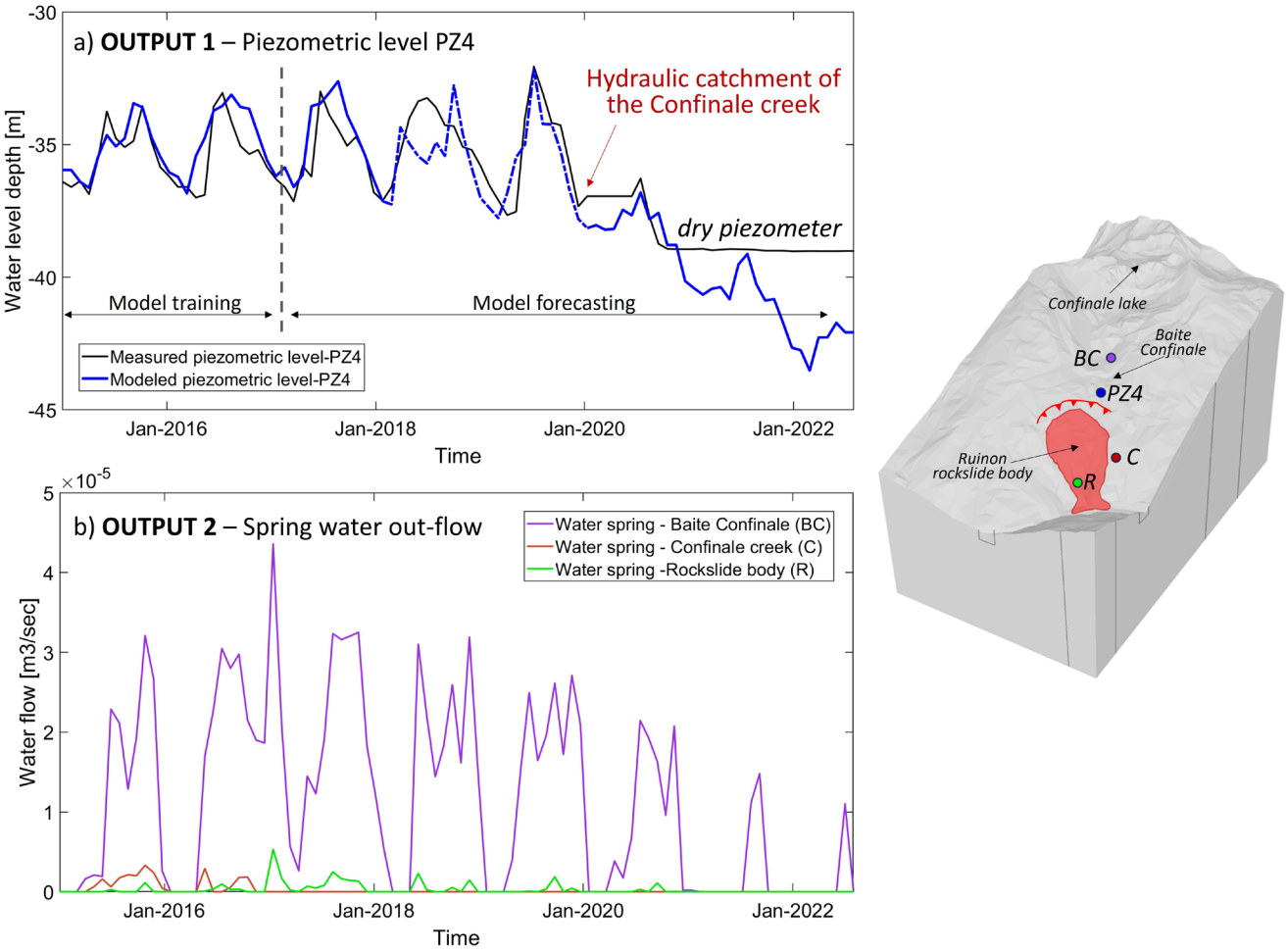

Figure 5.39 - Output of the hydrogeological transient analysis. a) Simulated piezometric level at monitoring point PZ4 during the period from 2015 to 2021, subdivided in training model (2015-2016) and forecasting model (2017-2021). Results represented by the dotted line have a degree of uncertainty given by the assumption made in the input data. c) Simulated outflow rate for different springs located along the slope.

An additional element monitored during the numerical analysis was the flow rate of water springs simulated along the slope. Spring discharge data with temporal continuity are not found in the literature for the Ruinon slope. The available data are only those measured in the geological campaign conducted in the summer 2022, in the framework of this work (Section 5.3.4). In detail, one semi-permanent spring at the "Baite di Confinale" locality, 3 seasonal springs along the Confinale creek, and 2 seasonal springs at the base of the active Ruinon rockslide body were monitored. As can be seen from the graphs in Figure 5.39c, the simulated flow rates have significant seasonal variation. The water spring at "Baite di Confinale" shows maximum flows (in the order of 0.05 l/s) in May-June and minimums in the fall period (0.02 l/s), until it dries up completely in the winter. These values are consistent with what measured in in July 2022 when flow values of 0.01 to 0.1 l/s were measured in springs at the same location (see S10-13 in Table 5.9). It can be observed that, as a result of the Confinale engineering works, the springs located downstream of the works come to dry up almost completely, even during late-spring periods, when maximum flow rates are expected. In contrast, the spring upstream of the works continues its water regime, with a reduction in flow rates probably linked to a lower rainfall input in the years 2021-2022.

5.6.3 Discussion

After a calibration process, where the most significant hydraulic parameters were verified, the performed numerical analysis, in both steady-state (i.e., considering the average annual water availability) and transient regime (i.e., considering the different water distribution throughout the year), allowed to simulate the groundwater flow in the 3D investigated volume. The hydrogeological model presented in Section 5.4 has been verified, validated, and numerically reproduced. The model results, expressed by pore pressure distribution along the slope, piezometric level trends, location of water springs, and water flow rates are congruent with the observations and field measurements carried out along the slope, as well as with the elaborations made following the results of chemical analysis on the water samples collected.

The main features controlling the groundwater circulation can be summarized as follow:

- *Hydraulic conductivity contrasts:* This process is well evident along the rockslide axis section, where the continuous interplay between low- and high-permeability bodies causes a multiple intersection between piezometric and topographic surfaces. The high-permeability unit upstream of the main rockslide body, causes a significant increment of infiltrated water, as well as a capture of groundwater flowing from the upstream recharge volumes. This causes a substantial lowering of the groundwater level in correspondence of the unit. Downstream, a piezometric level rise

occurs due to increased water availability related to (i) deep flow in fractured rock-mass and (ii) the presence of low-permeability deposits at the base of the slope that induce water accumulation. Moreover, the presence of low-permeability glacial deposits upstream of the rockslide body, causes a rise in the piezometric level by accumulation of groundwater flowing downstream

- *Morphological factors:* Morphological factors clearly control the presence or absence of water spring, driving the interaction between piezometric level and slope surface. As an example, at the Ruinon rockslide and along its left flank, the rising of the piezometric level is sufficient to define the development of water springs, while along the entire right flank, it is not sufficient to cross the topographic surface.
- *Presence of the Confinale creek*: With a continuous water infiltration supply, the presence of the Confinale creek causes a rise in the water table and the development of shallow water flow. This is evidenced by an increase in the frequency of water springs along the stream which can be related to more shallow flows, unrelated to the main piezometric evolution of the slope.

This results in the evidence of two preferential feeding zones represented by the area at the top of the slope and the unit of gravitative and morpho-structure elements.

The transient analysis, covering a time window of 6 years, allowed to simulate the pore pressure changes along the 3D investigated volume. The analysis showed a significant rise in piezometric level in the spring-summer period with the consequent activation of temporary water springs, in the same areas already highlighted for the stationary model. This observation is consistent with on-site measurements that had shown the presence of both permanent and seasonal springs. Increased water supply in the months with higher water availability goes to raise the level of the deep-water table to the point of partial saturation of the rockslide body. This mechanism could be the main responsible for triggering deep deformations that result in significant acceleration events in the rockslide body, as should be demonstrated by performing stress-strain analyses.

The 3D hydrogeological model was able to account to hydrological engineering works put in place along the Confinale creek and can thus represent a good tool for exploring further engineering solutions. The simulated engineering actions caused a reduction and flattening of the water table level. This in turn generates a significant reduction in the number of springs present downstream of the hydraulic engineering works, consistent with field observations. This aspect confirmed the significant role of the Confinale creek, which therefore represents a very important source of groundwater body supply. The relationship between piezometric level and Confinale creek supply is further confirmed during the simulation of piezometric levels in years 2018-2019, where stream flow data are completely absent. The well-calibrated model was able to return reasonable scenarios based on assumptions made, which can

be updated and supplemented with new data or different assumptions. In this study, an infiltration of water was assumed to be 5% of its flow rate along the entire stretch of the stream. Different infiltration values may be explored in future analyses.

The calibrated and validated model is therefore now available for the development and analysis of future hydrogeological scenarios, associated to engineering works or even those related to ongoing changes of the climatic variables. Moreover, the distribution of water pressures and the other simulated hydrogeological variables within the slope, or their evolution in response to hydro-climatic input scenarios, can be progressively introduced into numerical stress-strain modelling analyses to assess slope stability.

As every model, the presented Ruinon hydrogeological model developed within this work can be improved. First, enhancement and implementation of input data can be addressed:

- In the presented model, a time range of 1 month was used for the definition of the input factors. This allows to analyze the general hydrogeological evolution of the slope but prevents to investigate the response of the system to intense and short meteorological events. A reduction in the time range considered would allow an enhanced definition of water availability along the slope, a better simulation of the infiltration processes and consequently a better response of the piezometric level trend.
- Hydrogeologic properties defined on site investigations and field tests have led to a proper reconstruction of groundwater flow dynamics. Increasing data and knowledge on material properties, though, for example, hydraulic testing in future new boreholes, will improve the definition of the conductivity ranges, especially in superficial and fractured rock-masses whose description presents large uncertainty.
- The calculation of water seepage rate from the totality of water availability, can be improved through greater accuracy in defining homogeneous runoff regions.

Moreover, an increment of the model complexity can be addressed:

- More complex hydraulic models for defining the seepage rate in the unsaturated zone could be explored to better calibrate the infiltration rates and thus better define the mechanism of aquifer recharge.
- More accurate definition of hydrogeological units could be developed on a limited volume of the slope such as the rockslide area. This would allow greater detail and resolution of the mechanisms that affect the rockslide body.

- The use of software that allows for accurate simulation of the runoff process could lead to greater awareness of infiltration and recharge processes along the slope but especially at the rockslide body.

At last, to increase the validity of the model, it is deemed necessary to introduce or identify new hydrogeological monitoring points with sufficient temporal continuity to represent new elements on which better define the calibration/validation process.

5.7 Stability analysis of the Ruinon landslide: a 3D DEM numerical approach

Evidences from geotechnical monitoring investigations along the Ruinon active body, showed a close relation between climatic-hydrological inputs and the deformative evolution of the rockslide (Section 5.3.6). This relationship also strictly correlates with the evolution of the piezometric level: periods of high acceleration of the rockslide body are associated with a sudden rise in the piezometric level measured in the proximity of the high niche; in contrast, periods of water table lowering coincide with a quiescence state of rockslide activity, with no appreciable deformations. Recent hydraulic engineering works and water deviations of the Confinale creek, combined with a period of particularly dry climatic conditions, have resulted in a significant lowering of the piezometric level with an apparent stabilization of the landslide body (Section 5.3.5 and 5.3.6).

This process could be related to a hydro-mechanical (HM) interaction between the rockslide body and the groundwater table level in correspondence with the periods of maximum rise, which causes a reduction of the effective stress at the sliding surface. This could result in a considerable increase in strains along the shear band, resulting in a deep deformative acceleration of the rockslide body.

Such HM couplings were already highlighted in a preliminary stage of numerical modeling conducted in this work with a FEM approach (Section 5.5), where three representative and simplified piezometric levels were processed and introduced into a homogeneous mechanical model of the slope. The results of the analysis showed that a rise in the piezometric level corresponds to increases in simulated irreversible strains at the Ruinon rockslide body (Figure 5.34), confirming the observations described above. In Section 5.6, a hydrogeological analysis was developed allowing to simulate in detail the evolution of groundwater bodies in response to climatic inputs.

In this Section, the deformation and stability of the Ruinon rockslide body is explored by introducing the water pressure distributions simulated by the hydrogeological analysis (Section 5.6) and adopting a more complex geomechanical modelling approach of the slope. The aim is to develop a semi-coupled HM analysis in which the deformation responses of the rockslide body to the simulated hydrogeological inputs, are examined. The goal is to verify the HM coupling occurring in correspondence of the rockslide body, and evaluate its stability in relation to different hydrogeological inputs. Moreover, the purpose of the present analysis is to verify whether the simulated piezometric levels are able to reproduce the mechanical evolution of the slope detected in the field. The efficiency of the recently introduced hydraulic engineering works in the Confinale creek, in ensuring a degree of stability of the landslide

body and a reduction of the landslide hazard level, will be evaluated. Hence, the Ruinon HM 3D model can represent a useful tool for rockslide management, to develop new monitoring strategies, and to plan stabilization actions.

For the development of this study, a discrete element modeling approach (DEM) was adopted, allowing the introduction of the detected discontinuity system, along which plasticity failure could represent a key element in driving rockslide body acceleration processes. In addition, this approach allows to account for different state of fracturing and mechanical weathering degree detected along the slope, using the field geomechanical parameters obtained during characterization.

5.7.1 Methods

Numerical analysis of the Ruinon rockslide was performed using the 3D DEM code 3DEC (version 7.0 - Itasca Consulting Group 2019), suited to analyze the behavior of discontinuous media (Section 2.3).

The distribution of pore pressures is introduced into the model considering the outcomes of the hydrogeological analysis presented in Section 5.6. At each water pressure distribution, the HM equilibrium is calculated with the assessment of the induced stress-strain fields.

Changes in the stress state within the rock-mass domain will affect interfaces between intact blocks (discontinuities) for which an elasto-plastic behavior is assumed. As the stress state evolves, the shear stress at interfaces may reach failure conditions, thus inducing plastic straining.

In the above outlined framework, the effects of HM loading were analyzed, focusing on the development of deep shear strains along a surface comparable to the surveyed shear band of the Ruinon active body. The adopted method does not involve the introduction of predefined sliding surfaces, but only zones of different fracture intensity consistent with field observations. The slip surface of the active landslide is meant to be reproduced from the in situ detected geomechanical conditions and hydrogeological inputs.

5.7.1.1 Modelling approach, set-up and input data

The developed 3D geomechanical model has the same areal extent of the models defined in Section 5.4, 5.5 and 5.6 above (Figure 5.40a). Its extension is in fact appropriate to cover the main gravity-driven phenomena present along the slope. Moreover, the adoption of the same model size allows for a coupling with previous numerical simulations (i.e., export and import of simulated variables from one model to another), with a particular reference to the hydrogeological analysis.

The geomechanical model includes both discontinuities and deformable blocks obtained from the intersections of the joint network elements.

Geological-geomechanical domains

The geological model presented in Section 5.4 was here simplified to reduce the computational cost of HM couplings and to focus on the elements that most control the stress-strain evolution of the slope. In particular, surface deposits units and all the units that by areal dimensions and thicknesses are not considered to be significant for the overall mechanical evolution of the slope, were neglected at this stage. Moderately and intensely fractured rock-mass units of Section 5.4 model have been preserved, defined by regions of different fracture intensity (named respectively "slope" and "rockslide"). The active rockslide unit and the area of the gravity-driven trenches upstream the upper niche, were included in the domain of the intensely fractured rock-mass, considering the homogeneity of the mechanical properties detected in situ. This also allows to avoid possible mechanical interferences that would generally develop in the numerical model at the contact of three different units in the area of interest.

At average depths greater than 2000 m, a third domain was introduced simulating less fractured and stiffer rock-masses.

Distinct Fracture Network (DFN) generation

Discontinuities are represented by a multiple network defined by the four joint sets detected with geomechanical surveys (Section 5.3.3). The 3DEC built-in distinct fracture network (DFN) generator (Section 2.1) was used to reproduce, with a statistical approach, similar discontinuity patterns to those observed in the field (Figure 5.9).

First relevant geometrical parameters used for the Ruinon DFN generation procedure are the joint orientation ones (dip and dip direction). Following the Gaussian distributions, the dip and dip direction are described by four parameters: mean and standard deviation for the dip distribution, mean and standard deviation for the dip-direction distribution (Figure 5.40b-c). Next, the joint size (length of disk diameter) and the fracture intensity need to be described. Joint size follows a Gaussian statistical distribution described by mean and standard deviation values. The fracture intensity, is simulated through the mass density P32 parameter, defined as the area of joints per unit volume (Itasca Consulting Group 2019b). This parameter expresses the density of joints inside the rock-mass, considering joint spacing and persistency parameters (Zhen et al. 2020; Ojeda et al. 2023). The more a joint network is spaced with low persistence, the lower the fracturing intensity will be (i.e., low value of P32); the lower

the spacing and the higher the persistence, the higher the fracture intensity will be (i.e., high value of P32).

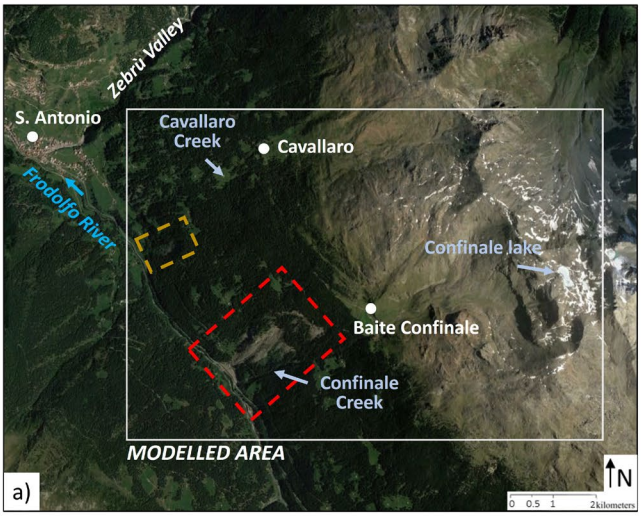

b) **Detected discontinuity network – geomechanical surveys (Section 5.3.3)**

SET	Orientation		Mean spacing [m]	Aperture [mm]	JRC	JCS [MPa]
	Dip direction [°]	Deep [°]				
K1	20 ± 30	25 ± 10	0.03	2	10	60
K2	230 ± 30	80 ± 15	0.09	3	8	70
K3	275 ± 10	75 ± 10	0.05	6	7	85
K4	150 ± 30	60 ± 10	0.2	4	8	72

c) **Modelled distinct fracture network (DFN)**

SET	Orientation		Mass - density			Size
	Dip direction [°]	Deep [°]	Slope	Rockslide	Z>2000 m	
K1	20 ± 30	25 ± 10	0.003	0.03	0.005	1200 ± 100
K2	230 ± 30	80 ± 15	0.002	0.02	0.005	850 ± 50
K3	275 ± 10	75 ± 10	0.003	0.03	0.005	850 ± 50
K4	150 ± 30	60 ± 10	0.001	0.01	0.005	850 ± 50

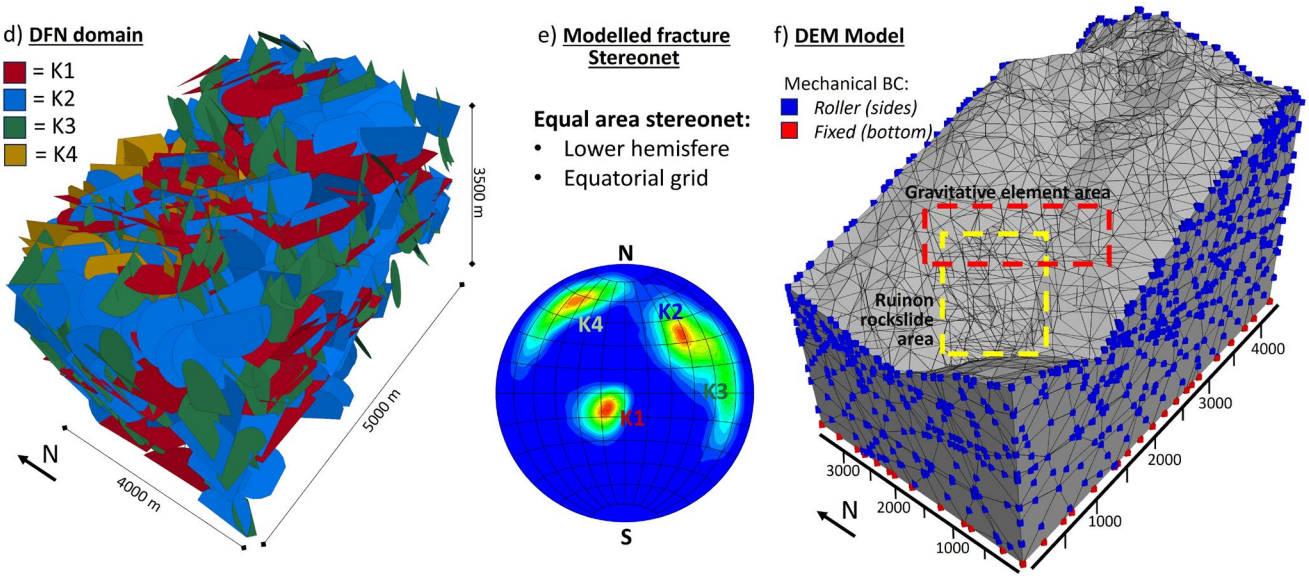

Figure 5.40 – a) DEM geomechanical model extension. b) Geomechanical properties defined in situ and useful for defining the DFN model. c) values used for the construction of the DFN model. d) Simulated DFN. e) Stereo-net showing the orientation of the component elements of the modeled DFN. f) DEM Ruinon geomechanical model and boundary conditions.

Joint size and fracture density parameters were defined based on representative values obtained from geomechanical field measurements performed on rock-masses outcropping along the slope (Section 5.3.3), scaled as specified below. Considering the scale effect, the mass-density factor calculated from geometrical values of geomechanical surveys, required a reduction factor of 100, which is used to enable numerical representation while maintaining the geometrical relationships detected. To account for the increased fracturing state characterizing the rockslide area, a smaller reduction factor of 10 was introduced for that unit. In addition, to speed up the computational calculation, for depths greater than

2000 m, a mass-density factor value of 0.005 was introduced, so as to introduce a fracture reduction with z, representing a stiffer rock-mass.
The developed DFN is shown in Figure 5.40d, with the corresponding orientations of the simulated objects in the stereo-network in Figure 5.40e.

Mesh generation and boundary conditions

Rock blocks, resulting from the intersection of discontinuities, were set as deformable and discretized into a triangular finite-difference mesh. A maximum mesh size value of 200 m was used, and increased to 20 m in the rockslide area to a better resolution and a more accurate simulation in the area of interest. Roller boundaries were applied to the lateral sides of the model, while the bottom boundary was applied a prevented displacement condition (Figure 5.40f). Considering that the sides of the model are placed sufficiently far away from the area of interest represented by the Ruinon rockslide, these boundary conditions are considered reasonable in order to simulate the stress-strain conditions that result in the development of slope failure.

Rock-mass and discontinuities properties

The constitutive Mohr-Coulomb plasticity model is used for describing the rock blocks behavior of both regions. Therefore, the required properties are: density ρ, Young's modulus E, Poisson's ratio μ, friction angle ϕ, cohesion c, and tensile strength σ_T. Mechanical properties were derived from laboratory tests and in-situ detailed field surveys, following results presented in Section 5.3.3 and 5.4.
Discontinuities were assigned an elasto-plastic Mohr-Coulomb constitutive law including slip-weakening of ϕ and c. The joint model aims at simulating displacement-weakening by loss of frictional, cohesive and tensile strength: once shear or tensile failure is reached, strength properties instantaneously drop from peak to shear residual values and null tensile strength. The required properties include normal stiffness k_N, shear stiffness k_S, friction angle ϕ (peak and residual) and cohesion c (peak and residual).
Joint strength parameters were derived from laboratory direct shear tests conducted on discontinuities sampled from the material drilled along the slope (Section 5.3.3). The same resistance and deformability values were assigned to all the DFN elements, consistent with field observations that had shown typical mechanical properties of weathered and smooth surfaces throughout the discontinuity set detected.
The mechanical properties of rock blocks and discontinuities used in the numerical modelling are summarized in Table 5.20.

Table 5.20 – Mechanical properties of blocks and discontinuity elements derived from laboratory tests.

Blocks					
ρ [Kg/m^3]	E [GPa]	μ	c [MPa]	ϕ [°]	σ_T [MPa]
2700	35	0.2	0.55	30	5
Blocks – Rockslide area					
ρ [Kg/m^3]	E [GPa]	μ	c [MPa]	ϕ [°]	σ_T [MPa]
2700	35	0.2	0.5	25	5
Discontinuity elements					
$c_{\_peak}$ [MPa]	$c_{\_residual}$ [MPa]	$\phi_{\_peak}$ [°]	$\phi_{\_residual}$ [°]	K_N [GPa/m]	K_S [GPa/m]
0.6	0	27	15	5	5

5.7.1.2 Modelling procedure

Numerical modeling involved different steps of analysis aimed at reconstructing the slope's stress state as well as the relationship between the evolution of hydrogeological bodies and the development of deformation processes.

- *Step 1*: a static analysis was performed under dry conditions and elastic mechanical parameters for both rock blocks and discontinuities.
- *Step 2*: the piezometric level representative of the stationary condition of 2014 was introduced into the mechanical model while maintaining elastic conditions.
- *Step 3*: once the elastic initialization was completed, the deformation state has been reset and the elasto-plastic properties were gradually introduced, first for the rock material and then also for the discontinuity elements, while updating equilibrium calculations.
- *Step 4*: the transient regime was then analyzed, introducing in the simulation the piezometric evolution evaluated from 2015 to 2021 with a time interval of 3 months. For each calculation step, the HM equilibrium under elasto-plastic conditions was recalculated, and the effects of changes in piezometric level from the previous step are evaluated. The introduction of hydrogeological factors every 3 months (March, June, September, December) allows to reproduce and analyze representative HM scenarios (i.e., winter, spring, summer, and fall) of each year, and, considering the wide time range analyzed, allows for reduced calculation time. The time period under consideration allows for the evaluation of HM scenarios that resulted in particularly significant accelerations of the landslide body, such as in the summer of 2016 and 2019. In addition, it will be possible to explore the effect of the hydraulic engineering works of

the Confinale creek on the stability of the rockslide, also evaluating their effectiveness considering future climate projections.

5.7.2 Results

The results of the analysis were evaluated in terms of change in the stress state, deformation state, and evolution of cumulative displacements along the slope. Elements that could significantly represent the state of activity of the Ruinon rockslide were examined, by using the 3DEC software tools. In particular, 2D cross-sections performed in NW-SE orientation along the active rockslide axis and monitoring points measuring the deformation and stress state of the grid points (i.e., point belonging to the rock-mass), were used.

Stationary condition – 2014 hydrogeological regime

Once the elastic initialization equilibrium was defined (*Step 1 and 2*), the modeling outputs of S*tep 3*, allowed to verify the validity of the model, reproducing the general stress-strain state of the slope.

Analyzing the distribution of 3D total displacements (Figure 5.41a), the maximum simulated values correspond to the Ruinon rockslide location, properly identifying the unstable body. The distribution of pore pressures follows the evolution discussed in Section 5.6, with location of the water table in correspondence of the rockslide body that reaches depths between 50 and 100 meters from the surface (Figure 5.41b).

Simulated effective stresses, are consistent with slope morphology and distribution of pore pressures (Figure 5.41c). An increase in effective stresses is present at elevations of about 2100 m a.s.l., probably related to the presence of subvertical discontinuity elements in a plastic state.

Considering the distribution of simulated displacements along 2D cross-sections running both longitudinally (Cross-section A - Figure 5.41d) and perpendicularly (Cross-section B - Figure 5.41e) through the rockslide axis, the development of a high-deformation body, consistent with field observations in terms of size, location and volume, is shown.

Figure 5.41f presents maximum values of horizontal displacements in correspondence of the “low” Ruinon rockslide body defined in previous Sections. On the other hand, Figure 5.41g shows maximum values of vertical displacements in correspondence of the “upper” body. This pattern highlights the development of subsidence and mass sliding processes along the vertical and horizontal axis, respectively, typical of a roto-translational evolutive mechanism.

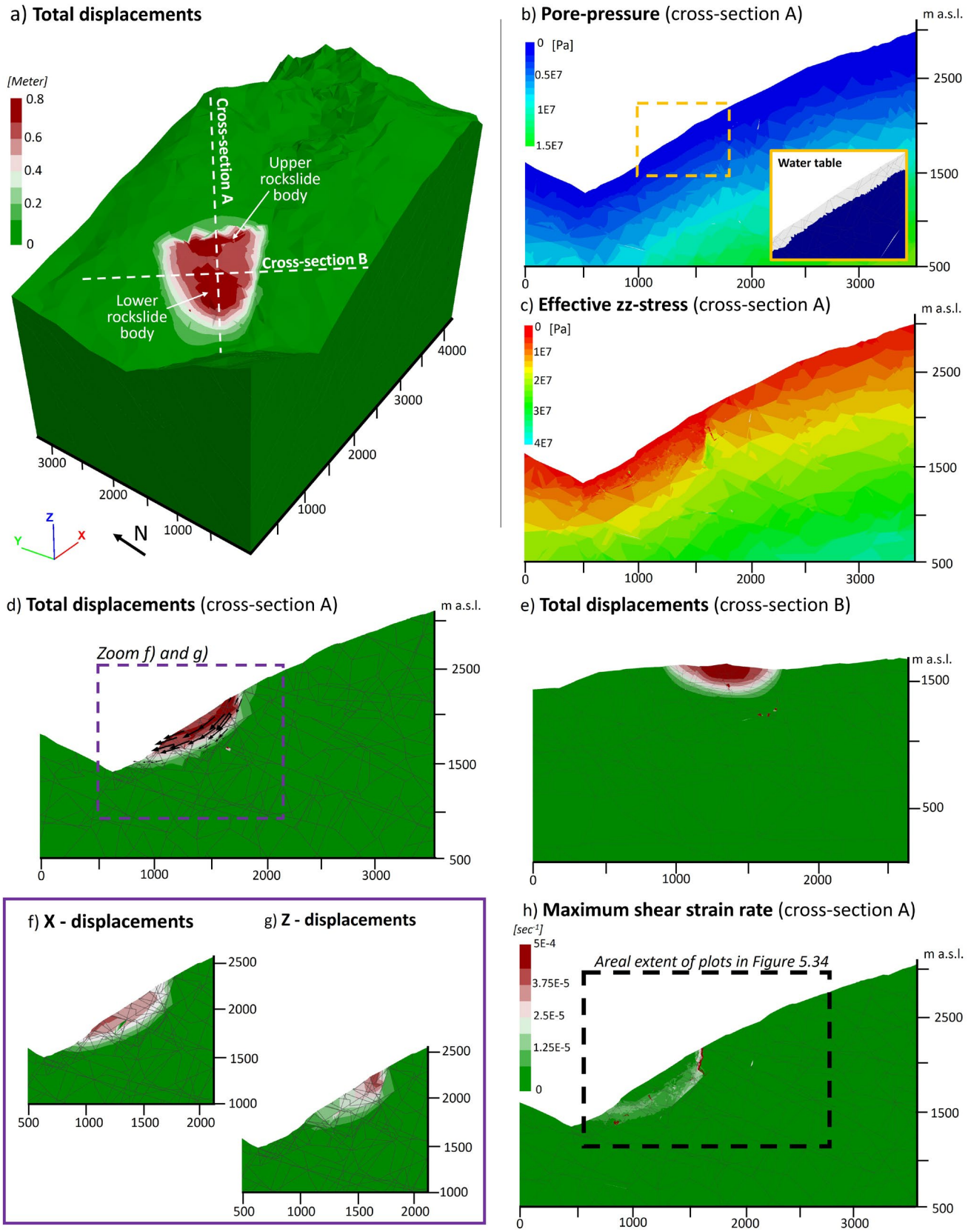

Figure 5.41 – Stationary condition – 2014 hydrogeological regime. a) Distribution of 3D total displacements. b) Pore pressure simulated along a cross section taken along the rockslide axis (A). c) ZZ effective-stresses simulated along same cross section A. d) Total displacements simulated along same cross section A. e) Total displacements simulated along a cross section taken perpendicular to the rockslide axis (B). f) X-displacements in correspondence of the simulated rockslide body. g) Z-displacements in correspondence of the simulated rockslide body. h) Maximum shear-strain rate simulated along the cross section A.

Moreover, by analyzing simulated shear-strain rates along the same cross-section A (Figure 5.41h), it is possible to detect the development of a shear band. At this step of the analysis, it does not exhibit sufficient continuity to result in mechanically unstable conditions for the slope. Nevertheless, it clearly defines the development of a rock-mass movement evolving separately from the surroundings (Figure 5.41d,h). The distribution of maximum shear strains follows sub-vertical joints (*K2-K3* sets) and minor discontinuity elements evolving approximately parallel to the slope morphology trend. A cluster of simulated maximum strain is highlighted at an altitude of 2100 m a.s.l., coincident with the location of the upper niche of the active rockslide body (Figure 5.41h).

Transient condition – 2015-2021 hydrogeological regime

Moving to *Step 4* of modeling (i.e., transient hydrogeological regime), the outputs of the analysis allowed to define the HM relationship between the evolution of the piezometric level and the simulated deformation state. This relationship is illustrated by analyzing the evolution of shear strains along the 2D cross section, already presented in Figure 5.41e. The piezometric level trend modeled in correspondence of the rockslide body (100 m depth) is shown in Figure 5.42a.

Figure 5.42b shows the simulated maximum shear strain increment in June of 2016, where, the development of a shear band is well defined. The simulated strain distribution is comparable with the slip surface of the Ruinon rockslide detected in Section 5.4, both in terms of depth and location. The maximum strain magnitude values are in correspondence of the high niche and the foot of the rockslide body.

Figure 5.42c shows the simulated deformation state during a winter hydrogeological scenario, corresponding to the month of December 2016. It is observed that the simulated deformation state at this stage shows conditions of greater mechanical stability with a distribution of strain values an order of magnitude lower than in the previous one. The distribution of maximum shear strains still shows the presence of deformation phenomena along the slope. Maximum deformations, however, are distributed in the shallower rockslide body and are no longer concentrated along a deep shear band. This corresponds to the possibility of unstable phenomena involving smaller volumes and superficial rock-masses.

Moving to the summer of 2019, when the piezometric level rises to the maximum values detected, unstable conditions are reached with the simulation of a well-developed shear surface at the same location defined in previous modelling steps. This is evidenced both by the development of plastic failure conditions (Figure 5.42d) and by the pattern of simulated maximum shear-strains (Figure 5.42d').

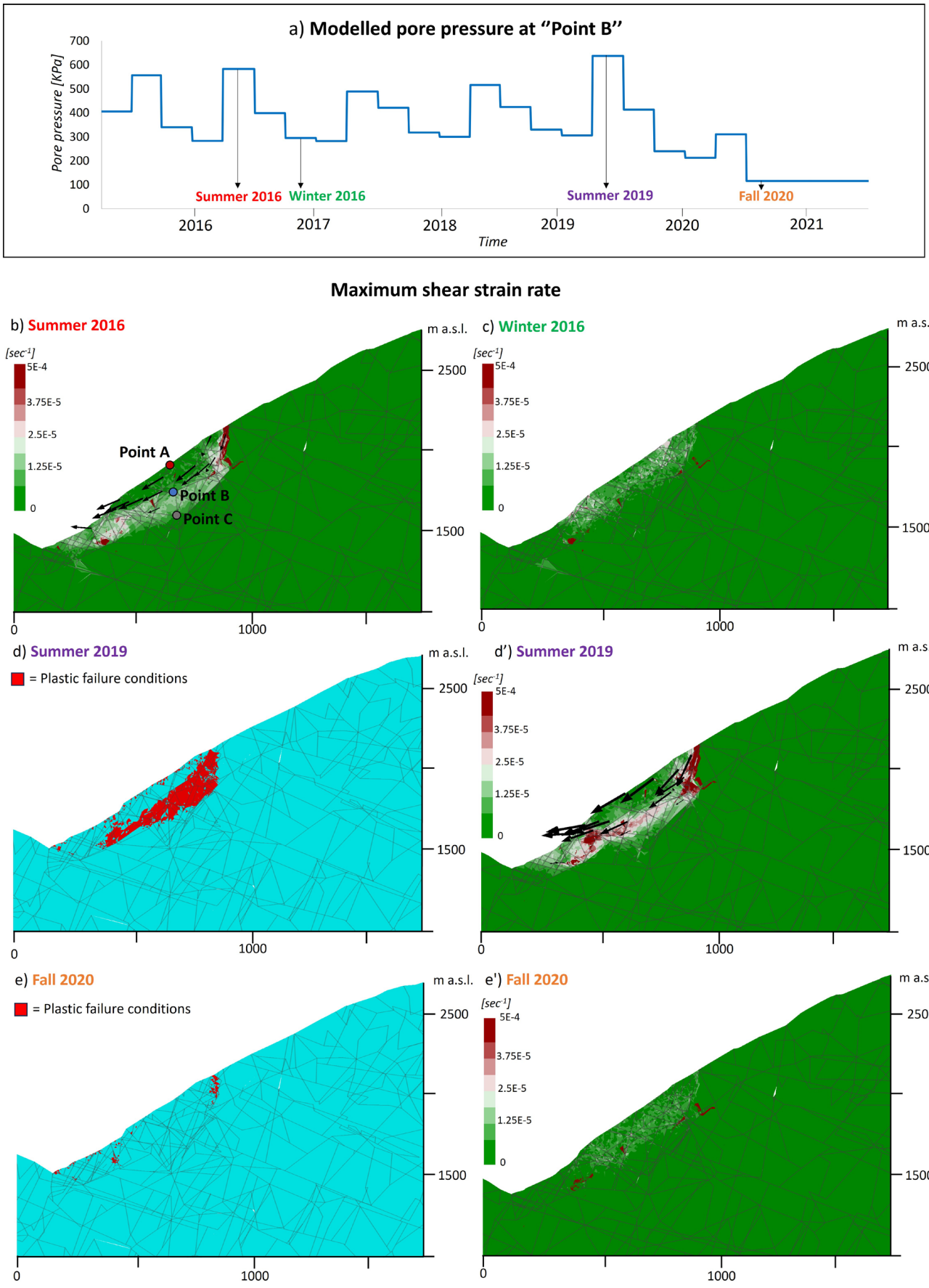

Figure 5.42 – a) modeled Pore pressure changes at point B. b,c,d',e') Maximum shear strain increment simulated at different stages of the transient hydrogeological regime. d,e) Plastic failure conditions.

The last modeling stage discussed, concerns the fall period of 2020, i.e., after the introduction of the Confinale creek water engineering works. As a result of the shift in effective stresses away from the failure conditions, no further plasticization is present, except limited to the high-niche zone (Figure 5.42e). As shown in Figure 5.42e', the distribution of deformation shows generally stable conditions, with a general absence of clustered strain regions. Small evidences of deformation are still present at the high niche, even if with very small, simulated values.

In general, these observations are consistent with the processed geotechnical monitoring data, which show more stable conditions in winter periods, when the water table level is low, and unstable conditions in the summer ones, when the piezometric level rises. The strain rates simulated by the model are referred to cyclical conditions of acceleration and deceleration/quiescence of the rockslide body during the same time periods, consistent with in situ observations. In fact, the displacements recorded by the GB-inSAR show a typical "stepped" evolution, defined by increased deformation in the summer months and static conditions in the winter ones.

Figure 5.43 shows the velocity and cumulative displacements values recorded by the monitoring points located along the slope (Figure 5.42b) at a depth of 0, 100 and 200 meters.

They show a "stepped" evolutive trend, that reflects the time-progression of the rockslide body detected by the geotechnical monitoring systems discussed above. Figure 5.43a shows the velocity (i.e., strain rate) simulated at the topographical surface (Point A), as well as above (Point B) and under (Point C) the modelled shear band. Peaks of strain rate (i.e. rockslide acceleration) are simulated during the summer period, and deceleration phases during the winter one. The highest velocities are reached in 2019 when the maximum piezometric level was measured and the simulated deformations take on maximum values. Moreover, it can be noted that the modelled velocities are highest along the topographic surface (point A) and almost the same within the entire simulated rockslide body (point B). A sharp decrease in velocity occurs at depths greater than the sliding surface (point C).

Figure 5.43b shows the cumulative displacements at the topographic surface in correspondence with the low landslide body, showing significant increments in the spring-summer periods and zero-deformation stages in the winter ones ("stepped" evolutive trend).

Although the deformative evolution of the rockslide body is correctly simulated by the model, a discrepancy between the magnitude of the simulated and measured values is reported (see for example Figure 5.26 and Figure 5.27), with measured values higher than modeled ones. This may be related to the simplifications that were necessary for model construction and HM simulation development. Among them is the size of the computational mesh, which, although sufficient to correctly simulate slope evolution, may not guarantee a sufficient level of detail in the simulation of stresses and strains. Added

to this is the 3-month time step used as the time interval at which to calculate HM equilibrium. A reduction of this time interval could allow a better definition of the distribution of stresses and failures. A fully coupled HM transient analysis, as well as the introduction of more complex mechanical constitutive laws, may allow better simulation of strain magnitude, but it is currently considered unfeasible for the computational effort required.

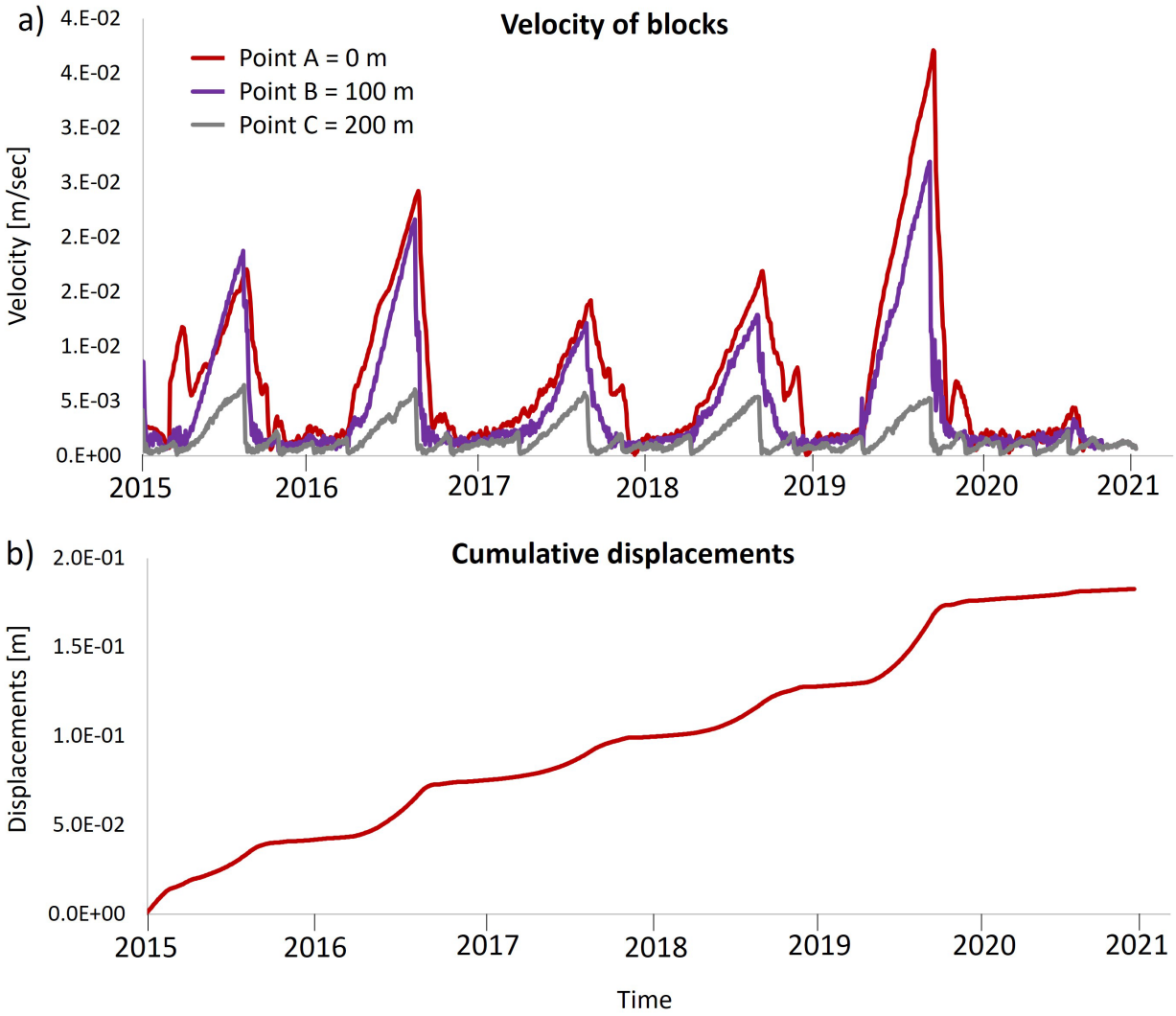

Figure 5.43 – a) Simulated block velocity at 3 monitoring points (Figure 5.42b). b) Simulated cumulative displacements along the topographical surface (Point A).

5.7.3 Discussion

The results of numerical modelling revealed a clear role of HM couplings in the stress-strain evolution of the slope, resulting in the development of a shear band already under steady-state hydrogeological conditions. In terms of location, geometry, and isolated volumes, this shear-region is coincident with the

sliding surface of the Ruinon rockslide, detected by in situ geological and geotechnical investigations (Section 5.3.3 and 5.4). The simulated shear band is developed at depths between 100 and 150 m, with a main slip surface at 100 m depth, reasonably representative of conditions observed in the field (70 to 100 m), considering the geometric simplifications required for the definition of the model (joint spacing and mesh dimensions).

Analyzing the transient hydrogeological regime, i.e. the 3D evolution of ground water availability, the close relationship between water pressures and the magnitude of simulated shear strains, was demonstrated, with maximum strain values in summer periods and minimum values in the winter ones. This is related to the fluctuation of the piezometric level, which during the rising phases interacts with the simulated slip surface promoting plastic failure, while in the decreasing phases remains below the identified surface without causing significant mechanical effects. These observations suggest that the location of the piezometric level and the distribution of hydrogeological bodies within the slope play a predominant role in the development of gravity-driven processes and the initiation of accelerated deformation phases.

By keeping the piezometric level below a given depth, a consistent reduction in the simulated deformations is shown. This is clear by analyzing the HM results of the years 2020 and 2021, when the piezometric level drops significantly due to the introduction of the hydraulic engineering works at the Confinale creek and drought weather conditions.

Analyzing the evolution of the deformative state and the trend of the measured variables at the modelled monitoring points, a good correspondence between the modeling outputs and the field evidences is observed. This attests the accuracy of the boundary conditions introduced and demonstrates the validity of both the mechanical and hydrogeological assumptions made during the numerical model set-up. In addition, these evidences allow validating the geological and geomechanical model elaborated in Section 5.4 from the data collected in situ, and used for the definition of the DEM model in Section 5.7.1.

The accuracy in the simulation of the mechanical evolution of the landslide body is mainly the result of a faithful reconstruction of the pore water pressures within the slope in response to climatic inputs. This confirms the importance adopting a 3D modeling approach for the stress-strain analysis of Alpine slopes, as already highlighted in Sections (3.2 and 5.5). In fact, in the present case study, the use of a 2D approach would not have allowed to capture the complex morphological, hydrological and geomechanical interactions, given their intrinsic 3D nature.

In the finite element analysis presented in Section 5.5, a close relationship between the evolution of the piezometric level and the magnitude of the simulated irreversible deformations had already been recognized. However, this analysis had a different purpose, of exploratory and parametric nature,

focused on verifying the role of morphology and mechanical properties in the development of the gravitational instability phenomena occurring along the Ruinon rock slope. Once the susceptibility of the slope to gravitational processes had been verified, the analysis presented in this section allowed to numerically describe the interaction between the evolution of the 3D hydrogeological bodies and the geomechanical setting of the slope. Combining the results of the two analyses, it can be concluded that the slope susceptibility to gravitational instability is mainly driven by the morphological and mechanical features of the slope, which are superimposed by the seasonal cyclical fluctuations of the piezometric level that modify the effective stress distribution and drive the development of plastic straining processes and acceleration phases of the main rockslide body.

Compared with the FEM analysis, the introduction of the discontinuity network allowed the geometries of the rockslide body to be simulated more accurately in terms of unstable mass volume and sliding surface depth, but especially in identifying the evolutionary dynamics of the simulated rockslide body (i.e., displacement distribution, positioning of shear surfaces, etc.). The failure mechanism mainly occurs along sub-vertical discontinuity surfaces that allow relative sliding of blocks by subsidence. On the other hand, principal sliding processes occur along less inclined discontinuity elements following the slope gradient.

The coupled HM modeling approach presented in this Section, represents a powerful tool for qualitatively verifying the stability of the rockslide body in relation to different hydrogeological inputs. In this regard, it was possible to observe that the introduction of the Confinale creek hydraulic engineering works, resulted in hydrogeological conditions that increased the stability of the rockslide body, at least considering the climatic conditions that occurred in the years 2020-2022. The highly unstable conditions that occurred in the year 2019 are associated with the achievement of critical depths of the piezometric level, which, in the summer of 2019, reached its maximum ever detected. The analysis of future evolution of groundwater bodies in response to climate change scenarios, can be explored and introduced into the present HM model for the verification of slope stability and deformative evolutionary state of the rockslide.

All the performed analyses demonstrated a clear relationship between changes in pore water pressure distribution and the deformative state of the rockslide body. These results emphasize the importance of distributed groundwater monitoring, which is currently only sufficient to set up, calibrate, and validate the presented HM model. However, if the numerical model is to be used to define new scenarios or to plan engineering solutions for slope stabilization, calibration and validation of the model should be performed dynamically, as soon as an adequate amount of new data is collected.

Finally, the relationship between pore water pressure variation and slope deformation, already defined in the processing of monitoring data (Section 5.3.6), can be further mathematically investigated, by focusing on the HM processes occurring at the slip surface, possibly also introducing more complex constitutive models. With this perspective, in the next Section, a 1D thermo-poro-mechanical model will be adopted to simulate and predict the velocity evolution of the landslide, obtaining critical values for measurable variables. The model will focus on the complex behavior of the shear band, in order to define the link between the external forcing (i.e. groundwater level) of the rockslide with its internal mechanical response. By deciphering this relationship, it will be then possible to predict the stability and velocity at the shear band and define the values of the input factors (driving factors) that result in unstable conditions of the system.

5.8 Stability analysis of the Ruinon rockslide: a novel physically based approach

Considering the field evidences of Ruinon rockslide activity (Section 5.3) and the results of numerical simulations showing a strong predisposition to gravitational instability processes (Section 5.5) as well as a key role of HM couplings in defining acceleration events (Sections 5.6 and 5.7), an advanced numerical analysis is now applied. By the development of a 1D thermo-poro-mechanical model, the aim is to reproduce the evolution of the rockslide, accounting for shear band material properties and the effect of pore pressure in promoting the evolution of different acceleration stages. The final goal is to forecast the stability and the velocity of the rockslide, by providing critical values of measurable variables as, for example, the groundwater level.

The analysis involves an accurate estimation of the mechanical and TM properties of the rock material by performing temperature-controlled triaxial cell tests. These tests will allow the definition of material parameters such as load-rate sensitivity and thermal sensitivity, useful in defining the THM behavior of the sliding surface.

The model developed in this Section represents a novel physics-based geomechanical tool to analyze landslide evolution, potentially useful for the implementation of early-warning and remediation strategies, that accounts for thermal and velocity sensitivity of shear band materials, as well as the effect of pore pressure in promoting acceleration events. The validated model can be also used as a predictive tool, to forecast the behavior of landslides taking into account future climate scenarios.

This modelling approach allows to take a step ahead toward the deciphering of climate forcings, a key research challenge that must be addressed to develop adaptation strategies for preventing and mitigating the impacts of ongoing climate change (Crozier 2010; Stoffel et al. 2014; Gariano and Guzzetti 2016; Paranunzio et al. 2019).

In this Section, the approach of analysis will be presented in detail, focusing on the application to the Ruinon rockslide. The model will be calibrated and validated against field data in the time interval 2014-2020, prior to the introduction of the hydraulic engineering works that resulted in a stabilization of the rockslide and an absence of significant deformation that could allow the calibration of the model. In Section 5.9, the developed model will be used to explore its application in assessing the impact of thermal variations related to climate change in the activity of large Alpine landslides, such as is the case of the Ruinon rockslide.

5.8.1 Methods

In recent years, several authors focused on the time-dependent behavior of shear band materials in large landslides (e.g. Vardoulakis 2002a; Goren and Aharonov 2007; Goren et al. 2010; Pinyol and Alonso 2010; Alonso et al. 2016). Veveakis et al. 2007 developed a model applied to the Vajont landslide, that accounts for heat production due to sliding friction in the shear band, relating the creeping motion to a thermally self-driven transient process. This creeping phase can be followed by progressive heating localization within the shear band that eventually triggers a catastrophic pressurization phase. Cecinato and Zervos 2012 proposed a generalized constitutive model accounting for heat generation and diffusion, pore pressure generation and dissipation, and thermal dependence of shear band materials, suitable to capture the final collapse dynamic evolution of large-scale landslides occurring in a coherent fashion. De Blasio and Medici 2017 studied the material response of the shear band due to friction and temperature increase related to acceleration steps of a sliding mass. Based on a number of experimental studies conducted on clayey material, that showed a dependence of mechanical properties on temperature (e.g., Hueckel et al. 2009; Ferri et al. 2010) and loading rate (Cappa et al. 2019; Bohloli et al. 2020), Seguí and Veveakis 2021 performed further laboratory tests on landslide shear band materials, demonstrating their thermal and load rate sensitivity.

Considering all the above evidences, Seguí et al. 2020 provided a time-dependent assessment tool for large landslides, combining internal and external factors acting on their sliding surface. This model assumes that the landslide body may be reproduced by a rigid block sliding on a thin visco-plastic shear band, undergoing thermal softening and velocity hardening. When the landslide moves, mechanical dissipation, due to friction, raises the basal temperature, while the shearing resistance of the shear-band material is reduced. This process can continue up to the point that the shear strength decreases uncontrollably, due to a thermal runaway instability (Gruntfest 1963).

In this Section the thermo-poro-mechanical mathematical model proposed by Seguí et al. 2020 and Seguí 2020 is applied to the Ruinon rockslide. The model assumes that the landslide deformation is concentrated on the basal shear band, representing the sliding surface: the landslide body is considered as a rigid block sliding on a thin visco-plastic shear band that undergoes thermal softening and velocity hardening. Shear stresses evolve with pore-pressure (i.e., groundwater level), defining the state of driving forces. When the landslide accelerates, mechanical dissipation occurs due to friction, that raises the basal temperature and reduces the shearing resistance of the shear-band material, up to a point that it can decrease uncontrollably due to a thermal runaway instability (Veveakis et al. 2007; Seguí et al. 2020). The system is so forced to become unstable, even when reducing the external driving factors (i.e.,

decreasing of the groundwater table), as it was shown to occur for the case of the Vajont landslide (Muller 1964, 1968).

The mathematical model and the constitutive equations used to forecast the behavior of the landslide were, first, proposed by Vardoulakis 2002, and further developed, among others, by Veveakis et al. 2007, Cecinato and Zervos 2012 and Seguí et al. 2020. The model has already been applied to the Vajont landslide (Italy) and to the Shuping landslide (Three Gorges Dam, China), to back analyze their stability and velocity evolution (Seguí et al. 2020), and to the El Forn Landslide (Andorra) as an early warning tool (Seguí and Veveakis 2021).

5.8.1.1 Numerical formulation

Starting from momentum, mass, and energy balance laws, and by assuming that the landslide shear band is fully saturated, without advection and volumetric changes ($\gamma_V = \gamma_{zz} = 0$), the governing equation describing temperature generation and diffusion within the sliding surface can be defined as:

$$\frac{\partial T}{\partial t} = D\frac{\partial^2 T}{\partial Z^2} + \left(\frac{\tau_d \dot{\gamma}}{\rho C_P}\right) \quad \text{(Equation 5.22)}$$

Where $D = \lambda/\rho C_P$ is the thermal diffusivity, ρ is the density, C_P is the specific heat capacity, λ is the thermal conductivity of the shear band material, τ_d is the shear stress acting on the sliding surface, $\dot{\gamma}$ is the shear strain rate, and T is temperature.

Considering the material to be visco-plastic, exhibiting a thermal and rate sensitivity behavior (Vardoulakis 2002a; Veveakis et al. 2007), a constitutive response for the irreversible part of the strain-rate is introduced in Equation 5.22. By assuming velocity hardening (i.e., the shear strength decrease as the shearing velocity increases) and thermal softening (i.e., when the temperature increases, the shear strength of the material decreases) the constitutive law for the shear-band material can be described by the following expression:

$$\dot{\gamma} = \dot{\gamma}_{ref}\left(\frac{\tau_d}{\tau_{ref}}\right)^{1/N} e^{m(T-T_0)} \quad \text{(Equation 5.23)}$$

Where $\dot{\gamma}_{ref}$ is the reference shear strain-rate, τ_{ref} is the reference shear stress, N is the frictional rate-sensitivity coefficient, m is the ratio of the temperature sensitivity coefficient (M) over the load-rate sensitivity coefficient (N), T is the temperature in the shear band, and T_0 is a reference temperature. Therefore, Equation 5.22 can be expressed as:

$$\frac{\partial T}{\partial t} = D\frac{\partial^2 T}{\partial Z^2} + \left(\frac{\tau_d}{\rho C_P}\right)\dot{\gamma}_{ref}\left(\frac{\tau_d}{\tau_{ref}}\right)^{1/N} e^{m(T-T_0)} \quad \text{(Equation 5.24)}$$

Equation 5.24 can be reduced to a dimensionless equation by considering the following:

$$z^* = z/(0.5 * z)$$

$$t^* = (\lambda_m/(0.5 * ds)^2) * t$$

$$T^* = m(T - T_0)$$

Where *ds* is the thickness of the active shear band. Equation 5.24 in dimensionless form, becomes:

$$\frac{\partial T^*}{\partial t^*} = \frac{\partial^2 T^*}{\partial Z^{*2}} + Gr\, e^{T^*} \quad \text{(Equation 5.25)}$$

where *Gr* is the Gruntfest number (Gruntfest 1963), defined as:

$$Gr = G_0 \left(1 + \frac{P_f}{P_{f0}}\right)^{1+\frac{1}{N}} \quad \text{(Equation 5.26)}$$

With:

$$G_0 = m \frac{\dot{\gamma}_{ref}}{D\rho C_P} \frac{ds^2}{4} \tau_{d,ref} \quad \text{(Equation 5.27)}$$

where P_f is the groundwater pressure and P_{f0} is the reference pressure.

The Gruntfest number introduced in Equation 5.25 is a dimensionless parameter representing a link between the external loading conditions and the internal response of the material, since it evolves with the pore water pressure and time (Equation 5.26).

Once the temperature is calculated by solving Equation 5.25, the next step is to define the velocity, *v*, and the cumulative displacement, *u*, of the landslide. This is achieved by integrating the strain rate over space and time. For the velocity:

$$v = \int_{-ds/2}^{ds/2} \dot{\gamma} dz = v_0 \int_0^1 \left(\frac{P_f}{P_{f0}}\right)^{1/N} e^{T^*} dz^* \quad \text{(Equation 5.28)}$$

Where v_0 is the reference velocity of the slope, which can be calculated from the slope displacement data detected outside the main landslide body.

As evidenced by Equation 5.25, the system depends on a single parameter, *Gr*, that expresses the ratio of the mechanical work converted into heat over the heat diffusion capabilities of the material.

Following the discussion presented in Seguí et al. 2020, the stability assessment can be performed by computing the steady-state response of the dimensionless temperature as a function of the Gruntfest number, through a numerical bifurcation analysis. If the combination of pore pressure (and consequently shear stresses), Gruntfest number and temperature is such that the state of the system remains within the area of stability (green area in Figure 5.44a), the system has the capacity to diffuse away the heat

generated inside the shear band due to friction and maintain a stable, slow creeping (Point A in Figure 5.44a). As soon as the shear stress or pore pressure lead *Gr* to increase above the critical value (Gr_c), or the (*Gr, T*) combination to lie outside the area of stability (Point B in Figure 5.44a), the system is entering a quasi-adiabatic regime (orange line in Figure 5.44b and c), where the heat generated due to friction cannot be diffused away, causing abrupt increase of the temperature leading to a so-called thermal runaway process (Gruntfest 1963).

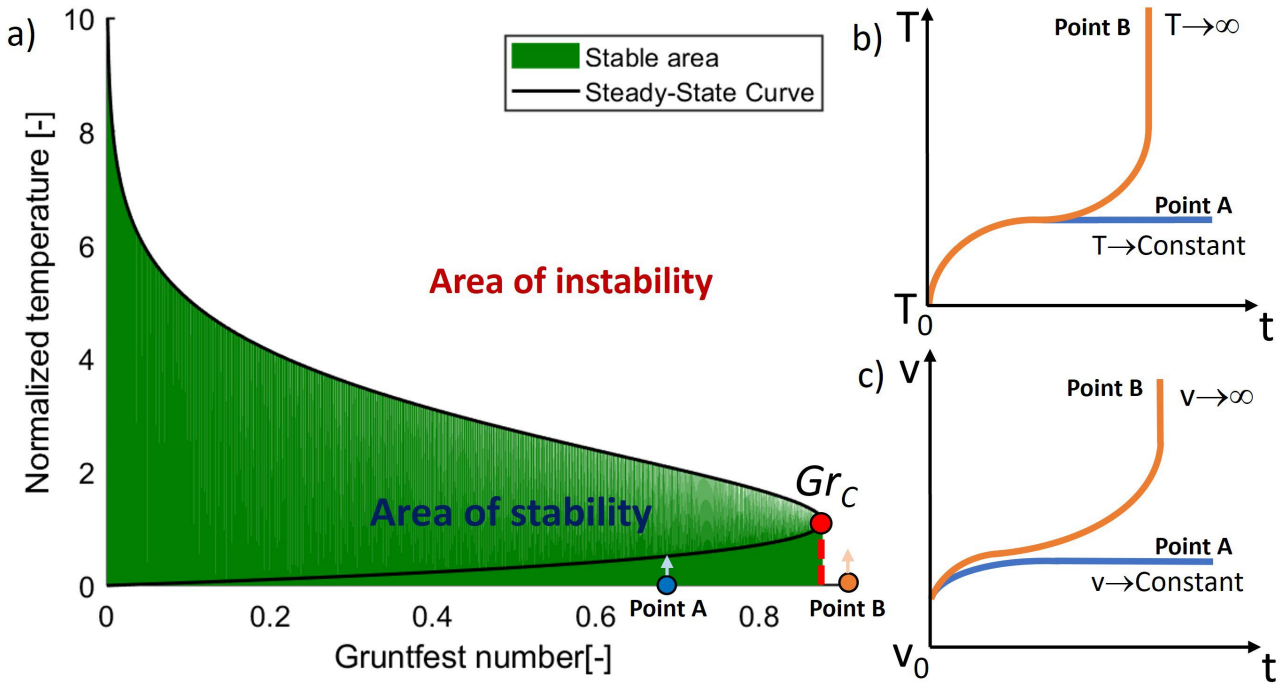

Figure 5.44 – Representation of the steady-state curve and area of stability of the dimensionless temperature as a function of the Gruntfest number. The value of critical Gruntfest is also highlighted in red. Points A and B represent two possible scenarios. b) Modeled temperature evolution for a point within (A) and outside (B) the stability area. c) Modeled velocity for the same points.

Based on the above presented mathematical formulation, the input data required by the model are the pore pressure, reference stress and velocity, as well as the initial temperature at the shear band and its thickness. In addition, to define the constitutive parameters of the shear band (modelled as a visco-plastic medium with thermal softening and velocity hardening, Equation 5.23), thermal and load rate sensitivity of the material must be measured or estimated, along with thermal diffusivity and density.

5.8.1.2 Definition of thermal and load rate material sensitivity

Experimental tests in a customized triaxial apparatus with velocity and temperature control were performed to explore the Ruinon material behavior and define thermal and load rate sensitivity

parameters. Although representative values have been suggested in the literature, they can only be fully determined through laboratory testing at different loading rates and temperatures. Because of the non-linear dependence of *Gr* on thermal and load rate sensitivity, the model is extremely sensitive to small variations of their values (especially for *N*), and thus an accurate definition of these parameters is decisive in the representativeness of the model. The thermal sensitivity parameter is mainly controlled by the mineralogical composition of the tested material and in particular by the clay content, as well as the rock fabric. In fact, at temperatures above 50° C, clay minerals can undergo chemical degradation processes that drastically change the behavior of the material. It follows that the higher the clay content in the rock, the greater its thermal sensitivity. Regarding the fabric of the rock, Seguí and Veveakis 2021 showed that if the minerals are oriented following one direction (e.g., direction of landslide sliding), the thermal sensitivity properties are very pronounced.

The material tested in this study was sampled from the rock cores sampled along the Ruinon slope during the drilling campaign of the years 2020-2021 (Section 5.3.3). Since the drilled boreholes are located outside the main rockslide body, no material is available from the shear band. Intact rock samples were collected at a depth of about 30 m from the locations closest to the rockslide body. Considering the rock slope model proposed in Section 5.4, which shows geological homogeneity along the rockslide, it is therefore reasonable to assume that the material composing the sliding surface has the same lithological properties as the main body, even if with a different degree of fracturing.

From the collected material, 6 cylindrical specimens (38mm diameter, 75mm height) were obtained (Figure 5.45). The rock material consists of phyllites with light bands composed of sericite, chlorite and sometimes graphite minerals and quartz bands. Quartz can also be present in veins or lenses (Montrasio et al. 1990; Griffini 2004).

The six available samples were divided into two groups of three samples each, one to be tested for the load rate sensitivity and one for the thermal sensitivity. Load-rate sensitivity tests were conducted in a triaxial apparatus by applying a lateral pressure of 1 MPa and a strain-controlled axial load until the specimen was led to a critical state or failure. Three different loading rates were tested: 0.005, 0.1 and 0.2 mm/min.

Thermal sensitivity tests were carried out by fixing the confining pressure and the loading rate at constant values of 1 MPa and 0.1 mm/min, respectively. During the first step, samples were heated to a specified temperature through a warming process with 3 °C steps, inducing a rate of 1.5 °C per hour before letting it equilibrate. Once the temperature had stabilized, the axial load was increased while keeping the strain rate of 0.1 mm/min constant, and the specimen was brought to failure (step 2). The temperature of the sample was monitored with a thermal probe less than 10 mm away from the sample, and the imposed

temperature was held constant until steady-state was achieved in the specimen. Four different temperatures (20, 35, 50 and 80 °C) were tested. By studying the relationship between deviatoric failure stress, loading rate (Figure 5.45a), and temperature (Figure 5.45b), the load rate sensitivity (N=0.075) and thermal sensitivity (M=0.006°C^{-1}) parameters were obtained.

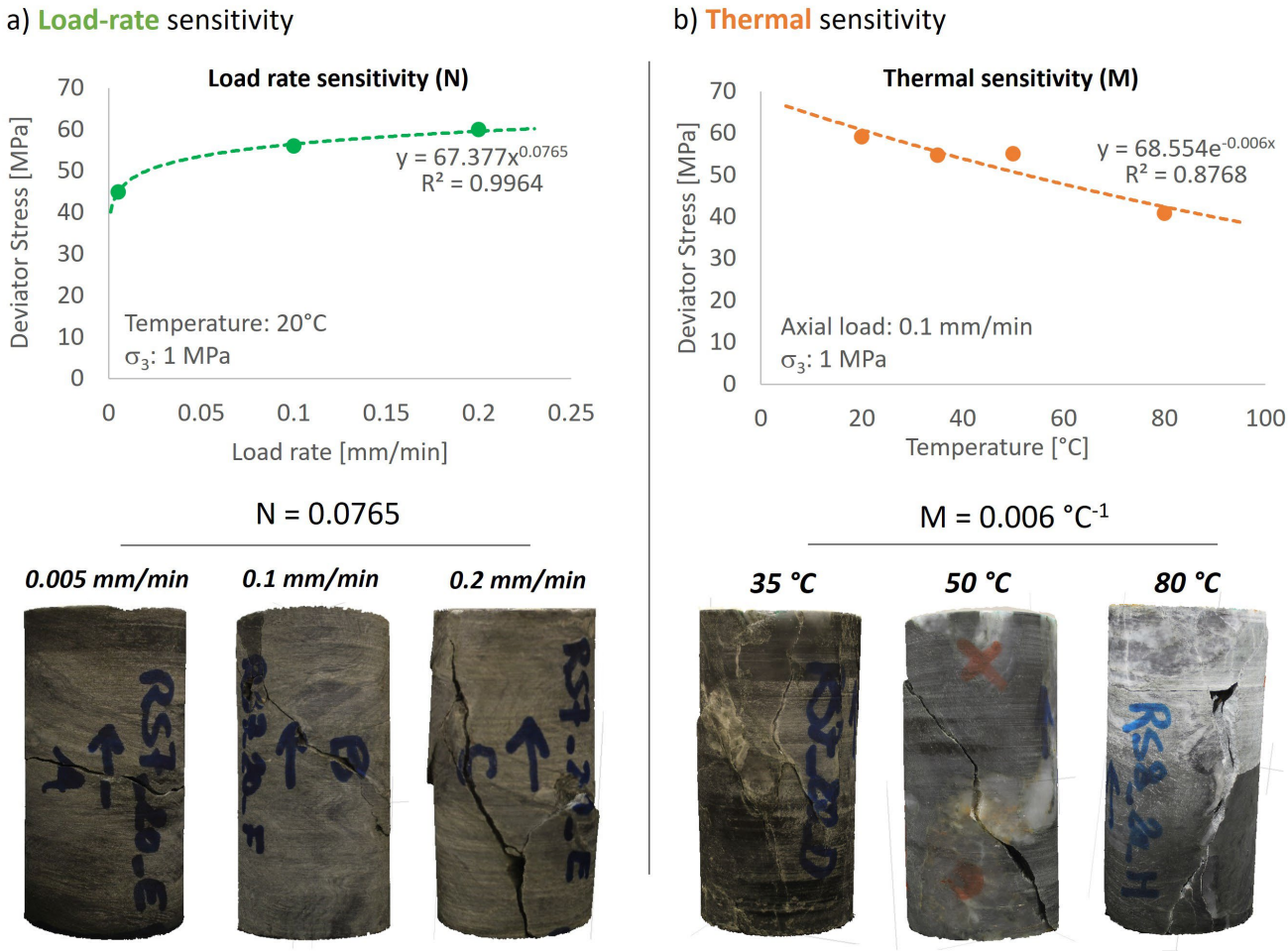

Figure 5.45 – a) Results of triaxial tests conducted at fixed temperature and lateral confinements, varying axial loading rates. Assessing the values of deviatoric stress at failure at different loading rates, allowed to define the load rate sensitivity parameter. b) Results of triaxial tests conducted at fixed load rate and lateral confinements, varying temperature. Assessing the values of deviatoric stress at failure at different temperature values, allowed to define the thermal sensitivity parameter.

By analysing the load-rate sensitivity results, a power interpolation fitting line was obtained, suggesting a load-rate hardening behaviour of the material (i.e., rock resistance increases as the speed of the load applied increases). On the other hand, the thermal sensitivity analysis shows an exponential interpolation line, suggesting a thermal softening behaviour (i.e., rock strength decreases with increasing temperature). These results are in accordance with the analysis conducted by Seguì and Veveakis 2021 and Seguì 2020 on similar rock materials. Compared with literature values, the tested material showed moderate load rate sensitivity and low thermal sensitivity, probably due to the nature of the material with a low component of clay minerals and a fabric not very well oriented given the presence of quartz veins.

5.8.1.3 Modeling input data

The input data required by the mathematical model presented above are represented by pore pressure at the sliding surface, and the shear band material properties. Groundwater levels measured by the piezometer *PZ4* (Section 5.3.6, Figure 5.46a) were used to calculate the pore pressure values by the relation $P_f = gH\rho_w$ (where g is the gravity acceleration, H the water head, and ρ_w the water density). Considering the stratigraphic data and the model presented in Section 5.4, a slip surface at 80 meters depth was assumed, and pore pressures were calculated in hydrostatic conditions considering the piezometric head above the sliding surface (Figure 5.46b). A time range from 2014 to 2020 was considered at this stage of the (back-)analysis. This time range allows for the inclusion of the two main Ruinon rockslide acceleration events that occurred in 2016 and 2019. In addition, this period precedes the introduction of hydraulic engineering works to regulate the Confinale creek and thus allows for the analysis of the interaction between pore pressures and the mechanical behavior of the shear band in its natural evolution.

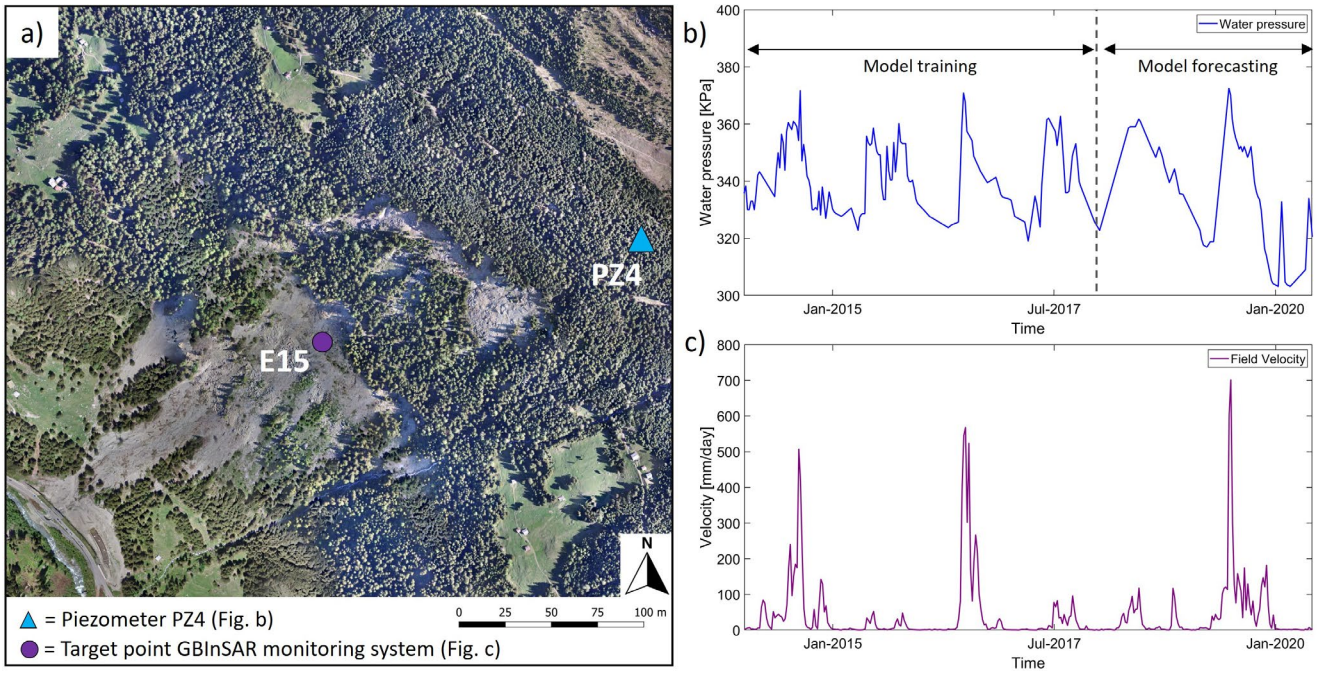

Figure 5.46 – a) Input factors introduced into the thermo-poro-mechanical model. a) Location of the piezometer used for pore pressure calculation and the GBInSAR monitoring point for landslide velocity assessment. b) Evolution of pore pressure introduced in the model. c) Evolution of landslide velocity used for model calibration and validation.

A reference temperature value of 10 °C was defined (T_0), which can be considered a representative average annual value for the slope at the considered sliding depths. This value agrees with the water temperatures measured at the springs around the "low niche". The thermal and mechanical parameters of the material derived from both laboratory tests and literature data, are presented in Table 5.21.

Table 5.21 – Shear band material parameters.

Parameter	Value	Detection method
Load rate sensitivity (N)	0.075	Laboratory test
Thermal sensitivity (M)	0.006 $°C^{-1}$	Laboratory test
Thermal diffusivity (D)	$6 \cdot 10^{-7}$ (m^2/s)	Cermak and Rybach 1982
Density (ρ)	2700 (Kg/m^3)	Laboratory test - Section 5.3.3
Heat capacity (C_P)	910 (J/Kg*K)	Cermak and Rybach 1982
Thermal conductivity (λ)	1.5 (W/(m*K))	Cermak and Rybach 1982
Reference slope velocity (V_0)	0.018 m/yr	In situ monitoring - Section 5.3.3
Reference stresses (τ_{ref})	$2 \cdot 10^5$ Pa	Stress-strain modelling – Section 5.5 and 5.7
Reference temperature (T_{ref})	10 °C	Assumption based on in-situ observations
Active shear band thickness (ds)	0.1 m	Inversion analysis - calibration
Initial Gruntfest number (G_0)	$2 \cdot 10^{-5}$	Inversion analysis - calibration

To constrain the loading stress acting at the sliding surface (τ_{ref}), results from the stress-strain models presented in Sections 5.5 and 5.7 were introduced. At a depth of about 80 meters, the models indicate shear stresses in a range of 0.2-0.5 MPa depending on the groundwater level and on the deformation state. In addition, HM stress-strain modeling allowed to assess the time-dependent evolution of the shear stress with piezometric level. As a first approximation, a simple linear equation to calculate the stress state along the slip surface of the landslide was introduced, depending only on the depth of the groundwater table.

The remaining parameter required in the expression of *Gr* is the active shear band thickness, *ds*. An initial value of 0.1 m was assumed, based on stratigraphic and geological data (Section 5.4). In a second step, the thermal sensitivity coefficient *M* and the reference values of the stress were used to infer the shear band thickness value through an inversion analysis (Seguí et al. 2020), described in the next Section.

The modelling analysis was divided into two different steps. In a first step defined "*training step*", the pore pressure data relevant to the years 2014-2018 were introduced as input factors. This step allowed to calibrate the model, by comparing the outputs of the model with the displacement and velocity data recorded by the landslide monitoring system. The normalized field data were fitted by the model calculated velocity using the time-dependent *Gr* number as an inversion parameter.

Once the model was calibrated, defining G_0 and *ds*, the second step (defined "*forecasting step"*) of the analysis involved the prediction of velocities by introducing pore pressure values relevant to years 2018-

2020. To validate the model, calculated output velocities were compared to the normalized field data recorded by the GBInSAR system (Figure 5.46c), which provided a sufficiently large dataset (Section 5.3.6). Point E15 (Figure 5.46a) was taken as a reference, considering that: (i) its location represents the center of mass of the landslide, (ii) it exhibits the largest displacements, which allows to evaluate the slope stability for the worst-case scenario. The choice of taking velocity data recorded at the slope surface as representative of the whole slope assumes the landslide mass to move as a rigid body with no change in velocity from the shear band to the topographic surface, as required by the model. This may be seen as a strong assumption and a limitation of the adopted approach, but it allows to perform a conservative analysis. In fact, all risk protection and mitigation actions refer to surface velocity values of the landslide body, which typically exhibit a similar trend to the deep ones but with higher magnitudes. In addition, surface deformations are the easier to measure in terms of both operability and cost. For the Ruinon case study, to date there are no monitoring systems installed that allow measurement of deep deformations at the sliding surface with temporal continuity. Therefore, the choice of using surface deformations for model calibration with all the associated assumptions is also related to the feasibility of the tool that is going to be defined. Furthermore, this assumption is consistent with the geomechanical modeling outputs of Section 5.7, that simulate small velocity reductions as depth above the slip surface increases.

5.8.2 Results

In a first step, the model was calibrated based on the fitting of the modeled velocities with the data recorded by the monitoring system, considering the interval between January 2014 and January 2018. All parameters required by the model were calibrated by qualitatively identifying the best fitting between simulated and monitored rockslide velocity (Figure 5.47a).

In this phase, the Gruntfest number was constrained by an inverse analysis: all parameters that define *Gr* are known, except for G_0. Different values of G_0 were then assumed, and a value of $2 \cdot 10^{-5}$ was fixed providing the best fitting velocity (Figure 5.47a). Moreover, the thickness of the shear band (*ds*) was constrained by solving Equation 5.27 as a function of *ds*. Considering the best-fit value of G_0, Equation 5.27 was applied to invert for the shear band thickness (*ds*) and the driving background stresses ($\tau_{d,ref}$). Using a range of thermal sensitivity values (*M*), different relations between $\tau_{d,ref}$ and *ds* were obtained (Figure 5.47b). Fixing the thermal sensitivity on the results of laboratory tests presented above, a value of *ds* could be defined by constraining the reference shear stresses on results of the stress-strain

modelling (Section 5.5). By evaluating the relationship between all the factors introduced in the plot of Figure 5.47b, a value of *ds* of 0.1 m was thus obtained.

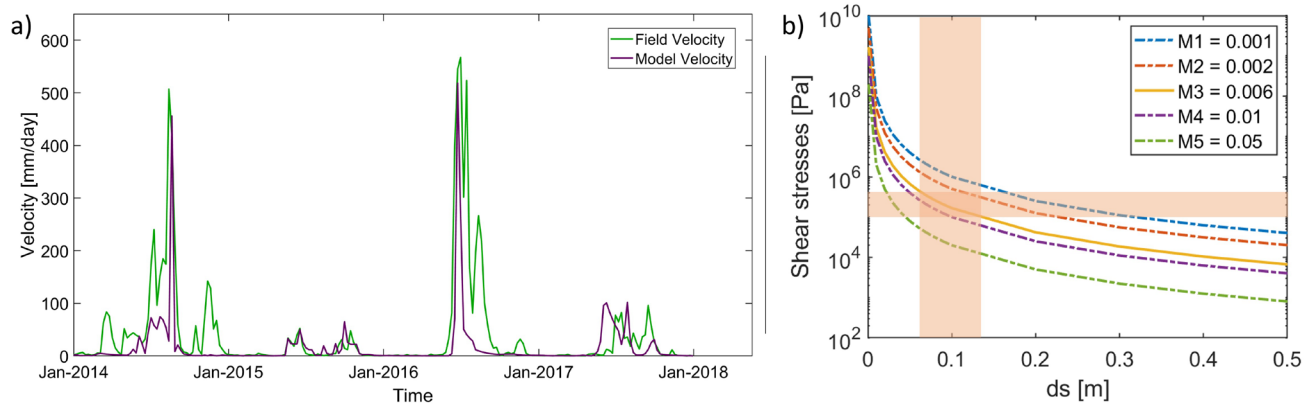

Figure 5.47 - Model calibration analysis. a) Best fitting obtained between modeled and monitored velocities. b) Evolution of the shear stress in relation to the active shear band thickness, with different scenarios of thermal sensitivity (M). Fixing the thermal sensitivity value by considering the results of laboratory tests (M=0.006), a value of ds was defined by constraining the reference shear stresses on results of the regional FEM modeling.

Once calibrated, the model was validated over the time range 2018-2020. A good fitting between recorded and simulated values of velocity was obtained (Figure 5.48a).

The model accurately reproduces the rockslide behavior, by adequately identifying periods of maximum acceleration of the sliding mass. The relationship between groundwater level trends and landslide velocity is well simulated. Deviations between the two curves in Figure 5.48a are mainly defined by differences in the magnitude and amplitude of a few velocity peaks.

Figure 5.48b-c respectively show the evaluated Gruntfest number (*Gr*) against normalized temperature in the model's phase space and the simulated basal temperature evolution over time. Figure 5.48b shows that *Gr* and basal temperature vary along the lower branch of the stable curve (i.e., within the stable area of the graph) with values close to the Gr_c, but never reaching it. The simulated mechanical state of the rockslide therefore remains stable in the secondary creep phase in agreement with the monitored evolution of the rockslide, which shows near-collapse conditions with significant accelerations and frequent gravitational-instability events. The calculated basal temperature (Figure 5.48c) follows the evolution of the effective shear stresses (and consequently the pore pressures) acting along the slip surface. It varies over a range of about 5°, with maximum temperature peaks corresponding to pore pressure peaks. During the years 2014, 2016 and 2019, significant landslide acceleration events occurred, in correspondence with a sudden increase in the piezometric level. This also resulted in a rise of the basal temperature, due to the increase of frictional heat, which may have modified the internal mechanical conditions and exacerbated the velocity values.

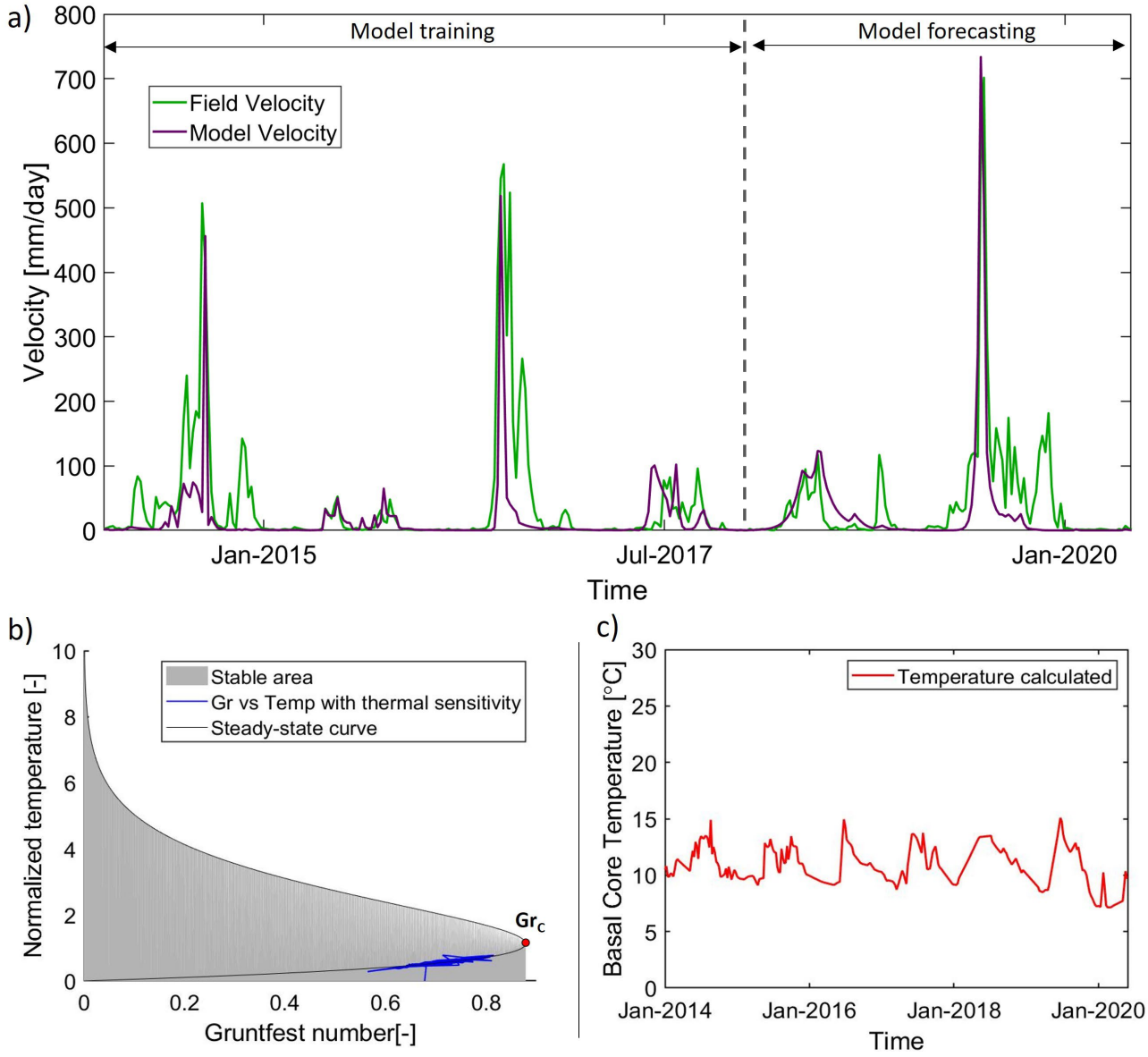

Figure 5.48 - a) Validation of the model by predicting velocities for the years 2018-2020 and comparing them with the monitored ones. b) Evolution of the Gruntfest number. c) Simulated basal temperature.

Once the model was calibrated and validated over the 2014-2020 time range, an explorative attempt was made to apply this modelling tool in predicting mechanical behavior of the landslide in relation to variations in external inputs. In particular, a rise of the piezometric level was hypothesized, with the goal of identifying the groundwater level (i.e., pore pressure value) sufficient for the development of critical conditions (i.e., collapse conditions). By a "trial and error" iterative process in which increasing pore pressures were progressively introduced in correspondence of the June 2019 conditions, the critical pore pressure value was identified. As shown in Figure 5.49, by introducing a pore pressure value of 390 kPa, which corresponds to the location of the groundwater level at a depth of 30 m from the topographic surface (instead of 32 m as measured), critical conditions are simulated.

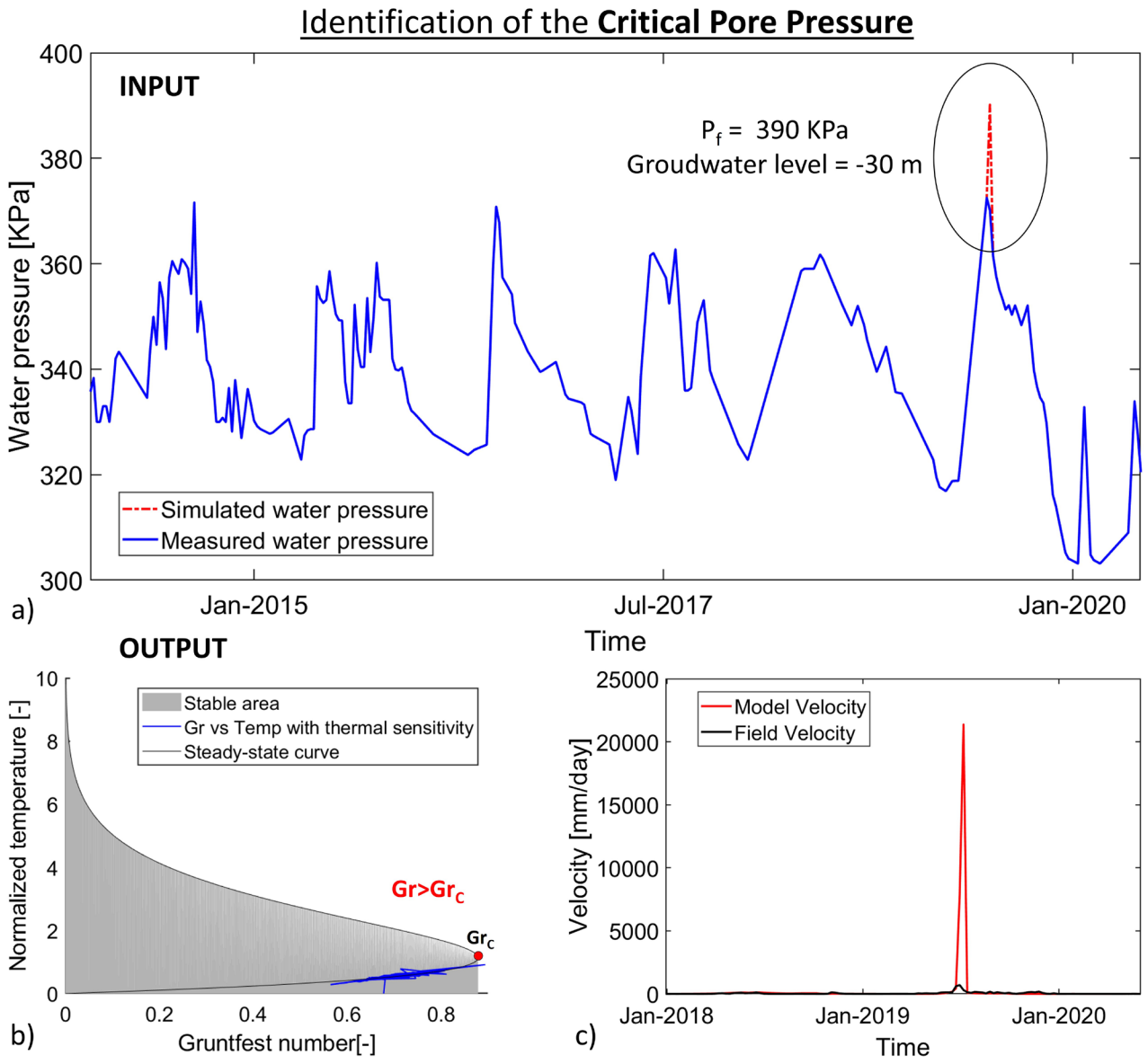

Figure 5.49 – a) Evolution of pore pressure introduced into the analysis. Values are coincident with those monitored, except for June 2019 when higher hydraulic pressure values were introduced. b) evolution of the gruntfest number against normalized temperature in the model's phase space. c) Simulated landslide velocity.

The evolution of the Gruntfest number against normalized temperature in the model's phase space (Figure 5.49b), reaches the critical value (Gr_c) representing conditions of quasi-adiabatic regime (orange line in Figure 5.44b and c). In this condition, the heat generated due to friction cannot be diffused away, causing abrupt increase of the temperature leading to a so-called thermal runaway process.

Simulated landslide velocities (Figure 5.49c) are in the range of 20 m/day, much larger than the value of 0.7 m/day measured in June 2019, when strong unstable conditions occurred. Therefore, the simulated critical scenario indicates strongly unstable conditions, and the pore pressure value introduced represents its critical value.

Regarding the conditions that triggered the acceleration stages of the rockslide body in the years 2014, 2016, and 2019 (Figure 5.50a), a unified criterion for a rigorous definition of waring thresholds has not yet been established. Analyzing the evolution of the Gruntfest number against normalized temperature in the model's phase space, it can be observed that in correspondence with acceleration events, the curve clearly shifts toward the Gr_c (Figure 5.50 b-c). Evolution occurs predominantly along the x-axis (i.e., *Gr*), consistent with field evidence that has demonstrated a strong dependency between the deformation state and pore pressures.

Thermal increases, on the other hand, are more limited and sometimes show an unclear trend, especially for the year 2014, when the rising of temperature occurred after the *Gr* peak, in contrast to the 2016 and 2019 events where a synchronous increment was observed (Figure 5.50 c). The evolution of simulated landslide velocities in relation to *Gr* shows a generally monotonous trend, with a rapid and well-defined change of slope at the onset of acceleration stages (Figure 5.50 d). Hence, *Gr* values of 0.735 can be qualitatively assumed to define pre-alert conditions for acceleration steps, which seem to occur at values of *Gr* higher than 0.74.

However, more evidence and numerical insights are needed to define a quantitative and reliable method to detect threshold values of *Gr*, pore pressure or temperature that can identify the initiation of acceleration stages of the landslide body in pre-collapse conditions (i.e., secondary creep). For civil protection and landslide risk management purposes, these values would represent pre-warning and warning thresholds that could be identified simply by continuously monitoring parameters such as piezometric level or temperature at the sliding surface. However, more efforts are still needed to achieve these goals. Some suggestions will be addressed below in the discussion Section 5.8.3.

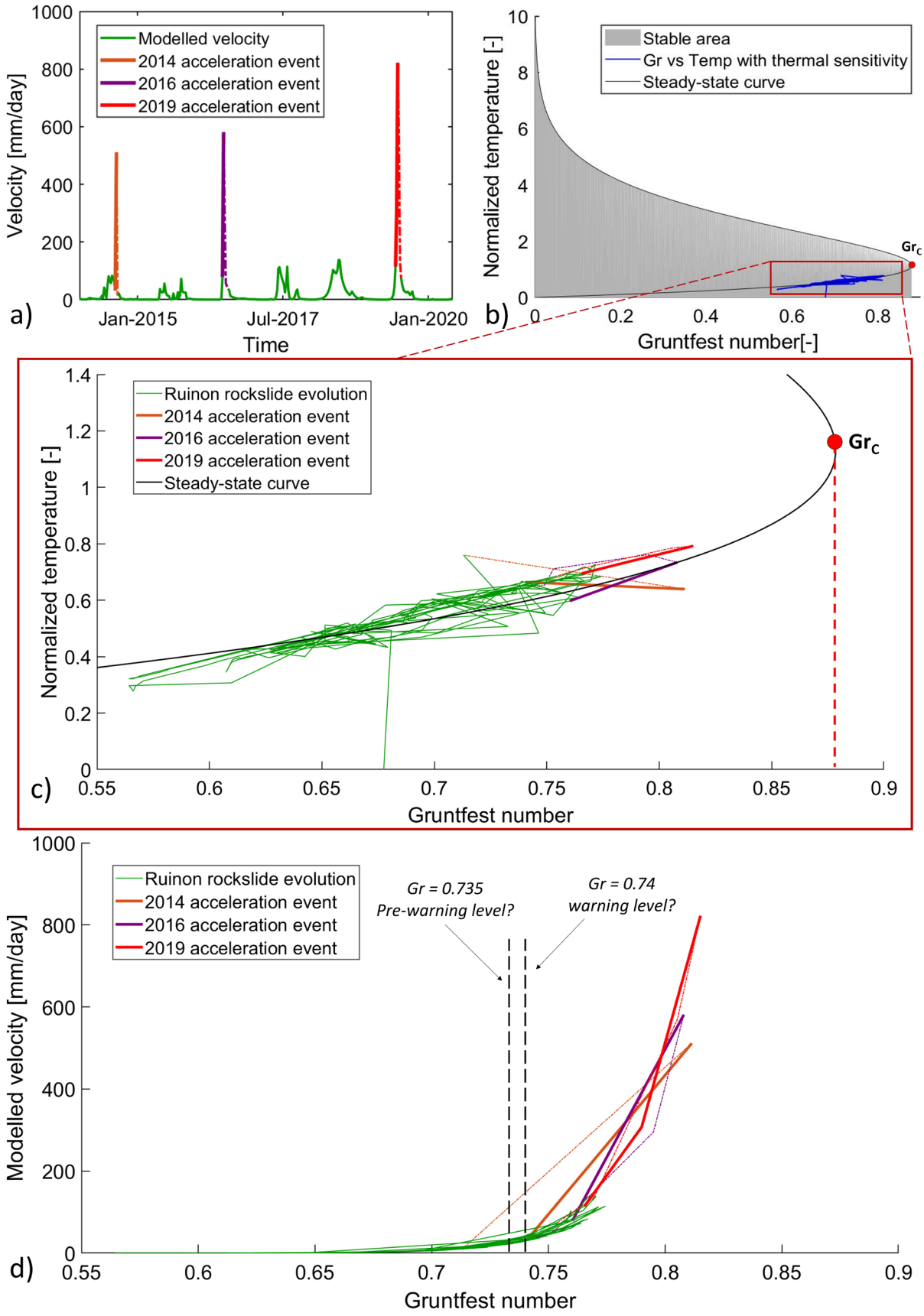

Figure 5.50 – a) Modeled velocity and identification of significant acceleration phases. b) evolution of the gruntfest number against normalized temperature in the model's phase space. c) Focus on the Ruinon rockslide evolution with the identification of the 2014, 2016 and 2019 acceleration events in the model's phase space. d) Modelled velocities vs Gruntfest number; two different values of Gr are hypothesized as pre-warning and warning levels based on the evolution of the curve.

Summarizing the above discussion, with current knowledge, a collapse threshold value was identified by calculating the critical value of *Gr* (i.e., of pore pressure). This represents the pore pressure value that, if exceeded, generates collapse (corresponding to tertiary creep). Below Gr_c, the rockslide is in unstable condition, where acceleration stages can occur (i.e., secondary creep). The numerical definition of the pre-warning and warning thresholds, representing progressive transition between stable and unstable conditions, cannot be currently provided with an objective criterion. In the present study, by analyzing the evolution of *Gr* with modelled velocity, a pre-warning and warning level of Gr = 0.735 and Gr = 0.74 were hypothesized, corresponding, following Eq. 5.26, to a pore pressure of 353 and 362 kPa respectively (Figure 5.51a).

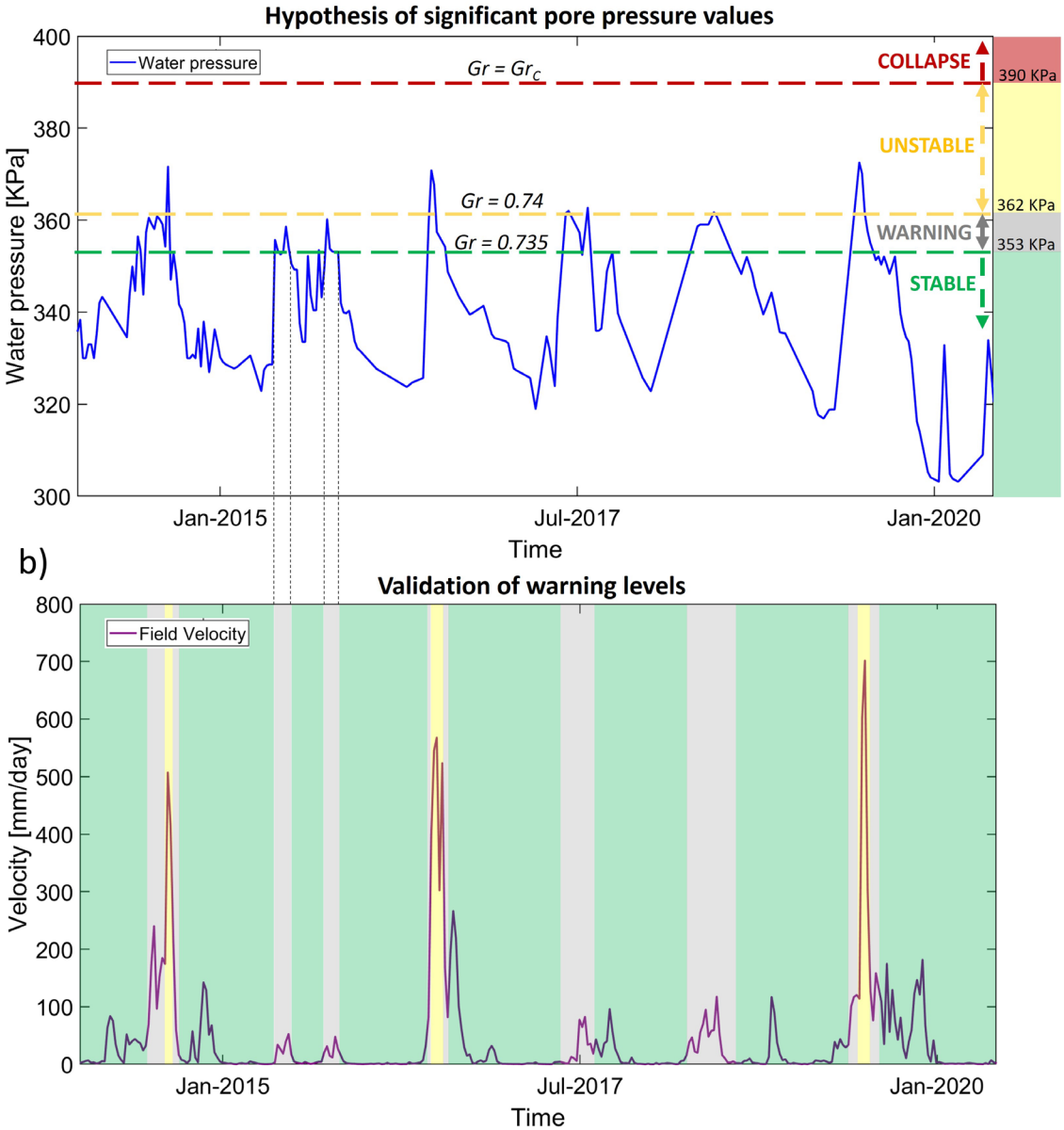

Figure 5.51 – a) Definition of pore pressure levels corresponding to Gruntfest values identified as potential thresholds. b) Validation of stability, pre instability and instability levels by highlighting the time periods corresponding to the relevant classes in the evolution of measured velocities.

It should be observed that the 2014, 2016 and 2018 acceleration events occurred above pore pressure values of 362 kPa, whereas between values of 353 and 362 kPa an increase in velocities was observed, but without generating significant instability events (Figure 5.51b). Below values of 353 kPa, no relevant deformation phases are reported, indicating stable conditions (Figure 5.51b).

5.8.3 Discussion

The thermo-poro-mechanical model developed in this Section is based on monitoring and numerical evidences that identified a clear relationship between piezometric level evolution and the deformation activity of the Ruinon rockslide body. The model combines external and internal factors that control the rockslide mechanical evolution, through the definition of the so-called Gruntfest number (*Gr*). The pore pressure evolution (P_f), due to groundwater fluctuations, represents the main external driving factor for the rockslide, while the mechanical weakening of the shear band, due to loading rate and temperature variations, defines its internal response.

The model results faithfully simulate the behavior of the rockslide during the considered time period. *Gr* values evolve close to critical stability in the model phase space, in accordance with field observations showing a significant landslide activity with displacements and velocity values close to a critical point (i.e., close to tertiary creep, or final acceleration of the landslide, representing catastrophic collapse).

Some small discrepancies between the calculated and monitored velocities are shown in terms of their magnitude and time lag, especially in correspondence of the velocity peaks. This may be explained considering the one-dimensional approach of the presented analysis, which neglects the complex natural 2- and 3-D evolution of the field variables. In addition, the fact that measured velocities are sometimes greater than simulated ones, may be ascribed to the fact that field velocities are related to a monitoring point located on the surface of the rockslide body, which may be affected by shallow secondary accelerations that are neglected by this modeling approach. However, considering all the necessary assumptions made in the mathematical model, the results obtained can be considered to faithfully simulate the general behavior of the landslide, by properly matching the velocity peaks and their time of occurrence.

The parameters introduced in the model are comparable with ranges reported in the literature. Concerning the values of G_0 and *ds* (which are the most uncertain parameters, as they cannot be directly measured or easily estimated), they were constrained through a calibration process, involving inverse analysis until the best match between modeled and measured velocities was achieved. By monitoring

the basal temperature of the landslide and performing a thorough mechanical characterization of the shear band material, G_0 and ds parameters could be better constrained, resulting in a reduction of model uncertainties.

A major factor of model uncertainty is represented by the temperature calculated at the sliding surface, as no monitoring data for this parameter are available. However, at this stage of modelling, the reference temperature (T_0) of 10°C is sufficiently representative of the slope under analysis, consistently with water temperature data recorded at springs near the lower landslide niche. This value is also in agreement with temperatures calculated in previous works, where the thermal evolution along an Alpine slope was simulated in similar geological and morphological conditions (Grämiger et al. 2018; Morcioni et al. 2022). Future numerical simulations of the slope could be performed to include thermal diffusion and groundwater-driven convection processes to better define the boundary temperature values at the sliding surface (T_0).

A key feature of the presented analysis lies in the consequentiality between the output of the regional stress-strain models (Sections 5.5 and 5.7) and the input of the present analysis. Compared with traditional numerical analysis, this approach allows a greater awareness of the interactions between external and internal variables through the definition of a complex mathematical relationship. Thanks to this numerical description, the link between pore pressure and deformation state of the rockslide, is fully defined through a mathematical treatment and no longer described qualitatively through comparison of simulated variables. Once validated, the presented mathematical model allows to simulate and predict any deformation state in response to variations in external factors such as the groundwater level. As a consequence, this tool could be useful for the identification of threshold levels below which the driving factors (e.g., the groundwater level) must lie to ensure mechanical stability conditions of the slope, thus providing a physically-based warning system.

This analysis can be considered as a preliminary step, developed to explore the potential of the presented method. For the definition of alert thresholds, further efforts are needed in order to verify the validity and applicability of the method in this field. To ensure that the model proposed by Seguí 2020 can be used as an early-warning tool, some additional efforts are needed both to reduce numerical assumptions (i.e., uncertainties) and to numerically identify alert thresholds. In fact, although the definition of the critical state (i.e., landslide collapse) is based on the resolution of the model equations, no numerical criteria have yet been proposed for the identification of the pre-collapse warning thresholds useful for civil protection and risk management activities. Even if some evidences have been detected in this work, there is still a lack of established criteria for defining pore pressure or temperature values related to

landslide body acceleration events (i.e., creep transitions) in the pre-collapse stage. Some recommendations for further research developments are summarized below.

Although it has been demonstrated that some of the input parameters required by the model can be assumed from the literature, greater site-specific characterization would lead to a reduction in modeling uncertainties. Some steps could be represented by:

- Site-specific monitoring of temperatures within the landslide body at different depths;
- Continuous monitoring of temperatures at the sliding surface;
- Increase knowledge of the mechanical properties and thermal sensitivity parameters of the slip surface materials by performing tests in a triaxial thermal cell;
- Define, through laboratory tests on cylindrical rock specimens, the thermal properties of the material (e.g., thermal conductivity, specific heat capacity, etc.).

Even if the model has already been applied to different case studies in which collapse scenarios have been correctly reconstructed (e.g., Seguí et al. 2020), applications of the method to landslides in which critical conditions have been reached and the main driving factors (e.g., pore pressure, velocity) are known, would allow to:

- Verify the correct numerical definition of the critical collapse condition (i.e., Gr_c), for the identification of the landslide instability/collapse limit;
- Verify the existence of a universal relationship between Gr (i.e., P_f) and $\dot{\gamma}$ or between T and $\dot{\gamma}$ in the promotion of acceleration stages, useful for the definition of the stability/instability threshold of the landslide.

The robustness of the modelling approach proposed by Seguì et al. 2020, Seguì 2020, Seguì and Veveakis 2021 has been demonstrated in this work, by applying it to a different geological, geomorphological, and geomechanical setting.

This analysis also highlighted the importance of the thermal factor. Thermal sensitivity in highly complex geomechanical systems, such as the sliding surface of a large rockslide, can significantly control the deformation state, the initiation of acceleration phases, and the transition to different creep states. This process, associated with frictional heat development, can be monitored in the field by simply installing a thermometer measuring the temperature at the sliding surface. Rapid increases in temperature may indicate the development of an accelerated deformation phase, triggered, for example, by a rise in the piezometric level, which can cause degradation of mechanical properties and the transition to a tertiary creep.

Especially when the model is adopted as a predictive and early-warning tool, temperature and pore-pressure monitoring would allow to check the real-time stability conditions of the landslide and continuously assess its positioning in the stability phase-space.

Compared with the TM simulations presented in the previous Chapter 4, temperature variations considered here are not directly caused by climatic effects but mostly driven by mechanical forcings. Although in this model, the climatic role in the temperature evolution is not predominant, the next Section will explore the possibility that ongoing climatic changes may lead to an increase in the reference temperature at the sliding surface, resulting in changes in the modeled basal temperature evolution. Because of the high degree of coupling between thermal sensitivity and the simulated deformation, even increments of a few tenths of a degree could result in considerable changes in rockslide deformation outputs.

5.9 Prediction of landslide evolution under climate change

As widely discussed in previous Chapters 3 and 4 and as shown by monitoring data and numerical analysis applied to the Ruinon case study, the mechanical evolution of rockslides is significant controlled by climate dynamics: different rainfall inputs can boost triggering mechanisms as well as an exacerbation of atmospheric temperatures can lead to significant induced TM stresses and accelerate mechanical degradation of rock-masses. As a consequence, variations in meteorological conditions connected to climate change may directly influence the evolution of rock-slopes, especially in the Alpine environment where climatic variations are brough to their extremes. Evidences of this are already noticeable nowadays with an increase in instability phenomena (Crozier 2010; Stoffel et al. 2014; Gariano and Guzzetti 2016; Paranunzio et al. 2019), also related to the development of new deformation processes, linked, for example, to permafrost melting.

To date, studies are mostly focused on the analysis of the future evolutionary trend of rock slopes, looking for the relationship between climate variables and the occurrence of instability phenomena, mainly rockfalls and shallow landslides. On the other hand, the impact of climate change on the evolution of active landslide phenomena, such as large Alpine landslides or slow deformation processes (e.g., DSGDS), has been little explored so far. Active landslides, as complex and delicate systems, will potentially be strongly influenced by novel dynamics of driving factors, with new evolutionary equilibria to be expected. Human activities may therefore be subject to a new level of risk that must be explored and addressed.

This section is aimed to explore the evolution of a large landslide under future climate scenarios by introducing different climate inputs. In particular, the 1D thermo-poro-mechanical numerical model, developed in the previous Section to simulate the Ruinon rockslide evolution, will be used to evaluate the impact of thermal changes at the sliding surface. This analysis should be intended as a parametric and exploratory study of the impact of atmospheric temperature variations on the state of activity of a large Alpine landslide. The results are not intended to be predictive of the mechanical evolution of the Ruinon rockslide, mainly because other factors that will not be considered in this analysis (including changes in hydrologic and hydrogeologic inputs), may be a potentially equally or more significant element.

To define the evolution of climate variables at the Ruinon rockslide area, bias-corrected Regional Climate Model outputs were evaluated and statistically downscaled using a two-step approach (change factors and weather simulators), considering different scenarios of warming increment above preindustrial temperatures of 1.5, 2.0, 3.0, 4.0°C, respectively. The future temperature evolution along the slope and specifically at the depth of the sliding surface was evaluated and introduced into the model

to verify its influence on the rockslide mechanical behavior. The analysis represents a first attempt in the formulation of a predictive tool of landslide behavior, aimed toward the definition of a novel physically based early warning strategy that can account for future climate scenarios.

5.9.1 Methods

The study has been carried out in different steps that initially involved the definition of future climate conditions on the slope surface from current values (reference period 2010-2020 – Section 5.3.5). The values obtained through a downscaling analysis from regional climate models and considering different climate scenarios are in a second step introduced into a thermal model simulating the evolution of temperature along the slope and at the depth of the sliding surface. Results are then introduced into the thermo-poro-mechanical model defined in the Section 5.8, calibrated and validated on the recorded rockslide velocity data, by keeping the evolution of pore pressures fixed to the dynamics recorded over the simulated time range.

5.9.1.1 Downscaling climate analysis

The temperature evolution at the slope surface was evaluated by performing a downscaling analysis from 27 regional climate models. Global Warming Levels (GWLs) of 1.5°C, 2.0°C, 3.0°C, and 4.0°C forced by the SSP5-8.5 scenario and available on the IPCC-WGI Atlas repository (Iturbide et al. 2021) were considered. A climate model reaches GWL when the change in global near-surface air temperature, averaged over successive 20-year periods, reaches that level of warming relative to the 1851-1900 climate simulation (IPCC 2014). Precipitation, minimum and maximum temperature data were downloaded for the Ruinon area, taking into account 27 Regional Climate Models RCMs (Table 5.22). Following a procedure consisting of calibration over the measured data at the Confinale climate station (Section 5.3.5), bias-correction (Cannon 2018) and downscaling (Wilby et al. 2004; Fowler et al. 2007), the analysis returns daily temperature and precipitation values for a 20-year period. In Figure 5.52a, an example of temperature evolution simulated by three different climate models and for three different climate scenario is presented. In Figure 5.52b is shown the mean of all the 27 models compared to the reference values, calculated for each month.

Table 5.22 - List of the 27 RCMs with their time intervals according to the WGLs corresponding to the climate scenarios investigated.

Regional Climate Models List

	CNRM – 6 models	IPSL - 2 models
	2030-2049 scenario 1	2015-2034 scenario 1
	2045-2064 scenario 2	2030-2049 scenario 2
	2067-2086 scenario 3	2050-2069 scenario 3
	2087-2100 scenario 4	2066-2085 scenario 4
Mod 1-6: CNRM-CERFACS-CNRM-CM5_rcp85_r1i1p1	**ICHEC _r3i1p1 - 3 models**	**MPI - 10 models**
Mod 10-12: ICHEC-EC-EARTH_rcp85_r3i1p1	2020-2039 scenario 1	2017-2036 scenario 1
Mod 13-16: ICHEC-EC-EARTH_rcp85_r12i1p1	2038-2057 scenario 2	2037-2056 scenario 2
Mod 17, 19: IPSL-IPSL-CM5A-MR_rcp85_r1i1p1	2067-2080 scenario 3	2071-2080 scenario 3
Mod 23-32: MPI-M-MPI-ESM-LR_rcp85_r2i1p1	2081-2100 scenario 4	2081-2100 scenario 4
Mod 33-34: NCC-NorESM1-M_rcp85_r1i1p1	**ICHEC_r1i1p1 - 4 models**	**NCC - 2 models**
	2018-2037 scenario 1	2032-2051 scenario 1
	2034-2053 scenario 2	2048-2067 scenario 2
	2060-2079 scenario 3	2072-2091 scenario 3
	2082-2100 scenario 4	

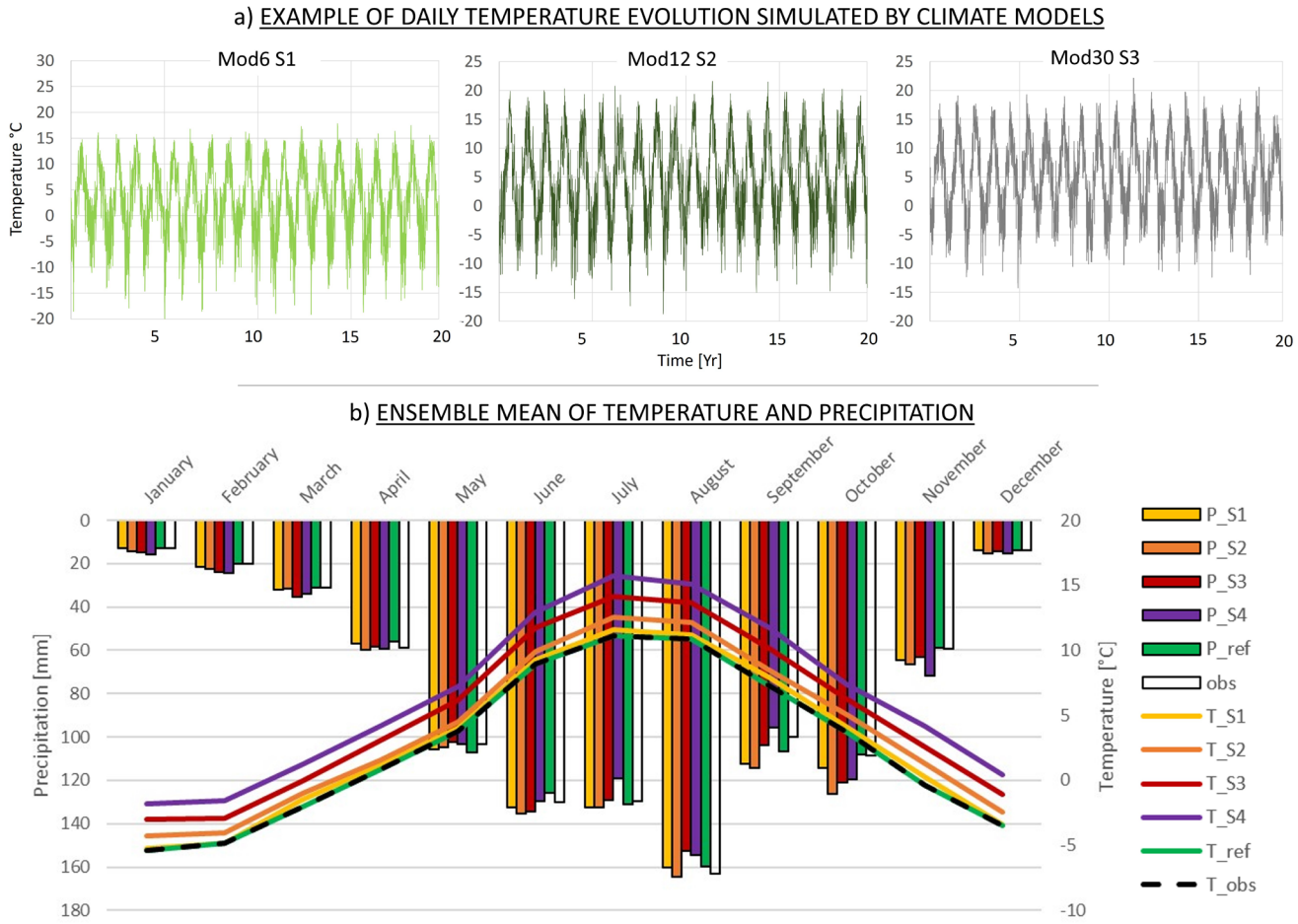

Figure 5.52 – a) Example of thermal evolution simulated by climate models for 3 different climate scenarios. b)Monthly average of temperatures and precipitation simulated by all the models considered in the downscaling analysis for the different climate scenarios.

5.9.1.2 Temperature evolution at the Ruinon Landslide sliding depth

To evaluate the impact of climate changes at the Ruinon rockslide sliding depth, a 2D thermal model was developed using the FEM software COMSOL multiphysics. A reference section taken along the rockslide axis was considered and the thermal distribution was simulated by introducing results of the climate downscaling analysis (Figure 5.53a).

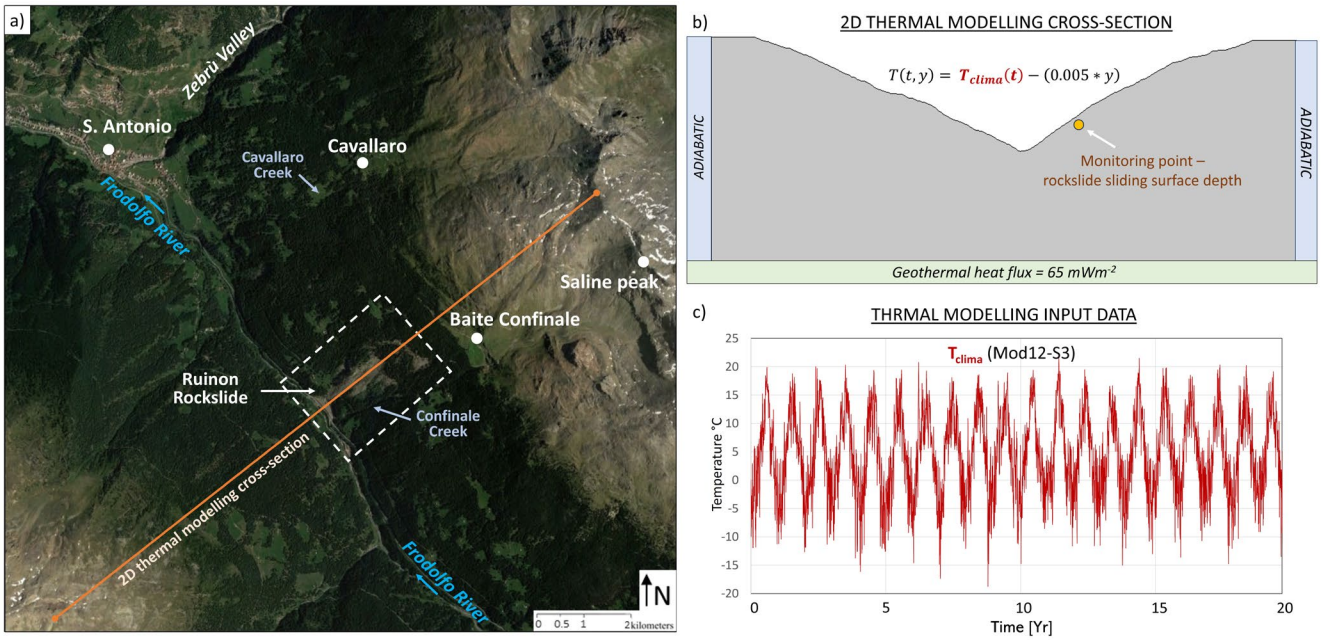

Figure 5.53 – a) Location of the 2D thermal modelling cross-section. b) Definition of thermal boundary conditions. c) Example of input factor introduced into the equation for defining the thermal evolution along the slope.

In the model, the process of heat transport is governed by thermal conduction processes defined by thermal diffusivity (D), which depends on thermal conductivity (λ), specific heat capacity (C_P) and rock density (ρ) following the relation $D = \lambda(\rho C_P)^{-1}$. Values of λ = 1.5 W m^{-1} K^{-1} and C_P = 910 J Kg^{-1} K^{-1} were chosen for the problem at hand, corresponding to generalized values for phyllites lithologies found in the literature (Cermak et al. 1982; Robertson et al. 1988).

Adiabatic boundary conditions define the lateral sides of the thermal model, while a constant vertical geothermal heat flux of 65 mW m^{-2} (Swisstopo, 1982) is applied along the lower boundary (Figure 5.53b). A temperature history was assigned to the slope surface, representing the main driver of temperature evolution within the rock-mass. Specifically, rock surface temperatures were set to depend on environmental conditions, as a function of altitude (y) and time (t). Rock surface temperatures were thus defined by:

$$T(t,y) = T_{clima}(t) - (0.005 * y) \quad \text{(Equation 5.29)}$$

where $T_{clima}(t)$ is the slope surface temperature evolution derived from the climate downscaling analysis, whereas 0.005°C m^{-1} represents the rate of temperature variation with altitude (y).

Initial slope temperature distribution was defined upon calculating steady-state thermal equilibrium under current values (T_{clima}=15° as mean year temperature). The transient thermal analysis, performed following equation 5.29, allowed to evaluate the temperature redistribution along the slope during the modelled 20-year period, considering climate conditions changing. In particular, the daily temperature evolution simulated by each model and for each climate change scenario were used as an input factor for the thermal analysis (Figure 5.52a, Figure 5.53c), returning a total of 106 temperature scenarios at the sliding surface.

By introducing a monitoring point along the 2D section (Figure 5.53b), the temperature at the depth of the rockslide sliding surface was evaluated for all the 27 climate models and for each climate scenario.

5.9.1.3 Assessment of landslide evolution

In a third step of the analysis, the temperature simulated by the 2D thermal model at the sliding depth was introduced into the governing equation of the thermo-poro-mechanical model (Section 5.8), representing the basal temperature factor (T_0). The thermo-poro-mechanical governing equation defined in the previous Section 5.8.1, is recalled below:

$$\frac{\partial T}{\partial t} = D\frac{\partial^2 T}{\partial Z^2} + \left(\frac{\tau_d}{\rho C_P}\right)\dot{\gamma}_{ref}\left(\frac{\tau_d}{\tau_{ref}}\right)^{1/N} e^{m(T-T_0)} \qquad \text{(Equation 5.30)}$$

Where $D = \lambda/\rho C_P$ is the thermal diffusivity of the shear band material, with ρ the density, C_P the specific heat capacity and λ the thermal conductivity. τ_d is the shear stress acting on the sliding surface, τ_{ref} is the reference shear stress, $\dot{\gamma}$ is the shear strain rate, m is the ratio of the temperature sensitivity coefficient (M) over the load-rate sensitivity coefficient (N), T is temperature in the shear band and T_0 is a reference temperature.

The reference temperature T_0, previously kept fixed at representative values of 10°C, is now influenced by the thermal evolution related to climate change. Increases in T_0, and consequently in the calculated temperature at the sliding surface (T), cause increment in the simulated velocities according to the Eq. 5.28.

At this stage, the evolution of pore pressure is kept fixed on the values introduced in the Section 5.8 for calibration and validation (2014-2020), in order to assess the thermal impact on the mechanical response of the landslide. As a result, compared to the analysis presented in the previous Section 5.8, the stability of the landslide is only affected by temperature. Analyzing the evolution of the stability curve in the

model's phase space, is therefore expected to observe changes only in the normalized temperature (i.e., along the y-axis). Compared with the simulated conditions of Section 5.8, variations along the x-axis (i.e. Gr), are not expected at this stage as the hydrogeological regime is kept constant. In this analysis, the achievement of critical conditions is therefore expected by reaching the upper branch of the stability curve (Figure 5.44). However, considering the limited changes in T that are expected as a short-term response to the ongoing climate changes, critical conditions should not be reached.

5.9.2 Results

The results of the 2D thermal modeling allowed the assessment of temperature evolution along the Ruinon slope considering different future climate scenarios. Thermal gradients are shown to be influenced by the altitude effect and, considering climate change, the slope is progressively exposed to increasing temperatures on the global mean.

Figure 5.54a shows the distribution of simulated temperatures under steady-state regime and representative of current conditions, which stand for a baseline for the subsequent transient analysis.

Introducing thermal evolution at the slope surface in response to climate change, it can be observed that the simulated temperature variations are restricted to the slope subsurface within a maximum depth of thermal diffusion of about 200 m. At the depth of the sliding surface, temperatures are shown to be increase on a magnitude of 0.1 to 1°, depending on the intensity of the temperature increase at the slope surface. Figure 5.54b shows an example simulated by considering inputs of the climate model 12 (ICHEC-EC-EARTH_rcp85_r3i1p1_ model) for climate scenario 3 (i.e., 3° above pre-industrial values).

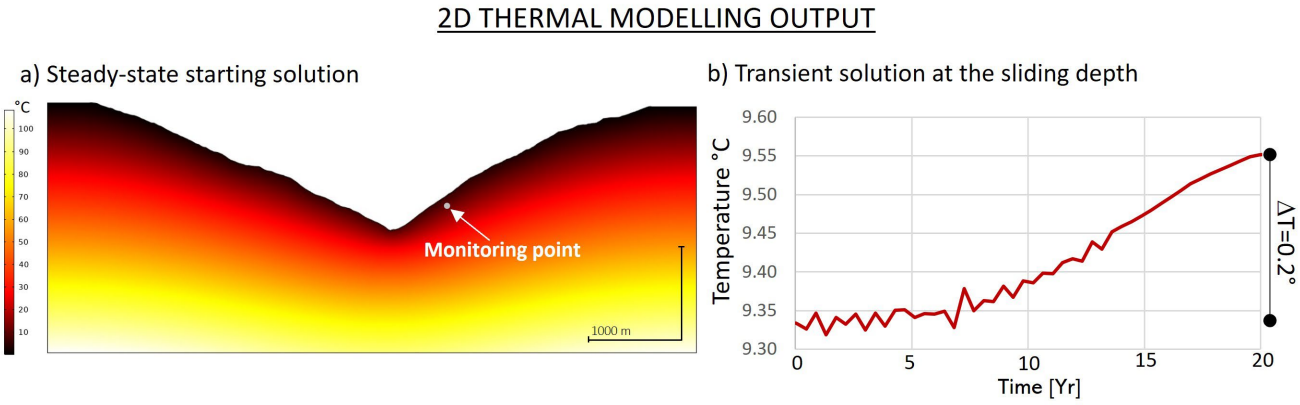

Figure 5.54 - 2D thermal modeling output. a) Temperature distribution (°C) along the slope corresponding to current thermal conditions. b) Temperature evolution at the depth of the sliding surface considering as an input the temperature simulated by climate model 12 (ICHEC-EC-EARTH_rcp85_r3i1p1_ model) in the climate Scenario 3.

The temperature evolution simulated by the 2D thermal model at the Ruinon sliding depth (Figure 5.54b), was subsequently introduced into the governing equation of the thermo-poro-mechanical model (equation 5.30), representing the reference temperature factor (T_0). The basal temperature at the sliding surface (T) is now affected by both the shear heating and the climate warming trend, which may affect the simulated landslide velocity following Eq. 5.28. Modeling outputs were analyzed in terms of simulated velocity, also compared with reference values measured in previous Section 5.8. In addition, the evolution of the Gruntfest number (Gr) was also analyzed to verify the stability of the landslide.

As an example, Figure 5.55 shows the Gr-T evolution, and the landslide velocity simulated by the thermo-poro-mechanical model by introducing temperature forecasted by model 12 (ICHEC-EC-EARTH_rcp85_r3i1p1_ model) for climate scenario 3.

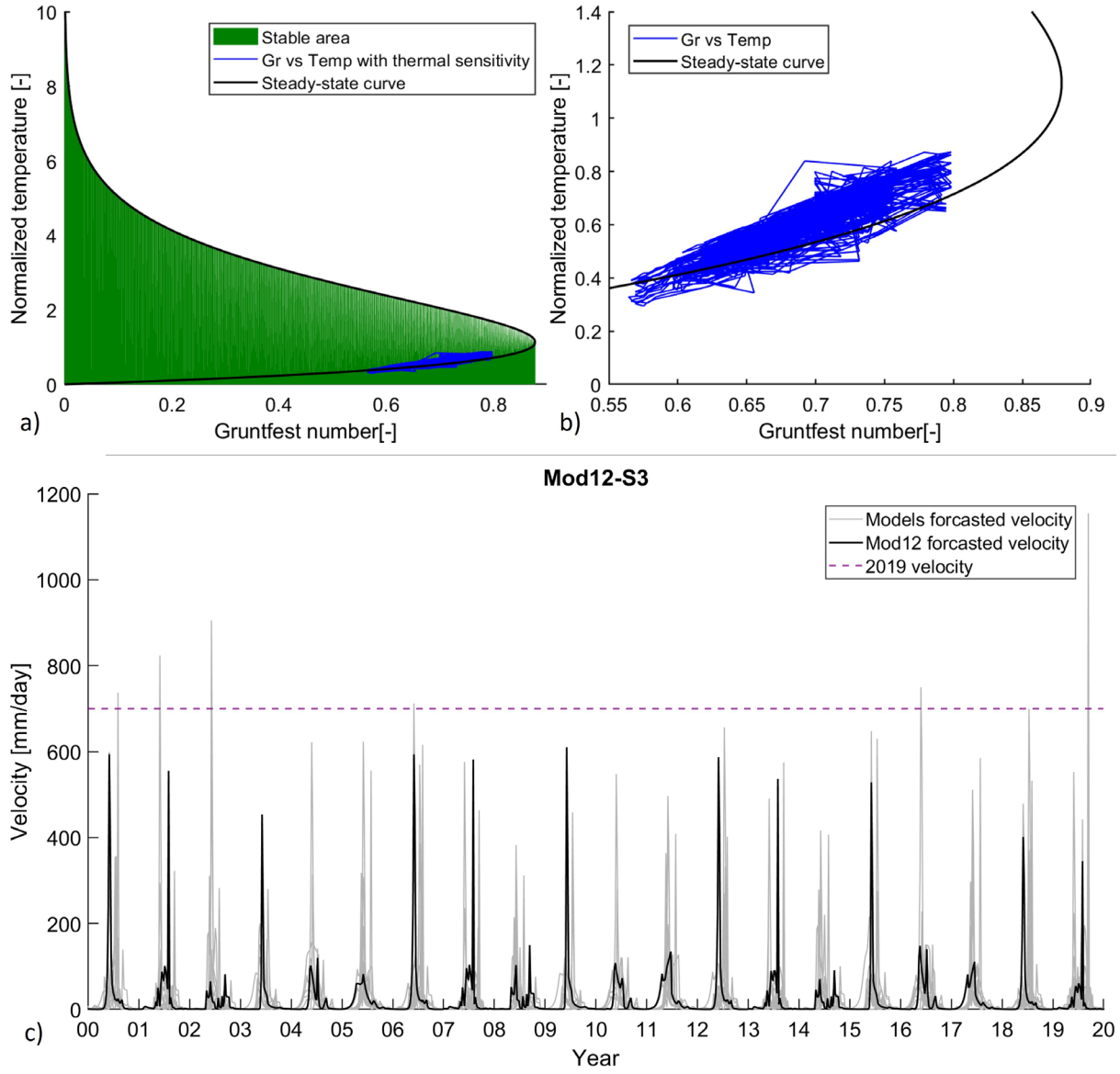

Figure 5.55 – Thermo-poro-mechanical modelling output resulting from the thermal input derived by the climate model 12 (ICHEC-EC-EARTH_rcp85_r3i1p1_ model) for Scenario 3. a) Modeled basal temperature evolution. b) Gruntfest number. c) Landslide velocity.

As can be observed in Figure 5.55a, the stability curve evolves in a range of *Gr* values comparable with the results of the previous analysis in Section 5.8 with, however, a wider normalized temperature range, consistent with what expected. *Gr* values, in fact, being dependent on pore pressure, do not differ from the previous analysis because the hydrogeological regime is kept unchanged. Variations in normalized temperature (i.e., y-axis), on the other hand, are larger due to the thermal warming trend introduced. Having variations in the range of 0.1-1° such amplitude is not very pronounced, allowing the rockslide to remain in the range of stability. By analyzing the simulated velocities (Figure 5.55b), however, the acceleration stages, primarily related to an increase in pore pressure (i.e., approaching Gr_c), are more pronounced and frequent. This is mainly related to the thermal effect that results in a shift of the peaks in the *Gr-T* curve toward values closer to the upper area of instability.

The results of the analysis showed an appreciable impact of basal thermal increment on the deformative evolution of the landslide. The modeled system appears to be sensitive to thermal changes, with a significant increase in the deformation activity, even for small magnitudes of temperature increments.

This relationship is clear when considering the set of all climate models examined for the present study. Figure 5.56 shows for each climate scenario (i.e., 1.5, 2, 3, 4° above pre-industrial values) the average velocities simulated by all 27 models (black line) and the maximum velocities of the 27 models (red line). For reference, the simulated velocities are also compared to the values reached by the rockslide in summer 2019 (dashed line) when a major acceleration event occurred (see Section 5.2.1).

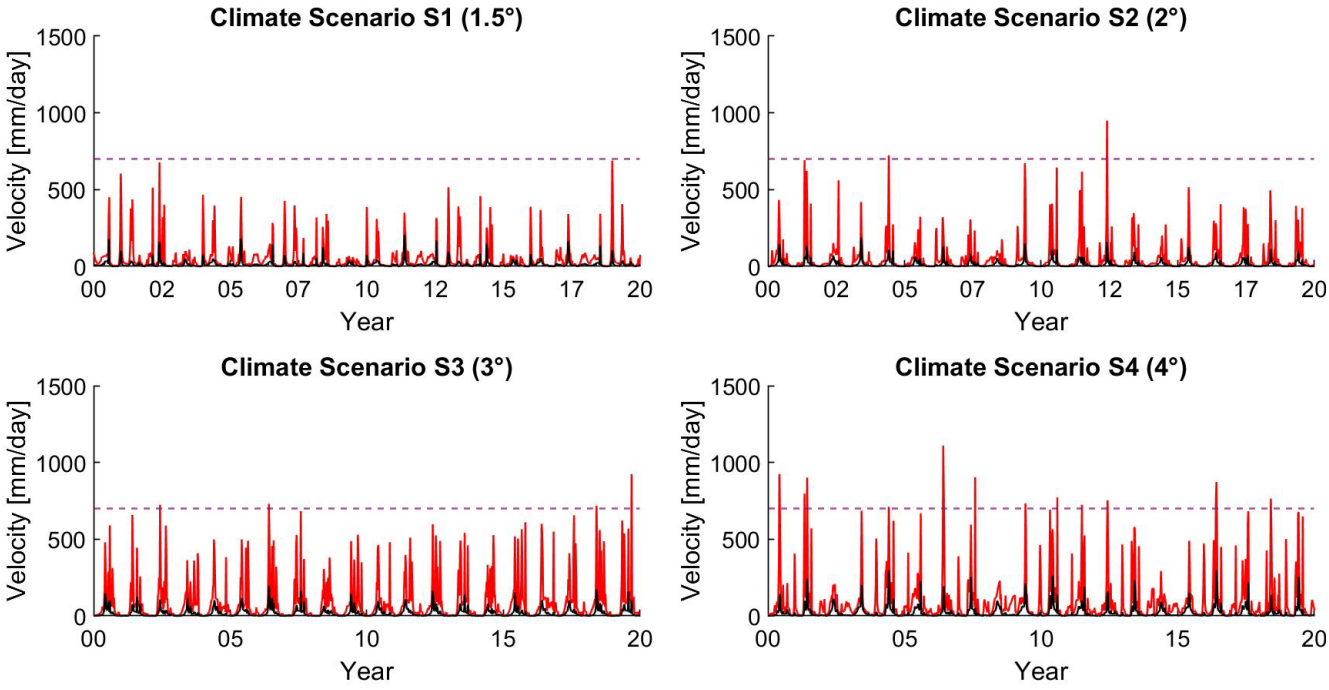

Figure 5.56 – Average (black line) and maximum (red line) velocities simulated by all the 27 for each climate scenario. The dashed line represents the 2019 landslide velocity as a reference.

As shown in the Figure 5.56, rockslide activity increase moving from climate scenario 1 to 4. The acceleration peaks become more intense, intersecting the line representing the speed reached by the landslide in 2019 several times in the graph. The 2019 event was taken as an indication of representative warning velocities, as it led to the development of significant gravitational instabilities testified by several episodes of rockfalls and debris. If the method of defining numerical alert thresholds discussed in Section 5.8 will be developed, the velocities simulated in this Section as a response to climate warming should be correlated with them.

A more quantitative method of assessing the thermal impact on rockslide evolution can be provided by checking the number of times the velocity reached by the rockslide was exceeded in 2019. This gives an exceedance frequency that can provide insight into the importance of thermal impact on the mechanical response of the rockslide. The histogram in Figure 5.57 shows the frequency of velocity exceedance for each model and for each climate change scenario. It can be noticed that moving from Scenario 1 to Scenario 4, the frequency increases with maximum values of 10 recorded for the most extreme models. Indeed, from this method it is also possible to evaluate models that propose the most extreme climate scenarios and consequently the most significant scenarios of simulated deformation evolution. In the present work they are represented by the ICHEC-EC-EARTH and MPI-M-MPI-ESM-LR models that show above-average exceedance frequencies.

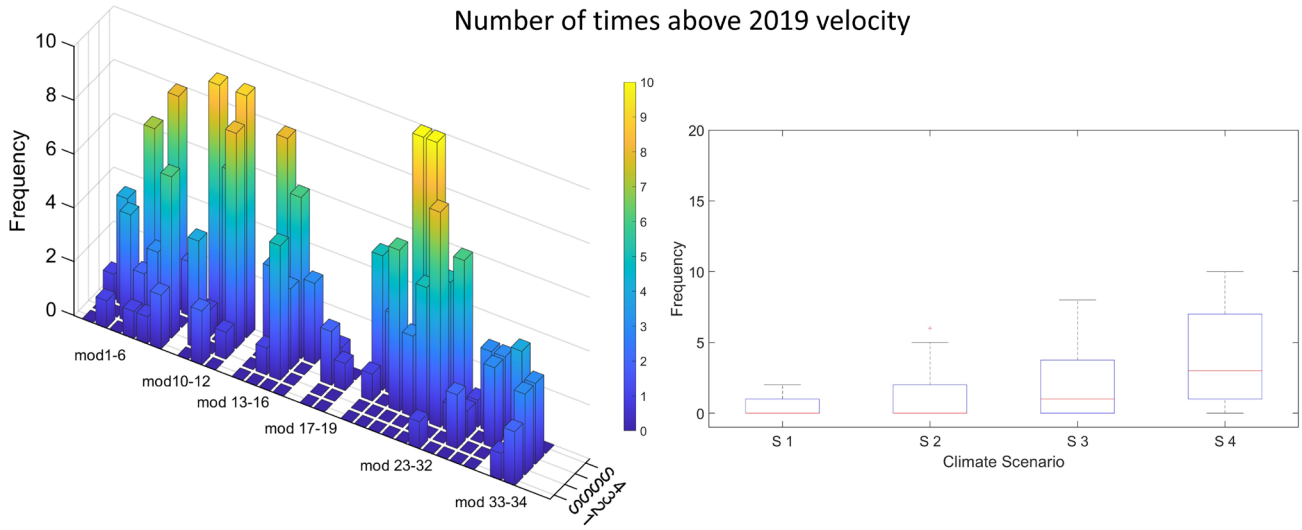

Figure 5.57 - Number of times the simulated velocity over the considered time range (20 years) exceeds the landslide velocity recorded in summer 2019 for each model and each climate scenario

5.9.3 Discussion

Through a multi-disciplinary approach, the study presented in this Section explored the impact of atmospheric temperature variations related to climate change on the activity of a large Alpine landslide such as that represented by the Ruinon. Through a downscaling process, thermal scenarios simulated by 27 climate models were analyzed considering four different evolutionary climate scenarios (1.5, 2, 3 and 4° above pre-industrial temperatures). The thermal scenarios, evaluated at the topographic surface, were subsequently introduced as input factors for the calculation of temperature at the depth of the rockslide sliding surface by using a thermal diffusion model. At this point, the simulated temperature changes were introduced into the previously calibrated and validated thermo-poro-mechanical model as the evolution of the reference temperature at the sliding surface, and the corresponding velocities were evaluated. Thus, this approach allowed to evaluate the role of atmospheric thermal variation in the state of rockslide activity.

Although temperature variations at the depth of the sliding surface in response to the ongoing climate change are in the range of 0.1 to 1 °C, the results showed a significant impact on the mechanical evolution of the rockslide. This is mainly related to the thermal sensitivity of the material defining the shear band. The nature of the material in the shear band, due to its state of strong mechanical degradation, makes it particularly sensitive to temperature changes. This is consistent with what has already been observed in the literature from both laboratory (Hueckel et al. 2009; Ferri et al. 2010; Seguí and Veveakis 2021) and site (Seguí and Veveakis 2021) evidences.

In general, the mean velocity values simulated by the model are consistent with in-situ evidences, following the natural evolution of the rockslide body highlighted in the time range between 2014 and 2020. However, when analyzing the simulated maximum velocity values, it is observed that the values reached in the summer of 2019 are exceeded with a frequency that increases moving from climate scenario 1 to climate scenario 4, highlighting the role of thermal evolution.

Considering the stability curve, the effect of the introduced warming trend is highlighted by changes along the temperature axis. The curve shifts toward the upper instability area even if with small changes. Comparing the results with what observed in Section 5.8, the impact of temperature on the stability of the rockslide, appears to be lower than the pore pressure factor. *Gr* changes driven by pore pressure fluctuations are in fact much more prominent and seem to control greater the triggering of rockslide body acceleration phenomena. This is consistent with evidences of previous TM analyses applied to slope stability (Section 4), where a preparatory role of temperature rather than triggering was highlighted. From a preliminary analysis performed starting from rockslide Gr-T conditions referred to

the year 2019, it is observed that to reach critical conditions by temperature evolution only, an increase in T_0 at the sliding surface of about 5° would be required (Figure 5.58).

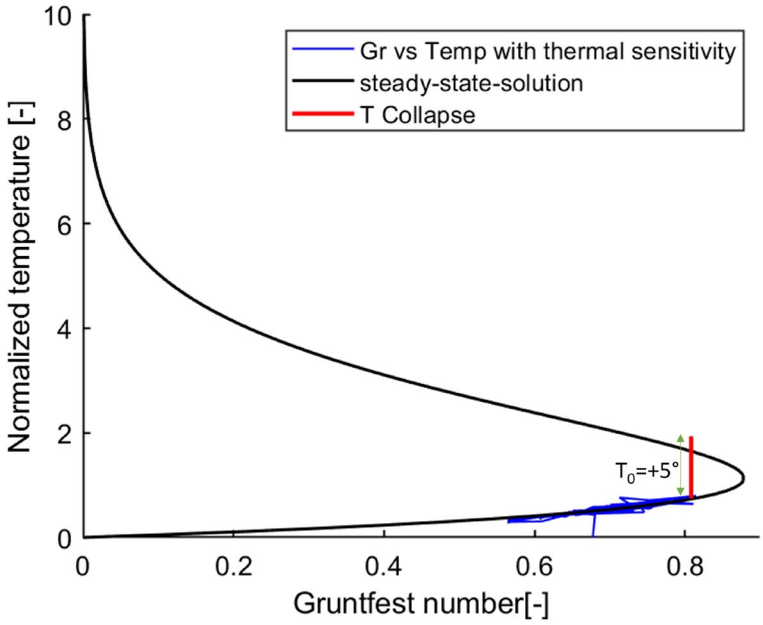

Figure 5.58 - Achievement of the model instability area by increasing T_0 from the rockslide conditions referring to the year 2019.

This seems to be outside the expected thermal scenarios for the near future, but interaction with new hydrogeological conditions could shift the curve toward the Gr_c and thus reduce the required thermal increase to reach the upper area of instability.

By increasing the observation time to very long time scales, considering completely different climatic conditions from the current one, such as the late Pleistocene thermal warming, a significant impact of temperature on the stability curve could be assessed. Atmospheric temperature increases of 10-12°C, such as that reconstructed for the Alpine region during the late Pleistocene age (Section 4), could result in major changes along the T-Gr curve, with a significant approach to the area of instability. Even if the temperature factor does not lead to instability initiation, it would still bring the system to mechanical degraded conditions, where the effect of other factors such as changes in pore pressure could have a more pronounced impact. This would explain the development and failure of numerous large landslides in the Alpine region occurred after the late-Pleistocene deglaciation process, which cannot be completely explained by the mechanism of tension release alone. During the deglaciation process, the slope is not only exposed to different stress conditions but also to significant climate variations, the effect of which needs to be explored more through a multiphysical approach such as what is proposed in this work.

The present analysis is not a predictive tool for the assessment of the evolutive history of the Ruinon rockslide, but should be intended as an explorative study to increase knowledge and scientific awareness of the impact that climate change may have on the evolution of Alpine rock slopes. It was possible to

show how, in addition to the hydrological component, which as well-known plays a key role in landslide stability, temperature can also considerably influence it. Studies, typically focused on the impact of hydrological factors, should therefore also consider the coupling with the thermal component.

The next step of the analysis will be to consider in a coupled way the effect of climate change on both temperature and hydrogeology, by considering the downscaled precipitation values (Figure 5.52). This can potentially result in a shift in the stability curve for both T and Gr (i.e., pore pressure) values toward unstable conditions.

The validity of the multiphysical approach proposed by Seguì et al. 2020, Seguì 2020, Seguì and Veveakis 2021 is further demonstrated in this Section. In addition, the potential use of this approach as a predictive tool for analyzing the evolution of landslides in response to changes in climatic input variables is highlighted.

5.10 Conclusion

In this Chapter 5, the Ruinon rockslide case study was analyzed. By following a multi-disciplinary methodological approach that included the collection of geological, geomorphological, geomechanical, hydrogeological, and climatic data, their processing and the development of numerical analyses, it was possible to obtain a solid knowledge of its mechanical evolution.

The availability of a good amount of data, thanks to the previous works carried out in the area, supplemented and validated by the field investigations conducted for the development of the present work, allowed the definition of a solid geological and hydrogeological model of the slope.

Its validity has been demonstrated through the development of numerical hydrogeological and mechanical (i.e., stress-strain) analyses, which accurately simulate the slope behavior. The outputs of the analyses were compared with the data recorded by the in situ monitoring system and field observations, showing a faithful correspondence.

As shown by both the in-situ investigation and modelling outputs, a close relation between climatic-hydrological inputs and the deformative evolution of the rockslide body is evident. The slope exhibits a complex hydrogeological setting governed by the presence of the Confinale creek, flowing on the left flank of the rockslide body, as well as gravitational elements (i.e. trenches and tensile fractures), promoting surface water infiltration. The groundwater circulation is driven by the presence of a high-permeability unit upstream of the main rockslide body, as well as low-permeability deposits that allow for water accumulation and piezometric rises. At the Ruinon rockslide and along the Confinale creek this process causes the development of water springs, while along the entire right flank of the landslide, the rise of the piezometric level is not sufficient to cross the topographic surface. The piezometric level trend at the rockslide body is strongly linked with the water flow of the Confinale creek, with peaks in correspondence of the highest water availability periods.

Through a numerical coupling process, the outputs of the hydrogeological modeling were used as inputs for the development of a HM analysis, which could explore the role of hydraulic pressures on the mechanical evolution of the slope. The results of the mechanical analyses showed that the susceptibility to gravitational instability of the slope is mainly driven by its morphological and mechanical features, which are superimposed by the seasonal cyclical evolutions of the piezometric level that drive the development of deformation processes and acceleration phases of the main rockslide body.

The adoption of both continuous and discontinuous modeling approaches, allowed to point out the role of the discontinuity network in the mechanical evolution of the slope. The development of simulated deformation processes is in fact mainly drove by the occurrence of failures and plastic deformations along discontinuous elements, in response to HM inputs. Compared with the FEM analysis, the

introduction of the detected joint network allowed a more faithful reproduction of the geomechanical and HM evolution of the slope. Considering such evidences, a simulation of the distribution of pore pressures obtained from modeling the groundwater circulation in the discontinuity network and not in a continuous medium as represented by the SEEP-3DEC coupling, could allow the values of the simulated deformative variables to be defined more faithfully.

At last, the application of a thermo-poro-mechanical model, allowed to achieve a complete awareness of the link between pore pressure and deformation state of the rockslide, through the definition of a mathematical relation. Once validated, the model allowed to simulate and predict deformation state in response to variations in external factors such as, groundwater levels or the reference temperature evolution in response to climate changes. It has also been demonstrated that this tool can be useful for the identification of threshold levels below which the driving factors must lie to ensure mechanical stability conditions of the slope. To reach the application of the model as an early-warning tool, however, some additional steps are needed for the numerical definition of pre-collapse warning thresholds

The coupling of the presented numerical analyses (i.e., hydrogeological, mechanical, mathematical), in addition to demonstrating the achievement of a good awareness of the geomechanical behavior of the Ruinon rockslide, represents a potentially significant tool for understanding and predicting evolutionary scenarios of active landslides. The analysis provides the basis for the development of a landslide early-warning system and a real-time assessment tool, used in combination with traditional monitoring methods. The approach allows to include the variability of climate forcings, for the prediction of the mechanical evolution of landslides, also taking into account future climate scenarios. This represents a step toward deciphering the role of climate factors for the development of adaptation strategies to prevent and mitigate the impacts of ongoing climate change.

Chapter 6
Concluding remarks

Through the adoption of a multi-disciplinary approach and the development of multiphysics numerical analyses, this work allowed to deepen knowledge of the quantitative relationships between climate factors and the stress-strain evolution of rock slopes, also providing suggestions for the development of new predictive and warning tools.

Four case studies of past and active rockslide events in the Alpine region were analyzed, for which the effects of different climatic factor was assessed. Through a methodological process that includes geological and geomechanical characterization of rock slopes and the definition of a geological conceptual model, the development of numerical analysis was carried out. The adoption of different numerical methods, from FEM, FDM and DEM strain-strain to more advanced mathematical models, led to the development of coupled analyses with HM, TM and THM approaches.

In Chapter 3, two case histories in which exceptionally heavy rainfall events led to slope failure were discussed and the dominant triggering role of HM couplings was verified. While for the 2012 Cimaganda rockslide, a 2D FEM approach was sufficient to correctly reproduce the mechanical behavior of the slope, the Piuro landslide required a 3D FDM approach because of its complex geological settings. Rainfall input of 267 mm over four days and of 345 mm over five days respectively, simulated the triggering pore pressure conditions and the slope failure geometries. In the Piuro case study, the introduction of 3D complex geometry allowed to verify the predisposing role of geological-structural elements in the development of large gravitational instabilities and to evaluate how 3D morphologies can significantly influence the distribution of pore pressures along a slope.

In Chapter 4, a coupled DEM-FEM 2D approach was adopted for the development of a TM analysis applied to the Cimaganda rock slope. The stress-strain effect of 1230 m ice melt coupled with seasonal to millennial thermal evolution from the late Pleistocene age to present, allowed to reproduce the mechanical conditions of the slope. Consistent with field observations, at the end of simulations the predisposition to rock slope instabilities was evident, highlighting the role of temperature as significant preparatory factor promoting joint failures and the occurrence of irreversible strain. In addition, a thermal monitoring system placed along the Cimaganda slope showed a daily thermally active layer ranging from 0.3 m in winter to 0.75 m in summer, and reaching 12° of seasonal temperature change at 2.5 m depth. Congruently with the modeling outputs, thermal variations are matched by reversible normal joint deformations in the range of 10^{-4} m at the daily scale and 10^{-3} m at the seasonal one.

In Chapter 5, the Ruinon case history was analyzed and the relationship between climate variables and the mechanical evolution of the rockslide was assessed. The complexity of the phenomenon led to the definition of a study over different steps. First, the role of morphological and mechanical factors in the predisposition to gravitative instability processes was verified via 3D stress-strain FEM analysis. By introducing the 2012 morphological conditions (prior to the recent acceleration events) and cohesion values varying between 0.2 and 1.0 MPa (covering the detected mechanical range), it was possible to faithfully reproduce the distribution of instability events along the slope. Three different representative piezometric levels (40, 30 and 20 m depths in correspondence of the piezometer PZ4) were also introduced, showing an increase in irreversible deformation at the Ruinon rockslide location as the groundwater level increases. Then, the hydrogeological regime of the slope was faithfully reconstructed through a 3D FEM analysis starting from a careful 3D reconstruction of the hydrological units and introducing the water availability along the slope calculated by considering rainfall, snowmelt, infiltration capacity and the presence of the Confinale creek in the time period 2014-2021. The model, calibrated and validated on the evolution of the piezometric level measured by the PZ4 (the only significant hydrogeological monitoring tool present), well reconstructed the distribution of springs and the groundwater flow. In particular, it was verified how the Ruinon hydrogeological regime is strongly influenced by: hydraulic conductivity contrasts, morphological factors, presence of gravitational morpho-structures and the Confinale creek seepage. Outputs of the hydrogeological model were subsequently imported into a 3D DEM model, where the role of HM factors in triggering the deformative acceleration stages of the rockslide was modelled. The peculiar “stepped” evolution of the rockslide following seasonal hydrological inputs was simulated, and the development of shear deformations along a localized surface at a depth of about 100 m was reconstructed. The maximum of the simulated deformations are observed in correspondence with the rises in the piezometric level, which was demonstrated to be the main driver of the rockslide evolution. By lowering the piezometric level, more stable conditions are simulated, as following the introduction of the hydraulic engineering works of the Confinale creek. At last, the application of a thermo-poro-mechanical model at the sliding surface, allowed to mathematically define the link between pore pressure and the mechanical evolution of the rockslide, simulating its velocity. By calibrating and validating the velocity outputs with the data recorded by the GBInSAR system, the 2014, 2016, and 2019 acceleration events were correctly simulated. Analyzing the evolution of Gr (i.e., pore pressure) and the simulated temperature at the sliding surface, a first attempt to define threshold values has been proposed. A critical pore pressure value of 390 kPa was obtained to which values of 352 and 362 kPa are added as pre-alert and alert thresholds. However, to reach the application of the model as an early-warning tool, some additional steps are

necessary for their rigorous numerical definition. Anyway, the analysis allowed to demonstrate the potential use of this physics-based model as a tool for defining transitions between different creep stages controlled by groundwater level, temperature and mechanical properties of the landslide shear surface. The model was also adopted to explore the impact of ongoing climate changes on large Alpine landslides, pointing out an increasing activity with the rise in the reference temperature at the sliding surfaces. It was possible to show how the effect of temperature on landslide stability, while significant, appears to be less impacting than the evolution of pore pressure, but that, a combined effect could result in the attainment of unstable conditions sooner than by considering the two processes separately.

For each case discussed, the multi-disciplinary method applied (i.e., field surveys, laboratory tests, definition of a conceptual model, numerical analysis), has been demonstrated to be a valid approach for the study of rock-slopes exhibiting gravitative instability phenomena. It led to an accurate geological and geomechanical characterization and to the development of solid numerical models, in which the effect of different climatic factors has been progressively examined. The effectiveness of the characterization method, as well as the validity of the numerical assumptions adopted, was demonstrated by the faithful reproduction of the instability phenomena analyzed. In the case of past events (i.e., Piuro and Cimaganda), where data availability is limited and the complete absence of monitoring systems leaves some variables undetermined, the simulation of landslides geometries and volumes was taken as an element to validate model results. In the case of the active Ruinon rockslide, the presence of an effective monitoring system enabled model calibration and validation based on the recorded deformation data. For this case study, thanks to the presence of a broad amount of geotechnical, hydrogeological and climatic data, it was possible to develop accurate and multi-disciplinary analyses that led to a deep knowledge of the mechanical evolution of the rockslide. This testifies to how data collection, supported by a consistent monitoring system, can lead to a solid understanding of gravity-driven processes, which is the basis for any analysis of slope stability, evolutionary prediction and hazards quantification. In view of the future development of complex and multiphysics stability models, data collection and the installation of efficient monitoring systems remain a key step in the definition of accurate and appropriate numerical tools. It is necessary, however, that research in this field also move toward a multiphysics approach, seeking innovative methods and unified procedures for monitoring nontraditional variables, such as for example the temperature at different slope depths.

Summarizing the main research outcomes, the groundwater triggering role in both slope collapses and landslides acceleration stages (i.e., creep transitions), was verified. It has been numerically demonstrated that even single rainfall events, in non-ordinary regime, are sufficient to generate overpressures relevant

to rock slope failure. As a result, the analysis of groundwater circulation processes, coupled with mechanical calculations, allows a better simulation of slopes evolutive scenarios, which overcomes traditional stability methods where only representative piezometric levels are introduced. The development of a 3D HM analysis also highlighted that slope morphology plays a major role in the distribution of water pressures, suggesting that a 3D approach should not be neglected especially in the presence of complex geological settings.

The study underlines the importance of developing a robust 3D hydrogeological model supporting and preliminary to mechanical analyses of slope stability. Transient groundwater circulation analyses should be more widely adopted for the simulation of the coupled stress-strain effect on slope stability, as well as to support the design of measures for landslide risk reduction. Hydrogeological models should also be considered as a valuable tool for planning the implementation of landslide monitoring networks (especially the deep one), allowing the identification in the 3D space of the most significant sites for monitoring the most influential variables.

In the TM analyses presented, atmospheric temperature fluctuations, while in the short-term predominantly result in reversible rock-mass deformations, in the long-term can induce considerable failure development and cumulative deformations. The larger the time scale considered, the more predominant the thermal effect becomes, both due to the accumulation of strains and the progressive degradation of mechanical properties by weathering processes (i.e., weakening of the rock-mass). While short-term cyclic thermal evolution significantly impacts surface rock-mass elements, long-term monotonic temperature rises can define significant effects even at depths generally coincident with the sliding surface of large landslides such as the analyzed historical Cimaganda rockslide. As a result, temperature factors should not be neglected when the stress-strain evolution of rock slopes is analyzed.

The approach adopted, which can be extended to different areas and time scales, clearly showed that temperature is a significant driver of rock mass degradation and a promoter of gravitational instability processes over time. These evidences indicate that areas subject to gravitative instability processes can change in distribution and extent over time, due to the progressive action of climatic factors. Future climate scenarios show an increase in global temperature with an exacerbation of thermal cycles and a potential significant impact on the stress-strain evolution of rock slope. New slope exposures due to glacial retreat, added to the development of processes such as permafrost melting, could result in new evolutionary dynamics in the Alpine regions, resulting in an extension of the areas subject to gravitational instability to higher altitudes. This confirms the need, recently emerged in this field of research, to introduce climatic forcings, including the thermal ones, into the assessment of landslide susceptibility and hazard levels in order to achieve dynamic 4D mapping in which also temporal

evolution is considered.

The magnitude of modelled and measured joint seasonal deformation (in the range of 10^{-3} m) is sufficient to define changes in the hydraulic opening of joints, resulting in a potential increase in the permeability of the rock-masses. This can induce to an increase in the infiltration capacity during spring periods, which, in the Alpine environment, generally coincide with a maximum water supply due to intense precipitation and snow melting. This interaction needs to be investigated in more detail in future developments of numerical analyses, as it could have a significant impact on slope stability especially in view of ongoing climate change.

The presented outcomes fit into the new research directions, which consider landslide processes as the result of a combination of factors. In the thermo-poro-mechanical model applied to the Ruinon rockslide, where water, temperature and thermal sensitivity of the material were considered together, these evidences were further confirmed. The introduction of the thermal factor in complex models such as the one presented in this work, can lead to greater awareness of the development of large landslides in the Alpine environment, with particular reference to post-glacial large landslides.

As an example of multiphysics and multi-disciplinary approach, the Ruinon analysis allowed to gain insight into the link between climate inputs and rockslides activity, also providing the basis for the development of a physics-based warning and predictive tool. Its potentiality lies in identifying thresholds based on trigger causes (e.g., groundwater level rises) and not on the effects (e.g., landslide velocity), thus leading to a greater awareness of the landslide process. This represents a step toward mitigating the impacts of climate change, for which the evolution of driving factors may undergo substantial changes, and traditional warning systems based on past landslide velocities may no longer be efficient.

Acknowledgments

For the case studies of Piuro and Cimaganda, I would like to acknowledge “Comunità Montana della Valchiavenna” for the access to local facilities and field work permissions, and the Interreg V-A Italy-Switzerland Cooperation Program, A.M.AL.PI.2018 “Alpi in Movimento, Movimento nelle Alpi. Piuro 1618-2018”- id 594274 for the data provision. For the Ruinon case study, the Author is grateful to ARPA Lombardia for making field monitoring data available.

Personal acknowledgments

I would like to thank Professor Tiziana Apuani, who gave me the opportunity to develop this doctoral project and supported me day after day during my approach to the world of scientific research. Special thanks also to Professor Francesco Cecinato for the valuable advice he has always been able to give me, especially in the field of numerical modeling.
I want to acknowledge all my colleagues, professors and collaborators in Milan and Chiavenna, who have helped and supported me throughout the project. Special thanks to Greta and Andrea, great traveling mates in this academic adventure.
I wish to thank Professor Manolis Veveakis from the Department of Civil and Environmental Engineering of Duke University, for welcoming me to his research group and helping me to improve my skills and knowledge about landslide modeling. Thanks to all the friends I met at Duke, who gave me an unforgettable experience.

Thanks to my parents who have supported me over the years and always allowed me to follow my passions and desires.
I could never have achieved this goal without my friends, who as faithful brothers always knew how to advise me on the right choice.
Special thanks to Giulia who supported me during the writing of the Thesis and the preparation of the dissertation, proving to be an essential reference point.

I would like to dedicate this Thesis to Paola, who I am sure would have been proud of my achievement.

References

Abbassi B, Russel D, Taghavi R (2013) FLAC3D mesh and zone quality. Contin Distinct Elem Numer Model Geomech 11–02

AGI (1977) Raccomandazioni sulla programmazione ed esecuzione delle indagini geotecniche. Assoc Geotec Ital 1:96

Agliardi F, Crosta G, Zanchi A (2001) Structural constraints on deep-seated slope deformation kinematics. Eng Geol 59:83–102. https://doi.org/10.1016/S0013-7952(00)00066-1

Albini P., Bellani A., Stucchi M (1988) Terremoti e frane nelle Alpi Centrali. Atti Del 1988 7:129–146

Aldighieri B, Mazzoleni G (2011) La Valchiavenna: un bacino pilota per il controllo dell'ambiente alpino. Quad di Geodin Alp e Quat 10

Aleotti P, Chowdhury R (1999) Landslide hazard assessment: summary review and new perspectives. Bull Eng Geol Environ 58:21–44. https://doi.org/10.1007/s100640050066

Alonso EE, Zervos A, Pinyol NM (2016) Thermo-poro-mechanical analysis of landslides: from creeping behaviour to catastrophic failure. Géotechnique 66:202–219. https://doi.org/10.1680/jgeot.15.LM.006

Apuani T, Scapozza C (2023) AMALPI TREK - Dal Maloja al Gottardo: Alpi in movimento, movimento nelle Alpi. Milano Univ Press. https://doi.org/https://doi.org/10.54103/milanoup.141

Archer NAL, Bell RA, Butcher AS, Bricker SH (2020) Infiltration efficiency and subsurface water processes of a sustainable drainage system and consequences to flood management. J Flood Risk Manag 13:e12629. https://doi.org/https://doi.org/10.1111/jfr3.12629

ASTM (2014) D7012-14 Standard Test Methods for Compressive Strength and Elastic Moduli of Intact Rock Core Specimens under Varying States of Stress and Temperatures. ASTM Int. https://doi.org/10.1520/D7012-14

ASTM (2008a) Standard Test Method For Determination Of The Point Load Strength Index Of Rock And Application To Rock Strength Classifications

ASTM (2004) Standard Test Method For Triaxial Compressive Strength Of Undrained Rock Core Specimens Without Pore Pressure Measurements

ASTM (2023) Standard Test Method for Splitting Tensile Strength of Intact Rock Core Specimens with Flat Loading Platens

ASTM (2008b) D5607 – 08 Standard Test Method for Performing Laboratory Direct Shear Strength Tests of Rock Specimens Under Constant Normal Force

ASTM (2008c) ASTM D5981-96(2008), Standard Guide for Calibrating a Groundwater Flow Model Application (Withdrawn 2017). West Consh

Ayachit U, Geveci B, Quammen C, et al (2018) ParaView: User guide. Kitware Inc 274

Baecher GB, Lanney NA, Einstein HH (1978) Statistical Description of Rock Properties and Sampling. Proc 18th US Symp Rock Mech 5C1-8

Bajni G (2022) Statistical methods to assess rockfall susceptibility in an alpine environment: a focus on climatic forcing and geomechanical variables. PhD Thesis, Univ degli Stud di Milano

Bajni G, Camera CAS, Apuani T (2021) Deciphering meteorological influencing factors for Alpine

rockfalls: a case study in Aosta Valley. Landslides 18:3279–3298. https://doi.org/10.1007/s10346-021-01697-3

Bajni G, Camera CAS, Apuani T (2023) A novel dynamic rockfall susceptibility model including precipitation, temperature and snowmelt predictors: a case study in Aosta Valley (northern Italy). Landslides 20:2131–2154. https://doi.org/10.1007/s10346-023-02091-x

Bakun-Mazor D, Hatzor YH, Glaser SD, Carlos Santamarina J (2013) Thermally vs. seismically induced block displacements in Masada rock slopes. Int J Rock Mech Min Sci 61:196–211. https://doi.org/https://doi.org/10.1016/j.ijrmms.2013.03.005

Bakun-Mazor D, Keissar Y, Feldheim A, et al (2020) Thermally-Induced Wedging–Ratcheting Failure Mechanism in Rock Slopes. Rock Mech Rock Eng 53:2521–2538. https://doi.org/10.1007/s00603-020-02075-6

Ballantyne CK (2002) Paraglacial geomorphology. Quat Sci Rev 21:1935–2017. https://doi.org/https://doi.org/10.1016/S0277-3791(02)00005-7

Barbosa R, Ghaboussi J (1990) Discrete finite element method for multiple deformable bodies. J Finite Elem Anal Des 1990;7145–58

Barla G, Barla M (2001) Investigation and modelling of the Brenva Glacier rock avalanche on the Mount Blanc Range. Rock Mech - a Chall Soc 35–40

Baroň I, Bečkovský D, Míča L (2014) Application of infrared thermography for mapping open fractures in deep-seated rockslides and unstable cliffs. Landslides 11:15–27. https://doi.org/10.1007/s10346-012-0367-z

Baroni C, Martino S, Salvatore MC, et al (2014) Thermomechanical stress-strain numerical modelling of deglaciation since the Last Glacial Maximum in the Adamello Group (Rhaetian Alps, Italy). Geomorphology 226:278–299. https://doi.org/10.1016/j.geomorph.2014.08.013

Barton N (1976) The Shear Strength of Rock and Rock Joints. Int J Rock Mech Min Sci Geotech 13:255–279

Barton N (1988) Barton, 1988. Rock mass classification and tunnel reinforcement using the Q-system. ASTM, STP 984

Barton N, Bandis S (1982) Effects of block size on the shear behavior of jointed rock. 23rd US Symp Rock Mech (USRMS) Soc Min Eng AIME, Berkeley, Calif

Barton N, Choubey V (1977) The shear strength of rock joints in theory and practice. Rock Mech 10:1–54. https://doi.org/10.1007/BF01261801

Bathe KJ. (1982) The finite element procedures in engineering analysis

Batista L dos S, Gomes Filho RR, Carvalho CM de, et al (2020) Water infiltration rate in the soil under different uses and covers in the Poxim River basin, Sergipe, Brazil. Int J Innov Educ Res 8:321–339. https://doi.org/10.31686/ijier.vol8.iss11.2756

Bazin S, Malet J-P, Damiano E, et al (2012) Guidelines for landslide monitoring and early warning systems in Europe – Design and required technology

Bertolini G, Pizziolo M (2008) Risk assessment strategies for the reactivation of earth flows in the Northern Apennines (Italy). Eng Geol 102:178–192. https://doi.org/https://doi.org/10.1016/j.enggeo.2008.03.017

Bettes P (1977) Infinite elements. Int J Numer Methods Eng 1977; 1153–64

Bhunya K, Mishra K, Ojha P, Berndtsson R (2004) Parameter Estimation of Beta Distribution for Unit

Hydrograph Derivation. J Hydrol Eng 9:325–332. https://doi.org/10.1061/(ASCE)1084-0699(2004)9:4(325)

Bieniawski ZT (1974) Estimating the Strength of Rock Materials. J South African Inst Min Metall 74:312–320. https://doi.org/10.1016/0148-9062(74)91782-3

Bieniawski ZT (1979) The geomechanics classifications in rock engineering applications. Proc 4th Congr Rock Mech ISRM

Bini A (1996) La massima estensione dei ghiacciai (MEG) nel territorio compreso tra il Lago di Como, il Lago Maggiore e le rispettive zone di anfiteatro. Geol Insubr 65–77

Bini A, Buoncristiani JF, Couterrand S, et al (2009) Die Schweiz während des letzteiszeitlichen Maximums (LGM), karte 1:500 000. Fed Off Topogr swisstopo

Bini A, Sciunnach D, Bersezio R, et al (2014) Note illustrative della Carta Geologica d'Italia alla scala 1:50.000. Foglio 96 - Seregno

Bishop AW (1955) The use of the Slip Circle in the Stability Analysis of Slopes. Géotechnique 5:7–17. https://doi.org/10.1680/geot.1955.5.1.7

Bishop JE (2009) Simulating the pervasive fracture of materials and structures using randomly close packed Voronoi tessellations. Comput Mech 44:455–471. https://doi.org/10.1007/s00466-009-0383-6

Blikra LH, Christiansen HH (2014) A field-based model of permafrost-controlled rockslide deformation in northern Norway. Geomorphology 208:34–49. https://doi.org/https://doi.org/10.1016/j.geomorph.2013.11.014

Bohloli B, Soldal M, Smith H, et al (2020) Frictional Properties and Seismogenic Potential of Caprock Shales. Energies 13:. https://doi.org/10.3390/en13236275

Bonsignore G, Borgo A, Gelati R, et al (1969) Note illustrative della Carta Geologica d'Italia, Foglio 8—Bormio. Serv Geol d'Italia, Roma

Bonzanigo L (1999) Lo slittamento di Campo Vallemaggia. PhD thesis, ETH Zurich

Borga M, Dalla Fontana G, Da Ros D, Marchi L (1998) Shallow landslide hazard assessment using a physically based model and digital elevation data. Environ Geol 35:81–88. https://doi.org/10.1007/s002540050295

Brabb EE (1984) Innovative approaches to landslide hazard mapping. 4th Int Symp Landslides 1:307–324

Brideau M-A, Pedrazzini A, Stead D, et al (2011) Three-dimensional slope stability analysis of South Peak, Crowsnest Pass, Alberta, Canada. Landslides 8:139–158. https://doi.org/10.1007/s10346-010-0242-8

Burman BC (1971) A numerical approach to the mechanics of discontinua. James Cook University of North Queensland

Burton A, Bathurst JC (1998) Physically based modelling of shallow landslide sediment yield at a catchment scale. Environ Geol 35:89–99. https://doi.org/10.1007/s002540050296

Camera C, Apuani T, Masetti M (2015) Modeling the stability of terraced slopes: an approach from Valtellina (Northern Italy). Environ Earth Sci 74:855–868. https://doi.org/10.1007/s12665-015-4089-0

Camera CAS, Bajni G, Corno I, et al (2021) Introducing intense rainfall and snowmelt variables to implement a process-related non-stationary shallow landslide susceptibility analysis. Sci Total

Environ 786:147360. https://doi.org/10.1016/j.scitotenv.2021.147360

Cannon AJ (2018) Multivariate quantile mapping bias correction: an N-dimensional probability density function transform for climate model simulations of multiple variables. Clim Dyn 50:31–49. https://doi.org/10.1007/s00382-017-3580-6

Canuti P (2002) Applicazione dell'interferometria radar da terra per il controllo dei movimenti franosi: la frana del Ruinon in Valfurva (SO). Tech Rep Pubblicazi

Canuti P, Casagli N, Catani F, Fanti R (2000) Hydrogeological hazard and risk in archaeological sites: Some case studies in Italy. J Cult Herit 1:117–125. https://doi.org/10.1016/S1296-2074(00)00158-8

Cappa F, Scuderi MM, Collettini C, et al (2019) Stabilization of fault slip by fluid injection in the laboratory and in situ. Sci Adv 5:eaau4065. https://doi.org/10.1126/sciadv.aau4065

Carlà T, Gigli G, Lombardi L, et al (2021) Monitoring and analysis of the exceptional displacements affecting debris at the top of a highly disaggregated rockslide. Eng Geol 294. https://doi.org/10.1016/j.enggeo.2021.106345

Carlà T, Nolesini T, Solari L, et al (2019) Rockfall forecasting and risk management along a major transportation corridor in the Alps through ground-based radar interferometry. Landslides 16:1425–1435. https://doi.org/10.1007/s10346-019-01190-y

Carrara A, Guzzetti F, Cardinali M, Reichenbach P (1999) Use of GIS technology in the prediction and monitoring of landslide hazard. In: Natural Hazards. pp 117–135

Casagli N, Catani F, Del Ventisette C, Luzi G (2010) Monitoring, prediction, and early warning using ground-based radar interferometry. Landslides 7:291–301. https://doi.org/10.1007/s10346-010-0215-y

Casagli N, Intrieri E, Tofani V, et al (2023) Landslide detection, monitoring and prediction with remote-sensing techniques. Nat Rev Earth Environ 4:51–64. https://doi.org/10.1038/s43017-022-00373-x

Cascini L, Fornaro G, Peduto D (2010) Advanced low- and full-resolution DInSAR map generation for slow-moving landslide analysis at different scales. Eng Geol 112:29–42. https://doi.org/https://doi.org/10.1016/j.enggeo.2010.01.003

Cecinato F, Zervos A (2012) Influence of thermomechanics in the catastrophic collapse of planar landslides. Can Geotech J 49:207–225. https://doi.org/10.1139/t11-095

Cermak V, Rybach L (1982) Thermal conductivity and specific heat of minerals and rocks. Landolt-Börnstein, New Ser. Gr. V, Geophys. Sp. Res. 305–343

Chen Z-Y, Morgenstern NR (1983) Extensions to the generalized method of slices for stability analysis. Can Geotech J 20:104–119. https://doi.org/10.1139/t83-010

Cheng Y (1966) The use of infinite element. Comput Geomech 1996;18(1)65–70

Cheng YM, Lansivaara T, Wei WB (2007) Two-dimensional slope stability analysis by limit equilibrium and strength reduction methods. Comput Geotech 34:137–150. https://doi.org/10.1016/j.compgeo.2006.10.011

Clayton C, Jackson A, Price J, et al (2020) Case study: analysis of a highwall toppling failure and development of a successful mine re-entry plan using RS2, RocFall and Dan-W at a coal mine in Canada. 383–398. https://doi.org/10.36487/acg_repo/2025_21

Collins BD, Stock GM (2016) Rockfall triggering by cyclic thermal stressing of exfoliation fractures. Nat Geosci 9:395–400. https://doi.org/10.1038/ngeo2686

Collins BD, Stock GM, Eppes MC (2017) Progressive Thermally Induced Fracture of an Exfoliation Dome: Twain Harte, California, USA. ISRM Progress. Rock Fail. Conf. ISRM-PRF-2017-006

Consortium PAGES 2k (2013) Continental-scale temperature variability during the past two millennia. Nat Geosci 6:339–346

Conti P, Manatschal G, Pfister M (1994) Synrift sedimentation, Jurassic and Alpine tectonics in the central Ortler nappe (Eastern Alps, Italy). Eclogae Geol Helv 87:63–90

Corominas J, Westen C Van, Frattini P, et al (2014) Recommendations for the quantitative analysis of landslide risk. 209–263. https://doi.org/10.1007/s10064-013-0538-8

Coulomb CA (1776) Essai sur une application des regles des maximis et minimis a quelquels problemesde statique relatifs, a la architecture. Mem Acad Roy Div Sav 7:343–387

Crosta G (2018) Servizio di modellazione geotecnica ed individuazione delle soglie di criticità nelle aree di frana monitorate dal CMG di ARPA del Lotto 1: Aree di Ruinon (Comune di Valfurva, SO) e Gera Lario (Comune di Montemezzo, CO) Volume I – Ruinon. Tech Rep

Crosta G, Agliardi F (2014) Long-and short-term controls on the Spriana rockslide (Central Alps, Italy). Landslide Sci a Safer Geoenvironment 243–249

Crosta G, Zanchi A (2000) Deep Seated Slope Deformations: Huge, Extraordinary, Enigmatic Phenomena. In: Landslides in Research, Theory and Practice. pp 1: 351-358

Crosta GB (2013) Revisione dei valori Soglia da dati GB_InSAR a seguito dell'evento novembre 2012. Tech Rep

Crosta GB, Agliardi F (2003) Failure forecast for large rock slides by surface displacement measurements. Can Geotech J 40:176–191. https://doi.org/10.1139/t02-085

Crosta GB, Agliardi F, Rivolta C, et al (2017) Long-term evolution and early warning strategies for complex rockslides by real-time monitoring. Landslides 14:1615–1632. https://doi.org/10.1007/s10346-017-0817-8

Crosta GB, Chen H, Lee CF (2004) Replay of the 1987 Val Pola Landslide, Italian Alps. Geomorphology 60:127–146. https://doi.org/10.1016/j.geomorph.2003.07.015

Crosta GB, di Prisco C, Frattini P, et al (2013) Chasing a complete understanding of the triggering mechanisms of a large rapidly evolving rockslide. Landslides 11:747–764. https://doi.org/10.1007/s10346-013-0433-1

Crozier MJ (2010) Geomorphology Deciphering the effect of climate change on landslide activity : A review. Geomorphology 124:260–267. https://doi.org/10.1016/j.geomorph.2010.04.009

Cruden DM, Varnes DJ (1996) Landslide types and processes. Turn AK, Schuster RL Landslides Investig mitigation, Transp Res board Spec Rep 247 National R:pp 36–75

Cundall P, Hart R (1992) Numerical modelling of discontinua. Eng Comput 9:101–113. https://doi.org/10.1108/eb023851

Cutter SL, Boruff BJ, Shirley WL (2003) Social Vulnerability to Environmental Hazards. Soc Sci Q 84:242–261

D'Amato J, Hantz D, Guerin A, et al (2016) Influence of meteorological factors on rockfall occurrence in a middle mountain limestone cliff. Nat Hazards Earth Syst Sci 16:719–735. https://doi.org/10.5194/nhess-16-719-2016

D'Angiò D, Lenti L, Martino S (2021) Microseismic monitoring to assess rock mass damaging through a novel damping ratio-based approach. Int J Rock Mech Min Sci 146:104883.

https://doi.org/https://doi.org/10.1016/j.ijrmms.2021.104883

Darnault R, Rolland Y, Braucher R, et al (2012) Timing of the last deglaciation revealed by receding glaciers at the Alpine-scale: Impact on mountain geomorphology. Quat Sci Rev 31:127–142. https://doi.org/10.1016/j.quascirev.2011.10.019

Davies O, Rouainia M, Glendinning S, et al (2014) Investigation of a pore pressure driven slope failure using a coupled hydro-mechanical model. Eng Geol 178:70–81. https://doi.org/10.1016/j.enggeo.2014.05.012

Davis BAS, Brewer S, Stevenson AC, Guiot J (2003) The temperature of Europe during the Holocene reconstructed from pollen data. Quat Sci Rev 22:1701–1716. https://doi.org/https://doi.org/10.1016/S0277-3791(03)00173-2

De Blasio FV, Medici L (2017) Microscopic model of rock melting beneath landslides calibrated on the mineralogical analysis of the Köfels frictionite. Landslides 14:337–350. https://doi.org/10.1007/s10346-016-0700-z

De Ojeda P, Sanz E, Galindo R (2021) Historical reconstruction and evolution of the large landslide of Inza (Navarra, Spain). Springer Netherlands

De Pedrini A, Ambrosi C, Scapozza C (2022) The 1513 Monte Crenone rock avalanche: numerical model and geomorphological analysis. Geogr Helv 77:21–37. https://doi.org/10.5194/gh-77-21-2022

Deere DU, Hendron AJ, Patton FD, Cording EJ (1966) Design Of Surface And Near-Surface Construction In Rock

Dei Cas L, Pastore ML, Bonetti D, Ferrarini F (2022) Problems and Solutions for the Management of a Unitary System of Landslide Monitoring Networks: an Experience in North Italy. Ital J Eng Geol Environ 2:41–57. https://doi.org/10.4408/IJEGE.2022-02.O-04

Dei Cas L, Pastore ML, Pavan A, Petrella N (2021) Geological monitoring networks for risk management close to large rock cliffs: the case history of Gallivaggio and Cataeggio in the italian Alps. Geogr Helv 76:85–101. https://doi.org/10.5194/gh-76-85-2021

Dejong JT, Soga K, Kavazanjian E, et al (2013) Biogeochemical processes and geotechnical applications: Progress, opportunities and challenges. Bio- Chemo- Mech Process Geotech Eng - Geotech Symp Print 2013 143–157. https://doi.org/10.1680/bcmpge.60531.014

Del Ventisette C, Casagli N, Fortuny-Guasch J, Tarchi D (2012) Ruinon landslide (Valfurva, Italy) activity in relation to rainfall by means of GBInSAR monitoring. Landslides 9:497–509. https://doi.org/10.1007/s10346-011-0307-3

Deppo (2002) Le verifiche idrauliche e la valutazione di rischio nei sistemi di drenaggio urbano. L'ambiente

DeWalle DR, Rango A (2008) Principles of snow hydrology. Cambridge University Press

Donald IB, Giam SK (1988) Application of the nodal displacement method to slope stability analysis. In: Fifth Australia-New Zealand Conference on Geomechanics: Prediction Versus Performance; Preprints of Papers: Prediction Versus Performance; Preprints of Papers. pp 456–460

Donati D, Stead D, Stewart TW, Marsh J (2020) Numerical modelling of slope damage in large, slowly moving rockslides: Insights from the Downie Slide, British Columbia, Canada. Eng Geol 273:105693. https://doi.org/10.1016/j.enggeo.2020.105693

Donnini M, Santangelo M, Gariano SL, et al (2023) Landslides triggered by an extraordinary rainfall event in Central Italy on September 15, 2022. Landslides 20:2199–2211.

https://doi.org/10.1007/s10346-023-02109-4

Draebing D, Krautblatter M (2019) The Efficacy of Frost Weathering Processes in Alpine Rockwalls. Geophys Res Lett 46:6516–6524. https://doi.org/https://doi.org/10.1029/2019GL081981

Drucker DC, Prager W (1952) Soil mechanics and plastic analysis or limit design. Q Appl Math 10:157–165

Durand Y, Laternser M, Giraud G, et al (2009) Reanalysis of 44 yr of climate in the French Alps (1958–2002): methodology, model validation, climatology, and trends for air temperature and precipitation. J Appl Meteorol Clim 48:29–449

Duvillard PA, Ravanel L, Deline P (2015) Risk assessment of infrastructure destabilisation due to global warming in the high French Alps. J Alp Res

Eberhardt E (2008) Twenty-ninth Canadian Geotechnical Colloquium: The role of advanced numerical methods and geotechnical field measurements in understanding complex deep-seated rock slope failure mechanisms. Can Geotech J 45:484–510. https://doi.org/10.1139/T07-116

Eberhardt E, Stead D, Coggan JS (2004) Numerical analysis of initiation and progressive failure in natural rock slopes-the 1991 Randa rockslide. Int J Rock Mech Min Sci 41:69–87. https://doi.org/10.1016/S1365-1609(03)00076-5

Einstein HH, Baecher GB (1983) Probabilistic and statistical methods in engineering geology - Specific methods and examples part I: Exploration. Rock Mech Rock Eng 16:39–72. https://doi.org/10.1007/BF01030217

Elmo D, Rogers S, Stead D, Eberhardt E (2014) Discrete Fracture Network approach to characterise rock mass fragmentation and implications for geomechanical upscaling. Min Technol 123:149–161

Elmo D, Stead D, Rogers S (2015) Guidelines for the Quantitative Description of Discontinuities for use in Discrete Fracture Network Modelling. 13th ISRM Int Congr Rock Mech Int Soc Rock Mech

Eppes MC, Magi B, Hallet B, et al (2016) Deciphering the role of solar-induced thermal stresses in rock weathering. GSA Bull 128:1315–1338. https://doi.org/10.1130/B31422.1

European Commission JRC (2020) Climate change and Europe's water resources. Publ Off LU

Falappi P (2012) La frana di Piuro in Bregaglia del 1618: fantasie e realtà

Falatkova K, Šobr M, Neureiter A, et al (2019) Development of proglacial lakes and evaluation of related outburst susceptibility at the Adygine ice-debris complex, northern Tien Shan. Earth Surf Dyn 7:301–320. https://doi.org/10.5194/esurf-7-301-2019

Fellenius W (1936) Calculation of the stability of earth dams. Proc 2nd Congr Large Dams 4:445–462

Ferrari F, Apuani T, Giani GP (2014) Rock Mass Rating spatial estimation by geostatistical analysis. Int J Rock Mech Min Sci 70:162–176. https://doi.org/10.1016/j.ijrmms.2014.04.016

Ferri F, Di Toro G, Hirose T, Shimamoto T (2010) Evidence of thermal pressurization in high-velocity friction experiments on smectite-rich gouges. Terra Nov 22:347–353. https://doi.org/10.1111/j.1365-3121.2010.00955.x

Fiorucci M, Marmoni GM, Martino S, Mazzanti P (2018) Thermal Response of Jointed Rock Masses Inferred from Infrared Thermographic Surveying (Acuto Test-Site, Italy). Sensors 18

Fischer L, Amann F, Moore JR, Huggel C (2010) Assessment of periglacial slope stability for the 1988 Tschierva rock avalanche (Piz Morteratsch, Switzerland). Eng Geol 116:32–43

Florineth D, Schlüchter C (1998) Reconstructing the Last Glacial Maximum (LGM) ice surface

geometry and flowlines in the Central Swiss Alps. Eclogae Geol Helv 91:391–407. https://doi.org/10.7892/boris.87056

Fowler HJ, Blenkinsop S, Tebaldi C (2007) Linking climate change modelling to impacts studies: recent advances in downscaling techniques for hydrological modelling. Int J Climatol 27:1547–1578. https://doi.org/https://doi.org/10.1002/joc.1556

Froitzneim N, Manatschal G (1996) Kinematics of Jurassic rifting, mantle exhumation, and passive-margin formation in the Austroalpine and Penninic nappes (eastern Switzerland). Bull Geol Soc Am 108:1120–1133. https://doi.org/10.1130/0016-7606(1996)108

Gariano SL, Guzzetti F (2016) Landslides in a changing climate. Earth-Science Rev 162:227–252. https://doi.org/10.1016/j.earscirev.2016.08.011

Gawin D, Schrefler BA, Galindo M (1996) Thermo-hydro-mechanical analysis of partially saturated porous materials. Eng Comput 13:113–143. https://doi.org/10.1108/02644409610151584

Geuzaine C, Remacle J-F (2023) Gmsh Reference Manual

Giandotti M (1934) Previsione delle piene e delle magre dei corsi d'acqua. Ist Poligr dello Stato 8

Gischig V, Amann F, Moore JR, et al (2011a) Composite rock slope kinematics at the current Randa instability, Switzerland, based on remote sensing and numerical modeling. Eng Geol 118:37–53. https://doi.org/10.1016/j.enggeo.2010.11.006

Gischig VS, Moore JR, Evans KF, et al (2011b) Thermomechanical forcing of deep rock slope deformation: 1. Conceptual study of a simplified slope. J Geophys Res Earth Surf 116:1–18. https://doi.org/10.1029/2011JF002006

Gischig VS, Moore JR, Evans KF, et al (2011c) Thermomechanical forcing of deep rock slope deformation: 2. the Randa rock slope instability. J Geophys Res Earth Surf 116:. https://doi.org/10.1029/2011JF002007

Godt JW, Baum RL, Savage WZ, et al (2008) Transient deterministic shallow landslide modeling: Requirements for susceptibility and hazard assessments in a GIS framework. Eng Geol 102:214–226. https://doi.org/https://doi.org/10.1016/j.enggeo.2008.03.019

Gonzalez FCG, Cavacanti M do CR, Nahas Ribeiro W, et al (2024) A systematic review on rainfall thresholds for landslides occurrence. Heliyon 10:e23247. https://doi.org/https://doi.org/10.1016/j.heliyon.2023.e23247

Google E (2022) Google Earth. earth.google.com/web/

Goren L, Aharonov E (2007) Long runout landslides: The role of frictional heating and hydraulic diffusivity. Geophys Res Lett 34:1–7. https://doi.org/10.1029/2006GL028895

Goren L, Aharonov E, Anders MH (2010) The long runout of the Heart Mountain landslide: Heating, pressurization, and carbonate decomposition. J Geophys Res Solid Earth 115:1–15. https://doi.org/10.1029/2009JB007113

Grämiger LM, Moore JR, Gischig VS, et al (2017) Beyond debuttressing: Mechanics of paraglacial rock slope damage during repeat glacial cycles. J Geophys Res Earth Surf 122:1004–1036. https://doi.org/10.1002/2016JF003967

Grämiger LM, Moore JR, Gischig VS, et al (2020) Hydromechanical Rock Slope Damage During Late Pleistocene and Holocene Glacial Cycles in an Alpine Valley. J Geophys Res Earth Surf 125:e2019JF005494. https://doi.org/https://doi.org/10.1029/2019JF005494

Grämiger LM, Moore JR, Gischig VS, Loew S (2018) Thermomechanical Stresses Drive Damage of

Alpine Valley Rock Walls During Repeat Glacial Cycles. J Geophys Res Earth Surf 123:2620–2646. https://doi.org/10.1029/2018JF004626

Grechi G, D'Angiò D, Martino S (2023) Analysis of Thermally Induced Strain Effects on a Jointed Rock Mass through Microseismic Monitoring at the Acuto Field Laboratory (Italy). Appl Sci 13:. https://doi.org/10.3390/app13042489

Grechi G, Fiorucci M, Marmoni GM, Martino S (2021) 3D Thermal Monitoring of Jointed Rock Masses Through Infrared Thermography and Photogrammetry. Remote Sens 13:1–25. https://doi.org/10.3390/rs13050957

Grechi G, Martino S (2021) Multimethodological Study of Non-linear Strain Effects Induced by Thermal Stresses on Jointed Rock Masses. Springer International Publishing

Gregnanin A, Valle M (1995) Deformation and metamorphism in the Austroalpine Oetztal-Stubai Complex (Part II); Early-Alpine evolution in basement and cover. Ital J Geosci 114:393–409

Griffini L (2004) Valutazione delle condizioni di stabilità della frana del Ruinon e aree limitrofe - Istituto di Ricerca per l'Ecologia e l'Economia Applicate alle Aree Alpine (IREALP). Tech Rep

Griffini L (2013) Intervento di protezione e valorizzazione dei territori dell'alta Valtellina attraverso la difesa degli abitati e delle infrastrutture dalla Frana del Ruinon di Valfurva - Progetto preliminare Progetto preliminare. Tech Rep

Griffini L (2020) Realizzazione di opere idrauliche diversive del Torrente Confinale e del bacino idrografico per la riduzione degli apporti idrici verso la frana del Ruinon in territorio comunale di Valfurva - Progetto esecutivo. Tech Rep

Griffini L (2021) By-pass idraulico del torrente Frodolfo nel tratto sotteso dalla Frana del Ruinon, Valfurva (SO). Tech Rep

Griffiths AA (1921) The phenomena of rupture and flow in solids

Griffiths D V, Lane PA (1999) Slope stability analysis by finite elements. Géotechnique 49:387–403. https://doi.org/10.1680/geot.1999.49.3.387

Grimstad E, Barton N (1993) Updating of the Q-system for NMT. Proc Int Symp Sprayed Concr Fagernes, Oslo, 22–26 Oct 1993

Grimstad E, Kankes K, Bhasin R, et al (2002) Rock Mass Quality Q Used in Designing Reinforced Ribs of Sprayed Concrete and Energy Absorption. Int Symp Sprayed Concr Davos, 22–26 Sept 2002

Grove AT (2001) The "Little Ice Age" and its Geomorphological Consequences in Mediterranean Europe. Clim Change 48:121–136. https://doi.org/10.1023/A:1005610804390

Gruber S, Peter M, Hoelzle M, et al (2003) Surface temperatures in steep alpine rock faces - a strategy for regional-scale measurement and modelling. Proc 8th Int Conf Permafr 1:325–330

Gruntfest IJ (1963) Thermal Feedback in Liquid Flow; Plane Shear at Constant Stress. Trans Soc Rheol 7:195–207. https://doi.org/10.1122/1.548954

Gu T, Wang J, Fu X, Liu Y (2015) GIS and limit equilibrium in the assessment of regional slope stability and mapping of landslide susceptibility. Bull Eng Geol Environ 74:1105–1115. https://doi.org/10.1007/s10064-014-0689-2

Guerin A, Jaboyedoff M, Collins BD, et al (2019) Detection of rock bridges by infrared thermal imaging and modeling. Sci Rep 9:13138. https://doi.org/10.1038/s41598-019-49336-1

Gunzburger Y, Merrien-Soukatchoff V, Guglielmi Y (2005) Influence of daily surface temperature fluctuations on rock slope stability: Case study of the Rochers de Valabres slope (France). Int J

Rock Mech Min Sci 42:331–349. https://doi.org/10.1016/j.ijrmms.2004.11.003

Guyennon N, Valt M, Salerno F, et al (2019) Estimating the snow water equivalent from snow depth measurements in the Italian Alps. Cold Reg Sci Technol 167:102859. https://doi.org/10.1016/j.coldregions.2019.102859

Guzzetti F, Carrara A, Cardinali M, Reichenbach P (1999) Landslide hazard evaluation: A review of current techniques and their application in a multi-scale study, Central Italy. In: Geomorphology. pp 181–216

Guzzetti F, Mondini AC, Cardinali M, et al (2012) Landslide inventory maps: New tools for an old problem. Earth-Science Rev 112:42–66. https://doi.org/https://doi.org/10.1016/j.earscirev.2012.02.001

Guzzetti F, Reichenbach P, Ardizzone F, et al (2006) Estimating the quality of landslide susceptibility models. Geomorphology 81:166–184. https://doi.org/https://doi.org/10.1016/j.geomorph.2006.04.007

Hall K (1999) The role of thermal stress fatigue in the breakdown of rock in cold regions. Geomorphology 31:47–63. https://doi.org/https://doi.org/10.1016/S0169-555X(99)00072-0

Hammah R, Yacoub T, Corkum B, Cuarran JH (2008) The Practical Modelling of Discontinuous Rock Masses with Finite Element Analysis. ARMA, Am Rock Mech Assoc

Hansmann J, Loew S, Evans KF (2012) Reversible rock-slope deformations caused by cyclic water-table fluctuations in mountain slopes of the Central Alps, Switzerland. Hydrogeol J 20:73–91

He K, Li Y, Ma G, et al (2021) Failure mode analysis of post-seismic rockfall in shattered mountains exemplified by detailed investigation and numerical modelling. Landslides 18:425–446. https://doi.org/10.1007/s10346-020-01532-1

Helmstetter A, Sornette D, Grasso J-R, et al (2004) Slider block friction model for landslides: Application to Vaiont and La Clapière landslides. J Geophys Res Solid Earth 109:1–15. https://doi.org/10.1029/2002jb002160

Hoek E (1988) The Hoek-Brown failure criterion-a 1988 update. Proc 15th Can Rock Mech Symp

Hoek E, Brown ET (1997) Practical estimates of rock mass strength. Int J Rock Mech Min Sci 34(8), 116

Hoek E, Brown ET (1980) Underground excavations in rock

Hudson JA, Harrison JP (1997) Engineering rock mechanics

Hueckel T, François B, Laloui L (2009) Explaining thermal failure in saturated clays. Géotechnique 59:197–212. https://doi.org/10.1680/geot.2009.59.3.197

Hungr O, Leroueil S, Picarelli L (2014) The Varnes classification of landslide types, an update. Landslides 11:167–194. https://doi.org/10.1007/s10346-013-0436-y

Icenhour C, Keniley S, Permann C, et al (2018) Multi-physics Object Oriented Simulation Environment (MOOSE). Idaho Natl Lab

Intrepid Geophysics (2014) Geomodeller; Version 3, User's Manual; Intrepid Geophysics, Inc

Intrieri E, Gigli G, Mugnai F, et al (2012) Design and implementation of a landslide early warning system. Eng Geol 147–148:124–136. https://doi.org/https://doi.org/10.1016/j.enggeo.2012.07.017

IPCC (2014) Climate Change 2014: Synthesis Report. Contribution of Working Groups I, II and III to the Fifth Assessment Report of the Intergovernmental Panel on Climate Change. IPCC, Gene:155

IPCC (2012) Managing the risks of extreme events and disasters to advance climate change adaptation: summary for policymakers. A special report of Working Groups I and II of the Intergovernmental Panel on Climate Change (IPCC)

Ismes (1994) Studi Sismici in Alta Valtellina. I Quad dell'Ismes 336

ISRM (2015) The ISRM Suggested Methods for Rock Characterization, Testing and Monitoring: 2007–2014. Comm Stand Lab F Tests Rock Mech ISRM

ISRM (1981) Rock Characterization, Testing and Monitoring. Comm Stand Lab F Tests Rock Mech ISRM

Itasca Consulting Group (2019a) FLAC3D—Fast Lagrangian Analysis of Continua; Version 7.0, User's Manual. Itasca Consult Group, Inc Minneapolis, MN, USA

Itasca Consulting Group (2018) UDEC—Universal distinct element code, Version 7.0, User's Manual

Itasca Consulting Group (2019b) 3DEC - Version 7.0, User's Manual

Iturbide M, Fernández J, Gutiérrez JM, et al (2021) Repository supporting the implementation of FAIR principles in the IPCC-WGI Atlas

Ivy-Ochs S (2015) Variaciones glaciares en los Alphs europoes al final de la última glaciación. Cuad Investig Geogr 41:295–315. https://doi.org/10.18172/cig.2750

Ivy-Ochs S, Kerschner H, Maisch M, et al (2009) Latest Pleistocene and Holocene glacier variations in the European Alps. Quat Sci Rev 28:2137–2149. https://doi.org/10.1016/j.quascirev.2009.03.009

Ivy-Ochs S, Kerschner H, Reuther A, et al (2006) The timing of glacier advances in the northern European Alps based on surface exposure dating with cosmogenic 10Be, 26Al, 36Cl, and 21Ne. Spec Pap Geol Soc Am 415:43–60

Jaboyedoff M, Oppikofer T, Derron M-H, et al (2011) Complex landslide behaviour and structural control: a three-dimensional conceptual model of Åknes rockslide, Norway. Slope Tectonics 351:0

Jaboyedoff M, Penna I, Pedrazzini A, et al (2013) An introductory review on gravitational-deformation induced structures, fabrics and modeling. Tectonophysics 605:1–12

Jaeger JC, Cook NGW (1969) Fundamentals of Rock Mechanics, 2nd Ed. Chapman hall

Janbu N (1973) Slope stability computations. Publ Wiley Sons, Inc

Jemec Auflič M, Bezak N, Šegina E, et al (2023) Climate change increases the number of landslides at the juncture of the Alpine, Pannonian and Mediterranean regions. Sci Rep 13:23085. https://doi.org/10.1038/s41598-023-50314-x

Jing L (2003) A review of techniques, advances and outstanding issues in numerical modelling for rock mechanics and rock engineering. Int J Rock Mech Min Sci 40:283–353. https://doi.org/10.1016/S1365-1609(03)00013-3

Keefer DK (1984) Rock Avalanches Caused by Earthquakes: Source Characteristics. Science (80-) 223:1288–1290. https://doi.org/10.1126/science.223.4642.1288

Kottek M, Grieser J, Beck C, et al (2006) World map of the Köppen-Geiger climate classification updated. Meteorol Zeitschrift 15:259–263. https://doi.org/10.1127/0941-2948/2006/0130

Kulatilake PHSW, Shreedharan S, Sherizadeh T, et al (2016) Laboratory Estimation of Rock Joint Stiffness and Frictional Parameters. Geotech Geol Eng 34:1723–1735. https://doi.org/10.1007/s10706-016-9984-y

Kulhawy FH (1975) Stress Deformation Properties of Rock and Rock Discontinuities. Eng Geol 9:327–

350

Lade P V (1977) Elasto-plastic stress-strain theory for cohesionless soil with curved yield surfaces. Int J Solids Struct 13:1019–1035

Lahai YA, Anderson KFE, Jalloh Y, et al (2021) A comparative geological, tectonic and geomorphological assessment of the Charlotte, Regent and Madina landslides, Western area, Sierra Leone. Geoenvironmental Disasters 8:16. https://doi.org/10.1186/s40677-021-00187-x

Lan H, Liu X, Li L, et al (2022) Remote Sensing Precursors Analysis for Giant Landslides. Remote Sens. 14

Lancaster-Jones PFF (1975) The interpretation of the Lugeon water-test. Q J Eng Geol 8:151–154. https://doi.org/10.1144/GSL.QJEG.1975.008.02.05

Lefranc E (1936) Procédé de mesure de la perméabilité des sols dans les nappes aquifères et application au calcul du débit des puits. Le Génie Civ CIX(15):306–308

Lefranc E (1937) La théorie des poches absorbantes et son application à la détermination du coefficient de perméabilité en place et au calcul du débit des nappes d'eau. Le Génie Civ CXI(20):409–413

Leith K, Moore JR, Amann F, Loew S (2014) Subglacial extensional fracture development and implications for Alpine Valley evolution. J Geophys Res Earth Surf 119:62–81. https://doi.org/10.1002/2012JF002691

Li A, Xu N, Dai F, et al (2018) Stability analysis and failure mechanism of the steeply inclined bedded rock masses surrounding a large underground opening. Tunn Undergr Sp Technol 77:45–58. https://doi.org/https://doi.org/10.1016/j.tust.2018.03.023

Liao Q, Hencher S (1997) Numerical modeling of the hydromechanical behaviour of fractured rock masses. Int J Rock Mech Min Sci 34(3–4)

Lignon S, Laouafa F, Prunier F, et al (2009) Hydro-mechanical modelling of landslides with a material instability criterion. Geotechnique 59:513–524. https://doi.org/10.1680/geot.7.00121

Liu B, He K, Han M, et al (2021) Dynamic process simulation of the Xiaogangjian rockslide occurred in shattered mountain based on 3DEC and DFN. Comput Geotech 134:104122. https://doi.org/10.1016/j.compgeo.2021.104122

Liu J, Pu S, Pu S, Rao J (2020) Visco-Elastoplastic Constitutive Fatigue Model for Rocks. Adv Civ Eng 2020:. https://doi.org/10.1155/2020/4292043

Liu SY, Shao LT, Li HJ (2015) Slope stability analysis using the limit equilibrium method and two finite element methods. Comput Geotech 63:291–298. https://doi.org/10.1016/j.compgeo.2014.10.008

Loew S, Gschwind S, Gischig V, et al (2017) Monitoring and early warning of the 2012 Preonzo catastrophic rockslope failure. Landslides 14:141–154. https://doi.org/10.1007/s10346-016-0701-y

Lorig L (1985) A simple numerical representation of fully bounded passive rock reinforcement for hard rock. Comput Geotech 1:79–97

Lorig LJ, Cundall PA (1989) Modeling of Reinforced Concrete Using the Distinct Element Method BT - Fracture of Concrete and Rock. In: Shah SP, Swartz SE (eds). Springer New York, New York, NY, pp 276–287

Løset F (1997) Engineering Geology - Practical use of the Q-method. NGI Rep 592046-4

Lotti F, Baiocchi A, D'Onofrio S, Piscopo V (2012) Hydrogeological site characterization of marly-silici-calcareous rocks through surveys of discontinuities and pumping tests. Acque Sotter - Ital J

Groundw 1:27–36. https://doi.org/10.7343/AS-002-12-0002

Lucas D, Herzog R, Iten M, et al (2020) Modelling of landslides in a scree slope induced by groundwater and rainfall. Int J Phys Model Geotech 20:177–197. https://doi.org/10.1680/jphmg.18.00106

Ma C, Li T, Zhang H (2020) Microseismic and precursor analysis of high-stress hazards in tunnels: A case comparison of rockburst and fall of ground. Eng Geol 265:105435. https://doi.org/https://doi.org/10.1016/j.enggeo.2019.105435

Ma Y, Sheng Q, Zhang G, Cui Z (2019) A 3D Discrete-Continuum Coupling Approach for Investigating the Deformation and Failure Mechanism of Tunnels across an Active Fault: A Case Study of Xianglushan Tunnel. Appl Sci 9:. https://doi.org/10.3390/app9112318

Macciotta R, Martin CD, Edwards T, et al (2015) Quantifying weather conditions for rock fall hazard management. Georisk Assess Manag Risk Eng Syst Geohazards 9:171–186. https://doi.org/10.1080/17499518.2015.1061673

Magnin F, Deline P, Ravanel L, et al (2015) Thermal characteristics of permafrost in the steep alpine rock walls of the Aiguille du Midi (Mont Blanc Massif, 3842 m a.s.l). Cryosph 9:109–121. https://doi.org/10.5194/tc-9-109-2015

Maidment D (1969) Handbook of hydrology

Maisch M, Haeberli W, Frauenfelder R, et al (2003) Lateglacial and Holocene evolution of glaciers and permafrost in the Val Muraglo, Upper Engadin, Swiss Alps. 8th Int Conf Permafr 717–722

Mann ME, Zhang Z, Rutherford S, et al (2009) Global Signatures and Dynamical Origins of the Little Ice Age and Medieval Climate Anomaly. Science (80-) 326:1256–1260. https://doi.org/10.1126/science.1177303

Maraun D, Knevels R, Mishra AN, et al (2022) A severe landslide event in the Alpine foreland under possible future climate and land-use changes. Commun Earth Environ 3:1–11. https://doi.org/10.1038/s43247-022-00408-7

Marinos P, Hoek E (2000) GSI: a geologically friendly tool for rock mass strength estimation. SRM Int Symp Int Soc Rock Mech

Marmoni GM, Fiorucci M, Grechi G, Martino S (2020) Modelling of thermo-mechanical effects in a rock quarry wall induced by near-surface temperature fluctuations. Int J Rock Mech Min Sci 134:104440. https://doi.org/10.1016/j.ijrmms.2020.104440

Martino S, Prestininzi A, Romeo RW (2014) Earthquake-induced ground failures in Italy from a reviewed database. Nat Hazards Earth Syst Sci 14:799–814

Masiol M, Zannoni D, Stenni B, et al (2021) Spatial distribution and interannual trends of δ18O, δ2H, and deuterium excess in precipitation across North-Eastern Italy. J Hydrol 598:125749. https://doi.org/https://doi.org/10.1016/j.jhydrol.2020.125749

Matsuoka N (2019) A multi-method monitoring of timing, magnitude and origin of rockfall activity in the Japanese Alps. Geomorphology 336:65–76. https://doi.org/https://doi.org/10.1016/j.geomorph.2019.03.023

Matsuoka N (2008) Frost weathering and rockwall erosion in the southeastern Swiss Alps: Long-term (1994–2006) observations. Geomorphology 99:353–368. https://doi.org/https://doi.org/10.1016/j.geomorph.2007.11.013

Mazzoccola D (1993) a dinamica dei versanti della media Valchiavenna (SO): analisi geomeccanica dei fenomeni di instabilità in atto e potenziali. PhD thesis

McColl ST (2012) Paraglacial rock-slope stability. Geomorphology 153–154:1–16. https://doi.org/10.1016/j.geomorph.2012.02.015

McCrea JM (1950) On the isotopic chemistry of carbonates and a paleotemperature scale. J Chem Phys 18:849–857. https://doi.org/10.1063/1.1747785

McNeel R (2010) Rhinoceros 3D; Version 6.0; Robert McNeel & Associates

Mergili M, Marchesini I, Rossi M, et al (2014) Spatially distributed three-dimensional slope stability modelling in a raster GIS. Geomorphology 206:178–195. https://doi.org/10.1016/j.geomorph.2013.10.008

Merizzi G (2002) Individuazione del reticolo idrico minore e delle relative fasce di rispetto, definizione delle attività vietate o soggette ad autorizzazione comunale.

Merizzi G (2015) – Relazione descrittiva dei sondaggi geognostici e delle indagini geofisiche progetto esecutivo: Realizzazione di opere idrauliche diversive del torrente Confinale e del bacino idrografico per la riduzione degli apporti idrici verso la frana del Ruinon in. Tech Rep

Meusburger K, Alewell C (2009) On the influence of temporal change on the validity of landslide susceptibility maps. Nat Hazards Earth Syst Sci 9:1495–1507

Mey J, Scherler D, Wickert AD, et al (2016) Glacial isostatic uplift of the European Alps. Nat Commun 7:13382. https://doi.org/10.1038/ncomms13382

Michoud C, Bazin S, Blikra LH, et al (2013) Experiences from site-specific landslide early warning systems. Nat Hazards Earth Syst Sci 13:2659–2673. https://doi.org/10.5194/nhess-13-2659-2013

Mises R v (1913) Mechanik der festen Körper im plastisch-deformablen Zustand. Nachrichten von der Gesellschaft der Wissenschaften zu Göttingen, Math Klasse 1913:582–592

Mogi K (1971) Fracture and flow of rocks under high triaxial compression. J Geophys Res 76:1255–1269

Montrasio A, Berra F, Cariboni M, et al (1990) Note illustrative della Carta Geologica d'Italia alla scala 1:50.000 - Foglio Bormio. Istituto Superiore per la Protezione e la Ricerca Ambientale Servizio Geologico d'Italia Organo cartografico dello Stato.

Montrasio A, Sciesa E (1988) Carta geologica della valle Spluga ed aree adiacenti, scala 1:50.000. CNR-Prog Strat Crosta Profond Milano

Montrasio L, Valentino R, Losi GL (2009) Rainfall-induced shallow landslides: a model for the triggering mechanism of some case studies in Northern Italy. Landslides 6:241–251. https://doi.org/10.1007/s10346-009-0154-7

Morcioni A, Apuani T, Cecinato F (2022) The Role of Temperature in the Stress–Strain Evolution of Alpine Rock-Slopes: Thermo-Mechanical Modelling of the Cimaganda Rockslide. Rock Mech Rock Eng 55:2149–2172. https://doi.org/10.1007/s00603-022-02786-y

Morcioni A, Apuani T, Cecinato F (2023a) Piuro Landslide: 3D Hydromechanical Numerical Modelling of the 1618 Event. Geosci 13:. https://doi.org/10.3390/geosciences13020049

Morcioni A, Apuani T, Cecinato F, Veveakis M (2023b) Landslide susceptibility evaluation in Alpine environment: 1. 3D Finite Element modeling of the Ruinon (IT) case study. Geomech energy Environ 36:. https://doi.org/https://doi.org/10.1016/j.gete.2023.100493

Morcioni A, Apuani T, Cecinato F, Veveakis M (2023c) Landslide susceptibility evaluation in Alpine environment: 2. Thermo-hydro-mechanical modeling for the response to climate-related variables. Geomech energy Environ 36:. https://doi.org/https://doi.org/10.1016/j.gete.2023.100494

Morgenstern NR, Price VE (1965) The Analysis of the Stability of General Slip Surfaces. Géotechnique 15:79–93. https://doi.org/10.1680/geot.1965.15.1.79

Muller L (1964) The rock slide in the Vaiont valley. Felsmech Ingenoirgeol 2:148–212

Muller L (1968) New considerations on the Vaiont slide. Felsmech Ingenoirgeol 6:1–91

Munjiza A, Andrews K, White J (1999) Combined single and smeared crack model in combined finite-discrete element analysis. Int J Numer Methods Eng 1999;4441–57

Munjiza A, Owen D, Bicanic N (1995) A combined finite-discrete element method in transient dynamics of fracturing solid. Int J Eng Comput 1995;12145–74

Nadim F, Einstein H, Roberts WJ (2005) Probabilistic stability analysis for individual slopes in soil and rock. Proc Int Conf Landslide Risk Manag

Naylor, DJ, Pande G, Simpson B, Tabb R (1981) Finite elements in geotechnical engineering. Pineridge Press

Neaupane K, Yamabe T (2001) A fully coupled thermo-hydro-mechanical nonlinear model for a frozen medium. Comput Geotech - Comput GEOTECH 28:613–637. https://doi.org/10.1016/S0266-352X(01)00015-5

Nigrelli G, Fratianni S, Zampollo A, et al (2018) The altitudinal temperature lapse rates applied to high elevation rockfalls studies in the Western European Alps. Theor Appl Climatol 131:1479–1491. https://doi.org/10.1007/s00704-017-2066-0

Norwegian Geotechnical Institute (2015) Using the Q-system. Nor Geotech Inst 57

Notti D, Wrzesniak A, Dematteis N, et al (2021) A multidisciplinary investigation of deep-seated landslide reactivation triggered by an extreme rainfall event: a case study of the Monesi di Mendatica landslide, Ligurian Alps. Landslides 18:2341–2365. https://doi.org/10.1007/s10346-021-01651-3

Ojeda P, Elmo D, Rogers S, Brzovic A (2023) Discrete Fracture Network (DFN) Analysis to Quantify the Reliability of Borehole-Derived Volumetric Fracture Intensity. Geosci 13:. https://doi.org/10.3390/geosciences13060187

Olhendorf C (1998) High Alpine Lake sediments as chronicles for regional glacier and climate history in the Upper Engadine, southeastern Switzerland.

Palis E, Lebourg T, Tric E, et al (2017) Long-term monitoring of a large deep-seated landslide (La Clapiere, South-East French Alps): initial study. Landslides 14:155–170. https://doi.org/10.1007/s10346-016-0705-7

Palmstrom A (1974) Characterization of jointing density and the quality of rock masses. Intern report, AB Berdal, Norw 26

Pande G, Beer G, Williams J (1990) Numerical methods in rock mechanics

Paranunzio R, Chiarle M, Laio F, et al (2019) New insights in the relation between climate and slope failures at high-elevation sites. Theor Appl Climatol 137:1765–1784. https://doi.org/10.1007/s00704-018-2673-4

Paranunzio R, Laio F, Chiarle M, et al (2016) Climate anomalies associated with the occurrence of rockfalls at high-elevation in the Italian Alps. Nat Hazards Earth Syst Sci 16:2085–2106. https://doi.org/10.5194/nhess-16-2085-2016

Parriaux A, Bonnard C, Tacher L (2010) Glissements de terrain: hydroge´ologie et techniques d'assainissement par drainage. Off Fe´de´ral l'Environnement (OFEV), Bern

Patton FD (1966) Multiple modes of shear failure in rock. Proc, 1st Int Cong Rock Mech, Lisbon 1:509–513

Perini M, Camin F, Corradini F, et al (2009) Use of δ18O in the interpretation of hydrological dynamics in lakes. J Limnol 68:174–182. https://doi.org/10.3274/JL09-68-2-02

Pigazzi E, Bersezio R, Marotta F, Apuani T (2023) Mapping landscape evolution in 3D: Climate change, natural hazard and human settlements across the 1618 Piuro landslide in the Italian Central Alps. Earth Surf Process Landforms. https://doi.org/10.1002/esp.5743

Pigazzi E, Bersezio R, Morcioni A, et al (2022) Geology of the area of the Piuro 1618 event (Val Bregaglia, Italian Central Alps): the setting of a catastrophic historical landslide. J Maps 1–10. https://doi.org/10.1080/17445647.2022.2057878

Pinarelli L, Nisi B, Vaselli O, et al (2014) Major, trace element, and Sr isotope geochemistry of surface and ground waters in the Chiavenna Valley (Sondrio, Northern Italy). Rend Online Soc Geol Ital 30:62–65. https://doi.org/10.3301/ROL.2014.13

Pinyol NM, Alonso EE (2010) Criteria for rapid sliding II. Thermo-hydro-mechanical and scale effects in Vaiont case. Eng Geol 114:211–227. https://doi.org/10.1016/j.enggeo.2010.04.017

Piper A. (1944) A graphic procedure in the geochemical interpretation of water analyses. Trans Am Geophys Union 25:914–923

Pistocchi A (2016) Simple estimation of snow density in an Alpine region. J Hydrol Reg Stud 6:82–89. https://doi.org/10.1016/j.ejrh.2016.03.004

Pollard D, Aydin A (1988) Progress in understanding jointing over the past century. Geol Soc Am Bull, 100, 1181–1204

Prager C, Zangerl C, Patzelt G, Brandner R (2008) Age distribution of fossil landslides in the Tyrol (Austria) and its surrounding areas. Nat Hazards Earth Syst Sci 8:377–407. https://doi.org/10.5194/nhess-8-377-2008

Preisig G, Cornaton F, Perrochet P (2012) Regional flow simulation in fractured aquifers using stress-dependent parameters. Groundwater 50

Preisig G, Eberhardt E, Smithyman M, et al (2016) Hydromechanical rock mass fatigue in deep-seated landslides accompanying seasonal variations in pore pressures. Rock Mech Rock Eng 49:2333–2351. https://doi.org/10.1007/s00603-016-0912-5

Priest SD, Brown ET (1983) Probabilistic stability analysis of variable rock slopes. Trans Inst Min Met (Sect A) 92 1-12

Pu S, Yu T, Ye L, et al (2022) Study on Instability Mechanism and Support Scheme of the Tunnel Face in Carbonaceous Phyllite Stratum under High Geo-Stress. Adv Civ Eng 2022:3870227. https://doi.org/10.1155/2022/3870227

Puglisi S, Zanframundo P (1978) Osservazioni idrologiche in piccoli bacini del subappennino dauno. G del Genio Civ 10-11–12:439–453

Racek O, Balek J, Loche M, et al (2023) Rock Surface Strain In Situ Monitoring Affected by Temperature Changes at the Požáry Field Lab (Czechia). Sensors 23:. https://doi.org/10.3390/s23042237

Racek O, Blahut J, Hartvich F (2021a) Observation of the rock slope thermal regime, coupled with crackmeter stability monitoring: Initial results from three different sites in Czechia (central Europe). Geosci Instrumentation, Methods Data Syst 10:203–218. https://doi.org/10.5194/gi-10-203-2021

Racek O, Blahůt J, Hartvich F (2021b) Monitoring of Thermoelastic Wave Within a Rock Mass Coupling Information from IR Camera and Crack Meters: A 24-Hour Experiment on "Branická Skála" Rock in Prague, Czechia. 41–48. https://doi.org/10.1007/978-3-030-60311-3_3

Ravanel L, Deline P (2010) Climate influence on rockfalls in high-Alpine steep rockwalls: The north side of the Aiguilles de Chamonix (Mont Blanc massif) since the end of the 'Little Ice Age.' The Holocene 21:357–365. https://doi.org/10.1177/0959683610374887

Rawat S, Gupta AK (2016) Analysis of a Nailed Soil Slope Using Limit Equilibrium and Finite Element Methods. Int J Geosynth Gr Eng 2:1–23. https://doi.org/10.1007/s40891-016-0076-0

Regione Lombardia (2022) Frana del Ruinon in comune di Valfurva (SO) - Variante in galleria alla SS 300 del Gavia. Tech Rep

Regione Lombardia (2015) DTM 5X5 - Modello digitale del terreno

Reichenbach P, Rossi M, Malamud BD, et al (2018) A review of statistically-based landslide susceptibility models. Earth-Science Rev 180:60–91. https://doi.org/https://doi.org/10.1016/j.earscirev.2018.03.001

Riva F (2017) Damage-Based Long-Term Modelling of Paraglacial To Postglacial Evolution of Alpine Rock Slopes. 267

Riva F, Agliardi F, Amitrano D, Crosta G (2017) Journal of Geophysical Research : Earth Surface to Postglacial Progressive Failure of Large Rock Slopes. J Geophys Res Earth Surf

Robertson EC (1988) Thermal Properties of Rocks. US Dep Inter Geol Surv 88–441

RocScience (2017) RS2 (Phase2 v 9.0)

Romana M, Tomás R, Serón JB (2015) Slope Mass Rating (SMR) geomechanics classification: Thirty years review. 13th ISRM Int Congr Rock Mech 2015-MAY:1–10

Rounce DR, McKinney DC, Lala JM, et al (2016) A new remote hazard and risk assessment framework for glacial lakes in the Nepal Himalaya. Hydrol Earth Syst Sci 20:3455–3475. https://doi.org/10.5194/hess-20-3455-2016

Rouyet L, Kristensen L, Derron M-H, et al (2017) Evidence of rock slope breathing using ground-based InSAR. Geomorphology 289:152–169

Rwechungula JC, Cheng Y (2021) Numerical analysis to estimate near-wellbore drilling induced failures area for fractured formation using Universal Discrete Element Codes (UDEC). Cogent Eng 8:1911591. https://doi.org/10.1080/23311916.2021.1911591

Saito M (1965) Forecasting the time of occurrence of a slope failure. Proc 6 th Int Conf Soil Mech Found Eng 537–541

Saito M (1969) Forecasting time of slope failure by tertiary creep. In: Proceedings of the 7th International Conference on Soil Mechanics and Foundation Engineering, Mexico City, Mexico. pp 677–683

Scaioni M, Marsella M, Crosetto M, et al (2018) Geodetic and Remote-Sensing Sensors for Dam Deformation Monitoring. Sensors 18

Scapozza C, Castelletti C, Soma L, et al (2014) Timing of LGM and deglaciation in the Southern Swiss Alps. Geomorphol Reli Process Environ 20:307–322. https://doi.org/10.4000/geomorphologie.10753

Scapozza C, Tognacca C, Ambrosi C, Seno S (2015) 20 maggio 1515: La "Buzza" che impressionò l'Europa. Boll Soc Ticin Sci Nat 103:78–88

Scaramellini G., Kahl G., Falappi GP (1995) La Frana di Piuro del 1618: Storia e Immagini di una Rovina, 2nd edizione. Assoc italo-svizzera per gli scavi di Piuro

Scaramellini G, Kahl G, Falappi GP (1988) La Frana di Piuro del 1618: Storia e Immagini di una Rovina. Assoc italo-svizzera per gli scavi di Piuro

Scavia C, Barbero M, Castelli M, et al (2020) Evaluating Rockfall Risk : Some Critical Aspects. 1–29. https://doi.org/10.3390/geosciences10030098

Schneider M, Oestreicher N, Ehrat T, Loew S (2023) Rockfall monitoring with a Doppler radar on an active rockslide complex in Brienz/Brinzauls (Switzerland). Nat Hazards Earth Syst Sci 23:3337–3354. https://doi.org/10.5194/nhess-23-3337-2023

Schoeller H (1962) Les eaux souterraines (The Underground Networks). Mason Cie 642

Schön JH (2015) Chapter 7 - Geomechanical Properties. In: Schön JHBT-D in PS (ed) Physical Properties of Rocks. Elsevier, pp 269–300

Seequent (2022) Heat and mass transfer modeling with GeoStudio. 73

Seguí C (2020) Analysis of the Stability and Response of Deep-Seated Landslides by Monitoring their Basal Temperature

Seguí C, Rattez H, Veveakis M (2020) On the Stability of Deep-Seated Landslides. The Cases of Vaiont (Italy) and Shuping (Three Gorges Dam, China). J Geophys Res Earth Surf 125:1–24. https://doi.org/10.1029/2019JF005203

Seguí C, Veveakis M (2021) Continuous assessment of landslides by measuring their basal temperature. Landslides 18:3953–3961. https://doi.org/10.1007/s10346-021-01762-x

Seguinot J, Ivy-Ochs S, Jouvet G, et al (2018) Modelling last glacial cycle ice dynamics in the Alps. Cryosphere 12:3265–3285. https://doi.org/10.5194/tc-12-3265-2018

Seibert J, Jenicek M, Huss M, Ewen T (2015) Snow and Ice in the Hydrosphere

Selby M (1982) Controls on the stability and inclinations of hillslopes formed on hard rock. Earth Surf Process Landforms 449–467

Senaldi M (2017) Indagine strutturale applicata all'area di frana del Ruinon, Valfurva (SO). Elabor di tesi Magistrale "Geologia Process risorse ed Appl Univ degli Stud di Milano"

Shao W, Bogaard T, Su Y, Bakker M (2016) Coupling a 1D Dual-permeability Model with an Infinite Slope Stability Approach to Quantify the Influence of Preferential Flow on Slope Stability. Procedia Earth Planet Sci 16:128–136. https://doi.org/10.1016/j.proeps.2016.10.014

Shi G, Goodman R (1985) Two dimensional discontinuous deformation analysis. Int J Numer Anal Methods Geomech 541–56

Siegenthaler U, Oeschger H (1980) Correlation of 18O in precipitation with temperature and altitude. Nature 285:314–317. https://doi.org/10.1038/285314a0

Simeoni L, Ronchetti F, Costa C, et al (2020) Redundancy and coherence of multi-method displacement monitoring data as key issues for the analysis of extremely slow landslides (Isarco valley, Eastern Alps, Italy). Eng Geol 267:105504. https://doi.org/https://doi.org/10.1016/j.enggeo.2020.105504

Singh P (2001) Snow and glacier hydrology. Springer Science & Business Media

Siva Subramanian S, Fan X, Yunus AP, et al (2020) A Sequentially Coupled Catchment-Scale Numerical Model for Snowmelt-Induced Soil Slope Instabilities. J Geophys Res Earth Surf 125:e2019JF005468. https://doi.org/https://doi.org/10.1029/2019JF005468

Sobrino JA, Frate F Del, Drusch M, et al (2016) Review of Thermal Infrared Applications and Requirements for Future High-Resolution Sensors. IEEE Trans Geosci Remote Sens 54:2963–2972. https://doi.org/10.1109/TGRS.2015.2509179

Sornette D, Helmstetter A, Andersen J V., et al (2004) Towards landslide predictions: Two case studies. Phys A Stat Mech its Appl 338:605–632. https://doi.org/10.1016/j.physa.2004.02.065

Sosio R, Crosta GB, Hungr O (2008) Complete dynamic modeling calibration for the Thurwieser rock avalanche (Italian Central Alps). Eng Geol 100:11–26. https://doi.org/https://doi.org/10.1016/j.enggeo.2008.02.012

Southwell R (1956) Relaxation methods in theoretical physics—a continuation of the treatise: relaxation methods in engineering science. Oxford Univ Press

Spencer E (1967) A Method of analysis of the Stability of Embankments Assuming Parallel Inter-Slice Forces. Géotechnique 17:11–26. https://doi.org/10.1680/geot.1967.17.1.11

Stocker T (2014) Climate change 2013: the physical science basis: Working Group I contribution to the Fifth assessment report of the Intergovernmental Panel on Climate Change. Cambridge university press

Stoffel M, Ballesteros Cánovas JA, Luckman BH, et al (2019) Tree-ring correlations suggest links between moderate earthquakes and distant rockfalls in the Patagonian Cordillera. Sci Rep 9:12112. https://doi.org/10.1038/s41598-019-48530-5

Stoffel M, Beniston M (2006) On the incidence of debris flows from the early Little Ice Age to a future greenhouse climate: A case study from the Swiss Alps. Geophys Res Lett 33:. https://doi.org/https://doi.org/10.1029/2006GL026805

Stoffel M, Huggel C (2012) Effects of climate change on mass movements in mountain environments. Prog Phys Geogr 36:421–439. https://doi.org/10.1177/0309133312441010

Stoffel M, Tiranti D, Huggel C (2014) Science of the Total Environment Climate change impacts on mass movements — Case studies from the European Alps. Sci Total Environ 493:1255–1266. https://doi.org/10.1016/j.scitotenv.2014.02.102

Strouth A, Eberhardt E (2009) Integrated back and forward analysis of rock slope stability and rockslide runout at Afternoon Creek, Washington. Can Geotech J 46:1116–1132. https://doi.org/10.1139/T09-048

Strozzi T, Farina P, Corsini A, et al (2005) Survey and monitoring of landslide displacements by means of L-band satellite SAR interferometry. Landslides 2:193–201. https://doi.org/10.1007/s10346-005-0003-2

Stumvoll MJ, Canli E, Engels A, et al (2020) The “Salcher” landslide observatory—experimental long-term monitoring in the Flysch Zone of Lower Austria. Bull Eng Geol Environ 79:1831–1848. https://doi.org/10.1007/s10064-019-01632-w

Sturzenegger M, Keegan T, Wen A, et al (2015) LiDAR and Discrete Fracture Network Modeling for Rockslide Characterization and Analysis. Eng Geol Soc Territ 223–227

Swisstopo (1992) Geothermische Karte der Schweiz 1:500.000

Tandon RS, Gupta V, Venkateshwarlu B, Joshi P (2022) An assessment of Dungale landslide using remotely piloted aircraft system (RPAS), ground penetration radar (GPR), and Slide & RS2 Softwares. Nat Hazards 113:1017–1042. https://doi.org/10.1007/s11069-022-05334-7

Tantardini D, Riganti N, Taglieri P, et al (2013) Glacier dynamics in San Giacomo valley (central Alps, Sondrio, Italy). Alp Mediterr Quat 26:77–94

Tantardini D, Stevenazzi S, Apuani T (2022) The Last Glaciation in Valchiavenna (Italian Alps): maximum ice elevation data and recessional glacial deposits and landforms. Ital J Geosci 141:259–277. https://doi.org/10.3301/IJG.2022.13

Tarchi D, Casagli N, Fanti R, Tarchi M (2003) Landslide monitoring by using ground-based SAR interferometry an example of application to the Tessina landslide. 68:15–30

Terzaghi K (1962) Stability of steep slopes on hard unweathered rock. Geotechnique 12(4), 251

Teza G, Marcato G, Castelli E, Galgaro A (2012) IRTROCK: A MATLAB toolbox for contactless recognition of surface and shallow weakness of a rock cliff by infrared thermography. Comput Geosci 45:109–118. https://doi.org/https://doi.org/10.1016/j.cageo.2011.10.022

Thiebes B, Bell R, Glade T, et al (2013) A WebGIS decision-support system for slope stability based on limit-equilibrium modelling. Eng Geol 158:109–118. https://doi.org/10.1016/j.enggeo.2013.03.004

Thiebes B, Bell R, Glade T, et al (2014) Integration of a limit-equilibrium model into a landslide early warning system. Landslides 11:859–875. https://doi.org/10.1007/s10346-013-0416-2

Tibaldi A, Pasquarè F (2009) Quaternary deformations along the 'Engadine–Gruf tectonic system', Swiss–Italian Alps. J Quat Sci 22:311–320. https://doi.org/10.1002/jqs

Tresca HE (1864) Sur l'ecoulement des corps solides soumis a de fortes pressions. Imprimerie de Gauthier-Villars, successeur de Mallet-Bachelier, rue de Seine

Tropeano D, Turconi L (2004) Using historical documents for landslide, debris flow and stream flood prevention. Nat Hazard 31:663–79

Tschuchnigg F, Schweiger HF, Sloan SW, et al (2015) Comparison of finite-element limit analysis and strength reduction techniques. Géotechnique 65:249–257. https://doi.org/10.1680/geot.14.P.022

Ureel S, Momayez M (2014) An Investigation of the Limit Equilibrium Method and Numerical Modeling for Rock Slope Stability Analysis. In: Rock Mechanics and Its Applications in Civil, Mining, and Petroleum Engineering. pp 218–227

Uzielli M, Nadim F, Lacasse S, Kaynia AM (2008) A conceptual framework for quantitative estimation of physical vulnerability to landslides. Eng Geol 102:251–256. https://doi.org/https://doi.org/10.1016/j.enggeo.2008.03.011

Valagussa A, Frattini P, Crosta GB (2014) Earthquake-induced rockfall hazard zoning. Eng Geol 182:213–225. https://doi.org/https://doi.org/10.1016/j.enggeo.2014.07.009

Valentino R (2023) FEM Modelling of Thin Weak Layers in Slope Stability Analysis. Geosciences 13

Vardoulakis I (2002a) Steady shear and thermal run-away in clayey gouges. Int J Solids Struct 39:3831–3844. https://doi.org/10.1016/S0020-7683(02)00179-8

Vardoulakis I (2002b) Dynamic thermo-poro-mechanical analysis of catastrophic landslides. Géotechnique 52:157–171. https://doi.org/10.1680/geot.2002.52.3.157

Varnes DJ (1978) Slope movement types and processes. Landslide Anal Control Transp Res Board, Spec Rep 176 11–33

Ventura G (1905) Bonificazione della Bassa pianura bolognese. G del Genio Civ 43

Veveakis E, Vardoulakis I, Di Toro G (2007) Thermoporomechanics of creeping landslides: The 1963 Vaiont slide, northern Italy. J Geophys Res Earth Surf 112:1–21. https://doi.org/10.1029/2006JF000702

Vinther BM, Buchardt SL, Clausen HB, et al (2009) Holocene thinning of the Greenland ice sheet. Nature 461:385–388. https://doi.org/10.1038/nature08355

Voight B (1988) A method for prediction of volcanic eruptions. Nature 332:125–130. https://doi.org/10.1038/332125a0

Volkwein A, Schellenberg K, Labiouse V, et al (2011) Rockfall characterisation and structural protection – a review. Nat Hazards Earth Syst Sci 11:2617–2651. https://doi.org/10.5194/nhess-11-2617-2011

Walter F, Amann F, Kos A, et al (2020) Direct observations of a three million cubic meter rock-slope collapse with almost immediate initiation of ensuing debris flows. Geomorphology 351:106933. https://doi.org/10.1016/j.geomorph.2019.106933

Wang H, Lin H (2018) Non-linear Shear Strength Criterion for a Rock Joint with Consideration of Friction Variation. Geotech Geol Eng 36:3731–3741. https://doi.org/10.1007/s10706-018-0567-y

Wang J, Wang X, Zhang Y, et al (2023) Simulation of Freeze–Thaw and Melting of Buried Ice in Longbasaba Moraine Dam in the Central Himalayas Between 1959 and 2100 Using COMSOL Multiphysics. J Geophys Res Earth Surf 128:e2022JF006848. https://doi.org/https://doi.org/10.1029/2022JF006848

Wang M-Y, Liu Y, Ding Y-N, Yi B-L (2020) Probabilistic stability analyses of multi-stage soil slopes by bivariate random fields and finite element methods. Comput Geotech 122:103529. https://doi.org/https://doi.org/10.1016/j.compgeo.2020.103529

Wang S, Ni P (2014) Application of block theory modeling on spatial block topological identification to rock slope stability analysis. Int J Comput Methods 11:. https://doi.org/10.1142/S0219876213500448

Wang Y, Li M (2021) Research on the Deformation Law of Jointed Surrounding Rock during Tunnel Excavation Based on Hydromechanical Coupling. Geofluids 2021:5583940. https://doi.org/10.1155/2021/5583940

Ward RD, Hann J (1911) Handbuch der Klimatologie. Bull Am Geogr Soc 43:935. https://doi.org/10.2307/200498

Wasowski J, Keefer DK, Lee C-T (2011) Toward the next generation of research on earthquake-induced landslides: Current issues and future challenges. Eng Geol 122:1–8. https://doi.org/https://doi.org/10.1016/j.enggeo.2011.06.001

Wei WB, Cheng YM, Li L (2009) Three-dimensional slope failure analysis by the strength reduction and limit equilibrium methods. Comput Geotech 36:70–80. https://doi.org/10.1016/j.compgeo.2008.03.003

Wels C, Mackie D, Scibek J (2012) J. Guidelines for Groundwater Modelling to Asses Impacts of Proposed Natural Resource Development Activities; Technical report; Report n◦194001. Br Columbia Minstry Environ Prot Sustain Branch

Wenk HR (1984) Brittle-ductile Transition Zone in the Northern Bergell Alps. Geol Rundschau 73:419–431. https://doi.org/10.1007/BF01820378

Wiebols GA, Cook NGW (1968) An energy criterion for the strength of rock in polyaxial compression. In: International Journal of Rock Mechanics and Mining Sciences & Geomechanics Abstracts. Elsevier, pp 529–549

Wilby RL, Charles SP, Zorita E, et al (2004) Guidelines for use of climate scenarios developed from statistical downscaling methods. Support Mater Intergov Panel Clim Chang available from DDC

IPCC TGCIA 27

Wirsig C, Zasadni J, Christl M, et al (2016) Dating the onset of LGM ice surface lowering in the High Alps. Quat Sci Rev 143:37–50. https://doi.org/https://doi.org/10.1016/j.quascirev.2016.05.001

Wittke W (1990) Rock mechanics—theory and applications. Springer

Wolter A, Havaej M, Zorzi L, et al (2013) Exploration of the kinematics of the 1963 vajont slide, Italy, using a numerical modelling toolbox. Ital J Eng Geol Environ 2013:599–612. https://doi.org/10.4408/IJEGE.2013-06.B-58

Wong DLY, Doster F, Geiger S, et al (2020) Fluid flow characterization framework for naturally fractured reservoirs using small-scale fully explicit models. Transp Porous Media 134:399–434

Wu D, Deng T, Duan W, Zhang W (2019) A coupled thermal-hydraulic-mechanical application for assessment of slope stability. Soils Found 59:2220–2237. https://doi.org/10.1016/j.sandf.2019.12.007

Wu JH, Hsieh PH (2021) Simulating the postfailure behavior of the seismically- triggered Chiu-fen-erh-shan landslide using 3DEC. Eng Geol 287:106113. https://doi.org/10.1016/j.enggeo.2021.106113

Wu L, Hou Z, Luo Z, et al (2023) Numerical simulations of supercritical carbon dioxide fracturing: A review. J Rock Mech Geotech Eng 15:1895–1910. https://doi.org/https://doi.org/10.1016/j.jrmge.2022.08.008

Xu Q, Fan X, Huang R, et al (2003) Advanced numerical techniques in rock slope stability analysis – applications and limitations. Nat Hazards Earth Syst Sci 3:423–433

Yin T, Chen Q (2020) Simulation-based investigation on the accuracy of discrete fracture network (DFN) representation. Comput Geotech 121:103487. https://doi.org/10.1016/j.compgeo.2020.103487

Zabuski L (2019) Three-Dimensional Analysis of a Landslide Process on a Slope in Carpathian Flysch. Arch Hydro-Engineering Environ Mech 66:27–45. https://doi.org/doi:10.1515/heem-2019-0003

Zerathe S, Lebourg T, Braucher R, Bourlès D (2014) Mid-Holocene cluster of large-scale landslides revealed in the Southwestern Alps by 36Cl dating. Insight on an Alpine-scale landslide activity. Quat Sci Rev 90:106–127. https://doi.org/https://doi.org/10.1016/j.quascirev.2014.02.015

Zhang X, Sanderson DJ, Harkness RM, Last NC (1996) Evaluation of the 2-D permeability tensor for fractured rock masses. Int J Rock Mech Min Sci Geomech 33:17–37. https://doi.org/10.1016/0148-9062(95)00042-9

Zhen CUI, Ping-Zhi C, Qian S (2020) Estimation of REV for Danba schist based on 3D synthetic rock mass technique. IOP Conf Ser Earth Environ Sci 570:. https://doi.org/10.1088/1755-1315/570/3/032001

Zhou C, Ng CWW (2015) A thermomechanical model for saturated soil at small and large strains. Can Geotech J 52:1101–1110. https://doi.org/10.1139/cgj-2014-0229

Zienkiewizc, Emson, Bettess (1983) A novel boundary infinite element. Int J Num Meth Eng 1983;19393–404